

Copyright  
by  
Bénédicte Stewart  
2010

**The dissertation committee for Bénédicte Stewart certifies that this is the approved version of the following dissertation (or treatise):**

**Numerical Simulations of the Flow Produced by a Comet Impact on the Moon and its Effects on Ice Deposition in Cold Traps**

**Committee:**

---

David B. Goldstein, Supervisor

---

Philip L. Varghese

---

Venkatramanan Raman

---

Laurence M. Trafton

---

Dana M. Hurley



**Numerical Simulations of the Flow Produced by a Comet Impact on the  
Moon and its Effects on Ice Deposition in Cold Traps**

**by**  
**Bénédicte Stewart, M.S.**

**Dissertation**

Presented to the Faculty of the Graduate School of  
The University of Texas at Austin  
in Partial Fulfillment  
of the Requirements  
for the Degree of

**Doctor of Philosophy**

**The University of Texas at Austin**  
**May 2010**

To Shaun

## **Acknowledgements**

I would like to thank my advisor, Dr. David Goldstein for his guidance, support and encouragement throughout the span of our research. I would also like to thank Dr. Elizabetta Pierazzo for her collaboration on this project. I also extend thanks to Dr. Philip Varghese and Dr. Laurence Trafton for the fruitful discussion and important suggestions during our regular group meetings.

I wish to acknowledge the previous work by my past colleague, Ju Zhang, without which our research would not have gone as far as it did. His efforts and help deserve my special thanks. I also wish to express my thanks to my other past and present colleagues: Chris Moore, Andrew Walker, James Strand, Kelly Stefani, Aaron Morris, Conrad Lee, Ju Zhang, Gerardo Colmenero, Kenji Miki and Kevin Marr. Notable thanks go to Chris Moore for the fruitful discussions.

Eternal thanks to my parents and my husband for their support and love.

I would also like to thank the Texas Advanced Computing Center for their computational resources. Funding for the work has been provided by NASA Planetary Atmospheres program, Grant No. NASA NAG5-11991.

# **Numerical Simulations of the Flow Produced by a Comet Impact on the Moon and its Effects on Ice Deposition in Cold Traps**

Publication No. \_\_\_\_\_

Bénédicte Stewart, Ph.D.  
The University of Texas at Austin, 2010

Supervisor: David B. Goldstein

The primary purpose of this study is to model the water vapor flow produced by a comet impact on the Moon using the Direct Simulation Monte Carlo (DSMC) method. Toward that end, our DSMC solver was modified in order to model the cometary water from the time of impact until it is either destroyed due to escape or photodestruction processes or captured inside one of the lunar polar cold traps.

In order to model the complex flow induced by a comet impact, a 3D spherical parallel version of the DSMC method was implemented. The DSMC solver was also modified to take as input the solution from the SOVA hydrocode for the impact event at a fixed interface. An unsteady multi-domain approach and a collision limiting scheme were also added to the previous implementation in order to follow the water from the continuum regions near the point of impact to the much later rarefied atmospheric flow around the Moon.

The present implementation was tested on a simple unsteady hemispherical expansion flow into a vacuum. For these simulations, the data at the interface were provided by a 1D analytical model instead of the SOVA solution. Good results were obtained downstream of the interface for density, temperature and radial velocity. Freezing of the vibrational modes was also observed in the transitional regime as the flow became collisionless.

The  $45^\circ$  oblique impact of a 1 km radius ice sphere at 30 km/s was simulated up to several months after impact. Most of the water crosses the interface under 5 s moving mostly directly downstream of the interface. Most of the water escapes the gravity well of the Moon within the first few hours after impact. For such a comet impact, only  $\sim 3\%$  of the comet mass remains on the Moon after impact. As the Moon rotates, the molecules begin to migrate until they are destroyed or captured in a cold trap. Of the 3% of the water remaining on the Moon after impact, only a small fraction,  $\sim 0.14\%$  of the comet mass, actually reaches the cold traps; nearly all of the rest is photo-destroyed. Based on the surface area of the cold traps used in the present simulations,  $\sim 1$  mm of ice would have accumulated in the polar cold traps after such an impact. Estimates for the total mass of water accumulated in the polar cold traps over one billion years are consistent with recent observations.

## Table of Content

List of Tables.....	xiii
List of Figures .....	xiv
Nomenclature .....	xxx
<b>CHAPTER 1.....</b>	<b>1</b>
Introduction .....	1
1.1 Motivation.....	1
1.2 Objectives .....	4
1.3 Dissertation Overview .....	5
<b>CHAPTER 2.....</b>	<b>6</b>
Literature Review .....	6
2.1 Water on the Moon .....	6
2.1.1 Observations.....	6
2.1.2 Modeling .....	14
2.2 Impact Simulations .....	22
2.2.1 Physics of the Impact Event.....	23
2.2.2 Impact Event Simulations .....	27
2.3 The DSMC Method .....	33
2.3.1 Planetary Atmosphere Applications.....	34
2.3.2 Parallel Implementation .....	35
2.3.3 Hybrid Implementations .....	38

2.3.4 Expansion Flows into a Vacuum.....	43
<b>CHAPTER 3.....</b>	<b>46</b>
Numerical Approach .....	46
3.1 Overview of The Present Numerical Approach.....	47
3.1.1 The General DSMC Procedure .....	47
3.1.2 Flow Conditions.....	51
3.2 Parallel Implementation.....	54
3.2.1 Overview.....	54
3.2.2 Performance Study.....	56
3.3 Unsteady Interface .....	68
3.3.1 SOVA Output.....	68
3.3.2 DSMC Input.....	72
3.4 Special Features: The Move Subroutine .....	76
3.4.1 Predictor-Corrector .....	76
3.4.2 Surface Temperature, Cold Traps and Residence Time.....	79
3.4.3 Photodestruction Processes .....	84
3.5 Special Features: The Collide Subroutine.....	86
3.5.1 Collision Limiter .....	86
3.5.2 Free Cells .....	94
3.6 Other Features: Unsteady Multi-Domain Calculations.....	94
<b>CHAPTER 4.....</b>	<b>98</b>
Simulations of 1D Unsteady Expansion Flow into a Vacuum .....	98
4.1 Objectives .....	98

4.2	Analytic Solution .....	99
4.3	DSMC Simulations .....	100
4.3.1	Region near the interface .....	109
4.3.2	Equilibrium region .....	113
4.3.3	Vibrational non-equilibrium region .....	116
<b>CHAPTER 5.....</b>		<b>122</b>
Late stages of a Comet Impact Simulations .....		122
5.1	Overview.....	122
5.2	Simulation Parameters .....	122
5.3	Comparison between the DSMC and SOVA Solutions Downstream of the Interface .....	126
5.3.1	Plume Contours in the Plane of Symmetry of the Impact: Vertical Impact....	126
5.3.2	Plume Contours in the Plane of Symmetry of the Impact: Oblique Impact....	128
5.3.3	Plume Macroscopic Data at a Secondary Interface: Oblique Impact.....	130
5.4	Time Evolution of the Expansion Plume for a 45° Oblique Impact .....	138
5.4.1	Interface Data .....	139
5.4.2	Near Field Data .....	156
5.4.3	Far Field Data .....	232
<b>CHAPTER 6.....</b>		<b>243</b>
Circum-Lunar Flow Results .....		243
6.1	Overview.....	243
6.2	Simulation Parameters .....	244
6.3	Migration of the Water Vapor Plume to the Polar Cold Traps .....	245



6.3.1 Total Mass Retained.....	246
6.3.2 Initial Fallback Pattern .....	248
6.3.3 Time Evolution of the Ice Deposits in the Polar Cold Traps .....	250
6.3.4 Deposition Pattern in the Polar Cold Traps.....	253
6.4 Migration of the Impact Crater Water to the Polar Cold Traps .....	254
6.4.1 Low Density Transient Atmospheric Flow .....	256
6.4.2 Time Evolution of the Ice Deposits in the Polar Cold Traps .....	264
<b>CHAPTER 7.....</b>	<b>270</b>
Conclusions .....	270
7.1 Summary .....	270
7.2 Future Work.....	274
Appendices .....	275
Appendix A .....	276
Parallel Computing.....	276
A.1 Parallel Computing .....	276
A.2 The Message Passing Interface (MPI) Method.....	278
A.3 Implementation .....	279
Appendix B.....	283
Preprocessing of the SOVA Data .....	283
B.1 Overview.....	283
B.2 Parallel Simulations .....	287

Appendix C.....	288
Spherical Coordinates Calculations needed for the Move Step.....	288
C.1 Predictor-Corrector Scheme.....	288
C.2 Surface Temperature Map.....	291
C.2 Location of the Cold Traps .....	294
C.3 Shadow Calculations.....	296
Appendix D .....	298
SOVA Solution in the Plane of Symmetry for the 45° Impact.....	298
Appendix E.....	302
Number of Molecules per Cell for the 45° Impact .....	302
References .....	310
Vita .....	321

## **List of Tables**

Table 2-1	List of reviewed observations looking for water on the Moon.....	7
Table 2-2	Modeling the possible accumulation of water in lunar cold traps.....	14
Table 3-1	Summary of the conditions used in Cases A to E.....	59
Table 3-2	Cold traps location and surface area.....	82
Table 4-1	Summary of the initial conditions used for Cases 1, 2 and 3.....	103
Table 6-1	Summary of the initial conditions used for Cases 1 to 4. Note that the subsolar point is assumed to be at longitude $0^\circ$ .....	256

## List of Figures

Figure 2-1	Impact site of fragment G of Comet Shoemaker-Levy 9 on Jupiter (Courtesy Hubble Space Telescope Jupiter Imaging Team and NASA).....	22
Figure 2-2	a) Early stages of an axisymmetric impact event. Vaporized impactor material start to expand away from the point of impact. The remaining part of the impactor lines the growing crater. The impact induced shock wave continues to propagate inside the target. b) Late stages of the impact event when the expansion plume can be approximated as a growing hemisphere of hot gas. (From Melosh, 1989).....	24
Figure 2-3	Geometry of the excavation flowfield. The shocked target material moves away from the point of impact. Below the original surface, the crater continues to expand while the target material ejected above it forms the ejecta curtain. The ejected target material forms an inverted cone that surrounds the vaporized materials. (From Melosh, 1989) .....	25
Figure 2-4	Definition of the angle of impact $\alpha$ . A vertical impact is defined by $\alpha = 90^\circ$ and a grazing impact is defined by $\alpha < \alpha_0$ where $\alpha_0$ is between 5 and $10^\circ$ .....	26
Figure 2-5	Peak shock pressure contours in the plane of symmetry of the Chixculub impact event for impact angles, $\alpha$ , of: $90^\circ$ , $60^\circ$ , $45^\circ$ , $30^\circ$ , and $15^\circ$ . An impactor 10 km in diameter is drawn for scale with the direction of impact being given by the vectors from the center of the projectile. The shock pressures chosen cover the range of shock melting for most of the materials of geologic interest. At 18 GPa, 50% of water initially at ambient temperatures vaporizes. Rocks typically melt for shock pressures between 30 to 150 GPa. At 250 GPa, most geologic materials will have vaporized and iron melts. (From Pierazzo and Melosh, 2000a) .....	31
Figure 3-1	Schematic of the DSMC algorithm. ....	50
Figure 3-2	Spherical coordinate system used for the DSMC simulations with temperature contours at the surface of the Moon. Note that for this figure, the axis of	

	rotation of the Moon is not aligned with the axis of symmetry of the spherical grid and that the white lines are latitude and longitude lines.....	52
Figure 3-3	Physical domain used in the DSMC simulations. Only three of the six boundaries of a single processor domain are presented (top, left and front boundaries) as the remaining three (bottom, right and back boundaries) are the respective opposite walls. ....	53
Figure 3-4	Speed-up versus number of processors for the simulations of an unsteady spherically symmetric expansion flow into a vacuum. ....	60
Figure 3-5	Parallel efficiency versus number of processors for the simulations of an unsteady spherically symmetric expansion flow into a vacuum. ....	61
Figure 3-6	Speed-up versus number of processors for the simulations of a 45° oblique impact of a comet on the Moon. ....	64
Figure 3-7	Parallel efficiency versus number of processors for the simulations of a 45° oblique impact of a comet on the Moon. ....	65
Figure 3-8	Average numbers of molecules per processor as a function of number of processors for Cases D and E. The error bars represent the smallest and largest number of molecules found on any processor at the end of the calculation. ....	67
Figure 3-9	Density contours in the impact plane of symmetry 2.5 s after a 2 km diameter comet impacted the surface of the Moon at 30 km/s for a vertical impact (left) and an oblique impact (right). The water density contours are represented in grey and the rock density contours are represented in green. The darker colors represent the denser areas of the flow. The red (left) and black (right) arcs represent the interface between the SOVA and DSMC codes. ....	69
Figure 3-10	Schematic of the impact event simulations by the SOVA hydrocode. The interface in which data are saved in the SOVA hydrocode is shown on the right. The interface is several Cartesian cells thick forming a shell with a radial thickness of at least 150 m everywhere. ....	70
Figure 3-11	Schematic of the impact event simulations by the SOVA hydrocode. The interface at which data are input into the DSMC code is shown in blue on the right. ....	73
Figure 3-12	Schematic of the DSMC molecule creation in the SOVA interface cells. ....	74

Figure 3-13	Schematic of the DSMC algorithm used for the comet impact simulations. Note that the steps related to the unsteady input condition at the interface with the SOVA hydrocode are shown in red. ....	75
Figure 3-14	Equatorial orbit with (left) and without (right) a predictor-corrector scheme used for the movement of the molecule with three different timesteps of 0.1, 10, and 100 s. Azimuthal angle color contours at the surface of the Moon with the location of the North Pole added for reference are plotted with the associated legend. The time at which the molecule is located at a given location is given by the color of the dots (the associated greyscale legend is presented below the figure). Note that for each cases, the total time the molecule has been orbiting is different (10000 s for $\Delta t = 0.1$ s vs. 100000 s for $\Delta t = 10$ s and 100 s). Also, for clarity, note that only some of the dots have been plotted. Finally, note that the size of the domain in the bottom two figures (for $\Delta t = 100$ s) is different from the previous four figures. ....	77
Figure 3-15	Ballistic trajectories for a molecule evaporating from the Moon's surface initially at a location where the surface temperature was 120 K (left) and 400 K (right) for four different timesteps of 0.1, 1, 10, and 100 s. The horizontal axis represents the distance along the surface of the sphere. Note that the axes are different for both figures. ....	78
Figure 3-16	Cold Trap locations at the poles of the Moon used in our simulations. ....	83
Figure 3-17	Equatorial orbits with shadow calculations for a timestep size of 10s. If the molecule is in the shadow of the Moon, it is represented by a blue dot if it is in the sun it is represented by a red dot. ....	85
Figure 3-18	Flowchart of the collision subroutine when the collision limiter is turned on. ....	91
Figure 3-19	Flowchart for a regular (left) and "modified" (right) collision. ....	92
Figure 3-20	Scaling of all the variables considered in the collision limiter subroutine for an under-resolved (in time) high density flow. The total number of accepted collisions is limited to a few per molecule. Equilibration of the translational modes and rotational modes is achieved through $N_{T-R}$ regular collisions. Energy exchange with the vibrational modes is then computed more quickly by	

	allowing $N_{VIB}$ additional “modified” collisions where the probability of translational-vibrational energy exchange is increased. ....	93
Figure 3-21	Schematic of the multi-domain approach used in the DSMC code. The inner domain is first run and as molecules exit the right and top boundaries they are saved to a file. Later, the molecular data are read in into a larger domain and molecules are input to the domain at the exact same time in the computation as they exited the inner domain. ....	96
Figure 3-22	2D density contours in the plane of impact for the water vapor plume induced by a 2 km diameter comet 3 s after impact on the Moon. The comet hits the surface at an angle of $45^\circ$ at 30 km/s from the left of the figure to the right. The red semi-circle represents the interface with the SOVA hydrocode and the grey lines represent the boundary of each DSMC domain used in the present unsteady sequential multi-domain simulation. ....	97
Figure 4-1	Plot of the ratio of specific heats, $\gamma$ , for water as a function of temperature. ....	102
Figure 4-2	Analytic temperature plots versus time at a distance of 20 km from the point of origin of the expansion for Cases 1, 2, and 3 (obtained from Eq. (4.1)). ....	103
Figure 4-3	Analytic density plots versus time at a distance of 20 km from the point of origin of the expansion for Cases 1, 2, and 3 (obtained from Eq. (4.1)). ....	104
Figure 4-4	Analytical radial velocity plots versus time at a distance of 20 km from the point of origin of the expansion for Cases 1, 2, and 3 (obtained from Eq. (4.1)). Note that the initial conditions do not influence the value of the radial velocity as it only depends on time and radial distance in this self-similar solution.....	104
Figure 4-5	Analytic Mach number versus time at a distance of 20 km from the point of origin of the expansion for Cases 1, 2, and 3.....	105
Figure 4-6	Analytic Knudsen number based on the density gradient versus time at a distance of 20 km from the point of origin of the expansion for Cases 1, 2, and 3. ....	105
Figure 4-7	Schematic of the approach used to simulate the expansion flow of water vapor into a vacuum. The 1D analytic solution is used at a hemispherical interface to create the DSMC molecules. The DSMC simulations provide 3D results that	

	are later sampled into radial bins. Finally, the sampled solution is compared to the analytic solution downstream of the interface. Plotted here as example is the analytic density plot for Case 2 as function of time at the interface as well as the density contours and profiles for Case 2 3s after the beginning of the expansion downstream of the interface. ....	107
Figure 4-8	DSMC density contours downstream of the interface for Case 2. The hatched area represents the parts of the domain that are ignored when the cell data are averaged into radial bins.....	109
Figure 4-9	DSMC and analytic density (a) and radial velocity (b) profiles 3 s after the beginning of the expansion downstream of the interface for Case 1 (blue) and Case 2 (red).....	110
Figure 4-10	DSMC and analytic temperature profiles 3 s after the beginning of the expansion downstream of the interface for Case 1 (a) and Case 2 (b). The vibrational temperatures were obtained by sampling the vibrational temperatures in each radial bin.....	111
Figure 4-11	DSMC and analytic temperature profiles 3 s after the beginning of the expansion downstream of the interface for Case 1 (a) and Case 2 (b). The vibrational temperatures were obtained by sampling the sampling the populations in each vibrational state. ....	113
Figure 4-12	DSMC and analytic density (a) and radial velocity (b) profiles 3 s after the beginning of the expansion downstream of the interface for Case 1 (blue) and Case 2 (red). Note that the analytic radial velocity only depends on the radial distance and time; therefore the analytic solution is the same for Cases 1 and 2...	114
Figure 4-13	DSMC and analytic temperature profiles versus radial distance from the point of origin of the expansion 3s after the beginning of the expansion for Case 1. The left hand-side figure (a) was obtained using a sampling of the <i>vibrational temperatures</i> in each radial bin while the right-hand side figure (b) was obtained using a sampling of the <i>populations</i> in each vibrational state. ....	115
Figure 4-14	DSMC and analytic temperature profiles versus radial distance from the point of origin of the expansion 3s after the beginning of the expansion for Case 2. The left hand-side figure (a) was obtained using a sampling of the vibrational	



	temperatures in each radial bin while the right-hand side figure (b) was obtained using a sampling of the populations in each vibrational state.....	116
Figure 4-15	Breakdown parameters versus radial distance away from the point of origin of the expansion 3.5 s after the beginning of the expansion for Case 3.....	118
Figure 4-16	Bird's parameters indicating departure from equilibrium for the vibrational modes versus radial distance away from the point of origin of the expansion 3.5 s after the beginning of the expansion for Case 3.....	119
Figure 4-17	DSMC and analytic temperature profiles versus radial distance from the point of origin of the expansion 3.5 s after the beginning of the expansion for Case 3. "CL" refers to the collision limited case and "No CL" refers to the regular DSMC simulations. The vibrational temperature components have been obtained using a sampling of the populations in each vibrational state in each radial bin. ....	120
Figure 5-1	Innermost DSMC domains used for the vertical (a) and oblique (b) impact events. The interface with the SOVA hydrocode is shown in red in the plane of impact (Note that in the simulations the SOVA interface is 3D). The comet diameter and the impact angle are to scale. For the oblique impact, the boundaries between processors are also shown exhibiting the non-uniform distribution used in the present simulations. ....	125
Figure 5-2	Hybrid SOVA and DSMC density contours of a vertical comet impact on the surface of the Moon after 5s. The SOVA hydrocode density contours are shown below the red interface (gray=ice; green=target) and by the black line outlining the limit between the water and the vacuum or rock above the interface. The collisionless DSMC contours are shown above the red interface with the associated legend (in kg/m <sup>3</sup> ). ....	128
Figure 5-3	Density contours in the plane of symmetry of the oblique impact after 1 s. The green and grey contours are from the SOVA calculations and represent the rock and water densities, respectively. The color contours above the red interface represent the DSMC water density contours with the attached legend. The black lines shown above the interface for reference represent the limit between rock	

	and water in the SOVA simulations. The grey line represents the limit between the dark and light grey SOVA contours above the interface. ....	130
Figure 5-4	Density contours from the SOVA hydrocode 1 s after a 45° oblique comet impact. The two red curves represent the SOVA interfaces at which data are provided.....	131
Figure 5-5	Density contours at interfaces {1} and {2}, 1s after the impact, from the (a) DSMC and (b) SOVA simulations. ....	133
Figure 5-6	Contours of the number of molecules per cell for the DSMC simulations 1 s after the beginning of the impact. ....	133
Figure 5-7	(a, b) $V_x$ , (c, d) $V_y$ , and (e, f) $V_z$ velocity contours at interfaces {1} and {2}, 1 s after the impact, from the (a, c, and e) DSMC and (b, d, and f) SOVA simulations.....	134
Figure 5-8	Contours of (a) DSMC rotational, (b) DSMC translational, (c) DSMC total and (d) SOVA temperatures at interfaces {1} and {2}, 1 s after the impact.....	135
Figure 5-9	(a) $v_1$ -, (b) $v_2$ -, and (c) $v_3$ -vibrational temperature contours at interfaces {1} and {2}, 1 s after the impact.....	137
Figure 5-10	2D projection of the DSMC density contours of the water vapor plume at the hemispherical interface with the SOVA hydrocode 1, 3, 5, 7, 9, and 11 s after impact. ....	140
Figure 5-11	2D projection of the DSMC density contours of the water vapor plume at the hemispherical interface with the SOVA hydrocode 13, 15, 17, 19 and 21 s after impact. ....	142
Figure 5-12	2D projection of the DSMC radial velocity contours of the water vapor plume at the hemispherical interface with the SOVA hydrocode 7, 9, 11, and 13 s after impact. ....	145
Figure 5-13	2D projection of the DSMC radial velocity contours of the water vapor plume at the hemispherical interface with the SOVA hydrocode 15, 17, 19 and 21 s after impact. ....	147
Figure 5-14	Total mass (red line) and instantaneous mass flux (blue line) into the DSMC domain at the 20 km in radius interface with the SOVA hydrocode as a function of time.....	150

Figure 5-15	Total mass flow (black line with triangle symbols) and spatially averaged directional mass flow (other colors) that crosses the interface between the SOVA and DSMC codes as a function of time. Note that the vertical axis uses a logarithmic scale.....	151
Figure 5-16	Instantaneous total mass flux (black line) and spatially averaged directional mass flux (other colors) of water that crosses the interface between the SOVA and DSMC codes as a function of time. Note that the vertical axis in the inset picture uses a logarithmic scale and that only the first ten seconds of the impact are shown.....	154
Figure 5-17	Location of the three 2D slices used to present the 3D water vapor plume results obtained from the DSMC simulations of a 45° comet impact. ....	157
Figure 5-18	Near-field density contours 1s after impact in the plane of symmetry (top), 45° off the symmetry plane (middle) and perpendicular to the plane of symmetry (bottom). ....	159
Figure 5-19	Near-field density contours 5 s after impact in the plane of symmetry (top), 45° off the symmetry plane (middle) and perpendicular to the plane of symmetry (bottom). ....	161
Figure 5-20	Near-field density contours 10 s after impact in the plane of symmetry (top), 45° off the symmetry plane (middle) and perpendicular to the plane of symmetry (bottom). ....	163
Figure 5-21	Near-field density contours 15 s after impact in the plane of symmetry (top), 45° off the symmetry plane (middle) and perpendicular to the plane of symmetry (bottom). ....	165
Figure 5-22	Near-field density contours 20 s after impact in the plane of symmetry (top), 45° off the symmetry plane (middle) and perpendicular to the plane of symmetry (bottom). ....	167
Figure 5-23	Near-field total temperature contours 1 s after impact in the plane of symmetry (top), 45° off the symmetry plane (middle) and perpendicular to the plane of symmetry (bottom). ....	171

Figure 5-24	Near-field rotational temperature contours 1 s after impact in the plane of symmetry (top), 45° off the symmetry plane (middle) and perpendicular to the plane of symmetry (bottom). .....	172
Figure 5-25	Near-field translational temperature contours 1 s after impact in the plane of symmetry (top), 45° off the symmetry plane (middle) and perpendicular to the plane of symmetry (bottom). .....	173
Figure 5-26	Near-field $v_1$ -vibrational temperature contours 1 s after impact in the plane of symmetry (top), 45° off the symmetry plane (middle) and perpendicular to the plane of symmetry (bottom). .....	175
Figure 5-27	Near-field $v_2$ -vibrational temperature contours 1 s after impact in the plane of symmetry (top), 45° off the symmetry plane (middle) and perpendicular to the plane of symmetry (bottom). .....	176
Figure 5-28	Near-field $v_3$ -vibrational temperature contours 1 s after impact in the plane of symmetry (top), 45° off the symmetry plane (middle) and perpendicular to the plane of symmetry (bottom). .....	177
Figure 5-29	Near-field total temperature contours 5 s after impact in the plane of symmetry (top), 45° off the symmetry plane (middle) and perpendicular to the plane of symmetry (bottom). .....	179
Figure 5-30	Near-field rotational temperature contours 5 s after impact in the plane of symmetry (top), 45° off the symmetry plane (middle) and perpendicular to the plane of symmetry (bottom). .....	180
Figure 5-31	Near-field translational temperature contours 5 s after impact in the plane of symmetry (top), 45° off the symmetry plane (middle) and perpendicular to the plane of symmetry (bottom). .....	181
Figure 5-32	Near-field total temperature contours 10 s after impact in the plane of symmetry (top), 45° off the symmetry plane (middle) and perpendicular to the plane of symmetry (bottom). .....	183
Figure 5-33	Near-field rotational temperature contours 10 s after impact in the plane of symmetry (top), 45° off the symmetry plane (middle) and perpendicular to the plane of symmetry (bottom). .....	184

Figure 5-34	Near-field translational temperature contours 10 s after impact in the plane of symmetry (top), 45° off the symmetry plane (middle) and perpendicular to the plane of symmetry (bottom). .....	185
Figure 5-35	Near-field total temperature contours 15 s after impact in the plane of symmetry (top), 45° off the symmetry plane (middle) and perpendicular to the plane of symmetry (bottom). .....	187
Figure 5-36	Near-field rotational temperature contours 15 s after impact in the plane of symmetry (top), 45° off the symmetry plane (middle) and perpendicular to the plane of symmetry (bottom). .....	188
Figure 5-37	Near-field translational temperature contours 15 s after impact in the plane of symmetry (top), 45° off the symmetry plane (middle) and perpendicular to the plane of symmetry (bottom). .....	189
Figure 5-38	Near-field total temperature contours 20 s after impact in the plane of symmetry (top), 45° off the symmetry plane (middle) and perpendicular to the plane of symmetry (bottom). .....	190
Figure 5-39	Near-field rotational temperature contours 20 s after impact in the plane of symmetry (top), 45° off the symmetry plane (middle) and perpendicular to the plane of symmetry (bottom). .....	191
Figure 5-40	Near-field translational temperature contours 20 s after impact in the plane of symmetry (top), 45° off the symmetry plane (middle) and perpendicular to the plane of symmetry (bottom). .....	192
Figure 5-41	Near-field pressure contours 1 s after impact in the plane of symmetry (top), 45° off the symmetry plane (middle) and perpendicular to the plane of symmetry (bottom). .....	197
Figure 5-42	Near-field ratio of vapor pressure to pressure contours 1 s after impact in the plane of symmetry (top), 45° off the symmetry plane (middle) and perpendicular to the plane of symmetry (bottom). .....	198
Figure 5-43	Near-field pressure contours 5 s after impact in the plane of symmetry (top), 45° off the symmetry plane (middle) and perpendicular to the plane of symmetry (bottom). .....	199

Figure 5-44	Near-field ratio of vapor pressure to pressure contours 5 s after impact in the plane of symmetry (top), 45° off the symmetry plane (middle) and perpendicular to the plane of symmetry (bottom). .....	200
Figure 5-45	Near-field pressure contours 10 s after impact in the plane of symmetry (top), 45° off the symmetry plane (middle) and perpendicular to the plane of symmetry (bottom). .....	201
Figure 5-46	Near-field ratio of vapor pressure to pressure contours 10 s after impact in the plane of symmetry (top), 45° off the symmetry plane (middle) and perpendicular to the plane of symmetry (bottom). .....	202
Figure 5-47	Near-field pressure contours 15 s after impact in the plane of symmetry (top), 45° off the symmetry plane (middle) and perpendicular to the plane of symmetry (bottom). .....	203
Figure 5-48	Near-field ratio of vapor pressure to pressure contours 15 s after impact in the plane of symmetry (top), 45° off the symmetry plane (middle) and perpendicular to the plane of symmetry (bottom). .....	204
Figure 5-49	Near-field pressure contours 20 s after impact in the plane of symmetry (top), 45° off the symmetry plane (middle) and perpendicular to the plane of symmetry (bottom). .....	205
Figure 5-50	Near-field ratio of vapor pressure to pressure contours 20 s after impact in the plane of symmetry (top), 45° off the symmetry plane (middle) and perpendicular to the plane of symmetry (bottom). .....	206
Figure 5-51	Near-field radial velocity contours 1 s after impact in the plane of symmetry (top), 45° off the symmetry plane (middle) and perpendicular to the plane of symmetry (bottom). .....	210
Figure 5-52	Near-field Mach number contours 1 s after impact in the plane of symmetry (top), 45° off the symmetry plane (middle) and perpendicular to the plane of symmetry (bottom). .....	211
Figure 5-53	Near-field radial velocity contours 5 s after impact in the plane of symmetry (top), 45° off the symmetry plane (middle) and perpendicular to the plane of symmetry (bottom). .....	212

Figure 5-54	Near-field Mach number contours 1 s after impact in the plane of symmetry (top), 45° off the symmetry plane (middle) and perpendicular to the plane of symmetry (bottom). .....	213
Figure 5-55	Near-field radial velocity contours 10 s after impact in the plane of symmetry (top), 45° off the symmetry plane (middle) and perpendicular to the plane of symmetry (bottom). .....	214
Figure 5-56	Near-field Mach number contours 10 s after impact in the plane of symmetry (top), 45° off the symmetry plane (middle) and perpendicular to the plane of symmetry (bottom). .....	215
Figure 5-57	Near-field radial velocity contours 15 s after impact in the plane of symmetry (top), 45° off the symmetry plane (middle) and perpendicular to the plane of symmetry (bottom). .....	216
Figure 5-58	Near-field Mach number contours 15 s after impact in the plane of symmetry (top), 45° off the symmetry plane (middle) and perpendicular to the plane of symmetry (bottom). .....	217
Figure 5-59	Near-field radial velocity contours 20 s after impact in the plane of symmetry (top), 45° off the symmetry plane (middle) and perpendicular to the plane of symmetry (bottom). .....	218
Figure 5-60	Near-field Mach contours 20 s after impact in the plane of symmetry (top), 45° off the symmetry plane (middle) and perpendicular to the plane of symmetry (bottom). .....	219
Figure 5-61	Near-field Knudsen number (based on the mean free path) contours 1 s after impact in the plane of symmetry (top), 45° off the symmetry plane (middle) and perpendicular to the plane of symmetry (bottom). .....	222
Figure 5-62	Near-field Knudsen number (based on the cell size) contours 1 s after impact in the plane of symmetry (top), 45° off the symmetry plane (middle) and perpendicular to the plane of symmetry (bottom). .....	223
Figure 5-63	Near-field Knudsen number (based on the mean free path) contours 5 s after impact in the plane of symmetry (top), 45° off the symmetry plane (middle) and perpendicular to the plane of symmetry (bottom). .....	224

Figure 5-64	Near-field Knudsen number (based on the cell size) contours 5 s after impact in the plane of symmetry (top), 45° off the symmetry plane (middle) and perpendicular to the plane of symmetry (bottom). .....	225
Figure 5-65	Near-field Knudsen number (based on the mean free path) contours 10 s after impact in the plane of symmetry (top), 45° off the symmetry plane (middle) and perpendicular to the plane of symmetry (bottom). .....	226
Figure 5-66	Near-field Knudsen number (based on the cell size) contours 10 s after impact in the plane of symmetry (top), 45° off the symmetry plane (middle) and perpendicular to the plane of symmetry (bottom). .....	227
Figure 5-67	Near-field Knudsen number (based on the mean free path) contours 15 s after impact in the plane of symmetry (top), 45° off the symmetry plane (middle) and perpendicular to the plane of symmetry (bottom). .....	228
Figure 5-68	Near-field Knudsen number (based on the cell size) contours 15 s after impact in the plane of symmetry (top), 45° off the symmetry plane (middle) and perpendicular to the plane of symmetry (bottom). .....	229
Figure 5-69	Near-field Knudsen number (based on the mean free path) contours 20 s after impact in the plane of symmetry (top), 45° off the symmetry plane (middle) and perpendicular to the plane of symmetry (bottom). .....	230
Figure 5-70	Near-field Knudsen number (based on the cell size) contours 20 s after impact in the plane of symmetry (top), 45° off the symmetry plane (middle) and perpendicular to the plane of symmetry (bottom). .....	231
Figure 5-71	Density contours 10 s after impact in: (a) the symmetry plane, (b) 45° off the symmetry plane and (c) perpendicular to the plane of symmetry.....	234
Figure 5-72	Total temperature contours 10 s after impact in: (a) the symmetry plane, (b) 45° off the symmetry plane and (c) perpendicular to the plane of symmetry. ....	235
Figure 5-73	Radial velocity contours 10 s after impact in: (a) the symmetry plane, (b) 45° off the symmetry plane and (c) perpendicular to the plane of symmetry. ....	236
Figure 5-74	Knudsen number (based on the mean free path) contours 10 s after impact in: (a) the symmetry plane, (b) 45° off the symmetry plane and (c) perpendicular to the plane of symmetry. ....	237



Figure 5-75	Density contours 20 s after impact in: (a) the symmetry plane, (b) 45° off the symmetry plane and (c) perpendicular to the plane of symmetry.....	239
Figure 5-76	Total temperature contours 20 s after impact in: (a) the symmetry plane, (b) 45° off the symmetry plane and (c) perpendicular to the plane of symmetry. ....	240
Figure 5-77	Radial velocity contours 20 s after impact in: (a) the symmetry plane, (b) 45° off the symmetry plane and (c) perpendicular to the plane of symmetry. ....	241
Figure 5-78	Knudsen number (based on the mean free path) contours 20 s after impact in: (a) the symmetry plane, (b) 45° off the symmetry plane and (c) perpendicular to the plane of symmetry. ....	242
Figure 6-1	Density (left) and speed (right) contours for the portion of the water vapor plume with speeds lower than 110% of the escape velocity, three hours after impact. The white arrow represents the direction of the comet at impact (note that the plane of impact is the XZ plane). The white sphere represents the Moon. Note that only cells with $Y > 0$ km have been plotted and that the viewing angle and viewing distance are different between the two figures. The black lines in the figure on the right represent the streamlines of the flow.....	247
Figure 6-2	Initial fallback pattern on an artificially uniformly cold lunar surface ( $T_{\text{surf}} = 120$ K) for the water vapor plume once 99.6% of the water has fallen back to the surface. Note that the Moon did not rotate for this simulation. ....	249
Figure 6-3	Grayscale contours for the mass of water stuck to the surface per square kilometer 3 hours, 7 days and 28 days after impact. Note that the inset picture indicates the location of the impact point at each time relative to the subsolar point.....	251
Figure 6-4	Line plots of the mass of water initially retained (black line), remaining on the Moon (both trapped and untrapped) (green line), destroyed (light blue line), and captured in the cold traps (red and blue lines for the cold traps located at the South Pole and North Pole, respectively) as a function of time. The inset figure zooms in early times. Note that the plot lines start three hours after impact when the intermediate simulations were started.....	252

Figure 6-5	Scatter plot of the deposition pattern of water ice in the North Pole cold trap (left) and in the South Pole cold traps (right). The color scale represents the time after impact at which the molecule was trapped.....	254
Figure 6-6	Translucent density contours (colored) for the atmospheric flow with superimposed grayscale contours for the mass of water stuck to the surface per square kilometer 10 minutes after impact for Cases 1, 2, and 3. Note that the inset picture indicates the location of the impact point at that time relative to the subsolar point.....	258
Figure 6-7	Translucent density contours (colored) for the atmospheric flow with superimposed grayscale contours for the mass of water stuck to the surface per square kilometer one hour after impact for Cases 1, 2, and 3. Note that the inset picture indicates the location of the impact point at that time relative to the subsolar point.....	260
Figure 6-8	Translucent density contours (colored) for the atmospheric flow with superimposed grayscale contours for the mass of water stuck to the surface per square kilometer one day after impact for Cases 1, 2, and 3. Note that the inset picture indicates the location of the impact point at that time relative to the subsolar point.....	261
Figure 6-9	Translucent density contours (colored) for the atmospheric flow with superimposed grayscale contours for the mass of water stuck to the surface per square kilometer seven days after impact for Cases 1, 2, and 3. Note that the inset picture indicates the location of the impact point at that time relative to the subsolar point.....	262
Figure 6-10	Translucent density contours (colored) for the atmospheric flow with superimposed grayscale contours for the mass of water stuck to the surface per square kilometer seven days after impact for Cases 2, and 4. Note that the inset picture indicates the location of the impact point at that time relative to the subsolar point.....	263
Figure 6-11	Line plots of the mass of water released (black line), remaining on the Moon (green lines), destroyed (light blue lines), and captured in the cold traps (red and blue lines for the cold traps located at the South Pole and North Pole,	

respectively) as a function of time. The square symbols represent Case 1, the circle symbols represent Case 2 and the triangle symbols represent Case 3. The inset figure zooms in early times. Note that the mass released (black line) is equal to 1% of the comet mass. .... 266

Figure 6-12 Line plots of the mass of water released (black line), remaining on the Moon (green lines), destroyed (light blue lines), and captured in the cold traps (red and blue lines for the cold traps located at the South Pole and North Pole, respectively) as a function of time. The square symbols represent Case 2, and the circle symbols represent Case 4. The inset figure zooms in early times. Note that the mass released (black line) is equal to 1% of the comet mass. .... 267

## Nomenclature

### Roman symbols

$A, Const$	constants
$c$	most probable thermal speed
$c_r$	relative speed between two molecules
$dist$	radial distance from the point of origin of the expansion
$e_{V, i}$	specific vibrational energy associated with the $i^{th}$ mode
$E(p)$	parallel efficiency
$f$	number of degrees of freedom
$F_{ACCEPTED}$	estimated fraction of accepted collisions in a cell during a given timestep
$F_N$	number of real molecules represented by a single DSMC molecule
$g$	gravity
$k$	Boltzmann's constant
$Kn$	Knudsen number
$M$	mass of the gas cloud
$M_{H2O}$	molecular mass of water
$M_V$	number of vibrational modes
$Mach$	Mach number
$N$	number of representative molecules
$N_k$	number of molecules in the $k^{th}$ excited vibrational level
$N_{ACCEPTED}$	number of accepted collision pairs
$N_{SELECT}$	number of selected collision pairs (Bird <sup>1</sup> Eq. (11.3))
$N_{SUBLIMATED}$	number of molecules to sublime from the impact crater
$N_{TR}$	limited number of collisions sufficient for the equilibration of the translational and rotational modes
$N_{VIB}$	additional number of collisions required for the possible equilibration of the vibrational modes
$NUM$	number of representative molecules in a cell
$p$	number of processors in a parallel computation
$P$	pressure
$P_{vapor}$	saturation vapor pressure of the gas
$P_{ionize, dissociate}$	probability for an in-flight molecule to ionize or dissociate
$P_{rot, vib}$	breakdown parameters for rotational and vibrational freezing
$Q$	total energy of the gas
$R$	radius of the sublimating crater
$\mathcal{R}$	specific gas constant
$R_0, T_0, \rho_0$	initial radius, temperature, and density of the gas cloud
$Radius_{MOON}$	radius of the Moon
$Rand$	random number

$r$	radial distance from the center of the Moon
$s$	distance from the point of impact along the surface
$S(p)$	speed-up for a parallel run with p processors over a serial run
$T$	temperature
$t$	time
$t_{reside}$	residence time
$V_r$	radial velocity component from the point of impact
$V_{max}$	velocity of the outer layers of the cloud
$V_{X, Y, Z}$	Cartesian velocity components
$V_C$	volume of computational cell
$X, Y, Z$	Cartesian coordinate axes centered at the center of the Moon, where X and Z define the plane of symmetry of the impact
$Z_{l, 2, 3}$	vibrational relaxation collision number for the vibrational modes
$Z_{rot}$	rotational relaxation collision number
$Z_{V, MIN}$	minimum vibrational relaxation collision number

#### Greek symbols

$\alpha$	impact angle
$\beta$	angle from the plane of symmetry of the impact
$\delta$	relative angle to the subsolar point
$\Delta t$	timestep size
$\Delta H$	binding energy
$\Gamma$	gamma function
$\gamma$	ratio of specific heats
$\lambda$	mean free path
$\nu_{l, 2, 3}$	vibrational mode number
$\nu_0$	lattice vibrational frequency of water within a water matrix
$\nu_{coll}$	collision frequency
$\varphi$	azimuthal angle in the old spherical coordinate system
$\Phi$	azimuthal angle in the new spherical coordinate system
$\rho$	density
$\sigma_T$	total collision cross-section
$\tau_{serial, p}$	wall clock time for serial and parallel computations
$\theta$	polar angle in the old spherical coordinate system
$\vartheta_{l, 2, 3}$	characteristic vibrational temperatures
$\Theta$	polar angle in the new spherical coordinate system
$\zeta$	fraction of the serial code that can be parallelized

# Chapter 1

## Introduction

### 1.1 MOTIVATION

In order to establish a base on the lunar surface, materials absent from the Moon will have to be brought from Earth at great cost. For that reason, research into the possible presence of important resources on the Moon, such as water, has been under way for years. Regolith samples from the Apollo missions have demonstrated that the equatorial regions of the Moon are extremely dry (Taylor, 1975). In fact, aside from some craters near the lunar poles, the surface temperature on the Moon was generally thought to be too high for any water deposits to accumulate. However, polar craters that are in permanent shadow, or cold traps, have a surface temperature low enough for water ice to remain there over geologic time scales (Ingersoll *et al.*, 1992). The sunny rim of such craters would provide a suitable location for a lunar base if water ice was actually present nearby. The main goal of this work is to consider scenarios for the possible accumulation of water ice in the cold traps at the lunar poles after a large comet impact by using the Direct Simulation Monte Carlo (DSMC) method.

Remote observations using either Earth based radars or detectors onboard lunar orbiters have investigated the possible presence of water ice at the lunar poles. Data from the Clementine (Nozette *et al.*, 1996) and Lunar Prospector (Feldman *et al.*, 1998) missions have been interpreted as the signature from possible water ice deposits at the lunar poles. But these findings have been questioned over the years by other groups (Simpson and Tyler, 1999 and Hodges, 2002). Some more recent missions have also provided a wide range of observations and results. Japan's Kayuga (also known as the SELEnological ENgineering Explorer, or SELENE) did not detect water ice on the Moon (Haruyama *et al.*, 2008). However, India's Chandrayaan-1 (Pieters *et al.*, 2009) orbiter as well as Cassini (Clark, 2009) and Deep Impact (Sunshine *et al.*, 2009) fly-bys of the Moon observed the signature from a possible thin layer of water not just localized inside the

polar cold traps but covering large areas of the Moon. Also, the ongoing Lunar Reconnaissance Orbiter (LRO) mission should soon provide some additional data about the presence of water on the Moon. In addition to the orbiter missions, both the Lunar Prospector (Goldstein *et al.*, 1999) and the recent Lunar Crater Observation and Sensing Satellite (LCROSS) missions went a step further by impacting a large mass in possible water reservoirs in order to observe water by-products in the impact induced plume. No conclusive result could be drawn from the Lunar Prospector data, but the LCROSS data showed the presence of water within the permanently shadowed regions of Cabeus crater near the lunar South Pole. While some of the most recent missions seem to indicate the presence of water possibly widely spread on the Moon, none of the above missions have yet provided irrefutable evidence as to the presence of water in the lunar cold traps and contradictory interpretations of the observations have provided little certainty as to the possible concentration and quantity of water at the lunar poles. In the end, only direct observations, for instance using rovers, can provide thorough investigation.

In parallel with the observations, several groups have simulated the transport of water molecules on the surface of the Moon using Monte Carlo approaches (Arnold, 1979, Morgan and Shemansky, 1991, Butler, 1997 and Crider and Vondrak, 2000). These approaches are well suited for the theoretical study of the gradual accumulation of water within a lunar cold trap from steady sources such as chemical reactions, solar wind interactions, lunar out-gassing and micrometeorites. In the gradual mode, the gas flow involves free molecular, random walk diffusion over an extremely dry regolith surface which is perhaps what was observed by Chandrayaan-1 (Pieters *et al.*, 2009), Cassini (Clark, 2009) and Deep Impact (Sunshine *et al.*, 2009). After a large comet impact event, however, the atmosphere is expected to be near continuum and transport could be pressure-driven rather than via diffusion.

The impact of a comet or meteorite on a planet is a very complex problem to study. As the impactor hits the surface of the planet some of its kinetic energy is transformed into heat, melting and vaporizing both impactor and target materials. Impact events are simulated using three-dimensional hydrocodes, such as SOVA (Shuvalov, 1999) or CTH (McGlaun *et al.*, 1990). Hydrocodes simulate the surface deformation, the strong shock wave physics and the changes of the state of materials during the impact providing multi-dimensional unsteady macroscopic data for each material. Due to the computational cost of such runs, however, the simulation is usually stopped only a few seconds after impact.

In the case when the target planet has a tenuous atmosphere or no atmosphere, the gases will expand rapidly following the impact, becoming transitional and then rarefied after a few minutes. In rarefied flows, the gas flow can no longer be represented by the Navier-Stokes equations and the Boltzmann equation must be used instead. Stochastic approaches, such as the DSMC method (Bird, 1994), are usually the method of choice used to solve the Boltzmann equation. In the DSMC approach, the gas flow is modeled by a large number of representative molecules ( $O(10^5-10^8)$ ). For dilute gases, the mean ballistic time between collisions is much larger than the collision time so the collisions can be treated as instantaneous. Using this assumption, the representative molecules in DSMC simulations are moved and then collided in separate substeps. At any given time, the molecular data can be sampled to obtain the macroscopic flow properties such as density, bulk velocity and temperature.

While the DSMC method is well suited to simulate transitional to rarefied flows, the computational cost of the DSMC simulations becomes high as the number density of the flow increases. For that reason, hybrid methods have been implemented to simulate flows where both high density regions and rarefied regions are present. Such hybrid methods have been used over the years to simulate complex expansion and nozzle flows into hard vacuums or into a rarefied background gas (Roveda *et al.*, 2000) as well as hypersonic flows around blunt bodies (Schwartzentruber *et al.*, 2008).

In order to simulate the deposition of water in lunar cold traps after a large comet impact, a hybrid method seems appropriate. This method would simulate the impact event with a hydrocode and use that solution as input for a Boltzmann solver to simulate the transitional to rarefied gas flow. The present work focuses on DSMC simulations of the unsteady expansion flow during the late stages of the impact event as well as the later transient atmosphere using the results obtained with the SOVA hydrocode as input. The unique features of the problem distinct from the familiar aeronautical engineering applications of the DSMC method are the significance of gravity, the variable surface temperature, the large variations in length and time scales, the different materials involved and the particular gas-surface interactions. However, the hybrid method developed here for unsteady expansions can also be used for other engineering applications, like detonations, laser ablation, micro-meteorite impacts on spacecraft and micro-thrusters for station keeping.



## 1.2 OBJECTIVES

The main objective of the current research is to develop a numerical approach appropriate for the study of three-dimensional supersonic planetary-scale expansion flows into a vacuum. The present DSMC simulations model the induced expansion plume and resulting deposition of water in a lunar cold trap after a comet impact on the Moon. The initial boundary conditions to the DSMC runs are provided by the SOVA hydrocode simulations of the impact event.

The expansion flow after a comet impact on an airless body such as the Moon goes from continuum to transitional to rarefied and finally to free molecular. The variations in the flow scales of this problem are very large: from a few microns for the mean free path near the point of impact to several thousand kilometers for the size of the full-planetary domain. The major goal of this work was to modify our implementation of the DSMC method in order to simulate such flow. The previous serial axisymmetric version of the code was modified as follows. First, it was converted into a three-dimensional parallel code. The unsteady interface between the hydrocode and the DSMC code also had to be implemented. Due to restrictions on the hydrocode solver, the interface location is fixed and the gas flow at the interface is highly continuum. Therefore, the DSMC code had to be adapted to handle such high density, high temperature flow by using a collision limiter scheme suitable for polyatomic molecules like water. In order to handle the large variations in the scales of the flow, an unsteady sequential multi-domain approach has been implemented. Several other features have also been added in order to model the water transport processes on the surface of the Moon. A residence time model, a photodestruction model, and a variable surface temperature model including the polar cold traps have all been implemented.

The second objective of this work was to validate the present DSMC implementation. Basic simulations, e.g. simulations of ballistic or orbiting trajectories, have been used to test the validity of the present DSMC code. In addition, two separate test cases have been run in order to validate the use of the present method to simulate unsteady expansion flows. First, a 1D spherically symmetric unsteady expansion flow into a vacuum has been computed. Such flow is a simplified version of the late stages of a comet impact and has the advantage of having an analytic solution. Then, the results obtained for a 3D comet impact using the hybrid hydrocode-DSMC method have been compared downstream of the interface with the hydrocode-only results where both schemes should be valid.

The final objective was to study both the induced expansion flow and the later circum-lunar flow after the comet impact. At first, the flow expands away from the point of impact and at that stage a large fraction of the comet mass is lost to space. After several days-to-weeks on the Moon, a transitional flow of the remaining water establishes itself as molecules sublimate from the sunlit regions of the Moon and then condense on the night side. As the flow transitions from the rarefied expansion plume to a much more uniform free molecular flow, the important loss mechanism becomes photodestruction instead of escape from the Moon. From these simulations, parametric depositional maps of water have been obtained.

### **1.3 DISSERTATION OVERVIEW**

In Chapter 2, a literature review of the background work related to the possible presence of water ice on the Moon, to comet impacts and to the DSMC method is presented. The DSMC method is examined in Chapter 3 with a detailed description of the present implementation focusing more specifically on the three-dimensional parallel implementation of the code, the interface with the hydrocode solver, and the specific features required for the comet impact simulations. Results obtained from the simulations of a spherically symmetric flow expansion in a vacuum are presented in Chapter 4. Results obtained from the simulations of the late stages of a comet impact on the Moon are given in Chapter 5. Simulations of the induced circum-lunar flow and results for the deposition of water in the polar cold traps are presented in Chapter 6. Concluding remarks are presented in Chapter 7.

## **Chapter 2**

### **Literature Review**

This chapter describes some of the work related to the possible presence of water on the Moon, to comet impacts and to the DSMC method. First, a chronological summary of missions searching for water ice deposits on the lunar surface is given. Then, the modeling work investigating the accumulation mechanisms of water inside the lunar cold traps are presented chronologically. The second part of this chapter details the characteristics of an impact event as well as the numerical tools used to simulate such an event. Finally, the last section of this chapter presents several examples of use of the DSMC method and, in particular, several hybrid implementations.

#### **2.1 WATER ON THE MOON**

##### **2.1.1 Observations**

Several Earth-based observations and orbiter missions have looked for water on the Moon. The present literature review focuses on some of the most recent Earth-based observations made using the Goldstone and Aricebo radars and on the data obtained by the Clementine, Lunar Prospector, Kayuga and Chandrayaan-1 orbiter missions and by the Cassini and Deep Impact spacecrafts during their fly-bys of the Moon. The findings from these projects are summarized in Table 2-1.

Table 2-1 List of reviewed observations looking for water on the Moon

Project	Authors	Year	Conclusions
<b>Bistatic radar experiment onboard the Clementine orbiter</b>	Nozette <i>et al.</i>	1996	Small patches of ice covered and mixed with regolith covering 90 to 135 km <sup>2</sup>
	Simpson and Tyler	1999	No evidence for ice but ice mixed with regolith at a concentration of less than 1% is undetectable
	Nozette <i>et al.</i>	2001	10 km <sup>2</sup> of dirty ice on the lower Earth-facing wall of Shackleton crater
	McConnochie <i>et al.</i>	2002	Inconclusive
<b>Neutron spectrometer experiment onboard the Lunar Prospector orbiter</b>	Feldman <i>et al.</i>	1998	Up to 6×10 <sup>9</sup> tons of water ice
	Starukhina and Shkuratov	2000	Hydrogen from the Earth's magnetotail plasma
	Feldman <i>et al.</i>	2000	1.98×10 <sup>8</sup> tons of water ice
	Hodges	2002	Inconclusive
	Lawrence <i>et al.</i>	2006	Hydrogen buried under 10±5 cm of dry regolith but estimated abundance is highly uncertain
	Eke <i>et al.</i>	2008	Hydrogen deposits localized inside polar cold traps
<b>Goldstone radar</b>	Margot <i>et al.</i>	1999	Possible ice mixed with regolith or alternate layers of ice and regolith
	Hensley <i>et al.</i>	2008	Provided an accurate topographic map of the Moon
<b>Aricebo 12.6 / 13-cm wavelength radar</b>	Stacy <i>et al.</i>	1997	No evidence for the presence of ice
	Campbell <i>et al.</i>	2006	No thick deposits inside Shackleton Crater
<b>Aricebo 70-cm wavelength radar</b>	Campbell <i>et al.</i>	2003	No thick deposits but possible ice mixed with regolith at a concentration of 1 to 2%
	Campbell and Campbell	2006	No thick deposits but possible ice mixed with regolith at a concentration of 1 to 2%
<b>Kayuga Terrain Camera</b>	Haruyama <i>et al.</i>	2008	No exposed pure ice inside Shackleton Crater

Project	Authors	Year	Conclusions
<b>Chandrayaan-1 Moon Mineralogy Mapper</b>	Pieters <i>et al.</i>	2009	OH/H <sub>2</sub> O widely distributed in the uppermost layers of regolith. More prevalent at higher latitudes and inside fresh craters
<b>Cassini Visual and Infrared Mapping Spectrometer</b>	Clark	2009	OH/H <sub>2</sub> O widely distributed in the uppermost layers of regolith. More prevalent in the polar regions and highlands
<b>Deep Impact HRI-IR Spectrometer</b>	Sunshine <i>et al.</i>	2009	OH/H <sub>2</sub> O widely distributed in the uppermost layers of regolith. Global presence only dependent upon the surface temperature

In 1996, the Clementine mission provided new observations of the lunar surface and especially of the lunar poles. Using the data from the bistatic radar experiment onboard Clementine, Nozette *et al.* (1996) studied the polarization ratio enhancement detected in the radar backscatter at the South Pole. The regions of enhanced backscatter were associated with permanently shadowed terrain. They concluded that small patches of ice covered and mixed with rocky material may be present over 90 to 135 km<sup>2</sup> of the South Pole.

Their results were, however, questioned a year later by Stacy *et al.* (1997). Using the Aricebo 12.6-centimeter wavelength radar system in a bistatic set-up similar to the Clementine experiment, Stacy *et al.* obtained detailed maps of the lunar poles. Because of large topographic features at the surface of the Moon, they were only able to observe 40% of the area above 85°N and 60% of the area below 85°S. Several regions of enhanced backscatter and high circular polarization ratios (CPR) were observed but their locations were not consistent with known permanently shadowed areas. Instead, some of these high CPR regions were located on the steep rims of several craters. From their observations, Stacy *et al.* concluded that most of the regions with high CPR were due to increased roughness of the surface at these locations near the poles and not from the presence of thick water ice deposits.

One year later, data from the Lunar Prospector orbiter mission became available. Feldman *et al.* (1998) used the neutron spectrometer onboard Lunar Prospector to look at the hydrogen signature at the lunar poles. From the spectrometer data, they found enhanced deposits of hydrogen at the poles with locations consistent with permanently shadowed areas. They argued that this hydrogen signature can be consistent with water ice deposits under 40 cm thick dry

regolith covering 1850 km<sup>2</sup> at both poles. If one assumes a 1.6 m thick water ice deposit in association with the previous estimate of the total surface area covered by such a deposit as much as  $6 \times 10^9$  tons of water could be on the Moon. Their observations, however, did not constrain the distribution of the water ice deposits within the cold traps. For instance, their observations can also be due to deposits with a lower concentration of water, or due to multilayered geometries with alternate layers of water ice and dry regolith.

In 1999, Margot *et al.* used the Earth based 3.5-centimeter wavelength Goldstone radar to observe both poles of the Moon. If a shallow layer of ice was buried under a dry regolith layer, their radar observations would have been able to detect it. But from their observations, they were not able to detect any thick water ice deposits. However, they noted that their findings can be consistent with the Lunar Prospector observations if the water ice at the poles is mixed with regolith or that alternate layers of ice and regolith are present.

While Clementine and Lunar Prospector provided a large amount of data from their remote observations of the lunar poles, questions concerning the interpretation of the results remained. Simpson and Tyler (1999) reanalyzed the data obtained with Clementine's bistatic radar experiment. Using a different processing approach to the radar data, they were unable to reproduce the findings of Nozette *et al.* (1996). However, they did not rule out the possible presence of water ice uniformly distributed in the regolith with a mixing ratio under 1%. Such deposits could explain the hydrogen signature observed by Lunar Prospector (Feldman *et al.*, 1998) but would not have been detected by the Clementine radar experiment.

In 2000, Starukhina and Shkuratov postulated that the hydrogen signature observed at the poles of the Moon by Lunar Prospector is actually due to protons trapped in the regolith. In their model, the protons originate from the Earth's magnetotail plasma. The localized presence of hydrogen at the lunar poles can then be explained by the low temperature inside the cold traps. Such low temperatures slow the diffusion and outgassing of the hydrogen sufficiently so that hydrogen would be predominantly present in the polar regions of the Moon. The same year, Feldman *et al.* (2000) revisited their previous findings in light of more recent observations of the Moon. When they first reported the possible presence of hydrogen deposits at the lunar poles (Feldman *et al.*, 1998), the Lunar Prospector mission was still ongoing. Additional high-altitude orbits ( $100 \pm 20$  km) and new low-altitude orbits ( $30 \pm 15$  km) provided them with additional data. In the mean time, radar observations (Margot *et al.*, 1999 and Simpson and Tyler, 1999)

provided more accurate locations for the polar cold traps and also added new constraints as to the possible form of water ice deposits. Using these new pieces of information, Feldman *et al.* concluded that hydrogen at the North Pole was either limited to small deposits or was uniformly distributed in the soil with an overall higher concentration than at the equator. The neutron data at the South Pole seemed to suggest the presence of more concentrated hydrogen deposits. These observations would be consistent with a mass fraction of water of  $1.5 \pm 0.8\%$  within the regolith. Using Margot *et al.* (1999) estimates for the surface area of the polar cold traps and assuming the hydrogen is all in water form inside the cold traps, about  $1.35 \times 10^8$  and  $0.62 \times 10^8$  tons are present at the South and North Poles, respectively.

In 2001, Nozette *et al.* went back to the available data from an Aricebo monostatic radar experiment, the Lunar Prospector spectrometer experiment and the newly processed data from the Clementine bistatic radar experiment. They focused more closely on the lower Earth-facing wall of Shackleton crater. They noted that data from all three experiments could be interpreted as dirty ice deposits covering about  $10 \text{ km}^2$ . In 2002, McConnochie *et al.* studied the Clementine images taken by the ultraviolet-visual camera and the near infrared camera. From all the images taken, they reconstructed multi-spectral maps of the lunar poles in the hope of detecting the presence of water frost at the surface of some of the permanently shadowed regions. Their results were inconclusive however, as the study of different bands provided inconsistent results.

The interpretation of the Lunar Prospector data has also been questioned in 2002 by Hodges. Hodges (2002) noticed that the neutron spectrometer data can be interpreted differently and that hydrogen deposits at the poles are not the only possible explanation for the observation. While a decrease in the epithermal neutron flux was noticed by the Lunar Prospector spectrometer, no increase in the thermal neutron flux was reported. Hodges states that only both trends would certify that the observations are due to hydrogen. Using a Monte Carlo approach, Hodges showed that deficit or excess of some minerals, such as CaO or SiO<sub>2</sub>, in the regolith could produce results similar to those observed by the neutron spectrometer onboard Lunar Prospector.

In 2003, Campbell *et al.* (2003) pointed out that 13-centimeter wavelength radars could not penetrate further than a few centimeters below the surface. Therefore, if water ice deposits were buried under a thick layer of regolith, Stacy, *et al.*'s experiment (1997) would not have detected such deposits. For that reason, Campbell *et al.* (2003) used the Aricebo radar with a

wavelength of 70 cm to observe the poles of the Moon. From their observations, they concluded that no thick ice deposits were present at the lunar poles. They also pointed out that if water is mixed with regolith at a concentration of 1 to 2%, this water could not be observed using a radar experiment. In 2006, Campbell *et al.* used the 13-centimeter Aricebo radar for a high resolution look at the bottom of Shackleton Crater concluding again that thick ice deposits were not present but that disseminated ice was possible. This result was consistent with Campbell and Campbell (2006) observation of the lunar South Pole with the Aricebo radar using a wavelength of 70 cm. Campbell and Campbell did not find a particular signature within Shackleton Crater that differed from nearby sunlit areas.

In 2006, Lawrence *et al.* (2006) used a Monte Carlo approach to study the epithermal neutron flux signature of hypothetical lunar soils by varying the abundances of several elements, such as Fe, Gd and Sm. Their goal was to compare the results obtained with their model to the Lunar Prospector data. Based on known mineral composition of lunar soils, they concluded that it would be very unlikely for the variations in the abundance of such elements to have produced the Lunar Prospector data but that the presence of hydrogen is more likely. Also, they noted that the high concentrations of CaO or SiO<sub>2</sub> as suggested by Hodges (2002) as a possible explanation for the Lunar Prospector observations were also unlikely. They noted that the concentrations proposed by Hodges (2002) would be higher than that observed in most lunar samples and these elements are usually only present with other elements that have not been observed at the lunar poles. In conclusion, they reaffirmed previous findings that the observed signature in the Lunar Prospector neutron spectrometer data is likely due to hydrogen deposits buried under dry regolith. Eke *et al.* (2008) post-processed the Lunar Prospector neutron spectrometer data creating a reconstructed image of the distribution of hydrogen at the poles by taking into account which areas were in permanent shadow. Using this reconstruction, they concluded that the hydrogen deposits observed at the lunar poles were not uniform but mostly localized inside the polar cold traps.

Using data from the Goldstone observations of the lunar South Pole in 2006, Hensley *et al.* (2008) are currently compiling an accurate topographic map with a planar accuracy of 40 m and a 5 m vertical accuracy. Results from Japan's Kayuga mission have also been reported in 2008. Haruyama *et al.* (2008) used the stereo camera onboard Kayuga with a resolution of 10 m to observe Shackleton Crater. Using infrared through visual wavelengths, they found that the



temperature at the bottom of the crater did not exceed 88 K and that the visual albedo of the crater floor was similar to those of the surroundings. The latter finding led them to conclude that no exposed pure water ice deposits were present within Shackleton Crater.

In late 2009, three different groups reported data from three different missions that would be consistent with the widespread presence of a very thin layer of water or OH on the surface of the Moon. In 1999, as Cassini flew by the Moon, the Visual and Infrared Mapping Spectrometer (VIMS) was used to look at the distribution of water on the lunar surface (Clark, 2009). First, Clark (2009) post-processed the spectral data obtained in the 0.35  $\mu\text{m}$  to 5  $\mu\text{m}$  range in order to remove the thermal emission component from the observed signal. Clark focused particularly on the 2.7 to 2.9  $\mu\text{m}$  and the 3  $\mu\text{m}$  lines as they could be due to adsorbed water or OH. The 3  $\mu\text{m}$  absorption line is characteristic of either materials with adsorbed water or water ice. In the post-processed data, absorption was shown to be stronger in the south polar region and also north of the Mare Crisium. Because of the location of the observed signature, Clark noted that the signature was probably due to adsorbed water and not ice with a water abundance ranging from 10 to 1000 parts per million (ppm) depending on the assumed model for the lunar soil composition. The 2.7 to 2.9  $\mu\text{m}$  absorption lines are characteristic of OH and showed stronger signatures in the polar regions and to a lesser extent along the lunar terminator. Clark noted that the relatively strong signature at the terminator could be due to either the diurnal cycle or simply to the viewing geometry from Cassini. Finally, Clark compared his observations to the data from the neutron spectrometer onboard Lunar Prospector (Feldman *et al.*, 1998 and 2000). While both datasets showed low water content in the maria regions of the Moon, the VIMS data showed a much more extended water and OH coverage than the Lunar Prospector data. Clark noted, however, that both results were not mutually exclusive because the neutron spectrometer detected large deposits up to 1 m deep and VIMS detected a thin layer up to a few millimeters thick at the lunar surface which would have been invisible to the neutron spectrometer onboard Lunar Prospector.

At the same time Clark (2009) published his findings, Sunshine *et al.* (2009) reported similar results from the fly-bys of the Moon by the Deep Impact spacecraft. Using the HRI-IR spectrometer onboard Deep Impact, Sunshine *et al.* (2009) searched for water in the uppermost layers of the lunar surface at three different times, once in December 2007 and twice in June 2009. On the first fly-by the spacecraft followed a path along the equator while on the later fly-

bys the spectrometer looked down on the northern hemisphere (from 20-60°N) following two paths one crossing the morning terminator and one crossing the evening terminator. Their observations focused on the hydration feature from 2.7 to 3.6  $\mu\text{m}$ . Similar to Clark (2009), the spectral data was post-processed to remove the thermal emission component from the lunar surface. From their analyses, Sunshine *et al.* (2009) found features on the Moon similar to features observed on Mars and on some asteroids consistent with OH and hydrated minerals. All three datasets showed that water or OH was present at all latitudes and that the hydration signatures decreased toward the subsolar point where no hydration was observed. They also noticed that both maria and highlands had similar steady-state hydration levels but that the hydration loss during the transient lunar day was more pronounced in the maria. Also, the most hydrated regions were near the North Pole with a possible water content of 0.3 wt.%. Because the hydration level observed in the evening was similar to the hydration level in the morning, and because of the rapid photo-destruction of water in the atmosphere, Sunshine *et al.* noted that solar wind bombardment of the lunar surface was the most probable source for the observed water.

Pieters *et al.* (2009) used the Moon Mineralogy Mapper ( $\text{M}^3$ ) onboard the Indian lunar orbiter Chandrayaan-1 to detect spectral absorption features of the lunar surface. The  $\text{M}^3$  spectrometer measured visible and near-infrared wavelength reflectance of the solar radiation off the surface. Similar to Clark (2009) and Sunshine *et al.* (2009), the thermal emission component of the spectra, which was as high as 30% of the total reflectance at the subsolar point, was removed. From the post-processed data, they observed global absorptions features at 2.8 to 3.0  $\mu\text{m}$  which are usually associated with the presence of OH or  $\text{H}_2\text{O}$  in silicates. These features were present all around the Moon but were noticeably stronger at higher latitudes and also inside fresh craters (possibly up to 770 ppm depending on the soil model). The observations were repeated over several orbits and, contrary to Sunshine *et al.*'s findings, the time of day did not seem to affect the signal. However, the Pieters *et al.* (2009) conclusions were obtained using only two observations, one in the morning and one in the afternoon. Noting the lack of correlation between the Lunar Prospector data and the  $\text{M}^3$  data, Pieters *et al.* (2009) concluded, similarly to Clark (2009), that their results were due to the presence of solar-wind deposited water in the upper few millimeters of the lunar surface.

### 2.1.2 Modeling

Several authors have modeled the possible means of accumulation of water ice at the lunar poles. The possible sources of water that have been considered are: liberation from the interior of the Moon, solar wind reduction of  $\text{Fe}^{++}$ , cometary, meteorite and micrometeorite impacts. The main losses mechanisms are direct loss after impact (through escape, dissociation or chemical reaction), Jean's escape, photodestruction and Lyman  $\alpha$  radiation. Each group considered some or all of the processes and investigated the possible presence of water ice deposits in cold traps. A summary of some of the major findings is presented in Table 2-2.

Table 2-2 Modeling the possible accumulation of water in lunar cold traps

Authors	Year	Assumed Sources	Main destruction mechanisms
<b>Watson <i>et al.</i></b>	1961	Liberation from the interior of the Moon	Photodestruction, losses from the cold traps
<b>Arnold</b>	1979	Solar wind reduction of $\text{Fe}^{++}$ , meteorites and comets impacts	Photodestruction, losses from the cold traps
<b>Morgan and Shemansky</b>	1991	Micrometeorites and comet impacts	Escape, high temperature dissociation, photodissociation, Lyman $\alpha$ radiation
<b>Hodges</b>	1991	Solar wind reduction of $\text{Fe}^{++}$ , meteorites and comets impacts	Photodestruction, losses from the cold traps
<b>Butler</b>	1997	Solar wind reduction of $\text{Fe}^{++}$ , meteorites and comets impacts	Photodestruction
<b>Berezhnoi and Klumov</b>	1998	Comet impact	Escape, chemical reactions within the temporary atmosphere
<b>Crider and Vondrak</b>	2000	Solar wind bombardment	Photodestruction, ionization
<b>Crider and Vondrak</b>	2002	Solar wind bombardment	Photodestruction, ionization
<b>Crider and Vondrak</b>	2003	Solar wind bombardment	Photodestruction, ionization, Lyman $\alpha$ radiation
<b>Ong <i>et al.</i></b>	2010	Comet and asteroid impact	Escape

The possible presence of trapped water ice at the poles of the Moon was first studied by Watson *et al.* (1961). Their model assumed a uniform source of water at the surface of the Moon, the presence of permanently shaded areas at high latitudes with a temperature low enough to trap water molecules and two main loss mechanisms for the molecules as they travel and accumulate in these cold traps. The main source of water was from liberation from the interior of the Moon and the main destruction mechanisms were photodissociation, and losses from the cold traps. Using the percentage of shaded area inside an equatorial crater as a function of daytime, Watson *et al.* estimated an approximate value for the fraction of the lunar surface that is permanently shaded. They found that about 0.5% of the lunar surface is permanently shaded and that water ice could be present in the lunar cold traps.

Arnold (1979) provided the next thorough study of the possible presence of water on the Moon. With increased knowledge about the Moon from the Apollo missions, his model improved upon that of Watson *et al.* (1961) but mostly provided a confirmation of Watson's findings. Arnold, first, focused more on data characterizing the cold traps. His model was based on a more detailed study of the duration of the trapping period, of the surface area of the traps, and of the heat balance in cold traps. From a study of the Moon orientation over its history Arnold assumed a trapping period of about 2 billion years and by using Lunar Orbiter data he confirmed that approximately 0.5% of the lunar surface is permanently shadowed at the poles. He also assumed that the temperature inside the cold trap depends on geothermal flow, solar wind bombardment, lateral conduction from nearby illuminated regions, and re-radiation. He found that the three first processes are the major ones and that because of the re-radiation term, the diameter of the cold traps must be greater than about 30 m for effective trapping. Because of the extraordinary dryness of the lunar samples brought back from the Apollo missions, the main source of water could no longer be from differentiation of the interior of the Moon. The water was thus assumed to come from solar wind reduction of  $\text{Fe}^{++}$  in the regolith, from meteorites containing  $\text{H}_2\text{O}$  and from comet impacts; each source strength provided about  $10^{16}$ – $10^{17}$  g over the assumed trapping period. The transport of water was calculated using a Monte Carlo approach where molecules hop around the Moon until they are destroyed or trapped. Molecules that hit the sunlit surface are instantaneously re-emitted because of the relatively high surface temperature of 250 to 400 K, while on the night side molecules are trapped at the surface until sunrise. Molecules can be destroyed while in flight or while stuck at the surface. The main destruction mechanisms were photodissociation for in

flight molecules, and solar wind sputtering or chemical decomposition and meteorite impacts for the captured molecules. Arnold concluded that if  $10^{16}$ – $10^{17}$  g of water accumulated on the Moon over 2 billion years, a 2 m deep layer with a 1–10% concentration by weight of water could be found at the cold traps. Finally, he also noticed that after a comet impact, a temporary atmosphere forms with an exosphere far above the surface and therefore ionization and UV radiation should be limited to a thin layer in the upper atmosphere. In this case ice should accumulate rapidly and be partially protected from the destruction mechanisms.

Morgan and Shemansky (1991) wrote the next major paper studying the possible accumulation of water ice at the lunar polar cold traps. The two main sources of water molecules they considered are micrometeorite and cometary impacts. Using assumptions based on impact experiments, they considered that for a micrometeorite impact, at least 25% of the water in the impactor should be lost after impact because of the large impact velocity. First, the early expansion cloud could have temperatures up to  $\sim 5000$  K which would dissociate much of the water present into OH and H. In addition, a large part of the early expansion cloud will have a velocity larger than the Moon's escape velocity. Therefore, most of the material present in the early expansion cloud would be lost after impact. However, most of the meteorite material, including water, is usually found in the late stage vapor cloud so at least 75% of the water should be retained. They assumed that 57.6 g/s of meteoric material impact the Moon and so for a composition similar to the Interplanetary Dust Particles (IDP) composition, i.e. about 5% by mass is water, the source rate for this process was found to be  $0.75 \times 10^{-17}$  g cm<sup>-2</sup> s<sup>-1</sup>. Looking at comet impacts, the average time between impacts is about 13.3 million years with an average incoming comet mass of about  $7 \times 10^{16}$  g. The source rate of water for this process is thus  $2 \times 10^{-16}$  g cm<sup>-2</sup> s<sup>-1</sup>. Again using impact experiments, they estimated that 75% of that water would be lost because the same loss mechanisms involved with micrometeorite impacts will be amplified by the size of the impactor. They also assumed that the requirements for trapping, such as a low enough temperature, are met by about 0.5% of the lunar surface regions that are localized at the poles. By taking into account the geothermal flux, the flux of solar wind protons and the interplanetary Lyman  $\alpha$  radiation they found that the surface temperature will be 26 K. If the re-radiation from nearby sunlit surface is also considered the temperature at which water should still be captured can be as high as 95 K. They also noticed that the limiting loss process inside the cold traps was due to Lyman  $\alpha$  flux from the Local Interstellar Medium (LISM) and had not been accounted for

before. Water molecules exposed on the surface of the cold traps should only have a lifetime of four years, which would prevent water ice accumulation from continuous sources such as micrometeorite impacts. For episodic deposits from comet impact, water ice may be partially preserved through burial as the destruction rate of water ice by Lyman  $\alpha$  radiation is smaller than the creation rate of new regolith. For the comet impact deposition rate, they simply assumed that 1 in 20 molecules reach the cold traps. In the end,  $1.8 \times 10^{15}$  g of water should reach the cold traps due to comet impacts which should cover 1 cm of the estimated permanently shadowed regions.

The same year, Hodges (1991) looked at the possible water ice accumulation from another point of view. Assuming that a total of about  $10^{17}$  g of water was created by reduction of  $\text{Fe}^{++}$  by solar wind hydrogen and that the same amount was deposited by comet and meteorite impacts, he looked at the possible loss mechanisms involved in the transport of the water molecules to the cold traps. By adding infrared radiation from the sunlit crater rims in the heat transfer model to look at the temperature in permanently shaded areas, the estimated cold trap area should be about 0.02% of the lunar surface instead of the 0.5% previously used. Using the previous loss rates in association with this new surface area for the cold traps, the rate of deposition of water could be as large as 30 times the loss rate. Hodges however looked further at the losses of water molecules during their transport to the cold traps and found severe limitations to this deposition to loss ratio. If photodissociation is ignored, given the large number of ballistic steps required for a molecule of water to reach a cold trap, a monolayer of water should be present on the night side of the Moon. However, this is in conflict with the requirements imposed by the large activation energy for Ar derived from the Apollo 17 mass spectrometer measurements. Those data imply that the surface of the regolith must be pristine for Ar to adsorb on the lunar surface at night. Moreover, Hodges calculated that the mean exposure time should be much larger than the photodestruction lifetime so most of the water molecules that reach cold traps will have to be recombined more than 30 times. But the probability of such numerous recombinations is only 0.0076 so most of the water molecules actually reaching the cold traps must be primaries. Hodges concluded from his study that the amount of water ice deposits at the lunar poles should be much lower than previously expected.

Butler (1997) modeled the transport of water molecules at the surface of the Moon to the polar cold traps using a Monte Carlo approach. From previous thermal models, he assumed that the permanently shaded areas at the poles were cold enough to allow for water ice accumulation

and retention for billions of years. In his model, the water molecules originated from comet and meteorite impacts and surface processes and he considered that the molecules were initially uniformly distributed on the lunar surface. Once the water molecules were released from the surface, they hopped around the Moon being acted upon by a variable gravity field. The new molecule location and time-of-flight were both calculated analytically. Each time a molecule hit the surface it was assumed to accommodate to the surface temperature. In his model, the Moon did not rotate and the surface temperature profile was longitudinally averaged varying only with latitude. During the transport process, the water molecules could be destroyed by photoionization, photodissociation, chemical reactions, escape, or solar wind interaction. In his simulations, Butler considered only the dominant loss mechanism, photodestruction, and ignored possible recombination. If a molecule was not destroyed, it continued to hop to a new location and the probability of it being trapped was a function of the fraction of the surface area that was a cold trap in that particular region. Under reasonable lunar conditions for the photodestruction mean time and the fraction of cold traps, Butler found that a range of 20 to 50% of molecules would be captured by the cold traps.

In 1998, Berezhnoi and Klumov considered a comet impact as the possible source for the hydrogen signature detected at the lunar poles by Lunar Prospector. They looked at a given impact event and modeled how much of the cometary water might be captured in a cold trap. They assumed a uniform expansion model with a relatively uniform mixing between the comet material and the excavated regolith. While some of the cometary material is lost due to escape, the remaining material forms an atmosphere. At a given temperature and pressure, the chemical composition of the atmosphere asymptotically freezes and is assumed to remain constant thereafter. Based on this known chemical composition of the atmosphere, they calculated the amount of volatiles that condense inside the lunar cold traps. Their model also assumed that ice deposits inside the cold traps are redistributed by micrometeorite impacts but with their assumptions not much material was lost by that process. From their model, a comet, 2 km in diameter, impacting the Moon would have deposited enough water inside the polar cold traps to account for the Lunar Prospector observations. They also noted that if water were to be present in the lunar cold traps, its origin could be determined by looking at the D/H ratio and also by the possible presence of other compounds present in a comet, such as SO<sub>2</sub> and CO<sub>2</sub>.

Crider and Vondrak (2000) used a Monte Carlo method to investigate the amount of hydrogen that would have reached cold traps over millions of years from solar wind bombardment of the lunar surface. The interaction of incident protons with the regolith can have several outcomes. Protons can be backscattered, hydrogen can be sputtered or desorbed, or the proton can be converted into H<sub>2</sub>, OH or H<sub>2</sub>O. In their simulations, Crider and Vondrak considered the transport of seven species, H, D, H<sub>2</sub>, HD, OH, H<sub>2</sub>O and HOD. The present summary will focus on their results for water. They first assumed that the lunar surface was saturated from solar wind bombardment. Molecules or atoms are uniformly distributed at the surface of the Moon and are released using a Maxwellian velocity distribution based on the local surface temperature. In their model, the surface temperature is a function of the solar zenith angle. The migration model then calculates the analytical trajectory of a particle assuming a collisionless flow. At each hop a particle can be lost to ionization or photodissociation as the by-products are eliminated from the calculation and recombination is thus not taken into account. If a particle lands at a latitude higher than 85° it has a certain probability of being trapped based on the assumed fraction of the surface that is a cold trap. This fraction is based on the estimates from Margot *et al.* (1999) for the cold traps surface area at both lunar poles. From their simulations, Crider and Vondrak found that an average of 4.2% of all the simulated water molecules will reach a cold trap. They noted that this process alone would have provided more than enough water to the permanently shadowed areas throughout the Moon history to account for the quantities of hydrogen observed by the Lunar Prospector orbiter (Feldman *et al.*, 2000). They noted that additional loss mechanisms such as losses from within the cold traps should also be taken into account. Their final remark was that their method would have to be modified in order to simulate the deposition of water after a comet impact because the induced flow is collisional.

In 2002, Crider and Vondrak refined their model by taking into account the probability for each species to be formed from solar wind reaction with the lunar surface. Assuming a saturated lunar surface, incident protons from the solar wind can be backscattered, or can interact with the surface, chemically react with a local atom, or be sputtered or diffused away. In their model, Crider and Vondrak assumed that 1% of the protons were backscattered, 27% were diffused away and the remaining 72% were released after reacting with the regolith. Of all the incident protons, only 1% were assumed to have produced water. Using the same computational approach as the one detailed in their previous paper (Crider and Vondrak, 2000), Crider and



Vondrak tracked the molecules to see how much hydrogen was deposited in the lunar cold traps. From their simulations they found that 0.04% of the incident protons will reach a cold trap as water. They also noticed that most of the hydrogen reaches a cold trap through OH migration and water only accounts for 6.8% of captured hydrogen. Finally, it would have taken 100 million years for the amount of hydrogen detected by Lunar Prospector (Feldman *et al.*, 2000) to accumulate assuming that only water could be retained over geologic time scales inside the cold traps.

In 2003, Crider and Vondrak refined their study by adding loss mechanisms for hydrogen deposited inside the lunar cold traps. The continuous loss of hydrogen from the cold traps can be due to sublimation and diffusion, but it is dominated by the interstellar Lyman  $\alpha$  radiation. In their simulations, the continuous deposition mechanisms are from migration and direct solar wind deposition. In addition to these continuous processes, discrete impact events need to be accounted for as they redistribute the surface material. A 5 m-deep column with the expected composition of the regolith in a cold trap is simulated for 1 billion years. Initially, interstitial hydrogen is uniformly mixed with the regolith, with a hydrogen content of 10 ppm. After 1 billion years, Crider and Vondrak found that a net accumulation of hydrogen, mostly as water, was observed in the uppermost 1.6 m of the column and that the final concentration in this top layer was comparable to the results obtained by Feldman *et al.* (2000) using the Lunar Prospector data. They found a final retention rate of water of 5.6% which is sufficient to account for the expected quantity of water deduced from the Lunar Prospector data.

More recently, Ong *et al.* (2010) used hydrocode simulations to estimate the amount of water deposited on the Moon over 1 billion years due to comet impacts. They simulated several comet impacts using the SAGE hydrocode and used modified equations of state in order to better model water. Their runs were axisymmetric and they impacted a 1 km diameter comet at five different impact velocities ranging from 5 to 60 km/s. The comet and the Moon's surface were made out of pure ice, and basalt, respectively. They assumed a background atmosphere based on the equations of state for solar wind flux. The atmospheric pressure they used was actually about  $10^6$  times larger than the actual pressure at the surface of the Moon but they saw little change in their results when the pressure was increased by three orders of magnitude. In order to estimate how much water is retained on the Moon after impact they used two methods: an outflow boundary and tracer particles. The former method compared the speed of each material within the

cells at the boundary of their domain, 24 km above the surface and 36 km away from the point of impact, to the escape velocity on the Moon. If the materials within the cell have a velocity larger than the escape velocity they are assumed to be lost. In the latter method, at the end of the calculation, they computed which tracer particles had a speed smaller than the escape velocity of the Moon. In order to validate their results, they used the analytical solution provided by Moses *et al.* (1999) to the problem of impact induced vapor plumes on terrestrial bodies. The analytical model assumed a spherically symmetric, well mixed, ideal gas cloud expanding into vacuum. Ong *et al.* ran their simulations up to 25 s after impact and computed how much of the water should remain on the Moon right after impact. Using the outflow method, they found that between 100% of the water (for the 5 km/s impact) to as little as a trace (for the 60 km/s impact) was retained on the Moon right after impact. These outflow results agreed well with the analytical solution even if they noted that the plume they obtained was not as well mixed as was assumed by Moses *et al.* (1999). In their simulations, the expanding plume was initially mostly made of the projectile while the target material was the main component of the later plume. Their results from the tracer particles were inconclusive as they used too few tracer particles in their simulations to resolve the amount of water retained in impacts with a velocity larger than 30 km/s. As their numerical domain extended to only a few tens of kilometers above the surface, they used data from the Butler (1997) and Crider and Vondrak (2003) computations in order to estimate the transport and cold trap losses for the remaining water. Finally, using estimates as to the flux and distribution size of comets that would have impacted the Moon over a one billion year period, they estimated that between  $1.3 \times 10^8$  and  $4.3 \times 10^9$  metric tons of water could have accumulated in the lunar cold traps over that period of time.

The possible presence of water at the lunar poles has been the subject of various remote observations as well as several numerical studies over the years. Unfortunately, no definitive answer as to the presence or absence of water in the lunar cold traps has yet been obtained. Remote observations of the lunar surface have two main limitations. First, some of the results obtained can be due to the presence of water but they can also be due to other phenomena such as surface roughness (Clementine) or other species (Lunar Prospector). Also, remote observations using different detectors have found several different deposits that are not always consistent with previous findings (see the Chandrayaan-1 data versus the Lunar Prospector data). Numerical

simulations have been run in parallel with the observations, to study the possible deposition and retention of water in the lunar cold traps. While possible sources, loss mechanisms, and cold trap capture processes appear fairly well understood, many unknowns remain within each process. Also, comet impact sources have only been crudely modeled and no models have yet followed the cometary water from the time of impact until it is lost or deposited into the lunar cold traps.

## **2.2 IMPACT SIMULATIONS**

Large impact events have left noticeable scars on the planets and moons of our Solar System. Astronomers consider that meteorites have produced the majority of the observed craters but they also believe that comet impact events have occurred throughout history. This idea was confirmed by the recent example of the Shoemaker-Levy 9 (SL9) comet impact on Jupiter in 1994 (Figure 2-1). The SL9 impact has been one of a few major comet impacts ever observed and has renewed interest in the study of such impact events.

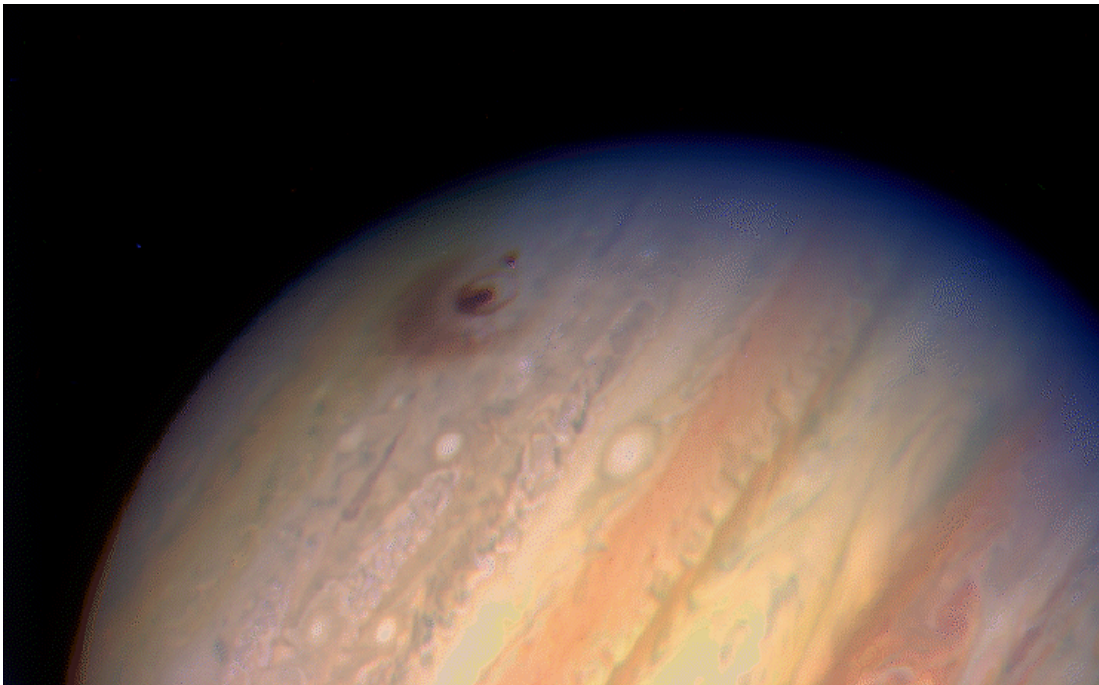


Figure 2-1 Impact site of fragment G of Comet Shoemaker-Levy 9 on Jupiter (Courtesy Hubble Space Telescope Jupiter Imaging Team and NASA)

### 2.2.1 Physics of the Impact Event

Melosh (1989) thoroughly reviewed the physics of the impact event which is similar for both meteorites and comets. The impact event is usually divided into two different stages: the contact and compression phase and the excavation phase. The contact and compression stage starts when the projectile hits the surface of the target. During this stage, the projectile kinetic energy is converted into internal and kinetic energy of both projectile and target. The high-speed projectile pushes material out of its path, compressing and accelerating it, while the target decelerates the projectile. Two shock waves propagate away from each other, one in the target and one in the projectile, mediating the velocity changes, and creating a strongly compressed contact zone between the projectile and the target. Locally, the pressure can reach up to thousands of GPa and jets may be present in these high pressure regions. The superheated vapor jets may be partially ionized and can reach velocities larger than the impact velocity. However, jets usually involve a minor amount of material and are made up of less than 10% of the projectile mass. The average shock pressure usually reaches hundreds of GPa and both impactor and target materials may melt or vaporize in the contact zone. As the shock wave continues to propagate in the projectile, it reaches the rear of the projectile and reflects as a rarefaction wave which travels at the speed of sound in the compressed material. At the same time, the compressed part of the projectile continues to move downward and the projectile coats the growing crater cavity (Figure 2-2a). As the rarefaction wave propagates in the projectile it unloads the material which starts to expand into the crater cavity and begins to move away from the impact site. The contact and compression stage ends when the rarefaction wave has fully unloaded the projectile. This stage usually lasts less than a second in a good sized comet.

During the excavation stage, the shock wave continues to expand into the target while inducing an excavation flow and a vapor plume above the crater. As the shock expands away from the impact site it becomes a hemisphere centered at about one projectile diameter below the surface. This isolated hemispherical shock starts to weaken due to its growing size and to irreversible processes. The shock first becomes a strong stress wave before ending up as an elastic wave carrying only about  $10^{-4}$  of the original impact energy away from the impact site. The mass of melted and vaporized target material is determined by the rate of decline of the shock wave strength and is proportional to the square of the impact velocity. Typically, the mass of melted

material is about ten times the mass of vapor and in the special case of water ice impactors, the impact velocity must be larger than 10 km/s for a significant amount of vaporization of the target to occur. As the shock propagates away from the impact site, the target material behind the shock is set in motion becoming the excavation flow that eventually opens the crater. The excavation stage can last seconds or minutes and at the end of it, about 90% of the kinetic energy of the projectile has been transformed into internal energy of the target.

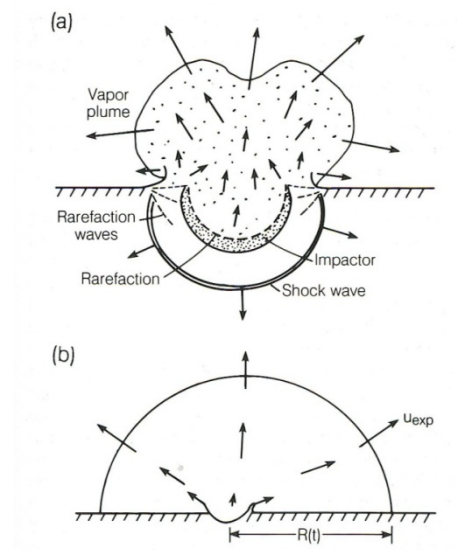


Figure 2-2 a) Early stages of an axisymmetric impact event. Vaporized impactor material start to expand away from the point of impact. The remaining part of the impactor lines the growing crater. The impact induced shock wave continues to propagate inside the target. b) Late stages of the impact event when the expansion plume can be approximated as a growing hemisphere of hot gas. (From Melosh, 1989)

The induced flow of material during the impact event is made of two separate components with noticeably different physics: the excavation flow and the vapor plume expansion. The excavation flow is made of target material and its velocity is usually between one-sixth and one-tenth of the impact velocity. As its maximum velocity decreases rapidly with time and distance away from the impact site, the excavation flow is mostly subsonic and can be considered incompressible. During the excavation phase, the target material moves mostly

outward and upward but the flow initiated below the impact point remains under the initial surface of the target and compresses the rocks under it, creating the expanding crater. The remainder of the excavation flow is ejected from the crater and becomes the ejecta curtain (Figure 2-3). The ejected material usually takes the shape of an inverted cone with its lower edge defining the outer lip of the growing crater. This ejecta curtain is made of fragments of material all shocked at different pressures and encompasses or largely surrounds the vapor plume.

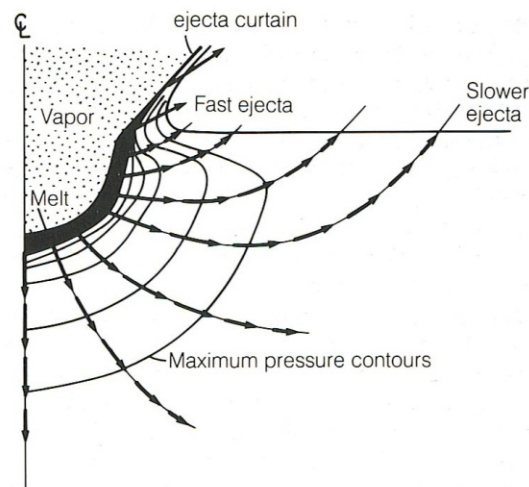


Figure 2-3 Geometry of the excavation flowfield. The shocked target material moves away from the point of impact. Below the original surface, the crater continues to expand while the target material ejected above it forms the ejecta curtain. The ejected target material forms an inverted cone that surrounds the vaporized materials. (From Melosh, 1989)

The vapor plume expansion begins as soon as the rarefaction wave unloads the rear of the projectile. If the unloaded material is in vapor phase, as is the case for high velocity comet impacts, a complex gas mixture begins to expand upward and outward at high speed. The initial part of the plume mostly originates from an annulus surrounding the projectile and is therefore made of both projectile and target material. In addition, each component of the plume has been shocked to different pressures, depending on its original location, thus providing a gas mixture with non-uniform initial temperatures. Also, initially, some material moves inward toward the crater center because the rear of the projectile has not yet started to expand creating a low

pressure region above the crater center. Once the vapor plume has expanded to several times the projectile diameter the flow can be approximated as an expanding hemisphere of hot gas (Figure 2-2b). Using this approximation, some analytic solutions, such as Zel'dovich and Raizer (1967), have been used to study the late stages of the expansion plume. In these models, the gas is usually defined as a perfect gas with a constant ratio of specific heats with some fixed simple initial pressure and density distribution. The analytic results provide some useful information as to the general trends observed in the expansion plumes. For instance, the analytic solutions show that the plume continues to accelerate as it expands into the vacuum. Also, the edge of the plume can move at about three times the mean gas velocity and for high velocity impacts the mean velocity of the gas can reach 10 km/s. Yet, these analytic solutions are only a very simplified version of the actual expansion plume and several physical phenomena such as the unsteadiness of the flow, the presence of solid and liquid particles and the effects of condensation are readily ignored.

The physics involved during a large hypervelocity impact event do not depend on the impact parameters such as impactor size, density, velocity and angle of impact. However, the resulting crater, deposition patterns and expansion plume are constrained by the impact parameters and are, in particular, highly variable with angle of impact. In reality vertical impacts are very unlikely. Shoemaker (1962) was the first to show that the probability for an impactor to hit a spherical target with a gravitational field at an angle between  $\alpha$  and  $\alpha+d\alpha$  is proportional to  $\sin(\alpha)\cos(\alpha)d\alpha$ , where  $\alpha$  is measured from the target surface (Figure 2-4).

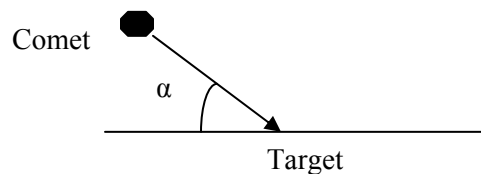


Figure 2-4 Definition of the angle of impact  $\alpha$ . A vertical impact is defined by  $\alpha = 90^\circ$  and a grazing impact is defined by  $\alpha < \alpha_0$  where  $\alpha_0$  is between 5 and 10°.

Therefore, the most probable angle of incidence for an impact is  $45^\circ$  and vertical and grazing impacts are uncommon. Several differences have been observed between oblique and vertical impacts. First, the crater is generally smaller for a given impactor mass and velocity as the angle of impact decreases. Also, while both vertical and oblique impacts can produce nearly circular craters for most impact velocities, the ejecta blankets are very dissimilar. In oblique impacts, a bilateral symmetry likened to a butterfly wing pattern can be observed. Furthermore, the expansion plume proceeds downrange of the impact point as the projectile preserves part of its horizontal component. Finally, in the extreme case of a very grazing impact, the crater formed may be elliptical and the projectile may even ricochet several times after the initial impact.

### **2.2.2 Impact Event Simulations**

For several decades, impact events could only be studied through studies of nuclear explosions, observations of craters on the surface of the Earth and other planets and more importantly experiments. Unfortunately, all of these approaches could only provide a partial understanding of impact events. First, the scale of nuclear explosions differs too much from that of possible meteorite and comet impacts. Then, the observation of already formed craters can not provide complete insight into the physics of the impact and, in particular, into the fate of the vapor plume. While experiments are important to understand the impact event itself, their results still have a limited scope. High velocity impacts have only successfully been reproduced in the lab since the 1950s and even now, experimental impact velocities can only be up to several km/s. In addition, because the results obtained are for very small scales, the findings can be hard to expand to planetary size impacts. For instance, the effect of gravity on crater formation cannot be deduced from small scale experiments. With the advances in computing power, a new complementary approach has been using numerical simulations to model impact events.

In 2004, Pierazzo and Collins provided an overview of hydrocode modeling of impact events. Hydrodynamic computer codes, or hydrocodes, have been used to simulate the first few seconds after an impact event to examine the surface deformation and gas release into the atmosphere. Hydrocodes model the shock waves produced during the impact as well as the induced changes in both target and impactor materials. To do so, a hydrocode combines three required models: the hydrodynamic equations, the equations of state and a constitutive model.



The hydrodynamic equations govern the flowfield and describe the conservation of mass, momentum and energy. The equations of state and the constitutive model represent all of the different materials involved and their response to pressure and stress.

For the simulations, a relatively small domain, a few tens of kilometers in each direction, is initially divided into a mesh of cells and the flow within this domain is solved as a function of time. Usually, the spatial and temporal resolutions are constrained by the Courant-Friedrichs-Lewy stability condition for numerical convergence. However, in order to obtain a stable solution even in the presence of shock waves an artificial viscosity must also be added to the numerical solution. For 2D and 3D simulations, the computational cost of a run scales as  $N^3$  and  $N^4$ , respectively, where  $N$  is the number of cells in one direction. For that reason, 2D simulations assuming axial symmetry are currently the most commonly used. Hydrocodes can usually be divided into two categories based upon the method used to solve the governing equations of the flow: Eulerian or Lagrangian based hydrocodes. In the Eulerian approach, materials flow through a mesh fixed in space which prevents the code from exactly representing the free surfaces and contact surfaces. For that reason, the mesh needs to be fine enough to resolve the interfaces accurately, therefore increasing the computational cost of a simulation. In the Lagrangian approach, the grid moves with the material so the free surfaces and contact surfaces are exactly represented. However, as material starts to expand, the Lagrangian grid starts to deform and can become inaccurate. This problem is usually resolved by regridding the domain as the run progresses which can again increase the computational cost of a simulation.

The equations of state and the constitutive model represent the response of the materials involved to stress. The equations of state are critical in the modeling of the early stages of the impact when the main component of stress is pressure. The equation of state relates the change in density and internal energy due to pressure, or volumetric stress. The equation is unique for each material and while simple for most gases can become more complex for solids and liquids. The first equations of state used in hydrocodes were analytical equations. Tillotson's equations of state are the most widely used for impact studies but they have severe limitations (Pierazzo and Collins, 2004). They do not provide any information on how to compute the temperature and they cannot compute melting and vaporization. A more recent approach has been to use computer codes to calculate the equations of state for each material. For instance, the ANEOS code relates

the pressure, density and temperature in a thermodynamically consistent way (Pierazzo and Collins, 2004). Such codes have the advantage of treating phase changes but one of their major limitations is that they treat all gases as monatomic or diatomic species. In order to speed-up the calculations, most hydrocodes use tabulated data, such as SESAME, derived from the equations of state codes (Pierazzo and Collins, 2004). While the equations of state are most important during the early stages of the impact, the constitutive model is fundamental to the modeling of the late stages of the impact. The final characteristics of an impact crater are highly dependent upon the constitutive model of the materials. This model links the strain or deformation of a material to the deviatoric stress. For many simple cases, simple models have been developed to represent the response of a material to shear, such as perfectly elastic model, Newtonian fluid model or perfectly plastic model. However, in the case of an impact event a more complex model must be constructed in order to get a better representation of the deformation of the materials. For instance, rocks are often represented as plastic materials whose yield strength depends on pressure. Using this model, permanent deformation of the rock occurs once it has been subjected to a stress larger than the yield strength. For most hydrocode simulations, the yield strength depends on depth, temperature and fragmentation of the material. Two of the main hydrocodes currently being used are CTH (McGlaun *et al.*, 1990) and SOVA (Shuvalov, 1999). CTH and SOVA are both Eulerian based hydrocodes.

Hydrocodes have been used to investigate several specific aspects of impact events. In 1999, Pierazzo and Melosh used the CTH hydrocode to study the effect of angle of impact on the production of melt and vapor by modeling the Chicxulub impact event. The Chicxulub structure in the Yucatan peninsula is one possible explanation for the mass extinction of the dinosaurs roughly 65 million years ago. Pierazzo and Melosh used the 3D version of the CTH hydrocode with bilateral symmetry for all their simulations. They divided the domain into 15 million cells and used 1000 mass-less tracer particles to track the thermodynamic history of given material points and the amount of melted/vaporized materials. The CTH hydrocode solves the equations of hydrodynamic flow in finite difference form using a 2-step Eulerian scheme. For all of their simulations, Pierazzo and Melosh used the SESAME tabular equations of state and they had no constitutive model for either impactor or target. The lithology of the target was assumed to be made of successive layers of sea water, sedimentary deposits, continental crust and mantle. The

impactor was a dunite asteroid 10 km in diameter hitting the surface at 20 km/s. The simulations were started with the impactor right above the surface. The simulations were stopped 5s after initial contact which is not long enough to describe the evolution of the vapor plume and the fate of the projectile. Five different angles of impact,  $\alpha$ , were used in their parametric study: 90°, 60°, 45°, 30°, and 15°. Pierazzo and Melosh found that the region of melting becomes shallower and shifts downrange as the angle of impact decreases. The amount of gas released from the sedimentary layer increases as the angle of impact,  $\alpha$ , decreases to 30° but almost no gas is released in the 15° case as the peak shock pressures are then too low to vaporize any material. However, they noted that the addition of a “strength model” to their simulations could change this result because at low impact angles shear heating might greatly increase the amount of melted and vaporized material. Finally, the amount of projectile material entrained in the vapor plume during the early phases of the impact increases as the angle of impact decreases. No projectile material is present in the vapor plume 5 s after impact for the vertical impact case as compared to more than 50% of the projectile for the 15° case.

In 2000, Pierazzo and Melosh (2000a) revisited their results from the 3D simulations of the Chicxulub impact event (Pierazzo and Melosh, 1999). Their objectives were to constrain the effect of angle of impact on the production of melt in impact events using general laws. In particular, they quantified the decrease in melt production with the decrease in angle of impact. As noted before (Pierazzo and Melosh, 1999), the region of melted material becomes shallower and moves downrange of the impact point as the angle of impact decreases (Figure 2-5). They found that the melt volume decrease by 20%, 50% and 90% from vertical impact to 45°, 30°, 15° impacts, respectively.

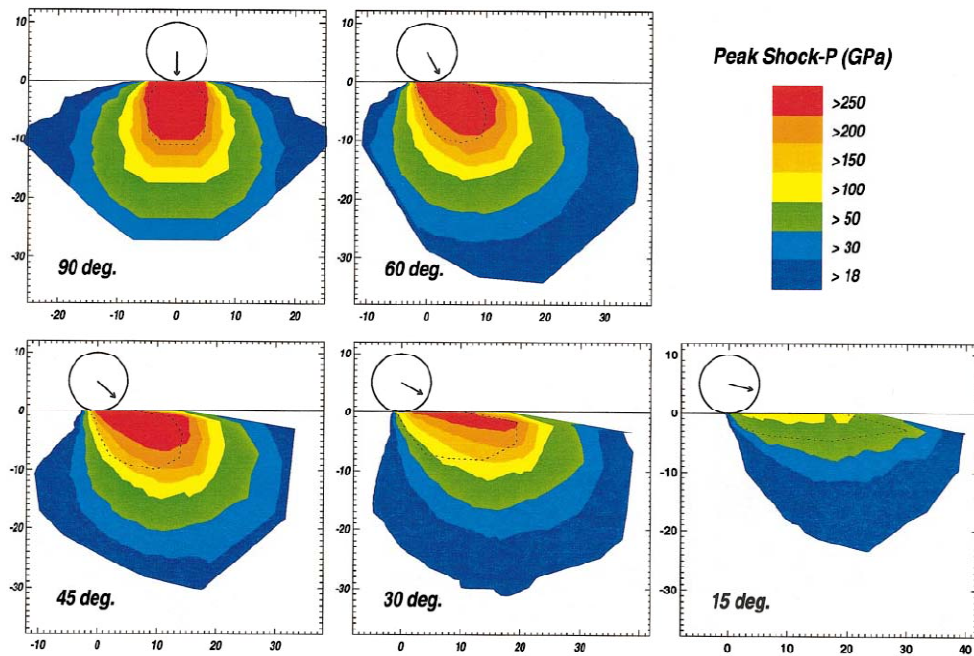


Figure 2-5 Peak shock pressure contours in the plane of symmetry of the Chicxulub impact event for impact angles,  $\alpha$ , of: 90°, 60°, 45°, 30°, and 15°. An impactor 10 km in diameter is drawn for scale with the direction of impact being given by the vectors from the center of the projectile. The shock pressures chosen cover the range of shock melting for most of the materials of geologic interest. At 18 GPa, 50% of water initially at ambient temperatures vaporizes. Rocks typically melt for shock pressures between 30 to 150 GPa. At 250 GPa, most geologic materials will have vaporized and iron melts. (From Pierazzo and Melosh, 2000a)

The same year, Pierazzo and Melosh (2000b) investigated the fate of the projectile after an oblique impact using their previous simulations of the Chicxulub impact (Pierazzo and Melosh, 1999). The fate of the projectile during and after impact is important to study the release of gases into the atmosphere and also to investigate the possible survival of organic material during an impact event. Using Lagrangian tracers inside the projectile, Pierazzo and Melosh observed that different parts of the projectile were subject to different conditions leading to widely ranging final states. The leading half of the projectile experiences the highest pressures and temperatures but mostly remains inside the expanding crater during the early phases of the impact. On the other hand, the rear half of the projectile is subject to lower pressures and temperatures and is ejected from the crater earlier with the exception of angles of impact of 60°

and  $90^\circ$ . Similar to the target material, the amount of melted and vaporized material decreases as the angle of impact decreases and becomes more localized to the leading half of the projectile. For a dense dunite projectile, the maximum amount of vaporization is obtained for angles of impact of  $60^\circ$  and  $90^\circ$  but only accounts for up to 30% of projectile material. At these large angles, the remaining part of the projectile is melted. At smaller angles, some of the projectile remains in the solid phase and the fraction of vaporized material decreases even further. From these results, Pierazzo and Melosh interpolated the results that would be obtained for different projectiles. For porous dunite, material representative of most stony asteroids, most of the projectile would melt even at low angles of impacts. Iron asteroids would mostly remain in the solid phase and no vaporization should occur. Finally, for comets, almost complete vaporization should be observed as ice is vaporized when subject to shock pressure smaller than 100 GPa. In addition to changing the amount of melt and vapor observed in the projectile, the angle of impact also influences where the projectile ends up. As the angle of impact decreases, material moves preferentially in the downrange direction. For very oblique impacts,  $\alpha = 15^\circ$  or  $30^\circ$ , a large amount of material moves downrange and upward at velocities larger than the escape velocity of the Earth. For larger angles of impact,  $\alpha = 45^\circ$ , the downrange velocity of the material is significant so most of the projectile is ejected out of the crater. For angles of impact,  $\alpha \geq 60^\circ$ , most of the projectile remains inside the crater during the first few seconds after impact.

The current simulations use the output from SOVA simulations run by Dr. E. Pierazzo at the Planetary Science Institute so this code will be described in more detail in the present section. The SOVA hydrocode simulates an impact event using a two-step Eulerian scheme to solve the equations of hydrodynamic flow in finite volume form (Shuvalov, 1999). The first step is a Lagrangian step during which the cells distort to follow the motion of the materials. The finite volume approximation used for the simulations conserves mass, momentum and energy. During this step, the otherwise discontinuous shock waves are modeled by adding a quadratic artificial viscosity to the previous equations. During the second step, or remesh, step, the distorted cells are mapped back to the initial Eulerian grid. Again, all the physical quantities are conserved during this step. In addition to the macroscopic data such as density, velocity, and temperature obtained with the Eulerian solver, the time evolution of each material point is followed by Lagrangian tracers initially distributed in both the target and the impactor.

In 2008, using the SOVA hydrocode, Artemieva and Shuvalov simulated the possible mass loss that the Moon may have experienced throughout its history due to meteorite and comet impacts. During a high-velocity impact, part of the target and of the impactor will have velocities larger than the escape velocity of the Moon thus possibly decreasing its overall mass. Using the 3D version of the SOVA hydrocode, they studied the high-velocity impacts of stony and icy bodies for angles of impact between  $15^\circ$  and  $90^\circ$ . Because most of the high velocity material is ejected during the early phases of the impact, they neglected both material strength and gravity in their simulations. Using these assumptions, the mass of the high-velocity ejecta can directly be scaled to the projectile mass. Jupiter-family comets can eject as much as 3.5 times the impactor mass for angles of impact larger than  $45^\circ$ . For low angles impacts, the ejected mass is less than twice the impactor mass. Moreover, as the angle of impact decreases, the portion of the projectile material lost due to escape increases from about 70% to nearly 100%. In the case of parabolic comets, as much as 10 to 12 times the impactor mass may be ejected during the impact. Asteroid impacts can eject as much as 4 times the impactor mass for angles of impact between  $30^\circ$  and  $60^\circ$ . However, in the case of asteroid impacts, the minimum ejected mass is obtained for vertical impacts, for which the mass of the ejecta is less than the impactor mass. Using several assumptions for the incoming impactor flux to the Moon, Artemieva and Shuvalov concluded that the Moon should have lost one hundredth of a percent of its mass throughout its history.

### 2.3 THE DSMC METHOD

For most engineering applications, gas flows can be modeled by the Navier-Stokes equations. However, when the mean free path of the gas becomes of the order of some representative length scale of the problem, the continuum assumption breaks down and the flow has to be represented by the Boltzmann equation. Two main categories of problems fall under these conditions: flows under atmospheric conditions inside small devices and rarefied gas flows. Unfortunately, the Boltzmann equation cannot generally be solved analytically due to the large number of unknowns and the difficulty of modeling the collision integral (especially for inelastic collisions). Therefore a molecular computational approach, such as the DSMC method (Bird, 1994), is generally chosen to solve non-continuum flows (Kannenberg and Boyd, 1999, Ngalande *et al.*, 2006 and Moss *et al.*, 2006). In actuality, the DSMC method solves the Boltzmann equation when a large number of representative molecules is used (Nanbu, 1986). The DSMC

method is capable of solving gas flow in any regime from continuum to transitional to rarefied to free-molecular and can also be applied to non-engineering applications, such as low density atmospheric flows. Due to computational cost considerations, the DSMC method has generally been used for transitional and rarefied flows. Nonetheless, the range of applications of the DSMC method is continuously being expanded to different flow regimes through the use of parallel and/or hybrid computing methods due to the method's robust ability to include complex molecular interactions. The DSMC method is described in more detail in Chapter 3.

### **2.3.1 Planetary Atmosphere Applications**

The DSMC method has been mostly developed for engineering applications, but it is also well suited for rarefied planetary scale problems when the atmospheric density is sufficiently low. In particular, the rarefied atmosphere on Jupiter's moon Io has been thoroughly studied over the years using the DSMC method first by Austin and Goldstein (2000) then later by Zhang *et al.* (2003, 2004) and more recently by Walker *et al.* (2009). The low density atmospheric flow on Io is believed to be sustained by two main sources: via sublimation of SO<sub>2</sub> from surface frost patches and from both continuous and sporadic volcanic eruptions.

In 2000, Austin and Goldstein studied the physics of the sublimation-driven SO<sub>2</sub> atmosphere on Io. The sublimation rate of SO<sub>2</sub> is highly variable within the temperature range observed on the surface of Io, producing supersonic winds moving from the dayside to the nightside of Io. As SO<sub>2</sub> sublimates from frozen deposits on the dayside, the gas begins to flow away from the high density regions until it reaches the nightside where it condenses. Austin and Goldstein simulated the sublimation driven supersonic flow inside a 2D axisymmetric cylindrical domain where the axis of symmetry was located at the subsolar point and where Io's surface was uniformly covered by a layer of SO<sub>2</sub> frost. In order to better model the gas flow conditions on Io, Austin and Goldstein added several physical mechanisms to their model, such as plasma heating, non-Local Thermodynamic Equilibrium (non-LTE) cooling by SO<sub>2</sub> rotational modes and a constant gravity field. Also, in order to simulate the large computational domain, Austin and Goldstein used variable weighting factors, an exponential grid in the vertical direction, and implemented a multi-grid sequential approach. They found that a strong atmospheric discontinuity can be observed near the terminator. The discontinuity is in the form of an oblique

curved shock near the surface and a hydraulic jump at high altitude. From their parametric study, they found that the strength and location of the shock depend on the assumed subsolar temperature. They also noticed that plasma heating and non-LTE cooling inflate the atmosphere while the presence of a non-condensable species prevents the expansion of SO<sub>2</sub> into the night side.

Expanding on Austin and Goldstein's work (2000), Zhang *et al.* (2003, 2004) studied Io's volcanic plumes and their interaction with Io's sublimation atmosphere. In their 2D axisymmetric calculations, SO<sub>2</sub> molecules were ejected from a hot, circular volcanic vent and sublimated from the surrounding frost covered surface after which they moved under a spatially varying gravity field. The collisions were computed using the Variable Hard Sphere (VHS) model. During a collision, energy exchange between translation and rotation or vibration was modeled using the standard and discrete Larsen-Borgnakke methods, respectively (Larsen and Borgnakke, 1974, Bergemann and Boyd, 1994). Zhang *et al.* (2003) also simulated radiative cooling of the gas from both rotational modes and discrete vibrational bands of SO<sub>2</sub>. In order to resolve the radiation features of the plume core accurately, they used a sequential multi-domain approach. This approach enabled them to use separate grids and timesteps in each domain but is only valid as long as the flow is supersonic.

In 2004, Zhang *et al.* studied the influence of particulates within the volcanic plumes. They assumed that the particles would not modify the gas flow for mass loading of particles much lower than the gas density. In order to simulate the presence of nano and micron-sized particles inside the plume they used two separate overlay methods. The first method they used for the smallest particle was a collision model where the particles are modeled as very large gas molecules. In the second method, the drag model, a frozen gas flowfield is used to calculate the drag acting on the particles. They then compared their results to shock height, deposition ring radius, brightness, and shadow observations of both Prometheus and Pele plumes.

### **2.3.2 Parallel Implementation**

Generally, accurate DSMC simulations require a large number of representative molecules ( $>10^6$ ) to be present inside a spatially resolved domain. Unfortunately, such



simulations are typically computationally expensive, especially for 3D problems. One obvious way to speed-up a simulation is to run it on a cluster of workstations or on a high performance computing system. To do so a parallel implementation of the DSMC solver has to be developed. Fortunately, the DSMC method is well suited to parallelization because the representative molecules only interact (through collisions) with other molecules in their cell. Therefore, a parallel implementation of the DSMC method only requires a decomposition of the physical domain between the processors. Once the computational domain is distributed among the processors, each processor creates, moves, and collides its own set of molecules. The communications between the processors are therefore limited to the transfer of representative molecules that cross a processor boundary and to the I/O functions. In order to obtain the most efficient implementation, the number of communications has to be kept to a minimum and the work load throughout the computation has to be evenly distributed among the processors.

In 1996, Dietrich and Boyd modified their DSMC code, MONACO, into a parallel version that could run on workstation clusters using the Message Passing Library (MPL). In doing so, they tried to limit the number of communications between processors. When a molecule crosses a processor boundary, the molecular data as well as the difference between the timestep and the time it took to reach the processor boundary are saved into a temporary array. Then, once the move step is done, all of the crossing molecules are sent to the appropriate processors in one global communication. Once the molecules are received by their destination processor, they are moved by their time remaining in the timestep. Because some molecules may cross several processors boundaries in one timestep this process is repeated until no more molecules exit the processor they were in. Dietrich and Boyd tested their implementation on three different problems: a diverging nozzle flow, a reentry planetary probe, and the flow in a neutral contactor. All of their results agreed well with both regular DSMC simulations and experiments. For each problem, Dietrich and Boyd distributed strips of cells aligned with the flow direction between the processors. By re-optimizing this domain decomposition as the run progresses, Dietrich and Boyd were able to obtain a parallel efficiency of about 90% where the parallel efficiency was defined as the ratio of computation time to the sum of computation and communication time. Dietrich and Boyd also noted that this large parallel efficiency could only be achieved if the problem size is scaled with the number of processors. For a constant problem size, as the number of processor

increases, the number of particles per processor decreases, in turn degrading the parallel efficiency for the problem.

LeBeau's Distributed DSMC Analysis Code (DDAC) (1999) is another example of a parallel implementation of the DSMC method. The DDAC solver uses the Message Passing Interface (MPI) implementation to run on distributed memory systems. In his simulations, one master processor oversees the I/O for the simulation while the DSMC algorithm is run by several slave processors. This implementation is not the most efficient because the I/O part of the simulation is not parallel but it ensures portability to systems where the slave processors have no access to disk space. Similar to Dietrich and Boyd (1996), LeBeau implemented dynamic domain decomposition for better load balancing. Molecules that cross processor boundaries are sent with their remaining timestep in one communication to the appropriate location and this process is repeated until all the molecules have been moved by a full timestep. LeBeau verified the efficiency of the DDAC implementation for uniform flow past a sphere with up to 512 processors using a fixed problem size. He considered two indicators to validate his parallel implementation: speed-up and parallel efficiency. The speed-up was computed as the ratio of the wall-clock time required by the scalar DAC code to that required by the DDAC code, while the parallel efficiency was defined as the ratio of the speed-up to the number of processors. First, LeBeau used a uniform grid for the simulations with and without dynamic domain decomposition. In these two cases, he found an overhead of 12% for DDAC over the serial DAC and observed a near linear speed-up of the simulations when the number of processors was increased. The parallel efficiency dropped rapidly for the static domain decomposition case but remained near constant for the dynamic domain decomposition case as the number of processors was increased. LeBeau then ran a slightly larger problem using an adapted grid with no fewer than 8 processors. For an adapted grid, both static and dynamic domain decompositions experienced a super-linear speed-up up to 128 processors. However, LeBeau noted that the good results obtained for the static domain decomposition cases can be explained by the relative simplicity of the flow. Finally, LeBeau simulated the X-38 reentry flow using a 5 species model inside an adapted Cartesian grid with up to 512 processors. For this complex problem no fewer than 64 processors were used and, as the number of processors was increased, the dynamic domain decomposition cases had much better parallel efficiency than the static cases.

More recently, Wu and Tseng (2005) presented their parallel implementation of the DSMC method with particular emphasis on their dynamic domain decomposition approach. Similarly to LeBeau (1999), Wu and Tseng used the MPI implementation for their parallel code. They also limited the number of communications between processors by grouping the molecules that are to be transferred into one global communication. Up to two transfer operations were computed at each timestep which Wu and Tseng assumed sufficient, for most simulations, for all molecules to have reached their final destination processor. Wu and Tseng noted that the use of a static domain decomposition is not optimal, especially for transient flow problems. They implemented a repartitioning tool that would periodically remap the domain as the run progressed so that near optimal load balancing could be achieved. At the end of the timestep, the domain may be remapped depending on the difference between the total idle time of all the processors and the computational cost of repartitioning. First, Wu and Tseng tested their implementation on a 2D cavity driven flow using up to 64 processors. Three different problem sizes were considered: a small case with 225,000 molecules, a medium case with 900,000 molecules and a large case with 3.6 million molecules. In all three cases, the simulations using dynamic domain decomposition were appreciably faster than the simulations using static domain decomposition. For the small problem size, Wu and Tseng observed a degradation of the parallel efficiency as the number of processors was increased, similar to Dietrich and Boyd's findings (1996). They also noted that the optimal frequency for repartitioning increased with increasing the problem size.

### **2.3.3 Hybrid Implementations**

The DSMC method can solve gas flows in any regime, from continuum to free-molecular, but due to its computational efficiency the method is mostly used to solve transitional-to-rarefied flows. Unfortunately, some flows of interest can have both continuum and non-equilibrium regions. For instance, hypersonic flows around reentry vehicles usually are mostly continuum, at lower altitudes, except in a few regions near the bow shock, inside the boundary layer and in the recirculation wake. Similarly, expansion flows in a low density environment are generally composed of three main components: a continuum core, a non-equilibrium region within the boundary layer and a rarefied expansion region. These complex flows cannot usually be accurately represented by a continuum solver and DSMC simulations can prove prohibitively expensive. For these problems, a hybrid method, where the continuum regions of the flow are

solved using a continuum solver and the non-equilibrium regions are simulated using the DSMC method, is most appropriate. Such hybrid methods have been used to simulate complex expansion and nozzle flows into a rarefied environment (Roveda *et al.*, 2000, Vashchenkov *et al.*, 2005 and VanGilder *et al.*, 2007) as well as hypersonic flows around reentry vehicles (Schwartzentruber *et al.*, 2008 and Burt and Boyd, 2009). The main issues related to hybrid methods are the mode of coupling (unidirectional or fully coupled), the mode of transfer (flux based or state based), and the positioning of the interface (static or moving).

In 2000, Roveda *et al.* implemented one of the first fully coupled hybrid methods and applied it to 2D, unsteady, pressure-driven slit flow impinging on a plate parallel to the slit. In order to obtain the best computational savings, the majority of the domain was simulated using the continuum solver and only a few small embedded regions were solved using the DSMC method. In their approach, the continuum regions of the flow were solved using the adaptive discrete velocity (ADV) scheme, an Euler solver (Nagida, 1995). The non-equilibrium flow regions were determined using three different breakdown parameters: the gradient-length Knudsen number for density, Bird's breakdown parameter, and the normalized local density gradient. The location of the interface between the continuum and non-equilibrium regions was updated at regular intervals as the flow evolves during the calculation but always comprised the boundary layers of the target plate and the slit walls. Also, in order to limit the amount of information to be transferred from one region to the other, a low pass filter was applied to the breakdown parameter contours in order to limit the effect of noise on the number of DSMC patches.

Roveda *et al.*'s hybrid method was fully coupled so information was transferred from either region to the other. The interface itself was an overlap region of DSMC reservoir cells, which transmit the information from the ADV domain to the DSMC domain, and ADV buffer cells, which transmit the information from the DSMC domain to the ADV domain. The coupling from the ADV domain to the DSMC domain used 2 reservoir cells to create the representative molecules that entered the DSMC domain based on the ADV thermodynamic properties. All of the representative molecules that did not exit the reservoir cells at the end of the current timestep were deleted.

The major issue involved in the data transfer from the DSMC domain to the ADV domain, was the statistical scatter in the unsteady DSMC macroscopic data. In order to decrease the noise level in the DSMC solution at the interface, Roveda *et al.* used ghost cells. At the interface, the DSMC cells were duplicated into ghost cells that contain clones of the DSMC particles present at the interface. The DSMC algorithm was then applied to each of the ghost cells creating independent samples that were ensemble averaged to reduce the noise in the macroscopic data transferred into the ADV domain.

In their simulations, a high pressure nitrogen gas was initially separated from a low density region by a diaphragm. At time  $t = 0$ , the diaphragm was removed and a supersonic jet expands through the slit. Roveda *et al.* found that the interaction of this jet with a downstream target plate resulted in a highly unsteady flow consisting of several complex structures such as a normal shock wave, a bow shock, a barrel-type structure downstream of the slit, and counter-rotating vortices emerging from the ends of the plate.

More recently, Vashchenkov *et al.* (2005) used a unidirectional sequential coupling between a Navier-Stokes solver and a DSMC solver to simulate supersonic plumes expanding into vacuum. First, Vashchenkov *et al.* simulated the high density part of the plume using a 2D axisymmetric Navier-Stokes solver with velocity slip and temperature jump at the walls. These continuum results were then used as input to their DSMC simulations using a Maxwellian distribution for their velocities. The DSMC solution did not feed back into the Navier-Stokes solver as the flow was supersonic at the interface between the two codes. Their hybrid simulations were in good agreement with previous experiments.

In 2007, VanGilder *et al.* simulated rocket and missile exhaust plumes using a unidirectional hybrid Navier-Stokes–DSMC solver. First, the fixed interface between the two solvers is located based on the value of Bird’s breakdown parameter as calculated by the Navier-Stokes solver. This approach generally provided them with a very complex interface so VanGilder *et al.* implemented a preprocessing tool that enabled them to create a smooth continuous interface between both continuum and non-equilibrium regions of the flow. Once the interface was determined, the continuum flow results were interpolated onto the DSMC inflow surfaces. In their simulations, the exhaust plumes were unsteady; therefore, VanGilder *et al.* used

ensemble averaging in the DSMC domain in order to reduce the statistical scatter. VanGilder *et al.* compared their solutions to other simulations for axisymmetric and low angle of attack missiles. For the axisymmetric case, the hybrid solution agreed well with the other simulations. For the low angle of attack case, the unidirectional coupling of the Navier-Stokes and DSMC solvers provided an acceptable solution for the far field even if it did not provide a very accurate solution in the near field.

In 2008, Schwartzentruber *et al.* implemented a fully coupled hybrid method to solve steady-state hypersonic flows and applied it to the 2D steady flow of nitrogen over a cylinder at Mach 3, 6 and 12. With a global Knudsen number of 0.01, such hypersonic flows are in the continuum regime in most of the domain with the exception of the bow shock (thermal non-equilibrium), the boundary layers (velocity slip and temperature jump), and the recirculation wake (rarefied conditions). The continuum regions of the flow were simulated using a Navier-Stokes solver, while the non-equilibrium regions were solved using the DSMC method. The breakdown parameter used to locate the interface between the two regions took into account both the values of the gradient-length Knudsen numbers for density, temperature and speed as well as the degree of thermal non-equilibrium of the gas (only within the DSMC region). Initially, a full Navier-Stokes simulation of the flow was used to calculate the value of the breakdown parameter. Once the initial non-equilibrium regions were flagged, an interface made of overlapping cells was created in order to transfer data from either region to the other. At this interface, information from the continuum region is transferred to the DSMC solver using a reservoir method (Roveda *et al.*, 2000). The molecular velocities are drawn from a Chapman-Enskog velocity distribution which agrees with the Navier-Stokes solution in the continuum regions. On the other side, temporal and spatial averages of the DSMC quantities were used to obtain the state properties at the boundaries of the continuum region. The interface between both regions was then allowed to move as the simulation proceeded. Once the interface location stopped changing, the interface was locked in place, the DSMC region was sampled and the continuum region was converged while information is still transferred from each region to the other. From their simulations, Schwartzentruber *et al.* found that the regions of non-equilibrium increased with Mach number. Overall, their solutions were in good agreement with full DSMC simulations. Finally, noticeable speed-ups, between 1.4

to 2.8 times faster, were observed in the hybrid simulations as compared to the full DSMC simulations.

Even more recently, Burt and Boyd (2009) implemented a hybrid particle method and simulated a Mach 6 hypersonic flow over a cylinder as well as a rarefied expansion flow. Most common hybrid methods couple a CFD solver with a DSMC code; however, hybrid schemes have some limitations due to the complexity of using two independent methods. An alternate approach is to use all-particle hybrid methods where a particle method is also used to solve the continuum regions of the flow. Unfortunately, such methods generally have large numerical diffusion errors on the scale of the cell size in the equilibrium regions of the flow. In order to circumvent this problem, Burt and Boyd (2009) used a modified particle method, the Low Diffusion (LD) method, to solve the regions of the flow in the continuum regime. The LD particle method was implemented such that the LD representative molecules mostly follow the streamlines of the flow by limiting their thermal motion. To do so, each Eulerian cell, used for sampling, was overlapped with a Lagrangian cell that deformed during each timestep. Burt and Boyd calculated the motion of each cell face based on the average value of the bulk velocity of the surrounding cells using kinetic theory. LD molecules were moved such that they kept a constant relative position within the Lagrangian cell. In addition to the Lagrangian cells, the LD scheme differs from the regular DSMC solver by the fact that the LD molecules had additional temperature and bulk velocity compared to regular DSMC molecules. In their hybrid method, Burt and Boyd located the interface using two Knudsen numbers: one based on a global characteristic length scale, the other based on a local gradient-length scale for density. They then updated the location of the interface at regular time intervals using a conservative approach where the interface was moved slightly further into the LD region and any small patch assigned to either method was removed. The interface itself was 4 buffer cells thick, made of 2 DSMC buffer cells next to 2 LD buffer cells. The information was transferred from one region to the other by creating duplicates of each molecule within the buffer zones. Each duplicate was of the opposite type as the original meaning that the DSMC molecules have LD duplicates and vice versa. The new DSMC molecules had velocity and internal energy distributions drawn using the LD data within the LD buffer cells. Simultaneously, the LD molecules were given a temperature and a bulk velocity using a temporal sub-relaxation scheme to calculate the velocities of the cell faces

at the interface between the DSMC and LD buffer cells. Molecules that did not enter the region associated with their type by the end of the timestep were deleted. This method only conserved quantities on average because of the relaxation scheme used to calculate the velocities of the cell faces.

Burt and Boyd first simulated the 2D, steady-state Mach 6 flow around a cylinder on 8 processors in order to validate the accuracy of their hybrid approach. They compared their hybrid solution to a full DSMC calculation using the exact same grid and timestep size. Good agreement was observed between both methods (outside of the shock, all properties were within 2%) with only a few discrepancies. They believed that the discrepancies were caused by the following: the non-exact conservation of quantities at the interface due to the sub-relaxation scheme, the assumption of homogeneous properties across the DSMC buffer cells, the lack of viscous transport, and the use of an equilibrium temperature within the LD domain. Because the cell size and timestep size requirement can be less stringent for the LD method, Burt and Boyd noted that both could be much larger within the LD regions possibly providing a solution faster than a full DSMC simulation. However, for the hypersonic flow around a cylinder, the location of the interface is not well known ahead of time which would require the implementation of an adaptive gridding scheme in order to modify the DSMC grid into a coarser LD grid. With a DSMC grid and timestep throughout the domain, the hybrid simulations were ~16% slower than the full DSMC simulations. Burt and Boyd then simulated a high-pressure, steady-state, axisymmetric converging-diverging nozzle flow which could not be accurately simulated using only the DSMC method. For this problem, the approximate location of the interface was known a-priori which enabled Burt and Boyd to use relatively large timestep and cell size in the LD region of the flow compared to what would be required by a DSMC code. Finally, they found that the LD solution was in very good agreement with a CFD solution in the continuum region of the flow.

#### **2.3.4 Expansion Flows into a Vacuum**

The expansion plume induced by a comet impact on the Moon is similar to several engineering problems involving expansion flows into a vacuum, such as nozzle plumes that occur on spacecraft (Kannenbergh and Boyd, 1999) and desorption or laser ablation from a surface (Bykov *et al.*, 2005). Due to the strong pressure gradient at the edge of the expansion, these flows are rarefied far enough away from the point of origin of the expansion. For that reason, the



DSMC method is often chosen to model these flows either alone or in combination with another solver that models the inner regions of the expansion plume. While early work has mostly focused on quasi-steady flows (Bird, 1970, Bird, 1994 and Kannenberg and Boyd, 1999), more recent research has examined unsteady flows (Bykov *et al.*, 2005 and VanGilder *et al.*, 2007).

Kannenberg and Boyd (1999) studied 3D quasi-steady thruster plume flow impingement on spacecraft surfaces. They used the DSMC method to model both a jet impinging on an inclined flat plate and hydrazine thruster plume impingement on solar arrays for two specific satellite architectures. Both problems were quasi-steady therefore Kannenberg and Boyd (1999) used time-averaging to reduce the noise in their DSMC simulations. They first compared their results for a rarefied nitrogen nozzle flow impinging on an inclined flat plate to both experiments and a free molecular analytic model by looking at surface pressure, shear stress and heat flux. They assumed that the isentropic nozzle flow expanded without boundary layer effects and that molecules were diffusely reflected off the flat plate. Their 3D simulations used an adapted grid with a variable timestep and were run on parallel machines with appropriate load balancing. Overall, they observed good agreement between experiments, DSMC and free molecular solutions with possible discrepancies due to uncertainty in the low pressure measurements. Kannenberg and Boyd (1999) then simulated an actual satellite architecture with the nozzle flow of hydrazine impinging on a solar array. In their model, due to the low temperature of the flow, they assumed that the flow was chemically and vibrationally frozen. Their simulations were divided into a two-step approach where axisymmetric simulations were used near the thruster exit. Then information was saved at a fixed breakdown surface and transferred to the next domain. They again used adapted grids with variable timesteps but also added variable weight in order to reduce on computational time. Their simulations showed relatively poor agreement with the free molecular solutions pointing to the difficulty of accurately modeling multi-species gas and boundary layer effects in a simple free molecular model.

Bykov *et al.* (2005) modeled the pulsed laser ablation of a target surface as is used, for instance, for surface micromachining and thin film deposition. They used a coupled hybrid approach to study the dynamics of the unsteady expansion of ablation products into a vacuum. In order to validate their approach, they compared their results for mass removed and time-of-flight

(TOF, which was the time variation of density at a given point of the plume) data to experimental data. In their model, they first solved for the laser radiation absorption by the surface and then calculated the surface induced heating and vaporization rates using a 1D heat flow equation. They then used the vaporization rate and surface temperature as input to a DSMC code that modeled the unsteady gas dynamics of the vaporization products. Finally, the DSMC solution was used to update the flux of particles and the velocity of the vaporization front. In their simulations, Bykov *et al.* (2005) considered three flow regimes, from near desorption (rarefied flow) to fairly developed ablation (near continuum), by using different laser fluences. For the most rarefied case, the plume is nearly axisymmetric but the plume moves mostly in the vertical direction for the near continuum case. For the near continuum case, TOF data and mass removal rate agreed well with experiments. Finally, at late times, Bykov *et al.* (2005) found that the flow became self-similar for all three cases.

## Chapter 3

### Numerical Approach

During the intermediate stages of a comet impact event, as the vapor plume of water expands away from the point of impact, the flow rapidly goes from continuum to rarefied. Only a small fraction of the water remains on an airless body such as the Moon but that remaining gas will stay collisional near the dawn terminator up to weeks or months after impact. Therefore, the Direct Simulation Monte Carlo (DSMC) method is best suited to solve the intermediate flows occurring between the early high density flow near the point of impact and the late free molecular flow established months later. The DSMC method models gas flows at the microscopic level using representative molecules. These simulated molecules are created and moved inside a meshed domain and typically each one represents a large number of real molecules ( $O(10^{20}-10^{30})$ ). The interactions between molecules are processed through binary collisions of neighboring molecules. For a large number of representative molecules, the basic DSMC collision models have been shown to accurately represent the collision integral of the Boltzmann equation (Nanbu, 1986). The DSMC method is inherently unsteady and at predetermined intervals, the molecular data can be sampled to obtain the macroscopic quantities of interest such as density, temperature and velocity.

DSMC simulations are not subject to the standard stability constraints of other numerical approaches but both timestep and cell sizes have to be chosen carefully to obtain meaningful results. In order to resolve a flowfield accurately, it is usually preferable for the timestep size to be smaller than the mean collision time and for the grid size to be of the order the mean free path. Also, the statistical fluctuations in the sampled macroscopic quantities are inversely proportional to the square root of the number of representative molecules. All these constraints mean that for most problems of interest, accurate DSMC simulations quickly become computationally expensive.

Several different versions of the DSMC method have been implemented over the years by independent groups. The present DSMC method differs from most DSMC implementations because it was written to simulate low density atmospheric flows. In particular, this code uses a three-dimensional spherical geometry, has temperature dependent molecular interactions with the lunar surface, and also takes its input data from a hydrocode simulation of an impact event. These features as well as some modifications added in order to simulate our large problems such as the parallel implementation, the collision limiting method and the sequential multi-domain approach are detailed in the following sections.

### **3.1 OVERVIEW OF THE PRESENT NUMERICAL APPROACH**

#### **3.1.1 The General DSMC Procedure**

The DSMC algorithm is usually divided in five substeps: the creation, the move, the indexing, the collision and finally the sampling steps (Figure 3-1). The DSMC algorithm goes through the move, indexing and collision steps at each timestep while the creation step is only called if needed and the sampling step is only called for at predetermined intervals. The first step in any DSMC simulation is to divide the domain into a grid, which is later used for both sampling and collision phases.

Once the grid has been initialized, the representative molecules can be created. In the present simulations, we are assuming that the Moon has no initial atmosphere so all the molecules have to flow into our domain from the comet impact site. In general, generation of inflow conditions can be divided into two categories: the state-based approach using reservoir cells and the flux-based approach at a boundary surface. For the cometary impact problem, both of these inflow conditions have been used. The first inflow condition is used to create the early expansion plume induced by the impact event. The data provided by the SOVA simulation of the impact event are used to create the DSMC molecules at a fixed interface made of reservoir cells. This inflow boundary is described in more detail in Section 3.3. The flux-based approach is used to create the water molecules that have remained inside the interface at the end of the SOVA simulations. These molecules are assumed to sublime from the impact crater some time after impact out of the presumed muddy caldera. Because the sublimating flux of molecules can be

expressed analytically for this problem, the flux-based approach was chosen over the state-based approach for this boundary. The flux of sublimating molecules is estimated based on the total mass of remaining water inside the interface, and on some predetermined sublimation timeline. Those newly created molecules are placed exactly at the inflow boundary, here the Moon's surface, and are moved into the domain using random partial timesteps.

In either case, once all the molecules have been created for the current timestep, all the molecules inside the domain are moved in the gravity field. The molecules thus follow a ballistic path in between collisions. During the move subroutine, molecules also interact with the boundaries of the domain as well as any surface present inside the domain. The most common interactions are specular and diffuse reflections, vacuum and reaction with the surface. The detailed boundary conditions used in the present simulations are presented in Section 3.1.2 while some of the features of the move step specific to our implementation are described in Section 3.4.

After all of the molecules have been moved, they are organized, or indexed, by cell. This step is required for the efficient computation of the collision and sampling steps. During the collision step, collisions partners have to be close-by which is achieved in the DSMC method by picking molecules from the same cell. During the sampling step, the molecular data inside each cell are used to calculate the macroscopic data.

Once all the molecules have been indexed, the molecular collisions are computed. The number of collision pairs to be selected in each cell is calculated using the No Time Counter (NTC) method (Bird, 1994). Collision pairs are then randomly selected until the number of selected pairs reaches the number calculated using the NTC method. For each selected collision pair, the collision event is accepted based on a given probability depending on the chosen molecular interaction model. The most commonly used model, and the model presently used here, is the Variable Hard Sphere (VHS) model (Bird, 1994) for which the collision cross-section depends on the relative collision velocity. Energy transfers between the translational modes and the rotational modes are modeled using the standard Larsen-Borgnakke model while the translational and vibrational mode energy exchanges are modeled using the discrete Larsen-Borgnakke model. In the simplest implementation of the DSMC method, collision cells are the

same as sampling cells. However, in order to minimize artificial diffusion effects from colliding molecules which are spaced far apart, sub-cells (subdivisions of the sampling cell) or free-cells (sub-cell centered on the first partner) can also be used. The free cell method has been implemented here and is presented in Section 3.5. Finally, in the high density regions of the flow where the flow is in local thermodynamic equilibrium, collisions only redistribute the energy and velocities at the microscopic level but the macroscopic properties remain unchanged. Therefore, because the collision step of the DSMC algorithm is the most expensive part of the simulation, a unique collision limiter has been implemented in the high density regions of the flow in order to decrease the computational cost of a simulation. This collision limiter is also presented in Section 3.5.

The final step, the sampling step, is used to obtain the macroscopic data, such as density, temperature and bulk velocity, from the microscopic data (molecule number, velocities and internal energies). A minimum number of molecules, typically  $\sim 10$ , must be present in any given cell to obtain physically meaningful values for the macroscopic data. However, even with an adequate number of molecules to properly simulate the flow, statistical noise in the macroscopic quantities can be too large. One way to improve the statistics of a DSMC simulation is by using averaging methods over uncorrelated samples. For steady flows, once steady state has been reached, temporal averages can be used to decrease the noise level of the simulation. This method is not applicable to unsteady flows but ensemble averaging over several runs with distinct random seeds can achieve the same result of decreasing noise.

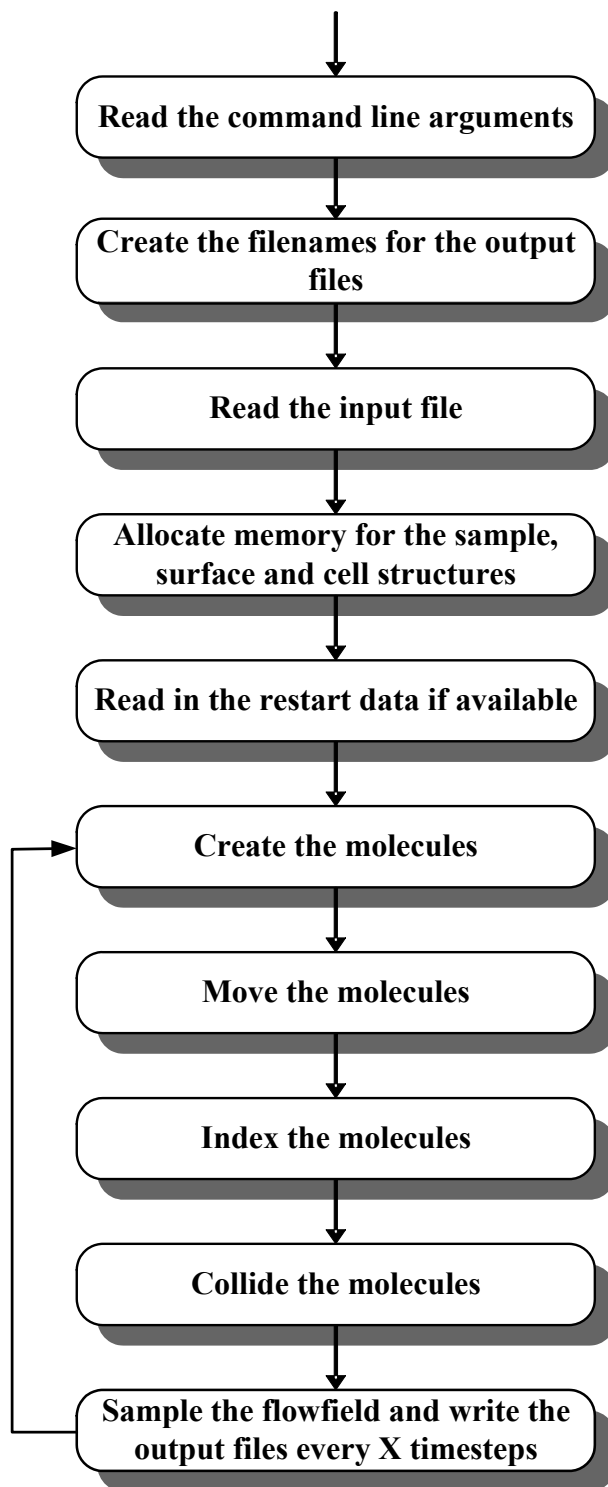


Figure 3-1 Schematic of the DSMC algorithm.

### 3.1.2 Flow Conditions

The present DSMC code is an extension of the axisymmetric code Zhang *et al.* (2003, 2004) used to simulate the sublimation atmosphere and volcanic plumes on Jupiter's moon Io. The original code was designed for the simulation of atmospheric flow with such specific features as a variable gravity field, multiple species (including solid grains and condensates), internal energy exchange, radiation from the rotational and quantized vibrational lines, and a spherical grid.

This previous implementation could only study axisymmetric problems so the code has been modified to simulate full planetary flows and non-axisymmetric plumes or expansions. The axisymmetric code was first modified into a fully three-dimensional code. Expanding on the axisymmetric implementation, the molecule location is now given by its radial distance from the center of the planet,  $r$ , and its polar and azimuthal angles from the axis of symmetry,  $\theta$  and  $\varphi$ , respectively (Figure 3-2).

The main advantage of the spherical coordinate system is that the surface of the planet is exactly represented by the lower boundary of the domain. On the other hand, the main limitations of the implementation are the increasing cell size with altitude and with polar angles near  $90^\circ$  and also the presence of two singular lines for polar angles equal to  $0^\circ$  and  $180^\circ$ . The first problem can be resolved by the use of a free cell subroutine that only collides close-by molecules in the regions where the cell size is large compared to the mean free path of the flow. The second problem is not directly addressed as we assume that no molecule will land *exactly* at either singularity at the end of a timestep. To prevent any problem, if a molecule actually lands at a singularity, the molecule is deleted and the event is reported to the user.

In order to take advantage of the fine gridding near the axis of symmetry of our spherical grid, the impact point in all our simulations is located at that axis (i.e. where  $r = 1738$  km (radius of the Moon) and  $\theta = 0^\circ$ ) and the surface properties (temperature, crater location) of the Moon are rotated such that the impact point is at the desired location on the lunar surface. In other words, unless the impact point is located at the poles of the Moon, the axis of rotation of the Moon will not be aligned with the axis of symmetry of the grid.



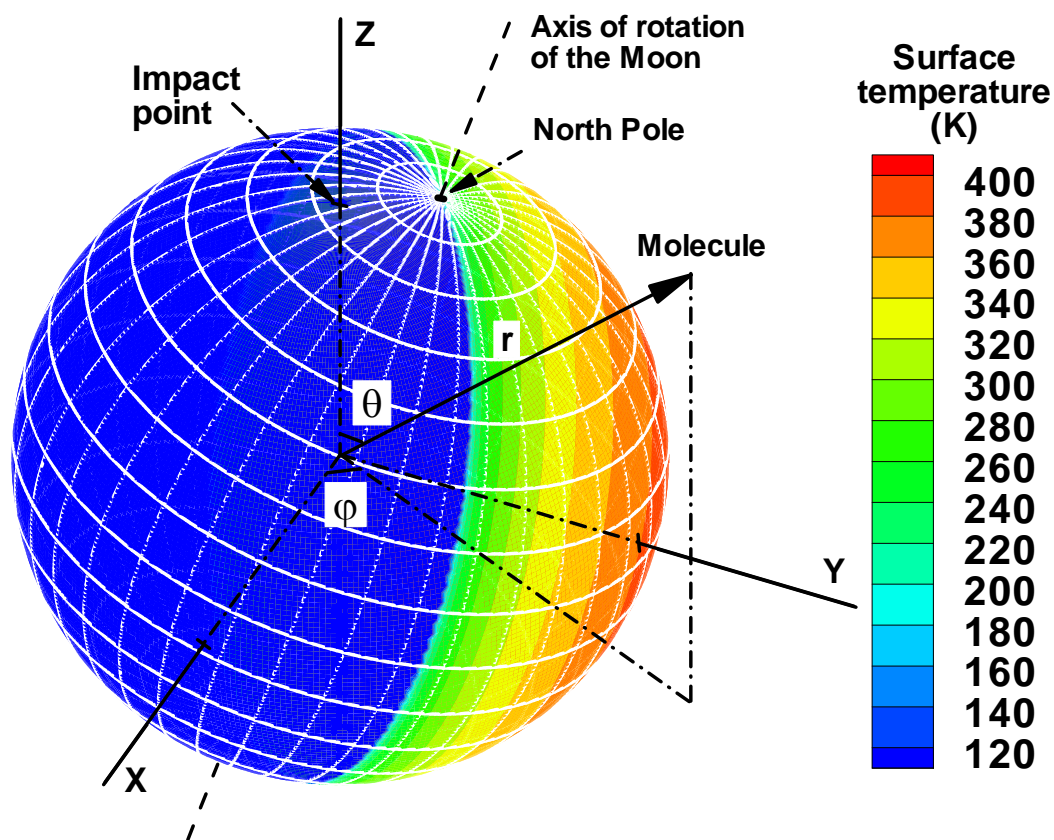


Figure 3-2 Spherical coordinate system used for the DSMC simulations with temperature contours at the surface of the Moon. Note that for this figure, the axis of rotation of the Moon is not aligned with the axis of symmetry of the spherical grid and that the white lines are latitude and longitude lines.

Three different domain decompositions have been used for our simulations (Figure 3-3). First, a “piece of pie” is used for the close-up simulations near the point of impact. This domain has been used for both serial and parallel simulations. For the full planetary parallel simulations, each processor simulates a “melon slice” that extends from the point of impact to its diametrical opposite (both points located on the axis of symmetry of the spherical domain). Finally, for the full planetary serial simulations, the entire planet can be simulated at once.

In Zhang’s axisymmetric simulations, the domain was bounded by the axis of symmetry, or left boundary, the surface of the planet, or bottom boundary, and the opposite right and top boundaries. In the present 3D simulations, the whole domain is enclosed by the addition of two

opposite boundaries, the front and back boundaries (Figure 3-3). Different boundary conditions can be implemented for each “wall” or “axis” depending on the simulation. General boundary conditions for all the walls include specular reflection and deletion (or “vacuum”) while other wall-specific boundary conditions can also be used. A molecule hitting the bottom wall can be directly (specularly) reflected, diffusely reflected after accommodating to the local surface temperature or it can stick to the surface for a given residence time. For some of the comet impact event simulations, a selective deletion is used at the top wall where only molecules with a speed larger than the escape velocity are deleted. The other molecules are saved for a later run using our multi-domain approach (See Section 3.6). In the case where the front and back walls are superimposed or for parallel simulations when a molecule crosses these walls, it is transferred to the appropriate cell or processor using a periodic boundary condition.

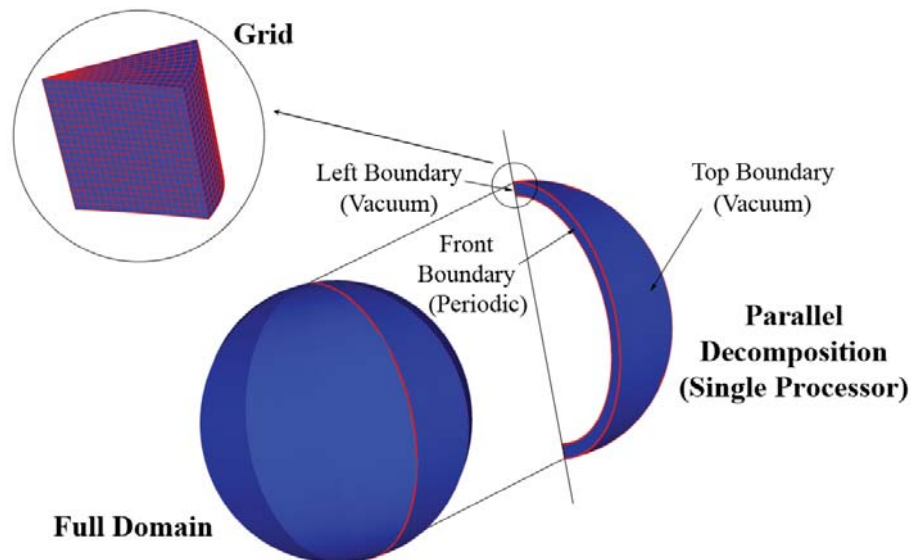


Figure 3-3 Physical domain used in the DSMC simulations. Only three of the six boundaries of a single processor domain are presented (top, left and front boundaries) as the remaining three (bottom, right and back boundaries) are the respective opposite walls.

For a full serial planet simulation, the left and right boundaries collapse into the axis of symmetry, the front and back walls are superimposed, the bottom wall represents the surface of the planet and the top wall is placed at the desired altitude (Figure 3-3). In this case, the left and right boundaries are singularities but again it has been assumed that no molecule will be exactly

at the wall location at the end of a timestep, so the boundary condition has been set as a vacuum. The front and back walls have a periodic boundary condition, the top wall is a vacuum and the bottom wall condition can be changed based on the assumptions made for the gas-surface interaction. In the present simulations, a molecule sticks to the surface of the Moon with a mean residence time, determined by the surface temperature, before being released from the surface. This boundary condition is required to simulate the late stages of the comet impact event because the few water molecules that have returned to the surface are expected to migrate around the Moon due to the variations in the surface temperature. Finally, while the main species used for Io's simulations was  $\text{SO}_2$  (Zhang *et al.*, 2003, 2004), all the results presented here have been obtained for  $\text{H}_2\text{O}$ .

Radiation, condensation and chemistry are not included in the present DSMC simulations. Also, all the water that crosses the SOVA interface is assumed to be in the vapor phase.

## 3.2 PARALLEL IMPLEMENTATION

In order to handle the large simulations necessary to model the full transient atmosphere around the Moon after a comet impact, our serial DSMC code was transformed into a parallel code that can be run on the Texas Advanced Computing Center (TACC) supercomputer Lonestar. The details of the implementation are given in Appendix A while the present section focuses on the issues of domain decomposition, load balancing and parallel efficiency.

### 3.2.1 Overview

Similar to Dietrich and Boyd (1996), and LeBeau (1999), our physical domain is divided among processors and each processor moves, collides and samples its own molecules. While many other methods (e.g. Dietrich and Boyd, 1996, LeBeau, 1999, Wu and Tseng, 2005) used a dynamic domain decomposition with noticeable improvements in their parallel efficiency, for reasons explained below, we decided to use a static domain decomposition. In other words, in the current implementation, each processor computes the same region of the domain throughout the entire run. For all our simulations, the point of impact is assumed to be at the axis of symmetry of the domain so a logical decomposition of the full domain is into smaller sub-domains in the azimuthal direction (Figure 3-3). While dynamic domain decompositions provided noticeable

savings on computational costs for complex flow problems, the savings for simpler flows were not as obvious. LeBeau (1999) noted that for a simple flow past a sphere problem using an optimal grid both static and dynamic domain decomposition runs provided very similar speed-up and parallel efficiency. In the present problem, we know that our flow is moving nearly radially away from the point of impact. In addition, our temperature is also relatively small ( $\sim 1000$  K) so we also expect the thermal velocity components to be relatively small compared to the bulk velocity of the flow (up to 40 km/s). Therefore, by using a domain decomposition in the azimuthal direction, we expect very little cross-flow from one processor to another, providing a relatively small amount of data to transfer at each timestep.

Another important factor coming into play in the domain decomposition and the parallel efficiency of the code is the load-balancing between processors. The most efficient parallel codes will have a near uniform workload across processors, so little time is wasted by idle processes. In the present simulations, we are using a domain decomposition specific to each impact condition. For an axisymmetric impact, load-balancing can be achieved by simply dividing the domain into equal azimuthal slices. For a fully 3D impact, however, the vapor plume will be more restricted, moving preferentially in one direction. For a  $45^\circ$  oblique impact, we found that most of the material moves downrange of the impact point with very little flow in the crossrange and uprange directions. Using a low resolution run to estimate the workload associated with each azimuthal degree, we implemented a non-uniform domain decomposition where processors in the downrange direction only simulate  $1^\circ$  of azimuth while crossrange and uprange processors simulate up to  $30^\circ$ . The load-balancing obtained for these simulations was not optimal because the flow was unsteady and the relatively narrow early plume tends to become fuller at later times. However, the non-uniform domain decomposition provides great improvement over a simple uniform decomposition (See Section 3.2.4).

### 3.2.2 Performance Study

Two different parameters are usually considered when studying the performance of a parallel implementation (LeBeau, 1999, Wu and Tseng, 2005): the speed-up and the parallel efficiency. The speed-up is generally computed as the ratio of the wall-clock time required by the serial code,  $\tau_{serial}$ , to that required by the parallel code,  $\tau_p$ :

$$S(p) = \frac{\tau_{serial}}{\tau_p} \quad (3.1)$$

The parallel efficiency is defined as the ratio of the speed-up,  $S(p)$ , to the number of processors,  $p$ :

$$E(p) = \frac{S(p)}{p} \quad (3.2)$$

Note that the parallel efficiency defined in Eq. (3.2) takes on values greater than one when the parallel speed-up is super-linear (Figure 3-4 and Figure 3-6), which may be observed due to improved cache usage, for instance. The performance of a parallel code can be evaluated without actually running the code by using Amdahl's law. If one can estimate the fraction,  $\xi$ , of the serial code that can be parallelized, Amdahl's law states that the speed-up for a constant problem size is given by:

$$S(p) = \frac{1}{(1-\xi) + \xi/p} \quad (3.3)$$

Using Amdahl's law, the speed-up of a parallel code will asymptote to a maximum theoretical speed-up, equal to  $1/(1-\xi)$ , as the number of processors is increased. This theoretical value is unfortunately hard to compute as the fraction of code that can be parallelized,  $\xi$ , may be hard to estimate. Also, Amdahl's law was derived for a constant problem size while most parallel codes have been written in order to simulate larger problems. Therefore, another way to look at the performance of a parallel code is to study the scalability of the parallel program by increasing

the problem size with the number of processors. A program is said to be scalable if a constant efficiency can be maintained by increasing the problem size with the number of processors.

The actual speed-up obtained with any parallel implementation is highly dependent on two factors: the number of communications per timestep and the total amount of idle time for all the processors. The number of communications between processors has to be limited so that the overhead of a simulation remains small as the number of processors is increased. In general, a communication can be divided into a start-up phase and the actual communication phase. The time required by the start-up phase is called latency and is independent of the amount of data transferred. Therefore, the number of communications should be limited in order to decrease the communication costs due to latency. The time taken by the actual communication phase is proportional to the amount of data being transferred and inversely proportional to the bandwidth of the network. Another source of degradation of the performance of parallel codes is due to the non-uniform load balancing between processors. If even one processor has a greater workload than all the other processors, the other processors will remain idle until that processor has caught up to them therefore decreasing the parallel efficiency.

In an approach similar to LeBeau (1999) and Wu and Tseng (2005), we used an increasing number of processors on a constant problem size in order to estimate the speed-up and efficiency of our parallel implementation. We considered two different problems: the unsteady expansion of a vapor cloud into vacuum and the 45° oblique impact of a comet on the Moon. A total of five different cases were run for the present parallel performance study and the important parameters for all cases are presented in Table 3-1. For all five cases, the point of origin of the vapor cloud was located at the axis of symmetry of our domain and we were only interested the parallel performance of our near field simulations. The number of communications between processors was fixed at four per timestep (see Appendix A) and static domain decompositions in the azimuthal direction were used.

The problem of an unsteady spherically symmetric cloud expanding into vacuum is studied in more detail in Chapter 4. In order to most resemble the comet impact simulations, the present DSMC simulations were fully three-dimensional using Tzuk *et al.*'s 1D analytic solution

(1993) as boundary condition at a hemispherical interface 20 km in radius from the point of origin of the expansion. The geometry of the interface is the same as for the 45° oblique impact simulations as provided by the SOVA hydrocode (see Section 3.3). The interface is made up of Cartesian cells between 50 and 200 m in size. The 1D analytic values for density, temperature and radial velocity were calculated at each timestep for all the SOVA interface cells based on the radial distance of the cell center from the point of origin of the expansion. In the present simulations, the analytic solution used the initial conditions for Case 3 presented in Section 4.3. The expansion flow only depends on the radial distance from the point of origin of the expansion, so we used a uniform domain decomposition between processors in the azimuthal direction. The present simulations of the spherically symmetric expansion flow inside a relatively large domain were used as the baseline for our parallel performance study (Case A in Table 3-1). Later, the same case but without output (Case B in Table 3-1) and a similar case with a smaller domain in the azimuthal direction (Case C in Table 3-1) were used to study both I/O and communication effects on the parallel performance of the DSMC code, respectively.

The remaining two cases (D and E in Table 3-1) simulated the expansion plume produced by a 2 km diameter water ice comet hitting the surface of the Moon at 30 km/s and at an angle of 45° (see Chapter 5). Again the DSMC simulations were fully three-dimensional. For these cases, the interface geometry as well as the data used at the interface were provided by the SOVA hydrocode simulations of the impact event. For this parallel performance study, we only used the SOVA data for the material that crossed the interface between 4.5 to 5 s after impact. The vapor plume resulting from an oblique comet impact is much more complex with noticeable asymmetries than the previous spherically symmetric flow. Early on (up to ~10 s for the 45° oblique impact), the vapor plume moves predominantly in the downwind direction with very little material moving upwind or crosswind. For the present simulations, we used a uniform decomposition as well as a non-uniform decomposition, with relatively larger domains for upwind processors as compared to the downwind processors, in order to study the possible benefits gained from the non-uniform decomposition.

Table 3-1 Summary of the conditions used in Cases A to E.

Case Number	Input	Domain Size	Azimuth grid	Timestep size (s)	Number of cells	Number of molecules	Number of timesteps	I/O
Case A	Analytic	32 km × 32 km × 64°	Uniform	0.01	13.1M	32.2M	50	Yes
Case B	Analytic	32 km × 32 km × 64°	Uniform	0.01	13.1M	32.2M	50	No
Case C	Analytic	32 km × 32 km × 0.64°	Uniform	0.01	6.55M	30.4M	50	No
Case D	SOVA	32 km × 32 km × 180°	Uniform	0.0005	18.4M	1.1M	1000	Yes
Case E	SOVA	32 km × 32 km × 180°	Non-uniform	0.0005	18.4M	1.1M	1000	Yes

For the spherically symmetric expansion flow, two different domains were considered: a large “piece of pie” 32 km × 32 km × 64° (Cases A and B) and a small “piece of pie” 32 km × 32 km × 0.64° (Case C). For Cases A and B, the DSMC cell size in the azimuthal direction is of the order the interface cell size but becomes much smaller than the interface cells for Case C. For all three cases, the simulations were started 2 s after the beginning of the expansion and were run for 50 timesteps with a timestep size of 0.01 s. As the number of processors was increased, the total number of cells remained constant at 13.1 and 6.55 million for Cases A and B and Case C, respectively. At the end of the simulations, the entire DSMC domain contained ~32 and 30.4 million molecules for Cases A and B and Case C, respectively. Because not all of the DSMC cells contained some material by the end of the simulations, the actual number of molecules per occupied cell was equal to ~20. Because of the relatively high densities near the interface, our collision limiter scheme (see Section 3.5.1) was used in all three cases. Up to 128 processors were used for Cases A and B and up to 64 processors were used for Case C. The speed-up obtained for these three cases is presented in Figure 3-4 while the parallel efficiency is presented in Figure 3-5.



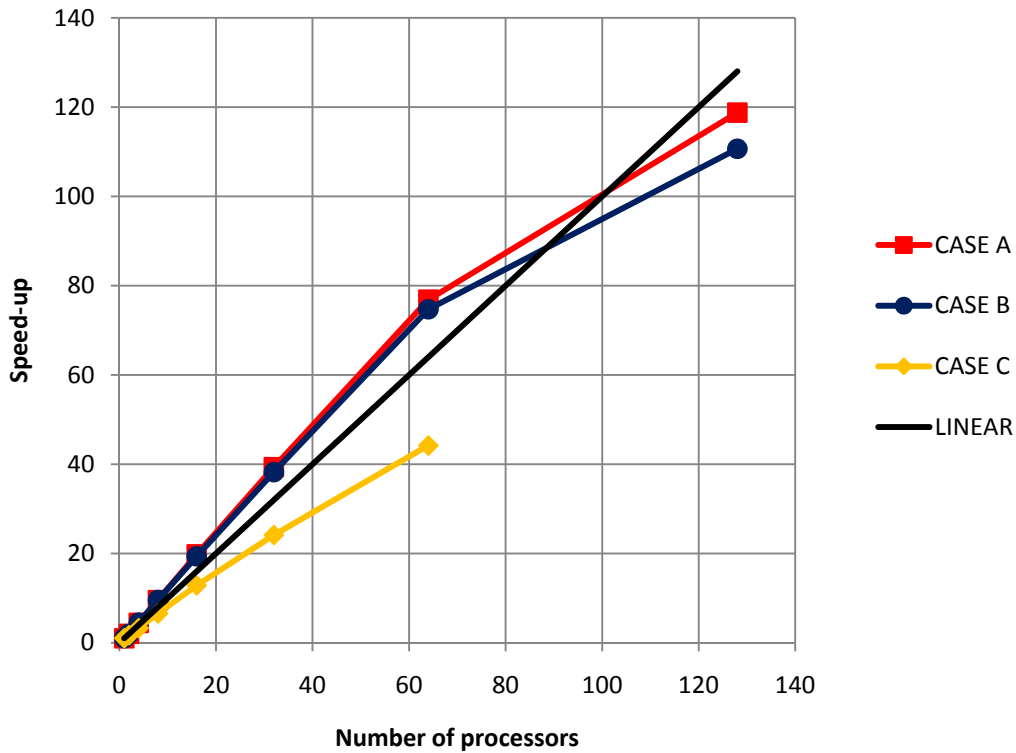


Figure 3-4 Speed-up versus number of processors for the simulations of an unsteady spherically symmetric expansion flow into a vacuum.

Cases A and B exhibit a noticeable super-linear speed-up for all the simulations using 64 processors or less. As the number of processors is further increased to 128, however, the speed-up for the simulations becomes sub-linear for both Cases A and B. For Case A, the parallel efficiency increases as the number of processors is increased from 2 to 8 processors. Then, the parallel efficiency remains nearly constant between 8 to 64 processors at  $\sim 1.2$ . For the 128 processor simulation, however, the parallel efficiency decreases rapidly to  $\sim 0.93$ . The trends for Case B are very similar as the trends for Case A but with a slightly smaller parallel efficiency for the simulations with a greater number of processors. For instance, the parallel efficiency for the 128 processor simulation is equal to  $\sim 0.86$  in Case B versus  $\sim 0.93$  in Case A. For Case C, the speed-up is sub-linear for all the parallel simulations and the parallel efficiency is always smaller than one. The parallel efficiency decreases nearly linearly from  $\sim 0.85$  for the 2 processors simulations to  $\sim 0.69$  for the 64 processors simulation.

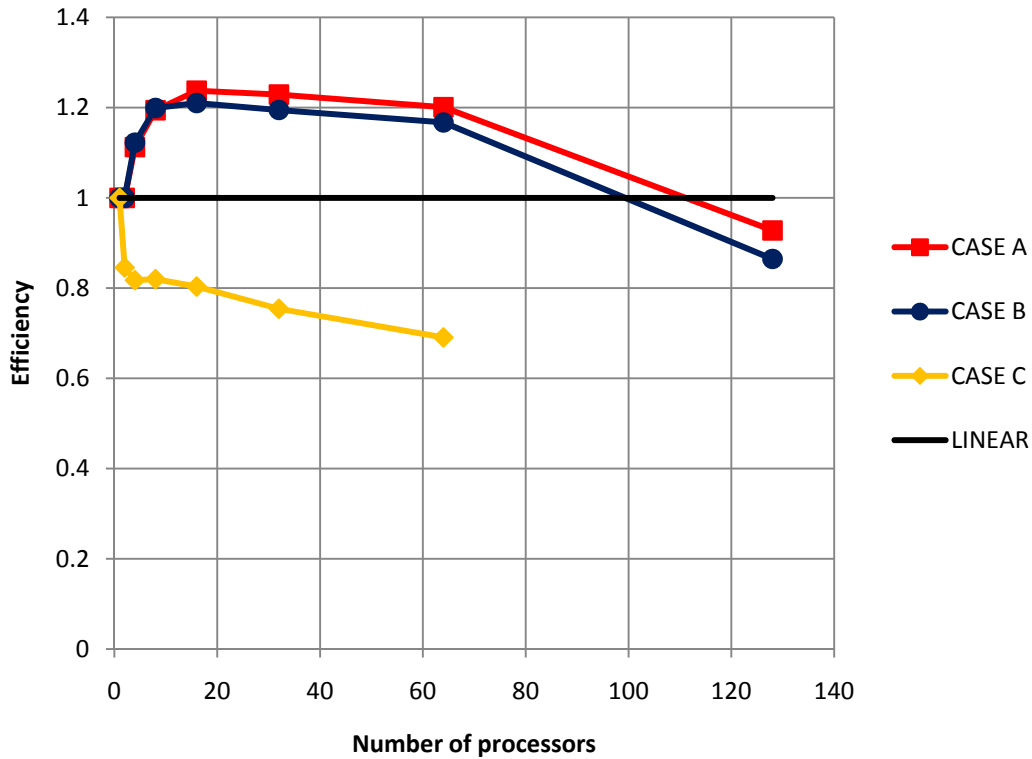


Figure 3-5 Parallel efficiency versus number of processors for the simulations of an unsteady spherically symmetric expansion flow into a vacuum.

The observed super-linear speed-up for Cases A and B with up to 64 processors is believed to come from several sources. As the number of processors increases, the size of the problem on each processor decreases. Therefore, better cache usage is probably partially responsible for the super-linear speed-up and the increased efficiency observed in Cases A and B (LeBeau, 1999 and Wu and Tseng, 2005). The improved cache usage however is not alone sufficient to observe a super-linear speed-up (see Case C). For all the simulations, the number of communications has been limited to four and the domain decomposition in the azimuthal direction is thought to provide very few molecules crossing processor boundaries at each timestep. For Cases A and B, the maximum number of molecules sent across by one processor to all the others is nearly constant at  $\sim 15000$ , so the ratio of molecules being transferred to the total number of molecules is no greater than 4% for the 64 processors simulation. Therefore, the overhead due to communications was kept relatively small in Cases A and B. Also, in the present

simulations, the total number of molecules present at any given timestep on one processor varies by less than 4.5% from one processor to another for all the simulations for Cases A and B. Because of the near uniform number of molecules distributed among the processors, the present simulations were fairly well load balanced. Finally, the super-linear speed-up for Cases A and B can also be partially due to the way we create molecules at our interface. The SOVA cells were used as reservoir cells where the DSMC molecules were created (see Section 3.3.2). Once the molecules were moved those that remained within the interface were deleted. This was achieved by searching through all the interface cells and checking if the molecule was within the boundaries of that cell. For the parallel simulations, the interface was divided among the processors so for the simulations with a greater number of processors the number of cells to search through when deleting molecules becomes smaller. Therefore, the search algorithm will speed-up as the number of processors is increased. While these can explain the super-linear speed-up up to 64 processors, the simulations with 128 processors have a lower parallel efficiency. This is probably due to some degradation in both load balancing and computation-to-communication cost ratio. For the 128 processors simulations, the difference in the number of molecules per processor increases to 7.5% and the ratio of molecules sent to total number of molecules reaches 7%.

Cases A and B exhibit similar trends and have near identical parallel efficiency for simulations with up to 32 processors. However, the simulations for Case B show a faster degradation in parallel efficiency for the 64 and 128 processors simulations. For Case A, the present simulations provided a restart file and an output flowfield file. As the total number of cells for each simulation was kept constant independently of the number of processors, the size of any output file for the simulations with a smaller number of processors was much larger than the size of the output file for any processor in the higher number of processor simulations. Therefore, some of the degradation of the parallel efficiency observed between Cases A and B for the simulations with the greater number of processors is believed to be due to the I/O cost. In Case A, the relative cost of I/O per processor decreases as the number of processors is increased therefore providing an additional increase in parallel efficiency. In summary, Cases A and B exhibit a super-linear speed-up due to improved cache efficiency, decreased cost of I/O, and decreased cost

of the reservoir boundary condition used at the interface as well as the relatively low communication cost overhead and the near uniform load among processors.

For Case C, instead of the super-linear speed-up observed Cases A and B, the speed-up is much smaller than ideal for a parallel efficiency of  $\sim 0.69$  for the 64 processors simulation. The initial 20% drop in parallel efficiency between the 1 processor and 2 processors simulations has been attributed to the added communication costs in the simulation using 2 processors. In addition, the main reasons for the observed differences between Case C and Cases A and B is again related to the overhead due to communications between processors. The bulk flow is moving radially away from the point of origin of the expansion but, due to relatively high temperatures ( $>1000$  K), the molecules may have a relatively large non-radial component. In Case C, the size of the processor domain in the azimuthal direction is relatively small so the number of molecules sent across at each timestep is very large. At each timestep, the ratio of the number of molecules sent by a processor to the total number of molecules in the processor varies between 3% for 2 processors and 84% for 64 processors. However, because the total number of molecules is constant for all the simulations, the number of molecules sent across per processor per timestep is between  $\sim 400,000$  and  $900,000$ . Therefore, the communication-to-computation cost is large enough in Case C to produce a sizeable degradation in parallel performance.

The  $45^\circ$  oblique impact simulations had as objective to evaluate the possible load-balancing of our DSMC simulations by comparing static uniform (Case D) and non-uniform (Case E) domain decompositions. For these simulations, the DSMC domain was a “piece of pie”  $32 \text{ km} \times 32 \text{ km} \times 180^\circ$  with 18.4 million cells. The simulations were run for 1000 timesteps with a timestep size of 0.5 ms, and  $\sim 1.1$  million molecules were present within the entire domain at the end of the computations. For both Cases D and E, the DSMC domain was divided between 2 to 180 processors and the observed speed-up and parallel efficiency presented in Figure 3-6 and Figure 3-7, respectively, were obtained by using the wall-clock time for the 2 processors simulation instead of the 1 processor simulation.

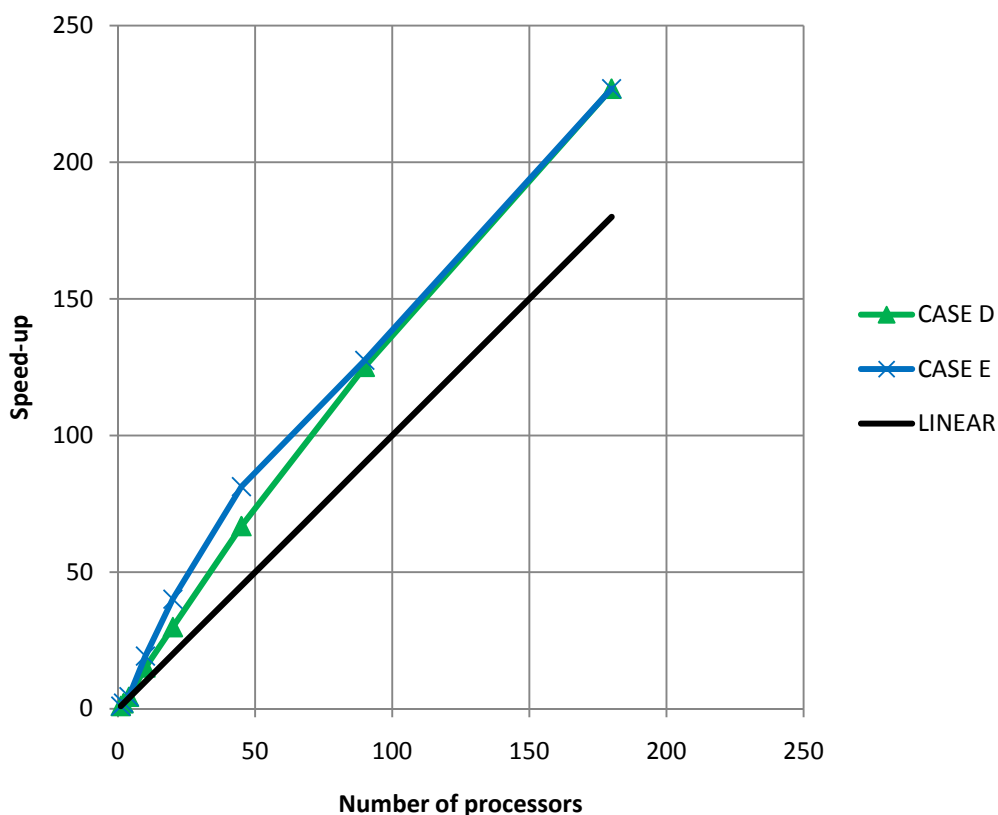


Figure 3-6 Speed-up versus number of processors for the simulations of a 45° oblique impact of a comet on the Moon.

For both Cases D and E, a super-linear speed-up can be observed for all simulations with more than 2 processors. For simulations with up to 4 processors, both uniform and non-uniform domain decomposition provide similar speed-up with parallel efficiencies of  $\sim 1.1$ . For simulations with 10 to 20 processors, the speed-ups begin to differ with a slightly better performance for Case E with the non-uniform domain decomposition. For these simulations, the parallel efficiencies increase up to  $\sim 1.5$  for Case D and  $\sim 2.0$  for Case E. As the number of processors is further increased, the parallel efficiency starts to drop and the differences between the two cases become negligible for 90 processors and above. As for the expansion flow simulations (Cases A-C), the super-linear speed-up can be partially attributed to improved cache efficiency. The total number of molecules per processor for Cases D and E is  $\sim 30$  times smaller than the total number of molecules for Cases A-C. Therefore, the CPU cache can be used even

more efficiently in Cases D and E which can be observed in the greater super-linear speed-up. In Cases A and B, the parallel efficiency is no greater than  $\sim 1.2$  but is as large as  $\sim 2.0$  in Case E with the non-uniform domain decomposition. The good parallel performance for these two cases can also be attributed to low communication costs. The ratio of molecules sent to the total number of molecules is less than 1% for all the simulations. Other factors such as the decreased cost of I/O, and decreased cost of the reservoir boundary condition used at the interface can also explain the noticeable speed-up.

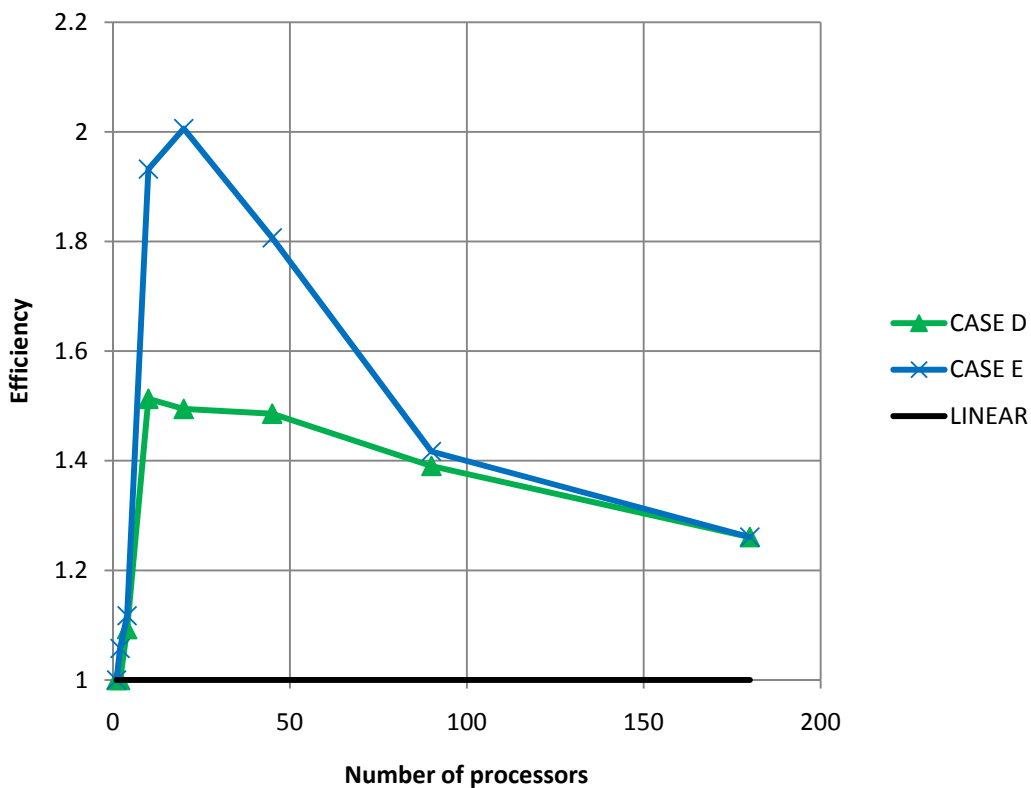


Figure 3-7 Parallel efficiency versus number of processors for the simulations of a  $45^\circ$  oblique impact of a comet on the Moon.

Interestingly, the overall load-balancing between processors is not as good for Cases D and E as for Cases A-C. Figure 3-8 shows the average number of molecules and smallest and largest number of molecules on any given processors for Cases D and E, respectively. Case D has

a very poor load balance among processors with a variation in the number of molecules across processors ranging from 65% for the 2 processors simulation up to 93% for the 90 processors simulation. Case E has a fairly good load balance up to 10 processors with less than a 10% variation but the variation increases to 75.5% and 50% for the 45 and 90 processors simulations. However, the total number of molecules in the simulations for Cases D and E is much smaller than for Cases A and B so better cache usage may be even more prominent in the former cases, limiting the effects of poor load balancing.

Another important parameter is the ratio of the largest number of molecules for one processor for Case D to the largest number of molecules for one processor for Case E. Because the total wall-clock time is directly linked to the computational time for the slowest processor, this ratio could explain some of the differences seen between Cases D and E. If the ratio is equal to one, both cases should have similar parallel performances. As the ratio increases, however, Case E should provide a more efficient solution. For the simulations with an intermediate number of processors between 10 and 45 processors, the ratio is equal to  $\sim 1.5$ - $1.6$  (Figure 3-8). Therefore, the parallel performance for Case D is expected to be worse than for Case E; this is observed in the present simulations. For the 90 processors simulations, the ratio drops to  $\sim 1.3$  so similar parallel performances are expected for Cases D and E which is again observed.

Therefore, in the present simulations, the parallel performance of a given simulation may be hard to estimate a-priori because of all the different parameters that have to be considered. Two of the main factors improving the parallel performance of our  $45^\circ$  oblique impact simulations are the improved cache usage and the very low communication costs. In addition, some other parameters such as the I/O cost, and the load-balancing may also be of importance in the overall parallel performance. Overall, the non-uniform domain decomposition provided a more efficient solution for an intermediate number of processors but very little difference has been observed for the small and large numbers of processors.

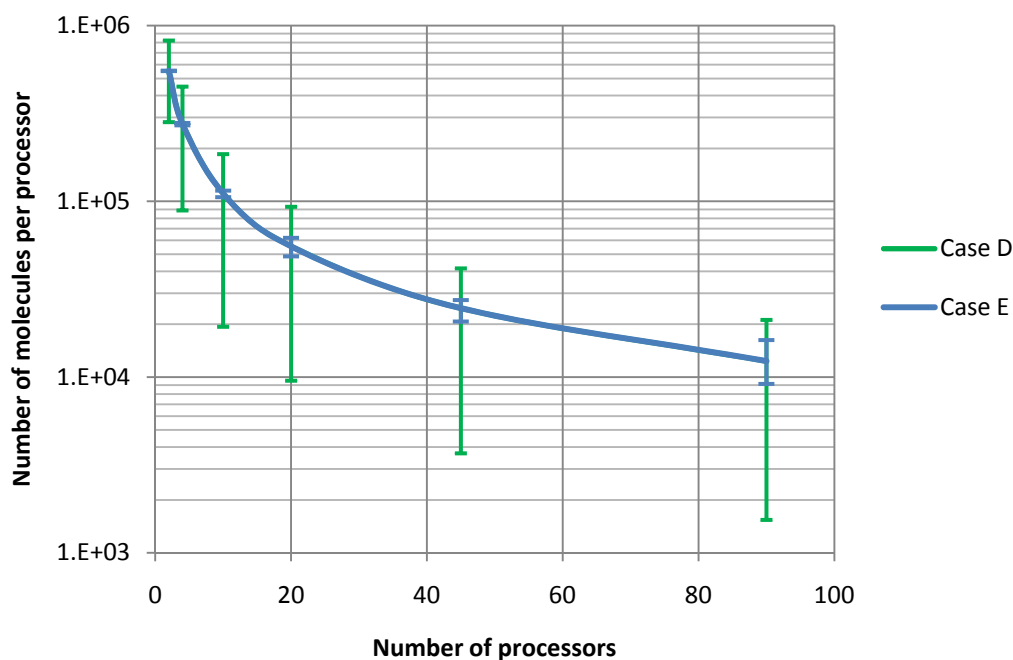


Figure 3-8 Average numbers of molecules per processor as a function of number of processors for Cases D and E. The error bars represent the smallest and largest number of molecules found on any processor at the end of the calculation.

In conclusion, our parallel implementation provides a super-linear speed-up under most circumstances for both uniform expansion flow and the non-uniform cometary vapor plume. In the present investigation of the cometary vapor plume we only considered a small time period after impact. However, the vapor plume and the spatial distribution of material are highly unsteady so the optimal parallel implementation for such flow would require a dynamic domain decomposition. In the present simulations, the static domain decomposition that is appropriate at a given time may not be efficient later on. However, even the uniform domain decomposition simulations provided a noticeably super-linear speed-up so all the parallel simulations in Chapter 5 use a fixed non-uniform domain decomposition that provides a near uniform load balancing at the time when most of the material is going through the interface.



### 3.3 UNSTEADY INTERFACE

The present computations use a multi-stage approach where the impact event is simulated with a hydrocode and the resulting subsequent transitional-rarefied flow is simulated with our DSMC code. As described in Section 2.3.3, several couplings between continuum solvers and kinetic solvers can be considered when running hybrid simulations. In the most general case, the coupling between the continuum solver and the DSMC code in hybrid methods must be fully integrated so information can be transferred from either region to the other (Roveda, 2000). However, in the limiting case where the flow is supersonic normal to the interface between the continuum and rarefied regions, a unidirectional coupling is sufficient because information cannot travel back upstream in supersonic flows. In the case of a comet impact, the flow near the point of impact remains supersonic for most (but not all) times. Therefore, the present hybrid method uses a unidirectional coupling from the SOVA hydrocode to the DSMC code similar to the unidirectional part of Roveda *et al.*'s coupling from the ADV domain to DSMC regions (2000). In our simulations, however, the SOVA computations are run first and at a chosen interface the unsteady macroscopic data (density, pressure, temperature, etc.) are saved. Later, the SOVA data are used as input to the DSMC simulations. The SOVA hydrocode simulations as well as the interface implementation in both SOVA and DSMC codes are described in the following sections in more detail.

#### 3.3.1 SOVA Output

The method of choice to simulate the physics of an impact event, such as surface deformation and material state changes, is by using a hydrocode. The present simulations use the output from the SOVA hydrocode simulations run by Dr. E. Pierazzo at the Planetary Science Institute in Tucson, Arizona. The present SOVA simulations were run for a sphere of water ice 2 km in diameter hitting the surface of the Moon at 30 km/s. Two different simulations were run with two different angles of impact of 90° and 45° (Figure 3-9). These two cases will be further referred to as the vertical and oblique impact cases for the 90° and 45° impact angles, respectively. For the vertical impact, the SOVA computational domain extends 21 km away from the point of impact in the horizontal plane and from 8 km below the surface to 23 km above it. Similarly, for the oblique impact, the SOVA computational domain extends 8 km below the

surface to 38 km above and from 21 km in the uprange direction to 37 km in the downrange direction. For both cases, the simulations were fully three-dimensional with non-uniform gridding in all three directions. The grid was finest near the surface at the point of impact with a cell width of 50 m in all three directions. The cell size was then incrementally increased in all three directions until the cell width reached a maximum of 200 m in all directions. At the beginning of the simulation, 1000 Lagrangian tracers were placed in both the impactor and target in order to track the peak pressure each material underwent. The comet itself is modeled as water ice and the surface of the Moon has the material properties of dunite. In order to properly initialize the SOVA hydrocode simulations, a background atmosphere is initially present inside all the computational cells that are neither inside the comet nor inside the target. While the actual density at the surface of the Moon is of the order  $10^{-14} \text{ kg/m}^3$  (Stern, 1999), the background atmosphere density was chosen to be  $5 \times 10^{-5} \text{ kg/m}^3$ . This relatively low value is not expected to modify the actual expansion plume (Ong *et al.*, 2010).

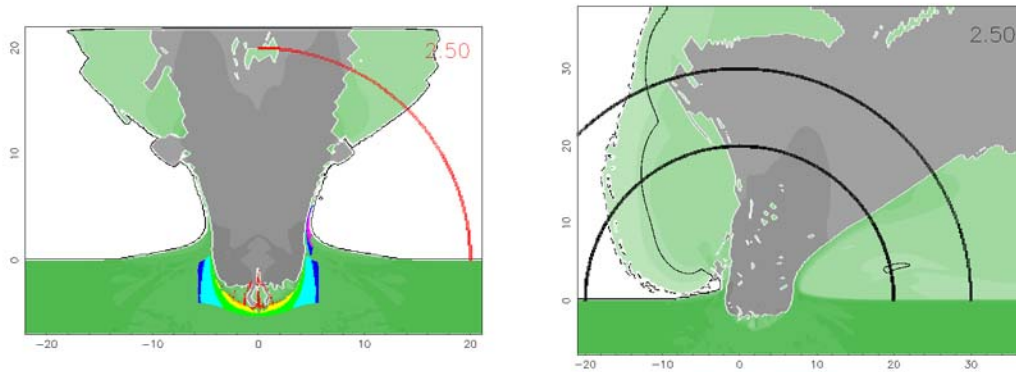


Figure 3-9 Density contours in the impact plane of symmetry 2.5 s after a 2 km diameter comet impacted the surface of the Moon at 30 km/s for a vertical impact (left) and an oblique impact (right). The water density contours are represented in grey and the rock density contours are represented in green. The darker colors represent the denser areas of the flow. The red (left) and black (right) arcs represent the interface between the SOVA and DSMC codes.

Hydrocode simulations do not usually provide time dependent data within the computational domain because the size of such output files would be very large (up to several tens of Gbytes per half second). Dr. Pierazzo modified the SOVA hydrocode in order to only

output the time-dependent data from a given set of (fixed) cells. This set of cells describes the SOVA-DSMC interface as seen from the SOVA hydrocode (Figure 3-9). For our purpose, we chose cells on a “connection hemisphere” several cells thick (Figure 3-10) over the Moon’s surface centered at the impact point. Obviously, other surfaces enclosing the impact point could be used. In each cell SOVA provides the concentration, density, partial pressure, temperature and bulk velocity of the materials present within the cell. The state of the materials is not given in the cell data.

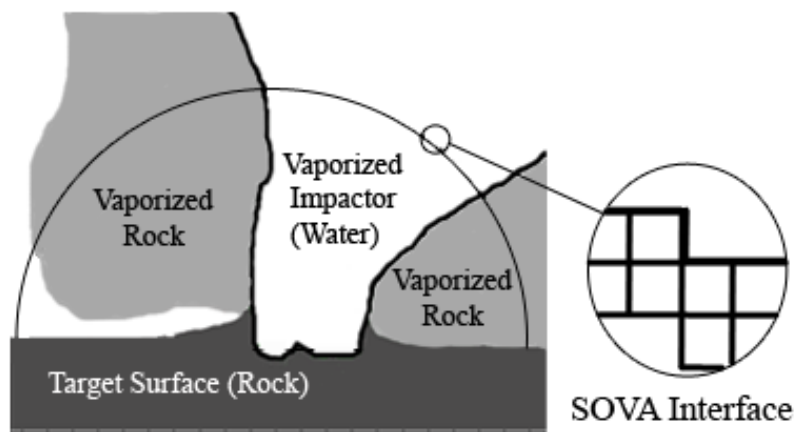


Figure 3-10 Schematic of the impact event simulations by the SOVA hydrocode. The interface in which data are saved in the SOVA hydrocode is shown on the right. The interface is several Cartesian cells thick forming a shell with a radial thickness of at least 150 m everywhere.

The radius of the connection hemisphere may vary with the size and velocity of the impactor. For this work, the radius had to be large enough so that densities in the selected cells are such that the computational cost of the DSMC simulations is acceptable. However, the SOVA code cannot run out to large distances away from the impact point for several reasons. First, the SOVA code cannot properly simulate very low densities as it is a continuum code. Then, the computational cost of a hydrocode simulation rapidly becomes too expensive as the domain size is increased. By looking at both vertical and oblique impact data, we decided that a reasonable distance should be at least 20 projectile radii away from impact point, i.e. a radius of 20 km for the connection hemisphere. For the oblique impact, the peak density at this hemisphere is smaller

than  $0.8 \text{ kg/m}^3$ . At this density the water vapor is dilute so the DSMC method can be used to model the flow even if the simulations will be computationally expensive. Therefore, a hemisphere with a 20 km radius was adopted for both vertical and oblique simulations as the interface between the SOVA and DSMC codes. In addition, a 30 km connection hemisphere was also used in the oblique impact simulations in order to compare the DSMC and SOVA solutions downstream of the interface.

In the present simulations, the water is assumed to be in the vapor phase only and is also assumed to remain as such within the DSMC domain. In reality, as the hot vapor plume expands and begins to cool, the gases within the plume may start to condense. However, it is believed that for planetary scale impacts, up to 50% of water vapor may remain in the monomer state and never condense (Melosh, 1989). In 2005, Zhong *et al.* studied the condensation of water within rocket exhaust plumes using classical homogeneous nucleation theory within their DSMC code. Several models have been presented over the years to represent the nucleation rate inside a supersaturated gas but no model has yet been able to satisfactorily fit most nucleation experiments. For that reason, Zhong *et al.* chose the popular classical nucleation theory (CNT) model which is dependent on, among other things, the temperature and density of the gas. Zhong *et al.* simulated the plume conditions of the Progress spacecraft's main engine exhaust that contained 30% water inside an axisymmetric domain downstream of the rocket's nozzle. They found that for such a nozzle flow expanding into a vacuum, the nucleation region was located 3 m downstream of the throat of the nozzle. The density of water clusters was largest in the nucleation region but was still 6 orders of magnitude lower than the gas density. The cluster density thereafter decreased further downstream due to the expansion of the gas. The average size of the clusters was found to be about 10 water molecules and the largest cluster was estimated to be 500 water molecules. The largest clusters were found in the densest regions of the flow downstream of the nucleation region, along the axis of symmetry. Under these conditions they found, however, that the flowfield without condensation was actually nearly unchanged when condensation was allowed. When a much larger (three order of magnitude larger) nucleation rate was used, Zhong *et al.* found that cluster sizes decreased but that the number of clusters increased. For this case, the flow conditions downstream of the nucleation region were noticeably different from the non-condensation case with a much lower water vapor number density and relatively hotter temperatures. Ongoing research (Li *et al.*, 2009) is still trying to improve the nucleation rate

models to be used in the DSMC simulations of condensation within an expansion plume. Presently, the influence of condensation on the overall flowfield has yet to be determined for a general expansion flow problem. One additional important feature from Zhong *et al.*'s work was that they only considered condensation due to supersaturation of the water vapor and did not study heterogeneous nucleation, the influence of foreign nuclei as possible initial source for cluster formations (which can dramatically increase the nucleation rate). For our comet impact simulations, we have the additional challenge of dust particles and molten droplets of target material within the expansion plume. However, these are not resolved within the SOVA cells and could only be estimated from analytical models. Therefore, while cluster formation may be important within an impact expansion vapor plume, it is beyond the scope of this work to explore its influence.

### 3.3.2 DSMC Input

First, the SOVA output had to be preprocessed in order to be used by the DSMC code. The SOVA data files were several tens of gigabytes with a lot of data that was not used in the DSMC simulations. Therefore, one of the objectives of the preprocessing was to decrease the size of the input file containing the SOVA data for the DSMC simulations. In addition, for the parallel simulations, we decided that each processor would have its own SOVA data file, again reducing the size of the file each processor would have to read. Therefore, the SOVA data had to be split among the processors based on the chosen decomposition. The details of the preprocessing computations are presented in Appendix B. For the cells containing pure water, the preprocessed data provides the density, temperature and velocity of the water at every SOVA timestep. Data from cells that contain *both* water and rock or just rock are currently not taken into account. The reason for this approximation is first that very high temperatures ( $\sim 5$  times larger than the temperatures inside the near-by cells containing only water) were observed in cells containing both water and rock. Also, we are assuming that all the water within the DSMC domain is in the vapor phase. In cells where rock and water are mixed, the presence of rock fragments and particles may accelerate the condensation of the water vapor which is not modeled in the present DSMC simulations. By ignoring the water present within the cells also containing some rock we neglect at most 3% of all the water that crosses the interface.

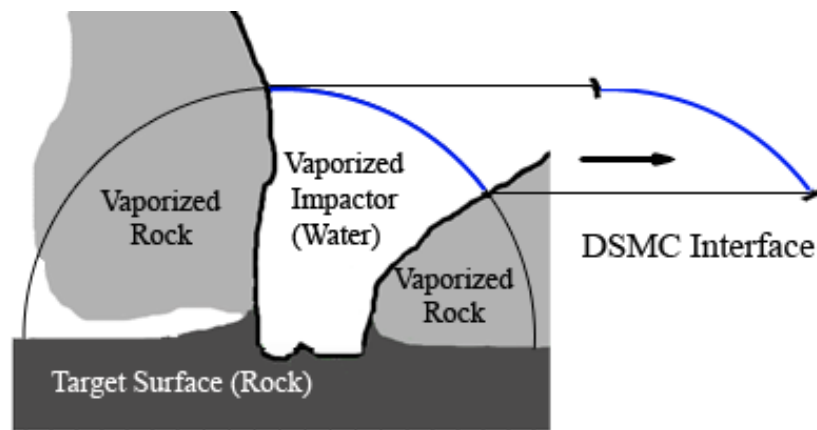


Figure 3-11 Schematic of the impact event simulations by the SOVA hydrocode. The interface at which data are input into the DSMC code is shown in blue on the right.

After choosing the type of coupling (unidirectional from SOVA to DSMC), and the location of the interface (a fixed hemispherical interface made-up of individual Cartesian SOVA cells), we needed to decide the type of DSMC boundary conditions that would be used at the interface. Generally, two different approaches can be implemented to create molecules in a DSMC code from macroscopic data at an interface (Schwartzentruber *et al.*, 2007): a flux-based approach or a state-based approach. When the interface between the two codes is defined as a simple line either method may be used interchangeably. In the present simulations, however, we are provided data within multiple cells that form a complex surface. In addition, the SOVA cells are Cartesian so they will not precisely overlap with the spherical DSMC cells (Figure 3-12). For that reason, we decided to use the SOVA cells as creation cells for a state-based interface. That is, each Cartesian SOVA interface cell is used as a reservoir cell for the DSMC domain (Lilley and Macrossan, 2003, Garcia and Wagner, 2006). An equilibrium distribution of molecules is created inside each reservoir cell and is allowed to drift into the spherical DSMC grid. Inside each reservoir cell, the number of molecules created is based on the SOVA density of water within that cell. Newly created molecules are then randomly distributed inside the cell. The SOVA temperature is then used to initialize the internal energy of each molecule as well as the thermal velocity component to be added to the bulk SOVA velocity within the cell. In the present simulations, the thermal components are drawn from a Maxwellian distribution. The molecules are moved by a full DSMC timestep and only the molecules exiting the reservoir cells are kept

(Figure 3-12). A simple search algorithm is used to see if a molecule remains within the reservoir cells.

When using reservoir cells for an inflow boundary condition, the timestep must be small enough so that not all of the molecules exit the creation cells. Also, the time interval between outputs in the SOVA hydrocode is variable. For both these reasons, the DSMC timestep was chosen independently of the SOVA timestep. The interface between the codes is unsteady and the DSMC molecules are created at each timestep based on the SOVA data at that time. If the SOVA timestep is larger than the DSMC timestep, which is the case in the present simulations, the data from a SOVA timestep is used to create molecules at each DSMC timestep until the DSMC simulation time has caught up to the SOVA time. Finally, for parallel simulations, due to different geometry between the SOVA and DSMC grids, some SOVA cells will be split up between multiple processors. In order to ensure that molecules within these cells are only created by one processor, processors will only consider the interface cells that have their cell centers within the processors' boundaries. If some of the newly created molecules are outside of the processor boundaries these molecules are transferred to the appropriate processor at the end of the creation step (see Appendix A).

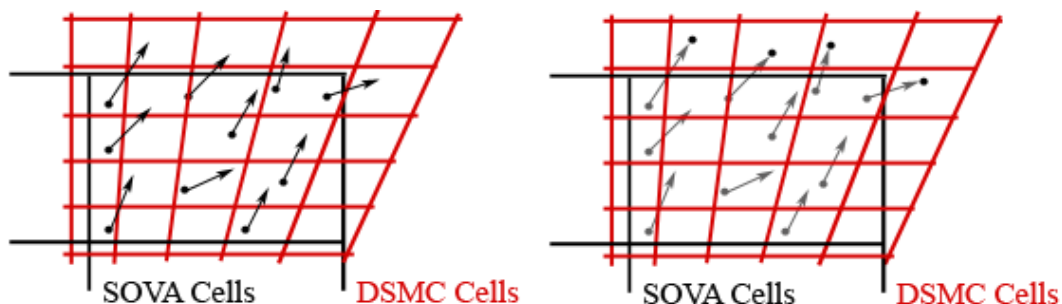


Figure 3-12 Schematic of the DSMC molecule creation in the SOVA interface cells.

Figure 3-13 summarizes the changes made to our DSMC implementation in order to use the SOVA data as input to our simulations. Only two changes were required: a new inflow subroutine had to be added to create molecules inside the SOVA interface cells and, after the molecules were created, a subroutine deleting the molecules remaining inside the reservoir cells had to be written.

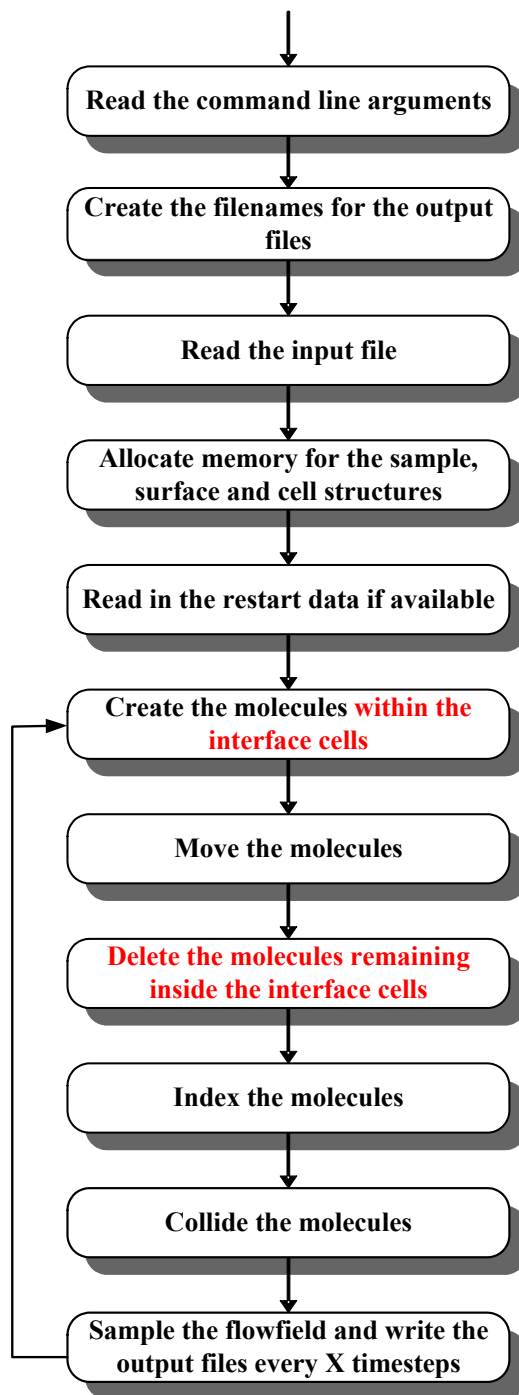


Figure 3-13 Schematic of the DSMC algorithm used for the comet impact simulations. Note that the steps related to the unsteady input condition at the interface with the SOVA hydrocode are shown in red.



### 3.4 SPECIAL FEATURES: THE MOVE SUBROUTINE

In order to simulate the late stages of a comet impact on the Moon as well as the induced circum-lunar flow up to months later, several new features have been implemented in our DSMC code. In the move subroutine, three main features have been added that are described in more detail below: a predictor-corrector scheme for the movement of the molecules, the molecular interaction with the lunar surface (with the required surface properties), and photodestruction processes for molecules in flight.

#### 3.4.1 Predictor-Corrector

In order to accurately model molecular movements, the present simulation uses a predictor-corrector scheme. The scheme is presented in Appendix C. An equatorial orbit, 300 km above the surface, is used to compare our solution with and without the use of the predictor-corrector scheme. In Figure 3-14, the three left-most figures have been obtained by using our predictor-corrector scheme. For timesteps equal to 0.1 and 10 s, the equatorial orbit was not unstable as a function of time. That is the molecule neither spiraled in nor out. For the larger timestep, equal to 100 s, the orbit seemed noisier than for the smaller timesteps but no obvious degradation was apparent (Figure 3-14). The right-most figures were obtained without the use of the predictor-corrector scheme. Contrary to the simulations with the predictor-corrector scheme, these three figures show large discrepancies between the simulated orbits after a few minutes. While the smallest timestep,  $\Delta t = 0.1$  s, was able to predict the orbit well enough so no degradation was obvious, both larger timesteps,  $\Delta t = 10$  and 100 s, were not able to resolve the movement of the molecule. As time increased, the molecule moved further away from the Moon until it would ultimately be lost from the simulation. Also, as the timestep was increased from 10 to 100 s, the degradation of the orbit was more pronounced. Note that the largest timesteps will not be used for the early stages of the impact simulations but the 10 s timestep will be used at late times when a nearly collisionless flow is established on the Moon.

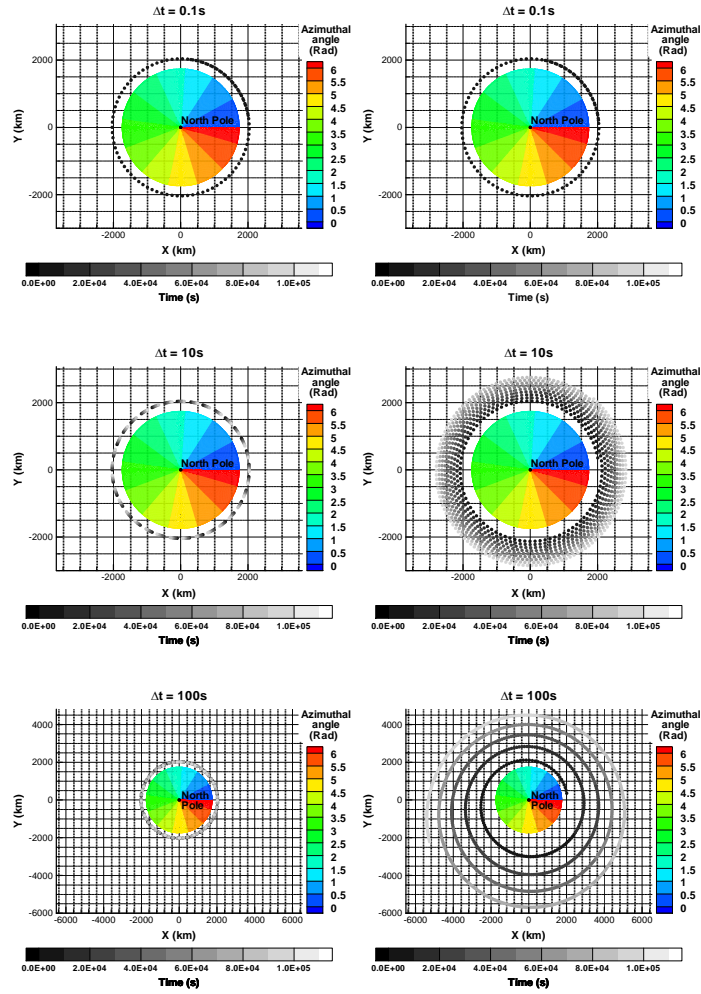


Figure 3-14 Equatorial orbit with (left) and without (right) a predictor-corrector scheme used for the movement of the molecule with three different timesteps of 0.1, 10, and 100 s. Azimuthal angle color contours at the surface of the Moon with the location of the North Pole added for reference are plotted with the associated legend. The time at which the molecule is located at a given location is given by the color of the dots (the associated greyscale legend is presented below the figure). Note that for each cases, the total time the molecule has been orbiting is different (10000 s for  $\Delta t = 0.1$  s vs. 100000 s for  $\Delta t = 10$  s and 100 s). Also, for clarity, note that only some of the dots have been plotted. Finally, note that the size of the domain in the bottom two figures (for  $\Delta t = 100$  s) is different from the previous four figures.

As a final validation of our predictor-corrector scheme, we simulated two ballistic trajectories for a molecule evaporating from the surface of the Moon with velocities representative of equilibrium temperatures of  $T_{MIN} = 120$  K and  $T_{MAX} = 400$  K, respectively. The timestep chosen for the circum-lunar flow calculations must resolve these trajectories for our solution to be relatively accurate. Figure 3-15 shows the ballistic trajectories for each initial surface temperature at the release location. Four different timesteps ( $\Delta t = 0.1, 1, 10$ , and  $100$  s) were used for the simulations and all the trajectories for each case are virtually identical except for the largest timestep. In that case, for the warmest initial surface temperature, the trajectory departs from the actual trajectory by about 70 km when the molecule finally hits the surface of the Moon again (two thousand kilometers away). In conclusion, from Figure 3-14 and Figure 3-15, we expect that the movement of our molecules will be resolved for the circum-lunar simulations as long as the timestep size remains smaller than 10 s.

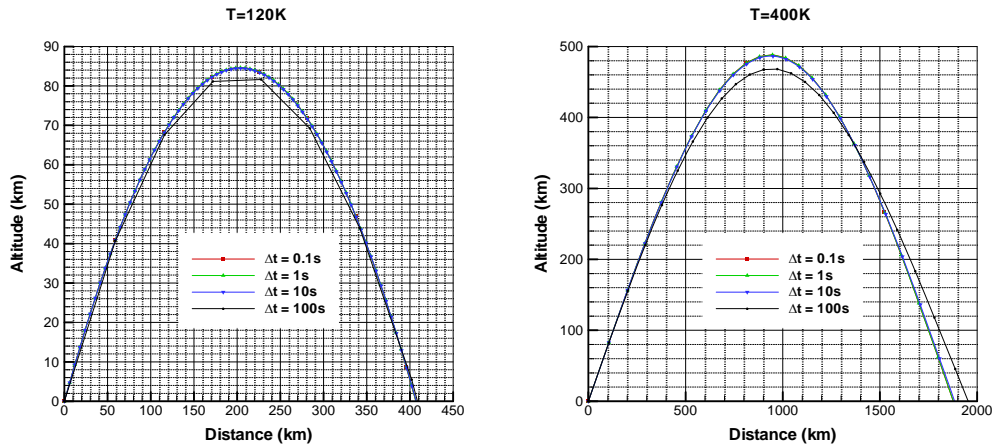


Figure 3-15 Ballistic trajectories for a molecule evaporating from the Moon's surface initially at a location where the surface temperature was 120 K (left) and 400 K (right) for four different timesteps of 0.1, 1, 10, and 100 s. The horizontal axis represents the distance along the surface of the sphere. Note that the axes are different for both figures.

### 3.4.2 Surface Temperature, Cold Traps and Residence Time

The Moon's surface temperature at given latitude and longitude depends on the location of this point relative to the subsolar point as follows (Butler, 1997):

$$T = (T_{MAX} - T_{MIN}) \times [\max(0, \cos \beta)]^{1/4} + T_{MIN} \quad (3.4)$$

where  $T_{MAX} = 400$  K,  $T_{MIN} = 120$  K and  $\beta$  is the subsolar zenith angle.

In the present simulations, the impact was chosen to be located at the axis of symmetry in our domain. For our parametric studies, however, the impact location had to be moved to different latitudes and longitudes. To do so, for each simulation, the lunar polar axis is rotated in our domain in order to reflect the desired location of the impact point on the Moon's surface. The details of the procedure are presented in Appendix B. In the reference frame associated with the surface temperature map, the location of a point on the surface of the moon is given by its angles,  $\Theta$  and  $\Phi$ . In this coordinate system, the North Pole is given by  $\Theta = 0^\circ$  and the subsolar point is assumed to lie at  $\Theta = \pi/2$ . Because of the relatively long timescales involved in our problem, the surface temperature at any point on the Moon's surface has to be time dependent to account for the rotation of the Moon around the Sun (similar to the temperature dependence in Walker *et al.*, 2009). We assumed that the Moon rotates around its polar axis (the tilt of the Moon axis is only  $1.5^\circ$  relative to the ecliptic plane) and we used a rotation rate of  $2.463 \times 10^{-6} \text{ s}^{-1}$  which is equivalent to a synodic period of 29 days 12 hours 37 minutes.

The objective of the present simulations is to investigate the possible accumulation of water ice in cold traps after a comet impact on the Moon. Over the years, several groups have modeled the conditions inside lunar polar craters in order to validate the existence of cold traps for water ice. In 1992, Ingersoll *et al.* investigated the stability of ice deposits at the poles of the Moon by calculating the surface temperature within a bowl-shaped crater. Using an energy balance between incoming scattered solar radiation and energy lost due to thermal radiation, they were able to determine the surface temperature of the shadowed regions of a crater. From their simulations, they found that the lowest latitude at which shadowed areas inside bowl-shaped craters would have a temperature of 102 K, and 117 K, is around  $77^\circ$  and  $72^\circ$ , respectively. Using

the evaporation rate from Watson *et al.* (1961), they noted that, for temperatures of 102 and 117 K, the evaporation rate would be 0.9 cm and 10 m over a billion years, respectively. In 1999, Vasavada *et al.* also studied the stability of water ice deposits at the lunar poles. They solved the 1D thermal diffusion equation as function of depth assuming incident solar radiation and emitted thermal radiation at the surface, and assuming temperature gradients at the bottom of their domain based on the lunar internal heat flux. In their simulations, they looked specifically at a list of lunar polar craters obtained from the observations by Nozette *et al.* (1996) and Margot *et al.* (1999). In addition, they used vapor pressure data to estimate the evaporation rates of water as function of temperature using a method similar to Watson *et al.* (1961) and found that 1 m of ice would take 1 billion years to sublimate at a temperature of 112 K or lower. From their model, they found that some of the observed craters had permanently shadowed areas with surface temperatures much lower than 110 K; so any water ice deposits inside these regions would be stable.

These two models seem to confirm that regions inside impact craters at the lunar poles have temperatures low enough to capture any water reaching those locations. In order to obtain a more precise location and total surface area for the lunar cold trap, several observational data sets can be used (Nozette *et al.*, 1996, Margot *et al.*, 1999, Elphic *et al.*, 2007, Noda *et al.*, 2008). Using data from the bistatic radar onboard the Clementine orbiter, Nozette *et al.* (1996) estimated that there were at least 6361 km<sup>2</sup> of permanently shadowed regions around the South Pole but only 530 km<sup>2</sup> around the North Pole. In 1999, Margot *et al.* used the Earth based Goldstone radar and estimated that the permanently shadowed areas should cover 1030 and 2550 km<sup>2</sup> at North and South Poles, respectively. More recently, Elphic *et al.* (2007) used elevation data sets from the observations of the lunar poles and combined them with a model for the illumination at the South Pole. From their simulations, they estimated that a total surface area of about 12,150 km<sup>2</sup> was in permanent shadow at the South Pole. Their model, however, did not provide estimates for the North Pole. Using data from the laser altimeter onboard Kaguya, Noda *et al.* (2008) estimated the illumination conditions at both lunar poles and found that above latitudes of 85°, 1236 km<sup>2</sup> and 4466 km<sup>2</sup> of permanently shadowed regions were present at the lunar North and South poles, respectively.

In the present simulations, we are using data from Elphic *et al.* (2007) and Margot *et al.*, (1999) for the location of our cold traps but the total surface area we are considering is more consistent with the Kaguya mission because these data are the most recent (Noda *et al.*, 2008). First, the latitude and longitude locations of the cold traps at the South Pole were based on the data presented in Table 1 in Elphic *et al.*'s 2007 paper. We then used Elphic *et al.*'s estimates for the actual shaded surface area and scaled our cold traps to cover the estimated permanently shadowed surface areas. In summary, our cold traps are disks, centered on the crater centers considered by Elphic *et al.* (2007), with a modified radius set to represent the actual surface area of the permanently shadowed areas. This approach is not an accurate representation of the distribution of the permanently shaded regions of the craters, but it is adequate considering our current resolution of  $1^\circ \times 1^\circ$  cells for the full planet simulations. But even with this approximation, we expect to obtain a fairly accurate determination of the total amount of water captured. For the North Pole cold traps, we only consider the three aligned craters around the  $315^\circ$  longitude and assign them a radius consistent with Noda *et al.*'s (2008) observed shadowed area at the North Pole. For our simulations, using our assumptions, the total surface areas of the shadowed regions are  $1257 \text{ km}^2$  and  $4575 \text{ km}^2$  at the North and South poles, respectively. These values are within 2.5% of Noda *et al.*'s estimates (2008). Table 3-2 summarizes the location and size of our lunar cold traps.

In order to know if a molecule that hit the surface of the Moon landed inside a cold trap, the code loops through the cold traps in Table 3-2 and checks if each molecule hitting the surface is within the cold trap radius. If so, the molecule is saved to a file with the time at which it landed and it is deleted from the calculation. More details about the search procedure are presented in Appendix C. Note that the Moon's surface is assumed to be smooth and that no elevation map was used in our calculations as we assume that terrain highs and lows tend to be small compared to water vapor scale height. Figure 3-16 shows the locations of the cold traps at the smooth poles of the Moon. The top figure shows the surface temperature contours with superimposed latitude and longitude lines. Oversized green molecules that are stuck in the cold traps are used to mark the location of the cold traps. The bottom figures are close-up views of the South (left) and North (right) poles with the actual locations and actual sizes of our cold traps.

Table 3-2 Cold traps location and surface area

Crater Name	$\Theta$ (°)	$\Phi$ (°)	Radius (km)	Surface Area (km <sup>2</sup> )
Unnamed (at SP)	177.5	356	20.34	1300
Shoemaker	178.1	45	19.34	1175
Cabeaus	174.5	322	16.93	900
Faustini	177.3	77	14.93	700
De Gerlache	178.5	273	9.77	300
Shackleton	179.7	110	7.98	200
Unnamed (at NP)	1.7	312	20.0	1257

In the case where a molecule hits the surface of the Moon outside of the cold traps, the surface interaction needs to be computed. The present simulations use the Langmuir (1916) and Frenkel (1924) model for the residence time of water on a water matrix:

$$t_{reside} = \nu_0^{-1} \times e^{\Delta H/kT} \quad (3.5)$$

where  $\Delta H = 6.65 \times 10^{-20}$  J is the binding energy,  $k$  is the Boltzmann constant,  $\nu_0 = 2.0 \times 10^{12} \text{ s}^{-1}$  is the lattice vibrational frequency of water within a water matrix, and  $T$  is the surface temperature (Sandford and Allamandola, 1993).

After a simulated molecule hits the surface of the Moon, at each subsequent timestep, the ratio of the timestep,  $\Delta t$ , to the residence time of the molecule,  $t_{reside}$  is compared to a random number. If the ratio is larger than the random number the molecule sublimates. It is released from the surface with velocities and internal energy representative of the local surface temperature.

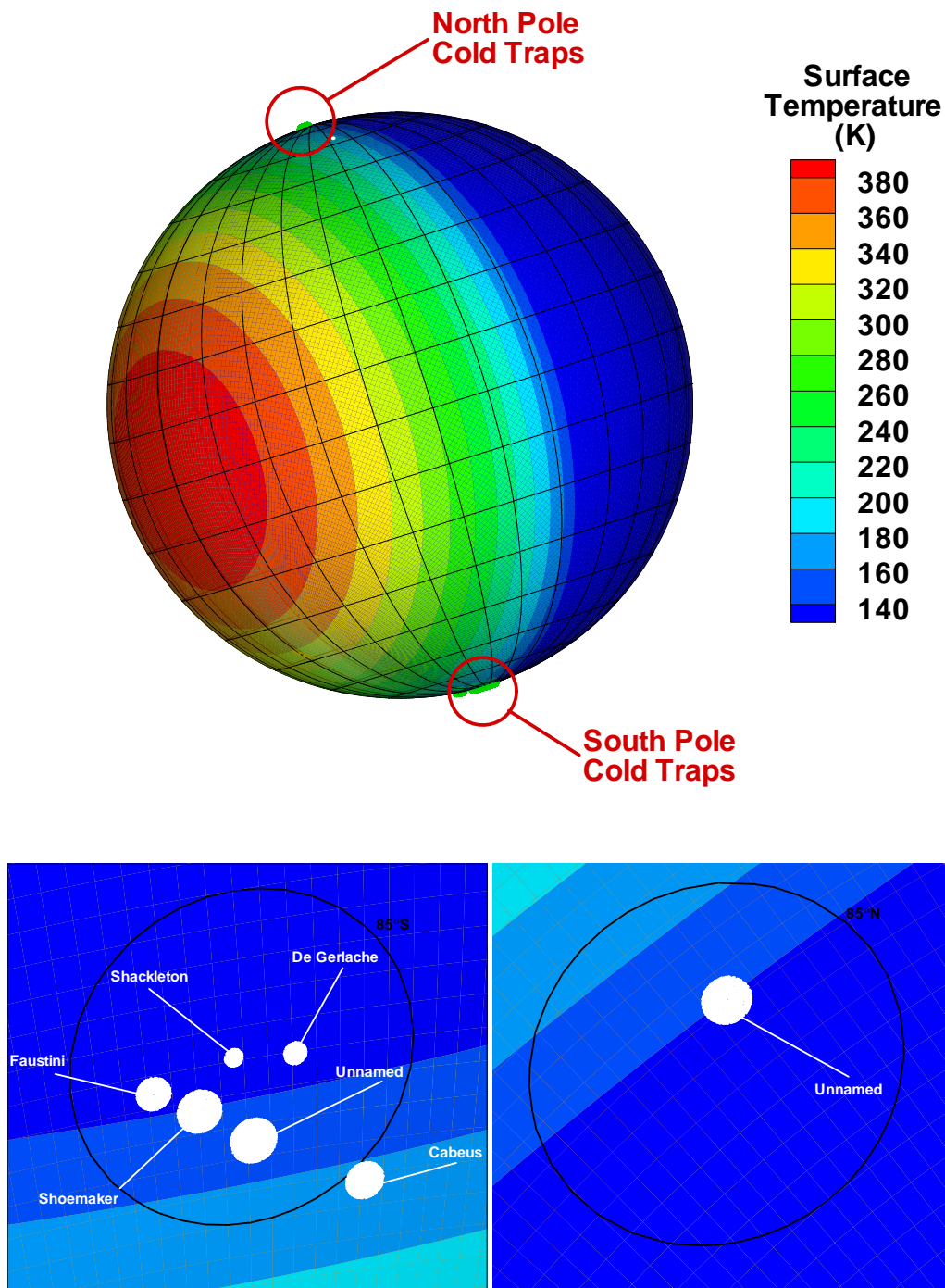


Figure 3-16 Cold Trap locations at the poles of the Moon used in our simulations.



### 3.4.3 Photodestruction Processes

Of all the loss processes the molecules may undergo while in the DSMC domain, we decided to restrict ourselves to escape and photodestruction processes for water molecules in-flight. While molecules hop around the Moon in the sunlit regions of the atmosphere, the water molecules will have certain probabilities to photodissociate and photoionize due to their interaction with solar photons (Goldstein *et al.*, 1999, Huebner, 1992):

$$\begin{aligned} P_{ionize} &= e^{-\Delta t / 2.45 \times 10^6} \\ P_{dissociate} &= e^{-\Delta t / 8.3 \times 10^4} \end{aligned} \tag{3.6}$$

At each timestep, for each molecule that is in the sunlit part of the atmosphere, a random number is compared to the previous probabilities in order to determine if the molecule is dissociated or ionized. If it is, the molecule is lost and is removed from the computation. One additional requirement is that we need to know when a molecule is in the sunlit part of the atmosphere. The details of the computation are presented in Appendix C. To validate our implementation, we used an equatorial orbit to plot when a molecule is in the shade versus in the sun (shown in Figure 3-17).

$\Delta t = 10s$

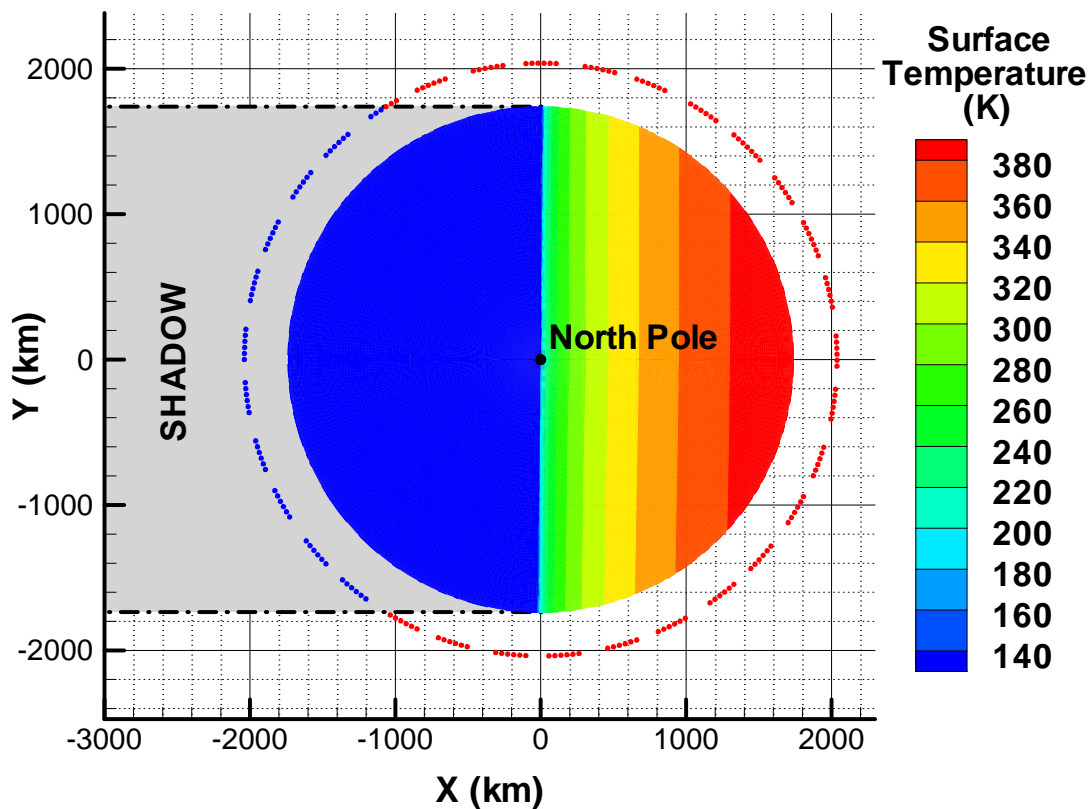


Figure 3-17 Equatorial orbits with shadow calculations for a timestep size of 10s. If the molecule is in the shadow of the Moon, it is represented by a blue dot if it is in the sun it is represented by a red dot.

### 3.5 SPECIAL FEATURES: THE COLLIDE SUBROUTINE

#### 3.5.1 Collision Limiter

DSMC simulations become computationally expensive as the density increases because of the large number of collisions that have to be computed and because the collision step is the most expensive part of the DSMC method. One way to decrease the computational cost of high density flow computations with non-equilibrium regions is by using hybrid CFD-DSMC methods. In these approaches, the regions of the flow in thermal equilibrium are solved using a CFD solver. An alternative way used to simulate the regions of the flow in thermal equilibrium has been to implement a modified DSMC method using a collision-limiting scheme (Titov and Levin, 2007, Macrossan and Geng, 2007, and Stewart *et al.*, 2009). In a resolved DSMC solution, the preferred cell size is of the order of the mean free path and the timestep should be smaller than the average time between collisions. However, in high density regions, these requirements are hard to match so a larger timestep and cell size are generally used. Unfortunately, the relaxation of these parameters means that a large number of collisions must be computed in every cell at each timestep. In general, in the local thermal equilibrium (L.T.E.) regions, some fraction of the total number of collisions bring the flow to equilibrium and the remainder only redistribute energy at the microscopic level leaving the macroscopic variables unchanged. Therefore, a collision limiter can be used in the high density regions of the flow in L.T.E. to decrease the computational time without significant loss of accuracy relative to a regular DSMC calculation. The Titov and Levin (2007) equilibrium DSMC (eDSMC) code utilizes a collision-limited approach to simulate high density flows, such as steady nozzle and supersonic channel flows. The eDSMC method is based on the DSMC method where the total number of collisions per cell per timestep is limited on average to two per molecule. For the flows that they studied, two collisions per molecule were sufficient to obtain a near equilibrium distribution in the cell. Their eDSMC method provided good agreement with high order Eulerian solvers for inviscid flows. For flows with both viscous and inviscid regions, a hybrid eDSMC-DSMC method is used, where the eDSMC method is used to simulate the inviscid regions of the flow and the regular DSMC method simulates the viscous regions. The results provided good agreement with full DSMC simulations with a noticeable speed-up. Macrossan and Geng (2007) also used a collision limited DSMC method in order to simulate steady rarefied flows with regions in thermal equilibrium. In

their approach, they used two possible breakdown parameters to determine which cells are in thermal equilibrium. The first parameter is the ratio of shear stress to pressure and the second parameter quantified the deviation of the temperature components from the mean kinetic temperature. Once the different regions of the flow have been characterized, the non-equilibrium regions are computed using the DSMC method and the equilibrium regions are computed using the collision-limited version of the DSMC method. The collision limited computations were in good agreement with full DSMC simulations with savings of about 10% of computational time.

The present DSMC implementation (Stewart *et al.*, 2009) is presented in detail in the following sections. In the modified “no time counter” scheme (NTC) used in the present DSMC implementation (Bird, 2007) the number of molecule pairs that need to be selected for potential collisions in a given cell is given by:

$$N_{SELECT} = \frac{1}{2} NUM(NUM - 1) F_N (\sigma_T c_r)_{max} \Delta t / V_C \quad (3.7)$$

where  $NUM$  is the number of representative molecules,  $F_N$  is the number of real molecules represented by a single DSMC molecule,  $(\sigma_T c_r)_{max}$  is representative of maximum value of the product of the collision cross section by the relative speed of selected pairs,  $\Delta t$  is the timestep size and  $V_C$  is the cell volume. In the present simulations, the collision cross-section,  $\sigma_T$ , is calculated using the Variable Hard Sphere (VHS) model for water.  $(\sigma_T c_r)_{max}$  is a parameter whose value is initially reasonably large but converges towards the maximum value of  $(\sigma_T c_r)$  for all the selected pairs in that cell. If the parameter  $(\sigma_T c_r)$  of an accepted pair is larger than  $(\sigma_T c_r)_{max}$  then  $(\sigma_T c_r)_{max}$  is updated. However, we want to keep the selection routine fairly efficient so we allow  $(\sigma_T c_r)_{max}$  in every cell to relax each timestep in order to avoid having the value of  $(\sigma_T c_r)_{max}$  be dictated by rare collision events with very large  $(\sigma_T c_r)$ . In order to relax  $(\sigma_T c_r)_{max}$ , we store the largest  $(\sigma_T c_r)$  of all selected pairs during the timestep,  $(\sigma_T c_r)_{largest}$ , and then, at the end of the timestep, set  $(\sigma_T c_r)_{max\_new}$  equal to:

$$(\sigma_T c_r)_{max\_new} = 0.95 \times (\sigma_T c_r)_{max} + 0.05 \times (\sigma_T c_r)_{largest} \quad (3.8)$$

At “worst” this relaxes  $(\sigma_T c_r)_{max}$  by 5% each timestep and, when  $(\sigma_T c_r)_{max}$  approaches the largest  $(\sigma_T c_r)$  in the cell, the change in  $(\sigma_T c_r)_{max}$  decreases as well. Therefore,  $(\sigma_T c_r)_{max}$  should not

tend to over-relax below the largest  $(\sigma_T c_r)$  in the cell unless the cell properties change or the cell is nearly collisionless (few collisions means that  $(\sigma_T c_r)_{largest}$  might not be equal to the largest  $(\sigma_T c_r)$  in the cell). This allows us to keep the ratio of the number of accepted pairs to selected pairs closer to unity if properties (temperature, etc.) of the cell have changed and speeds up the collision routine. Once a pair is selected, the collision is computed with the probability  $\frac{\sigma_T c_r}{(\sigma_T c_r)_{max}}$ . In our DSMC simulations of the comet impact event, the number of pairs to be selected, as given by Eq. (3.7), can be as large as  $\sim 10^6$  collisions per molecule per timestep (see Chapter 5). However, for a gas in thermal equilibrium, the translational and rotational energy modes of a molecule reach equilibrium with the other molecules in a cell after usually only a few collisions while the vibrational modes require anywhere from  $\sim 10^2$  to  $10^4$  collisions to equilibrate. The Titov and Levin (2007) and Macrossan and Geng (2007) collision limiters were used to simulate flows of monatomic and diatomic gases at low enough temperatures so that the vibrational modes would not be excited. Therefore, they were able to limit the total number of collisions to a small number (2 for Titov and Levin (2007)) in order to equilibrate the translational and rotational modes. In the present simulations, we are interested in the expansion flow of water vapor after a comet impact where the flow temperatures can be larger than 1000 K. Water is a triatomic molecule with three vibrational modes: the  $\nu_1$  and  $\nu_3$  stretching modes and the  $\nu_2$  bending mode. If a cell is in thermal equilibrium, each vibrational mode of the water molecules needs to be equilibrated also. However, the vibrational relaxation collision number for each mode ( $Z_1 = Z_3 = 100$  and  $Z_2 = 50$ ) is much larger than the rotational relaxation collision number ( $Z_{ROT} = 2.5$ ) and typically hundreds of collisions have to be computed before a vibrational mode will exchange energy with the other energy modes. Therefore, a two-level collision limiter is used in the present approach where the rotational and translational modes are equilibrated first using regular collisions, then the vibrational modes are brought to equilibrium using “modified” collisions where vibrational energy exchange is forced. Each one of these collisions represents hundreds of regular collisions and enables faster computation of the equilibration of the vibrational energy modes of a molecule. In addition to being applicable to high temperature flows of polyatomic molecules, the present method has the major advantage of not utilizing a breakdown parameter. As will be explained later in this section, as the collision rate of the flow decreases, the present collision-limiting scheme relaxes automatically to the regular DSMC collision scheme.

The algorithm for the collision subroutine in the case when the collision limiter is utilized is presented in Figure 3-18 (Stewart *et al.*, 2009). At the beginning of the collision subroutine, the number of pairs of molecules that should be selected per timestep per cell,  $N_{SELECT}$ , is calculated using Eq. (3.7). In addition, the collision limit,  $N_{T-R}$ , is also computed. In the current simulations, the rotational relaxation collision number,  $Z_{ROT}$ , is fixed at 2.5 and  $N_{T-R}$  is chosen to be 5 times the number of molecules in the cell so the translational and rotational modes can equilibrate. The code then starts to loop over the number of collisions. A pair of molecules is picked at random from the cell and the pair is accepted for collision based on the value of the product between its collision cross-section and the relative speed of the molecules. If the pair is accepted, the collision is computed. As long as the number of accepted collisions remains lower than  $N_{T-R}$ , a regular collision is computed. While selecting potential collision partners up to  $N_{T-R}$  accepted collisions, the number of selections needed is counted. This allows for the fraction of accepted collisions,  $F_{ACCEPTED}$ , to be estimated by the ratio of the number of accepted collisions over the number of needed selections.

After  $N_{T-R}$  collisions on average per molecule, the vibrational modes will not be equilibrated so  $N_{VIB}$  additional “modified” collisions are computed. In a “modified” collision, the probability of energy exchange between the vibrational and the translational mode is increased by the minimum average number of collisions for vibrational energy transfer ( $Z_{V,MIN}$ ) so each “modified” collision represents  $Z_{V,MIN}$  accepted regular collisions. Using this method, the probability of exchange of energy between the translational modes and several vibrational modes during one collision is very high. Unfortunately, from our initial simulations we found that modifying the order in which the modes were considered for energy exchange changed our computed solution. For an expansion flow, after the first vibrational-translational energy exchange, the amount of translational energy remaining for the next energy exchange was biased. This led to an unphysical overpopulation of molecules in higher vibrational states when equilibrium should have existed. Therefore, we modified our implementation to only consider one vibrational mode at a time during a “modified” collision. Using these assumptions, the number of “modified” collisions,  $N_{VIB}$ , to perform is given by

$$N_{VIB} = \frac{M_V \times (N_{ACCEPTED} - N_{T-R})}{Z_{V,MIN}} \quad (3.9)$$

where  $M_V$  is the number of vibrational modes (equal to three for water) and the term in parentheses is the number of accepted collisions remaining after the  $N_{T-R}$  collisions are performed. Unfortunately, in the NTC method,  $N_{ACCEPTED}$  is only known once all the collisions have been computed. Therefore, in the present simulations it has been approximated by  $F_{ACCEPTED} \times N_{SELECT}$  (Eq. (3.10)); fewer “modified” collisions will, in general, not result in full equilibration of all the vibrational modes. In addition,  $N_{VIB}$  is capped at 6 per vibrational mode per molecule since after that many “modified” collisions the vibrational modes will be equilibrated. Therefore, in our model the number of “modified” collisions,  $N_{VIB}$ , to perform is:

$$N_{VIB} = \text{Min} \left( \frac{M_V \times (F_{ACCEPTED} \times N_{SELECT} - N_{T-R})}{Z_{V,MIN}}, 6 \times M_V \times NUM \right) \quad (3.10)$$

All additional collisions beyond  $N_{T-R} + N_{VIB}$  are not performed because the gas in that cell is already in equilibrium.

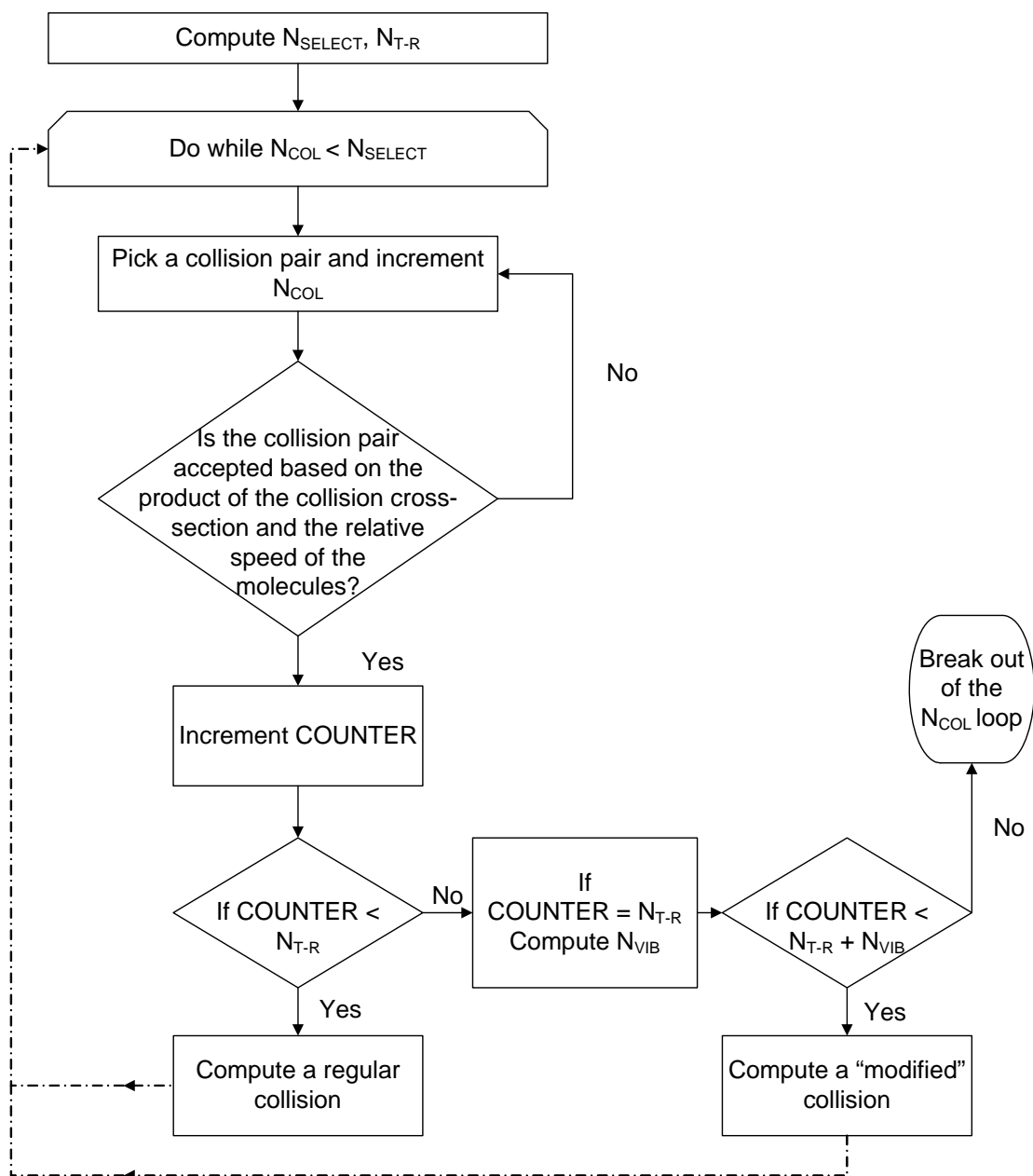


Figure 3-18 Flowchart of the collision subroutine when the collision limiter is turned on.

Figure 3-19 details the differences between regular and “modified” collisions. During a regular collision the probability of energy exchange between a vibrational mode and the translational mode is based on the vibrational relaxation collision number for that given vibrational mode (Bird, 1994). In a “modified” collision, the probability of a given vibrational



energy exchange is increased by multiplying the regular collision probability to the value of the minimum vibrational collision number for the entire simulation ( $Z_{V,MIN}$ ). In the current simulations,  $Z_{V,MIN}$  is equal to 50 but would be variable if the vibrational relaxation collision numbers were varying with temperature, for instance. The other major difference between the regular and “modified” collisions is that a “modified” collision considers only one vibrational mode picked at random for possible energy exchange instead of considering all three modes.

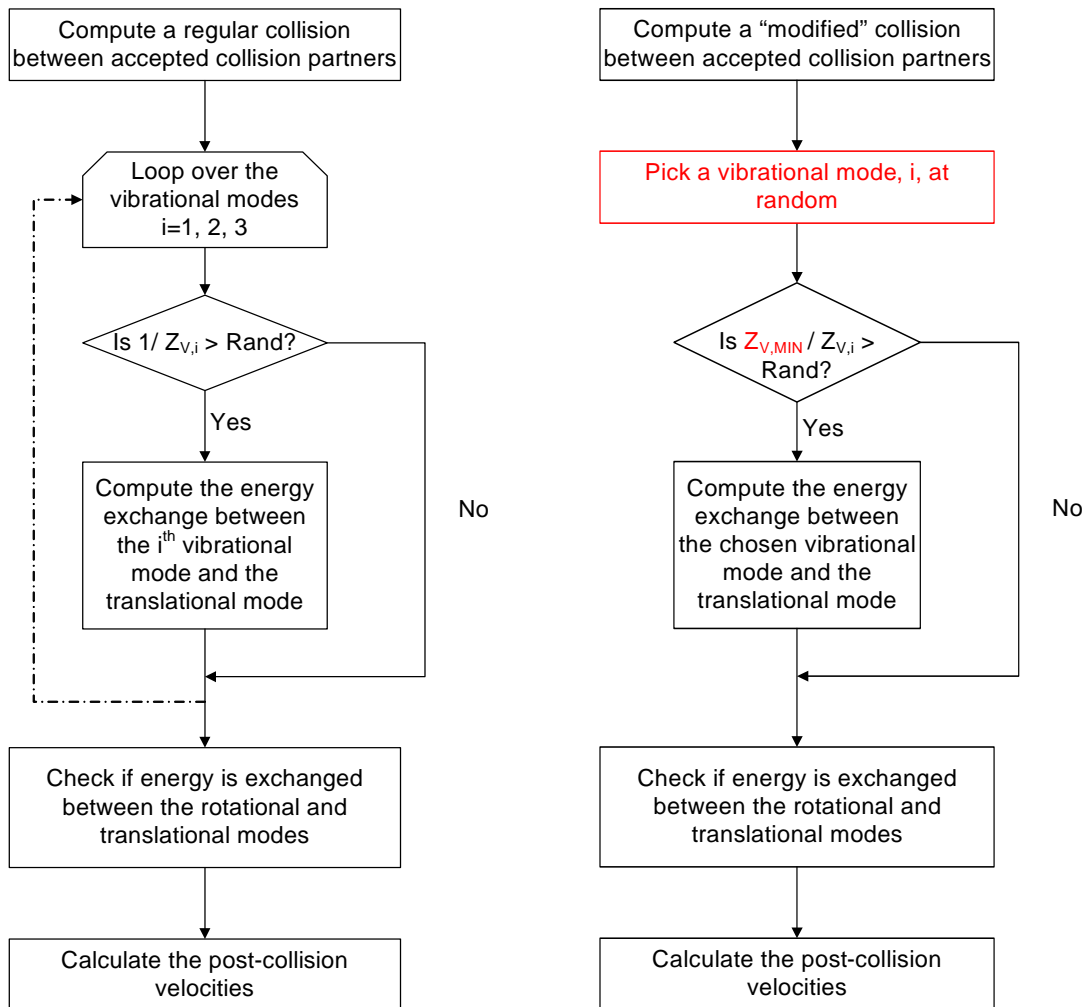


Figure 3-19 Flowchart for a regular (left) and "modified" (right) collision.

Figure 3-20 is a schematic representation of the scale of each collision number variable in a region of flow where the timestep is much larger than the mean collision time and therefore  $N_{SELECT} \gg NUM$  and, in general,  $N_{SELECT} > N_{ACCEPTED}$ . In the current simulations,  $N_{T-R}$  and  $N_{VIB}$  are of the order of the number of molecules in the cell ( $NUM$ ) but are much smaller than the number of selection pairs ( $N_{SELECT}$ ) given by Eq. (3.7). In our comet impact simulations, the total number of collisions computed is about 4 orders of magnitude smaller than  $N_{SELECT}$ .

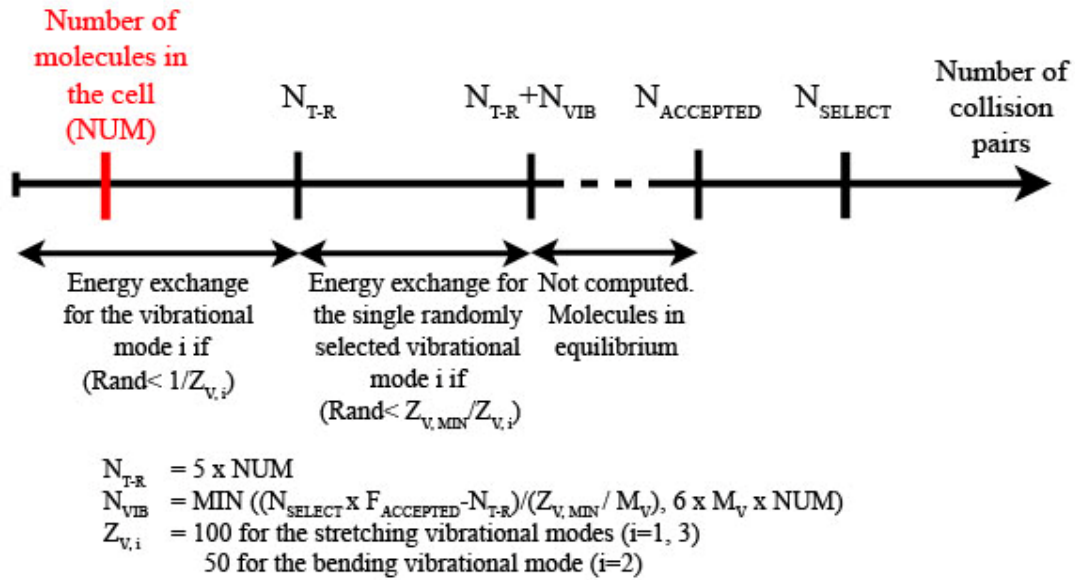


Figure 3-20 Scaling of all the variables considered in the collision limiter subroutine for an under-resolved (in time) high density flow. The total number of accepted collisions is limited to a few per molecule. Equilibration of the translational modes and rotational modes is achieved through  $N_{T-R}$  regular collisions. Energy exchange with the vibrational modes is then computed more quickly by allowing  $N_{VIB}$  additional “modified” collisions where the probability of translational-vibrational energy exchange is increased.

For a flow expanding into a vacuum, such as a comet impact on the Moon, the density of the flow drops rapidly away from the point of impact and the number of selected pairs ( $N_{SELECT}$ )

calculated using the NTC method (Eq. (3.7)) will also start to decrease. At some point,  $N_{SELECT}$  will be small enough (on the order of a few hundred) such that the vibrational modes should start to freeze out. In that case, in our collision-limited code,  $N_{VIB}$  will be equal to  $M_V \times (F_{ACCEPTED} \times N_{SELECT} - N_{T-R}) / Z_{V,MIN}$  instead of  $6 \times M_V \times NUM$  (Eq. (3.10)) which enables partial equilibration of the vibrational modes and freezing of the vibrational temperatures should be observed. Even later in the expansion,  $N_{SELECT}$  will become smaller than  $N_{T-R}$  and in that case the simulation is no longer collision-limited and it reverts to a classic DSMC computation.

### 3.5.2 Free Cells

The vapor plume produced by a comet impact on the Moon is mostly characterized by relatively low temperatures (less than 1000 K) and very large velocities (up to several tens of kilometers per second) (see Chapter 5). In addition, due to the large size of our computational domain (several kilometers in all three directions), the cell size is at least a few hundred meters for the near field plume calculations but can be as large as 30 km at the equator for the full planetary simulations. Under these conditions, in order to minimize the numerical viscosity induced by colliding molecules far apart (relative to the mean free path), we implemented a free cell method in our collision step similar to that of Roveda *et al.* (2000). For each first partner picked for a collision, a second partner must be picked within a certain region near the first partner. In the present simulations, the free cell region is  $1/10^{\text{th}}$  the cell size. If the second partner does not fulfill this condition another partner is picked. This process is repeated as many times as there are molecules in the cell and if no partner has been found, the size of the search region surrounding the first molecule is linearly increased. This overall process is repeated until a second partner is found or the size of the region has been expanded to the full cell. Our approach is, however, more simplistic than Roveda *et al.*'s as the size of our free cell does not depend on the characteristics of the flowfield.

## 3.6 OTHER FEATURES: UNSTEADY MULTI-DOMAIN CALCULATIONS

The cells in the near field of the impact need to be small enough in order to capture the physics of the expansion plume. However, it is currently impossible to run a full planet simulation with such small cells and even the use of free cells (see Section 3.5.2) can only help if the average separation between molecules is much smaller than the cell size. For that reason, a

restart capability has been implemented in the code so that molecules created in the near field can be transferred to a larger domain as they exit the inner domain. The present 3D unsteady multi-domain implementation is an extension of Zhang *et al.*'s (2003) 2D steady multi-domain sequential procedure. This multi-domain approach is valid for the present early stages of a comet impact event on the Moon as the induced flow is supersonic away from the impact point in the near field.

In Zhang *et al.*'s (2003) axisymmetric code, which was used to model steady volcanic plumes, a sequential approach is used to go from the inner domain to the outer domains. In the innermost domain, a relatively fine grid and small timestep are used to resolve such features as radiation from the vibrational bands within the core of volcanic plumes. The larger domains are used to resolve the entire plume that would be too computationally expensive to run with the resolution used in the innermost domain. Each stage is run until steady state is reached and at that time the molecules that exit the domain through the right and top boundaries are stored in a file. In their simulations, the left boundary is the axis of symmetry and the bottom boundary is the surface of Io. The saved molecules are read in during the next stage of the calculation in a larger domain. The number flux at the boundaries is preserved by using weighting factors. This process can then be repeated as many times as is required as long as the flow remains supersonic across the boundaries of the domain. While this approach was appropriate for the steady volcano plumes, the unsteadiness of the impact simulations required a slightly different approach.

In our implementation, instead of matching the number flux at the boundary, the molecules that exited the inner domain at a given time have to enter the outer domain at the same given time (Figure 3-21). Similarly to Zhang *et al.* (2003), the left boundary is at the axis of symmetry of the spherical domain and the bottom boundary is the surface of the Moon so we only need to transfer molecules that exit the inner domain through the right and top boundaries. In our code, such molecules are stored in a file while a second file keeps track of the time at which a molecule exited the domain (Figure 3-21). In the next step, the second file is used to track at which time a molecule is to be created inside the outer domain. When the timestep is not constant across domains, the move subroutine has been modified so the newly created molecules are moved by a partial timestep based on the actual time they exited the inner domain. For practical reasons, the unsteady approach has only been run using integer multiples of the timestep from one domain to the next.

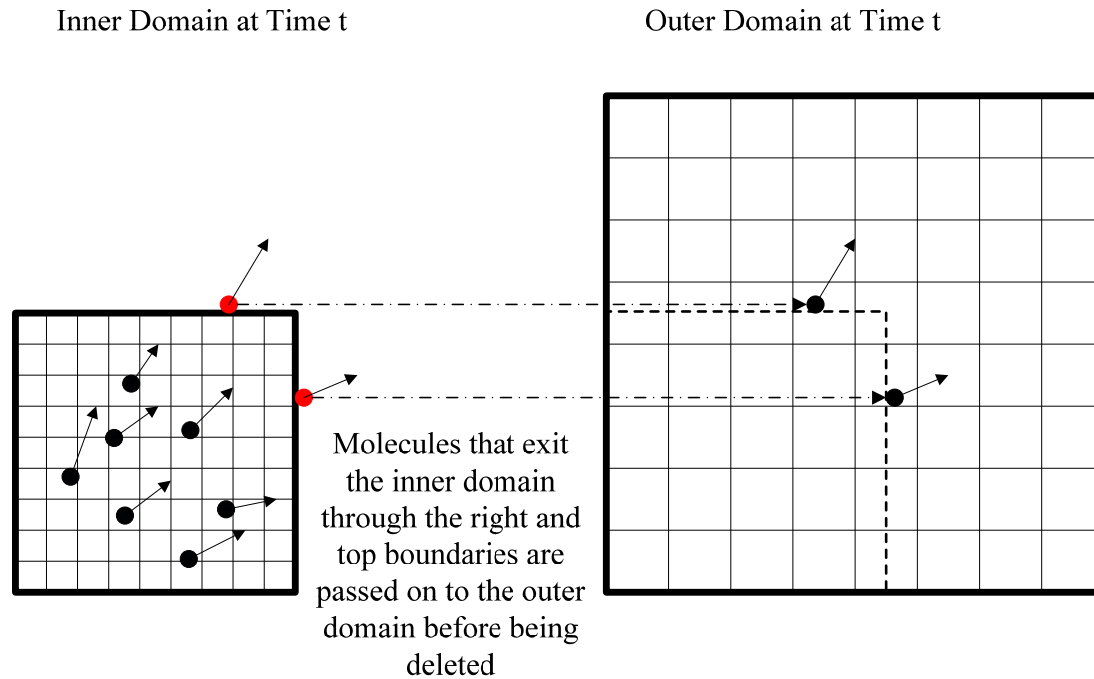


Figure 3-21 Schematic of the multi-domain approach used in the DSMC code. The inner domain is first run and as molecules exit the right and top boundaries they are saved to a file. Later, the molecular data are read in into a larger domain and molecules are input to the domain at the exact same time in the computation as they exited the inner domain.

One example of the use of our unsteady multi-domain approach is presented in Figure 3-22 for the  $45^\circ$  oblique impact of a 2 km diameter comet three seconds after the beginning of the impact. Four separate domains are shown in the figure, with the limits of each domain in the  $(X_{\beta=0^\circ}, Z_{\beta=0^\circ})$  plane being  $32 \text{ km} \times 32 \text{ km}$ ,  $60 \text{ km} \times 60 \text{ km}$ ,  $120 \text{ km} \times 120 \text{ km}$ , and  $240 \text{ km} \times 240 \text{ km}$ , from innermost to outermost. The cell size was increased from 100 to 200, 400, and finally 800 m in the outermost domain. The timestep size was 0.2 ms in the innermost domain and is fixed at 10 ms in all three outer domains. In order to present the data, the 3D results were interpolated onto a 2D Cartesian grid with a cell size of 500 m (See Section 5.4.2). The interpolated density contours shown in Figure 3-22 exhibit smooth transitions at the boundaries between the domains and several features can be observed across boundaries. For

instance, the mid-density feature ( $\sim 0.5\text{--}1 \times 10^{-2} \text{ kg/m}^3$ ) 40 km downstream of the point of impact can be traced from across the top boundary of the second domain to the third domain.

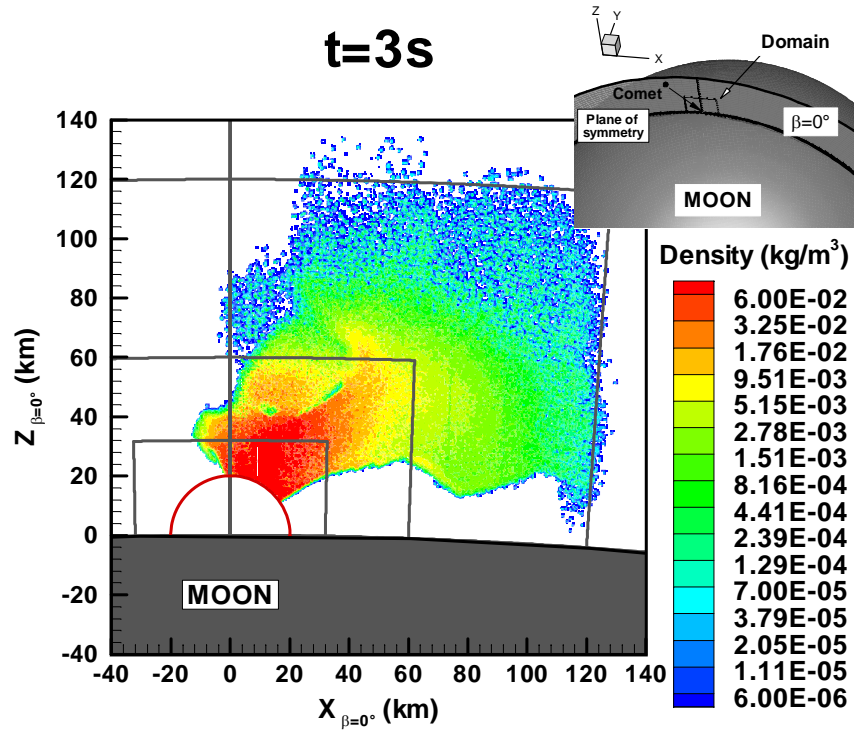


Figure 3-22 2D density contours in the plane of impact for the water vapor plume induced by a 2 km diameter comet 3 s after impact on the Moon. The comet hits the surface at an angle of  $45^\circ$  at 30 km/s from the left of the figure to the right. The red semi-circle represents the interface with the SOVA hydrocode and the grey lines represent the boundary of each DSMC domain used in the present unsteady sequential multi-domain simulation.

## Chapter 4

### Simulations of 1D Unsteady Expansion Flow into a Vacuum

#### 4.1 OBJECTIVES

Before simulating the relatively complex expansion flow induced by a comet impact, the present implementation of the DSMC method has been used to simulate a seemingly simple 1D unsteady expansion flow into a vacuum. The difficulties in simulating such flow with the DSMC method arise from the relatively high densities within the cloud and the unsteadiness of the flow. In this Chapter, we use an analytic solution to provide the required boundary conditions for the DSMC simulations in place of the SOVA hydrocode data. Within the DSMC domain, the DSMC results are then compared to the analytic solution in order to validate our approach. We chose to use the analytic solution derived by Tzuk *et al.* (1993) for the 1D unsteady expansion of a gas cloud into a vacuum. The initial conditions for the analytic solution have been chosen so that the flowfield generated resembles the flow produced by a comet impact. The analytic expansion plume is spherically symmetric, is made out of water vapor and is highly supersonic away from the point of origin of the expansion. In order to validate our 3D implementation, the present simulations were run fully 3D and a spatial average was used to compare our results to the 1D analytic solution. Also, we wanted to verify that we correctly implemented the reservoir boundary conditions for the complex geometry of the SOVA interface, so we used the SOVA interface geometry with the analytic solution data as our boundary condition for the DSMC simulations. In addition to verifying our implementation, we also used the present simulations to validate our model. In particular, we wanted to verify that the collision limiting scheme used in our code was valid, and that our spatially and temporally under-resolved simulations in the near field were still providing an acceptable solution. Finally, the 1D analytic solution also provided a relatively inexpensive way to observe the speed-up obtained with our parallel implementation (See Section 3.2.1).

## 4.2 ANALYTIC SOLUTION

Starting as early as the late fifties, appreciable effort was put toward modeling the sudden expansion of a gas into a background atmosphere or into a vacuum. Most of the early research groups derived analytic solutions to expansion flows using simplifying assumptions. While only valid under certain conditions, their solutions were quite successful at describing the overall behavior of expansion flows. In 1959, Sedov famously developed several self-similar solutions that could be applied to explosions from a point source or to spherical detonations. In order to derive his solutions, Sedov (1959) assumed that a finite amount of energy was deposited instantaneously at the point of origin of the explosion producing a strong expanding shock wave behind which the gas was set in motion. He further assumed that the expansion was inviscid without heat conduction or chemical reactions and that the gas was a perfect gas. Using this solution, Sedov (1959) was able to deduce the amount of energy liberated during an experimental American atomic bomb explosion using a series of photographs of the fireball observed after the explosion. All of Sedov solutions (1959) assumed a background gas; therefore they could not directly be applied to meteorite or comet impact events on the Moon. A few years later, however, Stanyukovich (1960) and Zel'dovich and Raizer (1967) provided analytical solutions for the problem of the expansion of a gas cloud into a vacuum. More recently, Tzuk *et al.* (1993) revisited the Stanyukovich (1960) and Zel'dovich and Raizer (1967) solutions. Tzuk *et al.*'s (1993) analytic solution is used in the present simulations and is described in more detail in the following section.

The analytic solution derived by Tzuk *et al.* (1993) assumes that the gas is an ideal gas with constant specific heats. The solution was derived for plane flows, flows with cylindrical symmetry and flows with spherical symmetry. In the present work, we are only interested in the spherically symmetric solution. The gas is initially confined inside a sphere of radius  $R_0$  when a large amount of energy is deposited into the gas sphere. At  $t = 0$ , the “separation” from the vacuum is removed, the initial energy is transformed into kinetic energy and the outer shells of the sphere begin to expand into the vacuum. This expansion flow is assumed to be isentropic and the initial density and pressure distributions inside the sphere have a specific form that allows for a self-similar solution to be found for the late times of the expansion, when the gas cloud size is



much larger than  $R_0$  (Tzuk *et al.*, 1993). The self-similar solution for the density, temperature, and radial velocity is as follows:

$$\begin{aligned}\rho &= \frac{AM}{V_{max}^3 t^3} \left[ 1 - \left( \frac{dist}{V_{max} t} \right)^2 \right]^{\frac{1}{\gamma-1}} \\ T &= T_0 \left( \frac{R_0}{V_{max} t} \right)^{3(\gamma-1)} \left[ 1 - \left( \frac{dist}{V_{max} t} \right)^2 \right] \\ V_r &= \frac{dist}{t}\end{aligned}\tag{4.1}$$

where  $V_{max}^2 = V_\infty^2 \frac{5\gamma-3}{3\gamma-3}$ ,  $V_\infty = \sqrt{\frac{2Q}{M}}$ ,  $A = \frac{\Gamma(\frac{5}{2} + \frac{1}{\gamma-1})}{2\pi\Gamma(\frac{3}{2})\Gamma(\frac{\gamma}{\gamma-1})}$ , and  $T_0 = \frac{(\frac{Q}{M})(\gamma-1)}{\mathcal{R}}$

(4.2)

and where  $\rho$  is the density,  $t$  is the time,  $V_r$  is the radial velocity component,  $dist$  is the distance from the center of the cloud,  $\gamma$  is the ratio of specific heats,  $T$  is the temperature,  $\mathcal{R}$  is the specific gas constant,  $M$  is the mass of the gas,  $Q$  is the total energy of the gas,  $\Gamma$  is the gamma function and  $V_{max}$  is the velocity of the outer layers of the cloud.

### 4.3 DSMC SIMULATIONS

The analytic solution above provides a simple model of a comet impact expansion flow. In order to most resemble the comet expansion plume flow, the gas used in the present simulations is water vapor. Again we are ignoring any chemical reactions and condensation within the DSMC domain. One of the main assumptions used in the derivation of Eq. (4.1) is that the ratio of specific heats,  $\gamma$ , of the gas being considered is constant. In the DSMC method, however, the ratio of specific heats varies with temperature as the degree of excitation of the vibrational modes may vary within the range of temperatures being considered. Therefore, in order to validate our DSMC simulations, we must choose appropriate initial conditions so the range of temperatures for the gas provides a near constant ratio of specific heats,  $\gamma$ , within the DSMC domain.

Using the number of degrees of freedom,  $f$ , of the gas, the ratio of specific heats,  $\gamma$ , is given by:

$$\gamma = \frac{f+2}{f} \quad (4.3)$$

Based on the principle of equipartition of energy, the number of degrees of freedom for the translational modes is always equal to three. Above a few Kelvins, the rotational modes of water will be fully excited. Because water is a nonlinear molecule, the contribution of rotational motion to the total number of degrees of freedom is equal to three. Within the temperature range being considered here, from a few hundred to a few thousand Kelvins, the vibrational modes of water go from partially excited to fully excited. Assuming that water is a harmonic oscillator, the effective number of degrees of freedom for each vibrational mode varies with temperature as follows:

$$f_{vib,i} = 2 \left( \frac{\vartheta_i}{T} \right)^2 \frac{e^{\vartheta_i/T}}{\left( e^{\vartheta_i/T} - 1 \right)^2} \quad (4.4)$$

where  $\vartheta_i$  is the characteristic temperature of the mode  $v_i$  and  $T$  is the temperature of the gas. The characteristic temperatures for the two stretching modes of water,  $v_1$  and  $v_3$ , are equal to 5261 K and 5404 K, respectively. The characteristic temperature for the bending mode of water,  $v_2$ , is equal to 2438 K. In summary, assuming that the temperature is high enough so the rotational modes are fully excited, the ratio of specific heats,  $\gamma$ , is equal to:

$$\gamma = \frac{3+3+f_{vib,1}+f_{vib,2}+f_{vib,3}+2}{3+3+f_{vib,1}+f_{vib,2}+f_{vib,3}} \quad (4.5)$$

This ratio of specific heats,  $\gamma$ , is plotted against temperature in Figure 4-1. One can see in particular that due to the relatively high characteristic temperatures for the three vibrational modes of water,  $\gamma$  varies from 4/3 at temperatures of a few hundred Kelvins to 7/6 at temperatures above 3000 K. All these results assume that the water molecules have not dissociated or been ionized.

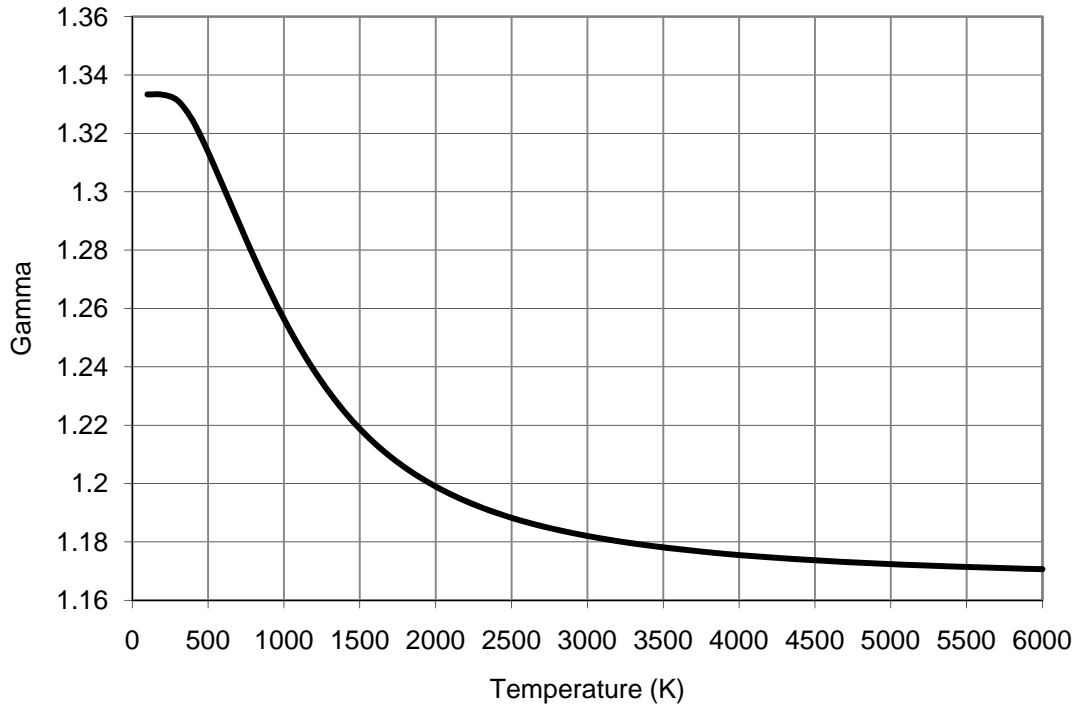


Figure 4-1 Plot of the ratio of specific heats,  $\gamma$ , for water as a function of temperature.

In order to validate our implementation of the DSMC method, we have used three different initial conditions for the analytic solution. The first and second sets of initial conditions produce a low temperature, low density solution (Case 1), and a high temperature, high density solution (Case 2), respectively. These two solutions are used to validate the creation of the molecules at the interface and our overall implementation for the simulation of unsteady expansion flows into a vacuum. The third set of initial conditions provides a low density solution at intermediate temperatures (Case 3). This third case is used to validate our collision limiting scheme and in particular the accurate modeling of vibrational freezing. In all three cases, the temperatures being considered at the interface are all within a small range so the ratio of specific heat can be assumed to be constant. Another assumption required in our simulations is that the flow is supersonic at the interface so information does not travel back upstream. With the chosen initial conditions, the flow is supersonic at all times at the interface (Figure 4-5). Finally, the initial conditions were chosen so that the density, temperature and radial velocity of the flow within the DSMC domain were representative of the values observed in the expansion plume

produced by a comet impact on the Moon. For the 45° impact, the density at the interface varies from about 0.8 to 0.1 kg/m<sup>3</sup>, the temperature varies from 3500 to 350 K, and the radial velocity varies from 50 to 1 km/s.

A summary of the initial conditions used for all three cases is presented in Table 4-1. We assumed that cloud was made out of water vapor with a specific gas constant of 461.5 J/(kg.K). The analytic solutions for density, temperature and radial velocity for Cases 1, 2, and 3 are presented as a function of time at a distance of 20 km away from the point of origin of the impact in Figure 4-2, Figure 4-3, and Figure 4-4. The Mach number of the flow is plotted in Figure 4-5.

Table 4-1 Summary of the initial conditions used for Cases 1, 2 and 3.

Case Number	$\gamma$	$\rho_0$ (kg/m <sup>3</sup> )	M (kg)	R <sub>0</sub> (m)	V <sub>max</sub> (m/s)
Case 1	1.33	$8.04 \times 10^{-1}$	$4.21 \times 10^8$	500	20000
Case 2	1.18	$8.04 \times 10^{-1}$	$3.37 \times 10^9$	1000	30000
Case 3	1.21	$2.16 \times 10^{-3}$	$3.57 \times 10^7$	1581	20000

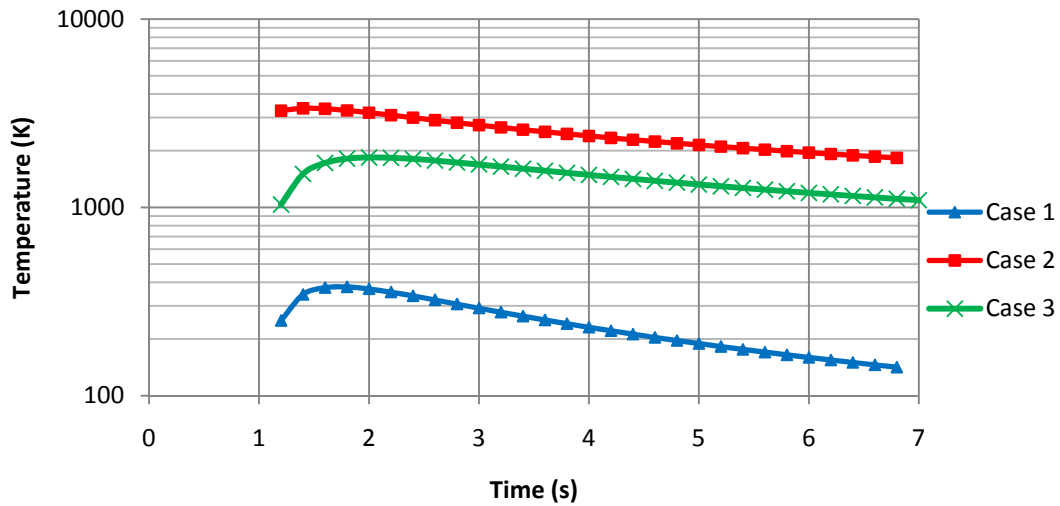


Figure 4-2 Analytic temperature plots versus time at a distance of 20 km from the point of origin of the expansion for Cases 1, 2, and 3 (obtained from Eq. (4.1)).

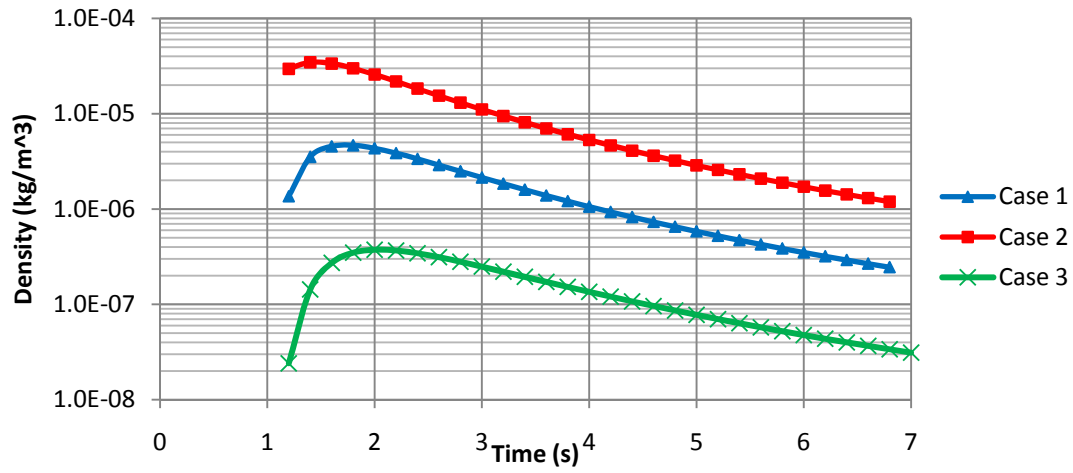


Figure 4-3 Analytic density plots versus time at a distance of 20 km from the point of origin of the expansion for Cases 1, 2, and 3 (obtained from Eq. (4.1)).

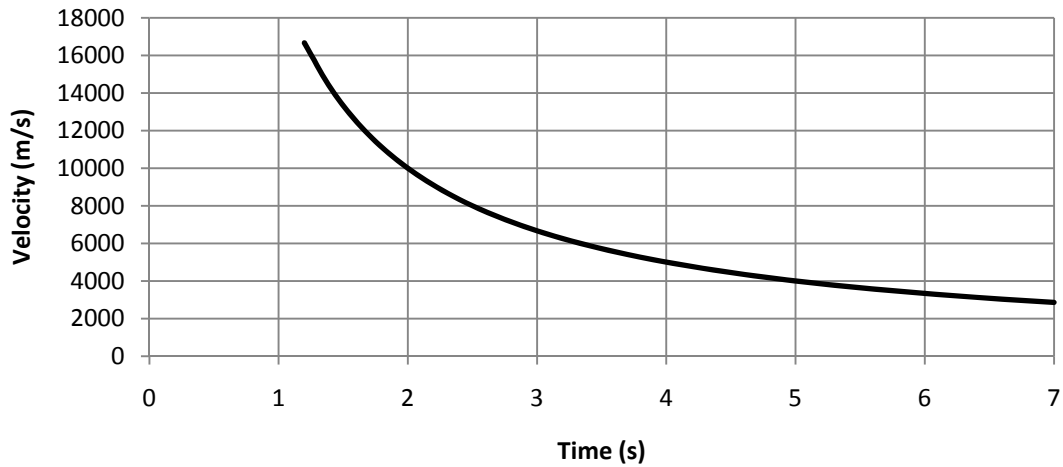


Figure 4-4 Analytical radial velocity plots versus time at a distance of 20 km from the point of origin of the expansion for Cases 1, 2, and 3 (obtained from Eq. (4.1)). Note that the initial conditions do not influence the value of the radial velocity as it only depends on time and radial distance in this self-similar solution.

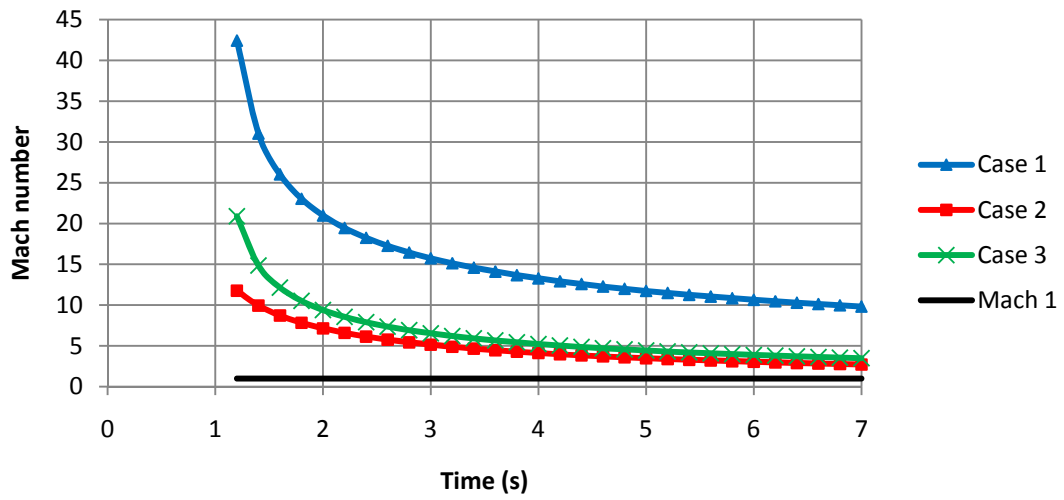


Figure 4-5 Analytic Mach number versus time at a distance of 20 km from the point of origin of the expansion for Cases 1, 2, and 3.

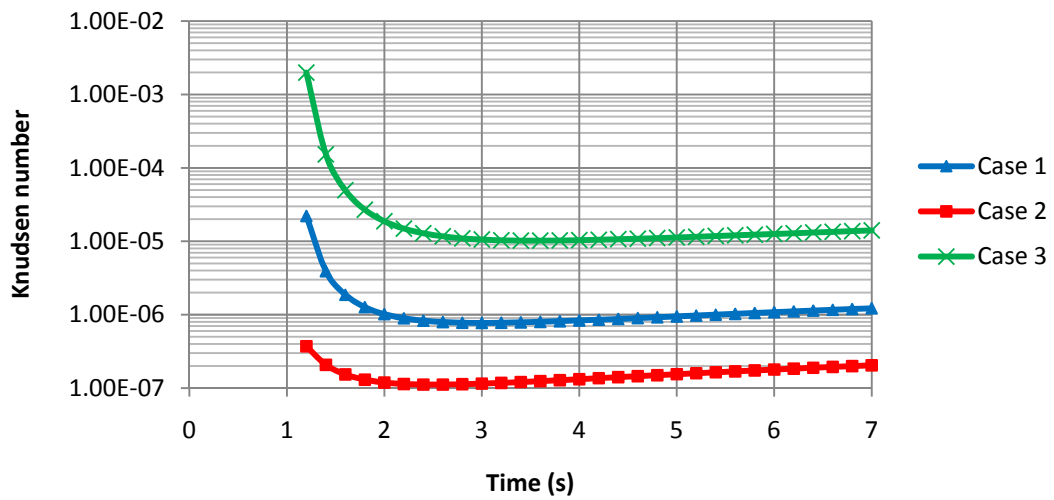


Figure 4-6 Analytic Knudsen number based on the density gradient versus time at a distance of 20 km from the point of origin of the expansion for Cases 1, 2, and 3.

With the prescribed initial conditions, 2 s after the beginning of the expansion, the Knudsen number based on the density gradient ( $Kn_{GLL}$  in Roveda *et al.*, 2000) at 20 km is about  $10^{-6}$  for Case 1,  $10^{-7}$  for Case 2, and  $10^{-5}$  for Case 3. In general, a flow is in the continuum regime for values of  $Kn_{GLL}$  equal or smaller than 0.01. From Figure 4-6, all three cases are within the continuum regime at the fixed interface 20 km away from the point of origin of the expansion. The analytic solution is used both as initial and boundary condition to our DSMC simulations but also as a benchmark we can compare our DSMC results to. The analytic results are one-dimensional and have been obtained assuming spherical symmetry for the flow. The main objective of the present simulations was to validate our DSMC implementation which is three-dimensional. Therefore, we chose to run the present simulations using the 3D version of our DSMC code with the point of origin of the expansion located at the axis of symmetry of our domain. The analytic solution was used as input to our DSMC calculations at a fixed hemispherical interface centered at the point of origin of the impact. Instead of creating a new interface, the geometry of the interface is exactly the same as the one used in the SOVA hydrocode simulations of the  $45^\circ$  impact (Figure 4-7). The interface is made of small Cartesian cells of a maximum cell size of 200 m that form a hemisphere 20 km in radius centered at the point of origin of the expansion. At each timestep, the analytic temperature, density and radial velocity are calculated at every SOVA interface cell based on the distance between the cell center and the point of origin. Using the reservoir boundary condition, DSMC molecules are created within the SOVA cells based on the analytic data and only the molecules that exited the SOVA cells at the end of the timestep are kept. Cases 1 and 2 were run in serial with the DSMC domain being a  $30 \text{ km} \times 30 \text{ km} \times 0.5^\circ$  “piece of pie” containing 180,000 cells for Cases 1 and 2. Case 3 was run in parallel on TACC’s Lonestar supercomputer using 16 processors. For this case, the entire DSMC domain was a  $50 \text{ km} \times 50 \text{ km} \times 0.64^\circ$  “piece of pie” containing 8 million cells. For all three cases the timestep was chosen to be 0.01s. Three seconds after the beginning of the expansion, Cases 1, 2 had 6.2, and 8.5 million molecules in the DSMC domain, respectively. Three and a half second after the beginning of the expansion, 76.6 million molecules were present in the DSMC domain for Case 3.

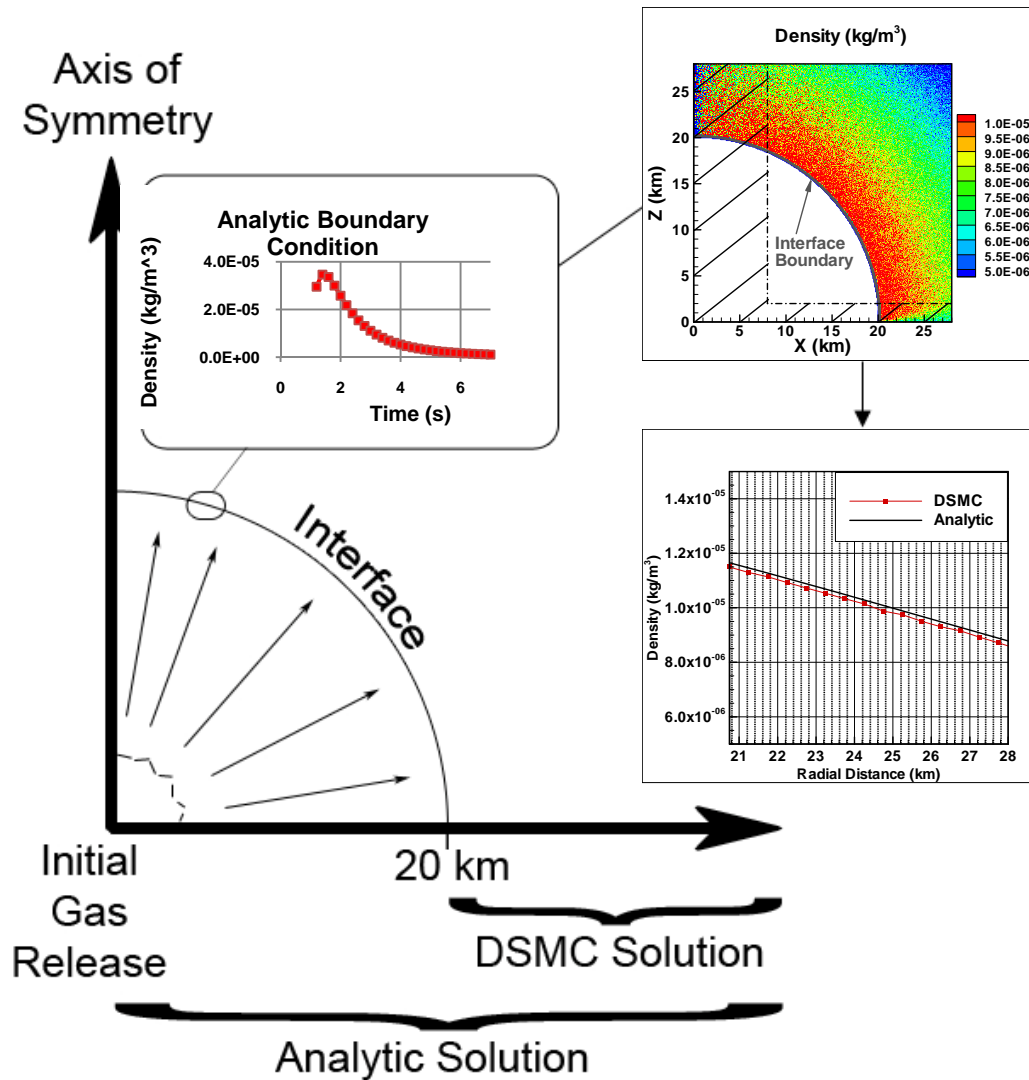


Figure 4-7 Schematic of the approach used to simulate the expansion flow of water vapor into a vacuum. The 1D analytic solution is used at a hemispherical interface to create the DSMC molecules. The DSMC simulations provide 3D results that are later sampled into radial bins. Finally, the sampled solution is compared to the analytic solution downstream of the interface. Plotted here as example is the analytic density plot for Case 2 as function of time at the interface as well as the density contours and profiles for Case 2 3s after the beginning of the expansion downstream of the interface.



For all three cases, the cell size and timestep size are not small compared to the mean free path and the mean collision time, respectively, but are representative of the cell size and timestep size that will be used in the comet impact simulations. If the DSMC solution agrees well with the analytic solution, these results would provide some validation of our under-resolved DSMC simulations of the impact event.

The 3D DSMC results presented in the following sections have been sampled in radial bins in order to be compared to the one-dimensional analytic solution (Figure 4-7). In all three cases, the radial bins are 500 m wide and the average values for the bins are obtained by averaging data only from the cells that have their cell centers within the boundaries of the radial bin. Because the present simulations are unsteady, a temporal average of the DSMC solution cannot be used. However, by running 3D simulations and using a spatial average over radial bins we can significantly reduce the noise in our simulations and show that the under-resolved solution still correctly models the flow. In the present computations, the 3D DSMC contours have been averaged into radial bins to be compared downstream of the interface to the analytic solution but only a subset of all the DSMC cells is being considered. Due to the spherical geometry of the domain, the cells near the axis of symmetry are very small and the number of molecules in them is not sufficient to obtain an acceptable solution. Also, the cells near the bottom of the domain have been ignored so the interaction of the molecules with that solid boundary is being ignored. The region of the DSMC domain that contains the cells being used to calculate the sampled quantities is presented in Figure 4-8.

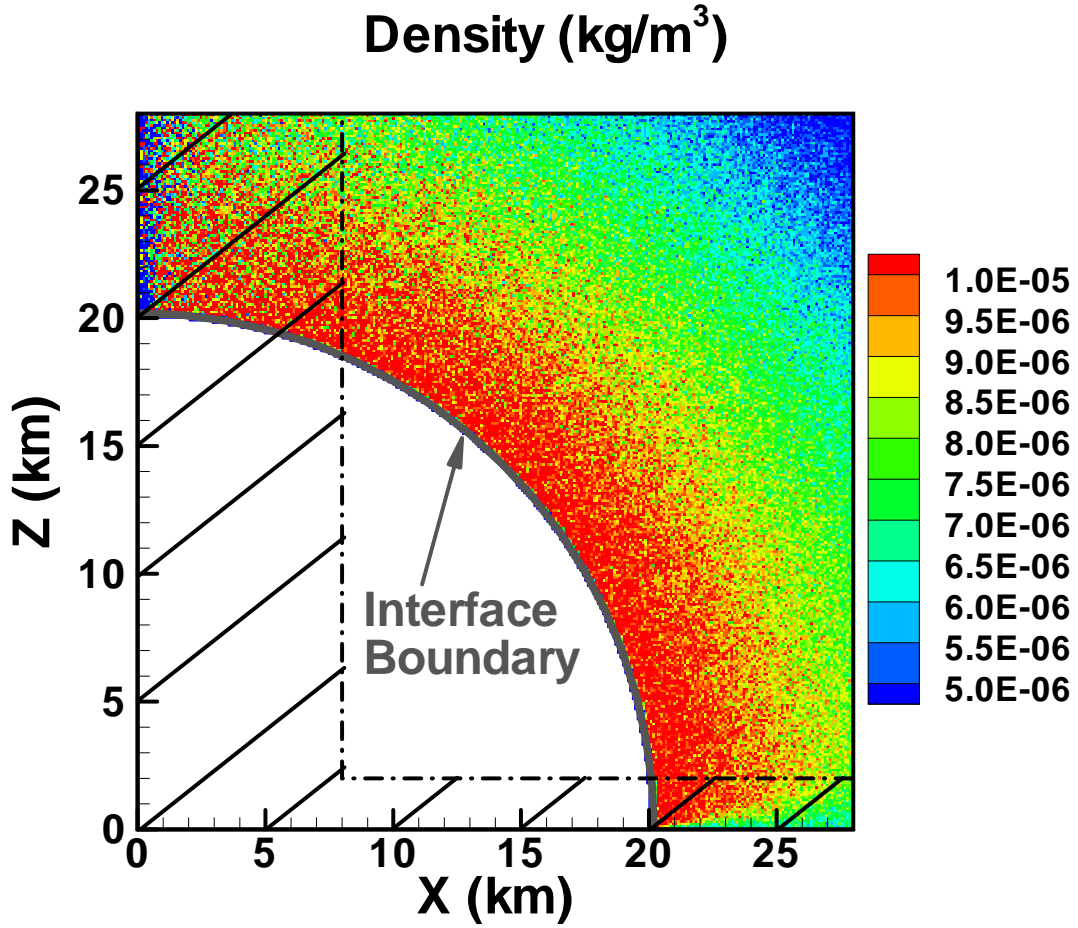


Figure 4-8 DSMC density contours downstream of the interface for Case 2. The hatched area represents the parts of the domain that are ignored when the cell data are averaged into radial bins.

#### 4.3.1 Region near the interface

The first objective of the DSMC simulations of a spherically symmetric expansion flow was to validate the implementation of the boundary conditions at the interface with the continuum solution. In the present section, the sampled DSMC results obtained 3 s after the beginning of the expansion are compared to the analytic solution near the interface for Cases 1 and 2.

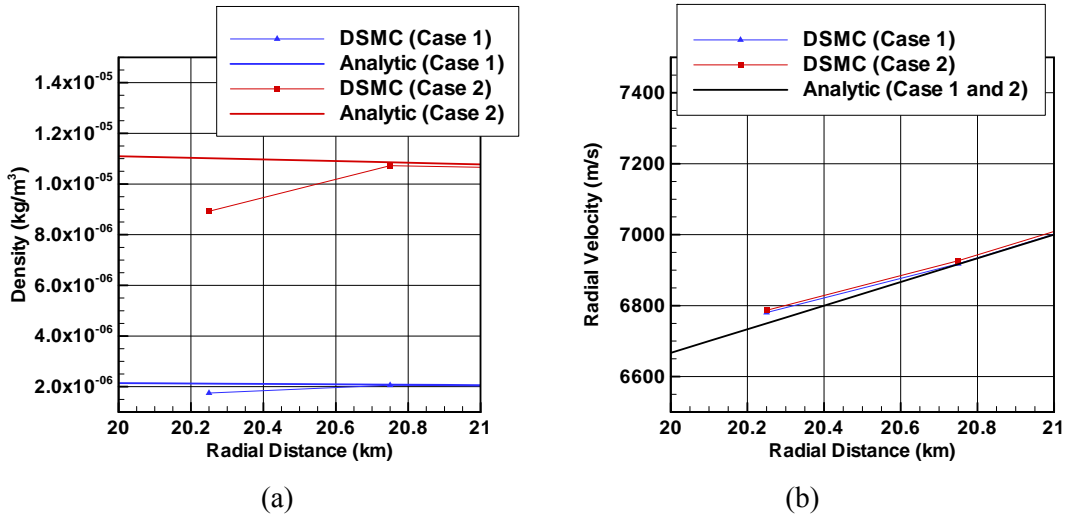


Figure 4-9 DSMC and analytic density (a) and radial velocity (b) profiles 3 s after the beginning of the expansion downstream of the interface for Case 1 (blue) and Case 2 (red).

The DSMC density and radial velocity profiles are within 1% of the analytical solution 1 km downstream of the interface (Figure 4-9). Closer to the interface, however, the DSMC density profiles do not match the analytic solution exactly. The differences can be explained by the fact that the DSMC cells and the SOVA interface cells are not superimposed. Some of the DSMC cells near the interface will have an apparent lower density as some of their volume contains the interface where no molecules are present. The temperature profiles near the interface are presented in Figure 4-10. For Case 1, the translational and rotational temperatures agree very well with the analytical solution but the vibrational temperatures do not. For Case 2, the temperature for all internal modes are all in agreement.

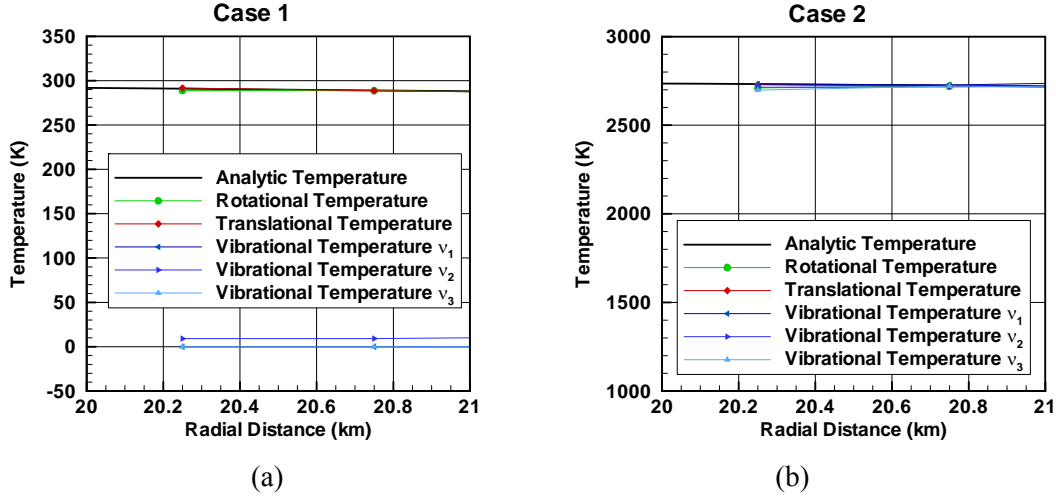


Figure 4-10 DSMC and analytic temperature profiles 3 s after the beginning of the expansion downstream of the interface for Case 1 (a) and Case 2 (b). The vibrational temperatures were obtained by sampling the vibrational temperatures in each radial bin.

The vibrational temperature of mode  $v_i$  can be calculated using the population distribution between the different energy levels of the mode:

$$T_{V,i} = \frac{\vartheta_i}{\ln(1 + \mathcal{R} \vartheta_i / e_{V,i})} \quad (4.6)$$

where  $\vartheta_i$  is the characteristic temperature of the mode  $v_i$ ,  $\mathcal{R}$  is the specific gas constant and  $e_{V,i} = \sum_{k=1}^{\infty} \mathcal{R} k \frac{N_k}{N} \vartheta_i$  with  $N$  being the total number of molecules and  $N_k$  the number of molecules in the  $k^{\text{th}}$  excited level. For a gas in equilibrium, as is the case here, the vibrational temperature of mode  $v_i$  can also be calculated using only the populations in the ground state and the first excited level:

$$T_{V,i} = \frac{\vartheta_i}{\ln(N_0/N_1)} \quad (4.7)$$

In Figure 4-10, the average vibrational temperatures for each bin have been obtained by *averaging the vibrational temperatures* in each DSMC cell. For Case 1, the vibrational

temperatures for the stretching modes  $v_1$  and  $v_3$  are equal to zero while the vibrational temperature for the bending mode  $v_2$  is very small but non-zero. In Case 2, due to the much larger temperature at the interface, the solution for the vibrational temperatures is in much better agreement with the analytic solution than for Case 1. The vibrational temperatures for the stretching modes agree well with the translational temperature while the bending mode temperature still underestimates the actual temperature. The discrepancies between the three vibrational temperatures are due to the fact that the vibrational stretching modes  $v_1$  and  $v_3$  have very similar characteristic temperatures,  $\vartheta_1 = 5261$  K and  $\vartheta_3 = 5404$  K respectively, that are about twice as much as the characteristic temperature for the bending mode  $v_2$ ,  $\vartheta_2 = 2438$  K. For Case 1, all three characteristic temperatures are much larger than the analytic temperature of several hundred Kelvins so a large number of molecules per cell is required to obtain an accurate solution in a single cell for the vibrational temperatures. Using Eq. (4.7), if we assume that one molecule in some cell is in the first excited level, the number of molecules required to be in ground level to obtain a temperature of 300 K for the stretching mode  $v_1$  is greater than 4 billion. That number decreases to a little more than 3000 molecules for the bending mode  $v_2$ . In the present simulations, we have at most 90 molecules per cell near the interface which is sufficient to represent the translational and rotational modes. Therefore, we know that we cannot resolve the temperatures associated with the stretching modes. For the vibrational mode  $v_2$ , the statistics are not sufficient so the number of cells without even a single vibrationally excited molecule (i.e. with a vibrational temperature of zero) is large and thus the averaged vibrational temperature is too low.

One way to obtain better statistics is to average the DSMC *molecular data* into larger cells. In Figure 4-11, we calculate the vibrational temperatures in a radial bin using the vibrational populations inside all the DSMC cells present in the entire bin. This can be seen as a spatial averaging that can be used in this case more readily than a standard ensemble averaging. In the present simulations, for both Cases 1 and 2, the spatial averaging provides  $\sim 400,000$  molecules per bin. For Case 1, the results obtained using population-averaging provide a much improved agreement between the vibrational temperature for the bending mode and the analytic temperature. The statistics for the stretching modes are however still insufficient to obtain a good solution for the  $v_1$  and  $v_3$  temperatures that are still equal to zero in this case. For Case 2, when

using the bin average, the agreement between all three vibrational modes and the analytic solution is very good.

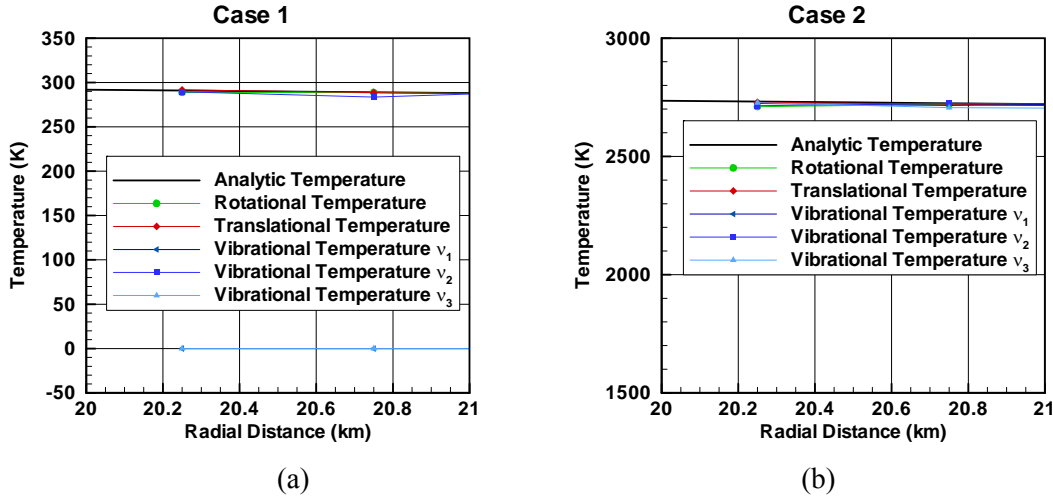


Figure 4-11 DSMC and analytic temperature profiles 3 s after the beginning of the expansion downstream of the interface for Case 1 (a) and Case 2 (b). The vibrational temperatures were obtained by sampling the populations in each vibrational state.

#### 4.3.2 Equilibrium region

The next objective of the present simulations was to validate the overall DSMC implementation by verifying that the DSMC solution would follow the analytic solution in the equilibrium regions of the flow. The sampled DSMC results obtained 3 s after the beginning of the expansion are compared to the analytic solution in Figure 4-12 to Figure 4-14 for Cases 1 and 2. The results are only compared in the region of the domain with good enough statistics up to 28 km from the point of origin of the expansion. The DSMC density profiles (Figure 4-12a) are in good agreement with the analytic solution for both cases. In Case 1, the spatially averaged DSMC solution is within 1% of the analytic solution while it is within 1.5% for Case 2. Similarly, the velocity profiles (Figure 4-12b) are in very good agreement with the analytic solution for both cases. In Case 1, the spatially averaged DSMC solution perfectly overlaps the analytic solution while it slightly diverges away for Case 2. Even in Case 2, the difference between the two solutions is less than 0.5%.

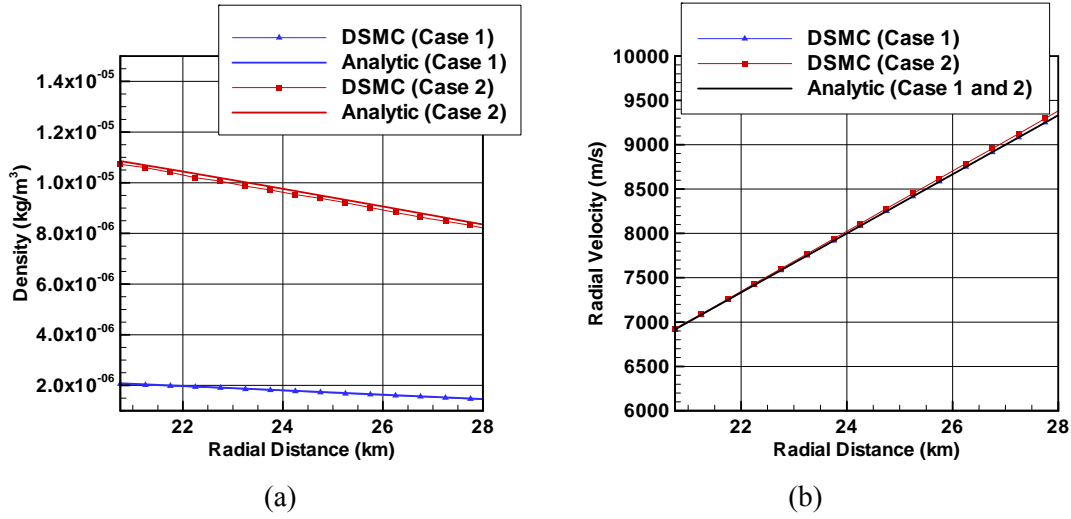


Figure 4-12 DSMC and analytic density (a) and radial velocity (b) profiles 3 s after the beginning of the expansion downstream of the interface for Case 1 (blue) and Case 2 (red). Note that the analytic radial velocity only depends on the radial distance and time; therefore the analytic solution is the same for Cases 1 and 2.

In Figure 4-13, the translational and rotational temperatures are in very good agreement with the analytic solution. The average vibrational temperatures, however, do not match the analytic solution at any location downstream of the interface. Similarly, to the results observed in Section 4.3.1, the stretching modes temperatures are equal to zero while the bending mode temperature is small at about 10 K. Using population-averaging to calculate the vibrational temperatures, the bending mode temperature is now of the same magnitude as the analytic temperature. That vibrational temperature is seen to oscillate around the analytic solution but the slope of the vibrational temperature seems to match that of the analytic solution. The statistics of the present simulations are not sufficient to obtain a non-zero temperature for the vibrational stretching modes even with the use of population averaging within the radial bins.

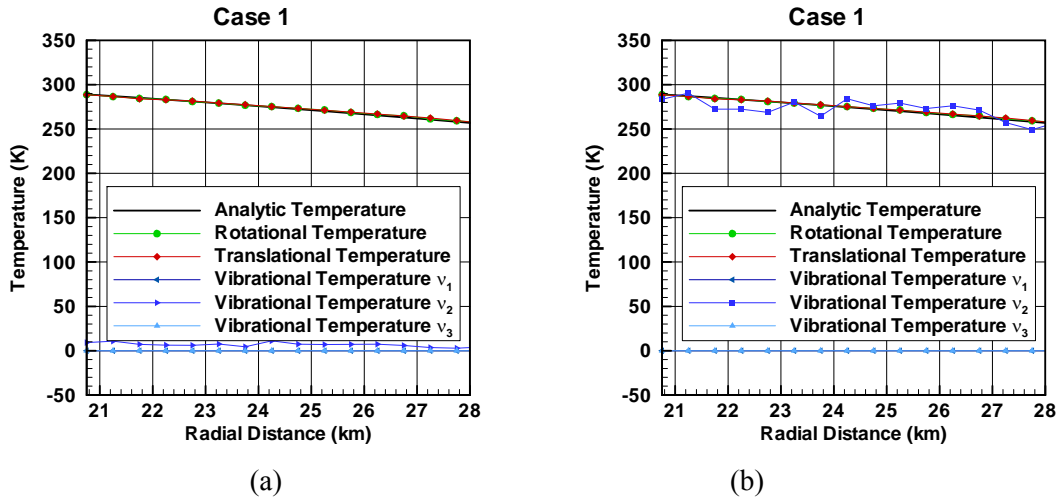


Figure 4-13 DSMC and analytic temperature profiles versus radial distance from the point of origin of the expansion 3s after the beginning of the expansion for Case 1. The left hand-side figure (a) was obtained using a sampling of the *vibrational temperatures* in each radial bin while the right-hand side figure (b) was obtained using a sampling of the *populations* in each vibrational state.

The results for the temperature components obtained in Case 2 are presented in Figure 4-14. Similarly to Case 1, the translational and rotational temperatures are in good agreement with the analytic solution, within 1% throughout the entire domain. In this case, due to the much larger temperature at the interface, the solution for the vibrational temperatures is much better than for Case 1. When using either the simple cell average (Figure 4-14a) or the bin average of populations (Figure 4-14b), the vibrational temperatures for the all three modes agree well with the analytic temperature. Note that the noise level in each vibrational temperature component is lower when using the bin average of populations (Figure 4-14b).



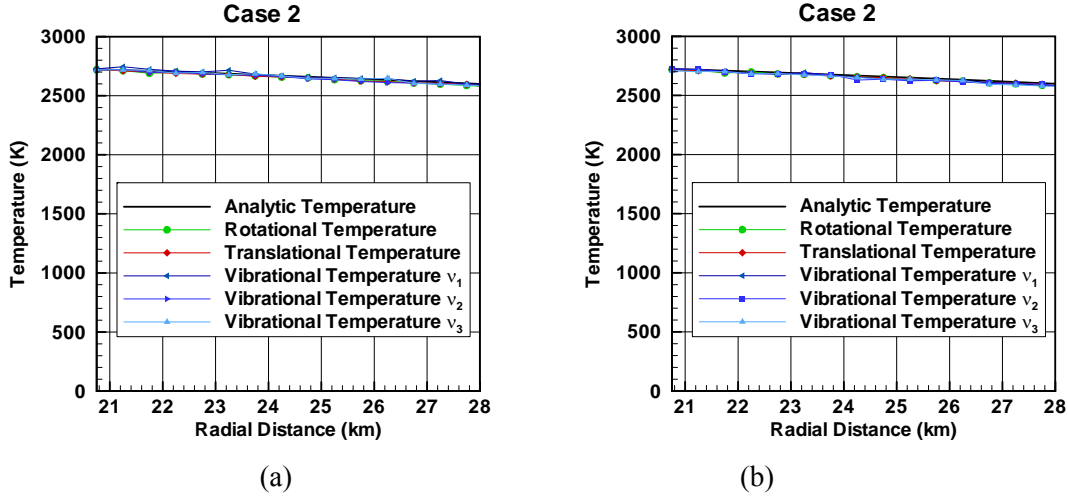


Figure 4-14 DSMC and analytic temperature profiles versus radial distance from the point of origin of the expansion 3s after the beginning of the expansion for Case 2. The left hand-side figure (a) was obtained using a sampling of the vibrational temperatures in each radial bin while the right-hand side figure (b) was obtained using a sampling of the populations in each vibrational state.

#### 4.3.3 Vibrational non-equilibrium region

The final objective of the simulation was to validate our collision limiter scheme and in particular the accurate description of the freezing of the vibrational modes. As the flow expands into a vacuum, the number density starts to decrease until the flow becomes collisionless. Before then, the vibrational and then the rotational modes will freeze and the temperature based on each mode will begin to depart from the translational temperature. In 1970 and later in 2002, Bird used the DSMC method to study freezing of the rotational and vibrational temperatures in steady rarefied expansion flows (Bird, 1970 and 2002). In his papers, Bird proposed the use of a breakdown parameter  $P$  in order to study the breakdown of rotational and vibrational equilibrium.  $P$  was defined as the ratio of the Lagrangian derivative of the logarithm of the density to the collision frequency of the gas,  $\nu_{coll}$ :

$$P_{rot} = \frac{1}{\nu_{coll}} \left| \frac{D \ln \rho}{Dt} \right| \quad (4.8)$$

Bird indicated a requirement for equilibrium was that  $P_{rot}$  must be small compared to unity ( $P_{rot} < 0.05-0.1$ ). The parameter  $P_{rot}$  can be extended to look at the breakdown in vibrational equilibrium by multiplying it by the vibrational relaxation number, giving the new parameter  $P_{vib}$ :

$$P_{vib} = Z_{vib} \times P_{rot} \quad (4.9)$$

Using the analytic expression for density presented in Eq. (4.1), we find:

$$\left| \frac{D \ln \rho}{Dt} \right| = \frac{3}{t} \quad (4.10)$$

The collision frequency of the gas can be expressed as a function of the mean free path,  $\lambda$ , and the temperature,  $T$ , of the flow (Vincenti and Kruger, 1965):

$$\nu_{coll} = \sqrt{\frac{8kT}{\pi m}} \times \frac{1}{\lambda} \quad (4.11)$$

Substituting Eqs. (4.10) and (4.11) into Eq. (4.8), and multiplying top and bottom by the radial distance,  $dist$ :

$$P_{rot} = \frac{3\sqrt{\pi}}{2} \times \frac{V_r}{c} \times \frac{\lambda}{dist} \quad (4.12)$$

where  $c = \sqrt{\frac{2kT}{m}}$  is the most probable thermal speed (Bird, 1994). This expression resembles the expression Bird derived for the parameter  $P_{rot}$  for a steady expansion flow (Bird, 2002). The parameter  $P_{rot}$  is proportional to the ratio of the flow velocity to the most probable speed times the Knudsen number based on the radial distance away from the point of origin of the expansion.

In order to observe freezing of the vibrational modes, we chose the initial conditions for Case 3 such that the parameter  $P_{vib}$  becomes of the order 0.1 within the DSMC domain. The breakdown parameters,  $Kn_{GLL}$ ,  $P_{rot}$ ,  $P_{vib}$  (for the stretching modes), and  $P_{vib2}$  (for the bending mode) are plotted in Figure 4-15. While the Knudsen number based on the density gradient and Bird's parameter  $P_{rot}$  indicate that the flow should be continuum within the entire DSMC domain,

Bird's parameters,  $P_{vib}$  and  $P_{vib2}$ , show that the vibrational modes should be freezing within the DSMC domain. Figure 4-16 shows a close-up view of the breakdown parameters for vibrational equilibrium as a function of distance from the point of origin of the expansion. For future reference,  $P_{vib}$  is equal to 0.05 at a distance of  $\sim 35$  km and  $P_{vib2}$  is equal to 0.05 at a distance of  $\sim 43$  km.

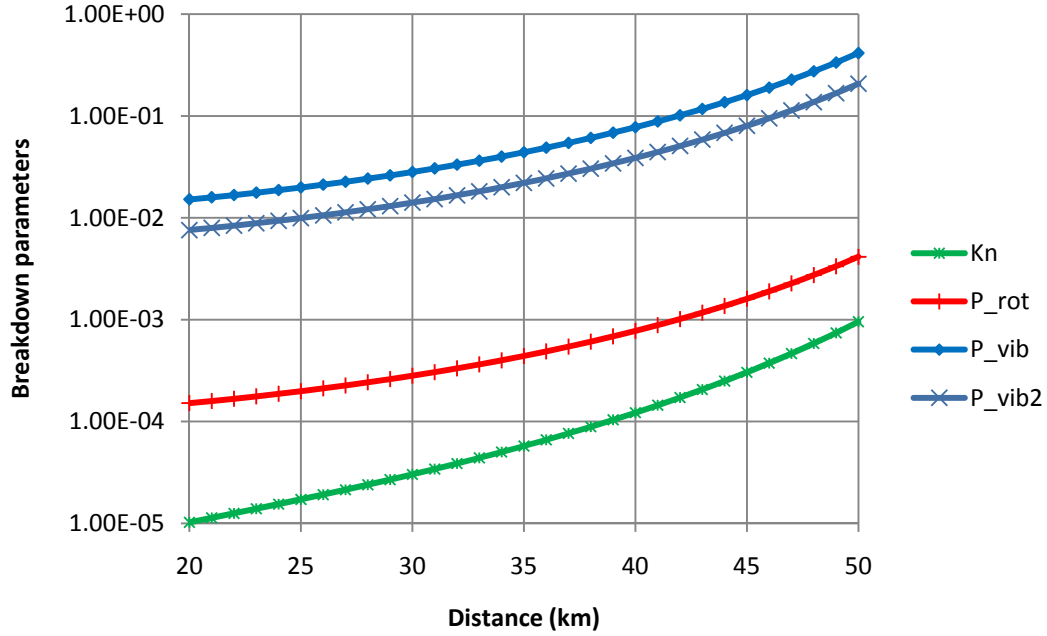


Figure 4-15 Breakdown parameters versus radial distance away from the point of origin of the expansion 3.5 s after the beginning of the expansion for Case 3.

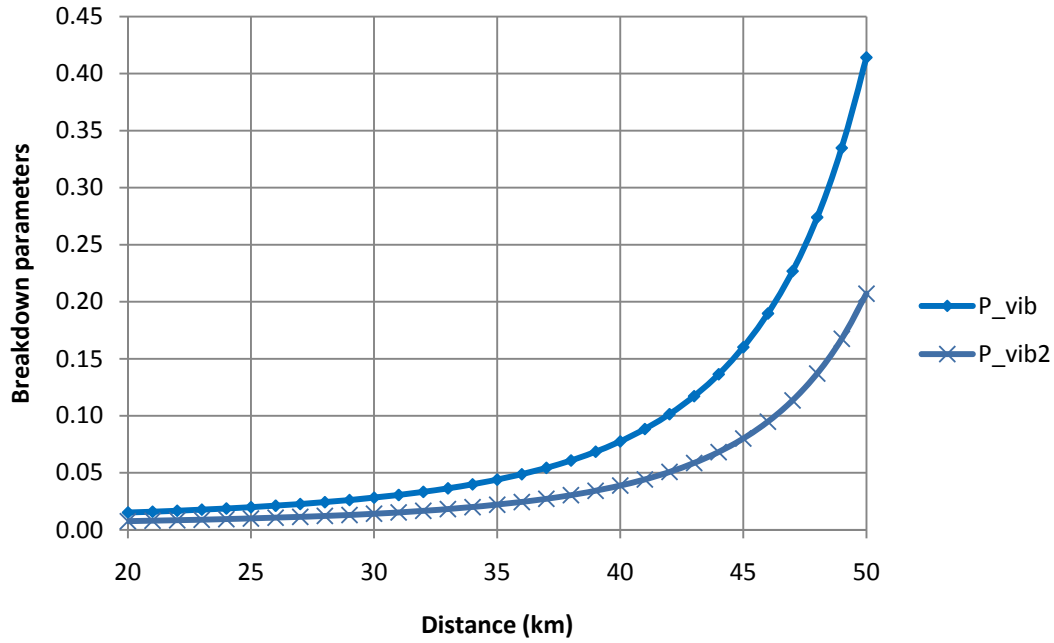


Figure 4-16 Bird's parameters indicating departure from equilibrium for the vibrational modes versus radial distance away from the point of origin of the expansion 3.5 s after the beginning of the expansion for Case 3.

All five DSMC temperature components for the translational, rotational and the three vibrational modes are shown in Figure 4-17. At the interface, all the temperature components are within 1% of each other. In that region of the flow, the  $P_{vib}$  and  $P_{vib2}$  parameters have values near 0.01. As the flow continues to expand away from the point of origin of the flow, the vibrational modes begin to depart from the rotational and translational modes that remain nearly identical within the entire domain. In the present simulations, the departure from the translational and rotational modes is gradual and has reached 3% and 1.4% for the stretching modes and the bending mode, respectively, 35 km from the point of origin. Downstream, 43 km from the point of origin of the expansion, the difference has increased 8.5% and 4%, respectively. Bird's results (2002) for a steady state expansion through a nozzle indicated that vibrational modes were in equilibrium with the translational and rotational modes for values of  $P_{vib}$  lower than 0.01. Then, as  $P_{vib}$  increased the vibrational modes began to freeze until a completely vibrationally frozen flow was observed when the vibrational breakdown parameter reached values near 1. The

freezing process was, however, gradual which we have observed in our simulations (Figure 4-17). Also, as expected, the vibrational modes with the largest vibrational relaxation number, the stretching modes, are beginning to freeze earlier than the bending mode with the lower vibrational relaxation number.

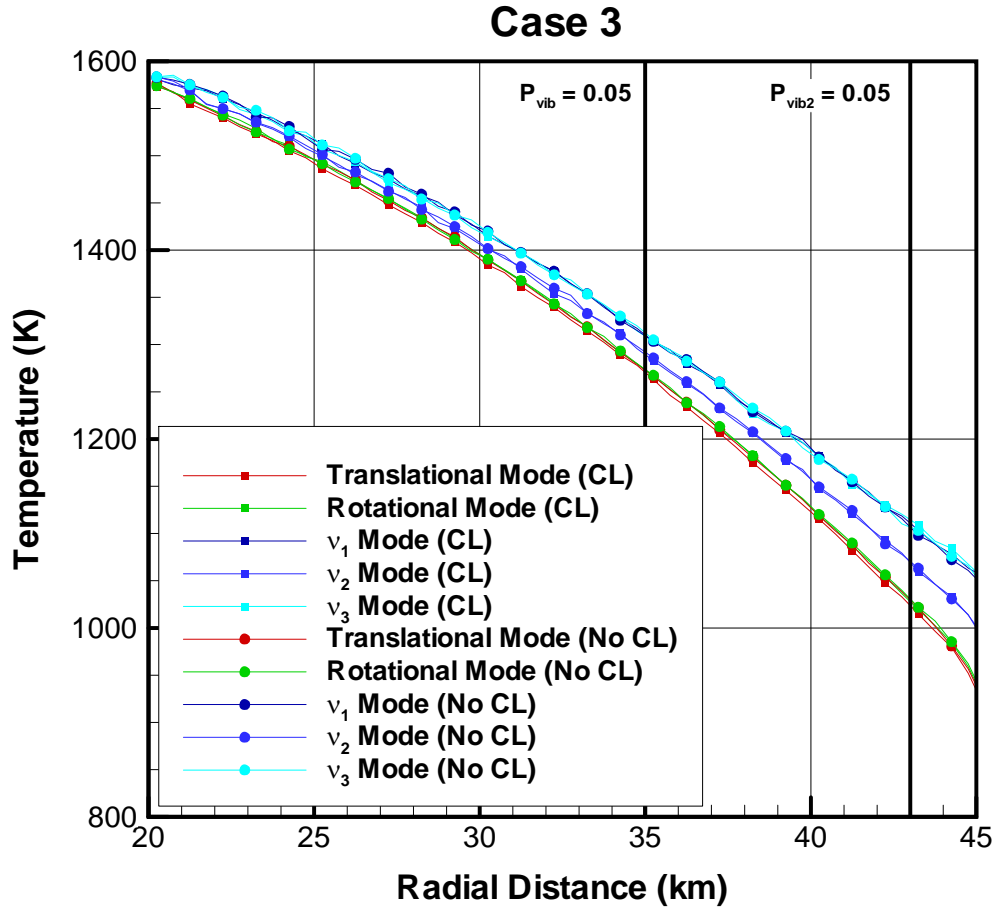


Figure 4-17 DSMC and analytic temperature profiles versus radial distance from the point of origin of the expansion 3.5 s after the beginning of the expansion for Case 3. “CL” refers to the collision limited case and “No CL” refers to the regular DSMC simulations. The vibrational temperature components have been obtained using a sampling of the populations in each vibrational state in each radial bin.

Finally, we have used Case 3 with its relatively low collision rate to study the validity of our collision limiter in the low density regions of the flow. Case 3 was run with and without the collision limiter turned on and the solution for the temperature components is shown in Figure 4-17. All five temperature components are in agreement within the entire domain. In particular, the fact that the “freezing rate” of the vibrational modes is identical shows that the collision limiting scheme is indeed correctly transitioning to the regular DSMC collision subroutine. Also, in this relatively low collision frequency region, the collision limited DSMC code is more than five times faster than the regular DSMC implementation.

## **Chapter 5**

### **Late stages of a Comet Impact Simulations**

#### **5.1 OVERVIEW**

In this chapter, the DSMC method is applied to study the time evolution of the water vapor plume produced by a comet impact on the Moon. The 3D unsteady expansion flow produced during the impact event is initially modeled by the SOVA hydrocode near the point of impact. The SOVA data are then used as input to the present DSMC simulations at a fixed interface within the continuum region of the flow. Near the interface, the flow is modeled using our under-resolved, collision limited DSMC method which is relaxed further away from the point of impact to the classic DSMC method. In order to follow the vapor plume as it expands and have a more resolved grid in the near field, we used our multi-domain approach presented in Section 3.6. The main parameters used in our DSMC simulations are presented in Section 5.2. In Section 5.3, the DSMC results downstream of the interface are compared to the SOVA data in the near field. Finally, in Section 5.4, we discuss the main characteristics of the late impact vapor plume for a 45° impact event as it expands up to 1000 km away from the point of impact.

#### **5.2 SIMULATION PARAMETERS**

The present DSMC computations simulate the impact of a 2 km diameter water ice comet on the Moon. The impactor hits the target with a velocity of 30 km/s and two impact angles are considered: a 90° (vertical) impact and a 45° (oblique) impact. The unsteady data provided by the SOVA hydrocode at a hemisphere 20 km in radius surrounding the point of impact are used as input to the DSMC simulations. Due to the geometry of our spherical grid, the point of impact is located at the axis of symmetry of our 3D DSMC domain where the azimuthal cell size is the smallest (Figure 5-1). For the oblique impact, several successive multi-domain DSMC runs were used to follow the water vapor from the comet as it expanded away from the point of impact. In

the present DSMC simulations, we neglected the rock inside the SOVA cells at the interface as well as water in cells containing both rock and water vapor. For the  $45^\circ$  oblique impact, the total mass of water neglected at the interface amounted to 3% of the comet mass. For the  $90^\circ$  vertical impact, the computations were only partial so we did not estimate how much water was neglected. In addition, the water was assumed to be purely in the vapor phase at the interface and to remain so within the DSMC domain. This validity of this assumption is studied in detail in Section 5.4.2.3. Because the SOVA hydrocode is a continuum solver, the SOVA results are only known to be valid in the continuum regions of the flow. Therefore, the interface between the SOVA hydrocode and the DSMC code is well inside the continuum region of the flow. The mean free path is of the order a few microns near the interface but the DSMC domain for the comet impact simulations is to be tens of kilometers in each direction. So at best, even for parallel computations, the cell size can only be in the meter range. For the proposed simulations, it will not be feasible to satisfy the usual constraints on cell size and timestep to obtain an accurate solution close to the impact point. However, we are mostly interested in the far field deposition of the water so an approximate approach to modeling the dense transitional regions was deemed acceptable. Hence, we choose to use an under-resolved collision-limited DSMC solution with “large” cells and a “large” timestep in the near field (see Sections 3.5.1 and 4.3) as a transition to a resolved far field DSMC solution. The overall effect of such an approximation is to misrepresent the transport coefficients (e.g., the effective viscosity is too large). Fortunately, the actual gradients of the flow are expected to be small, with length scales far greater than the cell size in the under-resolved regions of the flow and hence errors in the transport coefficients should have a minimal effect on the simulated flow. In addition, the inviscid SOVA code (aside from numerical viscosity) produces gradients only across its  $O(100\text{ m})$  sized cells. Since the flow is rapidly expanding, these lateral and radial gradients are dissipating and we expect that even our crude collision limited DSMC with collision free cells  $O(10\text{ m})$  can track them.

The first DSMC simulations of the late stages of a comet impact using the SOVA data as input were made for the vertical impact. For that impact, only material that crossed the SOVA interface in less than 6.6 s was available so this run was only used as a benchmark for the hybridization scheme (See Section 5.3.1). The axisymmetric vertical impact was simulated on a single processor and the present simulations were collisionless in order to limit their



computational cost. The SOVA data was provided for a small slice 100 m thick in the Y-direction. Because the SOVA cells are Cartesian, the DSMC domain had to extend up to  $90^\circ$  in the azimuthal direction in order to capture the SOVA cells in their entirety near the axis of symmetry. For these simulations, the DSMC domain was a  $20 \text{ km} \times 20 \text{ km} \times 90^\circ$  piece of pie (Figure 5-1a) and the cells were  $50 \text{ m} \times 50 \text{ m} \times 90^\circ$ . The low accuracy in the azimuthal direction was deemed acceptable as the present simulations were collisionless. Vacuum boundary conditions were used for the top, bottom, left and right boundaries so the molecules that hit these walls were deleted. For these simulations, the bottom wall is not located at the lunar surface but 10 km above it as no material crosses the interface below that altitude. In the present simulations, no molecule actually hit the bottom or left boundaries. In addition, the front and back walls were assumed to be specular. The SOVA data were provided on average every 0.1 s but the SOVA timestep interval between outputs was not constant. For that reason, the DSMC simulations used a much smaller timestep of 0.01 s in order to have an integer number of DSMC timesteps within each SOVA time interval. Then, the data from a SOVA timestep is used to create molecules at each DSMC timestep until the DSMC simulation time has caught up to the SOVA time. The ratio of real to simulated molecules was taken to be  $1 \times 10^{29}$ .

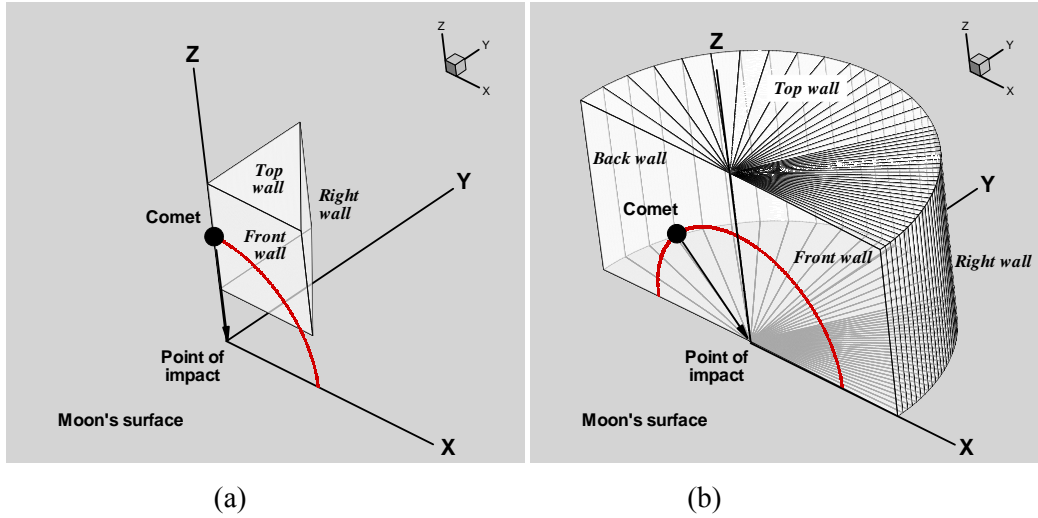


Figure 5-1 Innermost DSMC domains used for the vertical (a) and oblique (b) impact events. The interface with the SOVA hydrocode is shown in red in the plane of impact (Note that in the simulations the SOVA interface is 3D). The comet diameter and the impact angle are to scale. For the oblique impact, the boundaries between processors are also shown exhibiting the non-uniform distribution used in the present simulations.

For the 45° oblique impact, the SOVA simulations were run until most of the cometary water had crossed the interface. Therefore, this oblique impact event was more thoroughly studied than the vertical impact event. In particular, we looked at the late stages of the vapor plume (See Section 5.4) as well as the deposition patterns of water in the lunar cold traps after the impact event (See Chapter 6). In order to reduce the cost of the computations, the 3D SOVA and DSMC simulations took advantage of the symmetry of the problem (across the vertical plane containing the comet velocity vector before impact) by computing only half of the domain (Figure 5-1b). Even then, the more expensive collisional oblique impact simulations had to be run in parallel on the Lonestar supercomputer at the Texas Advanced Computing Center (TACC). We used 48 processors for these simulations. The domain decomposition was non-uniform using more processors in the downrange direction than in the uprange direction. The top, left and right boundary conditions were the same as for the vertical impact. However, the molecules crossing the top and right boundaries were saved to a file to be used later in a larger domain. Molecules hitting the bottom wall (the Moon's surface) stick to the lunar surface for a residence time depending on the local surface temperature. In the present simulations, the temperature was low enough so that molecules remain stuck on the timescale of the near field calculation (~20 s). In theory, if a large amount of warm rock falls back early on to the surface, the local surface temperature would increase and the water molecules residence time would noticeably decrease. This effect is, however, neglected in the present simulations because only a few simulated water molecules ( $O(10)$ ) actually come back to the surface during the first few tens of seconds after impact. The front and back walls of the overall domain, which represent the plane of symmetry of the impact, were assumed to be specular walls. The boundary condition at the other front and back walls between processors simply transfer molecules to the appropriate processor. For the present simulations, the ratio of real to simulated molecules was equal to  $5 \times 10^{29}$  and the timestep size was chosen to be initially 0.5 ms. The inner domain was a  $32 \text{ km} \times 32 \text{ km} \times 180^\circ$  piece of pie with cells of  $100 \text{ m} \times 100 \text{ m} \times 1^\circ$ . The downrange processors contained two azimuthal cells and

the uprange processors had 8 azimuthal cells. In order to limit the artificial smearing of gradients created by colliding molecules far apart in the cell, a free-cell approach was used (Roveda *et al.*, 2000).

### **5.3 COMPARISON BETWEEN THE DSMC AND SOVA SOLUTIONS DOWNSTREAM OF THE INTERFACE**

Two set of tests, one qualitative and one quantitative, were used to validate our DSMC results against the SOVA solution. Due the very large amount of data to be output from the SOVA simulations, the SOVA data were only provided at one 2D hemispherical interface for the vertical impact and at two 3D hemispherical interfaces for 45° oblique impact simulations. Also provided were pictures of the SOVA simulations' density contours for the expansion plume in the plane of symmetry of the impact. The first tests compared the SOVA results to the DSMC contours downstream of the interface in order to verify the overall shape of the expansion plume. Because these comparisons were only qualitative, they have only been done at one fixed time for both the vertical and oblique impacts. The quantitative set of tests was only done for the 45° oblique impact comparing the SOVA and DSMC solutions at both hemispherical interfaces. The comparison at the innermost interface, at which the DSMC molecules are created, aimed to validate our creation scheme. The comparison at the outermost interface was made to compare our DSMC model against the continuum SOVA solution in a region where the SOVA solution was still valid.

#### **5.3.1 Plume Contours in the Plane of Symmetry of the Impact: Vertical Impact**

Hybrid SOVA and DSMC density contours from the simulation of a vertical comet impact on the surface of the Moon are shown 5 s after impact in Figure 5-2. The SOVA picture has been modified where the data above the interface, represented by the red line, have been blanked except for the outer limit of the plume. Instead, above the interface, the DSMC results are shown with the associated legend. Five seconds after a vertical impact, the material is mainly expanding directly above the growing crater. The water vapor plume has reached altitudes greater than 30 km above the surface and extends horizontally up to 20 km away from the point of impact. In addition, very little rock is still above the crater walls. The ejecta curtain is so sparse, being only made of small chunks of rock, that the water plume actually extends outside of the

ejecta curtain. Also, near the axis of symmetry of the impact, the rocky material that will later form the central peak of the crater can be seen rising ~8 km above the surface. Five seconds after impact, the crater is ~5 km wide and ~6 km deep with the crater walls being ~4 km above the initial surface location. Overall, Figure 5-2 shows a good qualitative agreement between the two codes across the interface. The present comparison can only be qualitative as no legend was associated with the SOVA contours. In the SOVA region of Figure 5-2, the shades of green represent the rock contours and the shades of grey represent the water contours; the denser areas being represented by a darker shade. The black line above the red boundary represents the limit of the SOVA water contours. Right above the interface, the presence of rock in the SOVA code can be matched with a “hole” in the DSMC contours. The rock fragments that are observed further downstream of the interface in the SOVA simulations are not as well matched, however. Because the rock is not modeled in the DSMC simulation, water has diffused into these “holes”, completely filling them. In addition, the extent of the water in the DSMC simulation does not perfectly match the boundary for the water plume in the SOVA simulation shown in Figure 5-2 by the black line above the interface. The present simulations use a constant weighing factor for the molecules so the low density regions of the flow near the edge of the plume don’t have enough molecules per cells to have good statistics. Therefore, the plume shape cannot be perfectly recreated in the DSMC simulations.

The DSMC code, however, accurately captures the higher density regions of the flow. For instance, the peak of denser material ~3 km off the axis near the interface, as seen by the darker grey converging contours in the SOVA domain, can be traced well from the SOVA region to the DSMC region. Finally, there are some noticeably lower values in the density contours from the DSMC simulations near the axis of symmetry of the impact. This low density region is thought to be linked to an insufficient number of molecules near the axis. This problem has been observed before in the axisymmetric simulations of volcano plumes (Zhang *et al.*, 2004) which was also caused by poor statistics near the axis. This problem could be resolved by using either a greater number of molecules and/or radial weighting.

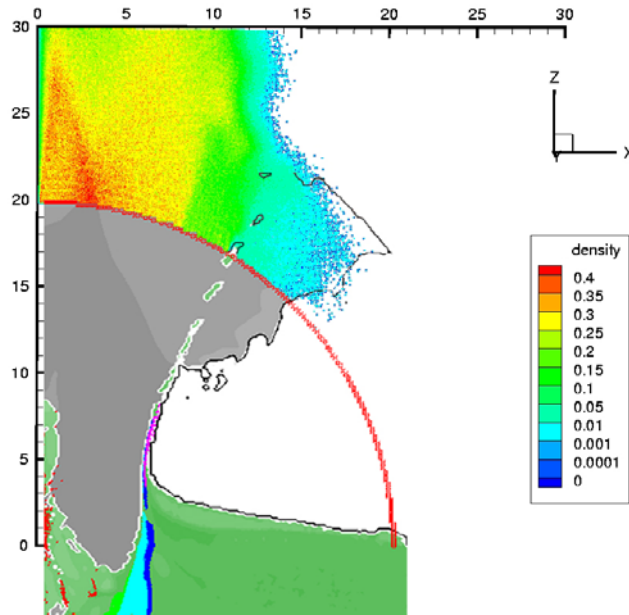


Figure 5-2 Hybrid SOVA and DSMC density contours of a vertical comet impact on the surface of the Moon after 5s. The SOVA hydrocode density contours are shown below the red interface (gray=ice; green=target) and by the black line outlining the limit between the water and the vacuum or rock above the interface. The collisionless DSMC contours are shown above the red interface with the associated legend (in  $\text{kg/m}^3$ ).

### 5.3.2 Plume Contours in the Plane of Symmetry of the Impact: Oblique Impact

Figure 5-3 presents the hybrid SOVA-DSMC density contours in the plane of symmetry of the  $45^\circ$  oblique impact 1 s after impact. The comet comes in at a  $45^\circ$  angle from the left and the plume expands away mostly in the downrange direction to the right. Compared to the vertical impact, the expansion plume for oblique impact develops earlier, moves with greater velocities, and expands preferentially in the downrange direction for similar impactor sizes and velocities. For the  $45^\circ$  impact, the expansion plume has already risen to at least 30 km above the initial surface in less than 1 s. The downrange extent of the plume is much greater than the lateral extent of the vertical impact as some of the plume has moved more than 30 km away from the point of impact. Also, the ejecta curtain is much more obvious in this case and clearly surrounds the entire water vapor plume. In addition, some large regions mostly comprising rock can also be observed within the vapor plume. The crater is still in the early formation phase being  $\sim 3$  km deep and

~5 km wide. The SOVA grey and green contours below the red interface represent water and rock, respectively, with the darker shades representing the denser regions of the flow. The black and grey lines above the red interface are from the SOVA simulation of the impact event. The black lines represent the limit between rock and water while the grey line represents the limit between the dark grey and light grey SOVA contours.

The color contours above the interface, with the associated legend, are from the DSMC simulation using the SOVA data at the interface as input. The DSMC data matches most of the features of the SOVA plume above the interface. First, the overall shape of the plume is preserved as the DSMC contours fill in the region of the plume where water was present in the SOVA simulation. In particular, the limit between the rock and water nearest to the surface matches very well between the SOVA and DSMC contours. However, similar to the vertical impact, the DSMC contours for the lowest density regions of the plume, high above the surface, are the least resolved. Also, the elongated area lined by the black line that was filled with rock (starting at  $X = 12$  km,  $Y = 17$  km) can be observed as an empty area in the DSMC contours. One should note again that as the water plume convects downstream, such regions will be slowly filled by water diffusing in from the surrounding regions. In the DSMC simulations, letting water diffuse to areas containing rock in the SOVA simulations should have a minimal effect on the total mass of water retained on the Moon after impact because these rock fragments are very small and because rock and water in neighboring cells have similar velocities and temperatures.

Finally, the dense region of the water plume represented by the red contours in the DSMC simulation matches well the higher density region from the SOVA simulation bordered by the grey line downstream of the interface. Overall, the comparison between the SOVA and DSMC contours in the plane of symmetry of the impact showed that the present under-resolved DSMC simulations provided a qualitatively reasonable solution downstream of the interface.

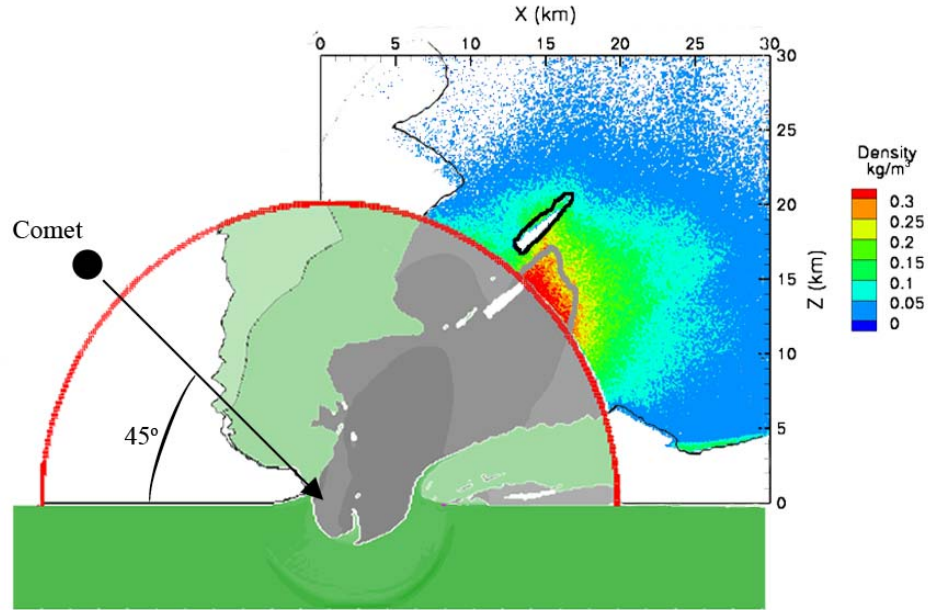


Figure 5-3 Density contours in the plane of symmetry of the oblique impact after 1 s. The green and grey contours are from the SOVA calculations and represent the rock and water densities, respectively. The color contours above the red interface represent the DSMC water density contours with the attached legend. The black lines shown above the interface for reference represent the limit between rock and water in the SOVA simulations. The grey line represents the limit between the dark and light grey SOVA contours above the interface.

### 5.3.3 Plume Macroscopic Data at a Secondary Interface: Oblique Impact

The following section aims to verify the quantitative agreement between the SOVA and DSMC solutions downstream of the interface between the two codes. Figure 5-4 shows the location of both SOVA interfaces, shown in red, for the 45° oblique impact event. For these simulations, interfaces {1} and {2} are concentric hemispheres 20 and 30 km in radius respectively. Macroscopic data, such as density, temperature and bulk velocity, were provided by SOVA at both interfaces. In the present DSMC simulations, the SOVA data at the innermost interface (interface {1}) were used to create the molecular data. The present validation runs

compare macroscopic data at both interfaces {1} and {2} obtained from the full SOVA simulations and from the DSMC simulations. The comparison at interface {1} aims to validate our particle creation scheme while the objective of the comparison at interface {2} is to validate our under-resolved DSMC scheme. Because of the differences between the SOVA Cartesian grid and the DSMC spherical grid, the DSMC and SOVA solutions could not be subtracted so the present section only compares the contours for both solutions. In addition, because of the two different grids, the radius of interface {2} differs slightly between the SOVA solution, at 30.2 km, and the DSMC solution, at 31 km.

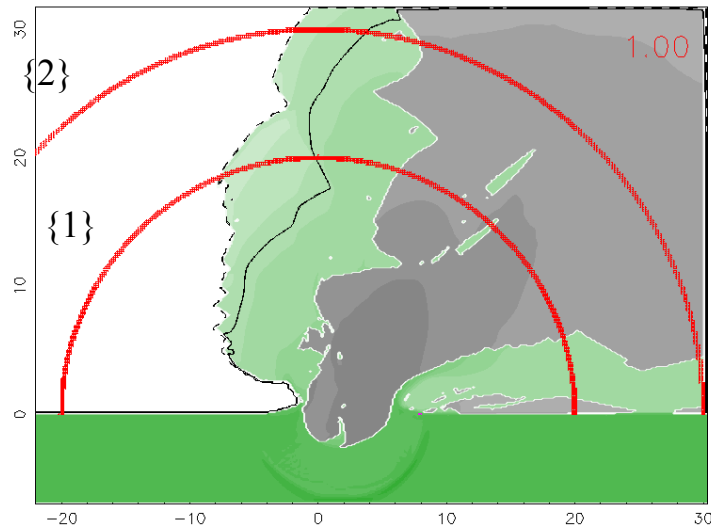


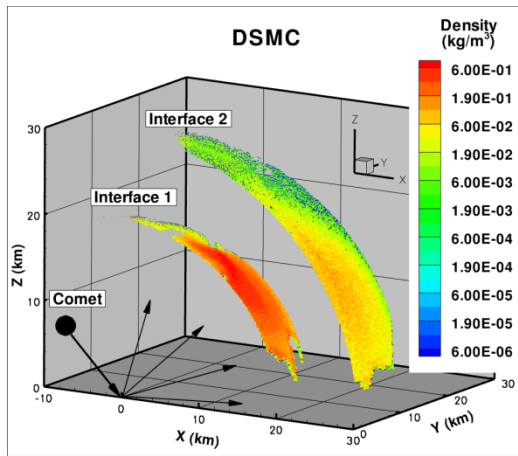
Figure 5-4 Density contours from the SOVA hydrocode 1 s after a 45° oblique comet impact. The two red curves represent the SOVA interfaces at which data are provided.

The following results show the water vapor plume 1 s after the beginning of the impact. At that time, the DSMC simulations had a total of ~7.3 million simulated molecules. The collision limiter numbers for rotational-translational energy exchange and for vibrational-translational energy exchange were fixed at 3 and 9 per molecule, respectively. Figure 5-5 to Figure 5-9 show density, number of molecules per cell, velocity and temperature contours at the interfaces {1} and {2} as seen from the plane of symmetry of the impact. First, the overall shape of the expansion plume is similar between the codes at both the creation interface (interface {1}) as well as the downstream interface (interface {2}). The main differences can be observed near

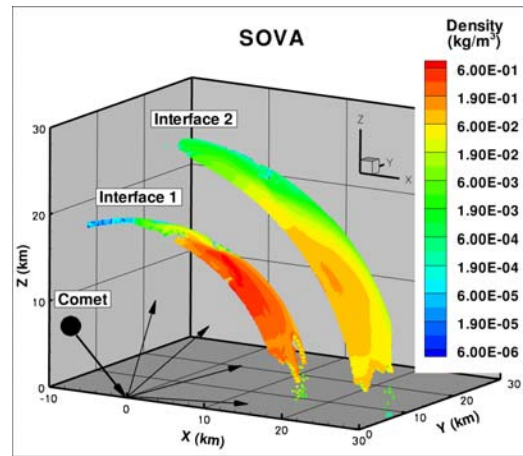


the axis of symmetry of the DSMC domain (right above the point of impact), away from the plane of symmetry of the impact as well as near the lunar surface. The differences in the extent of the plume between the two codes are due to the overall poor representation of the low density regions in the DSMC simulations. The regions of the plume that are not represented well in the DSMC code have densities no greater than  $\sim 0.0005 \text{ kg/m}^3$  (Figure 5-5). These values are  $\sim 100$  times smaller than the maximum density of  $0.78 \text{ kg/m}^3$  (Figure 5-5). In the present simulations, in the densest regions of the flow, near interface {1}, up to 130 molecules are present in every cell (Figure 5-6) and so virtually none can be found in the regions with the lowest densities. In order to resolve these regions, the ratio of real to simulated molecules (FNUM) would have to be decreased.

Outside of the low density regions, the DSMC and SOVA density contours agree well at both interfaces. At the creation interface, the high density contours are nearly identical between the two codes. At the downstream interface, the overall contours are similar but the DSMC density contours are very noisy. While more than 100 molecules are present in the high density cells near interface {1}, as the flow expands away from the interface the maximum number of molecules per cells has decreased to less than 40 in most areas at interface {2}. This number of simulated molecules per cell is sufficient to correctly model the flow but the solution is noticeably noisier at that interface. The relatively large noise level observed in the present DSMC contours was expected because the present contour plots are obtained using the instantaneous data. In most cases, DSMC solutions are plotted using temporal averaging to decrease the noise level in the results but this cannot be used here as the flow is unsteady. Also, because of the relatively high computational cost of the DSMC simulations, ensemble average is not presently used. The main features of the plume are however captured by the DSMC solution.



(a)



(b)

Figure 5-5 Density contours at interfaces {1} and {2}, 1s after the impact, from the (a) DSMC and (b) SOVA simulations.

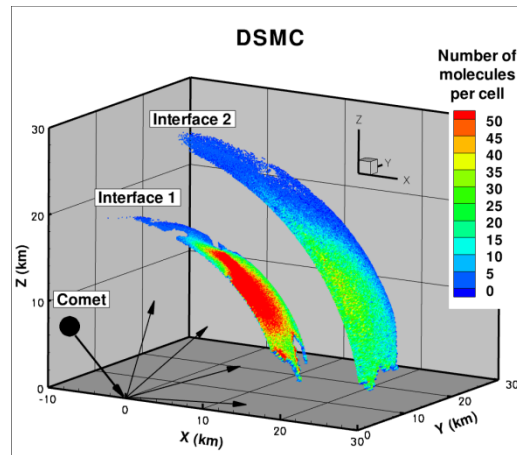
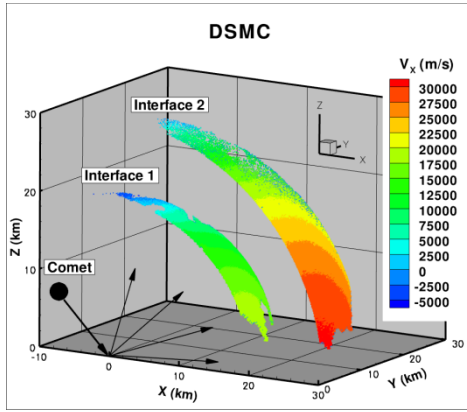
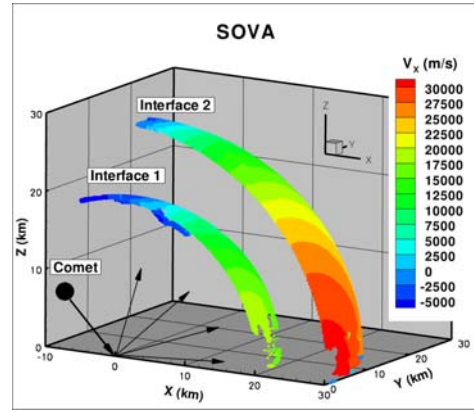


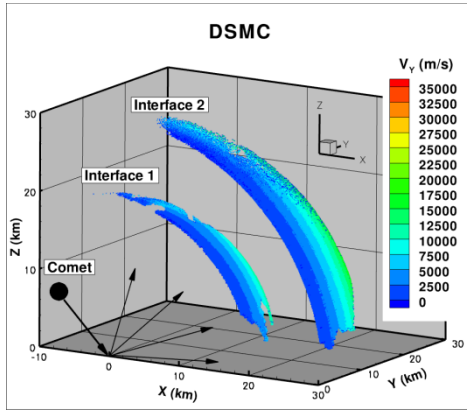
Figure 5-6 Contours of the number of molecules per cell for the DSMC simulations 1 s after the beginning of the impact.



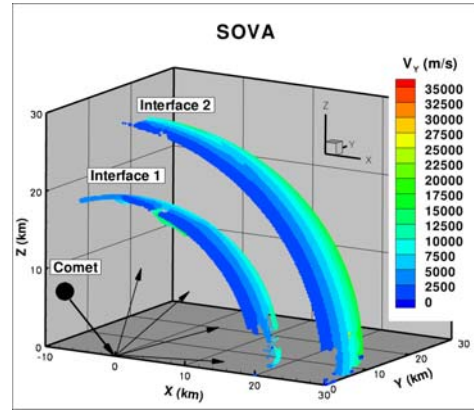
(a)



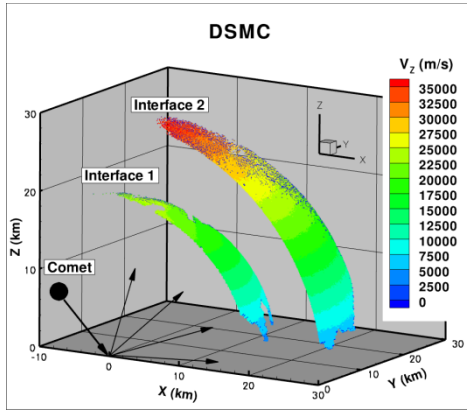
(b)



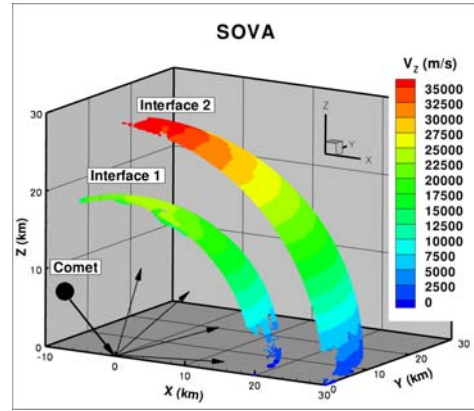
(c)



(d)



(e)



(f)

Figure 5-7 (a, b)  $V_x$ , (c, d)  $V_y$ , and (e, f)  $V_z$  velocity contours at interfaces {1} and {2}, 1 s after the impact, from the (a, c, and e) DSMC and (b, d, and f) SOVA simulations.

The velocity components for the SOVA and DSMC contours are plotted in Figure 5-7. The agreement at interface {1} is very good for all three components. At interface {2}, however, for the X- and Z-components of the velocity vector, some small discrepancies can be observed. Overall, the DSMC contours exhibit some slightly larger velocities than the SOVA contours at interface {2} for an error smaller than 1%. The discrepancies are due to the slight difference in the radius of interface {2} in the following contours, the SOVA and DSMC solutions being plotted at 30.2 km and 31 km, respectively.

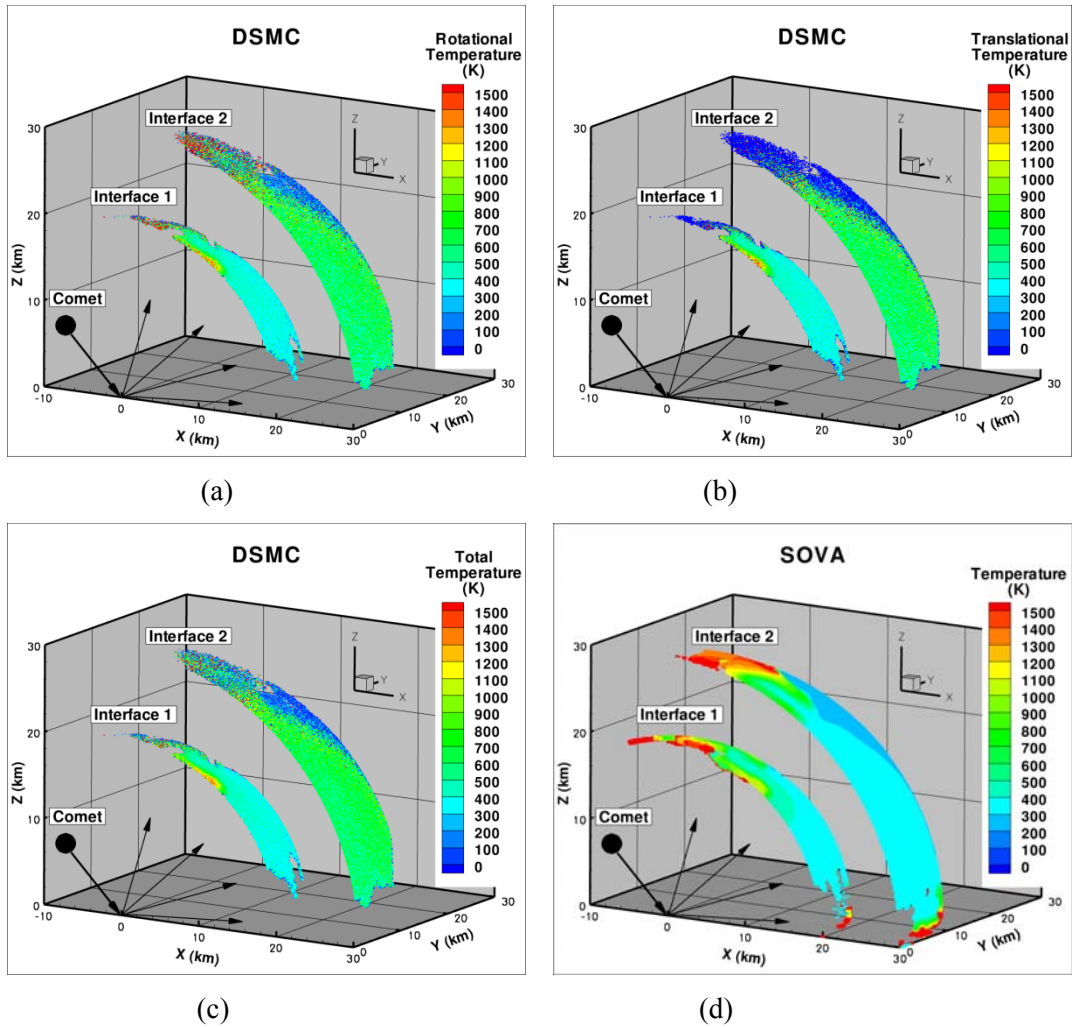


Figure 5-8 Contours of (a) DSMC rotational, (b) DSMC translational, (c) DSMC total and (d) SOVA temperatures at interfaces {1} and {2}, 1 s after the impact.

The DSMC rotational, translational and total temperatures are nearly identical at both interfaces (Figure 5-8) which was consistent with a flow being in Local Thermodynamic Equilibrium (LTE). The only differences between the three temperatures are observed near the axis of symmetry of the DSMC domain. In this region, the rotational temperature is noticeably hotter than the translational temperature and in somewhat better agreement with the SOVA solution. But overall the high temperature region right above the impact point is not well captured in the DSMC simulations. Because of the small DSMC cell size near the axis of symmetry of the spherical domain, this region has only a few representative molecules per cell and an accurate solution cannot be expected. Overall, at interface {1}, the rotational (Figure 5-8a), translational (Figure 5-8b), and total (Figure 5-8c) temperatures are in fairly good agreement with the SOVA temperature (Figure 5-8d). At interface {2}, however, the temperature from the DSMC simulation is very noisy and does not match well the SOVA solution. Near the plane of symmetry of the impact, the SOVA temperature is  $\sim 400$  K while the DSMC temperature is  $\sim 500$  K. As we move away from the plane of symmetry, the SOVA temperature remains nearly constant but the DSMC temperature increases up to  $\sim 700$  K. Even further away, the SOVA temperature drops to 300 K while the DSMC temperature only reaches  $\sim 200$  K in these regions. The low DSMC temperature observed is localized in the low density regions of the flow and has been attributed to the low resolution of the DSMC simulation in these regions. The much higher DSMC temperatures are observed in the higher density regions of the flow that are better resolved. The discrepancies there may be due to the relatively large cell size used in the DSMC simulations compared to the flow mean free path. Another possible origin for the discrepancies may be due to noise in the SOVA data at the interface. Even small variations in bulk velocity between neighboring cells may produce a higher temperature downstream of the interface. Also, possible differences in the physical models used in the DSMC and SOVA codes could be observed in different cooling rates.

Finally, as previously noted in Chapter 4, the vibrational temperatures for the present problem are extremely hard to resolve due to the relatively low temperatures (generally lower than 1000 K) as compared to the characteristic temperatures of a water molecule (between 2400 and 5400 K). This is directly observed in Figure 5-9 where the simulated vibrational temperatures are nearly zero everywhere even at interface {1}. The  $v_1$  and  $v_3$  have similar characteristic high temperatures, at 5261 K and 5404 K, and therefore almost no excited simulated molecule is present in the domain ( $\sim 700,000$  molecules per cell are required to average one excited molecule

at a temperature of  $\sim 400$  K for these two modes). The temperature for the  $v_2$  mode is better resolved due to the lower characteristic temperature for that mode (only a few hundred molecules per cell are required to get one excited molecule). Also, while very noisy, the non-zero  $v_2$ -vibrational temperatures seems to be consistent with the translational, and rotational temperature components in the high density region of the flow.

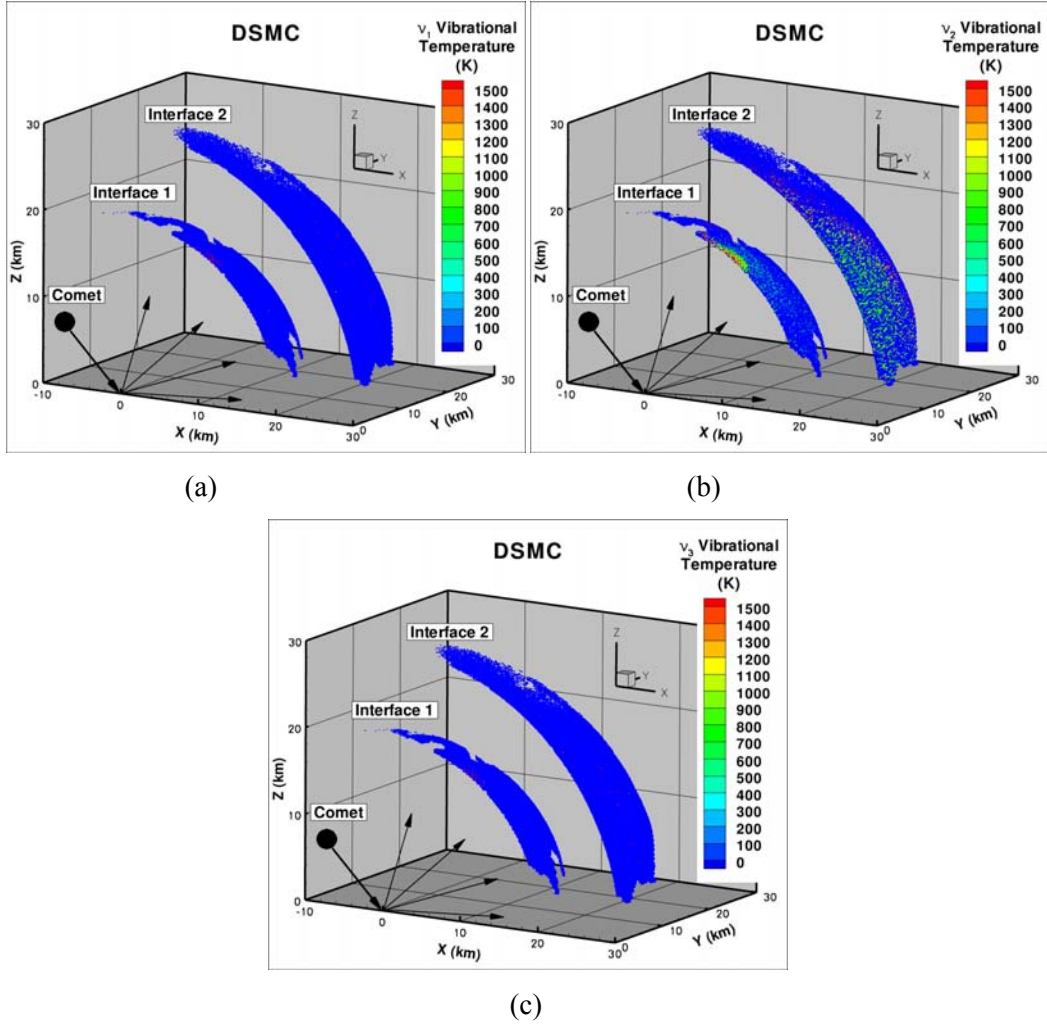


Figure 5-9 (a)  $v_1$ -, (b)  $v_2$ -, and (c)  $v_3$ -vibrational temperature contours at interfaces {1} and {2}, 1 s after the impact.

The under-resolved DSMC simulations seem to capture the physics of the flow fairly accurately, but the solutions are very noisy. In order to obtain a smoother solution, more simulation molecules could have been used or ensemble averaging as well as temporal averaging could have been used to plot the DSMC contours presented in Figure 5-5 to Figure 5-8. While the present simulations only took 24 h on 48 processors, they also only represent the first of the long series of runs required to simulate the entire water vapor plume up to 1000 km away from the point of impact. Therefore, computational cost dictated that having a fairly good representation of the plume at the downstream interface {2} was sufficient. Also, the focus of the project is to follow the water until it is destroyed or falls back on the lunar surface. Hence, the good agreement between the DSMC and SOVA densities and velocities and modestly good agreement on temperature should provide us with accurate enough results for the later circum-lunar part of the simulations.

#### **5.4 TIME EVOLUTION OF THE EXPANSION PLUME FOR A 45° OBLIQUE IMPACT**

The SOVA hydrocode simulations of the 45° oblique impact provided macroscopic data at the 20 km radius hemispherical interface from the beginning of the impact up to 21 s later. At that time, most of the cometary water had crossed the interface so the whole vapor plume can be studied in detail within the DSMC domain. In particular, the present simulations provide a direct way to estimate the total water mass retained on the Moon after impact as well as a detailed description of the vapor plume as it expands away from the point of impact. Also, the present simulations will track the water that falls back on the Moon and follow its migration to the polar cold traps months after impact. First, the overall plume shape and mass distribution of water within the plume are described using the DSMC data at the interface (Section 5.4.1). Then, 2D slices of the DSMC data in the near-field (up to 30 km from the point of impact) and far-field (up to 1000 km from the point of impact) are presented for several variables in order to analyze the characteristics of the plume. Because the DSMC computations ignore the rock, as a complement to our solution, the near-field density contours in the plane of symmetry of the impact provided by the SOVA simulations are shown in Appendix D.

### 5.4.1 Interface Data

A 2D projection of the DSMC water density and radial velocity contours at the interface with the SOVA hydrocode (interface {1} in Figure 5-4) are shown at 2 s intervals in Figure 5-10 to Figure 5-13. In the figures, the point of view is from directly above the point of impact, so the material further away from the origin is also closer to the lunar surface. The red circle marks the intersection of the interface with the surface of the Moon. The comet comes from the left and hits the surface at 30 km/s. Three different “planes” that are used to study the characteristics of the plume in the following sections are also shown in the figures: the plane of symmetry of the impact ( $\beta = 0^\circ$ ), the plane perpendicular to it ( $\beta = 90^\circ$ ), and an intermediate plane at  $\beta = 45^\circ$ . The DSMC solution for the half domain has been mirrored across the  $\beta = 0^\circ$  plane in order to show the entire plume. For easier reference in the following sections, the X-axis in the  $\beta = 0^\circ$ ,  $45^\circ$ , and  $90^\circ$  planes is referred to as  $X_{\beta=0^\circ}$ ,  $X_{\beta=45^\circ}$ , and  $X_{\beta=90^\circ}$ , respectively.

Initially, one second after the beginning of the impact, the plume is highly asymmetric with most of the material moving directly downrange of the point of impact (to the right in Figure 5-10a). Some water is only a few kilometers above the lunar surface and no water is moving through the interface directly above the point of impact. In the plane of symmetry of the impact ( $\beta = 0^\circ$ ), the water plume covers about two thirds of the downrange interface but in the intermediate ( $\beta = 45^\circ$ ) and perpendicular ( $\beta = 90^\circ$ ) planes the plume is restricted to some very narrow regions. Overall, the water vapor plume covers less than one fourth of the projected surface area of the hemispherical interface with the plume being nearly entirely confined between the  $\beta = -45^\circ$  and  $\beta = +45^\circ$  planes. The outer edge of the plume is also noticeably jagged which is probably a reflection of the shape of the rock ejecta curtain surrounding the water vapor plume (See Appendix D).



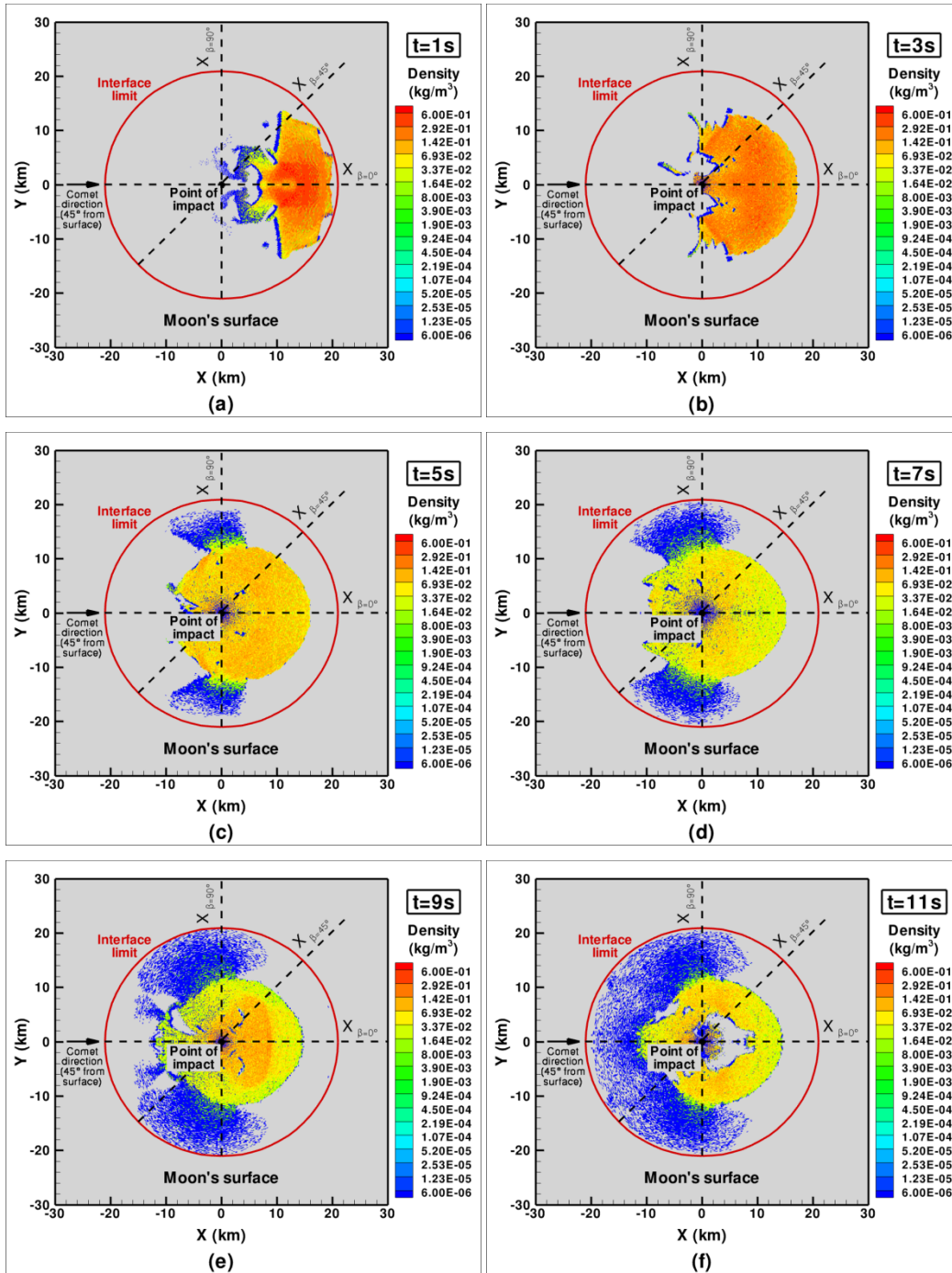


Figure 5-10 2D projection of the DSMC density contours of the water vapor plume at the hemispherical interface with the SOVA hydrocode 1, 3, 5, 7, 9, and 11 s after impact.

Three seconds after the beginning of the impact (Figure 5-10b), the boundary of the plume downrange of the interface takes a near-circular shape that it will retain at least up to 21 s after impact. Melosh (1989) pointed out that the ejecta curtain formed after impact will take on the shape of an inverted cone some time after impact. If the water plume is surrounded by that ejected curtain, as is the case in the SOVA contour plots (Appendix D) the outer limit of the water plume is also expected to resemble an inverted cone in the near-field. The near-circular boundary of the plume observed downrange of the interface in Figure 5-10b represents the intersection of this inverted cone with the SOVA interface. Three seconds after impact, the boundary of the water vapor plume intersects the interface at  $X_{\beta=0^\circ} = 17$  km and  $X_{\beta=45^\circ} = 15$  km, respectively. The overall shape of the plume at the interface is nearly identical in both the plane of symmetry and the intermediate ( $\beta = 45^\circ$ ) plane filling most of the downrange interface. In addition to the changes in the shape of the outer edge of the downrange plume, some water is now moving uprange of the point of impact three seconds after impact. The uprange boundary of the vapor plume is however not smooth. Overall, the plume now extends to the  $\beta = -90^\circ$  and  $\beta = +90^\circ$  planes but in the plane perpendicular to the impact plane, the plume is still much smaller than in the other two planes. The water vapor is localized to two regions: within a 4 km-wide region right above the point of impact and within a 5 km-wide region centered at  $X_{\beta=90^\circ} = 8$  km.

Two seconds later, five seconds after the beginning of the impact (Figure 5-10c), two separate regions can be observed at the interface: a main dense plume and a secondary low density plume. First, the 2D projection of the main plume is now nearly circular with a center located at ( $X = 4$  km,  $Y = 0$  km). In both the plane of symmetry and the intermediate ( $\beta = 45^\circ$ ) plane, the downrange boundary of the plume is retracting while the uprange boundary is further expanding. In the plane of symmetry of the impact, the downrange and uprange limits of the plume are now at  $X_{\beta=0^\circ} = 15$  km and  $X_{\beta=0^\circ} = -6$  km, respectively. In the intermediate  $45^\circ$  plane, the limits are at  $X_{\beta=45^\circ} = 15$  km and  $X_{\beta=45^\circ} = -8$  km, respectively. Major changes happened in the plane perpendicular to the impact plane where the previous two separate regions have now merged to form a single plume. In addition, a low density region can be observed close to the surface in the crossrange direction ( $\beta = \pm 90^\circ$ ). While initially most of the material was moving directly downrange of the point of impact, in the  $\beta = 0^\circ$  plane, now the plume is broader in the  $\beta = 90^\circ$ , and  $\beta = 45^\circ$  planes.

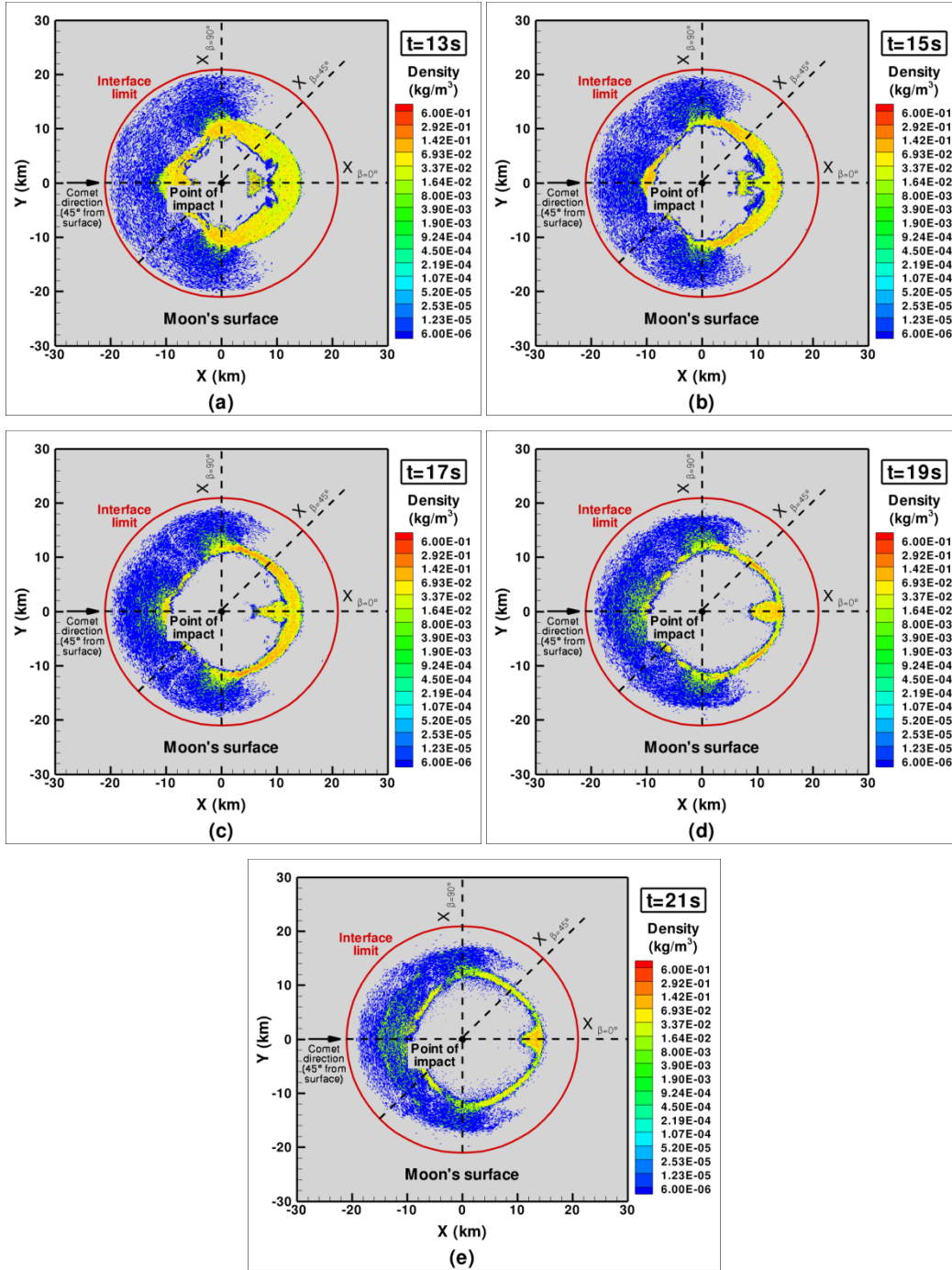


Figure 5-11 2D projection of the DSMC density contours of the water vapor plume at the hemispherical interface with the SOVA hydrocode 13, 15, 17, 19 and 21 s after impact.

In the next few seconds (Figure 5-10d), the overall shape of the plume is nearly unchanged. Seven seconds after impact, the plume continues to expand further uprange of the point of impact distorting the projected shape of the main plume into an oblong region with the limits of the plume shifting upstream to  $X_{\beta = 0^\circ} = -10$  to 15 km, and  $X_{\beta = 45^\circ} = -12$  to 14 km, respectively. The previous low density area is also now more prominent uprange of the point of impact extending to the  $\beta = 135^\circ$  plane. In the plane perpendicular to the impact plane, the plume fills nearly the whole interface with some material passing through the interface very close to the surface of the Moon. The radial velocity contours shown in Figure 5-12 and Figure 5-13 have been blanked for cells with a radial velocity greater than the escape velocity at the surface of the Moon (i.e. 2.38 km/s). Seven seconds after impact is the first time at which some of the material within the plume has a bulk radial velocity smaller than the escape velocity (Figure 5-12a). The slow material within the high density plume is mostly localized in the regions of the plume close to the rocky ejecta curtain as well as within the low density part of the plume.

Two seconds later, nine seconds after impact, the overall surface area covered by the main plume at the interface begins to shrink, while the low density part of the plume uprange of the point of impact continues to spread. The fullest plume is again observed in the plane perpendicular to the plane of symmetry with water leaving the interface just a few kilometers above the surface. The high density part of the plume is made of two distinct regions (Figure 5-10e): a high density region, in the form of a right triangle with vertex at ( $X = -8$  km,  $Y = 0$  km) and extending out at  $\pm 45^\circ$ , and an intermediate density region surrounding it. The densest region also corresponds to a high velocity region in the radial velocity contours (Figure 5-12b). At that time, most of the plume is now moving with a velocity smaller than the escape velocity except for that triangular region and most of the downrange plume which have been blanked out in the radial velocity contours. The origin of the high density, high velocity region can be explained by studying the contours observed eleven seconds after impact.

Eleven seconds after the beginning of the impact (Figure 5-10f), the overall plume shape at the hemispherical interface has changed dramatically. The outer boundary of the high density region is still circular but a large hole is now observable near its center slightly downrange of the point of impact. By examining the SOVA contours in Appendix D, this hole becomes attributable to some rocky material rising far above the point of impact. This material ultimately forms the central peak that can be observed in most large impact craters. The central peak of rocky material

is present above the initial lunar surface from about 5 s after impact (Appendix D) but reaches the 20 km radius interface around 11 s after impact. Because of this rocky material moving nearly straight up from the point of impact, the water above it is being pushed out of the way. This resulted in the contours observed nine seconds after impact where a dense and relatively faster section of the plume was observed just above the point of impact at the interface. Simultaneously, the low density material observed crossrange of the point of impact, at five seconds after impact, covers now most of the uprange half of the interface. In the plane of impact, the main plume uprange and downrange limits are at  $X_{\beta=0^\circ} = -12$  km and  $X_{\beta=0^\circ} = 14$  km, respectively, and the low density plume extends uprange to  $X_{\beta=0^\circ} = -19$  km. In the  $45^\circ$  intermediate plane, the plume overall characteristics remain unchanged and the main plume extends from  $X_{\beta=45^\circ} = -6$  to 13 km, while the low density plume extends uprange up to  $X_{\beta=45^\circ} = -20$  km. The broadest plume is still observed in the plane perpendicular to the impact plane with no noticeable changes from the previous time. In this plane, the main plume ranges up to  $X_{\beta=90^\circ} = 10$  km away from the point of impact and the low density plume to almost  $X_{\beta=90^\circ} = 20$  km. At that time, the entire plume is moving with a velocity smaller than the escape velocity but mostly still faster than 2 km/s. Overall, the main plume is moving faster than the low density part of the plume and the fastest material is found at the edges of the water plume with the central peak rocky material.

Thirteen seconds after impact (Figure 5-11a), the surface area of the interface covered by the rocky central peak material is even greater at the interface, further reducing the high density water vapor plume to a ring. Again, the high density material moves faster than the low density part of the plume. Differences in the velocities within the dense region can now be observed as the velocity in the uprange plume is greater than 2 km/s but is as low as 1.5 km/s in the downrange part of the plume. Overall, the fastest material is found at the boundary of the water vapor plume with the central peak rocky material. In the plane of the impact, the rocky plume is centered at  $X_{\beta=0^\circ} = 2$  km and is about 10 km wide. In the intermediate plane, the rocky material peak is also centered at  $X_{\beta=45^\circ} = 2$  km but it is also larger being 14 km wide. In the plane perpendicular to the impact plane, the extent of the rocky material is widest at 16 km. The ring of denser water vapor is thickest directly uprange and downrange of the point of impact, with width of 6 km and 9 km, respectively, as compared to 2 km and 6 km in the  $\beta = 45^\circ$  plane and 4 km in the  $\beta = 90^\circ$  plane. Finally, the low density plume can still be observed uprange of the ring with relatively lower radial velocities than the main plume.

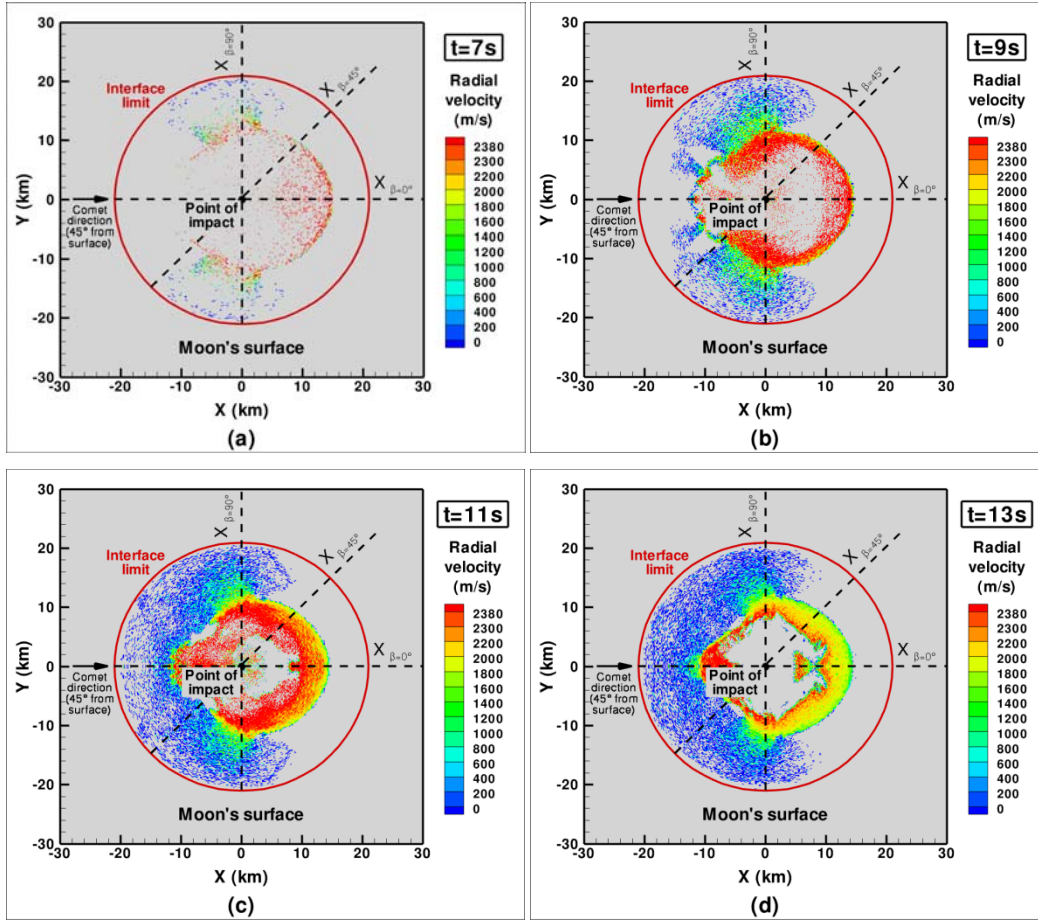


Figure 5-12 2D projection of the DSMC radial velocity contours of the water vapor plume at the hemispherical interface with the SOVA hydrocode 7, 9, 11, and 13 s after impact.

Two seconds later, at  $t = 15$  s, the previous trends continue with a noticeable decrease in the high density ring's thickness and the continued presence of the low density region uprange of the ring. First, the outer edge of the ring seems to stabilize at  $X_{\beta=0^\circ} = 14$  km and  $X_{\beta=45^\circ} = 13$  km, respectively. Also, the thickness of the ring decreases faster uprange than downrange of the point of impact. In the plane of impact, the rocky material forms a 14 km-wide gap in the center of the plume at the interface and the uprange and downrange ring thicknesses are 3 km and 8 km, respectively. The plume is very similar in the intermediate plane, with an even more pronounced imbalance between the uprange and downrange water vapor plumes. The uprange high density region has nearly disappeared and the uprange plume is now mostly constituted of low density

material. At the same time, the downrange plume is now limited to a 5 km-wide spray. In the plane perpendicular to the impact plane, the rocky material crossing the interface extends even further with the rocky plume width at the interface boundary being nearly 18 km. The high density part of the plume is only 2 km thick and the low density region is 10 km wide. Overall, in all three planes, the outer limits of the low density plume retreat slightly by a few kilometers toward the point of impact and the low density uprange plume is relatively denser in the crossrange direction. In the radial velocity contours the previous trends are continued. The downrange plume moves more slowly around 1.5 km/s at the outer edge and 2 km/s at the inner edge. The uprange dense material is usually moving faster than 2 km/s while the low density material remains slow.

At seventeen seconds after impact, the plume is very similar to the plume observed two seconds earlier. The limit of the rocky material above the point of impact is now nearly circular with a 9 km radius centered 1 km downrange of the point of impact (at  $X = 1$  km,  $Y = 0$  km). In the plane of symmetry of the impact, the dense plume is 9 km wide downrange of the point of impact but is only 2 km wide uprange. The dense plume is 2 km wide in the intermediate plane but is barely discernable in the  $\beta = 135^\circ$  plane. In the perpendicular plane, the plume is not as dense but the high density region is almost 3 km wide. The low density region of the plume is slightly denser directly uprange and crossrange of the point of impact and the uprange material is now moving more slowly through the interface.

Nineteen seconds after the beginning of the impact, the downrange plume is still noticeably denser than the uprange plume but it is also more localized than before. Hardly any material is moving downrange in the intermediate  $45^\circ$  plane where the water vapor is localized to a 2 km-wide spray. The downrange plume in the plane of symmetry continues to shrink with a thickness of 5 km. In the crossrange and uprange directions, the plume is almost entirely made of low density material. The densest uprange plume is observed in the plane of impact and in the plane perpendicular to it and the extent of the plume is now greater directly uprange of the point of impact ( $X_{\beta = 0^\circ} = -19$  km to  $X_{\beta = 90^\circ} = -17$  km). The radial velocity of the dense ring material continues to decrease to values lower than 1.5 km/s.

Twenty one seconds after impact (Figure 5-11e), the main change observed 19 s after impact continues. In the plane perpendicular to the impact plane, the outer edge of the low density plume has retracted to  $X_{\beta = 90^\circ} = 16$  km and the plume in that plane has a noticeably smaller

footprint than in the other two planes at the interface. The widest plume is observed in the plane of symmetry of the impact and in that plane the dense plume now seamlessly merges with the low density plume uprange of the interface. At the same time, the radial velocity of the water vapor crossing the interface continues to decrease to about 1.2 km/s in the dense part of the plume and to less than 1 km/s in the low density part of the plume.

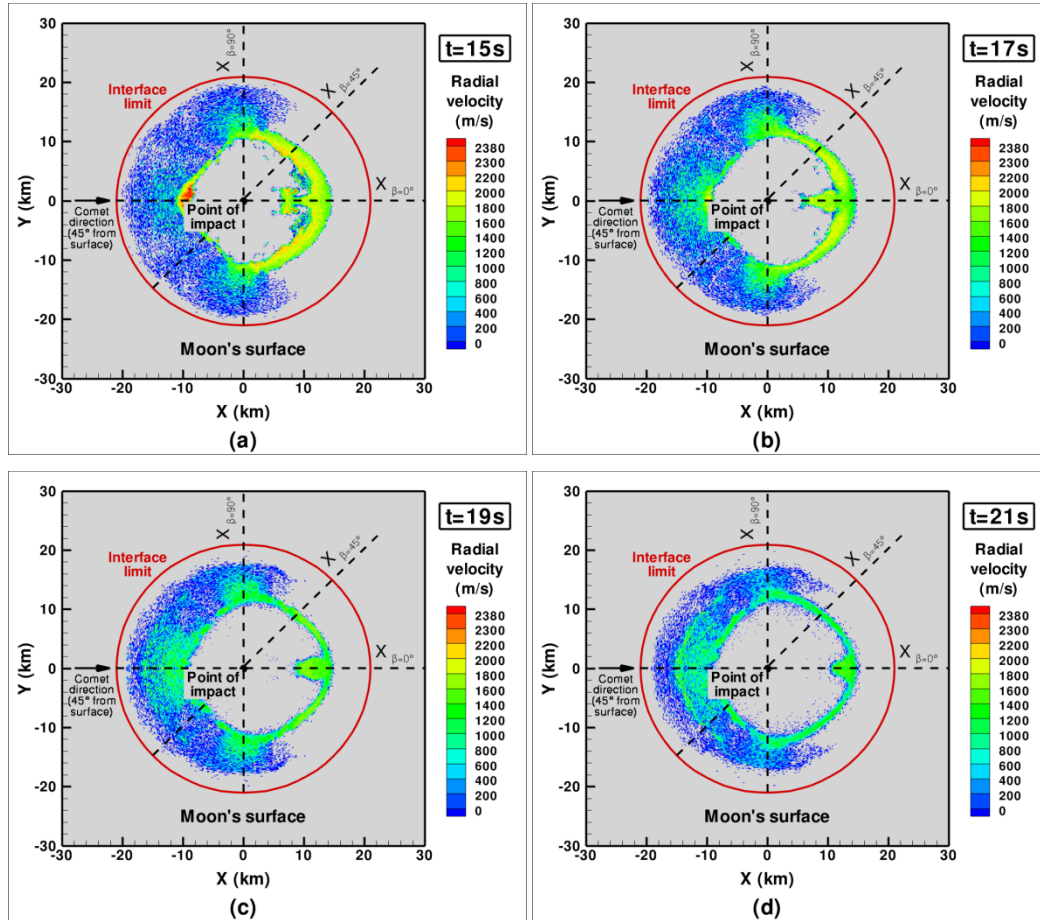


Figure 5-13 2D projection of the DSMC radial velocity contours of the water vapor plume at the hemispherical interface with the SOVA hydrocode 15, 17, 19 and 21 s after impact.

In summary, the water vapor plume undergoes several major shape changes during the early seconds of the impact event. Initially, the plume is strongly directional in the downrange direction. After about five seconds, however, the plume becomes more symmetric around a



location 4 km directly downrange of the point of impact and is clearly taking the shape of an inverted cone. A secondary low density plume is also appearing in the crossrange direction. Four seconds later, the next major change occurs when the central peak of rocky material reaches the interface. This rocky material is preceded by some relatively high density, high velocity water vapor that is moved out of the way as the rocky material moves directly above the point of impact. Once the rocky central peak material reaches the interface, the main water vapor plume is largely confined to a simple ring. In parallel, the low density plume continues to spread uprange of the dense plume until it fills the entire uprange hemisphere 11 s after impact. Interestingly, oblique impacts are known for the butterfly ejecta deposition pattern that can be observed with a depleted deposition of rock in the uprange direction (Melosh, 1989). Using Appendix D, we can see that initially some rock is displaced uprange but that the rocky plume seems to be made of lower density material compared to the downrange material. In particular, a dense ejecta curtain can be observed downrange of the point of impact but not uprange from three seconds on. Then, at later times ( $t \geq 9$  s), when the water vapor is generally moving much more slowly - at speeds lower than the escape velocity - the uprange plume is only constituted of water vapor. In the case of a comet impact, the cometary water that actually falls back on the Moon will be transported later around the Moon and not form a thick deposit near the impact crater. So the fast moving low density rock and slow moving low density water in the uprange direction seem to be consistent with depleted uprange deposits known as the butterfly ejecta pattern observed in oblique impact experiments. Finally, one can note that the contours above the point of impact are noisier than further away which is due to the fact that the point of impact is located at the axis of symmetry of our spherical DSMC domain. However, water vapor is only moving above the point of impact early during the impact event ( $3 \leq t \leq 9$  s) and from the radial velocity contours it was observed that this part of the water vapor plume was moving at velocities greater than the escape velocity of the Moon. Therefore, the relatively poorly resolved contours near the axis of symmetry of the DSMC domain probably do not influence our final solution concerning the total amount of water retained on the Moon.

The present DSMC simulations provide the number of simulated molecules entering the DSMC domain at each timestep at the interface. From these data, the total mass and instantaneous mass flux of water through the interface can be studied as a function of time and azimuthal angle. The total mass of water that has crossed the interface and instantaneous mass flux at the interface

are presented versus time in Figure 5-14. The same quantities are also plotted on a log scale for five different azimuthal angles ( $\beta = 0, 45, 90, 135$ , and  $180^\circ$ ) in Figure 5-15 and Figure 5-16. The line plot for each azimuthal angle represents the average total mass and average instantaneous fluxes of water that crossed a  $45^\circ$  ( $\beta = 0$ , and  $180^\circ$ ) or  $90^\circ$  ( $\beta = 45, 90$ , and  $135^\circ$ ) azimuthal slice of the interface centered at the given angle as a function of time. The angles of  $\beta = 0, 45, 90, 135$ , and  $180^\circ$  represent the downrange, intermediate downrange, crossrange, intermediate uprange, and uprange directions, respectively.

The total mass of the comet is  $4.65 \times 10^{12}$  kg, and 21 s after the beginning of the expansion, the total mass that has crossed the interface has asymptoted to  $4.46 \times 10^{12}$  kg of water, or 96% of the total comet mass (Figure 5-14). This, however, does not imply that 4% of the cometary water remains inside the 20 km in radius interface 21 s after impact. Indeed, in our DSMC simulations, we neglected 3% of the water mass crossing the interface because of the presence of rock in some of the SOVA cells. With our assumptions in the DSMC domain, such as the absence of chemistry or condensation, we considered that our computations could not model that water accurately and it was therefore neglected. By accounting for this 3%, the total amount of water remaining within the interface 21 s after impact is lowered to 1% of the initial comet mass. The mass remaining within the interface 21 s after impact is currently assumed to deposit back onto the lunar surface in and around the impact crater. The transport of that water into the lunar cold traps is studied in Chapter 6. Figure 5-14 provides some relatively good estimates as to the water distribution within the vapor plume. The fastest material crosses the interface in under 0.4 s and, assuming it originated at the point of impact, travels at nearly 50 km/s. The maximum mass flux at the interface is achieved around 1 s after impact and lasts about 0.5 s. During this time interval, the mass flux of water crossing the interface is  $1.85 \times 10^{12}$  kg/s. In addition, it takes less than 2 s for half of the comet mass to cross the interface and 90% of the comet mass has crossed the interface in less than 10 s. As expected, our data show that most of the cometary material is moving faster than escape velocity and will be blown off the Moon. In Figure 5-14 and Figure 5-16, a secondary peak can be observed in the instantaneous mass flux at the whole interface 9 s after the beginning of the impact (blue line in Figure 5-14 and black line in Figure 5-16). The secondary peak is believed to be due to the relatively high density material moving directly above the point of impact (Figure 5-10e). At the end of the SOVA simulations, the mass flux of water at the interface has dropped to  $5 \times 10^9$  kg/s (not shown).

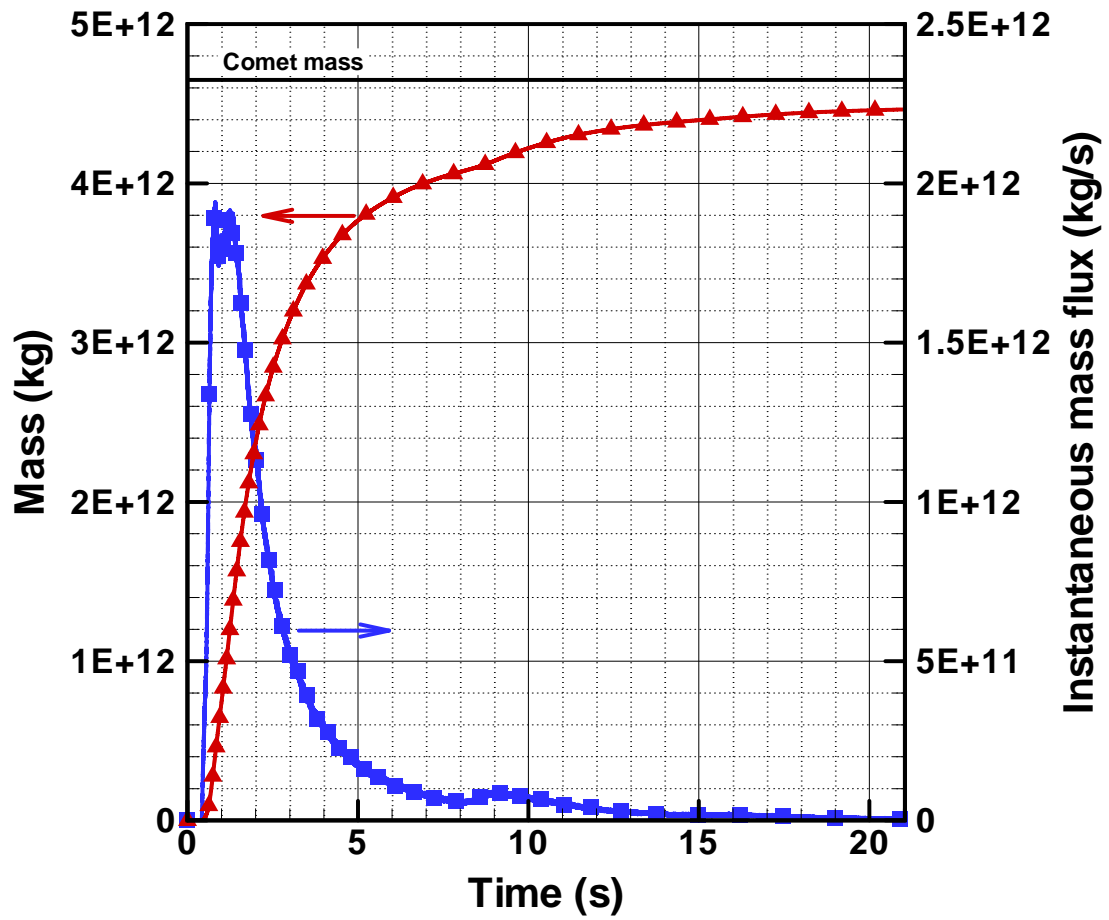


Figure 5-14 Total mass (red line) and instantaneous mass flux (blue line) into the DSMC domain at the 20 km in radius interface with the SOVA hydrocode as a function of time.

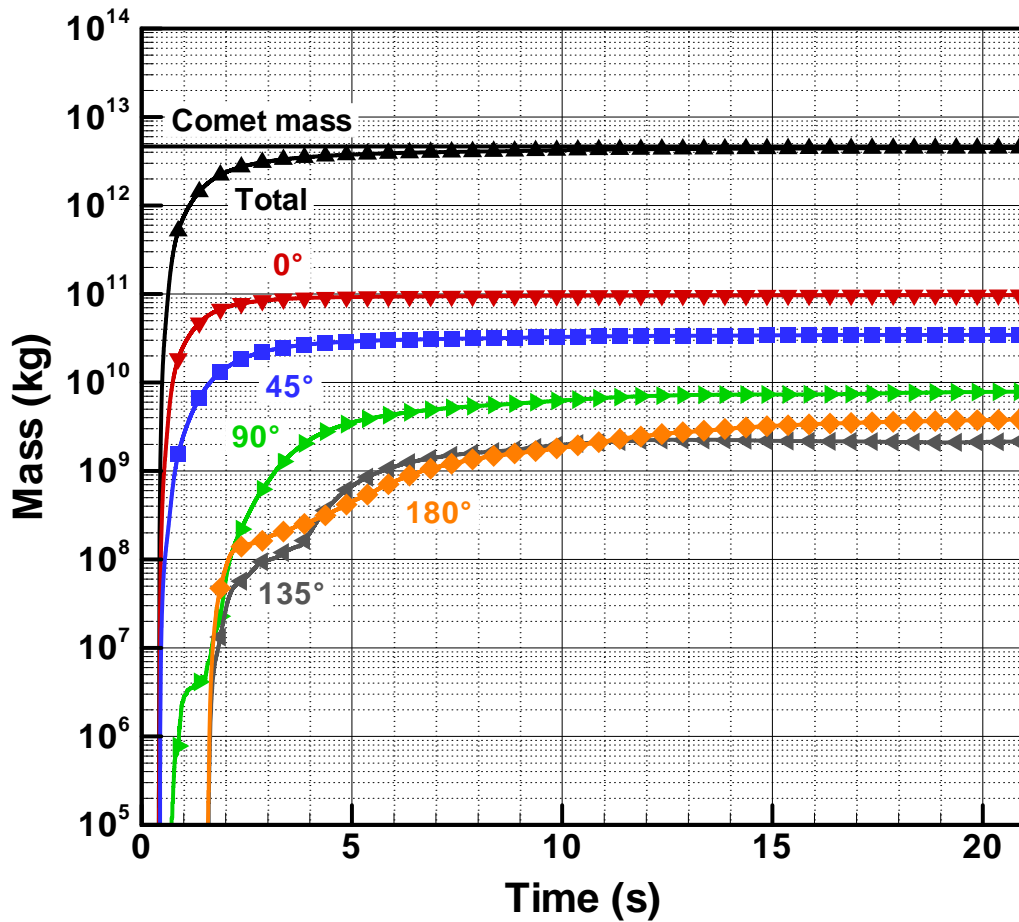


Figure 5-15 Total mass flow (black line with triangle symbols) and spatially averaged directional mass flow (other colors) that crosses the interface between the SOVA and DSMC codes as a function of time. Note that the vertical axis uses a logarithmic scale.

Figure 5-15 and Figure 5-16 provide some additional information concerning the mass loading of the water vapor plume. Initially, the water vapor plume travels preferentially in the downrange direction and crosses the interface 0.4 s after the beginning of the impact in that direction ( $\beta = 0^\circ$ , and  $45^\circ$ ). The plume only reaches the interface 0.9 s after the beginning of the impact in the crossrange direction ( $\beta = 90^\circ$ ) and it takes an additional 0.7 s for the water to cross the interface uprange of the point of impact ( $\beta = 135^\circ$ , and  $180^\circ$ ). The actual mass distribution of water within the plume can be obtained by multiplying the spatially averaged mass for each

azimuthal angle by the size of the angular region they each represent (due to the symmetry of the problem across the plane of impact the angular region around each azimuthal plane is equal to  $45^\circ$  for  $\beta = 0$ , and  $180^\circ$  and is equal to  $90^\circ$  for  $\beta = 45, 90$  and  $135^\circ$ ). We found that for this case 52.3% of the water moves directly downrange of the interface ( $\beta = 0^\circ$ ) and 87.7% moves in the general downrange direction ( $\beta = 0$  and  $45^\circ$ ). Most of the remaining portion of the water moves in the crossrange direction (8.3% for  $\beta = 90^\circ$ ) and very little water actually moves in the uprange direction with only 1.9% and 2.1% of the water crossing the interface in the directions centered on  $\beta = 135^\circ$  and  $\beta = 180^\circ$ , respectively.

In order to smooth the DSMC data, Figure 5-16 has been obtained by averaging the mass crossing the interface for azimuthal region over 200 DSMC timesteps. So each data point used in the line plot represents the spatially averaged amount of water crossing the interface during a 0.1 s interval. The data shown in Figure 5-16 is noticeably noisy but the actual noise level is believed to be only a few percent and any larger variation between two data points can be attributed to some actual physical phenomena. In the downrange direction ( $\beta = 0^\circ$ ), most of the water vapor has crossed the interface within 10 s of the beginning of the impact with a maximum spatially averaged mass flux of  $7 \times 10^{10}$  kg/s between 0.6 and 1.3 s after impact. The mass flux then decreases rapidly before a secondary peak, 8.5 s after impact, occurs with an instantaneous mass flux of  $7 \times 10^8$  kg/s. Afterwards, the influx at the interface in that direction stabilizes around  $2 \times 10^8$  kg/s until 18 s after impact. Near the end of the calculation, very little water is actually crossing the interface in that direction ( $< 10^8$  kg/s). The water vapor plume reaches the interface at the same time in the intermediate downrange direction ( $\beta = 45^\circ$ ) as in the downrange direction but the peak mass flux (1.5 s after impact) is only  $1.5 \times 10^{10}$  kg/s, and only lasts 0.2 s. In that region, the secondary peak is also observed slightly later than in the downrange direction, 9 s after impact, with a similar instantaneous mass flux of  $7 \times 10^8$  kg/s. The instantaneous mass flux then decreases to a near uniform value of  $2 \times 10^8$  kg/s until 17 s after impact. Afterwards, however, an interesting feature can be observed where the mass flux in that region of the interface begins to oscillate around zero. The fact that a negative instantaneous flow rates means that in that region at that time more water is falling back through the interface towards the lunar surface than is rising above the interface. In our present computations, the SOVA hydrocode simulations can be run first and the output can be used as input to our DSMC simulations. This sequential approach is

only valid in the case where there is no feedback from the DSMC domain towards the SOVA domain. In the present simulations we do observe some weak feedback with the negative instantaneous mass flux at the interface at late times. The only two regions with mass coming back to the surface through the interface are the downrange and uprange intermediate regions. The total mass falling back through the interface is  $\sim 0.3\%$  and  $\sim 6.7\%$  of the total mass crossing the interface in the intermediate downrange region and in the intermediate uprange region, respectively. This amounts to a total mass of water coming back to the surface through the interface of  $\sim 0.1\%$  of the total mass of water through the interface for the entire domain. Given the relatively low fraction of water coming back to the surface through the interface, the weak negative mass should not have any noticeable influence on the SOVA contours. In addition, this water is accounted in our estimate of the total comet mass remaining after impact near the crater. Therefore, the present sequential unidirectional calculations should provide us with fairly good estimates as to the total mass of water retained on the Moon after a comet impact.

In the crossrange direction ( $\beta = 90^\circ$ ), the peak mass flux ( $1.5 \times 10^9$  kg/s) is observed between 3 and 4 s after impact. The secondary peak lasts from 8.5 to 10.5 s after impact and has a net flux of incoming water at the interface of  $4.5 \times 10^8$  kg/s. The fullest plume has generally been observed in that plane from five seconds on (Figure 5-10 and Figure 5-11) but because the majority of the plume is made out of low density material, the total mass of water crossing the interface in that plane is relatively small (Figure 5-15). In the intermediate uprange direction ( $\beta = 135^\circ$ ), most of the material crosses the interface between 4 and 8 s after the beginning of the impact and during that time the greatest mass flux of water at the interface ( $5.5 \times 10^8$  kg/s) is observed 4.5 s after impact. The secondary peak is also observed 9 s after impact. Afterwards, the mass flux decreases rapidly and even becomes negative at most times during 13 s to 19 s after impact. Finally, directly uprange of the point of impact ( $\beta = 180^\circ$ ), most of the water moving in that direction crosses the interface 2 s after impact and during the time interval 5 s to 15 s after impact. Two similar peaks in the mass flux are observed 6 and 11 s after impact, with a peak value of  $4 \times 10^8$  kg/s.

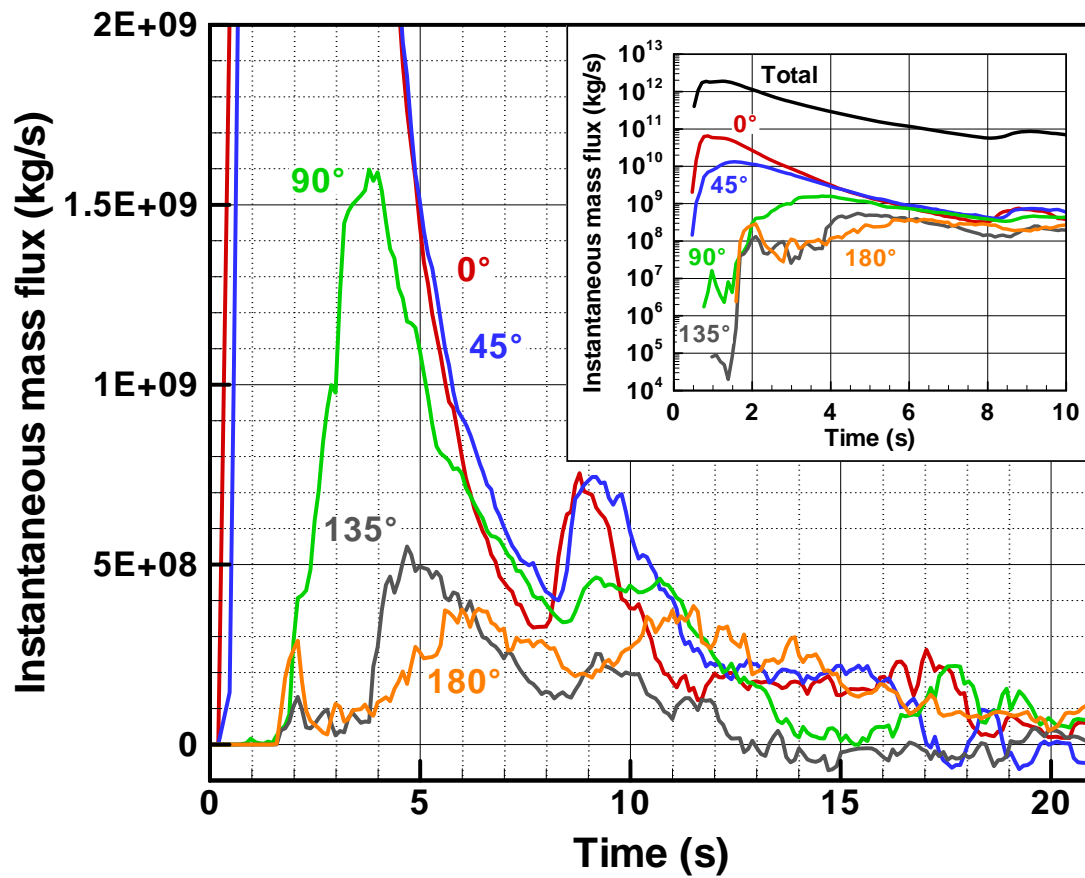


Figure 5-16 Instantaneous total mass flux (black line) and spatially averaged directional mass flux (other colors) of water that crosses the interface between the SOVA and DSMC codes as a function of time. Note that the vertical axis in the inset picture uses a logarithmic scale and that only the first ten seconds of the impact are shown.

The fraction of water that crosses the interface with velocity lower than the escape velocity can be estimated from the time it takes for the water to cross the interface. At a radial velocity of 2.38 km/s, which is the value for the escape velocity at the Moon's surface, material originating at the point of impact would take 8.4 s to reach the interface. From our DSMC contours for the radial velocity at the interface (Figure 5-12), some of the water vapor has a radial velocity lower than the escape velocity as early as 7 s after the beginning of the impact. This water vapor probably originated further away from the point of impact and had a shorter distance to travel to reach the interface therefore crossing the interface under 8.4 s while travelling at less than 2.38 km/s. Also, some of the water vapor crossing the interface 9 s after impact moves faster than the escape velocity (for instance the water vapor above the central peak rocky material). Exact estimates will be obtained from our multi-domain DSMC calculations as to the mass of water retained on the Moon after impact (see Chapter 6) but in the present section we use the plots for the mass flow rate of water at the interface as first order estimates. From Figure 5-14, the amount of water that crossed the interface between 8.4 s and 21 s after the beginning of the impact is  $3.68 \times 10^{11}$  kg or 7.9% of the original comet mass. Of this mass 16.8% crossed the interface in the downrange direction ( $\beta = 0^\circ$ ), and an additional 34.1% crossed the interface in the intermediate downrange direction ( $\beta = 45^\circ$ ). Of the remaining mass, a large amount (28.6%) was moving in the crossrange direction ( $\beta = 90^\circ$ ). Finally, the least amount (5.2%) of water crossed the interface in the intermediate uprange direction ( $\beta = 135^\circ$ ) while 15.2% of the mass retained on the Moon was moving in the uprange direction ( $\beta = 180^\circ$ ). In conclusion, the distribution of remaining water on the Moon after impact is more uniform than the overall distribution of water within the entire plume. Some preferential directions are still observed in the plume, however, with most of the water moving in the crossrange to intermediate downrange direction (62.7%), 32.1% of the remaining water moved either directly uprange or downrange of the point of impact and only 5.2% moved in the intermediate uprange direction ( $\beta = 135^\circ$ ).

Our estimate for the total amount of water retained on the Moon after impact should be higher if one accounts for the amount of water neglected at the interface. After 8.4 s, up to 10% of the total water mass crossing the interface is neglected due to the coexistence of rock and water within some of the SOVA cells. The relatively higher proportion of water ignored at later time is attributed to a larger contact area between the water and the rock. Therefore, under the present



assumptions, the total amount of water with a velocity smaller than the escape velocity could be as high as 8.7% of the total comet mass. These estimates are compared in Section 6.3.1 to the “actual” mass retained as obtained in our DSMC simulations of the water vapor plume to much later times when most of the cometary water has been lost due to escape.

#### 5.4.2 Near Field Data

While the present DSMC simulations are fully three dimensional, in order to study the plume in more detail, the 3D simulations have been post-processed. At several instants in time, the vapor plume has been sliced in three directions in order to study its characteristics (Figure 5-17). The first slice is in the plane of symmetry of the impact ( $\beta = 0^\circ$ ), while the second slice is in perpendicular to it ( $\beta = 90^\circ$ ). The final slice is located halfway in between the first two slices at a  $\beta$  of  $45^\circ$  (Figure 5-17).

Contours of various gas properties for the  $45^\circ$  oblique impact plume are presented as a function of time in Figure 5-18 to Figure 5-70. Each figure represents a given instant in time and shows contours for a specific gas property in all three directional slices ( $\beta = 0^\circ$ ,  $45^\circ$ , and  $90^\circ$ ). Adjacent to each separate slice is a schematic inset that shows the orientation of the 2D plane of interest. In each slice, the domain is 60 km in the horizontal direction ( $X_\beta$ ) and 30 km in the vertical direction ( $Z_\beta$ ). Unless otherwise noted, the cell size in both directions is 200 m and the present data have been interpolated using an “inverse distance weighting” scheme with a 500 m radius sphere of influence in order to smooth the data. Note that to observe the full plume, we took advantage of the symmetry of the problem where gas properties for  $X_{\beta = 45^\circ} < 0$  are taken from the DSMC data at  $\beta = 135^\circ$  in azimuth and where the data for  $X_{\beta = 90^\circ} < 0$  have been obtained by mirroring the data for  $X_{\beta = 90^\circ} > 0$ . First, we want to study the results near the interface with the SOVA hydrocode. The overall shape of the plume as well as several macroscopic properties, such as density, temperature, radial velocity and Mach number, will be examined. Some other parameters more relevant to the computational aspects of the simulations, such as the Knudsen number and mean free path, will also be studied.

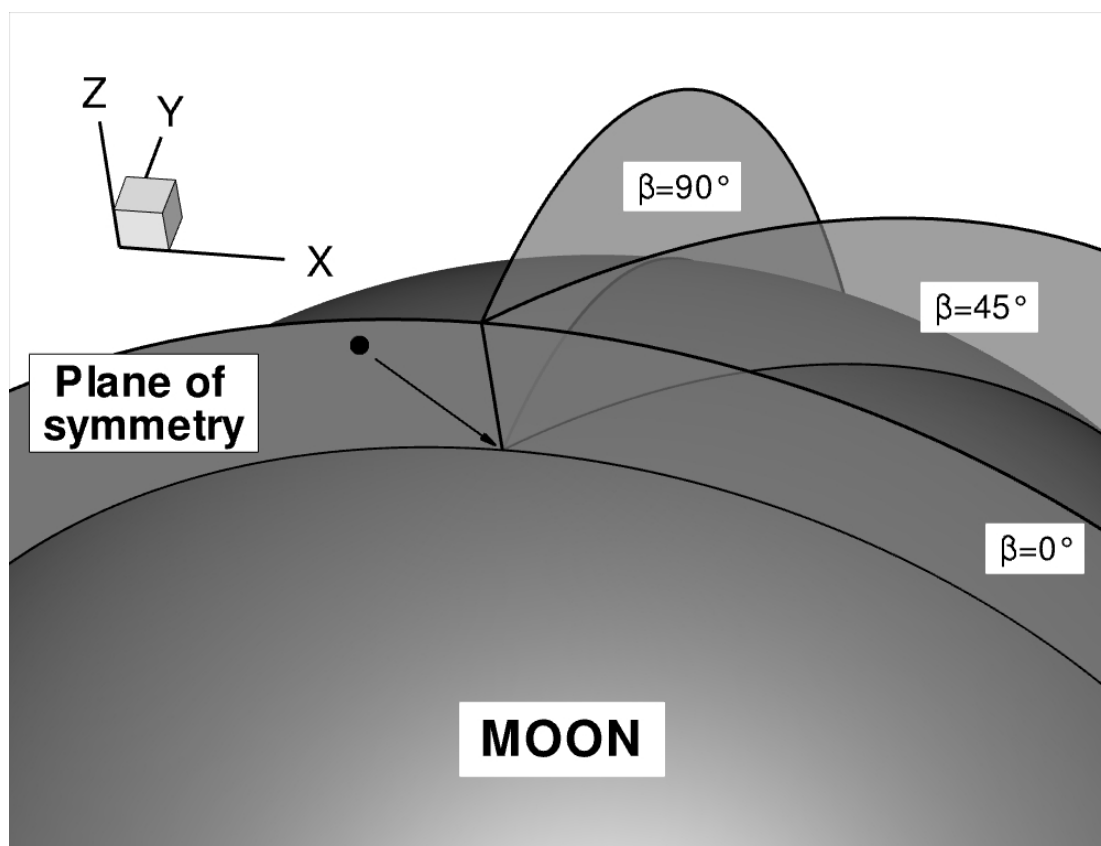


Figure 5-17 Location of the three 2D slices used to present the 3D water vapor plume results obtained from the DSMC simulations of a  $45^\circ$  comet impact.

#### 5.4.2.1 Density Contours

The density contours for the 45° oblique impact plume are presented as a function of time, 1, 5, 10, 15, and 20 s after the beginning of the impact, in Figure 5-18 to Figure 5-22. A consistent feature is noisier and slightly depleted density contours right above the point of impact in all three planes for times greater than five seconds after impact. This feature is not due any real physical process but is attributed to the spherical geometry of the DSMC domain. In the DSMC domain, the cells near the axis are smaller and each cell has on average only one or two molecules. Because of the poor statistics in that region of the flow, the noise in the number of molecules per cell is apparent when the molecular data are sampled to obtain the macroscopic properties, such as density. Even with our interpolation scheme, the contours remain noisy and appear depleted near the axis of symmetry of the domain for all quantities at all times.

The densest material crosses the interface early on. One second after the beginning of the impact, the water vapor plume is densest near the plane of symmetry of the impact. In addition, the densest material can be found near the interface (Figure 5-18) and the density decreases noticeably as the flow expands radially away from the interface. The peak density is  $\sim 0.42 \text{ kg/m}^3$  and is localized to a small region between  $X_{\beta=0^\circ}$  of 13 and 17 km and is 4 km thick radially away from the interface. Outside of that region, the density uniformly decreases radially away from the interface forming concentric contours, down to a low value of  $\sim 0.001 \text{ kg/m}^3$  furthest away from the interface. In the 45° intermediate plane (middle of Figure 5-18), an interesting feature can be observed. Early on, a widespread plume crossed the interface and then convected downstream to 28 km radially away from the point of impact, one second after impact. This region of the flow contains little material with a density of  $\sim 0.0005 \text{ kg/m}^3$ . Simultaneously, the plume near the interface originates at two separate locations with  $X_{\beta=45^\circ}$  limits of 1 to 9 km, and 12 to 18 km, respectively. The spray furthest from the point of impact has the highest density in the plane at  $0.08 \text{ kg/m}^3$ . In the plane perpendicular to the plane of symmetry (bottom of Figure 5-18), the plume is very small and at the interface the  $X_{\beta=90^\circ}$  limits of the plume range from 2 km to 6 km. In that plane, the plume only extends up to 5 km above the interface and the plume density is at most  $0.001 \text{ kg/m}^3$ .

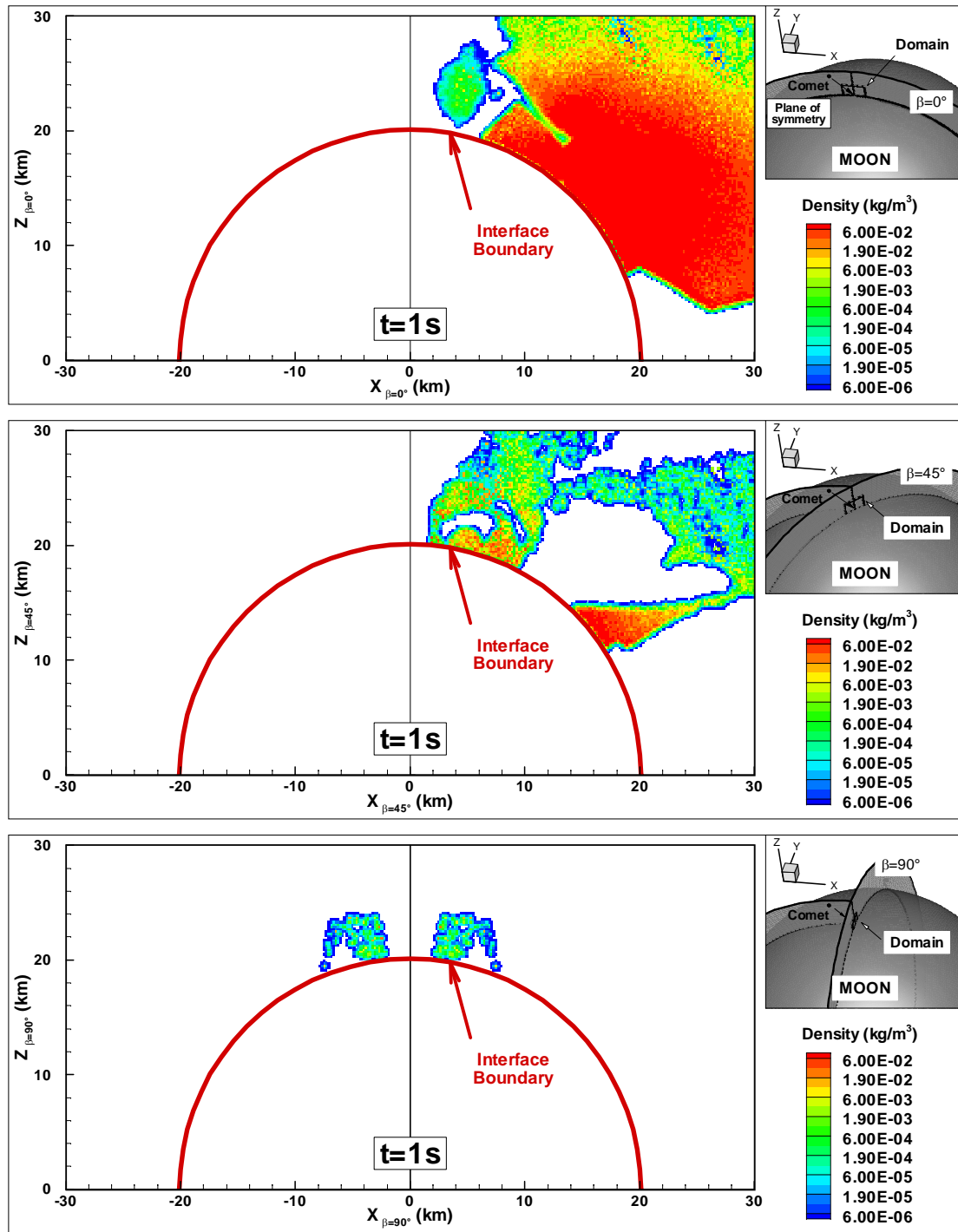


Figure 5-18 Near-field density contours 1s after impact in the plane of symmetry (top), 45° off the symmetry plane (middle) and perpendicular to the plane of symmetry (bottom).

Five seconds after the beginning of the impact (Figure 5-19), in the plane of symmetry of the impact, the densest material (up to  $0.08 \text{ kg/m}^3$ ) is found near the center of the plume between  $X_{\beta=0^\circ}$  of -5 km and 15 km filling the entire region downstream of the interface. A relatively low density region, 6 km downrange of the point of impact and extending from 4 km downstream of the interface to the top of the domain, can be observed within that dense region of the plume. This region is consistent with the location of four small patches of rock 3 km wide seen in the SOVA contours (Appendix D). In the DSMC simulations, the rock is not modeled so this now empty space is filled up by the water as the flow convects downstream producing the relatively low density region observed in our DSMC contours. The uprange boundary of the plume is located at  $X_{\beta=45^\circ}$  of -10 km and while dense material is crossing the interface uprange at that time, some low density material ( $\rho = 0.002 \text{ kg/m}^3$ ) is observed near the top of the domain 6 km above the interface. In the downrange section of the water vapor plume, the density drops 5 km downstream of the interface to around  $0.02 \text{ kg/m}^3$ . In the intermediate plane, the water vapor density contours are similar to the ones in the plane of symmetry of the impact with now a slightly greater maximum density of  $0.12 \text{ kg/m}^3$ . A low density region is observed 5 km downstream of the point of impact and that extends vertically to the limit of the domain which has again been attributed to the presence of rock at that location. In the plane perpendicular to the impact plane (bottom of Figure 5-19), the plume is mostly made of dense material, with a maximum density of  $0.08 \text{ kg/m}^3$ , within the  $X_{\beta=90^\circ}$  limits of -12 km and 12 km. Outside of that dense region, a small region of material can be observed just downstream of the interface with much lower densities around  $0.005 \text{ kg/m}^3$ .

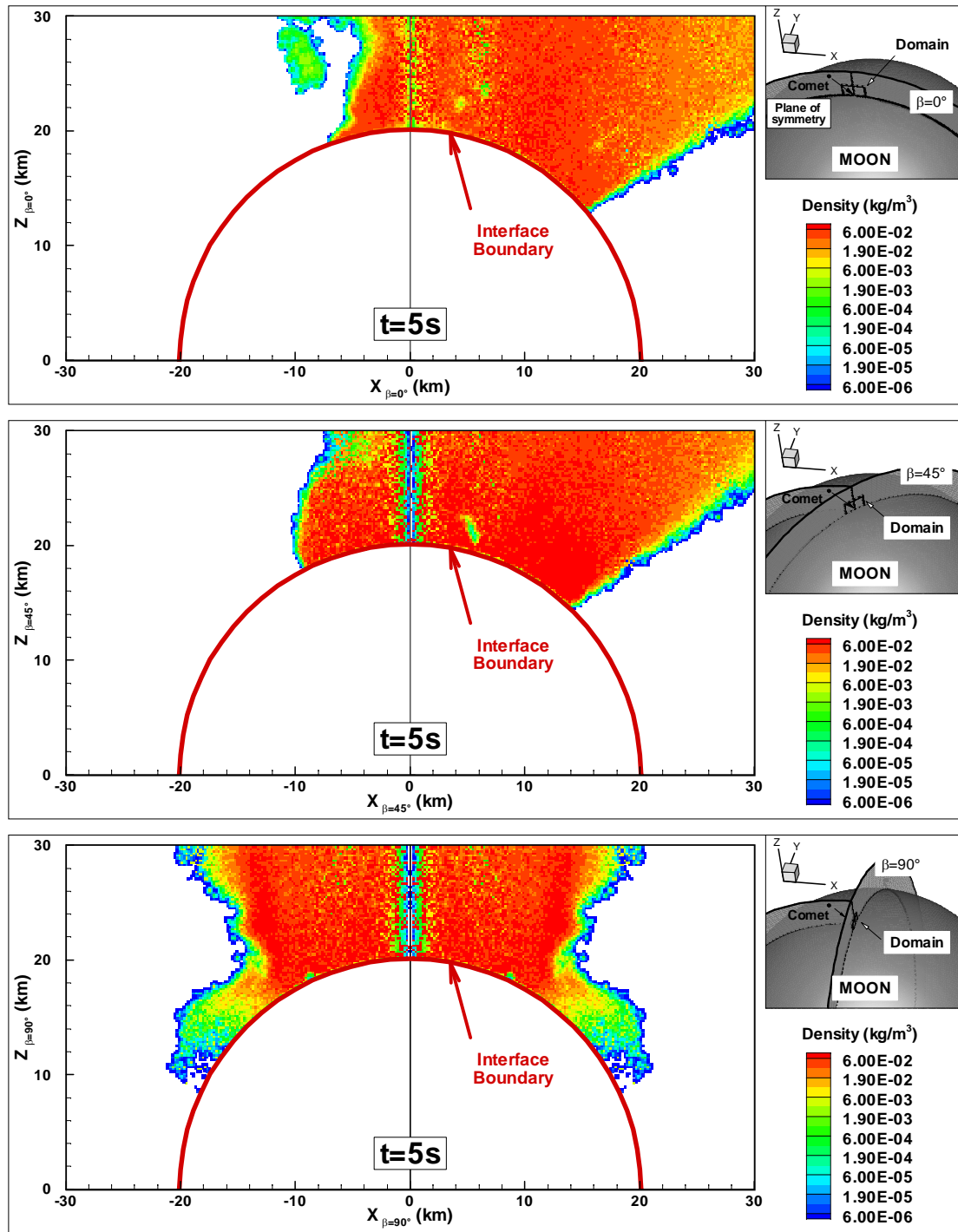


Figure 5-19 Near-field density contours 5 s after impact in the plane of symmetry (top), 45° off the symmetry plane (middle) and perpendicular to the plane of symmetry (bottom).

Later on, ten seconds after the beginning of the impact (top of Figure 5-20), the plume tends to become more symmetric across the point of impact but the average density continues to decrease with time. In the plane of symmetry of the impact, a dense region of material can be seen near the interface extending from 8 km uprange of the point of impact to 12 km downrange. This region is between 4 and 10 km thick and is thickest at  $X_{\beta=0^\circ} = 10$  km. The high density region is associated with the rise of rocky material from the bottom of the expanding crater; material that will later form the central peak of the crater (Appendix D). Because the rocky material is pushing water vapor out of its way (Figure 5-10), the water density ( $\sim 0.08 \text{ kg/m}^3$ ) in the region above the point of impact is noticeably larger than the density of the surrounding material, and is on the order of the peak density observed near the interface 5 s after impact. Surrounding the high density part of the plume, a mid-range region can be observed with densities greater than  $0.01 \text{ kg/m}^3$  with the exception of a small region 4 km downrange of the point of impact attributed to the presence of rock in the SOVA data (Appendix D). Also, the downstream part of the downrange plume has a relatively lower density than the uprange plume at the same radial distance. Finally, a separate spray of material, 2 km thick, is observed at the interface extending from  $X_{\beta=0^\circ} = -18$  km to  $-14$  km. In the  $45^\circ$  intermediate plane (middle of Figure 5-20), the same high density region (up to  $0.09 \text{ kg/m}^3$ ) can be observed above the point of impact due to the rise of the central peak rocky material. The region extends from  $X_{\beta=45^\circ} = -7$  km to 12 km, is between 4 and 6 km thick. Ten seconds after impact, in the  $45^\circ$  intermediate plane, a 6 km- thick low density spray of water vapor, with an average density of  $0.0005 \text{ kg/m}^3$  is observed downstream the interface uprange of the main plume. Outside of that burst, the plume shapes resembles an inverted cone in that plane. The fullest plume is observed in the plane perpendicular to the plane of symmetry (bottom of Figure 5-20) with material leaving the interface just 2 km to 4 km above the surface. A dense region is again observed above the point of impact, extending up to 11 km away from the axis of symmetry of the DSMC domain. Its thickness reaches 6 km right above the point of impact before decreasing to 3 km near its edges. An intermediate region with densities around  $0.02 \text{ kg/m}^3$  is seen above the high density region, with the exception of a low density region 6 km away from the axis of the domain where rock should be present. Outside of the intermediate region, the plume is more rarefied with densities in that region lower than  $0.001 \text{ kg/m}^3$ .

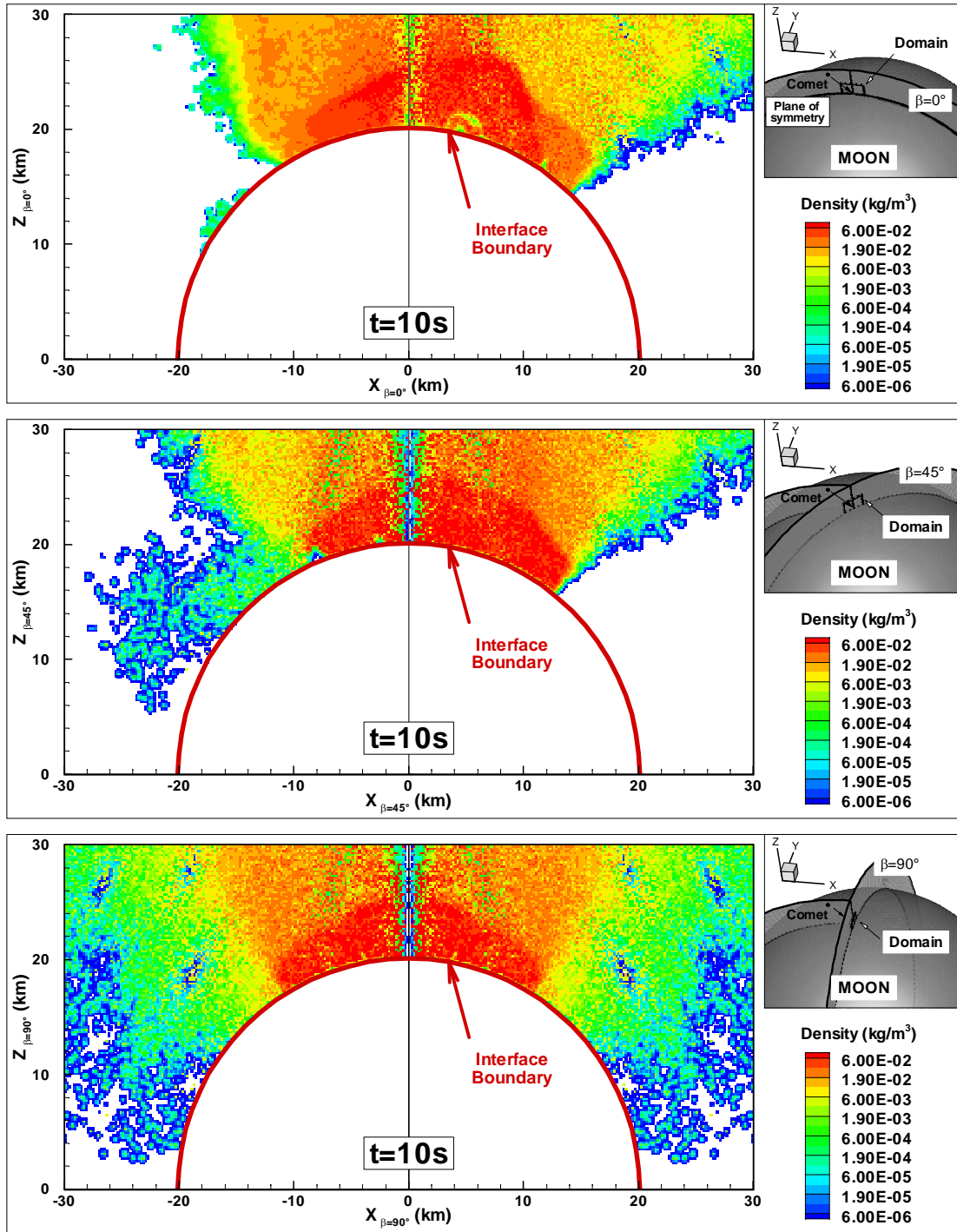


Figure 5-20 Near-field density contours 10 s after impact in the plane of symmetry (top), 45° off the symmetry plane (middle) and perpendicular to the plane of symmetry (bottom).



Fifteen seconds after impact, the rocky central peak material has already crossed the interface producing a hole in the water vapor contours above the point of impact. In the plane of impact (top of Figure 5-21), above the interface, the rocky material takes a triangular shape, with a 12 km base and a 6 km height, directly above the point of impact. At the interface, the water vapor plume is more widespread on the uprange side of the point of impact but the high density region of the plume is only localized to a small region 4 km-wide in that part of the plume. Downstream of the central peak material and uprange of the point of impact, the water vapor is being pushed out of the way by the rocky central peak material with intermediate values for density of at least  $0.01 \text{ kg/m}^3$ . Downrange of the point of impact, the dense plume covers most of the interface but the downrange peak density ( $0.05 \text{ kg/m}^3$ ) is slightly lower than the uprange peak density ( $0.08 \text{ kg/m}^3$ ). Also, the density downstream of the central peak material is noticeably lower downrange of the point of impact than it was uprange. Intermediate values for density are observed directly above the dense material crossing the interface from  $X_{\beta = 0^\circ} = 6 \text{ km}$  to  $14 \text{ km}$ . The plume in the  $45^\circ$  intermediate plane (middle of Figure 5-21) exhibits an even more pronounced unbalance between the uprange and downrange plumes and a much smaller footprint at the interface than the plume in the plane of symmetry of the impact. The downrange plume is limited to a 5 km-wide spray with a maximum density of  $0.06 \text{ kg/m}^3$ . Uprange, high density water vapor is limited at the interface to small region a few hundred meters wide with a density of  $0.01 \text{ kg/m}^3$  while the rest of the plume has an average density of  $0.001 \text{ kg/m}^3$ . The gap formed in the center of the plume is again triangular in shape with a base width of 8 km (from  $X_{\beta = 45^\circ} = -8$  to  $10 \text{ km}$ ) and a height of 8 km above the point of impact. In the plane perpendicular to the impact plane (bottom of Figure 5-21), the surface area covered by the rocky material crossing the interface is similar to that covered in the  $45^\circ$  intermediate plane but the shape of the hole is more square. The gap at the interface extends up to 9 km away from the axis of symmetry and the height of the plume increases from 6 km at the edge of the water plume to 10 km above the point of impact. Overall, the plume in that plane remains fuller than in the other two planes. Also, the high density region (with  $\rho = 0.07 \text{ kg/m}^3$ ) is limited to a few hundred meters wide dense spray, 11 km off the axis. An intermediate region (with  $\rho > 0.02 \text{ kg/m}^3$ ), 4 to 6 km wide, is observed above the high density region while the remainder of the plume has a relatively low density smaller than  $0.005 \text{ kg/m}^3$ .

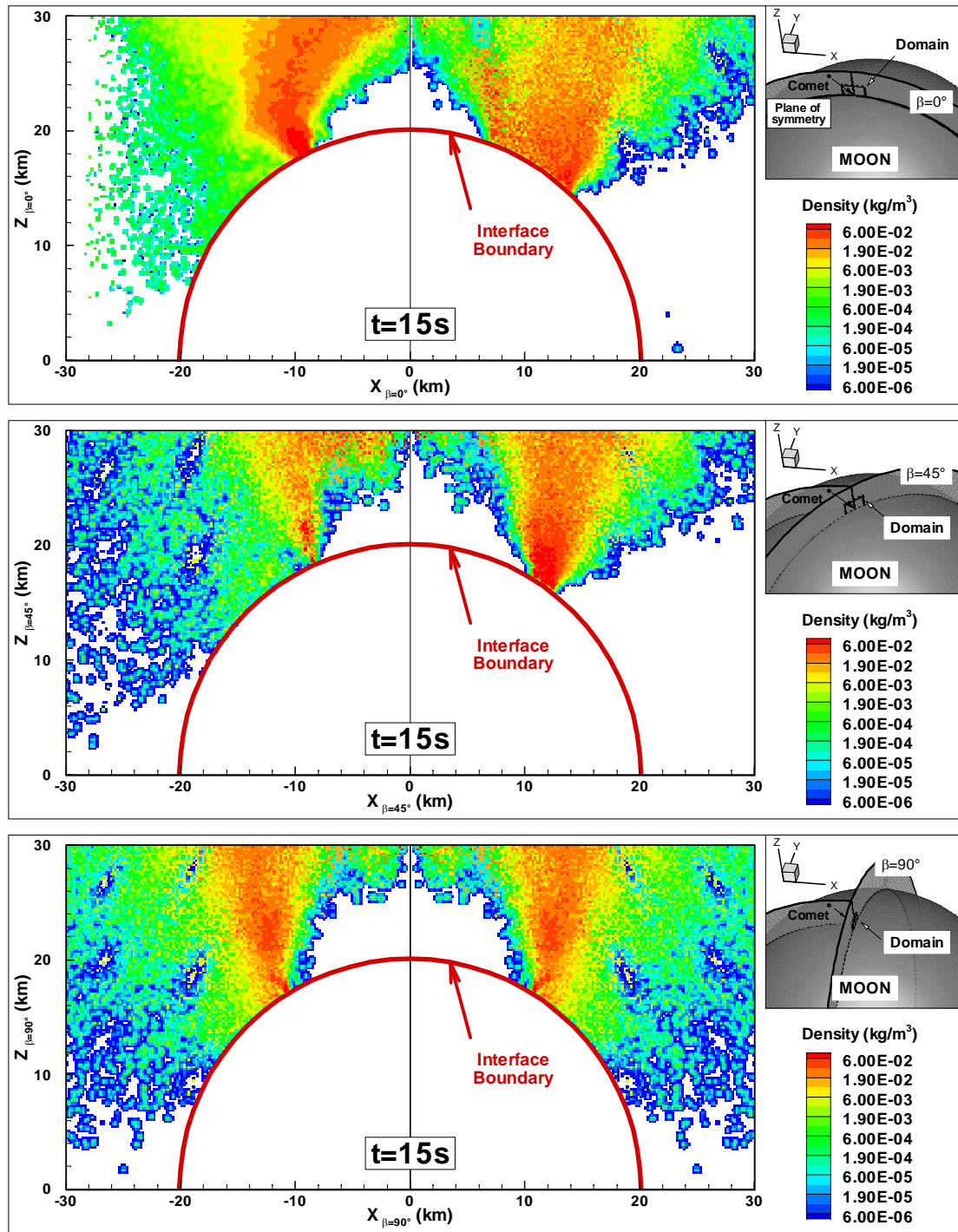


Figure 5-21 Near-field density contours 15 s after impact in the plane of symmetry (top), 45° off the symmetry plane (middle) and perpendicular to the plane of symmetry (bottom).

Twenty seconds after impact, the rocky central peak material continues to rise above the interface expanding the hole in the water vapor contours above the point of impact. In the plane of impact (top of Figure 5-22), the central peak rocky material at the interface extends from  $X_{\beta=0^\circ} = -9$  km to 10 km and nearly no material is present directly above the point of impact in the near-field. While still more widespread at the interface, the uprange vapor plume is noticeably less dense than the downrange plume with peak densities of  $0.01 \text{ kg/m}^3$  and  $0.08 \text{ kg/m}^3$ , respectively. In addition, most of the downrange water vapor plume is made of intermediate density material ( $> 0.01 \text{ kg/m}^3$ ) while the uprange plume is made of low density material ( $0.001 \text{ kg/m}^3$ ). In both uprange and downrange plumes, the least dense material is found near the edges of the plume at the boundary with rock. The amount of water vapor crossing the interface in the  $45^\circ$  intermediate plane (middle of Figure 5-22) decreases noticeably from fifteen seconds to twenty seconds after impact. The footprint of the water vapor plume is similar but the high density regions within the plume are even smaller than before. The central peak rocky material extends from  $X_{\beta=45^\circ} = -9$  km to 12 km at the interface and from  $X_{\beta=45^\circ} = -6$  km to 8 km, 30 km above the point of impact. The high density parts of both downrange and uprange plumes are limited to a few hundred meters wide sprays with peak densities of  $0.05 \text{ kg/m}^3$  and  $0.01 \text{ kg/m}^3$ , respectively. Also, the uprange spray only extends up to 5 km downstream of the interface and most of the uprange water vapor plume has densities less than  $0.005 \text{ kg/m}^3$ . In the plane perpendicular to the impact plane (bottom of Figure 5-22), the surface area covered by the rocky material crossing the interface is greater than that covered in the other two planes up to 11 km away from the axis of symmetry. Thirty kilometers downstream of the point of impact, the rocky material extends up to 7 km away from the axis of symmetry. The high density material ( $> 0.01 \text{ kg/m}^3$ ) is localized to a 100 m-wide spray at  $X_{\beta=90^\circ} = 11$  km that is only present up to 6 km downstream of the interface. The remainder of the plume has densities around  $0.005 \text{ kg/m}^3$  inside the plume and around  $0.0005 \text{ kg/m}^3$  near the edges of the plume.

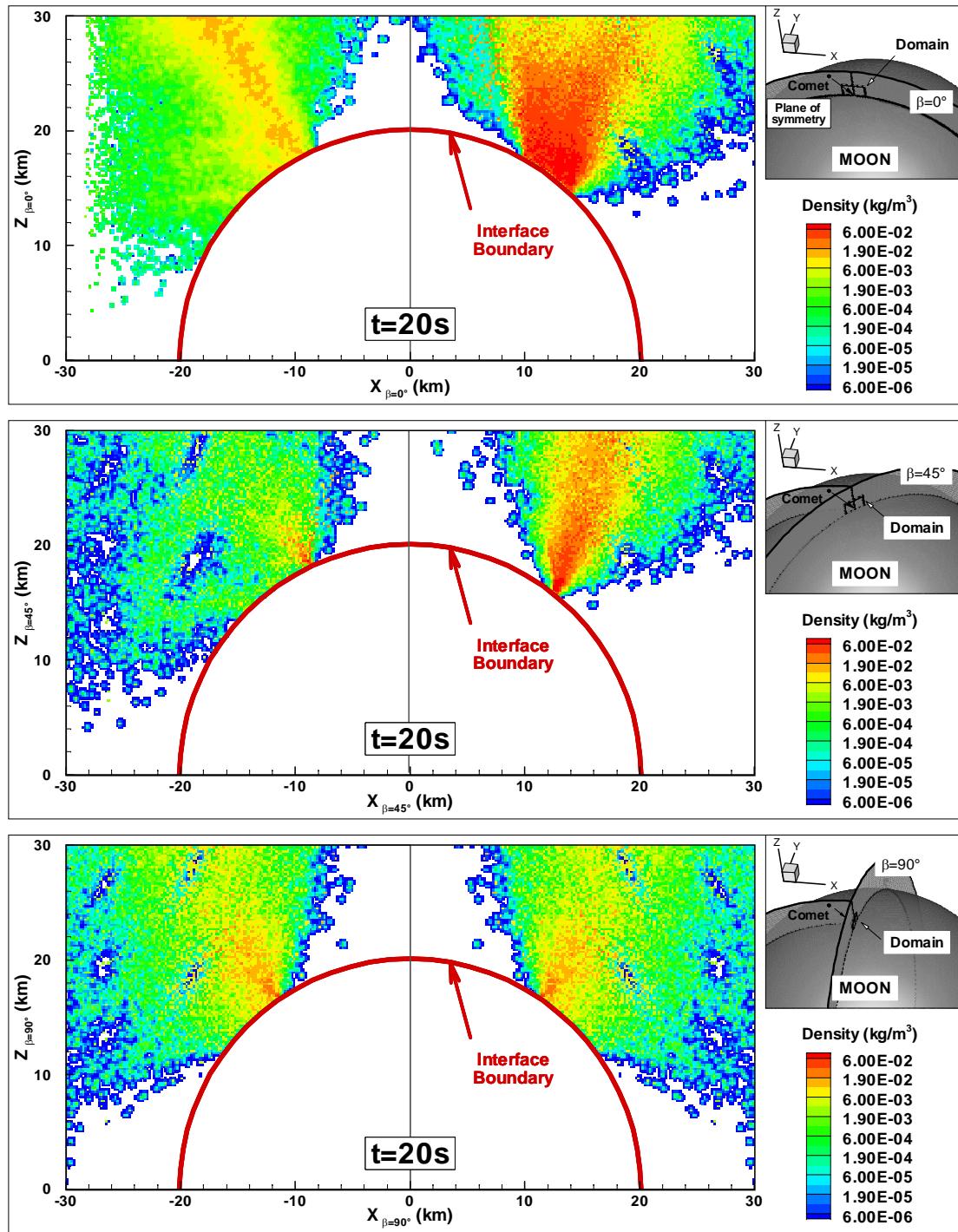


Figure 5-22 Near-field density contours 20 s after impact in the plane of symmetry (top),  $45^\circ$  off the symmetry plane (middle) and perpendicular to the plane of symmetry (bottom).

Several trends can be observed in the DSMC density contours within the water vapor plume downstream of the interface with the SOVA hydrocode. Overall, the density of the water vapor is highest in the early phases of the expansion with densities as high as  $0.4 \text{ kg/m}^3$  near the interface one second after impact. As the water vapor expands within the DSMC domain, the density decreases with radial distance away from the point of impact. The average density also continuously decreases with time until the central peak material reaches the interface (between 10 and 11 s after impact). At that time, a relatively high density region ( $\rho = 0.08 \text{ kg/m}^3$ ) can be observed directly above the point of impact. Once the central peak rocky material reaches the interface, the plume is separated into an uprange and downrange plume with very localized dense material crossing the interface at these times (from 11 s to 21 s after impact). At most times, several regions have been identified as containing rock (Appendix D). These regions are slowly filled up with water vapor as they convect downstream but they are still recognizable due to their relatively lower density compared to their surroundings. During the late phases of the expansion, the plume consists mostly of low density material with densities around  $0.005 \text{ kg/m}^3$  near the interface.

#### 5.4.2.2 Temperature Contours

The total, translational, and rotational temperature contours are presented in all three 2D slices 1, 5, 10, 15, and 20 s after the beginning of the impact (Figure 5-23 to Figure 5-40). The vibrational temperatures will only be shown one second after the beginning of the impact since the total temperature decreases rapidly with time to temperatures ( $< 500$  K five seconds after impact) too low to resolve the vibrational temperatures in the present simulations. The total temperature was obtained from the average of the translational, rotational and vibrational temperatures. Note that in all the translational temperature contours, cells with a translational temperature or density equal to zero have been blanked out. In the low density regions of the plume as well as near the axis of symmetry of the DSMC domain, the number of molecules per cell may be less than two which provides a translational temperature of zero. The blanking out of these cells generally reduces the overall footprint of the water vapor plume. Note that due to the rapid cooling of the water vapor plume with time, the scale of the color contours one second after impact (from  $T = 0$  to 1600 K) is different than the scale used at all later times (from  $T = 0$  to 400 K). Finally, similar to the translational temperature contours, for each vibrational mode, the cells with zero vibrational temperature have been blanked out in the vibrational temperature contours

In the plane of impact, one second after the beginning of the impact, the maximum total temperature,  $\sim 1700$  K, is localized to a small region  $3 \text{ km} \times 6 \text{ km}$  located 2 km downstream of the interface at  $X_{\beta=0^\circ} = 8 \text{ km}$  (top of Figure 5-23). A low temperature region can be observed further downrange of the point of impact starting at  $X_{\beta=0^\circ} = 12 \text{ km}$  with temperatures in the 400 to 450 K range. Contrary to a steady state expansion, the temperature does not always decrease with distance from the point of impact in the present vapor plume. Nearly 10 km downstream of the low temperature region there is a higher temperature region in the 700 to 800 K range. The translational and rotational temperature contours resemble the total temperature contours except for a small region near the uprange edge of the vapor plume (Figure 5-24 and Figure 5-25). In that region of the flow, the rotational temperature is very high while the translational temperature is very low. These discrepancies have been attributed to a low number of molecules per cell in that region. The low number of molecules means that only a few collisions between molecules will be computed at each timestep. As the water vapor expands into the vacuum, the translational temperature decreases rapidly but, because of the low number of collisions, energy transfer

between the translational and rotational modes does not happen. Therefore, downstream of the interface, in the regions of the flow with less than two molecules per cell, the rotational temperature remains hot while the translational temperature cools.

In the intermediate plane, three different regions can be observed with three distinct temperature profiles (middle of Figure 5-23). The region of the plume downstream of the interface ( $Z_{\beta = 45^\circ} > 16$  km and  $X_{\beta = 45^\circ} > 14$  km) has the lowest total temperatures in the 100 to 200 K range. The top part of that region however is much hotter at ~500 K. Near the interface the jet furthest away from the axis of symmetry of the DSMC domain has a near uniform temperature around 350 to 400 K. The jet closest to the axis of symmetry has higher temperatures of at least 800 K. Overall, the temperature in that plane is lower than in the plane of symmetry of the impact. This may mean that the material moving in that plane has been shocked to lower pressure than the material in the plane of symmetry. The translational and rotational temperatures agree within the uprange jet near the interface as well as within the downrange jet but the contours are greatly different in the outer part of the uprange jet and in the downstream regions (middle of Figure 5-24 and Figure 5-25). The rotational temperatures within the uprange jet downstream of the interface reach values as high as 1200 K. The rotational temperature in the region of the plume far downstream is very hot at its top edge (~1000 K) but decreases rapidly to lower values below that region near 150 K. In both these regions, the translational temperature is very cold around 200 K. The discrepancies between the high rotational and low translational temperatures may be due to the combination of two factors: the very high flow velocities and the overly large timestep and cell sizes.

In the plane perpendicular to the plane of impact, the total temperature contours are very noisy with high temperatures near 1000 K. These regions are associated with very high rotational temperatures of ~3000 K. On the contrary, the translational temperature is equal to zero almost everywhere (bottom of Figure 5-23 to Figure 5-25).

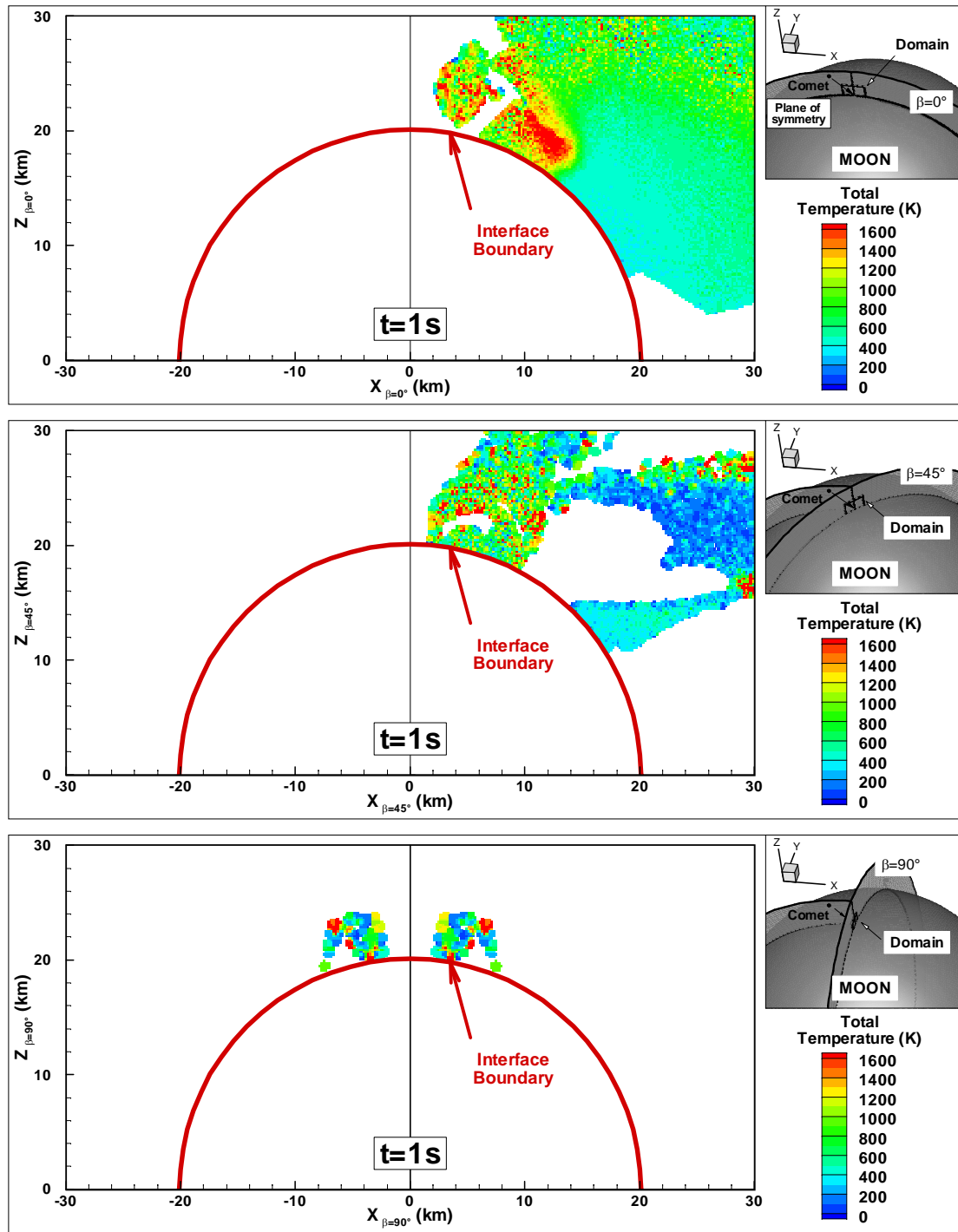


Figure 5-23 Near-field total temperature contours 1 s after impact in the plane of symmetry (top), 45° off the symmetry plane (middle) and perpendicular to the plane of symmetry (bottom).



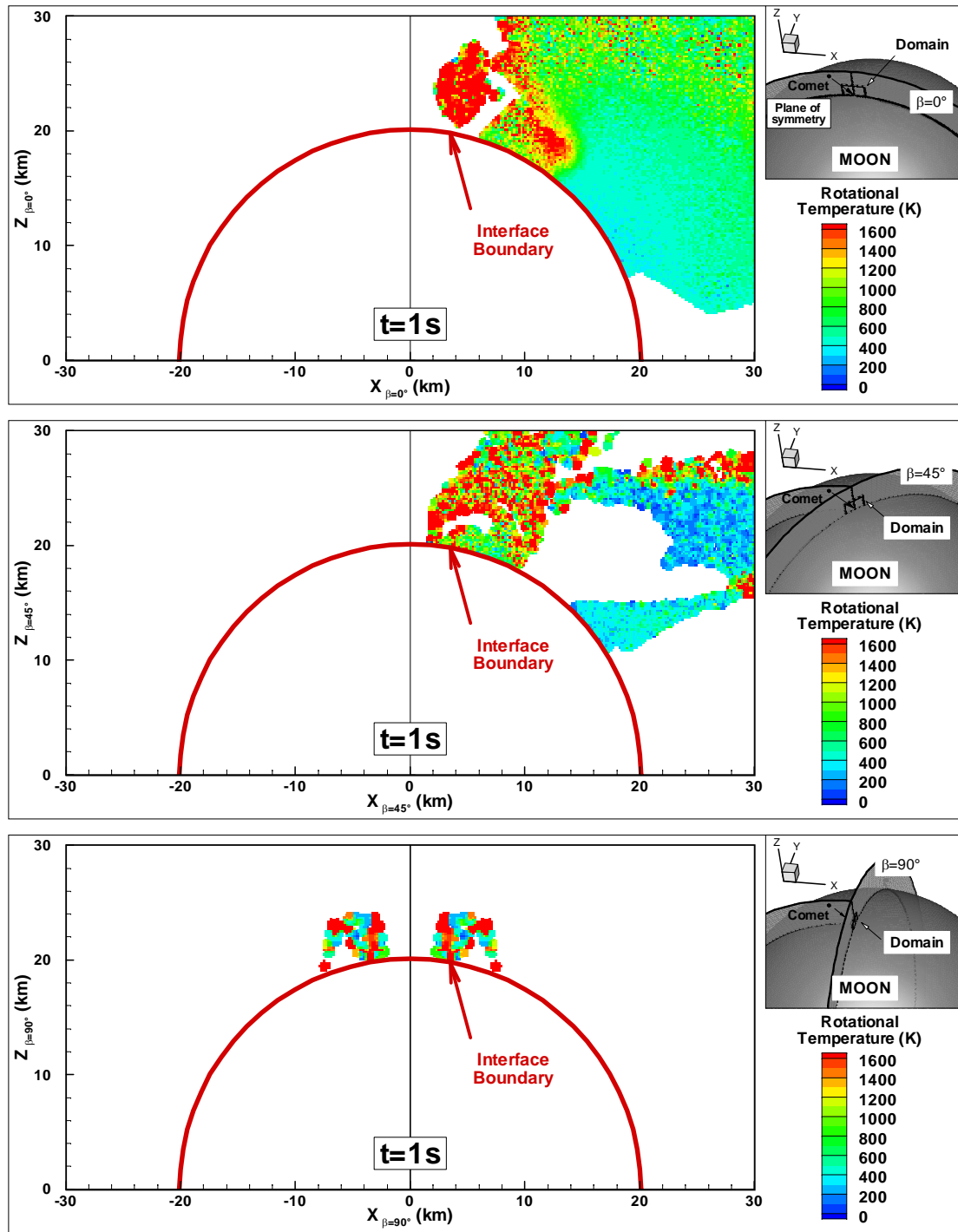


Figure 5-24 Near-field rotational temperature contours 1 s after impact in the plane of symmetry (top),  $45^\circ$  off the symmetry plane (middle) and perpendicular to the plane of symmetry (bottom).

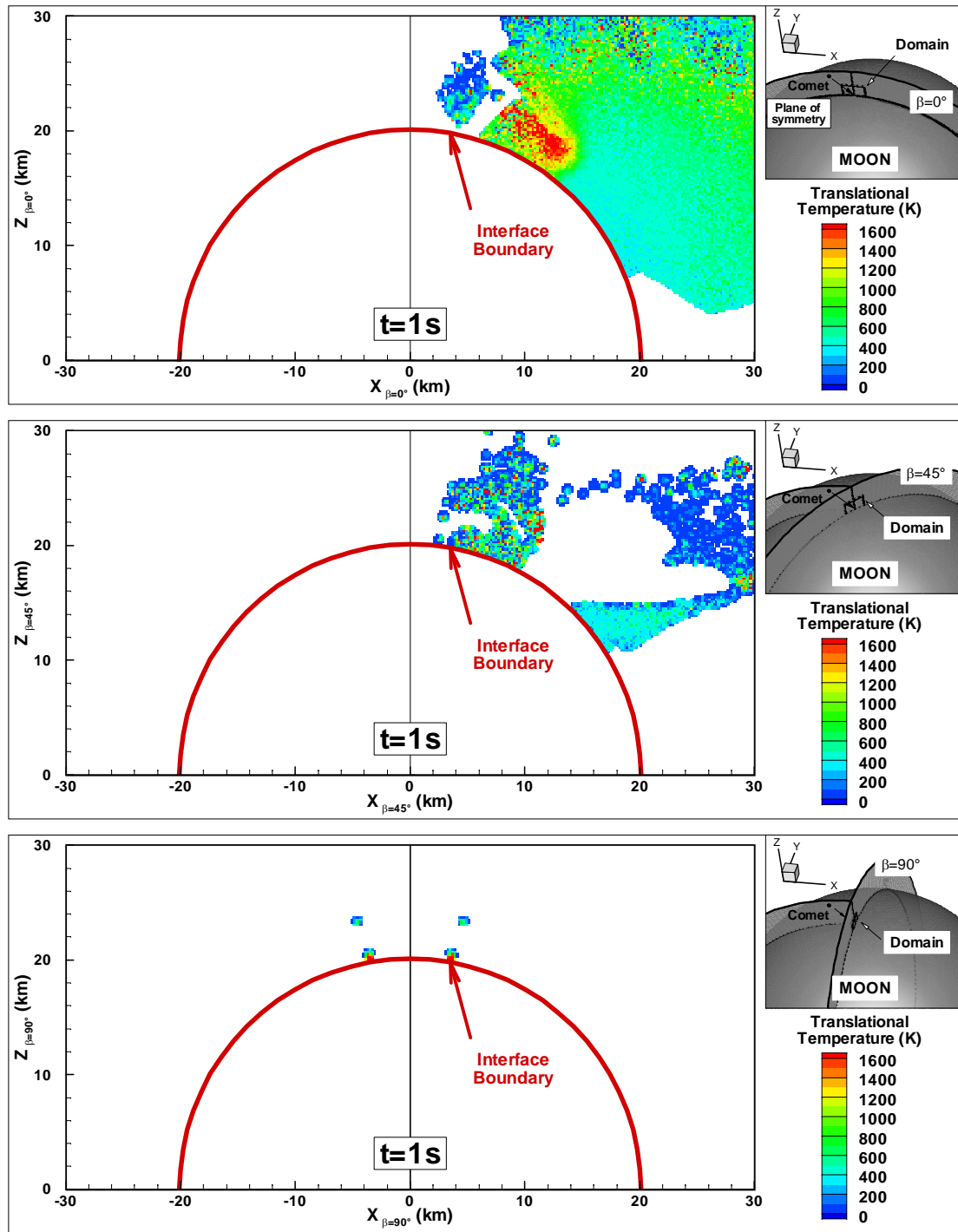


Figure 5-25 Near-field translational temperature contours 1 s after impact in the plane of symmetry (top), 45° off the symmetry plane (middle) and perpendicular to the plane of symmetry (bottom).

The vibrational temperatures (Figure 5-26, Figure 5-27, and Figure 5-28) are not resolved in the present simulations because the temperatures ( $< 2000$  K in the hottest regions and  $< 1000$  K within most of the plume) are low compared to the characteristic vibrational temperatures of water ( $\vartheta_1 = 5261$  K,  $\vartheta_2 = 2438$  K, and  $\vartheta_3 = 5404$  K). In thermal equilibrium at these low temperatures, many more molecules per cell are required than are presently simulated in order to have several in an excited state.

One second after impact, in the plane of symmetry of the impact (top of Figure 5-26, Figure 5-27, and Figure 5-28), the  $v_2$ -vibrational mode has the lowest characteristic temperature which provided temperature contours that more closely resemble the total temperature contours. The high  $v_2$ -vibrational temperature region is localized to a  $2 \text{ km} \times 2 \text{ km}$  region 12 km off axis. Regions of the plume with total temperatures near 1000 K have very noisy  $v_2$ -vibrational temperature contours with only a few cells with non-zero temperatures. Only the hottest part of the plume can be observed in the  $v_1$ - and  $v_3$ -vibrational temperature contours due to their high characteristic temperatures. Even in these regions, the vibrational temperatures underestimate the total temperature by a few hundred Kelvins. Note that because of the poor resolution for the vibrational temperature the total temperature obtained in our calculations actually underestimates the actual total temperature of the flow. In the  $45^\circ$  intermediate plane, all three vibrational temperatures are equal to zero within most of the plume (middle of Figure 5-26, Figure 5-27, and Figure 5-28). A small region in the jet nearest to the point of impact has some  $v_2$ -vibrational temperatures  $\sim 400$  K. In the plane perpendicular to the impact plane, the vibrational temperatures are equal to zero almost everywhere (bottom of Figure 5-26, Figure 5-27, and Figure 5-28).

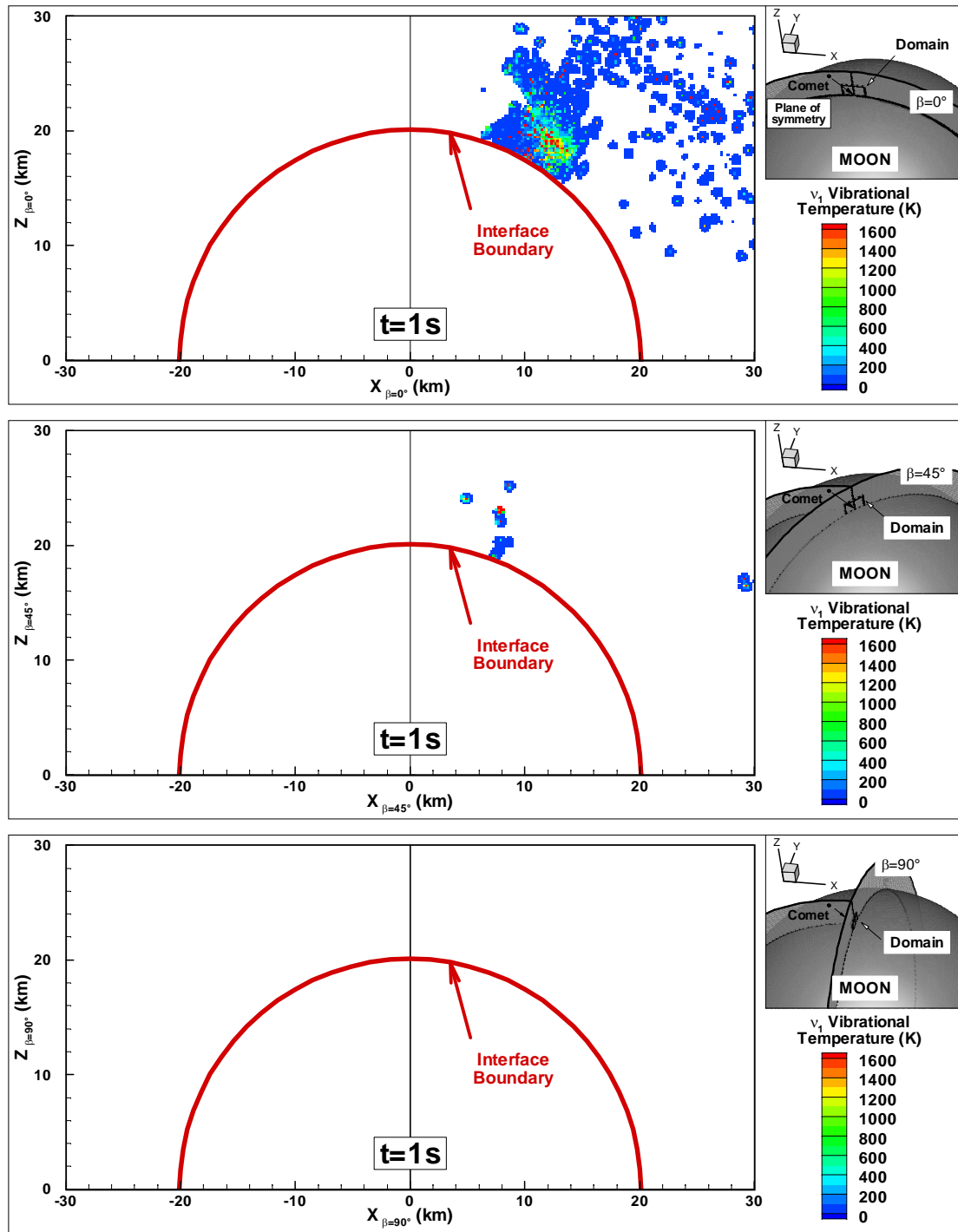


Figure 5-26 Near-field  $v_1$ -vibrational temperature contours 1 s after impact in the plane of symmetry (top),  $45^\circ$  off the symmetry plane (middle) and perpendicular to the plane of symmetry (bottom).

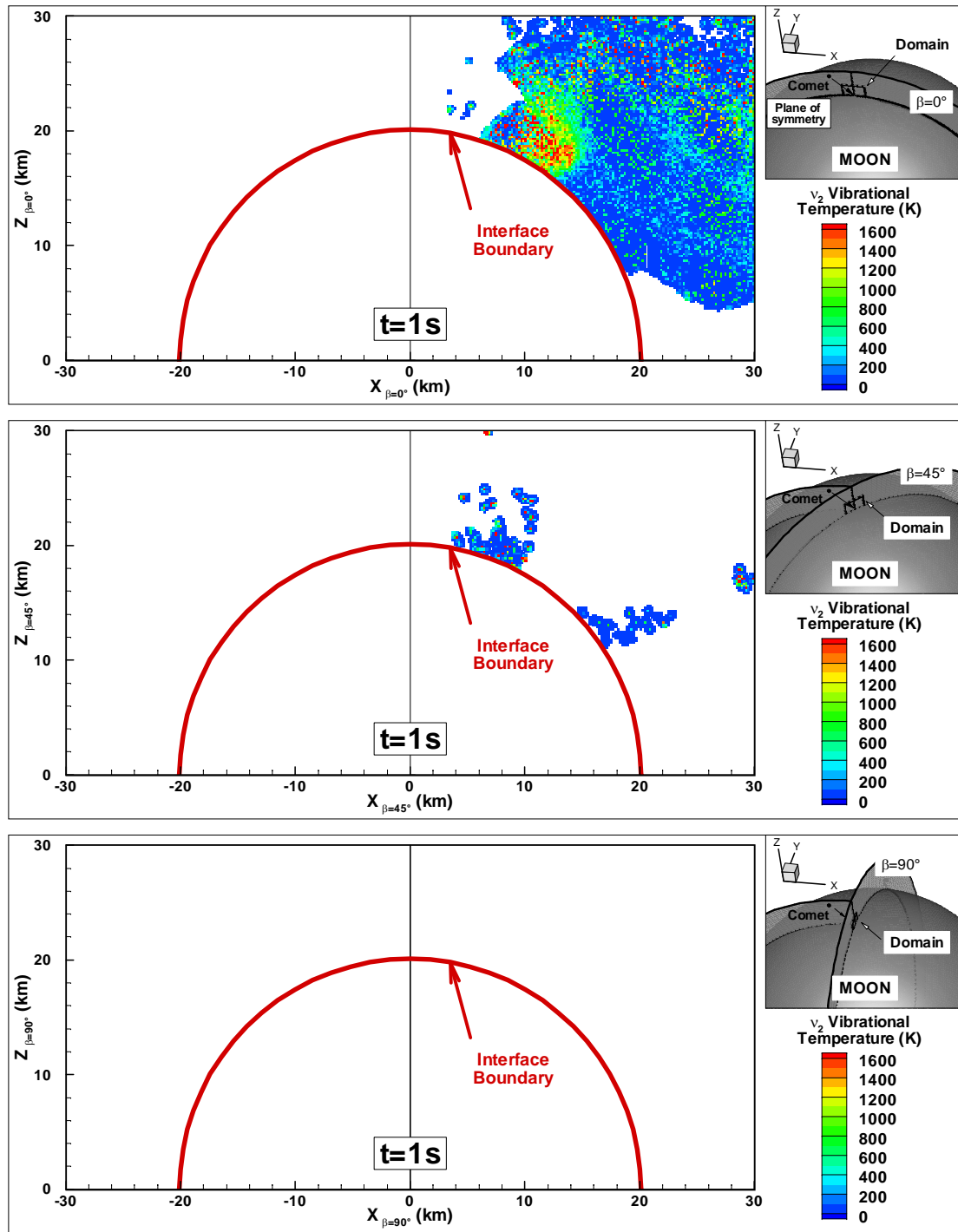


Figure 5-27 Near-field  $v_2$ -vibrational temperature contours 1 s after impact in the plane of symmetry (top),  $45^\circ$  off the symmetry plane (middle) and perpendicular to the plane of symmetry (bottom).

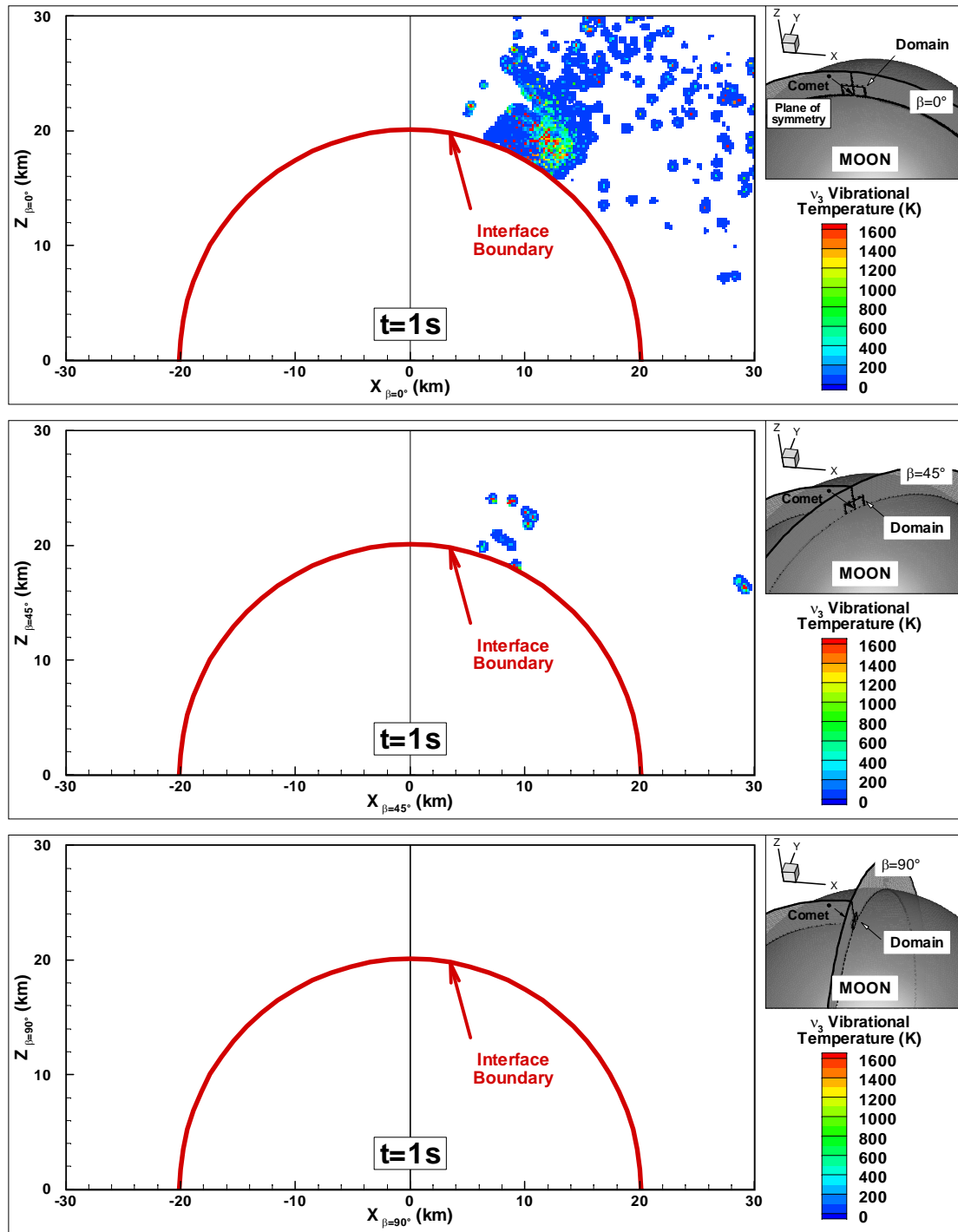


Figure 5-28 Near-field  $v_3$ -vibrational temperature contours 1 s after impact in the plane of symmetry (top),  $45^\circ$  off the symmetry plane (middle) and perpendicular to the plane of symmetry (bottom).

Five seconds after the beginning of the impact, the total temperature contours have changed noticeably. Instead of small localized high and low temperature regions, the total temperature in the plane of symmetry of the impact is nearly uniform around 300 K (top of Figure 5-29). The rotational and translational temperatures are in good agreement except in the region above the point of impact along the symmetry axis (top of Figure 5-30 and Figure 5-31). In that part of the plume, the rotational temperature is as high as 400 K and the translational temperature is as low as 50 K. The non-equilibrium between the two modes is again attributed to the low number of molecules per cell in that region of the plume. This translates into an artificially low collision rate and relative freezing of the internal modes of the molecules. Therefore, as the flow expands the translational temperature starts to decrease but the rotational temperature remains nearly constant. The same problem is observed in the intermediate plane and in the plane perpendicular to the plane of symmetry of the impact. In the intermediate plane (middle of Figure 5-29), the contours are not as uniform as in the plane of impact with slightly higher temperatures near the interface ( $\sim 350$  K) than further downstream ( $\sim 250$  K). Similarly to the results in the plane of symmetry of the impact, the rotational and translational temperature contours agree well with the total temperature contours outside of the region near the axis of symmetry of the DSMC domain (middle of Figure 5-30 and Figure 5-31). In the plane perpendicular to the impact plane (bottom of Figure 5-29), the temperature is not uniform but varies from relatively low total temperatures near the axis ( $\sim 200$  K due to an artificially low translational temperature) to much higher temperatures near the outer edge of the main plume ( $\sim 350$ - $400$  K). In the small burst of material observed on the outer edges of the main plume, the total temperature is also relatively small,  $\sim 150$  K. The total temperature is also smaller downstream of the interface at  $\sim 300$  K. In the perpendicular plane, the rotational contours are nearly uniform within the entire domain between 300 and 350 K (bottom of Figure 5-30). The translational contours, however, vary more with low temperatures near the axis of symmetry ( $\sim 100$  K) and in the burst ( $\sim 100$  K) to peak temperatures of more than 350 K in other regions (bottom of Figure 5-31). The temperatures for all three vibrational modes are equal to zero everywhere which was expected given the low temperatures within the plume ( $< 500$  K).

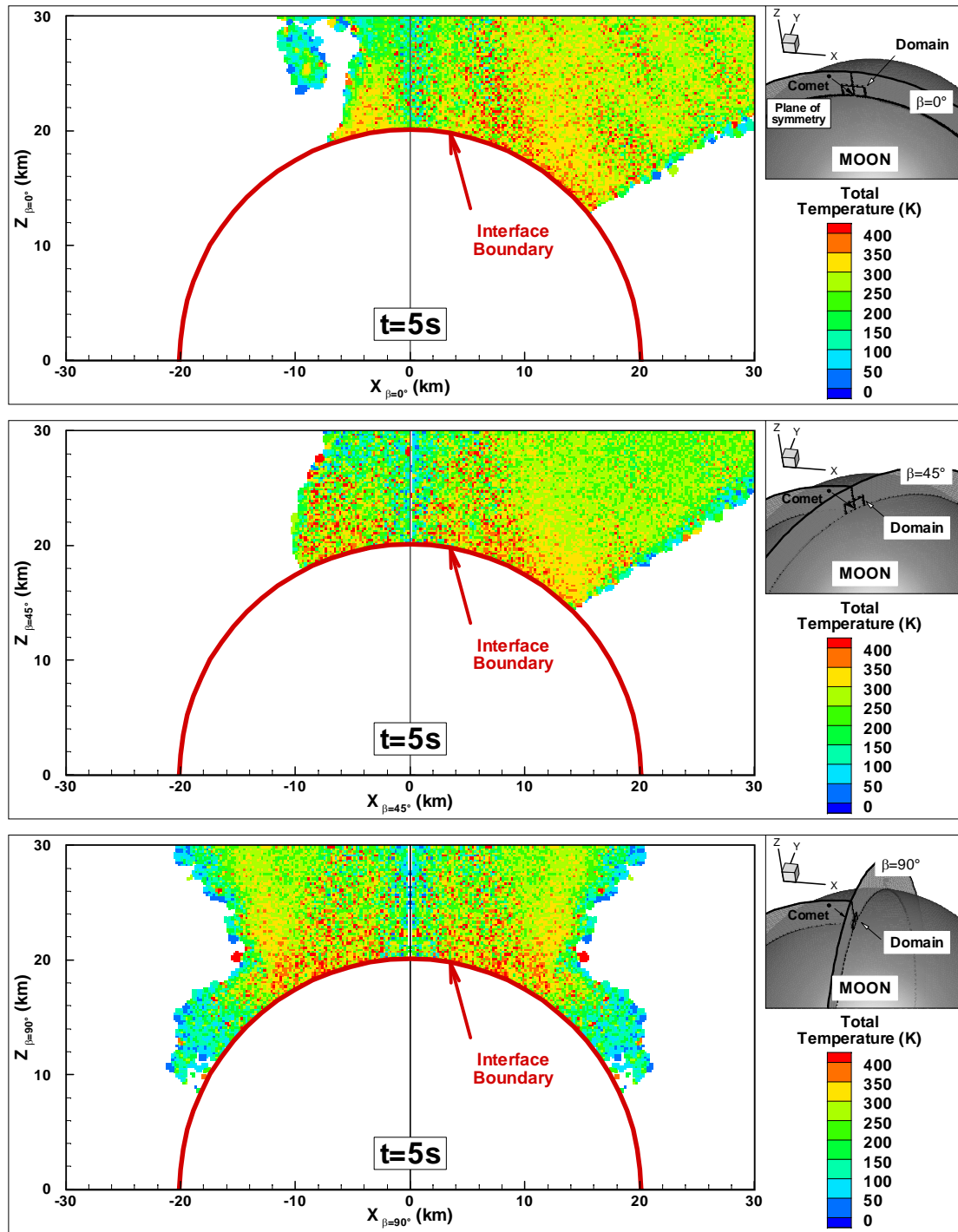


Figure 5-29 Near-field total temperature contours 5 s after impact in the plane of symmetry (top),  $45^\circ$  off the symmetry plane (middle) and perpendicular to the plane of symmetry (bottom).



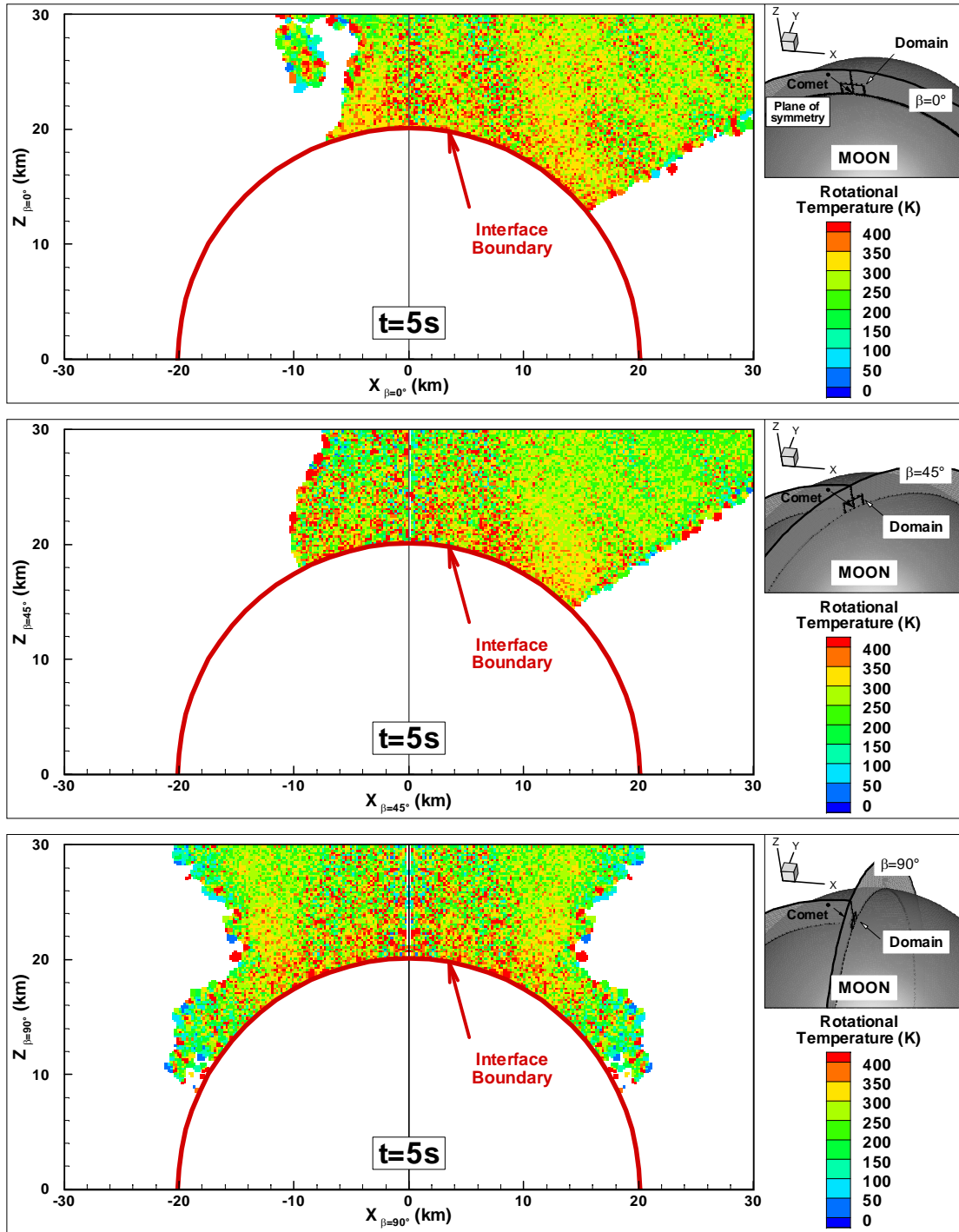


Figure 5-30 Near-field rotational temperature contours 5 s after impact in the plane of symmetry (top),  $45^\circ$  off the symmetry plane (middle) and perpendicular to the plane of symmetry (bottom).

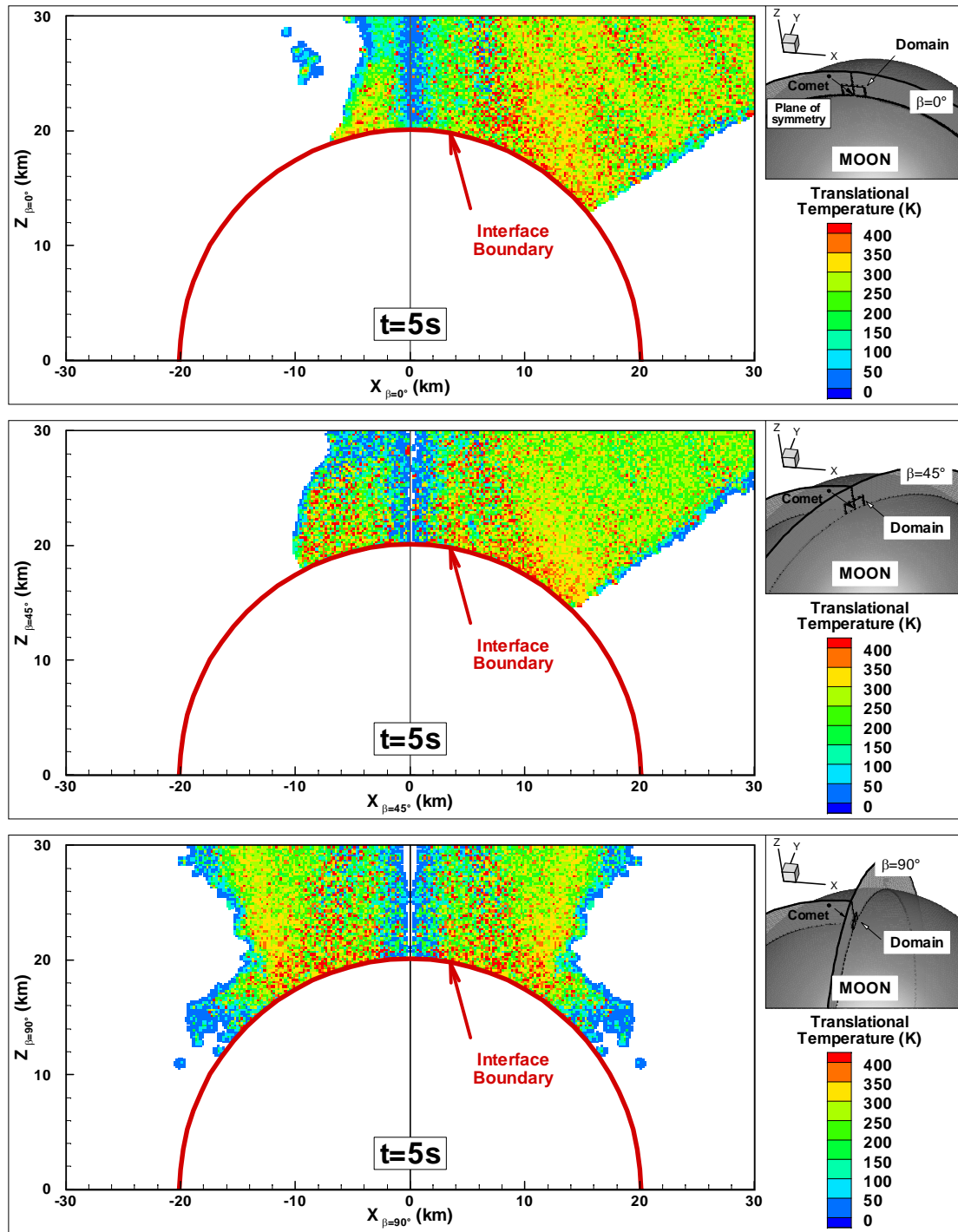


Figure 5-31 Near-field translational temperature contours 5 s after impact in the plane of symmetry (top), 45° off the symmetry plane (middle) and perpendicular to the plane of symmetry (bottom).

Ten seconds after impact, the temperature inside the plume is no longer uniform: the high density region observed in the density contours (Figure 5-20) is also associated with relatively higher total temperatures (Figure 5-32). In the plane of symmetry of the impact (top of Figure 5-32), away from the interface the temperature is  $\sim 250$  K but near the interface that temperature rises to more than 450 K. The rotational temperature contours are similar but the temperature in the region far downstream of the interface is generally hotter ( $\sim 300$  K) (top of Figure 5-33). The translational temperature is generally lower with temperatures around 200 K downrange and downstream of the interface (top of Figure 5-34). In the intermediate plane, a relatively higher temperature region ( $\sim 350$  K) is again observed in association with the high density region observed in Figure 5-20 (middle of Figure 5-32). The temperature away from the interface is  $\sim 200$  K. The translational temperature varies from 350 K near the interface to 150 K away (middle of Figure 5-34). The rotational temperature is more uniform and the high temperature region is not as well defined but the rotational temperature still decreases from  $\sim 350$  K on average near the interface to  $\sim 250$  K downstream of it (middle of Figure 5-33). In addition to the main plume, a recent burst of material extends the plume further uprange with total and rotational temperatures around 150 K and 200 K, respectively. That region is almost not present in the translational contours where cells with a zero translational temperature have been blanked out. In the plane perpendicular to the impact plane, a noticeable hotter region extending up to 10 km away from the axis of symmetry can be observed in the total temperature contours consistent with the high density region in that plane (Figure 5-20 and Figure 5-32). The temperature within that region is  $\sim 350$  K as compared to the lower temperatures in the 150 K to 200 K range away from the interface. Similar trends are observed in the translational and rotational contours (bottom of Figure 5-33 and Figure 5-34) with slightly higher rotational temperatures especially in the low density regions of the plume (bottom of Figure 5-20). Once again the vibrational temperatures are equal to zero in most of the domain.

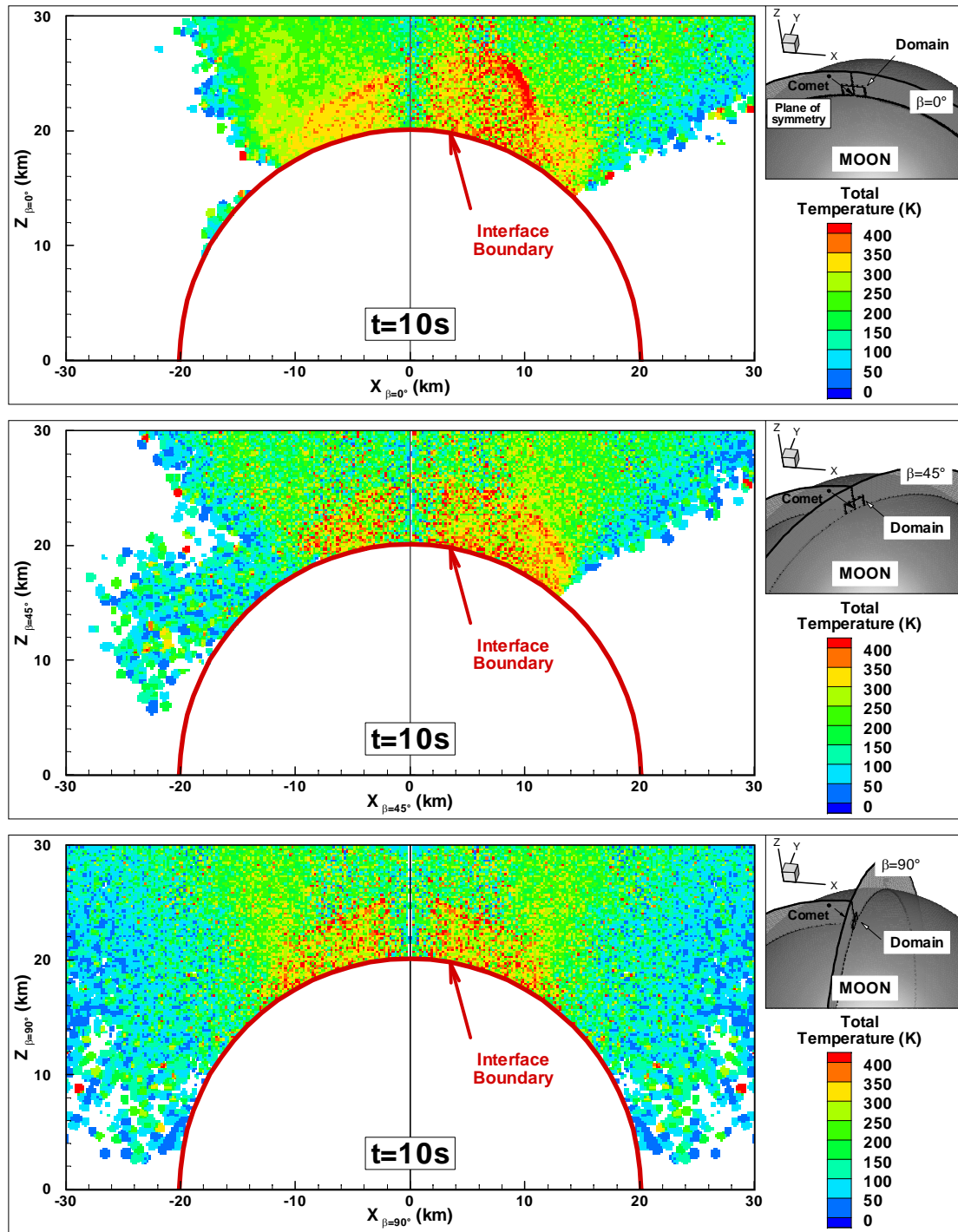


Figure 5-32 Near-field total temperature contours 10 s after impact in the plane of symmetry (top), 45° off the symmetry plane (middle) and perpendicular to the plane of symmetry (bottom).

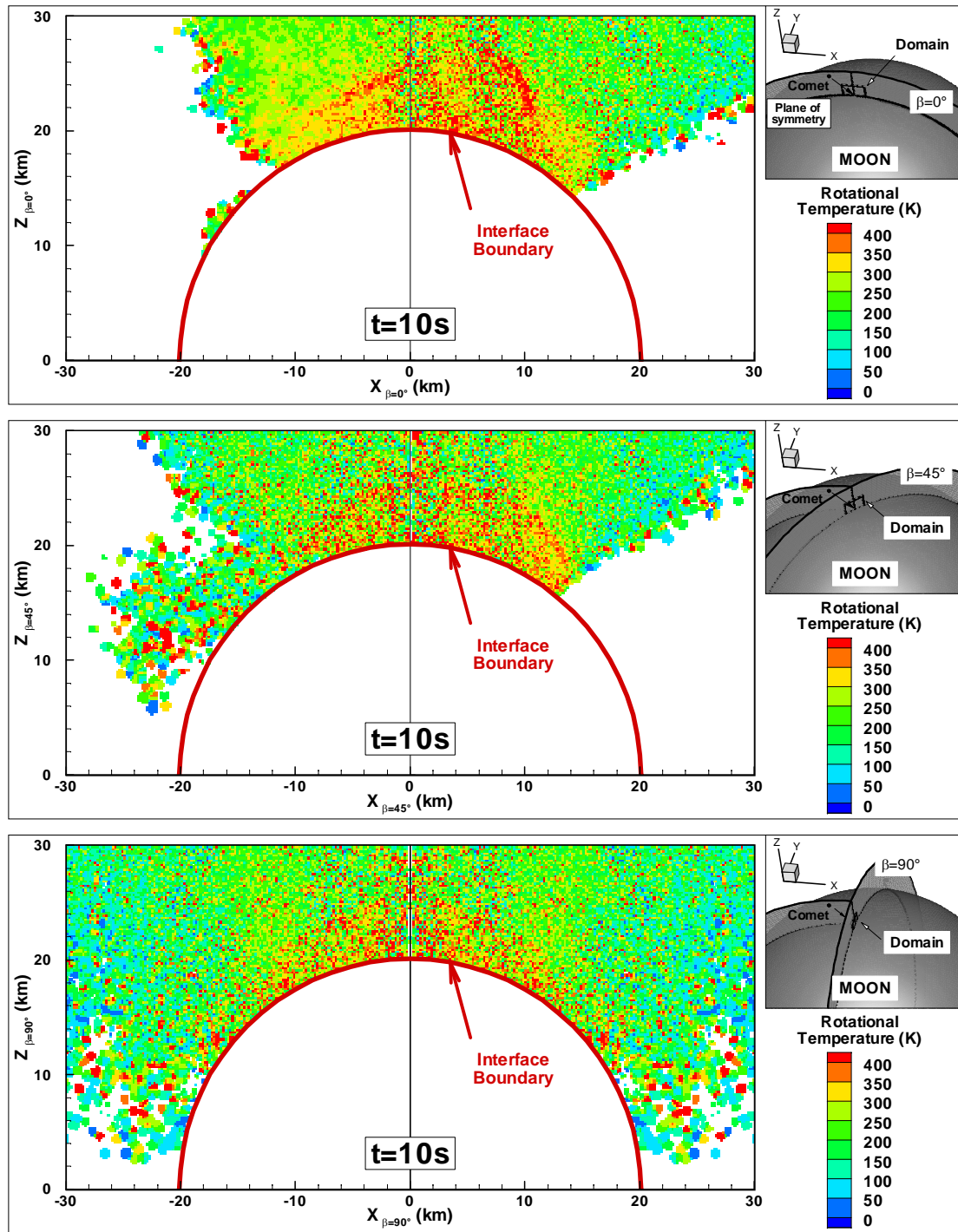


Figure 5-33 Near-field rotational temperature contours 10 s after impact in the plane of symmetry (top), 45° off the symmetry plane (middle) and perpendicular to the plane of symmetry (bottom).

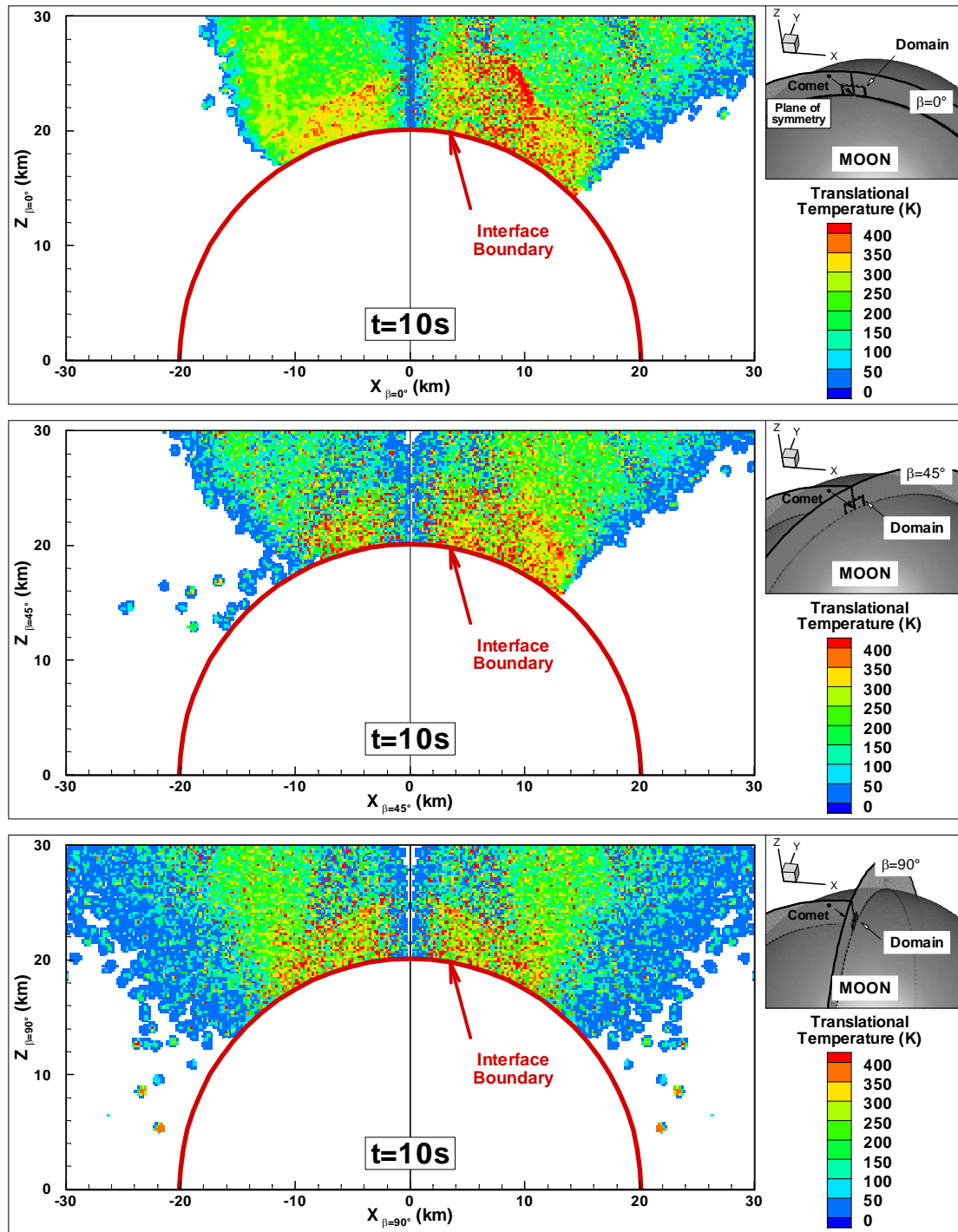


Figure 5-34 Near-field translational temperature contours 10 s after impact in the plane of symmetry (top),  $45^\circ$  off the symmetry plane (middle) and perpendicular to the plane of symmetry (bottom).

Fifteen seconds after the beginning of the impact, some interesting features can be observed in the plume. In the plane of symmetry of the impact, the high density regions uprange and downrange of the point of impact (Figure 5-21) have a slightly higher total temperature (~350 K) than the surrounding plume (~200 K) (top of Figure 5-35). In the intermediate plane (middle of Figure 5-35), the total temperatures in the plume uprange of the point of impact are lower than in the impact plane, ranging from 100 K in the low density region of the plume to 300 K closer to the central peak rocky material. Downrange of the point of impact, the total temperature contours are more uniform around 250 K. Finally, in the plane perpendicular to the impact plane (bottom of Figure 5-35), the plume is warmer closer to the central peak rocky material near the interface. The temperature in that region is around 300 K as compared to regions further away from the point of impact where the temperature is between 100 and 150 K. In all three planes, the rotational and translational temperatures agree well with the total temperature in the high density regions of the plume. In the low density regions, the rotational temperature is generally hotter (Figure 5-36) while the translational temperature is generally colder than the total temperature. In the translational temperature contours, the plume appears to be much smaller due to the blanking of the cells with a zero translational temperature (Figure 5-37).

Twenty seconds after impact, the total temperature within the center part of the uprange water vapor plume is nearly uniform around 200 K (top of Figure 5-38). Near the interface, the total temperature rises to 300 K due to a relatively higher rotational temperature in that region of the plume. In the downrange part of the plume, good agreement is observed between total, translational and rotational temperatures in the high density part of the plume with temperatures around 350 K. Near the edges of the plume, the number of molecules in the DSMC cells is too low to provide accurate temperatures. In the 45° intermediate plane (middle of Figure 5-40), the translational temperature is only resolved in the high density region of the downrange plume with temperatures from 350 K near the interface to 200 K downstream of it. Finally, the coldest overall water vapor is observed in the plane perpendicular to the impact plane (bottom of Figure 5-38) with temperatures lower than 250 K within the entire plume.

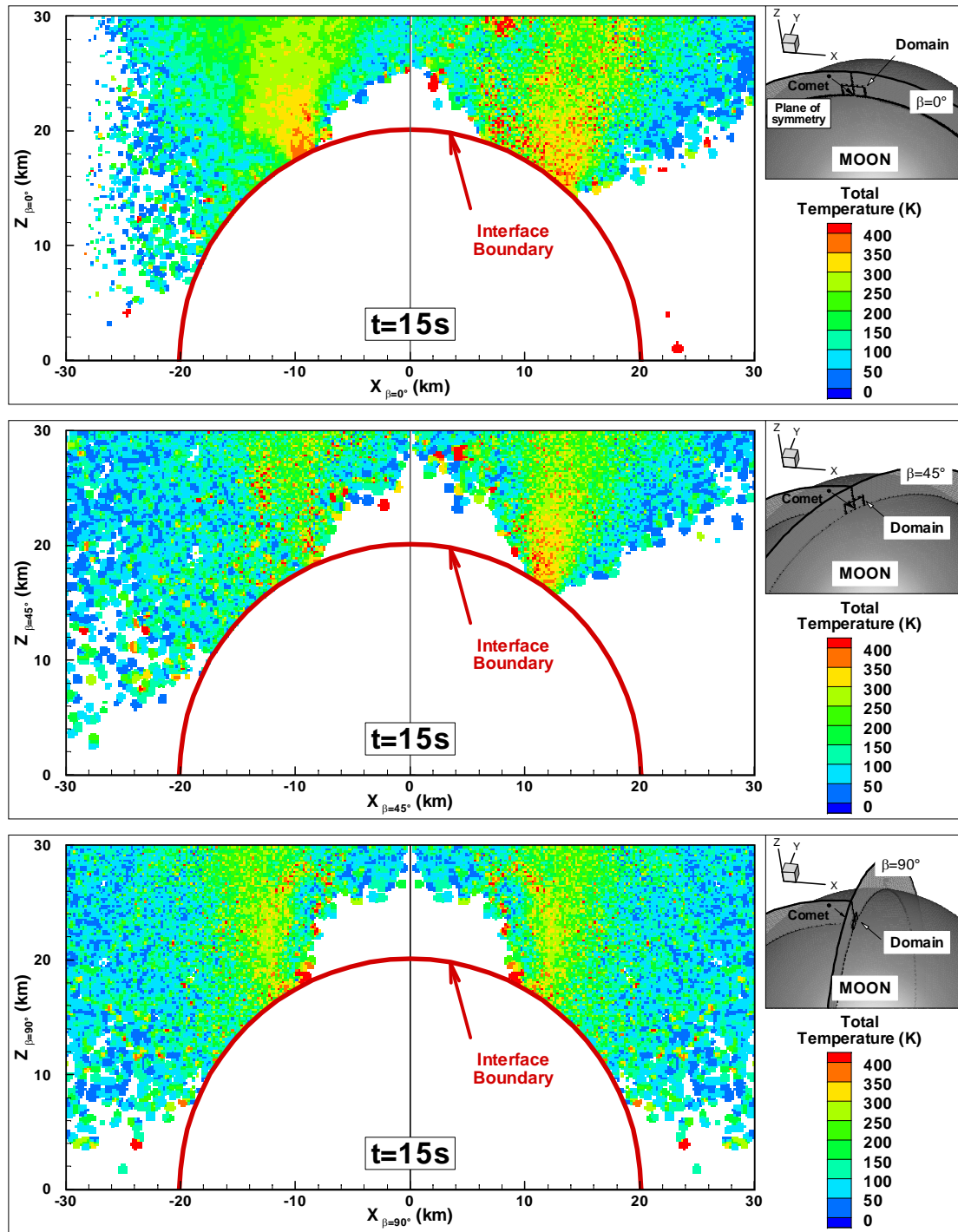


Figure 5-35 Near-field total temperature contours 15 s after impact in the plane of symmetry (top),  $45^\circ$  off the symmetry plane (middle) and perpendicular to the plane of symmetry (bottom).



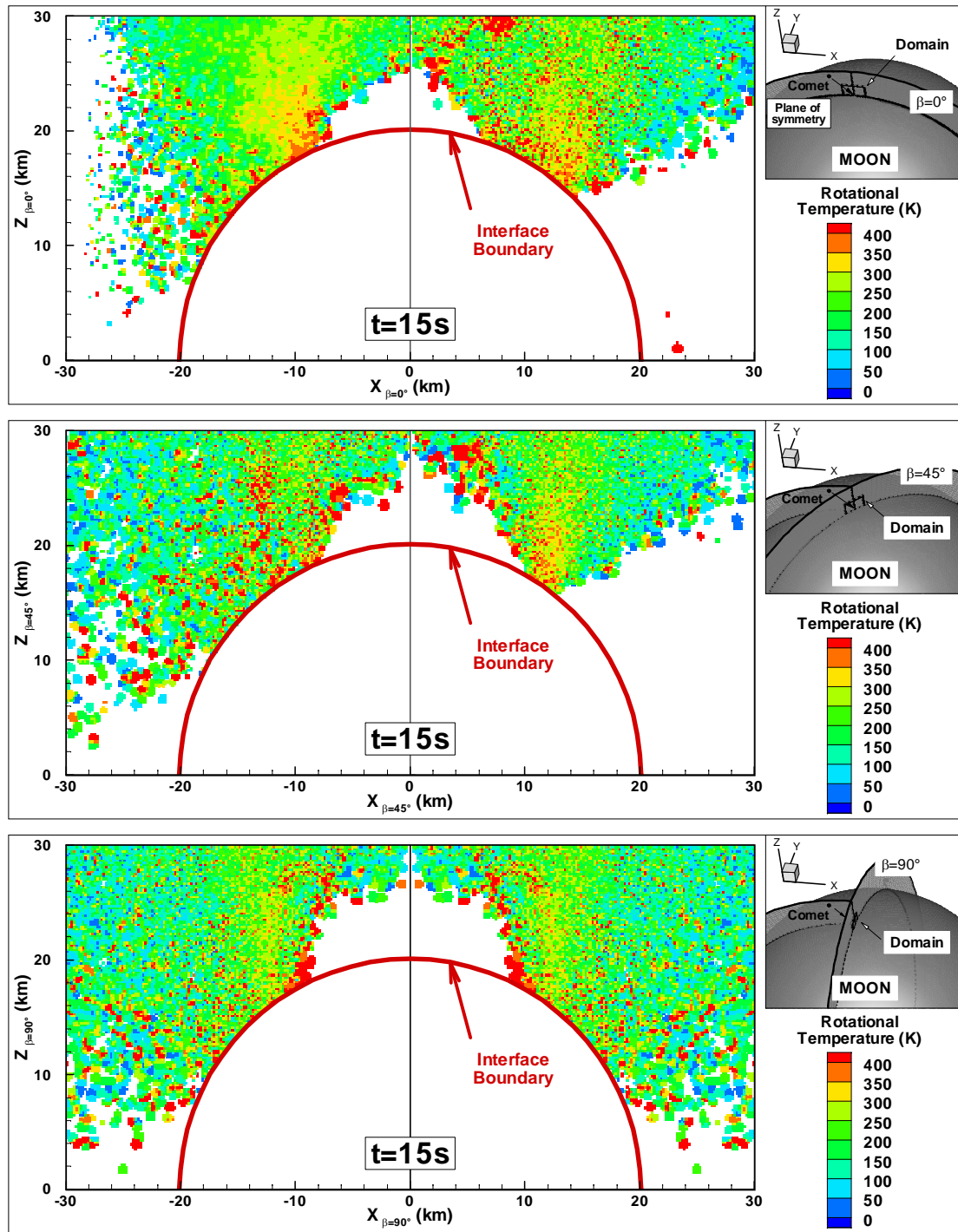


Figure 5-36 Near-field rotational temperature contours 15 s after impact in the plane of symmetry (top),  $45^\circ$  off the symmetry plane (middle) and perpendicular to the plane of symmetry (bottom).

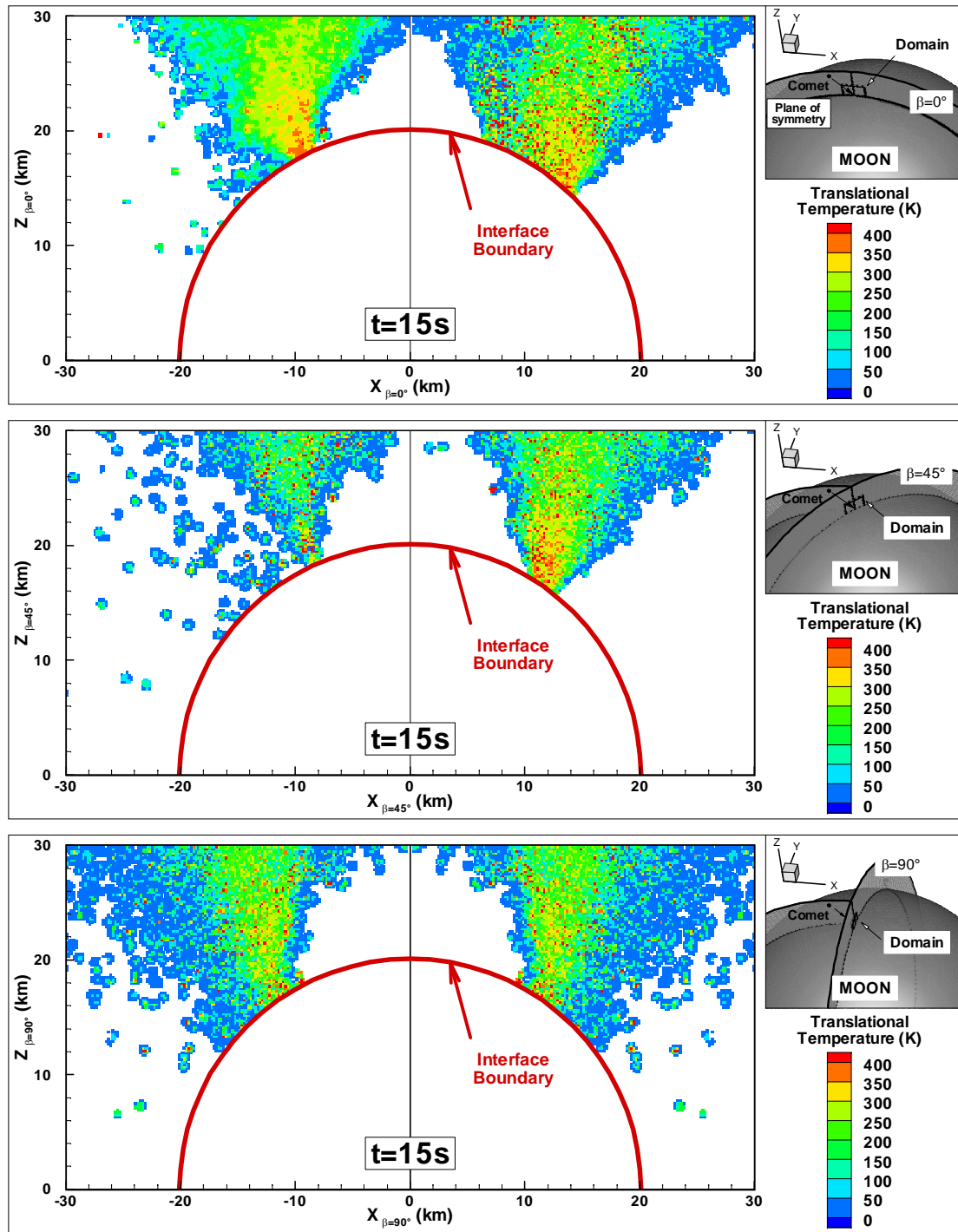


Figure 5-37 Near-field translational temperature contours 15 s after impact in the plane of symmetry (top),  $45^\circ$  off the symmetry plane (middle) and perpendicular to the plane of symmetry (bottom).

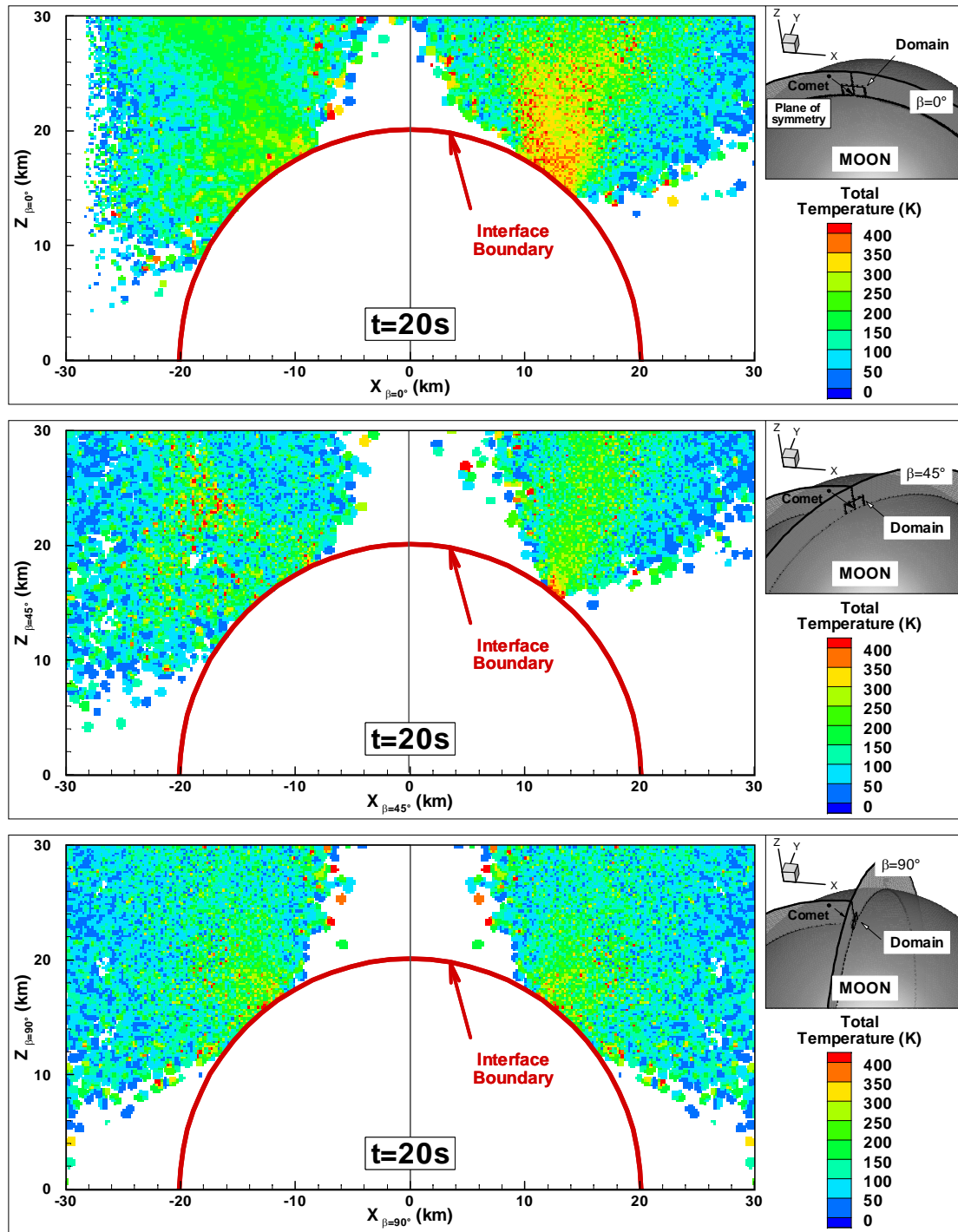


Figure 5-38 Near-field total temperature contours 20 s after impact in the plane of symmetry (top), 45° off the symmetry plane (middle) and perpendicular to the plane of symmetry (bottom).

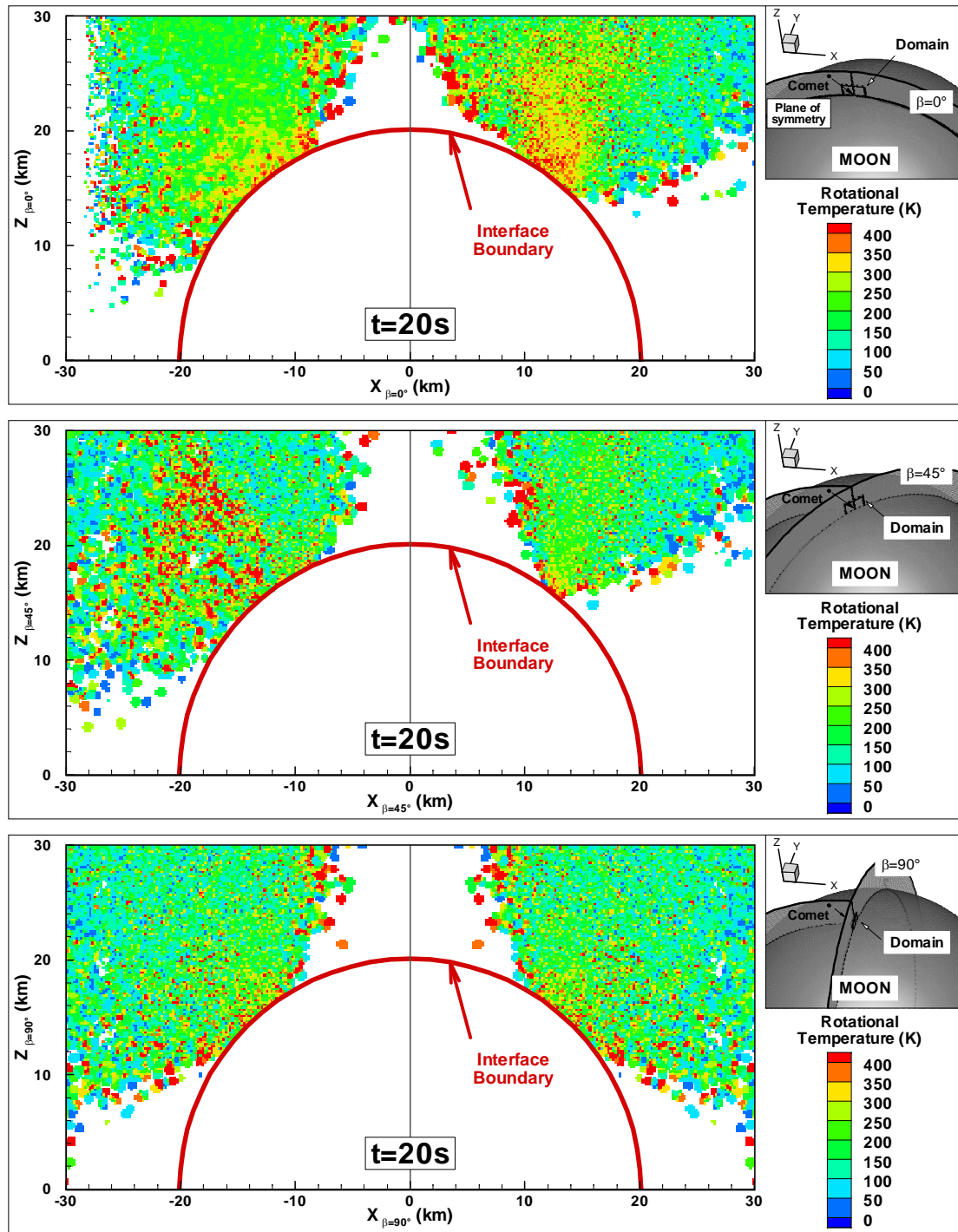


Figure 5-39 Near-field rotational temperature contours 20 s after impact in the plane of symmetry (top),  $45^\circ$  off the symmetry plane (middle) and perpendicular to the plane of symmetry (bottom).

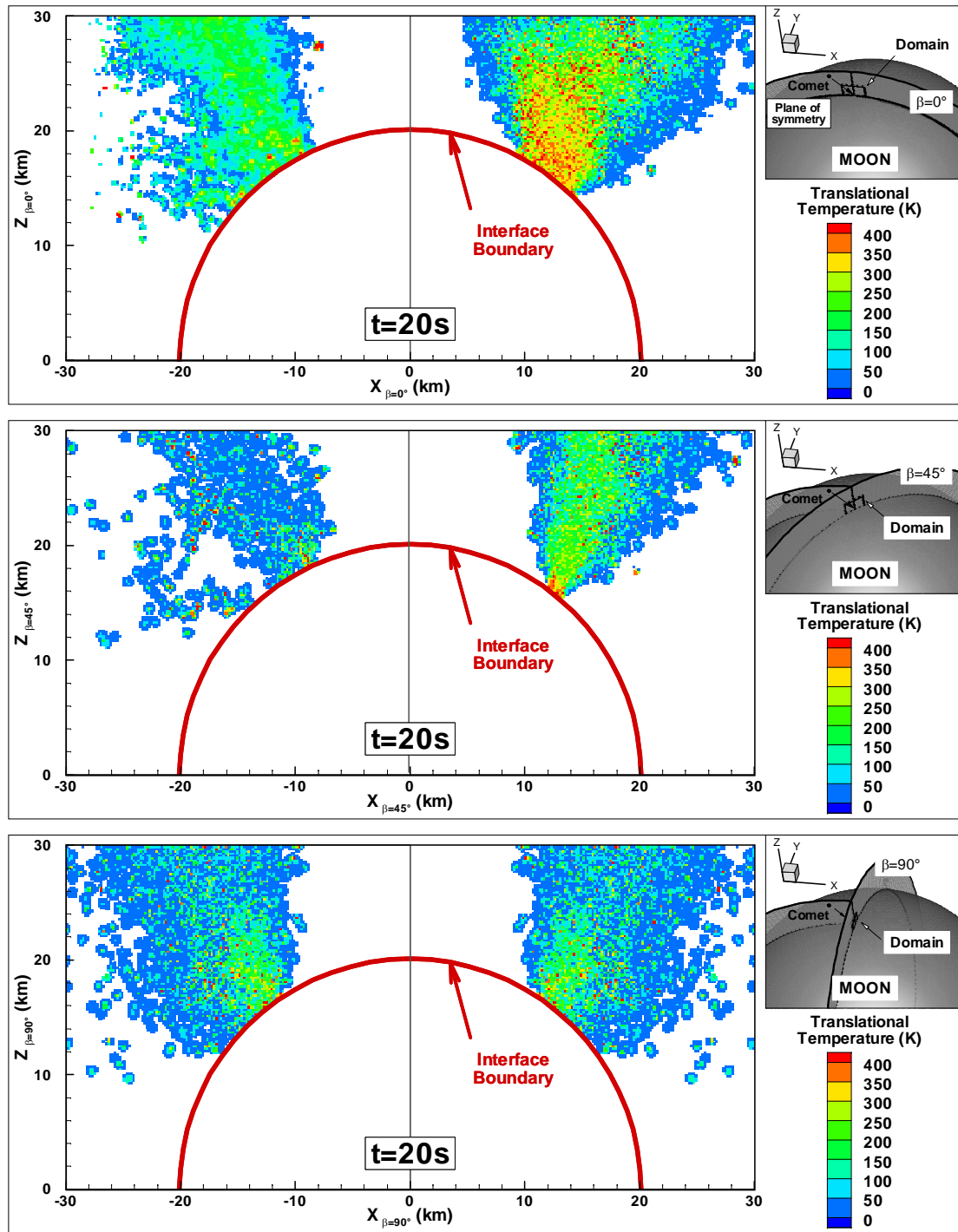


Figure 5-40 Near-field translational temperature contours 20 s after impact in the plane of symmetry (top),  $45^\circ$  off the symmetry plane (middle) and perpendicular to the plane of symmetry (bottom).

Because our DSMC solution has a relatively low number of molecules per cell, the temperature contours are especially noisy but some overall trends can still be observed. Early on, the total temperature within the plume reaches values as high as 1700 K locally. The plume, however, tends to cool very rapidly. From five seconds after impact on, temperatures lower than 500 K are observed within most of the plume. Overall the temperature contours are very different from what is expected in simple steady expansion flow into a vacuum. The temperature contours show some regional trends that are related to the location of the material in the comet and therefore to the conditions the water underwent during the impact event. As the flow expands, the temperature of a given volume of water vapor decreases but because of the non-uniform shock conditions the water vapor plume underwent, the temperature may be hotter downstream of the interface than near it. The rotational and translational temperatures are not in perfect agreement with a usually higher rotational temperature component than the translational temperature component. This is maybe most obvious near the axis of the domain and in the low density regions of the plume. Also, the vibrational modes are generally not excited resulting in simulated vibrational temperatures equal to zero throughout the domain at most times. These two problems have been associated to a lack of statistics in these regions and not to non-equilibrium physics within the plume.

### 5.4.2.3 Pressure

The total pressure,  $P$ , within the water vapor plume has been calculated assuming that the vapor is an ideal gas and that water is the only species. The pressure is given in Eq. (5.1) as a function of the number density,  $n$ , the translational temperature,  $T_{tr}$ , and Boltzmann's constant,  $k$  ( $= 1.38 \times 10^{-23} \text{ JK}^{-1}$ ).

$$P = n k T_{tr} \quad (5.1)$$

Condensation within the water vapor plume can occur when the pressure within the plume exceeds the vapor pressure of water at the temperature of the gas. Many additional physical processes may, however, accelerate the condensation process such as the presence of dust particles as possible nucleation sites for cluster formation (Zhong *et al.*, 2005). Because these processes are not modeled in the present simulations, we are only focusing on the possible condensation of the water vapor due to supersaturation. Because of the relatively large variations in temperature within the plume, from more than 1000 K early on to less than 200 K in some locations at later times, different phase transformations should be considered (Schroeder, 1999). For temperatures greater than the critical temperature ( $\sim 647 \text{ K}$ ), there is no distinction between the liquid and vapor phase and vapor cannot condense due to increase in pressure. For temperatures between the critical temperature and the triple point temperature ( $\sim 273 \text{ K}$ ), under the appropriate pressure conditions, water vapor condenses into water liquid. Finally, for temperatures lower than the triple point temperature, the vapor may deposit directly into the solid ice phase under high enough pressures. In the present section, we use the supersaturation equation for water vapor pressure over liquid for temperatures greater than 373 K and the supersaturation equation for water vapor pressure over ice for temperatures smaller than 373 K ice (Eq. (5.2)) (Fleagle and Businger, 1980).

$$\begin{aligned} P_{\text{Vapor over liquid}} &= 2.504 \times 10^{11} \times e^{-5417/T_{tr}} \\ P_{\text{Vapor over ice}} &= 3.27 \times 10^{12} \times e^{-6119/T_{tr}} \end{aligned} \quad (5.2)$$

Because the expression for the supersaturated vapor pressure has the translational temperature in an exponent, the noise level in the vapor pressure contours was too high for the previously interpolated contours. For this reason, the contours for the gas pressure and ratio of vapor pressure to gas pressure shown in Figure 5-41 to Figure 5-50 have been interpolated to a coarser grid with a larger sphere of influence. In each figure, the cell size in either direction is 500 m and the present data have been interpolated using a 2 km radius sphere of influence in our “inverse distance weighting” scheme. Note that because of the use of the coarser grid, the plume shape for pressure is slightly different from the plume shape observed in the density contours (Figure 5-18 to Figure 5-22). Similarly, the plume shape for the ratio of vapor pressure to pressure is somewhat different from that observed in the translational contours (Figure 5-25, Figure 5-31, Figure 5-34, Figure 5-37, and Figure 5-40). Finally, the thick white line in the contours for the ratio of the water vapor pressure to the gas pressure represents the location at which the ratio is equal to one. Cells with a ratio below one might be expected to see condensation due to supersaturation.

Early on, the pressure within the plume reaches Earth atmospheric level around 100 kPa in the plane of symmetry of the impact near the interface (Figure 5-41). Thereafter, the pressure decreases rapidly downstream of the interface to around 1000 Pa. Because of the relatively high temperatures within the plume at that time, the saturation vapor pressure is much higher than the pressure within the plume (Figure 5-42). The vapor pressure is lowest in the low temperature region observed near the interface far downrange of the point of impact. But even in that region, the vapor pressure is about one order of magnitude greater than the gas pressure. In the intermediate and perpendicular planes, some of the low density regions had no usable temperature data because of the poor statistics in our simulations. These regions therefore have a vapor pressure lower than the gas pressure. This is, however, a numerical effect and not a physical one. Therefore, one second after impact, it appears that no region of the plume is supersaturated. Five seconds after impact, the temperature has noticeably decreased within the entire plume to values lower than 500 K (Figure 5-31). Therefore, the vapor pressure is much lower at this time compared to one second after impact (Figure 5-44). Simultaneously, the density has been decreasing at the interface but only by a factor of at most five (Figure 5-43). Therefore, at that time, a few localized regions have a pressure lower than the saturation vapor pressure but most of



the plume is supersaturated. Ten seconds after impact (Figure 5-45), the pressure decreases to at most a few tens of thousands Pascals in the region of the plume being pushed outward by the central peak rocky material. In that region of the plume, the vapor pressure is maybe one order of magnitude greater than the gas pressure (Figure 5-46). Outside of that dense and hot region, the pressure is a few hundred to a few thousand Pascals and the vapor pressure appears to be lower than the gas pressure. Fifteen and twenty seconds after impact, the gas pressure decreases slightly to a few hundred to ten thousand Pascals (Figure 5-47 and Figure 5-49). The vapor pressure appears to become lower than the pressure within most of the plume with the exception of the high density, high temperature sprays observed both uprange and downrange of the point of impact (Figure 5-48 and Figure 5-50).

In conclusion, condensation may not be a factor in the fast moving, hot water vapor that crosses the interface early on after the impact. However, in the slower part of the plume that contains the water that will remain on the Moon after impact, condensation due to supersaturation should be expected.

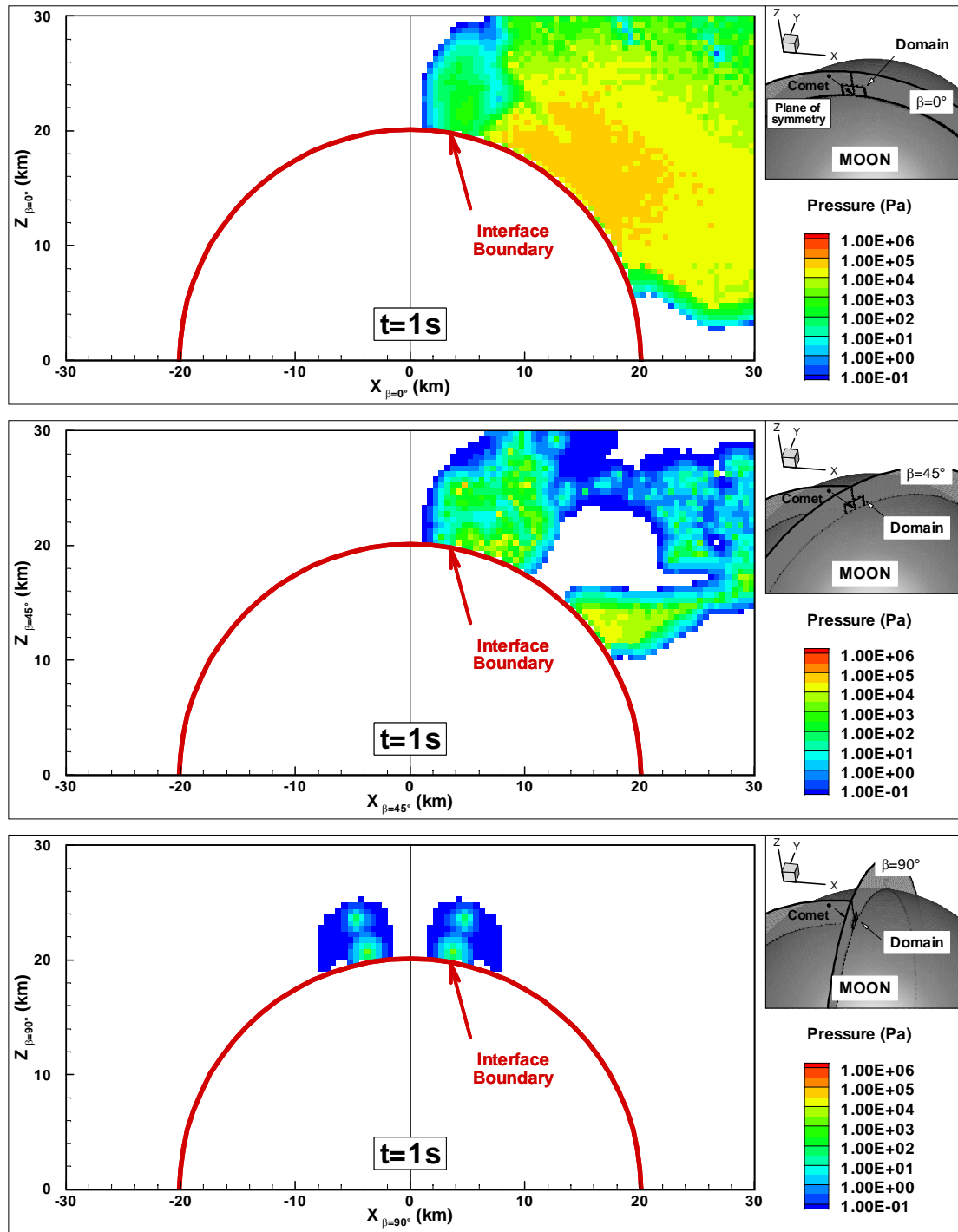


Figure 5-41 Near-field pressure contours 1 s after impact in the plane of symmetry (top),  $45^\circ$  off the symmetry plane (middle) and perpendicular to the plane of symmetry (bottom).

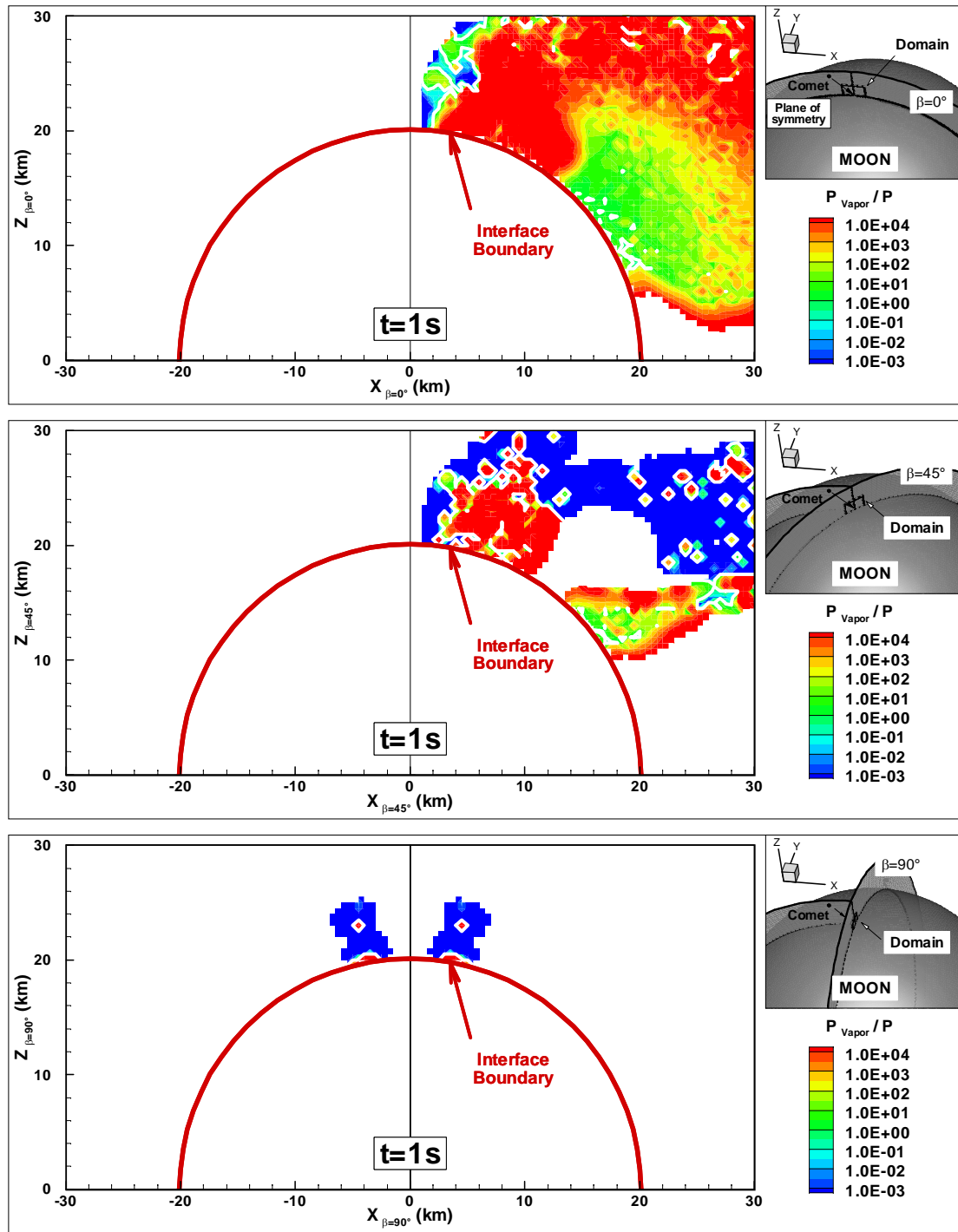


Figure 5-42 Near-field ratio of vapor pressure to pressure contours 1 s after impact in the plane of symmetry (top),  $45^\circ$  off the symmetry plane (middle) and perpendicular to the plane of symmetry (bottom).

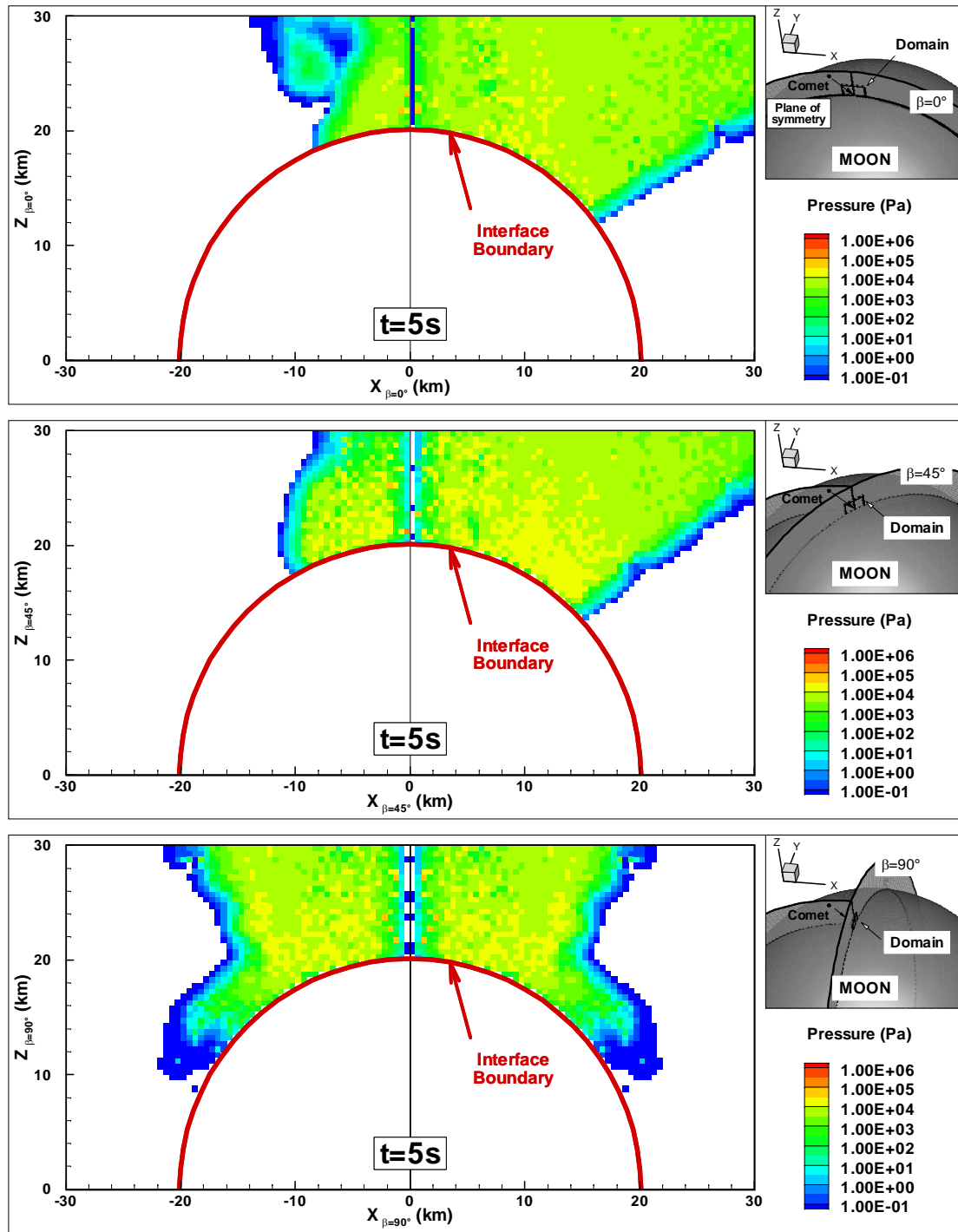


Figure 5-43 Near-field pressure contours 5 s after impact in the plane of symmetry (top),  $45^\circ$  off the symmetry plane (middle) and perpendicular to the plane of symmetry (bottom).

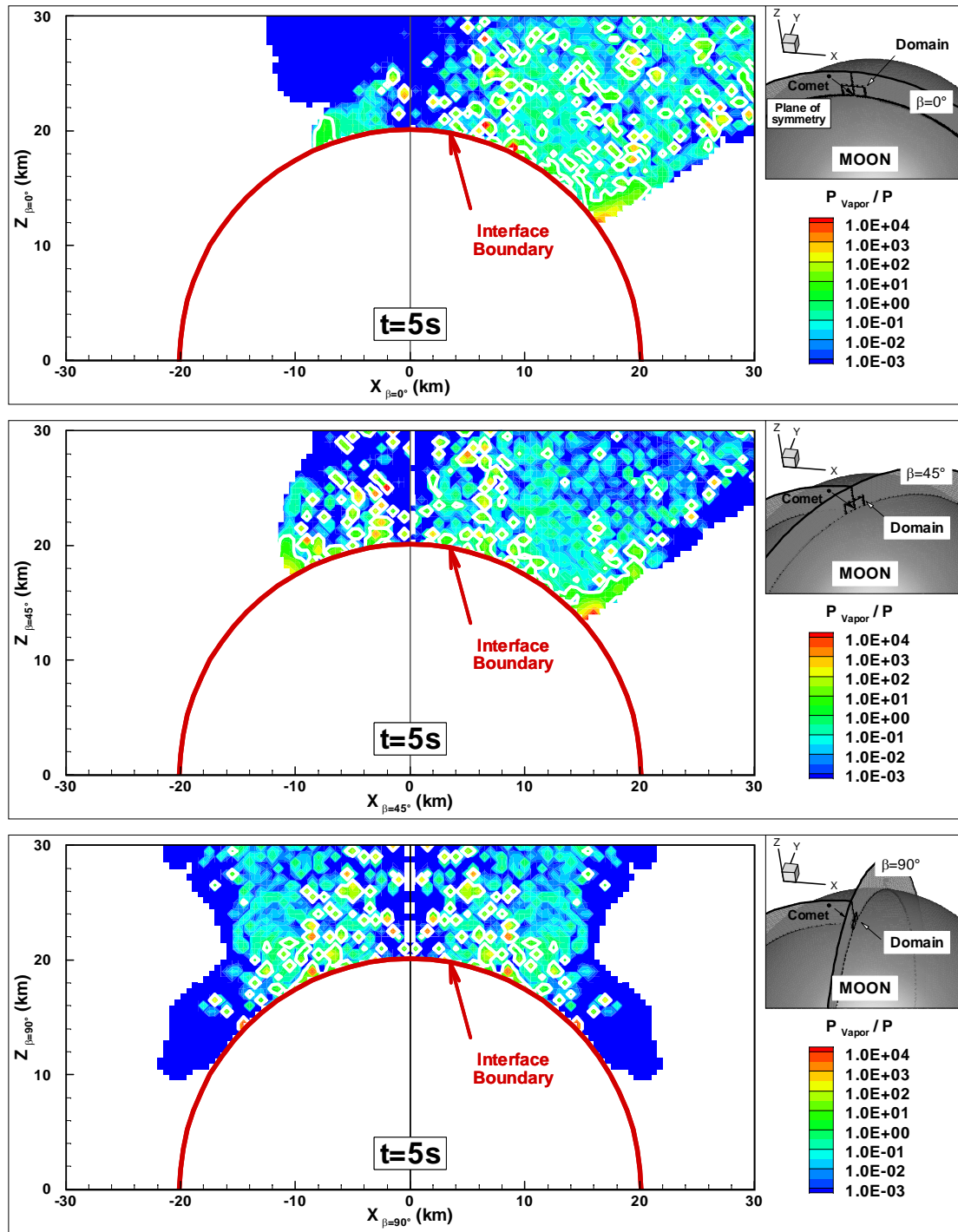


Figure 5-44 Near-field ratio of vapor pressure to pressure contours 5 s after impact in the plane of symmetry (top),  $45^\circ$  off the symmetry plane (middle) and perpendicular to the plane of symmetry (bottom).

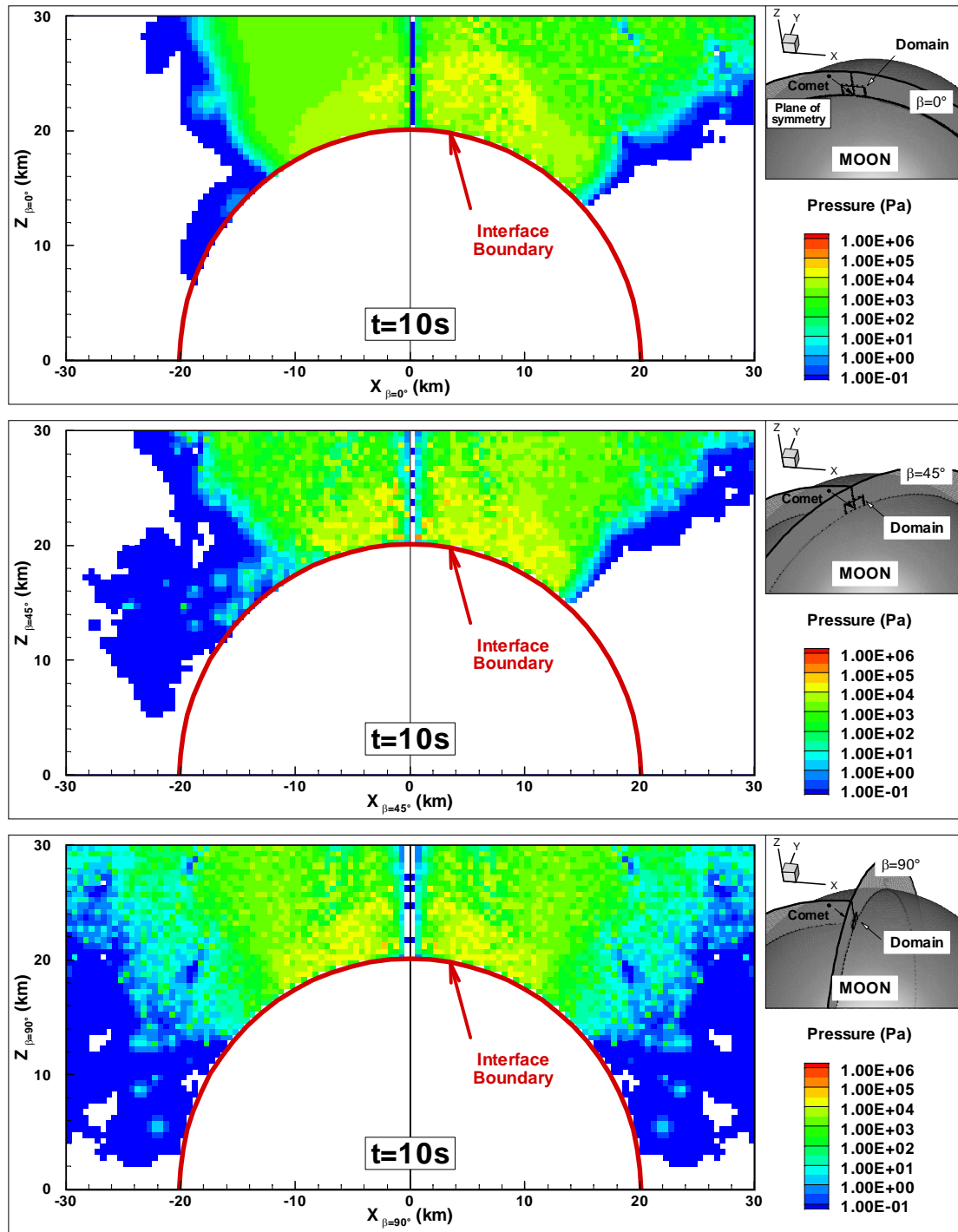


Figure 5-45 Near-field pressure contours 10 s after impact in the plane of symmetry (top),  $45^\circ$  off the symmetry plane (middle) and perpendicular to the plane of symmetry (bottom).

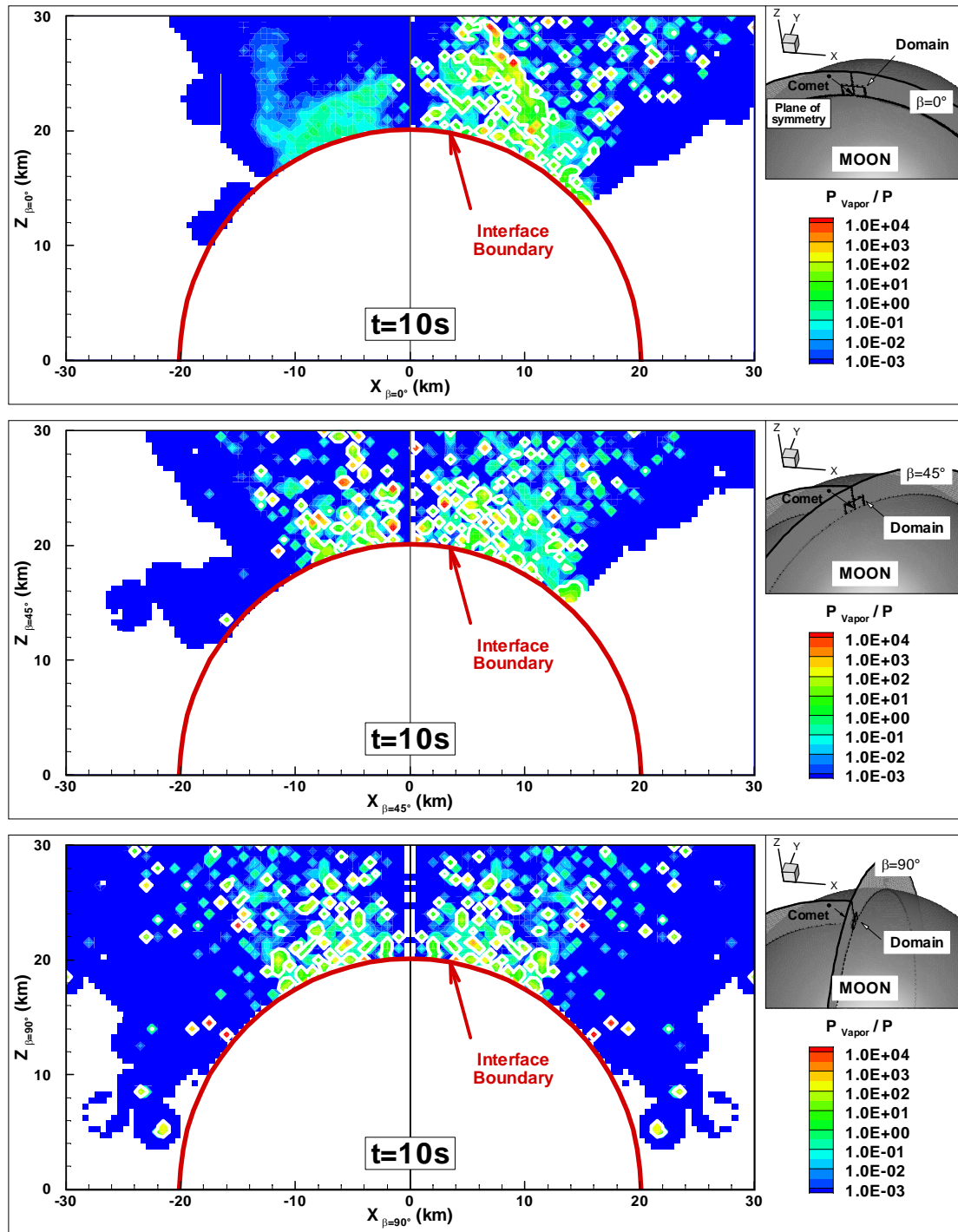


Figure 5-46 Near-field ratio of vapor pressure to pressure contours 10 s after impact in the plane of symmetry (top), 45° off the symmetry plane (middle) and perpendicular to the plane of symmetry (bottom).

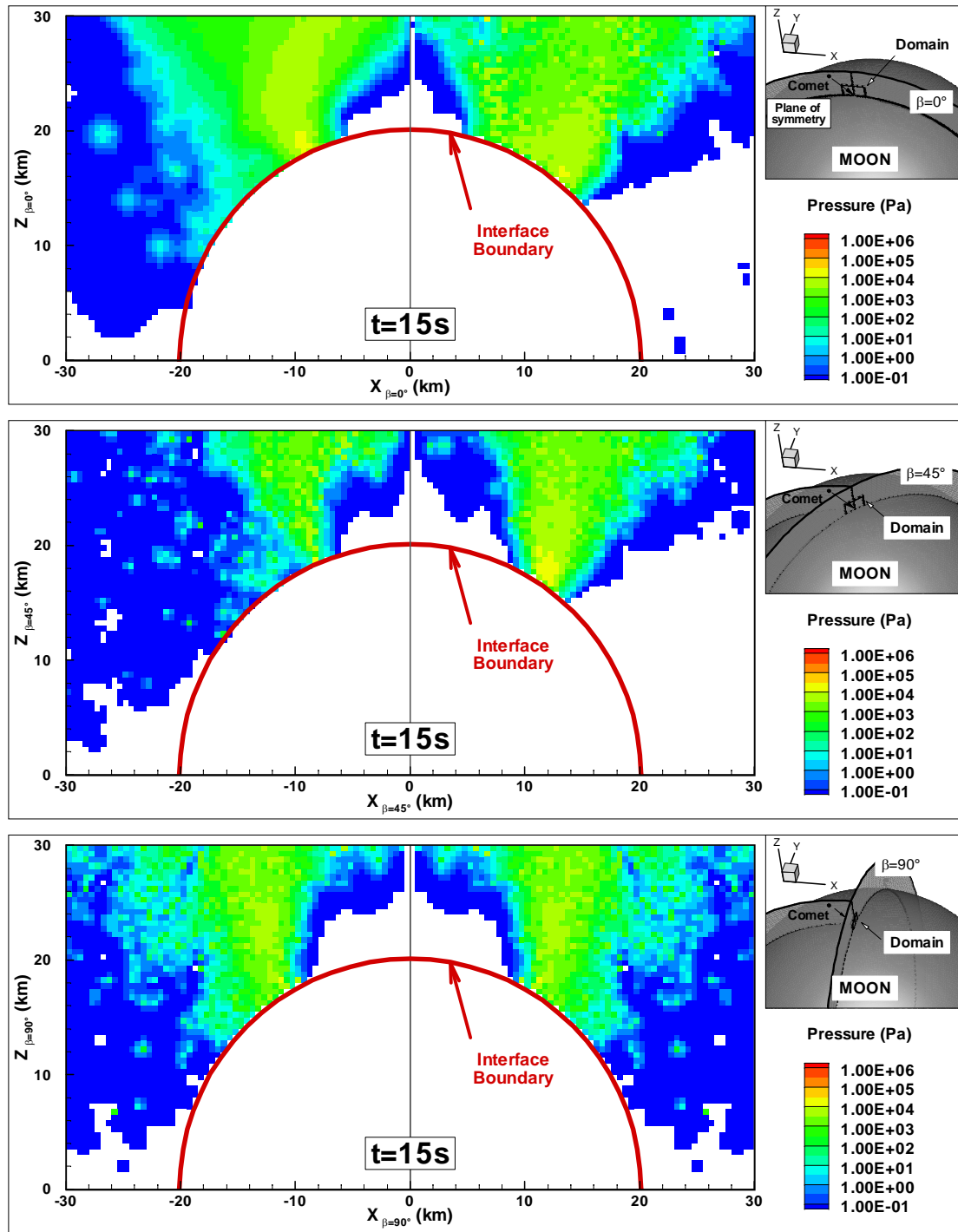


Figure 5-47 Near-field pressure contours 15 s after impact in the plane of symmetry (top),  $45^\circ$  off the symmetry plane (middle) and perpendicular to the plane of symmetry (bottom).



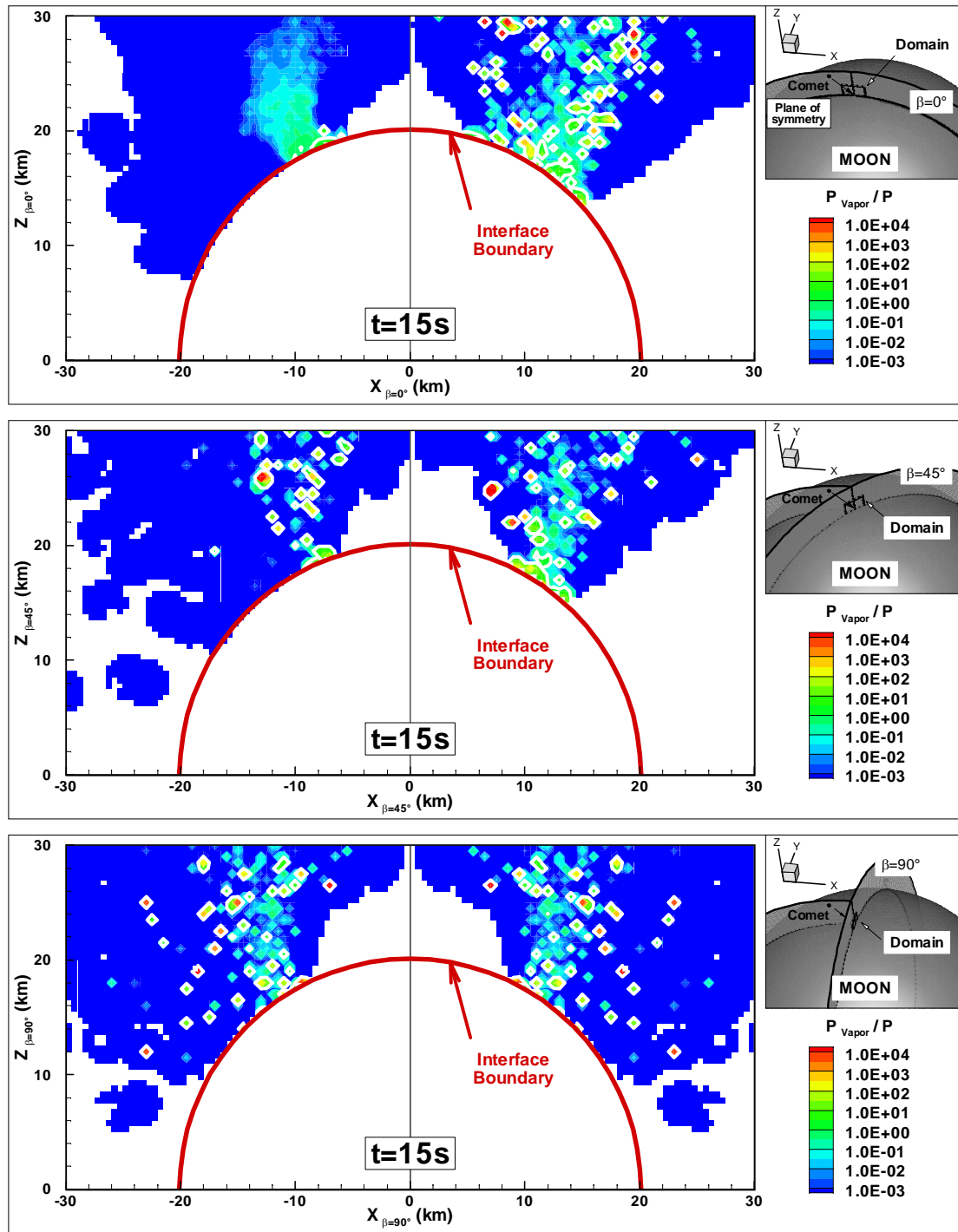


Figure 5-48 Near-field ratio of vapor pressure to pressure contours 15 s after impact in the plane of symmetry (top),  $45^\circ$  off the symmetry plane (middle) and perpendicular to the plane of symmetry (bottom).

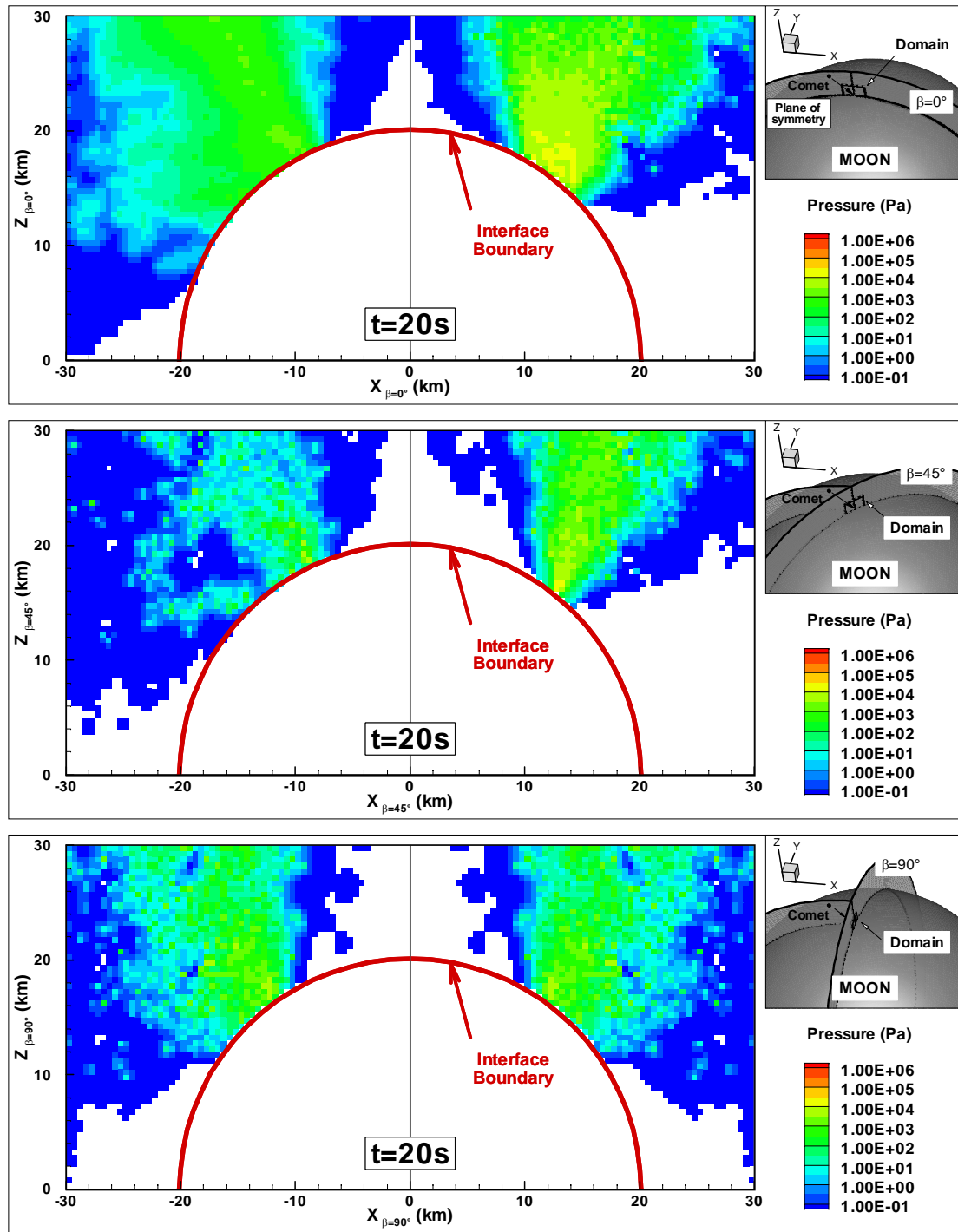


Figure 5-49 Near-field pressure contours 20 s after impact in the plane of symmetry (top),  $45^\circ$  off the symmetry plane (middle) and perpendicular to the plane of symmetry (bottom).

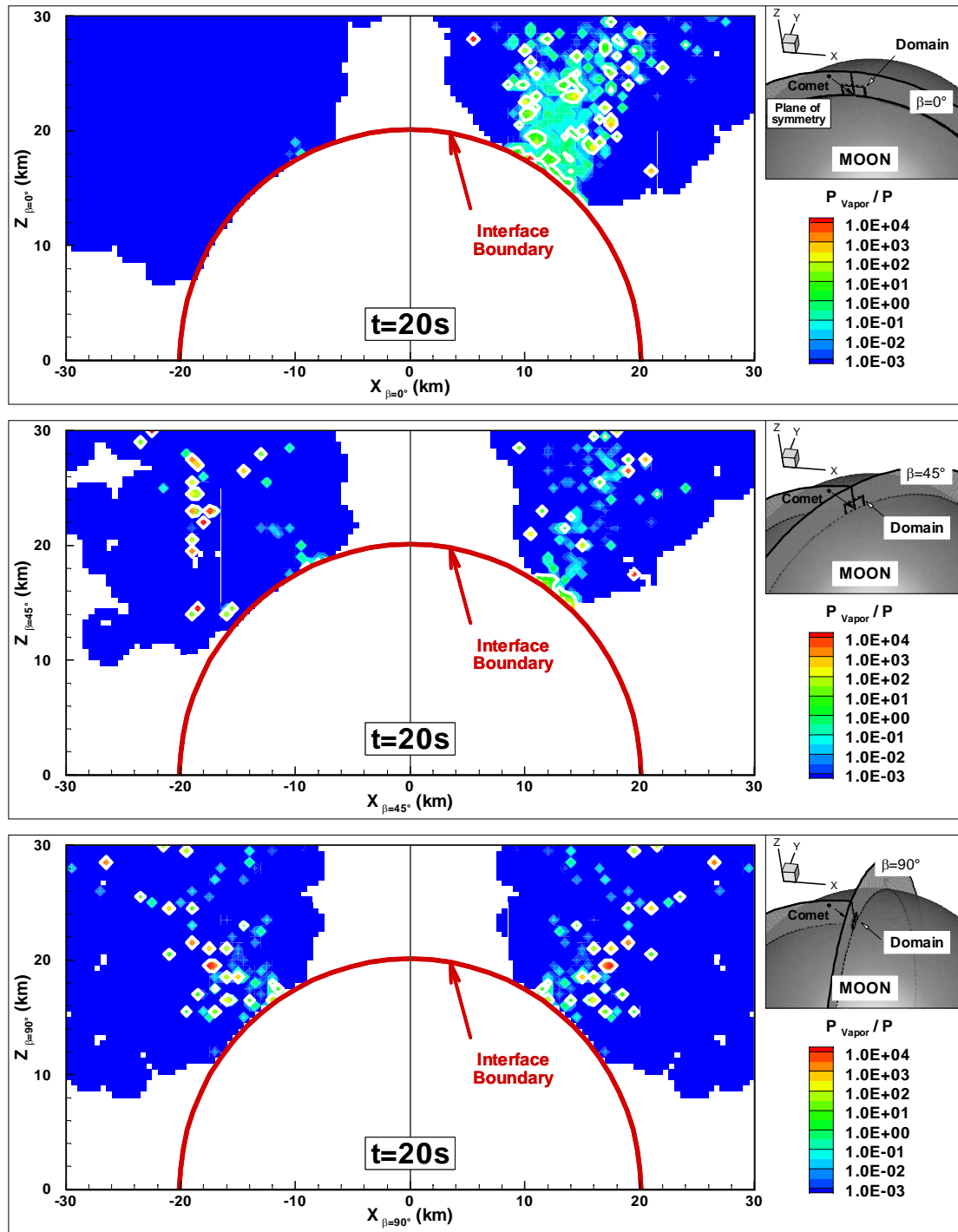


Figure 5-50 Near-field ratio of vapor pressure to pressure contours 20 s after impact in the plane of symmetry (top),  $45^\circ$  off the symmetry plane (middle) and perpendicular to the plane of symmetry (bottom).

#### 5.4.2.4 Radial Velocity from the Point of Impact and Mach Number

The radial velocity from the point of impact and the speed based Mach number are plotted in Figure 5-51 to Figure 5-60, 1, 5, 10, 15, and 20 s after the beginning of the impact. The radial velocity is calculated using Eq. (5.3) and the Mach number is calculated using Eq. (5.4). In theory, the ratio of specific heat,  $\gamma$ , should vary with temperature but for practical reasons its value has been fixed in Eq. (5.4) at an intermediate value of 1.3 which is representative of a water vapor temperature around 600 K ( $\gamma = 1.33$  at 200 K and  $\gamma = 1.21$  at 1700 K).

$$V_r = \left( \frac{X}{distance} \right) \times V_X + \left( \frac{Y}{distance} \right) \times V_Y + \left( \frac{Z-1738}{distance} \right) \times V_Z \quad (5.3)$$

Here,  $X$ ,  $Y$ , and  $Z$  are the coordinates of the cell center (note that the value of  $Z-1738$  (in km) represents the altitude of the cell center above the lunar surface),  $V_X$ ,  $V_Y$ , and  $V_Z$  are the velocity components in the Cartesian coordinate system presented in Figure 5-1, and  $distance = \sqrt{X^2 + Y^2 + (Z - 1738)^2}$ . Similar to the temperature contours, due to the rapid slow down of the water vapor plume with time, the scale of the color contours one second after impact (from  $V_r = 0$  m/s to 40000 m/s) is different than the scale used at all the later time (from  $V_r = 0$  m/s to 8000 m/s). Finally, the white line observed in the radial velocity contours 10 s, 15 s, and 20 s after impact represents the limit at which the water vapor has a radial velocity equal to the escape velocity at the surface of the Moon. Eq. (5.4) provides the expression used in the present section to calculate the Mach number:

$$Mach = \frac{\sqrt{V_X^2 + V_Y^2 + V_Z^2}}{\sqrt{\gamma \mathcal{R} T_{tr}}} \quad (5.4)$$

where the numerator is the speed of the gas and the denominator is the speed of sound within the gas. Note that in the Mach number contours, cells with a zero translational temperature have been blanked out. Also, we verified that the Mach number is greater than one within the entire plume at all times in the near field.

One second after impact, the radial velocity contours radially increase from the point of impact except within 15 km downrange of the point of impact where the radial velocity contours flatten out (Figure 5-51). Near the interface, beyond 15 km downrange, the water vapor has a relatively slower velocity,  $\sim 21$  km/s, compared to the water vapor crossing the interface nearer to the point of impact, moving at  $\sim 24$  km/s. Also, this region has a relatively lower average temperature (Figure 5-23), which means that the water vapor in that region went through some weaker acceleration than the rest of the water crossing the interface near that time. Because of the relatively lower velocity, this material started at a location further away from the point of impact than most of the water crossing the interface at that time, assuming that each volume of material travelled along a linear path from its point of origin to the interface. One second after impact, the flow is highly hypersonic within the entire domain (Figure 5-52), with the lowest Mach number, around Mach 25, being observed in the high temperature region of the flow (Figure 5-23).

Five seconds after impact, the water vapor velocity at the interface has decreased by a factor of five with velocities between 4 and 4.5 km/s in all three planes (Figure 5-53). The largest velocities near the interface are observed directly above of the point of impact. The Mach number contours five seconds after impact (Figure 5-54) are very noisy near the axis of symmetry of the DSMC domain, in the low density regions (Figure 5-19) and at the edges of the water plume; these have been attributed to the increased noise level in these regions in the translational temperature contours. In general, however, the Mach number increases with radial distance from the point of impact. The Mach number is as low as Mach 8 near the interface and increases up to Mach 25 at the top boundary of our domain.

Five seconds later, ten seconds after impact, the radial velocity contours are now more uniform within the entire plume, with velocities between 2.5 and 4 km/s (Figure 5-55). Some relatively slower velocities, slower than the escape velocity on the Moon, are observed at the edges of the water plume just downstream of the interface in all three planes and in the low density region of the plume observed in the intermediate and perpendicular planes (Figure 5-20). Overall, the Mach number takes relatively lower values near the interface,  $\sim 7$ , than further downstream,  $>10$  (Figure 5-56).

Fifteen and twenty seconds after impact, the entire water plume crossing the interface has a radial velocity lower than the escape velocity of the Moon at the surface (2.38 km/s) (Figure 5-57 and Figure 5-59). Twenty seconds after impact, most of the near-field water vapor plume has a radial velocity slower than the Moon's escape velocity. Simultaneously, the Mach number continues to decrease to values near Mach 3, fifteen and twenty seconds after impact (Figure 5-58 and Figure 5-60). The flow, however, is still supersonic everywhere downstream of the interface at these times.

In summary, initially, the radial velocity contours are nearly concentric meaning that most of the water crossing the interface early was vaporized in a small region near the point of impact. As the plume continues to expand, however, some noticeable differences begin to appear between the velocities of the low density and high density regions of the plume with the low density plume moving generally slower than the high density plume. In addition, the flow remains supersonic at all times during the first 21 s of the impact event downstream of the SOVA interface. The flow is hypersonic early on ( $Mach \gg 20$ ) before slowing down later to simply supersonic ( $Mach \sim 3$ ).

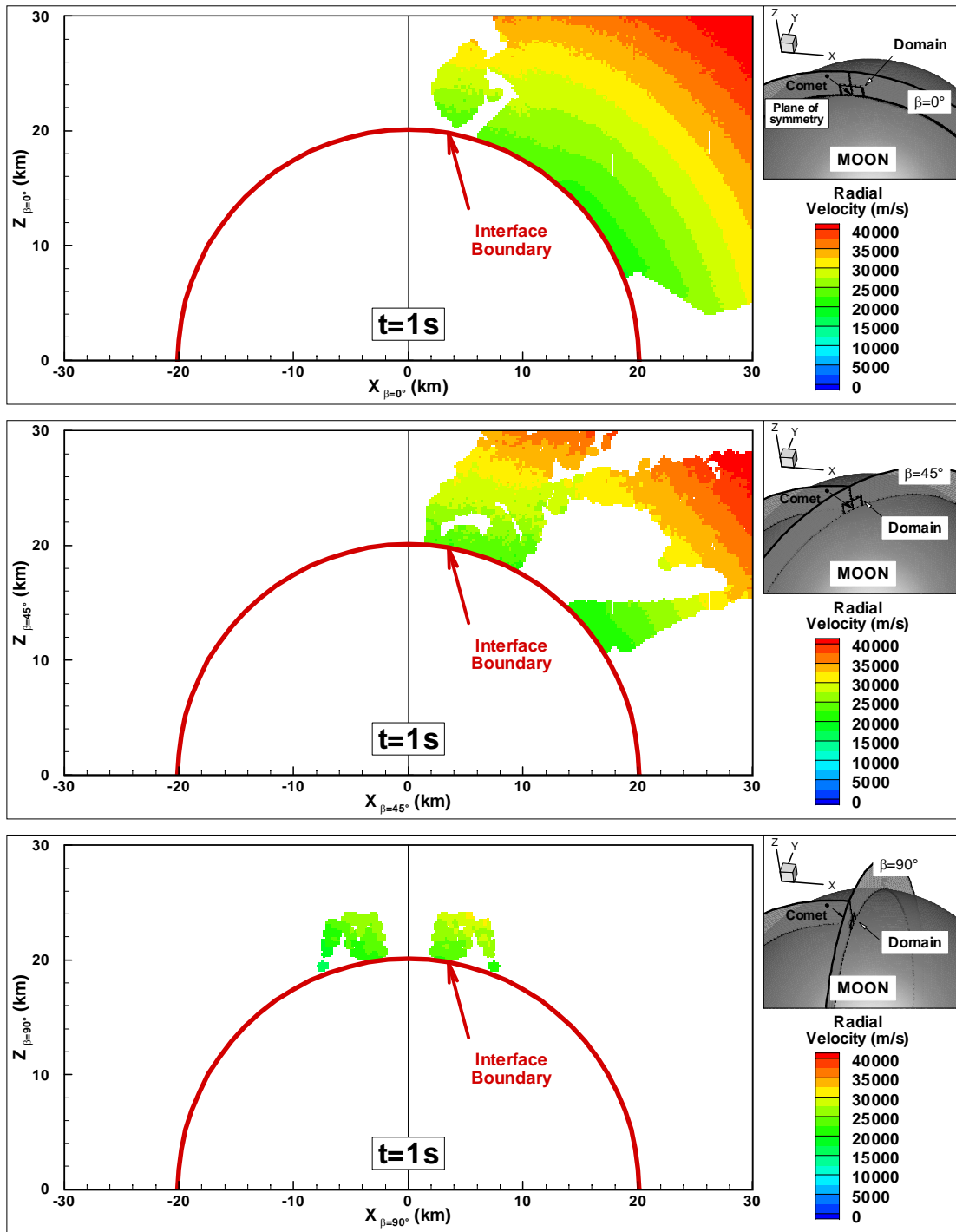


Figure 5-51 Near-field radial velocity contours 1 s after impact in the plane of symmetry (top),  $45^\circ$  off the symmetry plane (middle) and perpendicular to the plane of symmetry (bottom).

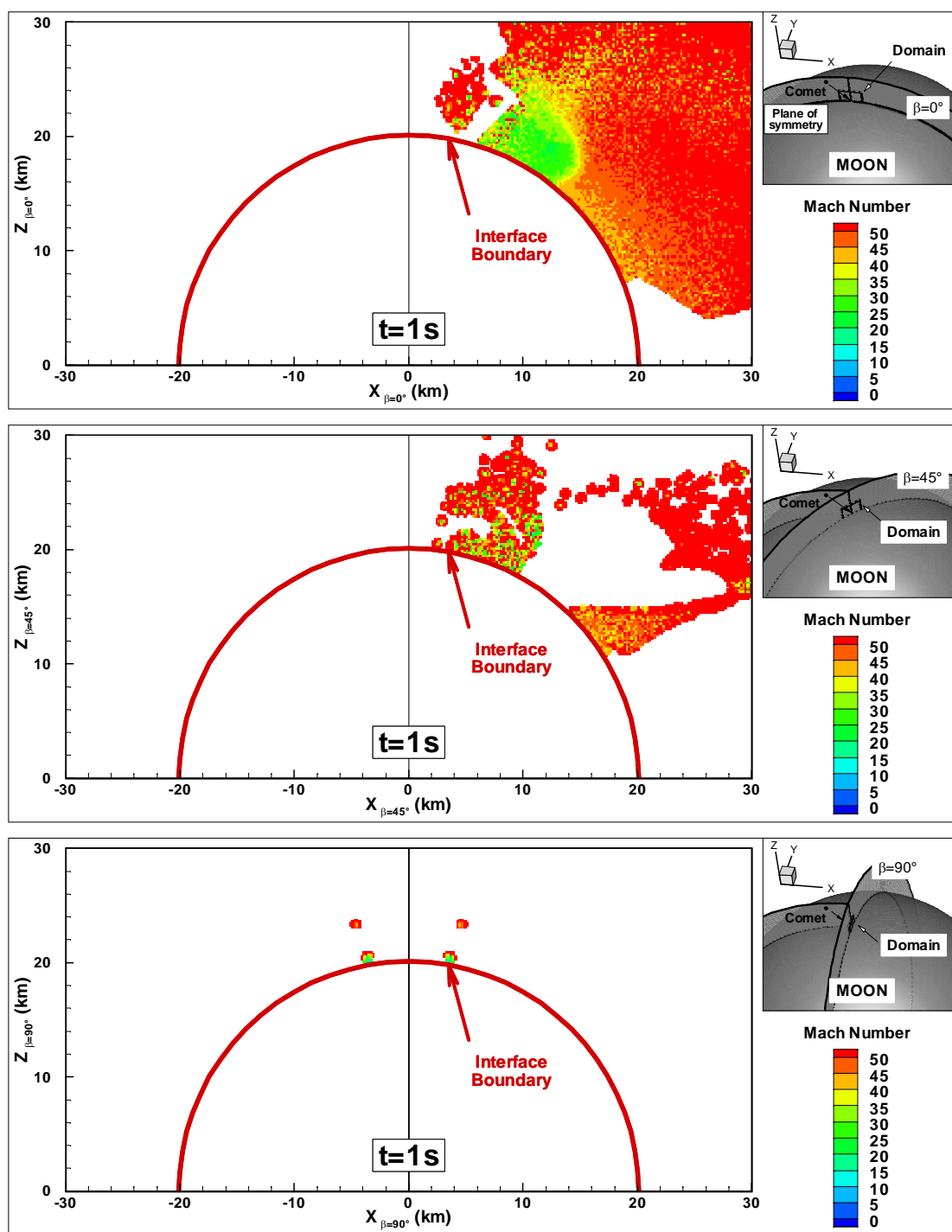


Figure 5-52 Near-field Mach number contours 1 s after impact in the plane of symmetry (top),  $45^\circ$  off the symmetry plane (middle) and perpendicular to the plane of symmetry (bottom).



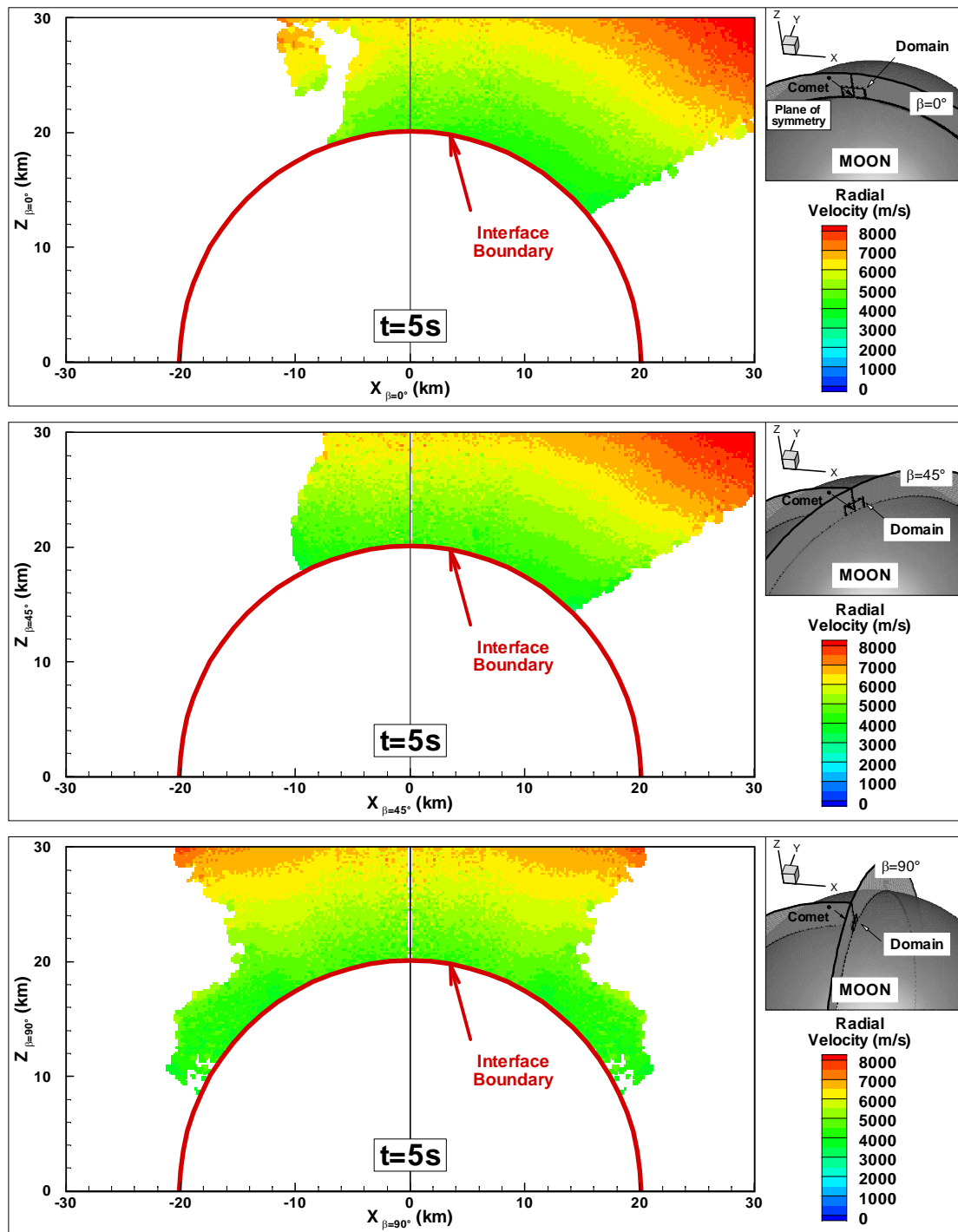


Figure 5-53 Near-field radial velocity contours 5 s after impact in the plane of symmetry (top), 45° off the symmetry plane (middle) and perpendicular to the plane of symmetry (bottom).

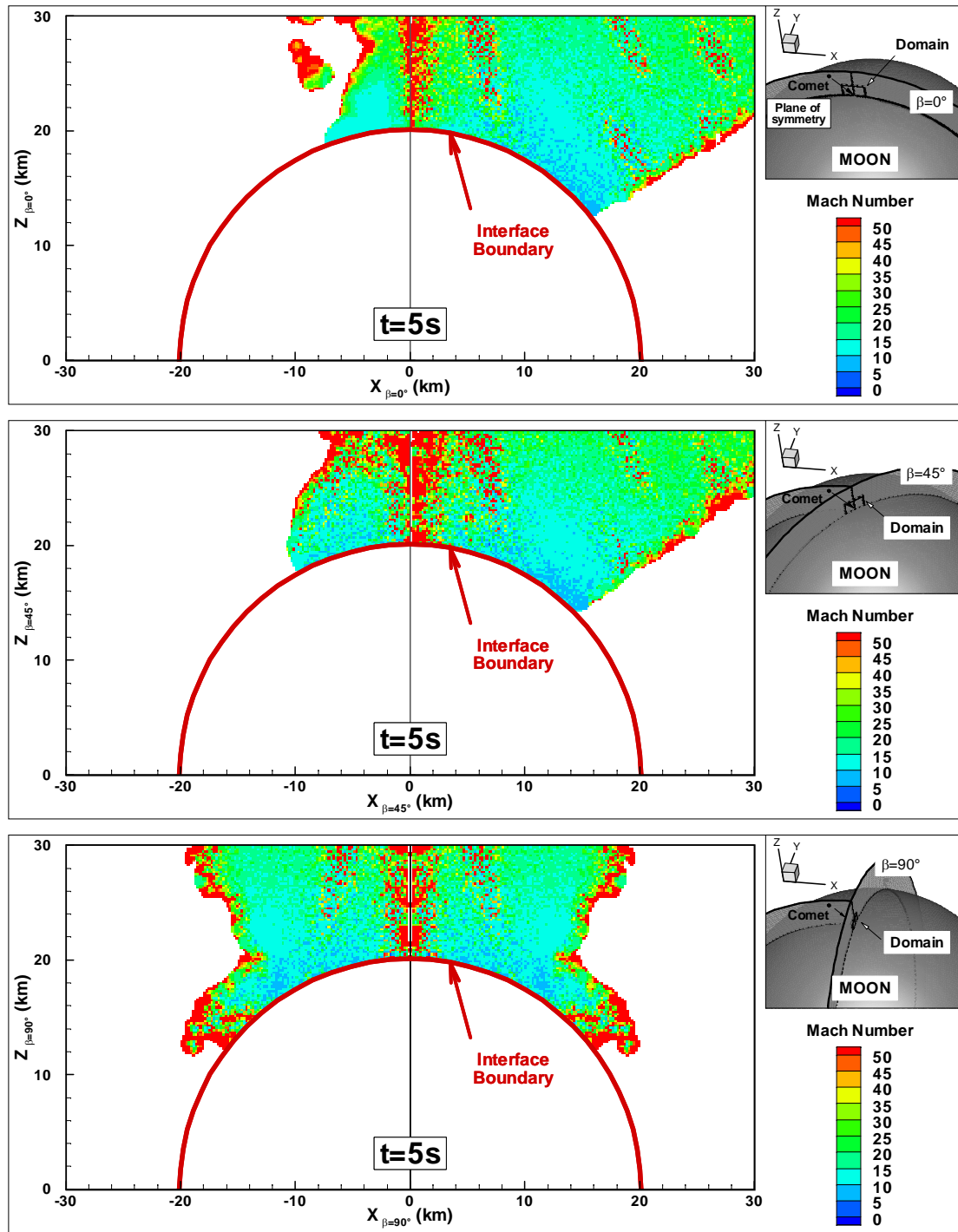


Figure 5-54 Near-field Mach number contours 1 s after impact in the plane of symmetry (top),  $45^\circ$  off the symmetry plane (middle) and perpendicular to the plane of symmetry (bottom).

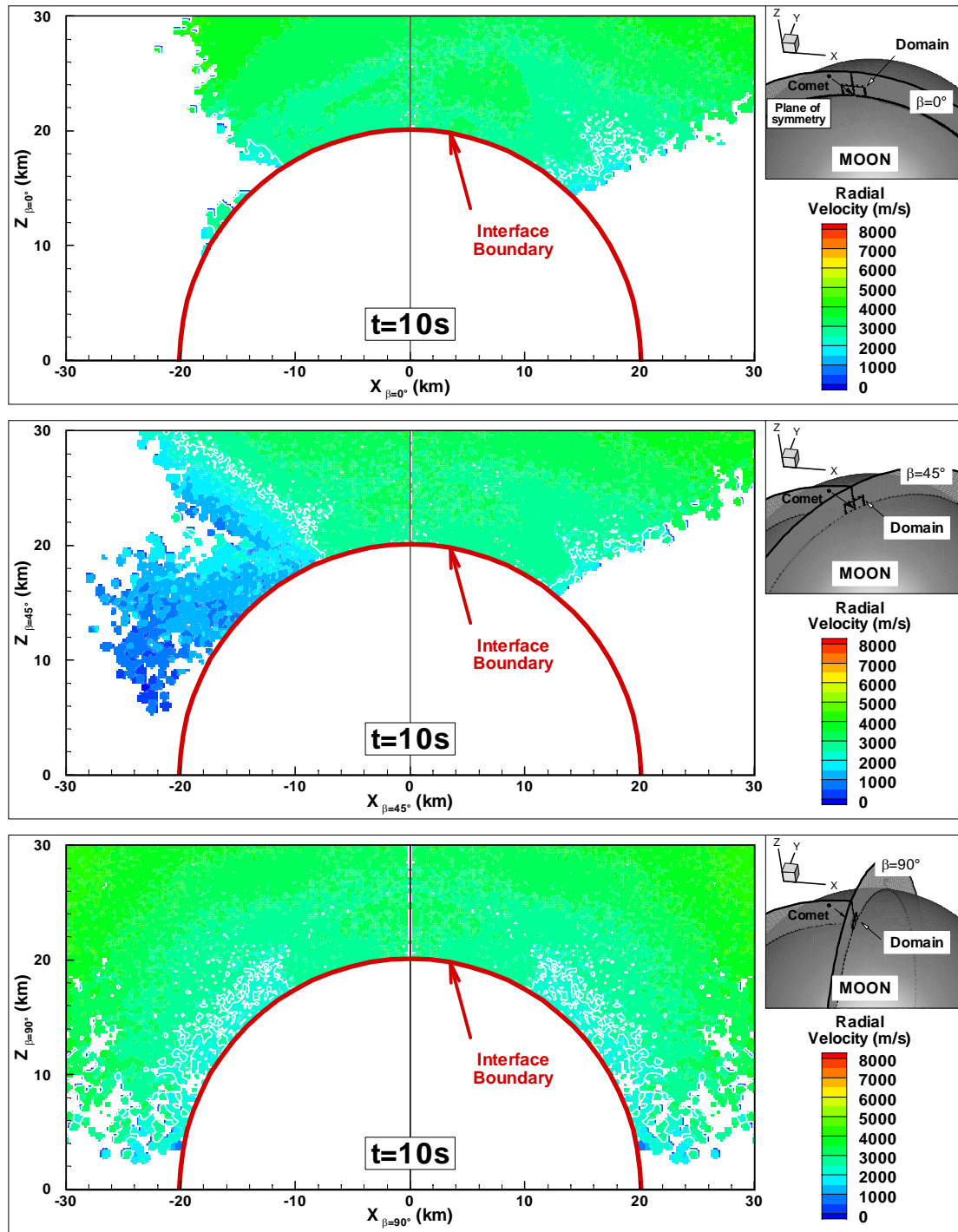


Figure 5-55 Near-field radial velocity contours 10 s after impact in the plane of symmetry (top), 45° off the symmetry plane (middle) and perpendicular to the plane of symmetry (bottom).

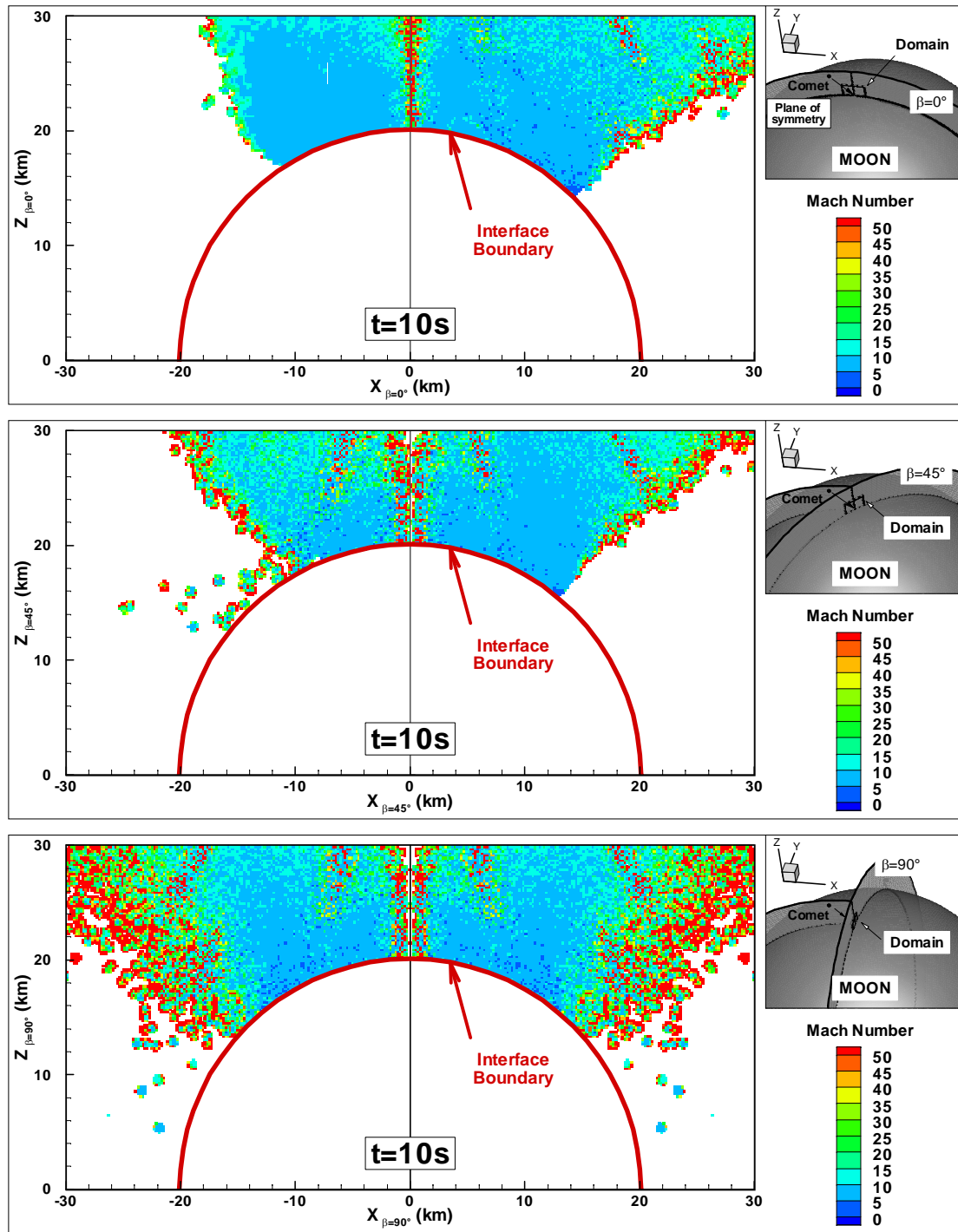


Figure 5-56 Near-field Mach number contours 10 s after impact in the plane of symmetry (top), 45° off the symmetry plane (middle) and perpendicular to the plane of symmetry (bottom).

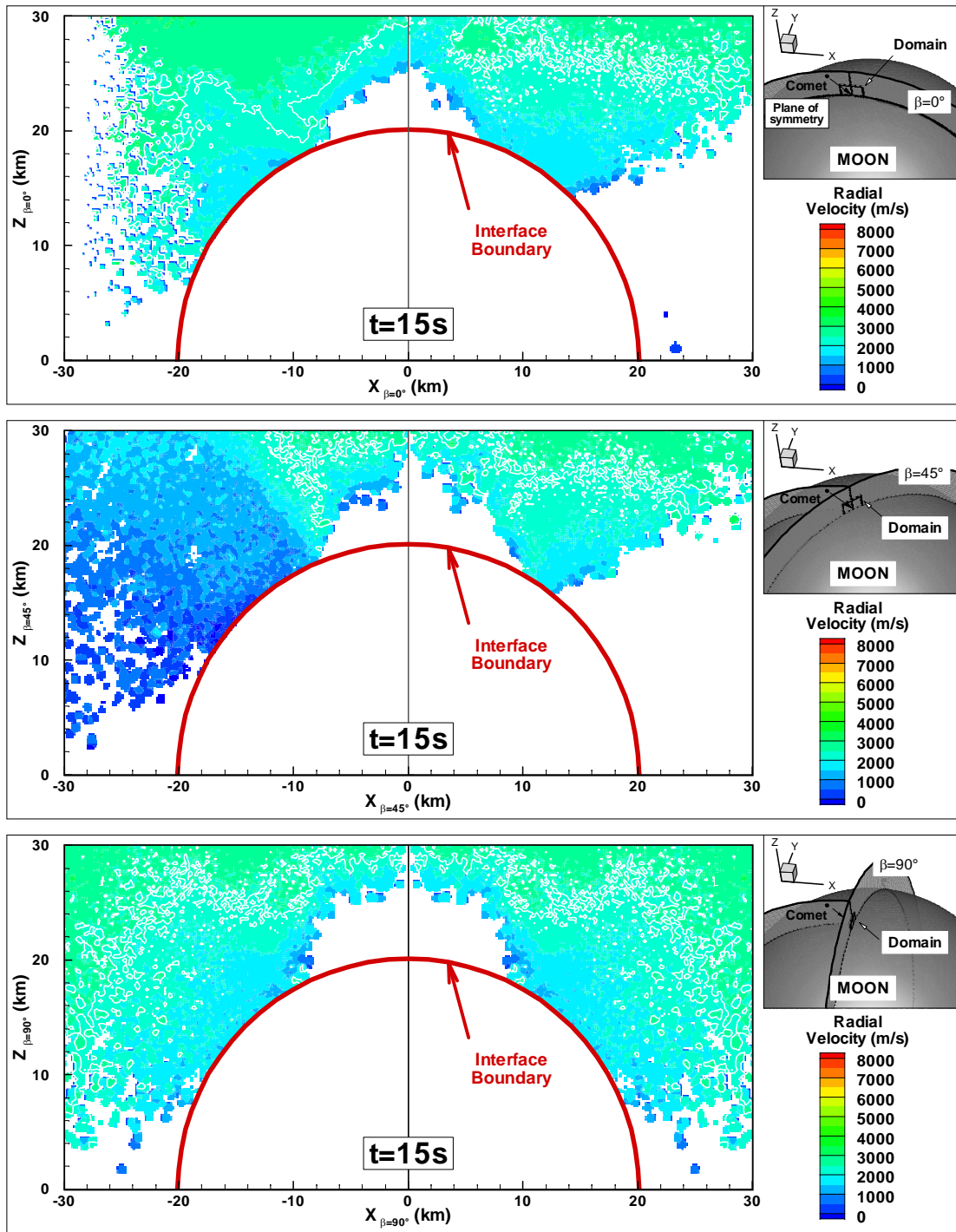


Figure 5-57 Near-field radial velocity contours 15 s after impact in the plane of symmetry (top),  $45^\circ$  off the symmetry plane (middle) and perpendicular to the plane of symmetry (bottom).

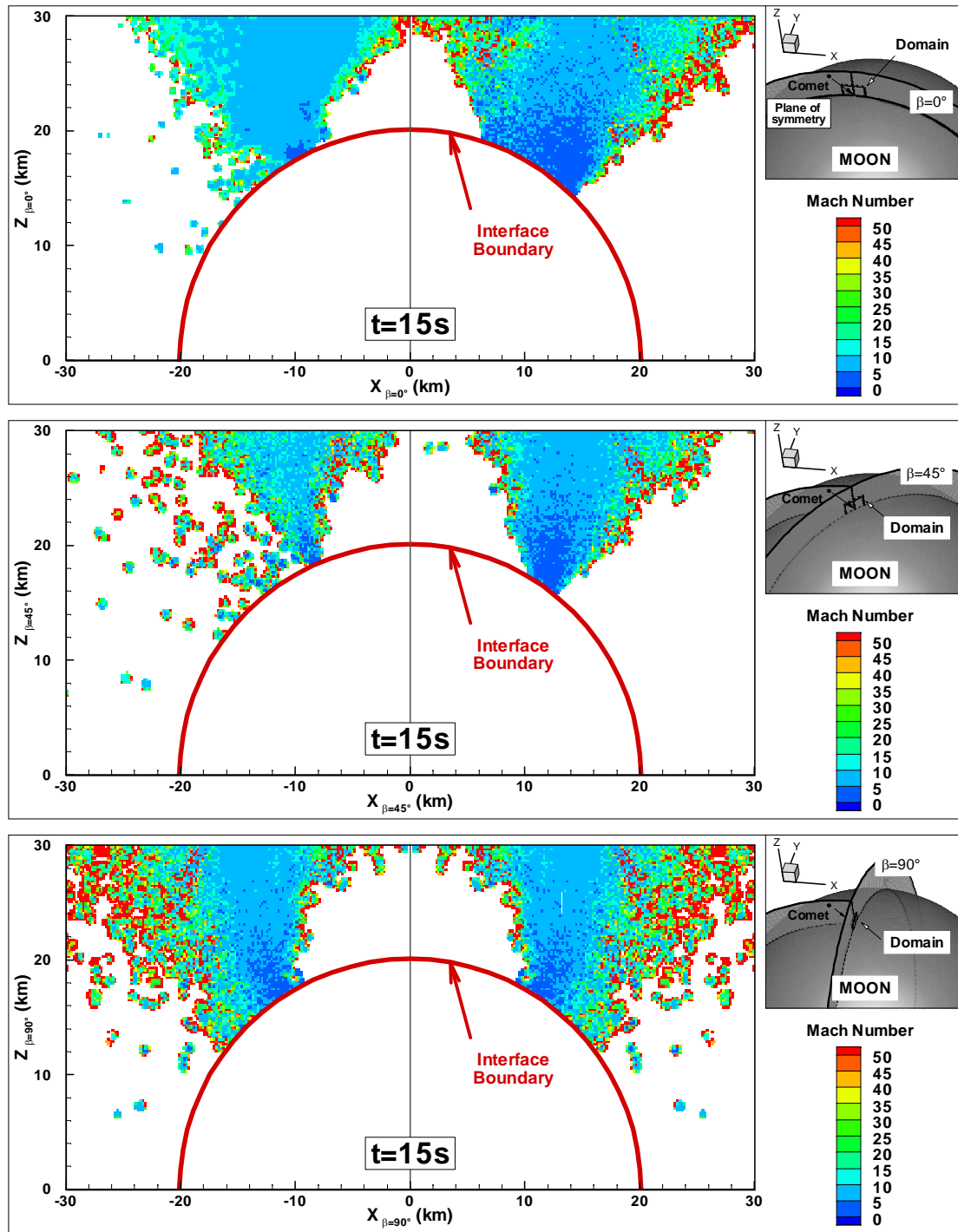


Figure 5-58 Near-field Mach number contours 15 s after impact in the plane of symmetry (top),  $45^\circ$  off the symmetry plane (middle) and perpendicular to the plane of symmetry (bottom).

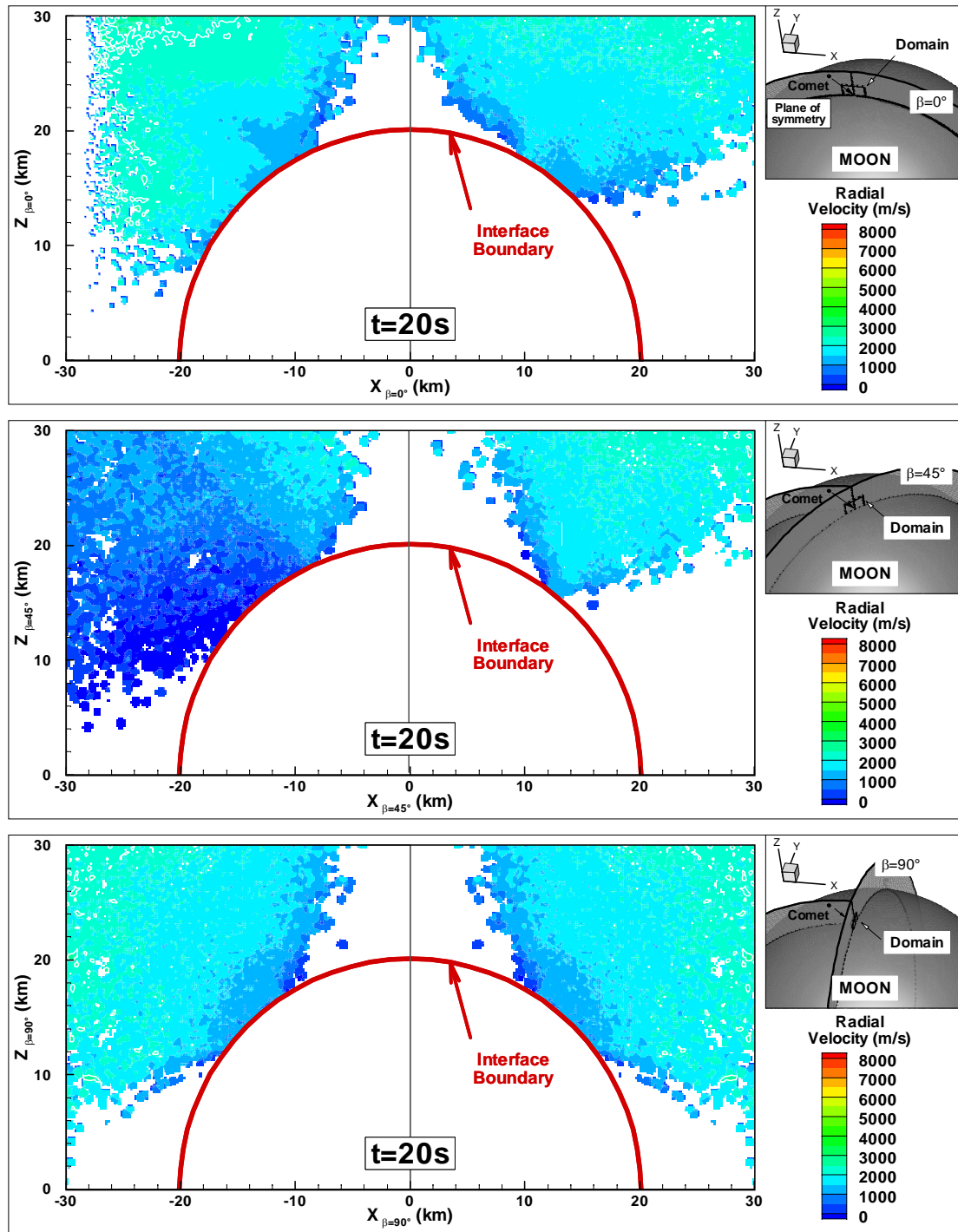


Figure 5-59 Near-field radial velocity contours 20 s after impact in the plane of symmetry (top), 45° off the symmetry plane (middle) and perpendicular to the plane of symmetry (bottom).



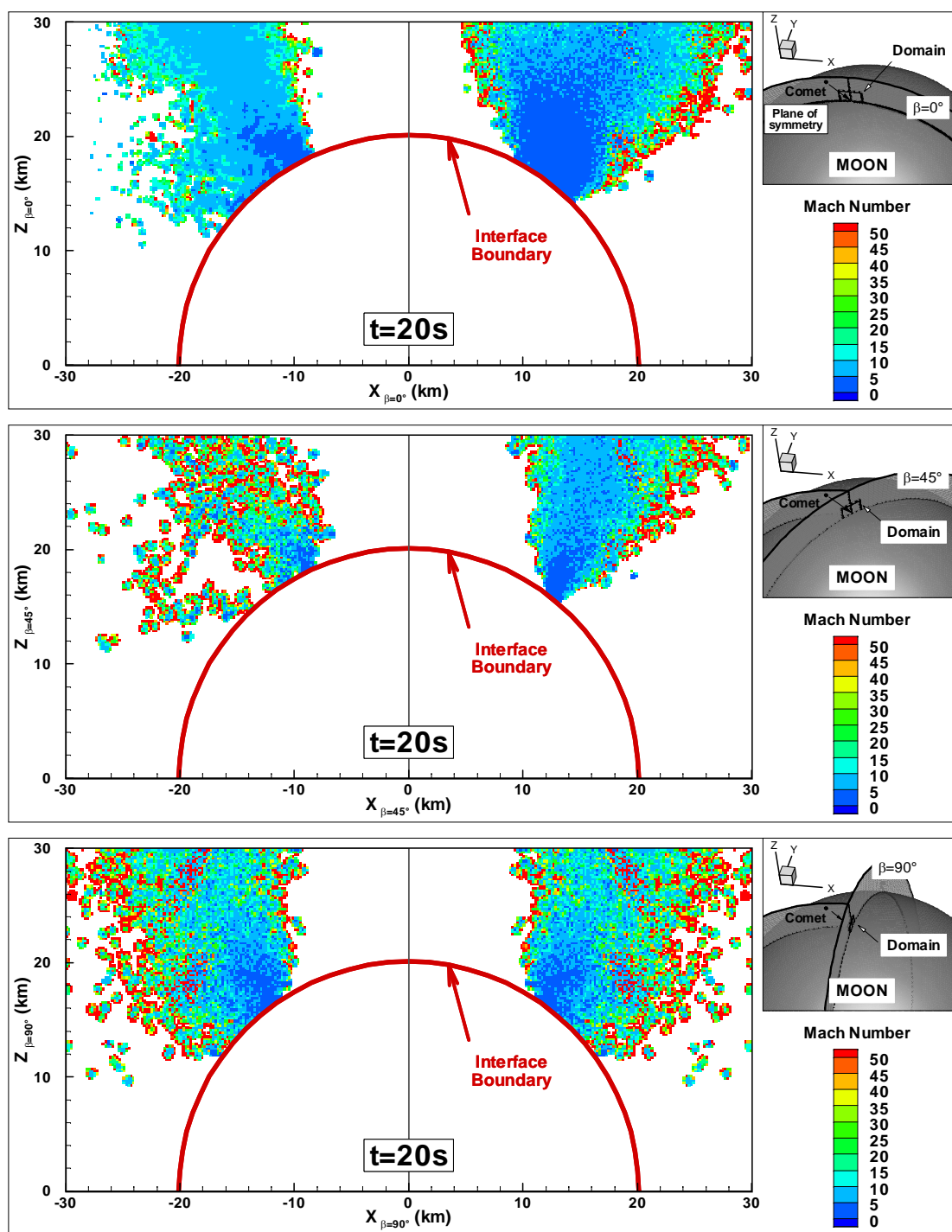


Figure 5-60 Near-field Mach contours 20 s after impact in the plane of symmetry (top),  $45^\circ$  off the symmetry plane (middle) and perpendicular to the plane of symmetry (bottom).



#### 5.4.2.5 Knudsen Numbers

Two different Knudsen numbers are being considered in the present section: the Knudsen number based on the mean free path and the Knudsen number based on the cell size. In both cases, the reference length scale is the density gradient length. The density gradient length that would optimally be used is in the direction of the flow but because our interpolated data is on a 2D Cartesian grid, we conservatively approximate the density gradient as the maximum between the value for the density gradient in the horizontal ( $X_\beta$ ) and vertical directions ( $Z_\beta$ ). The Knudsen number based on the mean free path can help determine the level of rarefaction within the plume while the Knudsen number based on the cell size can help determine if the cell size appropriately captures the gradients of the flow.

The mean free path of the flow was calculated using Eq. (5.5) for an equilibrium gas.

$$\lambda = \frac{1}{\sqrt{2}\pi d^2 n} \quad (5.5)$$

where  $\pi d^2$  is the cross-section of the gas in the Hard Sphere (HS) model ( $d = 3.9 \times 10^{-10}$  m for water) and  $n$  is the number density of the gas.

The Knudsen number based on the mean free path and the Knudsen number based on the cell size are calculated using Eq. (5.6) and Eq. (5.7), respectively.

$$Kn_\lambda = \frac{\lambda}{\rho} \max \left( \left| \frac{d\rho}{dX_\beta} \right|, \left| \frac{d\rho}{dZ_\beta} \right| \right) \quad (5.6)$$

$$Kn_{CELL} = \frac{\Delta x}{\rho} \max \left( \left| \frac{d\rho}{dX_\beta} \right|, \left| \frac{d\rho}{dZ_\beta} \right| \right) \quad (5.7)$$

The contours for Knudsen numbers based either on the mean free path or on the cell size 1, 5, 10, 15, and 20 s after impact are presented in Figure 5-61 to Figure 5-70 on the coarser grid also used to present the pressure results. Note that, the high values for both Knudsen numbers observed at all times at the edges of the water plume are artificial due to the differentiation between cells with and without water vapor. One second after impact, the Knudsen number based on the mean free path is as low as  $10^{-11}$  near the interface but increases up to  $10^{-9}$  further downstream (Figure 5-61). A gas flow is considered to be in the continuum regime as long as the

Knudsen number based on the mean free path is  $\leq 0.1$ . Therefore, most of the plume is in the continuum regime downstream of the interface one second after impact. The Knudsen number based on the cell size is smaller than 0.1 within most of the plume which means that the density gradient length is at least one order of magnitude larger than the cell size (Figure 5-62). Five seconds after impact, the contours for the Knudsen number based on the mean free path are much noisier with values ranging between  $10^{-9}$ - $10^{-10}$  (Figure 5-63) while the contours for the Knudsen number based on the cell size are in a similar range as that observed one second after impact (Figure 5-64). Ten seconds after impact, the Knudsen number based on the mean free path varies between  $10^{-9}$  away from the interface to  $10^{-10}$  near the interface within the dense regions of the plume and is of order  $10^{-5}$  in most parts of the low density regions of the plume (Figure 5-65). The Knudsen number based on the cell size is much noisier in the low density part of the plume where the gradient length looks to be of the same order as the cell size (Figure 5-66). This may however be due to the relatively high noise level in this region. Fifteen and twenty seconds after impact, both Knudsen numbers take on similar values as observed ten seconds after impact (Figure 5-67 to Figure 5-70).

The water vapor flow in the near field is mostly in the continuum regime at all times with Knudsen numbers based on the mean free path smaller than microns inside the plume. The standard recommendation of using cell sizes of the order the mean free path cannot be followed in the present DSMC simulations with cell sizes of the order of one hundred meters. However, the density gradient length of the flow is generally larger than the cell size and is therefore resolved in the present simulations. Indeed, the gradient-lengths are directly related to the SOVA cell size at the interface which is on the same scale as the cell size used in the present DSMC simulations.

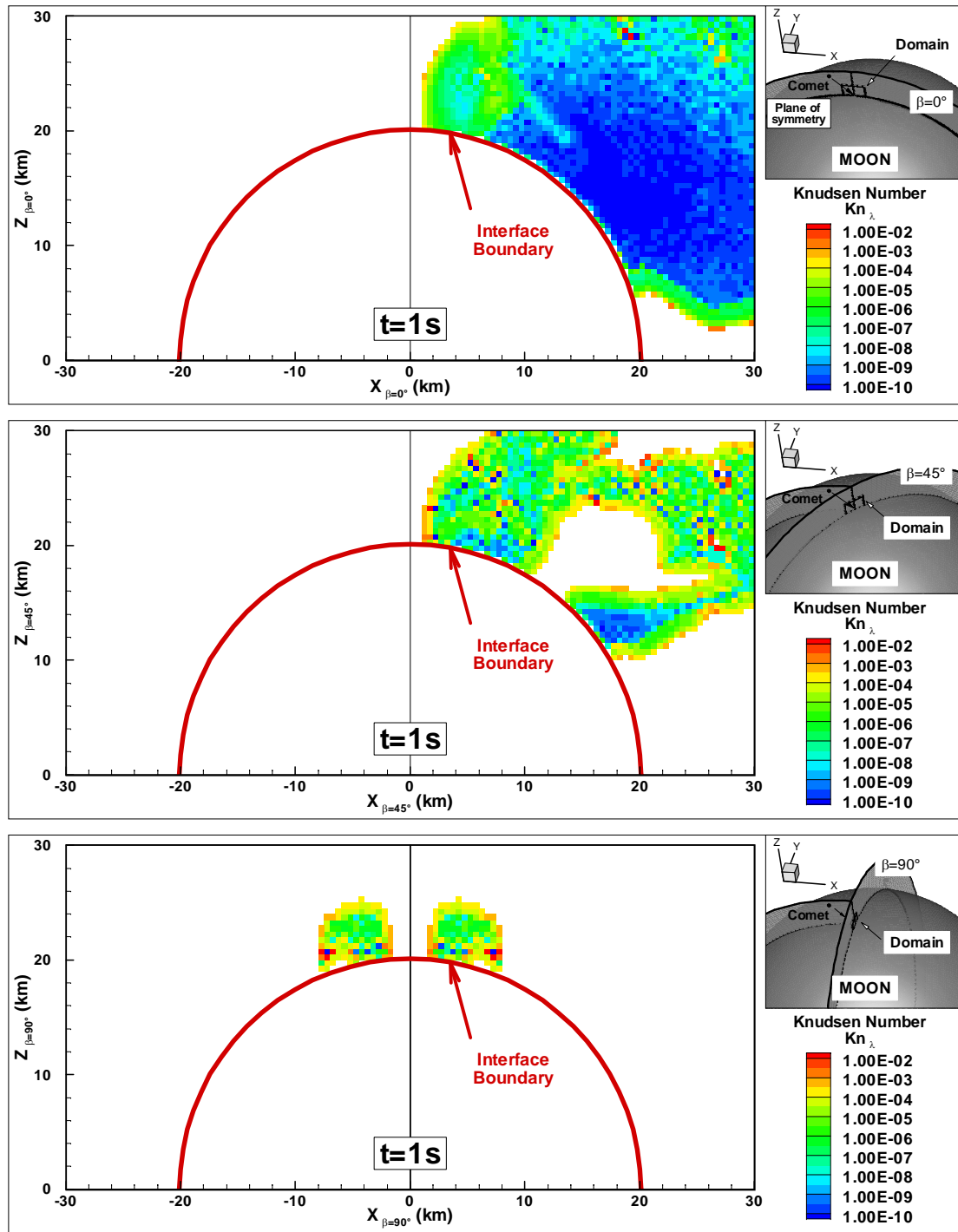


Figure 5-61 Near-field Knudsen number (based on the mean free path) contours 1 s after impact in the plane of symmetry (top), 45° off the symmetry plane (middle) and perpendicular to the plane of symmetry (bottom).

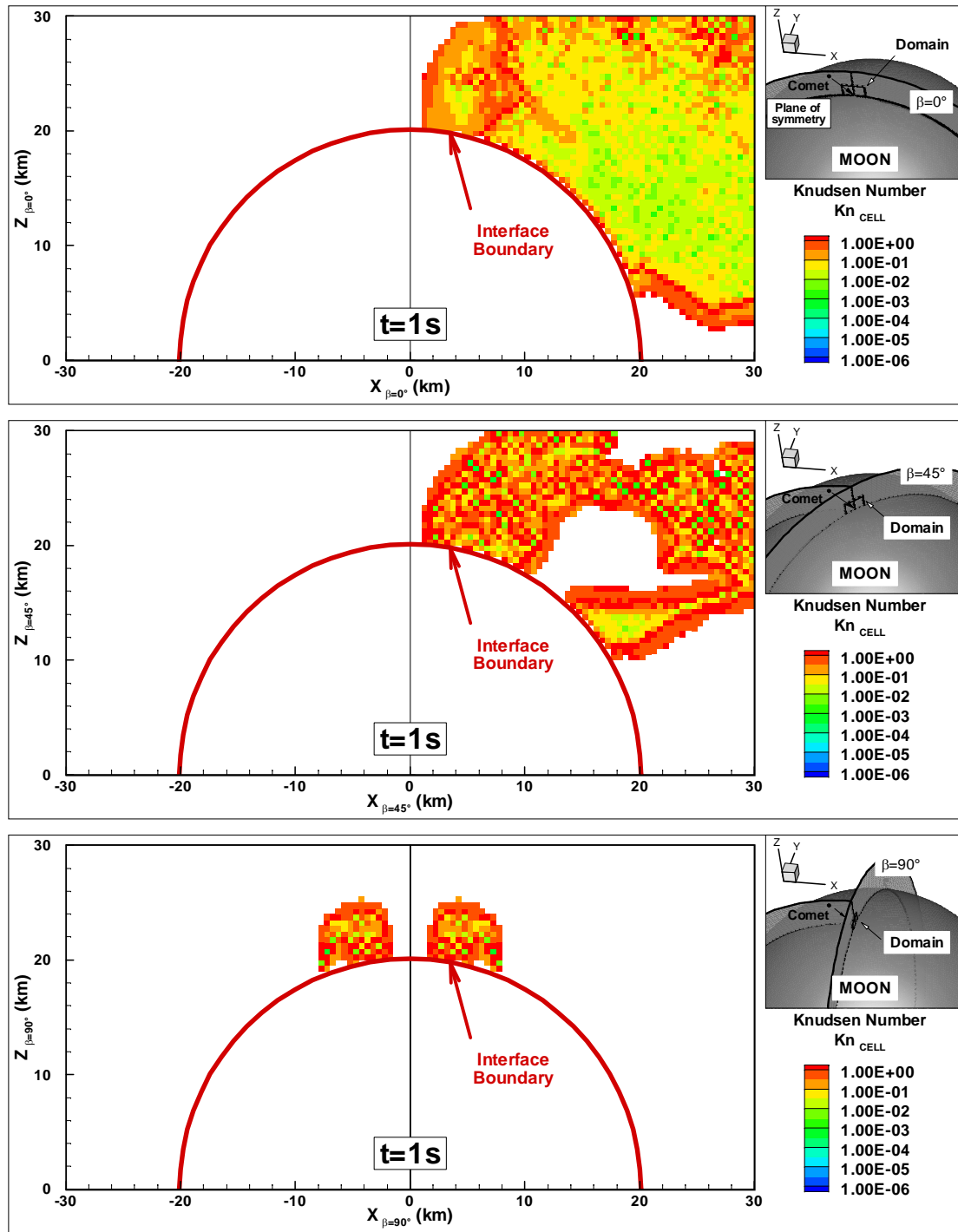


Figure 5-62 Near-field Knudsen number (based on the cell size) contours 1 s after impact in the plane of symmetry (top), 45° off the symmetry plane (middle) and perpendicular to the plane of symmetry (bottom).

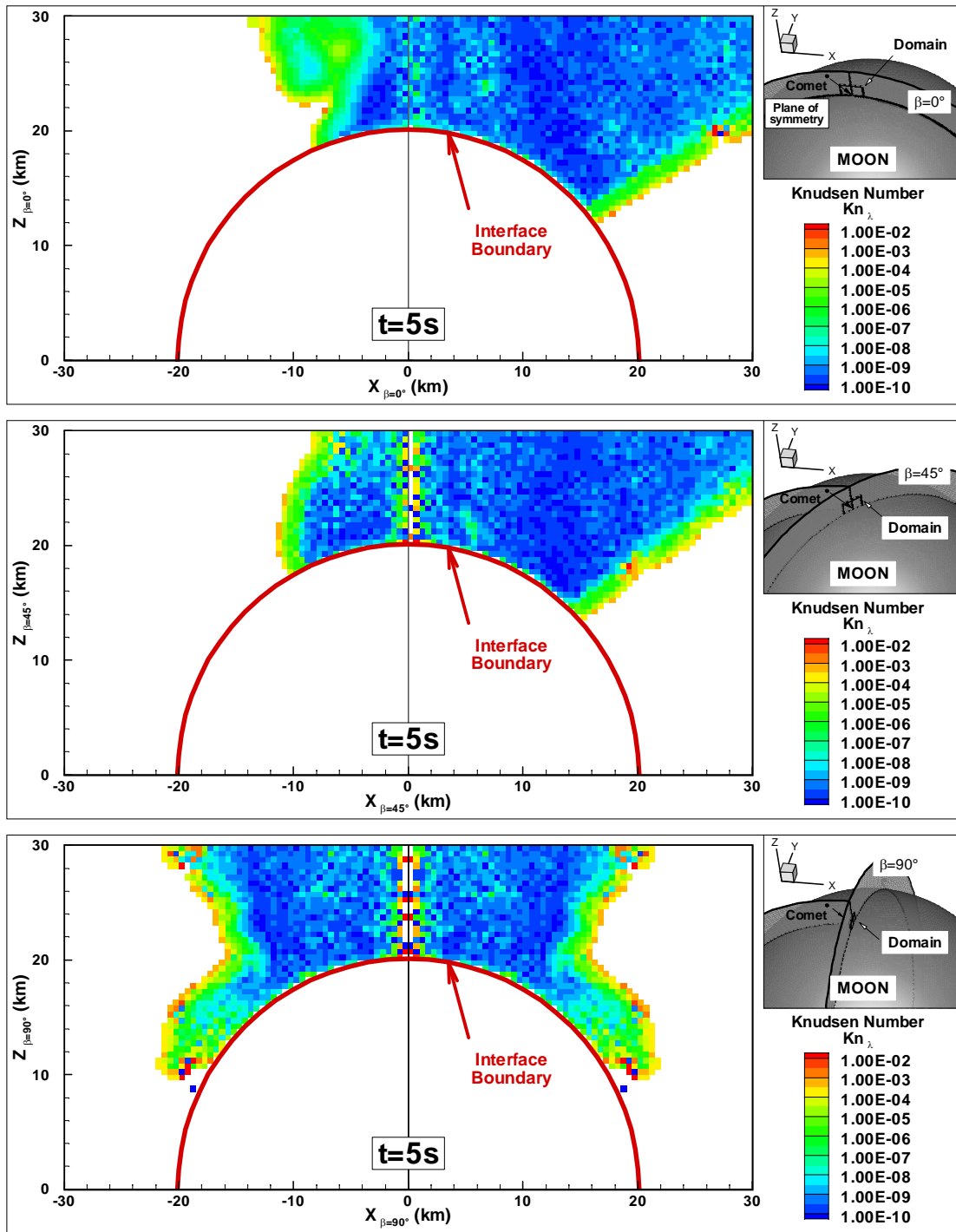


Figure 5-63 Near-field Knudsen number (based on the mean free path) contours 5 s after impact in the plane of symmetry (top), 45° off the symmetry plane (middle) and perpendicular to the plane of symmetry (bottom).

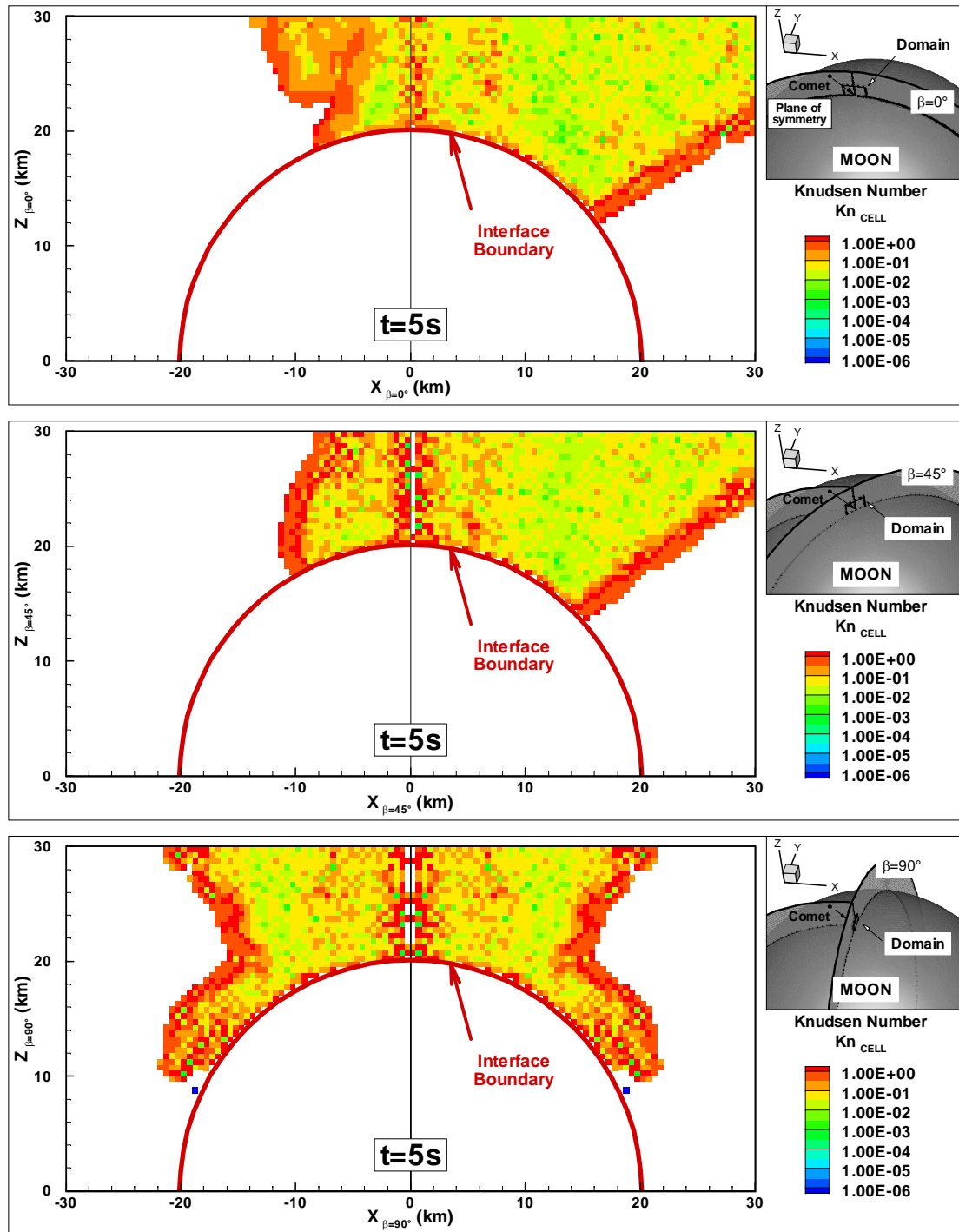


Figure 5-64 Near-field Knudsen number (based on the cell size) contours 5 s after impact in the plane of symmetry (top),  $45^\circ$  off the symmetry plane (middle) and perpendicular to the plane of symmetry (bottom).

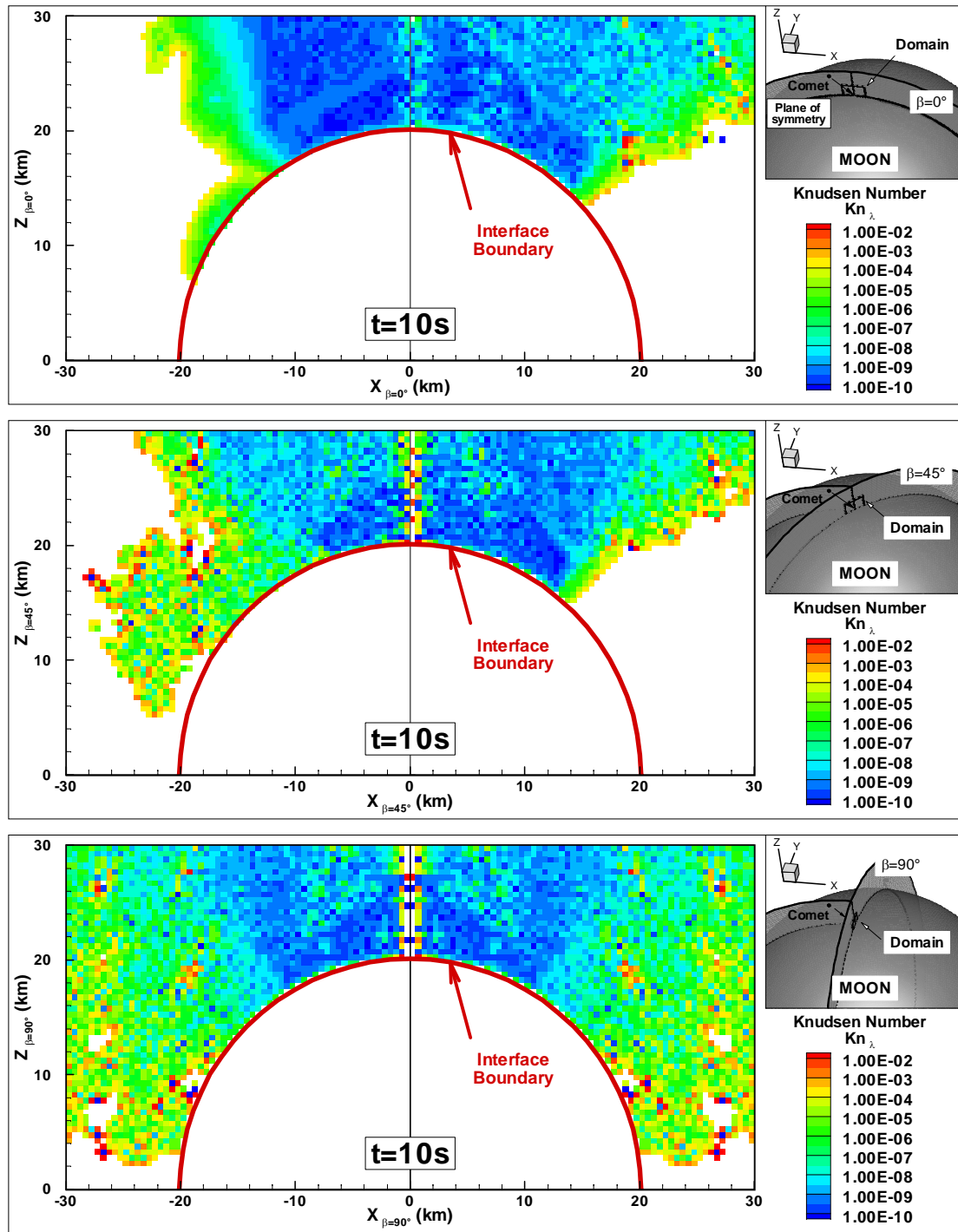


Figure 5-65 Near-field Knudsen number (based on the mean free path) contours 10 s after impact in the plane of symmetry (top),  $45^\circ$  off the symmetry plane (middle) and perpendicular to the plane of symmetry (bottom).

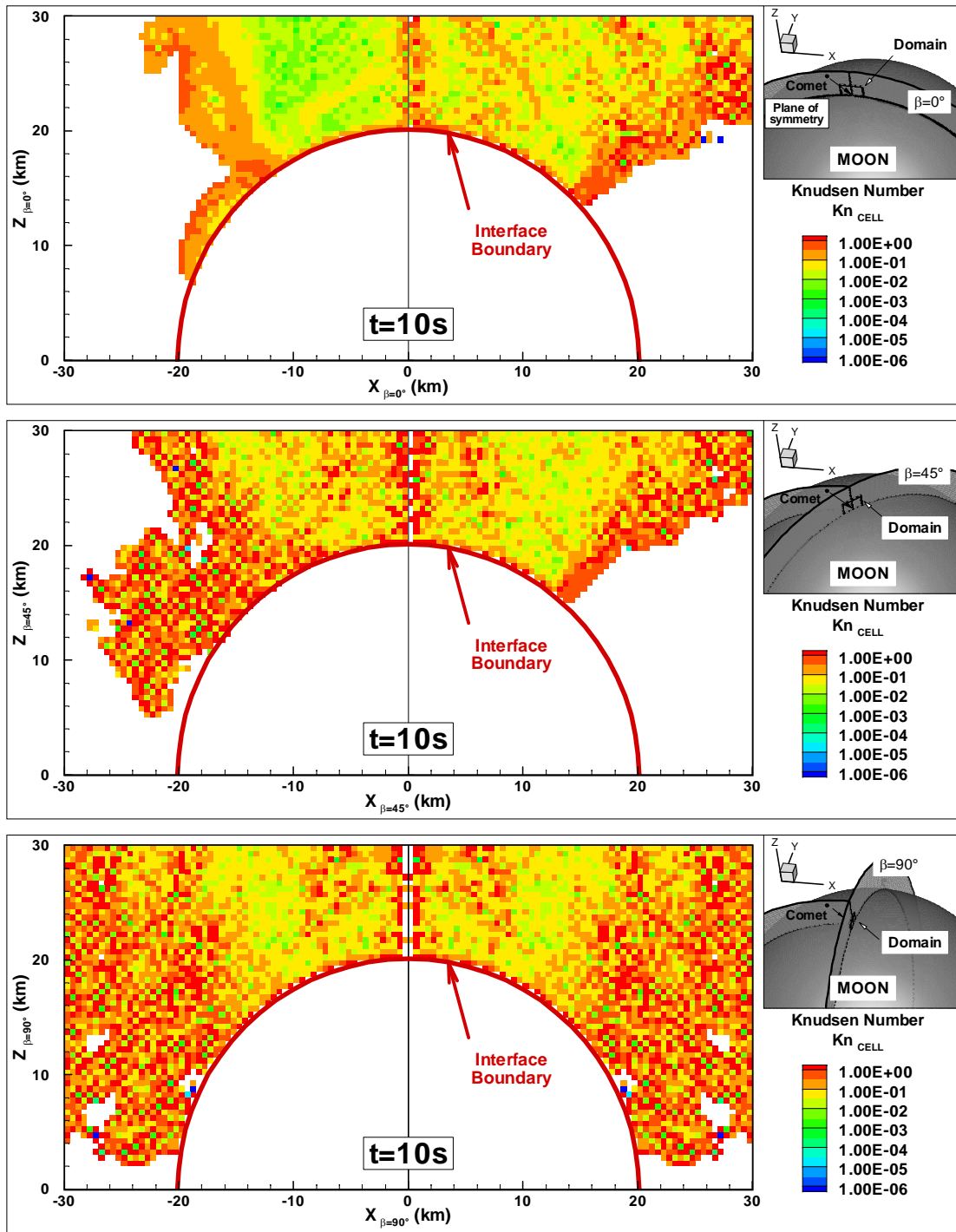


Figure 5-66 Near-field Knudsen number (based on the cell size) contours 10 s after impact in the plane of symmetry (top), 45° off the symmetry plane (middle) and perpendicular to the plane of symmetry (bottom).



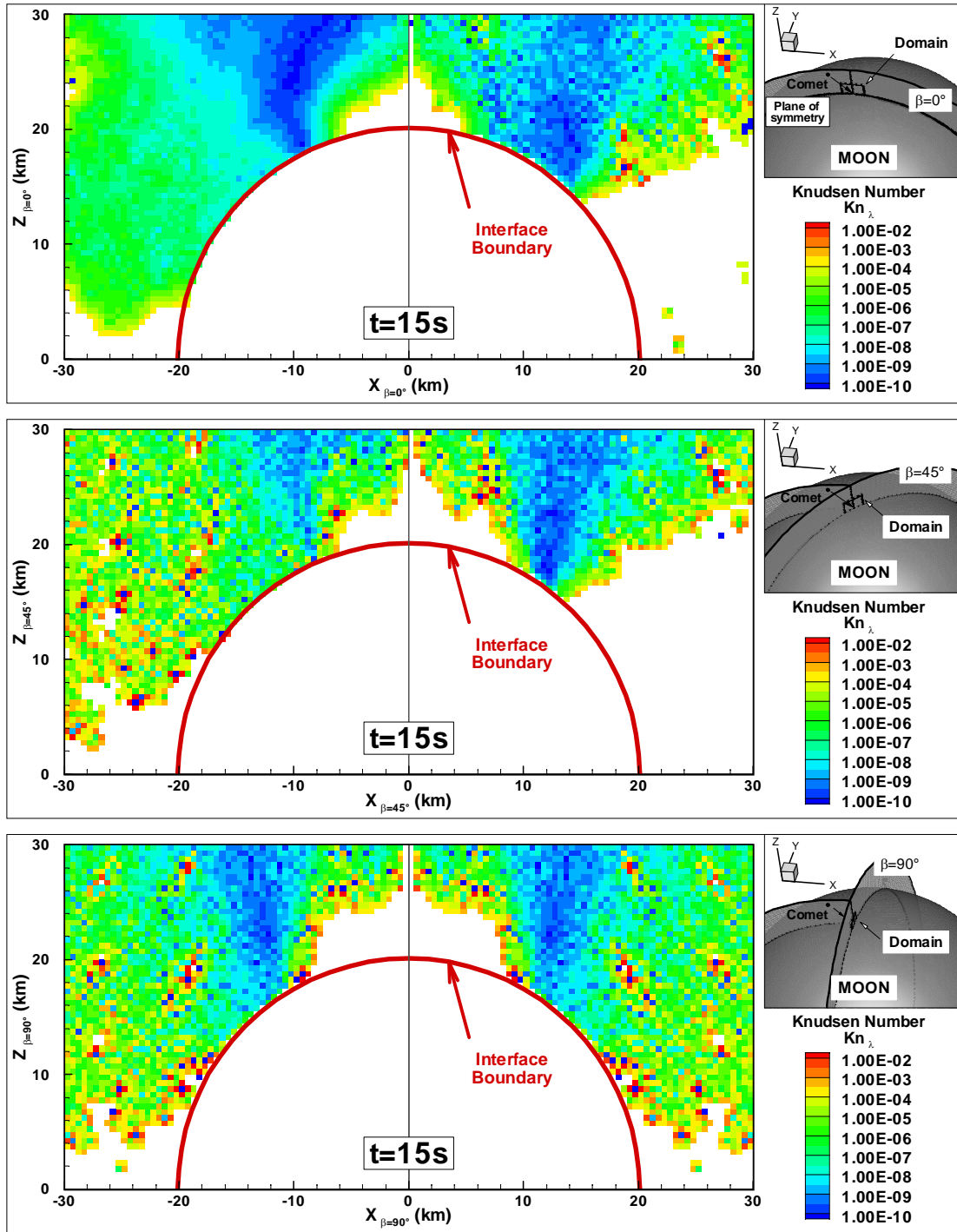


Figure 5-67 Near-field Knudsen number (based on the mean free path) contours 15 s after impact in the plane of symmetry (top),  $45^\circ$  off the symmetry plane (middle) and perpendicular to the plane of symmetry (bottom).

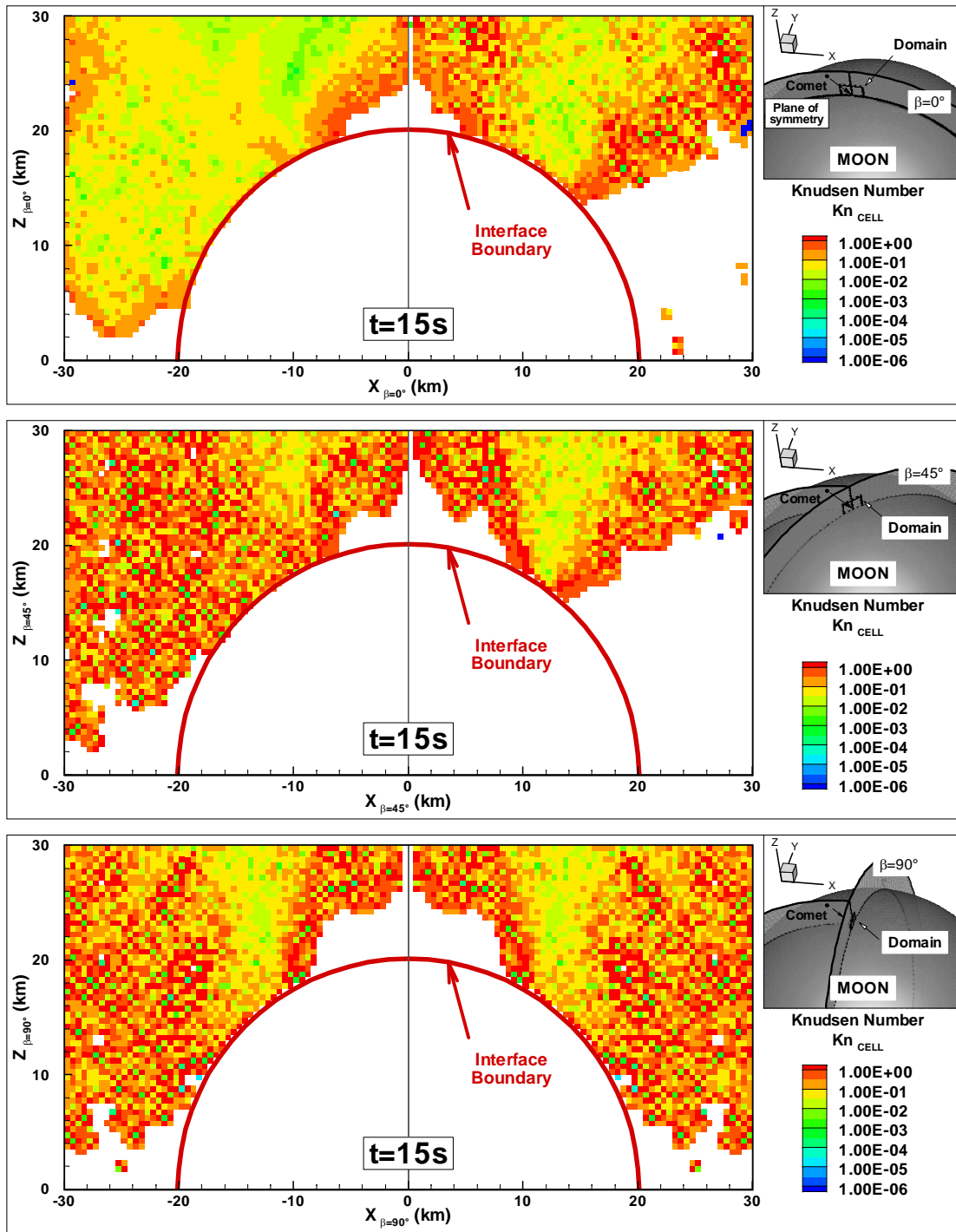


Figure 5-68 Near-field Knudsen number (based on the cell size) contours 15 s after impact in the plane of symmetry (top), 45° off the symmetry plane (middle) and perpendicular to the plane of symmetry (bottom).

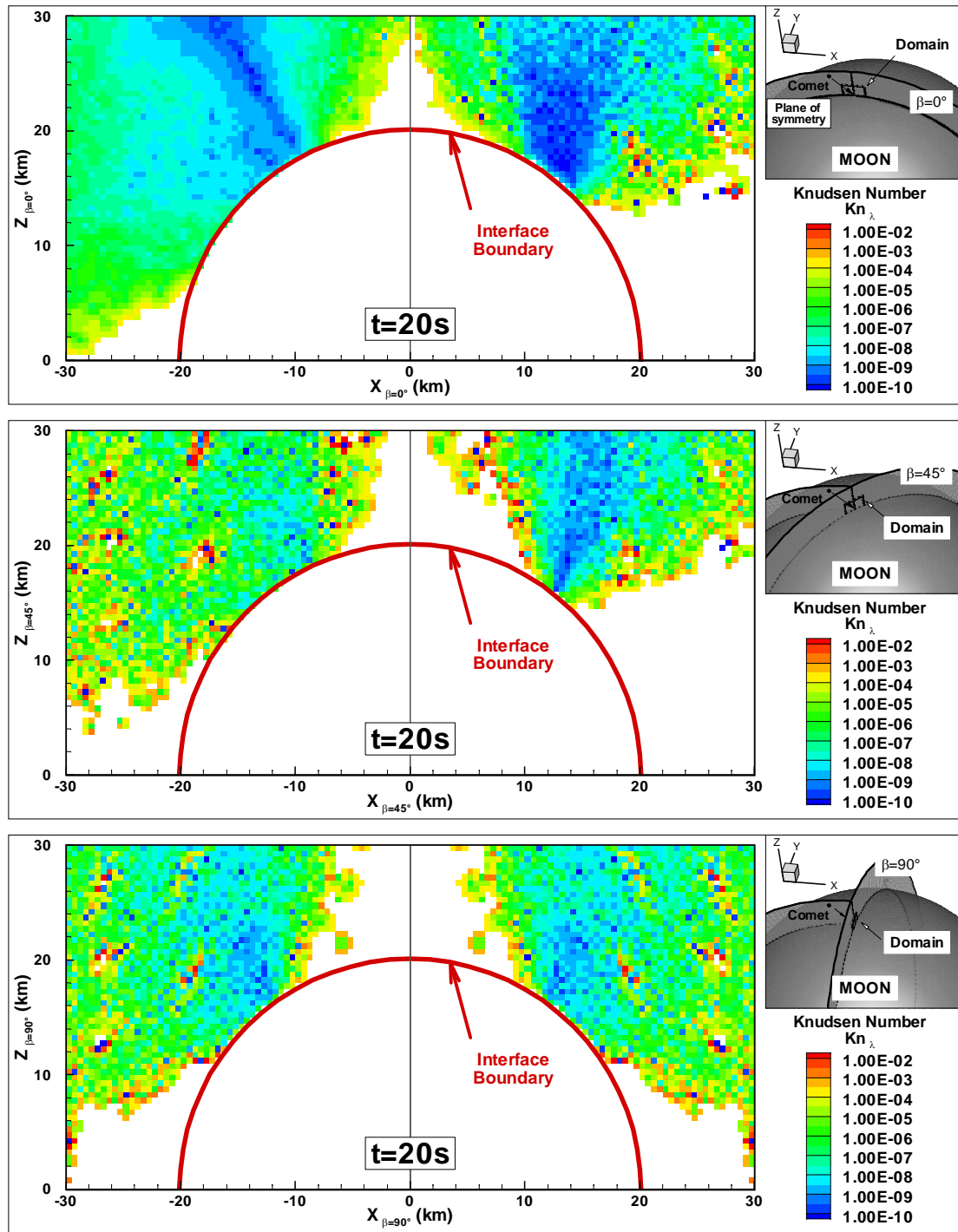


Figure 5-69 Near-field Knudsen number (based on the mean free path) contours 20 s after impact in the plane of symmetry (top), 45° off the symmetry plane (middle) and perpendicular to the plane of symmetry (bottom).

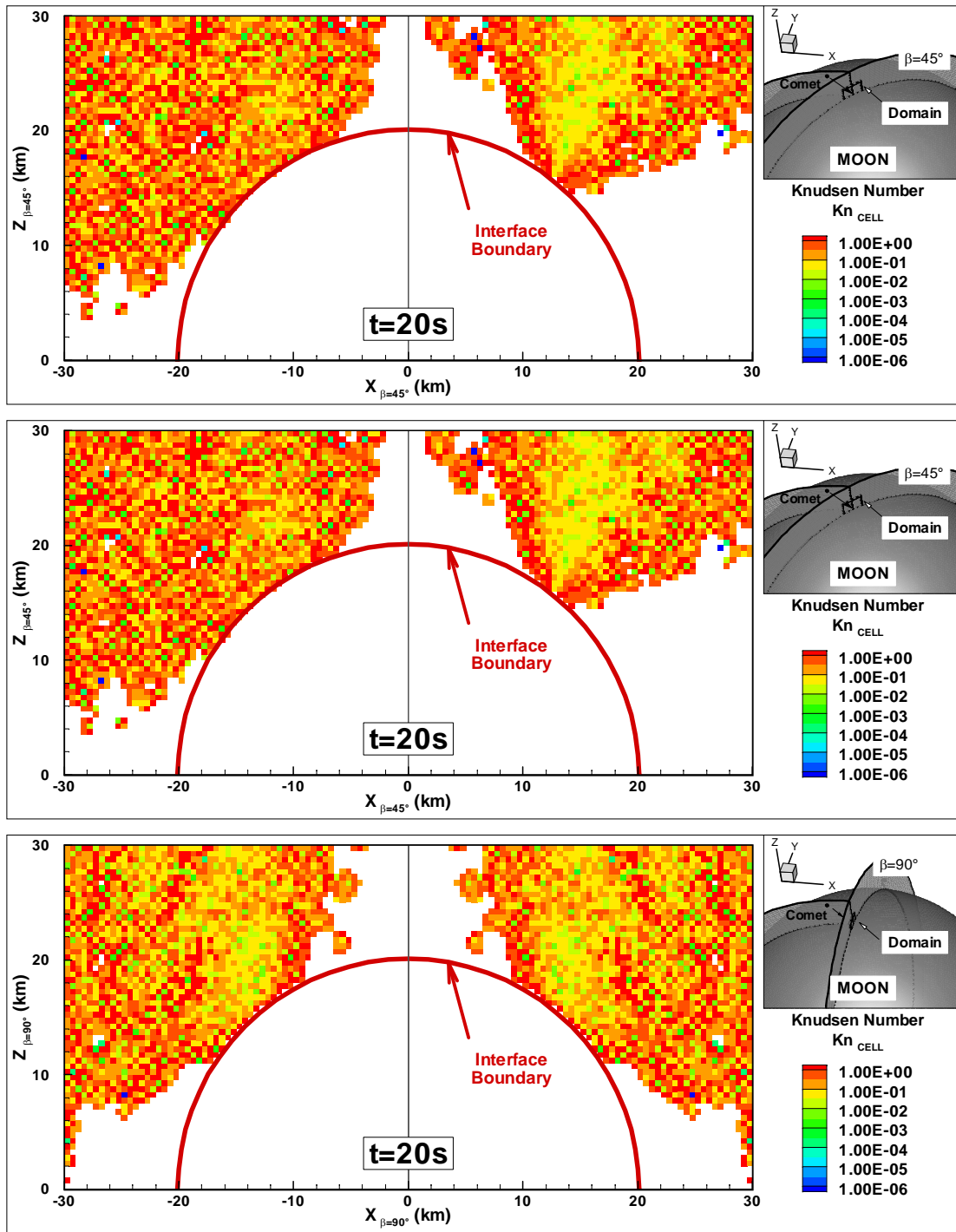


Figure 5-70 Near-field Knudsen number (based on the cell size) contours 20 s after impact in the plane of symmetry (top),  $45^\circ$  off the symmetry plane (middle) and perpendicular to the plane of symmetry (bottom).

### 5.4.3 Far Field Data

The near-field data presented in the previous section provided a fairly detailed description of the time evolution of the water vapor plume near the SOVA interface. The objective of the present section is to study the entire plume at two instants in time, 10 s and 20 s after the beginning of the impact (Figure 5-71 to Figure 5-78). In order to follow the water vapor plume as it expands away from the point of impact, the present simulations use the sequential unsteady multi-domain approach presented in Section 3.6. A series of four domains was used in the present simulations. The innermost domain, shown in the previous section, is  $32 \text{ km} \times 32 \text{ km} \times 180^\circ$  piece of pie with a cell size of 100 m and a timestep size of 0.0005 s. The first intermediate domain is a  $100 \text{ km} \times 100 \text{ km} \times 180^\circ$  piece of pie with a cell size of 250 m and a timestep size of 0.005 s. The second intermediate domain is a  $400 \text{ km} \times 400 \text{ km} \times 180^\circ$  piece of pie with a cell size of 1 km and a timestep size of 0.01 s. Finally, the outermost domain is a  $1000 \text{ km} \times 1000 \text{ km} \times 180^\circ$  piece of pie with a 2.5 km cell size and a 0.05 s timestep size. The boundary conditions for each domain are the same as the conditions used for the innermost domain (Section 5.2) except for the top and right wall boundary conditions for the outermost domain. In this domain, molecules that cross the top or right wall with a speed greater than 110% of the escape velocity are permanently deleted from the calculation. The other molecules are saved to a file to be read in at a later time in the full planetary domain to study the deposition of water in the lunar cold traps (see Chapter 6). The results in the present section are in a format similar to that used in Section 5.4.1. For each property, contour plots are shown in the plane of symmetry of the impact ( $\beta = 0^\circ$ ), in the  $45^\circ$  intermediate plane ( $\beta = 45^\circ$ ) and in the plane perpendicular to the plane of symmetry of the impact ( $\beta = 90^\circ$ ) (Figure 5-17). The present data has been interpolated using an “inverse distance weighting” scheme with a sphere of influence 2 km in radius for the 10 and 20 s data. The cell size in either direction for the interpolated contours is 2 km, 10 s and 20 s after impact. Also, in order to observe the full plume, the  $\beta = 45^\circ$  slice uses the DSMC data near  $45^\circ$  and  $135^\circ$  in azimuth and the  $\beta = 90^\circ$  slice uses the symmetry of the problem where the positive  $X_\beta$  data has been mirrored to obtain the data for negative  $X_\beta$ . With each contour plot, a small inset sub-figure shows the plane being considered. Contour plots for density, total temperature, radial velocity, and Knudsen number based on the mean free path are presented in the following sections.

#### 5.4.3.1 Ten Seconds after Impact

Ten seconds after impact, the water vapor plume is very different in the three planes being presently considered. The largest plume is observed in the symmetry plane where some of the fastest moving material has reached an altitude of  $\sim 500$  km. The plume also extends up to  $\sim 400$  km downrange and  $\sim 100$  km uprange of the point of impact, respectively. Because most of the plume is hypersonic, very little spread due to thermal motion can be observed so the downrange edge of the plume is relatively smooth and takes on the shape of an inverted cone in the near-field up to ( $X_{\beta=0^\circ} = 200$  km,  $Z_{\beta=0^\circ} = 80$  km). Up-range, the water vapor is mostly moving vertically and the uprange edge of the plume is not as well defined as the downrange edge possibly due to the fact that the flow carries less mass and less momentum in that direction. In the  $45^\circ$  intermediate plane (Figure 5-71b), the plume is noticeably smaller than in the symmetry plane. The main differences are observed far downstream of the point of impact where the full plume in the symmetry plane has been replaced by the two-sprays observed in the near-field one second after impact. However, the section of the plume located within 160 km of the point of impact is very similar to that observed in the symmetry plane. Overall, the fastest water vapor has reached an altitude of  $\sim 400$  km and the plume extends as far as  $\sim 350$  km downrange and  $\sim 50$  km uprange of the point of impact, respectively. In the intermediate plane, the downrange edge of the plume does resemble an inverted cone while the uprange edge is a near vertical line from afar. In the plane perpendicular to the impact plane (Figure 5-71c), the plume extent is the smallest and covers only a small fraction of the plume seen in the plane of symmetry. The fastest material has only reached an altitude of  $\sim 320$  km and most of the water vapor is within  $\sim 100$  km of the point of impact in the crossrange direction. Overall, the water vapor in this view looks like it is mostly moving straight up from the impact crater. One noticeable feature, at  $Z_{\beta=90^\circ} = \sim 100$  km, is the presence of three spikes: one directly above the point of impact and the other two off axis at  $X_{\beta=90^\circ} = \pm 50$  km.

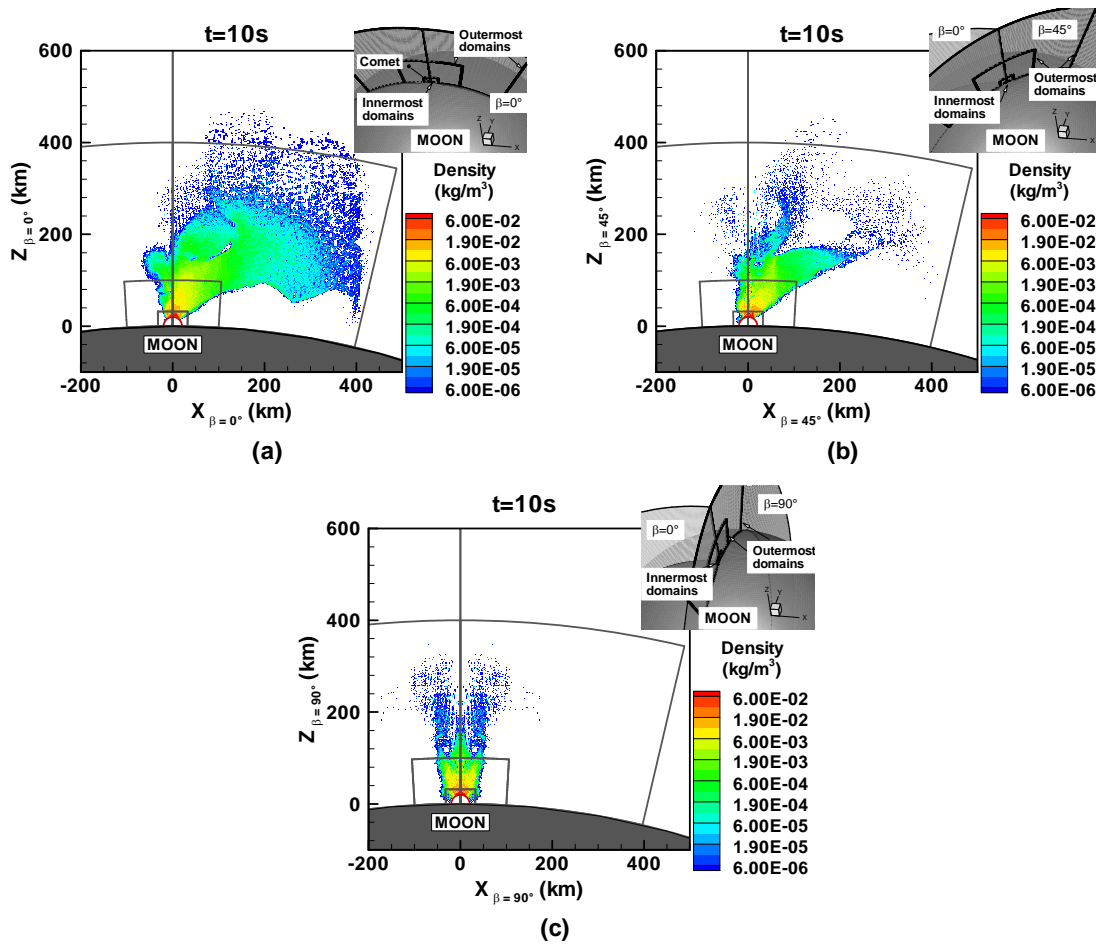


Figure 5-71 Density contours 10 s after impact in: (a) the symmetry plane, (b) 45° off the symmetry plane and (c) perpendicular to the plane of symmetry.

As was shown in Sections 5.4.1 and 5.4.2, most of the water vapor crosses the interface early on. However, because this material is also moving at large velocities (up to 50 km/s) into a vacuum, the expansion rate of the early plume material is such that ten seconds after impact, the densest material in the DSMC domain is observed near the interface with the SOVA hydrocode (Figure 5-71). In all three planes, the density decreases by about two orders of magnitude between the locations near the SOVA interface and the regions at an altitude of  $\sim 100$  km above the lunar surface.

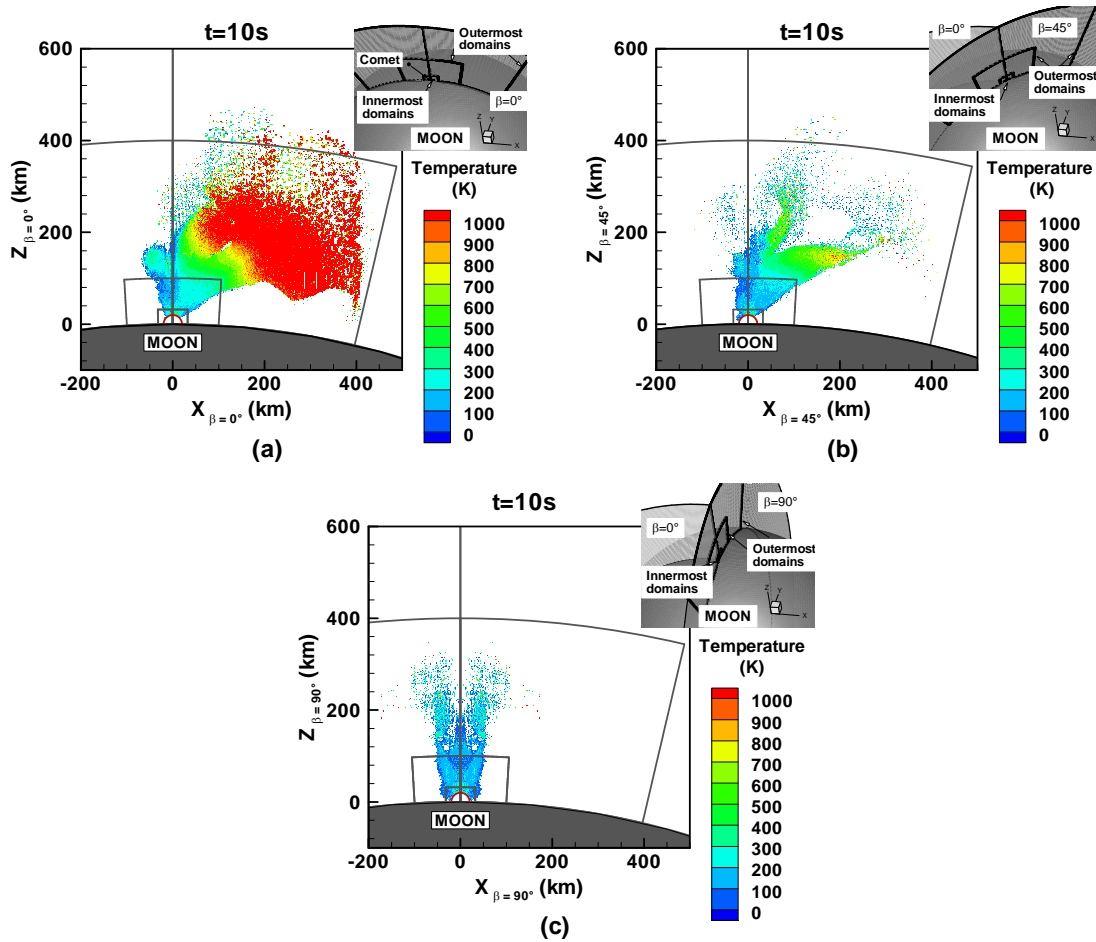


Figure 5-72 Total temperature contours 10 s after impact in: (a) the symmetry plane, (b) 45° off the symmetry plane and (c) perpendicular to the plane of symmetry.

The total temperature contours are shown in Figure 5-72. One of the most important features differentiating an oblique impact plume from a simple expansion flow is the temperature dependence on radial distance. In the present plume, more noticeably in the symmetry plane and in the 45° intermediate plane (Figure 5-72a and b), the water vapor is hottest downstream ( $> 1000$  K in the symmetry plane) and not upstream. The cooling of the flow associated with the expansion of the gas is not sufficient to overcome the initial temperature differences observed in the near-field. In Section 5.4.2, we saw that the gas temperature within the plume stabilizes around 250 K to 350 K from five seconds after impact. Therefore, due to the gas expansion, the entire plume is colder in the region between 32 and 100 km from the point of impact ( $< 300$  K).



The temperature of the water vapor in the plane perpendicular to the impact plane is very different from the temperature in the other two planes (Figure 5-72). Overall, the gas is colder than in the other two planes and the temperature is also much more uniform, being between  $\sim 100$  and  $\sim 300$  K.

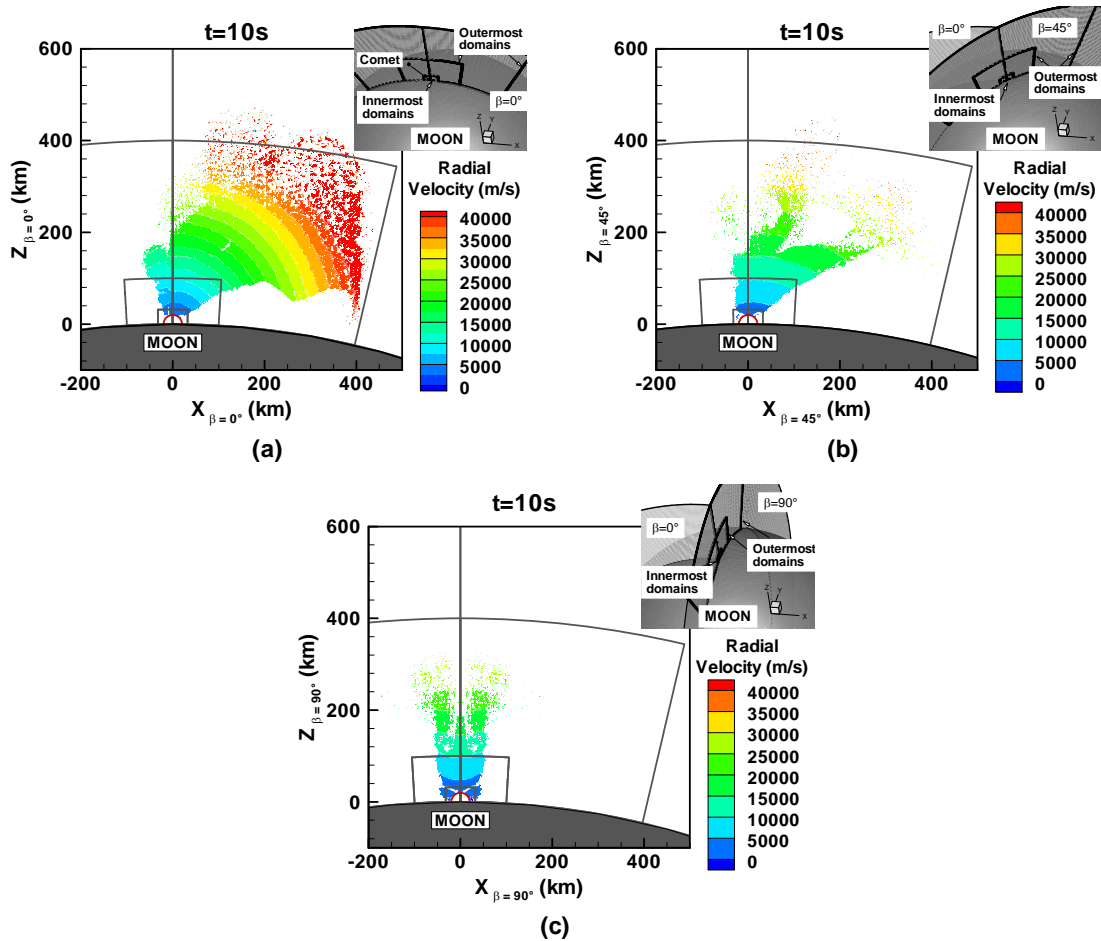


Figure 5-73 Radial velocity contours 10 s after impact in: (a) the symmetry plane, (b)  $45^\circ$  off the symmetry plane and (c) perpendicular to the plane of symmetry.

In the radial velocity contours, the white line seen near the SOVA interface represents the locations at which the radial velocity is equal to the escape velocity at the surface of the Moon. Overall, in the symmetry plane and in the intermediate plane, the radial velocity contours are nearly concentric with only some small local variations (Figure 5-73). The fastest vapor is

moving at more than 40 km/s and with the present temperature distribution most of the plume is hypersonic ( $M > 20$ ). In both planes, a very small fraction of the plume, near the interface at the outer edges of the plume, has a velocity smaller than the escape velocity. In the plane perpendicular to the symmetry plane, the radial velocity contours look somewhat inverted with the outer edges of the plume being slower than the center of the plume at the same altitude. Also, a small but noticeable region of the plume is moving in this plane with velocities slower than the Moon's escape velocity.

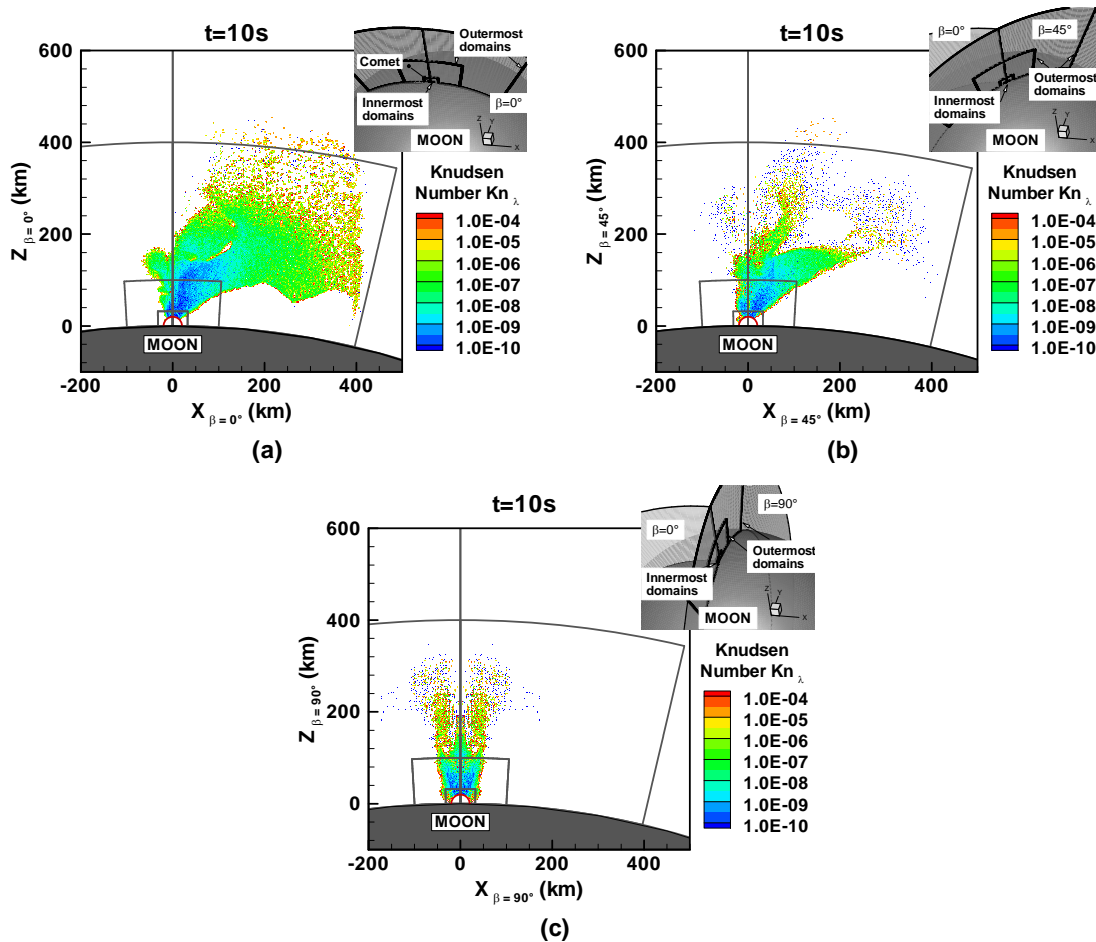


Figure 5-74 Knudsen number (based on the mean free path) contours 10 s after impact in: (a) the symmetry plane, (b) 45° off the symmetry plane and (c) perpendicular to the plane of symmetry.

Contours of the Knudsen number based on the mean free path presented in Figure 5-74 show that 10 s after impact, the water vapor plume is still entirely in the continuum regime. Overall, the Knudsen number increases with radial distance but remains lower than  $10^{-5}$ , which places the flow entirely in the continuum regime. In the continuum regions of the flow, the total number of collisions to be computed in the NTC method becomes prohibitively large. In the present simulations, we use a collision limiting scheme that enables us to simulate the continuum regions of the flow relatively efficiently (See Section 3.5). As the water vapor expands into the vacuum, the collision rate of the flow will begin to decrease and our collision limited scheme will revert to the standard DSMC collision routine. In the present simulations, because the water vapor plume is still in the continuum regime ten and twenty seconds after impact, the flow is collision limited within most of the plume ten and twenty seconds after impact.

#### ***5.4.3.2 Twenty Seconds after Impact***

Twenty seconds after impact, the shape of the water vapor plume is very similar to that observed ten seconds after impact. In fact, it resembles a rescaled image to that observed ten seconds after impact. The largest plume is observed in the symmetry plane where some of the fastest moving material has reached an altitude of  $\sim 900$  km (Figure 5-75a). The plume also extends up to  $\sim 800$  km downrange and  $\sim 100$  km uprange of the point of impact, respectively. The density is now greater away from the interface in the region of the plume directly above the rocky central peak material up to  $\sim 60$  km above the lunar surface. In the  $45^\circ$  intermediate plane (Figure 5-75b), the plume up to  $\sim 300$  km from the point of impact is very similar to that observed in the symmetry plane. Overall, the fastest water vapor has reached an altitude of  $\sim 800$  km and the plume extends as far as  $\sim 600$  km downrange and  $\sim 80$  km uprange from the point of impact, respectively. In the intermediate plane, the density contours are again decreasing with altitude with the maximum density observed above the rocky central peak material ( $0.01 \text{ kg/m}^3$ ). In the plane perpendicular to the impact plane (Figure 5-75c), the main plume only covers a fifth to a sixth of the surface area of the plume in the symmetry plane. The fastest material has reached an altitude of  $\sim 600$  km and most of the water vapor is within  $\sim 200$  km of the point of impact in the crossrange direction. Overall, the water vapor mostly moves straight up from the impact region and most of the water is located within  $\sim 300$  km of the point of impact in that plane. In all three

planes, as the water vapor continues to expand, the density of a given section of the plume has decreased by at least a factor of eight as compared to ten seconds after impact.

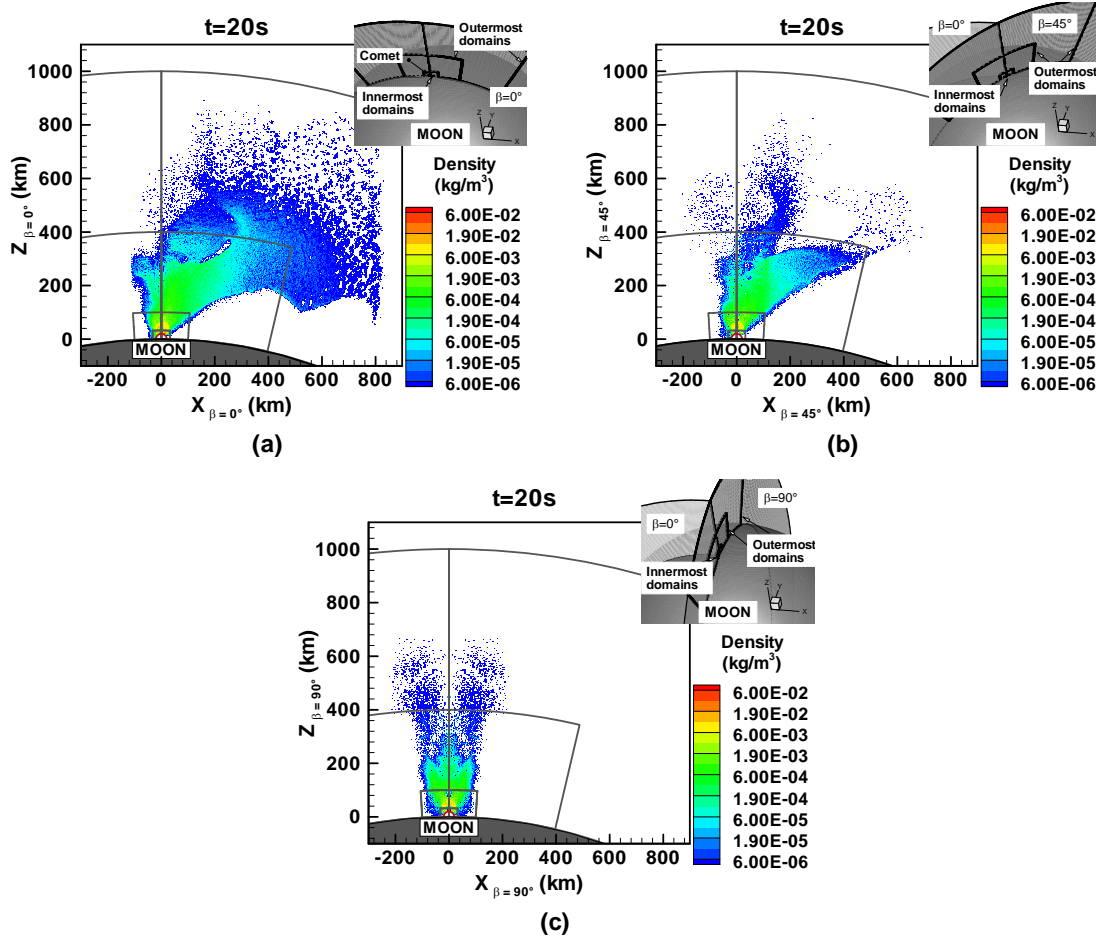


Figure 5-75 Density contours 20 s after impact in: (a) the symmetry plane, (b) 45° off the symmetry plane and (c) perpendicular to the plane of symmetry.

Total temperature contours, twenty seconds after impact, are shown in Figure 5-76. The region located 60 km above the point of impact where the relatively denser material was observed above the rocky central peak material is relatively warmer than the water vapor directly above or below it (Figure 5-76). The hottest temperatures are observed in the plane of symmetry of the impact where the downstream part of the plume still remains hotter than 1000 K. Overall, the

cooling rate of the water vapor appears to be relatively slow with the hot downstream material cooling by only a few tens of Kelvins between 10 s and 20 s after impact.

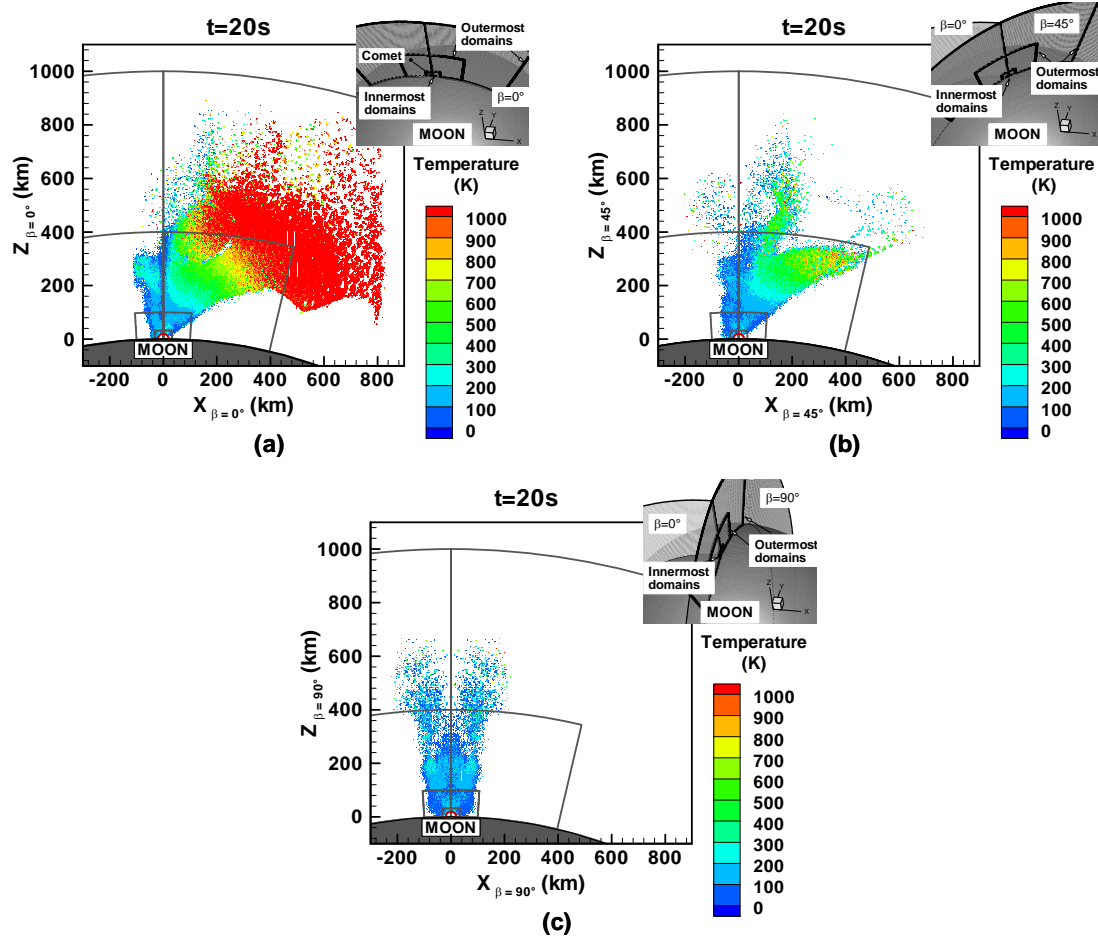


Figure 5-76 Total temperature contours 20 s after impact in: (a) the symmetry plane, (b) 45° off the symmetry plane and (c) perpendicular to the plane of symmetry.

Similar to the earlier time, but now in all three planes, twenty seconds after impact, the radial velocity contours appear to be near concentric circles with the fastest material moving at more than 40 km/s (Figure 5-77). The flow remains mostly in the hypersonic regime twenty seconds after impact with the smallest Mach numbers being observed near the interface with the SOVA hydrocode where the water vapor is the slowest ( $M \sim 5$  and  $V_r < 2$  km/s). The vapor with a radial velocity smaller than escape velocity has now reached the boundary of the innermost

domain. Note that in the intermediate plane, this region is much more prominent uprange of the point of impact than downrange.

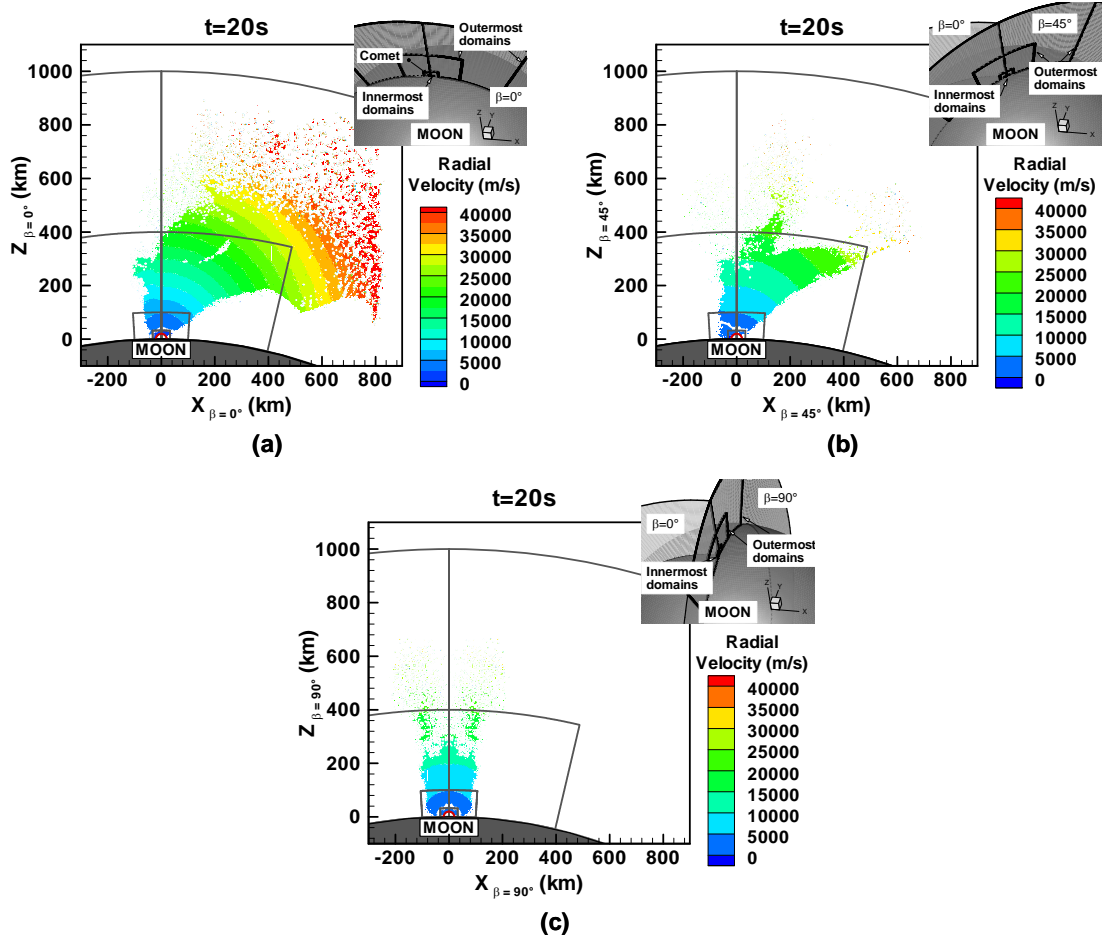


Figure 5-77 Radial velocity contours 20 s after impact in: (a) the symmetry plane, (b) 45° off the symmetry plane and (c) perpendicular to the plane of symmetry.

As the water vapor continues to expand into the vacuum, the Knudsen number based on the mean free path within the vapor plume continues to decrease (Figure 5-78). In some parts of the downstream section of the plume, the Knudsen number is now greater than  $2 \times 10^{-5}$  but the entire plume still remains in the continuum regime as far as 800 km from the point of impact.

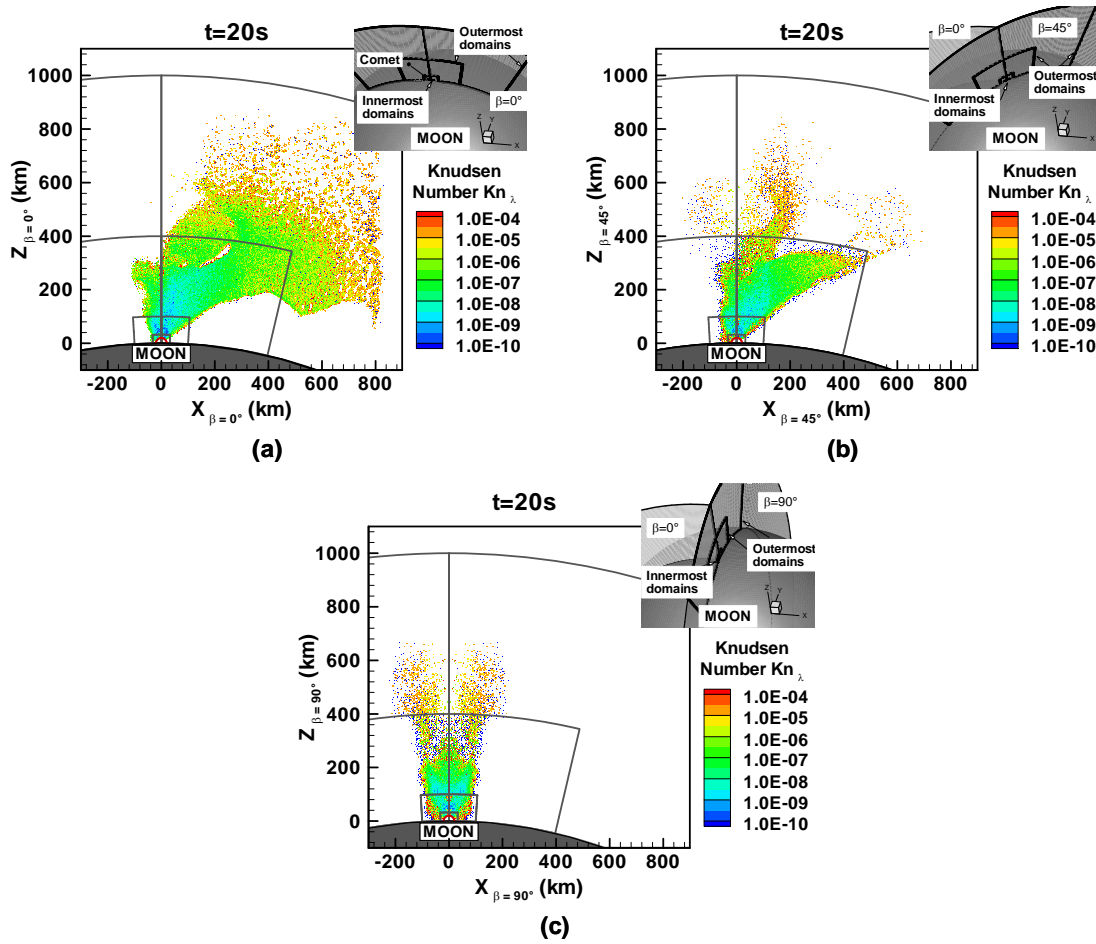


Figure 5-78 Knudsen number (based on the mean free path) contours 20 s after impact in: (a) the symmetry plane, (b)  $45^\circ$  off the symmetry plane and (c) perpendicular to the plane of symmetry.

## Chapter 6

### Circum-Lunar Flow Results

#### 6.1 OVERVIEW

After an icy comet impact on the Moon, some of the cometary water will remain within the sphere of influence of the Moon's gravity field and fall back onto the lunar surface. Due to large variations in the lunar surface temperature, those remaining water molecules will start a slow process of migrating around the Moon as the water molecules readily hop off the hot dayside surface and stick on the colder surfaces. During their migration, molecules may be destroyed while in flight due to photodestruction processes or be lost due to escape. However, some water molecules will land and possibly accumulate into sizeable deposits inside the lunar cold traps where they will remain over geologic times (Crider and Vondrak, 2003). The objective of the present chapter is to simulate the amount of water captured in the polar cold traps after a comet impact on the Moon. In our DSMC simulations of the  $45^\circ$  oblique impact of a 1 km radius comet at 30 km/s (See Section 5.4), we found that most of the water crossed the top boundary of our outermost domain with velocities greater than escape velocity. In the present chapter, we are interested in the small fraction of water that is retained on the Moon after impact. Most of that water was part of the water vapor plume simulated in the DSMC domain in Chapter 5. However, not all of the water had crossed the SOVA interface after 21 s, and so we are also interested in the water that remained within the SOVA interface at the end of the SOVA calculation. Because we have no actual knowledge of the distribution of that water on (and below) the lunar surface at later times, we used a simple model to constrain how this water is released into the lunar atmosphere (See Section 6.4). Simulation parameters are presented in Section 6.2 while the results for the transport to the cold traps of the "vapor plume water" and of the "impact crater water" are presented in Section 6.3 and Section 6.4, respectively.



## 6.2 SIMULATION PARAMETERS

For both simulations of the migration of the water vapor plume and of the impact crater water, the DSMC computations simulated the Moon's entire water vapor atmosphere due to each respective source up to 10,000 km above the lunar surface. The present computations used  $250 \times 180 \times 360$  uniform cells in the  $r$ ,  $\theta$ ,  $\varphi$  directions, respectively, and the timestep was initially equal to 1 s and was increased gradually to 10 s. The simulations were run in parallel on TACC's Lonestar and Ranger supercomputers using 36 processors with a uniform domain decomposition among the processors. The surface temperature varied between 400 K at the subsolar point to 120 K on the nightside of the Moon as described in Eq. (3.4). Equation (3.5) provided the relationship between the residence time and the local surface temperature and the cold trap locations were given in Table 3-2. Finally, the photodissociation and photoionization probabilities were given in Eq. (3.6) assuming an optically thin atmosphere, so there was no reduction in the incident radiative flux through the atmosphere. Note that by accounting for such reduction in the incoming radiative flux, the lifetime of the transient atmosphere may be increases by several order of magnitudes (Vondrak, 1974).

For the simulations of the transport of the remaining water vapor plume, the point of impact was located at  $45\text{S}^\circ$  latitude and at a longitude opposite to the longitude of the subsolar point at that time (i.e. at local midnight). The comet impact was oriented such that the downrange direction was toward the South Pole of the Moon. This location and orientation were judged to be favorable to the deposition process as some of the initial fallback material should land directly in the southern cold traps.

The location of the point of impact was parametrically varied in the "impact crater water" simulations in order to study its influence on the capture rate of water in the cold traps (See Section 6.4). Three different impact locations were chosen: at  $45\text{S}^\circ$  latitude and at a longitude opposite to the subsolar point longitude (i.e. at local midnight), at  $45\text{N}^\circ$  latitude and at the longitude of the subsolar point (i.e. at local noon), and at the North Pole. These three impact point locations have been considered because they cover a wide range of the parametric field in a relatively small number of runs, thus conserving our limited computational time.

### 6.3 MIGRATION OF THE WATER VAPOR PLUME TO THE POLAR COLD TRAPS

The present computations model the migration of the portion of the vapor plume simulated in the DSMC domain that is initially retained on the Moon. The water vapor that crossed the 20 km radius SOVA hemisphere in less than 21 s was simulated in successive domains extending as high as 1000 km above the lunar surface in Chapter 5. The computations presented in Chapter 5 were continued until most of the water had left the outermost domain and the majority of the remaining water molecules present in the domain were falling back to the surface. The portion of the water vapor plume that left the outermost domain used in Chapter 5 had to be computed in a larger domain. We chose to use a domain extending up to 50,000 km above the lunar surface, almost up to the Moon's Hill sphere (at a radius of  $\sim 60,000$  km), for the intermediate computations of the water vapor plume. Because the water vapor plume is supersonic everywhere 21 s after impact, and because the faster bulk velocities were observed downstream of the relatively slower flow, we assumed that molecules leaving the outermost domain with speeds greater 110% of the escape velocity at their altitudes would be lost due to escape (see Section 5.4.3). We use 110% of the escape velocity to mostly account for small speed changes that may occur due to collisions in the cold expanding gas. Using this assumption, we only needed to simulate the "slow" portion of the water vapor plume in our intermediate computations, thereby limiting the computational cost. The intermediate simulations were computed until the majority of the water vapor had come back to within 10,000 km of the lunar surface. At that time, molecules remaining within the intermediate domain, or the outermost domain used in Chapter 5, were distributed among the 36 processors used in our full planetary simulations. Because the simulations used in Chapter 5 and the intermediate simulations took advantage of the symmetry of the problem across the plane of impact, each of the molecules to be input inside our full planetary domain had to be mirrored in order to model the entire water vapor plume. Note that in the present simulations, Coriolis effects were ignored because the rotation rate of the Moon is slow. The results obtained in the full planetary simulations are presented first in the present section with a particular focus on the total mass of water initially retained on the Moon after impact and the shape of the primary deposition fallback pattern. The transport of the remaining water vapor plume was then simulated up to six months after impact and results for the time evolution of the polar ice deposits are presented.

### 6.3.1 Total Mass Retained

In the present section, we first study the overall shape of the water vapor plume three hours after impact before discussing how much water is retained on the Moon in our simulations. Figure 6-1 shows the gas density and gas speed three hours after impact for the portion of the water vapor plume with speeds lower than 110% of the escape velocity. In Figure 6-1, the point of impact is located at the “North Pole” of the Moon with the comet moving, before impact, in the  $XZ$  plane towards increasing  $X$ . Note that the symmetry of our problem across the  $XZ$  plane has been utilized in Figure 6-1 and only cells for  $Y > 0$  km have been plotted. Also, note that a constant surface temperature of 120 K is used in the present simulations. In addition to the gas speed contours, streamlines have been plotted at several locations. Note that because some of the streamlines travel in and out of the  $Y = 0$  plane, they appear to be discontinuous.

Three hours after impact, the water vapor plume has morphed into a very large cloud fully encompassing the Moon. The overall shape of the cloud is that of a “flying saucer” with the furthest molecules being found on the “southern” hemisphere in the crossrange (i.e.  $Y$ ) direction (up to 35,000 km). Molecules in the “northern” hemisphere are much more concentrated near the Moon only reaching altitudes of  $\sim 10,000$  km. The densest material is observed along the axis of symmetry of our spherical domain but we believe that this high density is artificial and can be attributed to the geometry of our grid and the poor statistics in that region. The overall density is actually greater in the “northern” hemisphere near the point of impact with the densest region extending further downrange of the Moon than uprange. The speed contours presented in Figure 6-1 show the presence of a low velocity region three radii from the Moon’s center. In that region of the cloud, molecules are turned around and stop moving in the upward  $Z$  direction. Instead, some of the molecules begin to fall back toward the point of impact while others (with a greater tangential component) go onto different orbital paths. Some of the molecules follow a near circular trajectory and hit the “southern” hemisphere of the Moon. Finally, the remaining molecules follow some elliptical trajectory that initially takes them away from the Moon at speeds greater than 1 km/s.

The cloud is not symmetric in the plane of impact (the  $XZ$  plane). In the “southern” hemisphere, the cloud extends further away from the lunar surface uprange than it does downrange. The differences have been attributed to the low density material uprange of the main water vapor plume at late times. This water vapor travels closer to the surface, some of it at

velocities near escape velocity, and is therefore expected to expand uprange of the Moon. On the other hand, even at late times (Figure 5-75), the outer edge of the downrange plume follows that of an inverted cone and water vapor moves in directions angled at more than  $45^\circ$  from the lunar surface. Possibly related to this initial condition, the water vapor mostly falls back toward the Moon on the “southern” hemisphere and does not expand away from the Moon.

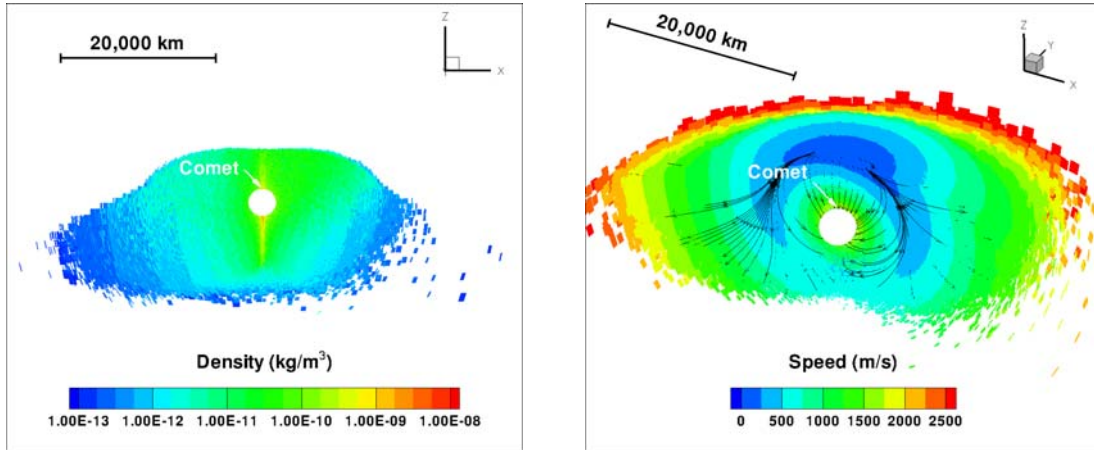


Figure 6-1 Density (left) and speed (right) contours for the portion of the water vapor plume with speeds lower than 110% of the escape velocity, three hours after impact. The white arrow represents the direction of the comet at impact (note that the plane of impact is the XZ plane). The white sphere represents the Moon. Note that only cells with  $Y > 0$  km have been plotted and that the viewing angle and viewing distance are different between the two figures. The black lines in the figure on the right represent the streamlines of the flow.

The mass of vapor plume water initially retained on the Moon after impact is equal to  $\sim 2.1\%$  of the comet mass. By also accounting for the amount of water that remained within the interface 21 s after impact, we find that the total retention rate for the water after the impact is  $\sim 3.1\%$ . In Section 5.4.1, we estimated the mass of water retained based on the time taken for molecules to travel from the point of impact to the hemispherical interface, and based on the mass flow rate at the interface (Figure 5-14). We calculated that between 7.9% and 8.7% of the water would be retained on the Moon which is much greater than what we found here to be actually retained. The main source of error in our preliminary estimate is due to the fact that we assumed that all the water vapor originated at the point of impact. This assumption was overly simplistic as

we saw in Figure 5-12a and b that material with low speeds crossed the interface under 8.4 s and more importantly that a relatively dense region of the plume (being pushed up by the rocky central peak material) crossed the interface later than 8.4 s after impact but with speeds greater than the escape velocity of the Moon.

The improved estimate for the mass retained is more in line with recent results obtained by Ong *et al.* (2010). Ong *et al.* (2010) used the results from their hydrocode simulations to estimate the fraction of water retained on the Moon after a vertical comet impact. In their paper, Ong *et al.* (2010) estimated the mass of water retained by comparing the plume velocity at the edge of their domain to the escape velocity. For a vertical impact at 30 km/s, Ong *et al.* (2010) found that ~1.5% of the cometary water had a velocity smaller than the escape velocity. Using Moses *et al.*'s (1999) analytical approach, Ong *et al.* (2010) noted that a 45° impact can be expected to retain ~3.4 times more water than a 90° impact. Thus, using their estimates of ~1.5% for a vertical impact, a 45° impact should retain ~5.1% of the cometary mass. Our results are located somewhere in between their solution for a vertical impact and their estimates for a 45° impact. Several simplifying assumptions in their analytical solution could be the source of the discrepancies between our 45° impact solution and their 45° impact estimate. Moses *et al.*'s (1999) analytic solution assumed the hemispherical expansion of an ideal gas mixture made of equal parts comet and target material by mass. The hemispherical assumption is appropriate for a vertical impact and Ong *et al.*'s solution (2010) agrees fairly well in this case with the analytic solution. Both assumptions are, however, questionable when extended to oblique impacts because the water plume is non-hemispherical (Figure 5-10 and Figure 5-11) and water and rock are fairly well separated (Appendix D).

### **6.3.2 Initial Fallback Pattern**

As the water vapor plume falls back to the lunar surface, the water molecules begin to migrate based on the local surface temperature at their landing site. In order to observe the actual shape of the initial fallback pattern, we set-up an independent simulation where the lunar surface temperature is artificially fixed everywhere at 120 K and where the Moon does not rotate. At this low temperature, the water molecules all stick to the surface and the initial fallback pattern can be observed without the migration of water molecules from the dayside to the nightside that would occur with a realistic surface temperature distribution. The mass of water stuck on the surface per

square kilometer is presented seven days after impact at a time where 99.6% of the water molecules that do not escape have fallen back to the lunar surface (the others are still present in the atmosphere at great altitudes or have entered orbit and will require additional time to fall back to the surface).

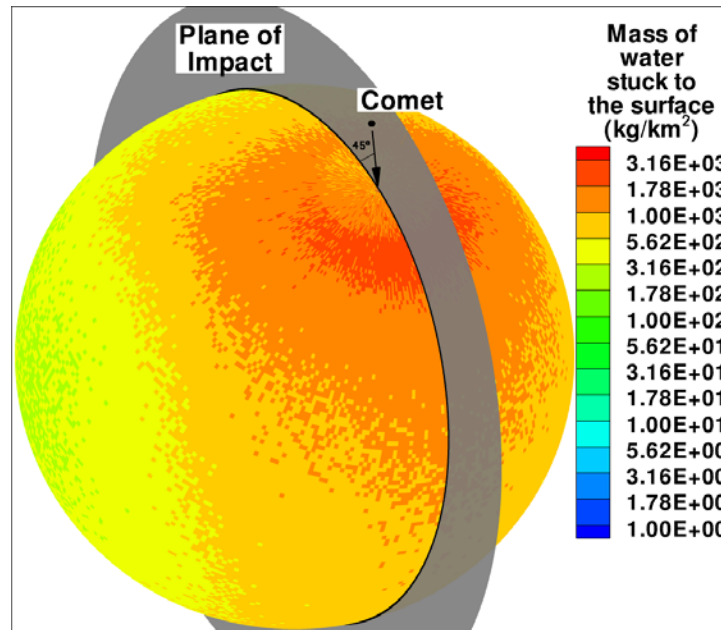


Figure 6-2 Initial fallback pattern on an artificially uniformly cold lunar surface ( $T_{\text{surf}} = 120 \text{ K}$ ) for the water vapor plume once 99.6% of the water has fallen back to the surface. Note that the Moon did not rotate for this simulation.

Figure 6-2 shows the mass of water stuck to the lunar surface per square kilometer seven days after impact. In our simulations of the water vapor plume (See Chapter 5), we noted that most of the water vapor plume moved in the downrange direction early on but it appeared that at a later time, when the flow speed was similar to the escape velocity at the surface of the Moon, the water vapor plume was much more symmetric around the point of impact (Figure 5-10 to Figure 5-13). In Figure 6-2, we see that most of the water vapor plume remaining on the Moon after impact landed in the downrange direction with some material depositing in the crossrange direction and relatively little water landing directly upstream of the point of impact. The thickest deposits ( $\sim 2000 \text{ kg/km}^2$ ) form a 200 km wide arc 200 km downrange of the point of impact.

Closer to the point of impact, the deposits are not as thick which can be attributed to the fact that the water vapor remaining within the hemispherical interface 21 s after impact was not simulated in the present computations. Twenty seconds after impact, the water vapor crossing the interface had radial velocities of  $\sim 1$  km/s (Figure 5-59). These molecules could land up to 600 km from the point of impact assuming a ballistic trajectory and a  $45^\circ$  angle for the initial velocity vector (molecules with velocities of  $\sim 0.5$  km/s could land at most 150 km from the impact crater). Overall, the thickest parts of the primary deposit resemble an arrowhead pointing in the same direction as the pre-impact comet velocity vector. The extent of the primary deposition pattern is very broad with dense deposits (orange contours) being observed  $\sim 4000$  km downrange and  $\sim 1000$  km crossrange of the point of impact. Up-range of the point of impact, the dense water deposits are only observed up to  $\sim 400$  km from the point of impact. Surrounding the thick deposits, some water actually landed all around the Moon. This entire surface coverage is consistent with the water cloud surrounding the Moon that was observed three hours after impact (Figure 6-1).

### **6.3.3 Time Evolution of the Ice Deposits in the Polar Cold Traps**

For the simulations of the transient flow around the Moon, we fixed the point of impact at the  $45^\circ$  latitude at local midnight. The comet comes in at  $45^\circ$  from the lunar surface heading toward the South Pole. That orientation was thought to provide favorable trapping rates as some of the thick primary deposits would directly land inside the South Pole cold traps. The deposition patterns for the water molecules are shown three hours, seven days, and twenty eight days after impact in Figure 6-3. We can see that three hours after impact, most of the water deposited on the lunar surface is stuck on the nightside south of the equator or near the terminator (thickest deposits have  $\sim 4000$  kg/km<sup>2</sup>). No deposits are observed on the dayside because even at a relatively low dayside surface temperature of 200 K, molecules stick to the lunar surface for less than 0.02 s on average in our current residence time model. Seven days after impact, the point of impact is now located at the dawn terminator. At that time, the water deposits are still asymmetric North-South but twenty eight days after impact, the surface contours are nearly symmetric across the equator. At that time, most of the water deposits are located near the poles and near the dawn terminator (thickest deposits have  $\sim 10,000$  kg/km<sup>2</sup>) with very small water deposit present near the dusk terminator (not shown). Also note that the point of impact has almost returned to its initial

position relative to the subsolar point but its actual location is barely discernable in the contours. Therefore, one month after impact, the transient atmospheric lunar flow has been fully established on the Moon. From then on, the gas flow is only sustained by the sublimation of the water deposits located near the dawn terminator as the Sun rises above their location.

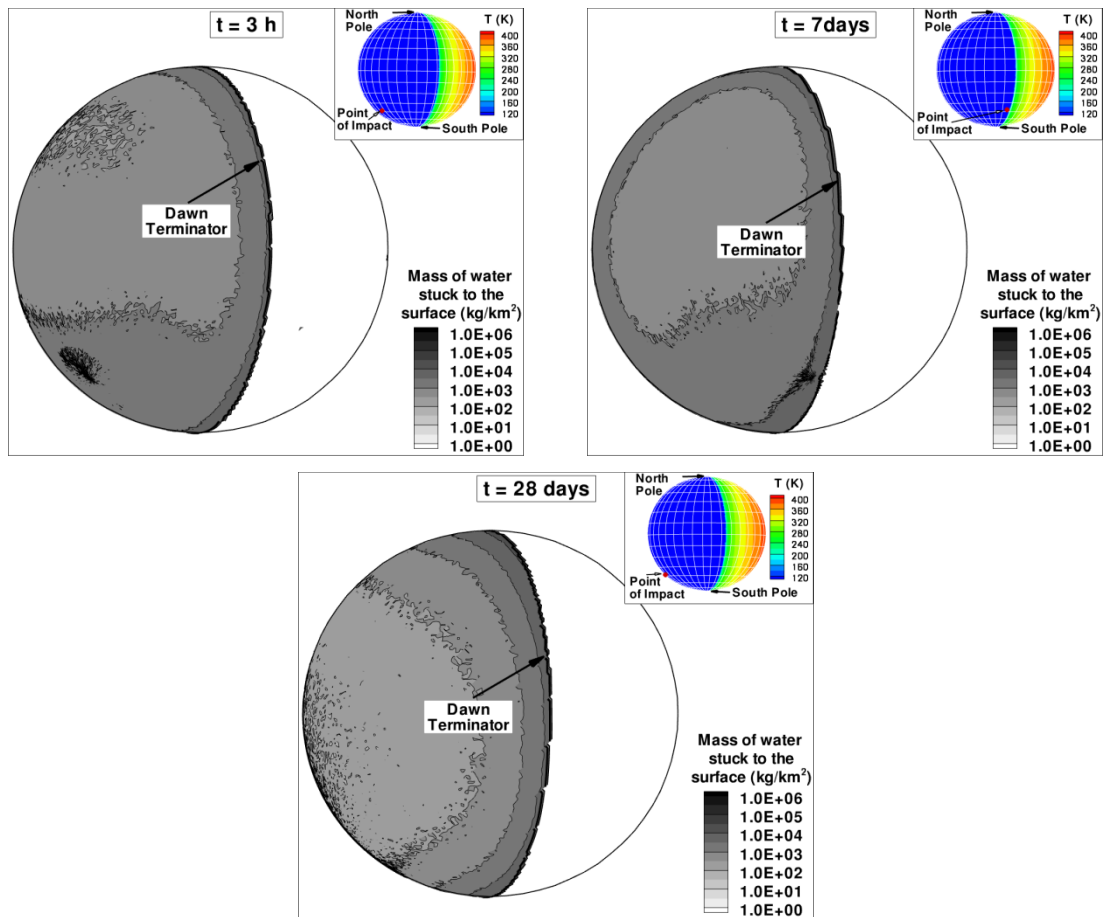


Figure 6-3 Grayscale contours for the mass of water stuck to the surface per square kilometer 3 hours, 7 days and 28 days after impact. Note that the inset picture indicates the location of the impact point at each time relative to the subsolar point.



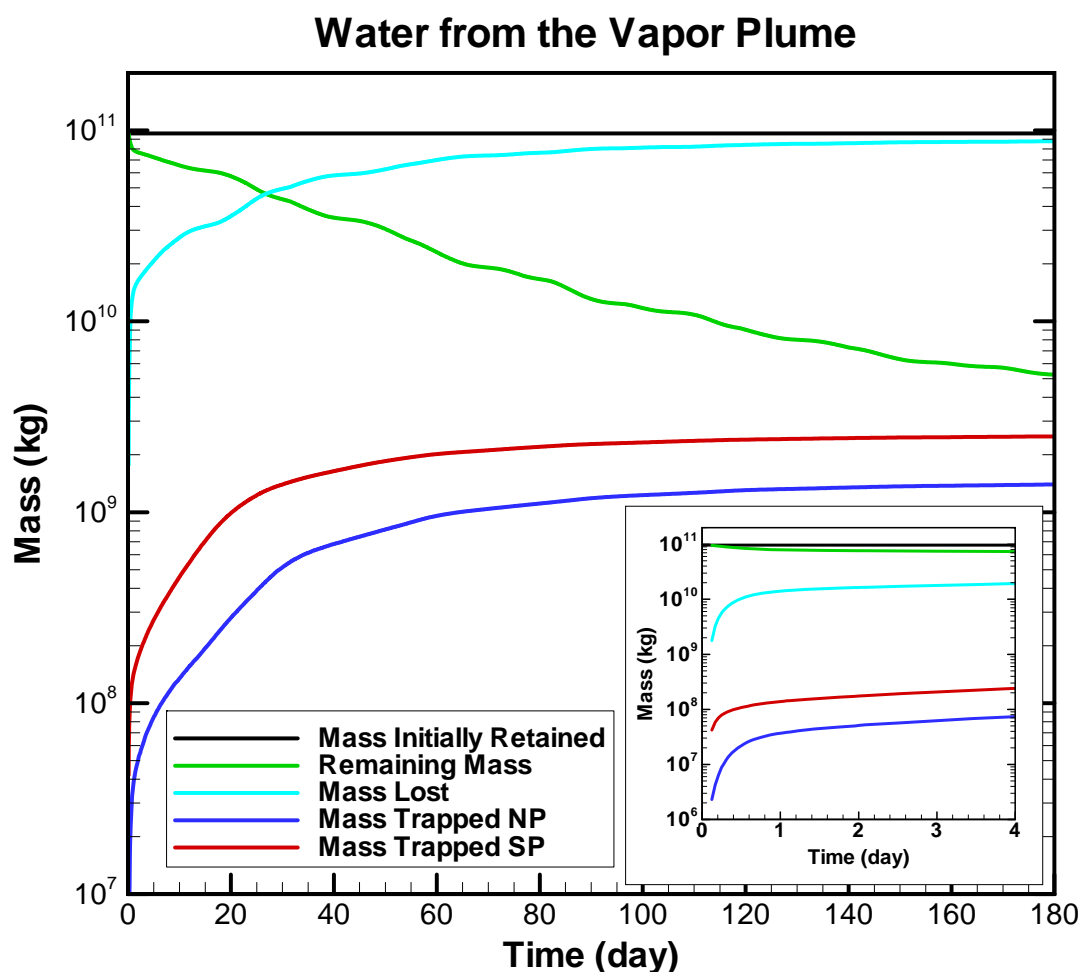


Figure 6-4 Line plots of the mass of water initially retained (black line), remaining on the Moon (both trapped and untrapped) (green line), destroyed (light blue line), and captured in the cold traps (red and blue lines for the cold traps located at the South Pole and North Pole, respectively) as a function of time. The inset figure zooms in early times. Note that the plot lines start three hours after impact when the intermediate simulations were started.

Line plots for the mass of water captured in the polar cold traps are shown in Figure 6-4. Capture of the cometary water starts early on during the migration process (inset in Figure 6-4). Ten hours after impact almost  $\sim 10^8$  kg of water was captured in the South Pole cold traps. In comparison, only  $\sim 1.5 \times 10^7$  kg was captured in the North Pole cold trap by that time. The photo-

destruction of the water is, however, noticeably faster than the capture rate as  $\sim 9 \times 10^9$  kg has already been destroyed by that time. In the present simulations, we assume that the atmosphere is thin so the incident photons can hit any molecule present in the dayside atmosphere. This assumption is, at least initially, believed to be conservative as some of the lower layers of the dayside atmosphere may be partially shielded from photo-reaction processes.

As the Moon rotates, water molecules continue to accumulate into both southern and northern poles at similar rates. The small oscillations that are more noticeably observed in the remaining mass line (green line) have been attributed to an increased/decreased number of molecules in the lunar atmosphere due to the Sun rising over relatively larger/smaller deposits around that time. Six months after impact,  $\sim 2.5 \times 10^9$  kg of water is trapped at the South Pole and  $\sim 1.4 \times 10^9$  kg is trapped at the North Pole. These quantities account for 74% of the water remaining on the Moon at that time. Assuming that the rates for all quantities from six months on are equal to the rates observed between 160 and 180 days after impact, we find that most of the water will have been trapped or destroyed  $\sim 8$  months after impact. At that time we estimate that  $\sim 0.086\%$  of the comet initial mass has been trapped in the lunar cold traps for an impact point located at a latitude of  $45S^\circ$  and an impact event occurring at local midnight.

#### **6.3.4 Deposition Pattern in the Polar Cold Traps**

The deposition pattern of water inside the modeled cold traps is shown six months after impact in Figure 6-5. The surface area covered by the polar cold traps is much smaller than the distance travelled by a molecule during a ballistic hop at the mean temperature observed on the lunar surface (Figure 3-15). Therefore, the location at which a molecule landed in a polar cold trap is random and a near uniform distribution is observed in the cold traps. Figure 6-5 also shows that molecules landed first in the South Pole cold traps which can be related to the chosen location for the point of impact.

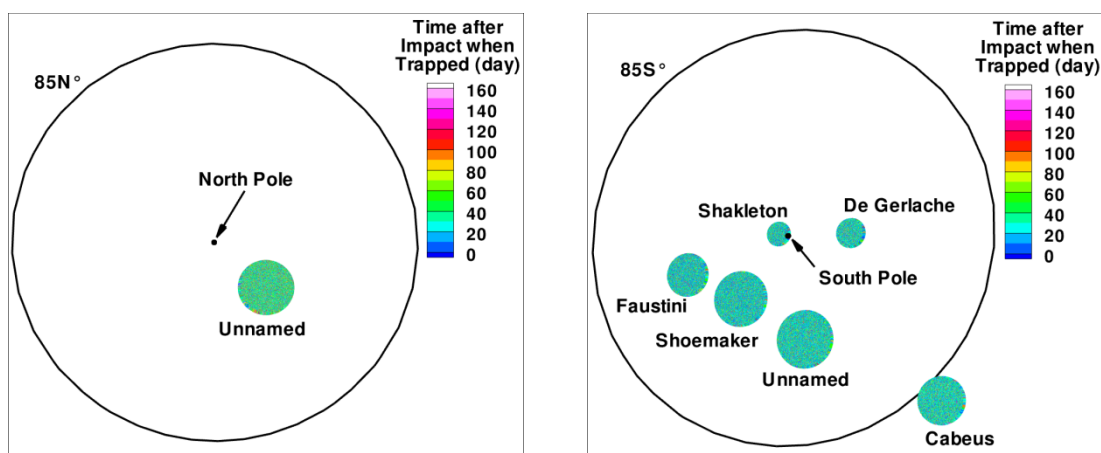


Figure 6-5 Scatter plot of the deposition pattern of water ice in the North Pole cold trap (left) and in the South Pole cold traps (right). The color scale represents the time after impact at which the molecule was trapped.

#### 6.4 MIGRATION OF THE IMPACT CRATER WATER TO THE POLAR COLD TRAPS

The water that did not cross the SOVA interface in under 21 s was never modeled in our DSMC simulations of the water vapor plume and therefore it was simulated independently. Because we do not know the thermal properties and spatial distribution of that residual water, we chose a fairly simple model to study the migration of that water to the polar cold traps. Note that these simulations ignore the presence of the vapor plume water because we want to distinguish between the two origins for the trapped water. This assumption may influence the time at which the transient atmosphere becomes collisionless but should not greatly impact the capture rate of water in the cold traps. The “impact crater” water was also assumed to fall back on the lunar surface near the point of impact. This assumption may not be accurate as some of that water may move at  $\sim 1$  km/s (which was the radial velocity of the water vapor 20 s after impact at the interface (Figure 5-59)) and travel hundreds of kilometers before landing back on the Moon. However, some of the water may also remain trapped inside the crater or may condense on rock that falls back closer to the impact crater. Because of all these uncertainties we chose to simply sublimate the residual impact crater water from a 30 km radius “crater” over a fixed period of time. Material inside the impact crater will be relatively hotter than the surroundings right after impact but even at an intermediate temperature of 400 K (equal to the subsolar point local

temperature), 1% of the comet mass is sublimated in less than 1 s. In order to avoid a spike in the release rate, we arbitrarily chose to sublimate water in 10 minutes with 50% of the water being sublimated in less than one minute. In order to show that this arbitrary function does not impact the final retention rate of water we also ran a case where water takes one month to sublimate from the crater. This slow sublimation is not relatable to any physical process but is used to show that the arbitrary model used to sublimate the water does not influence our solution. The number of molecules released from the crater was specified by the equilibrium vapor pressure (Eq. (5.2) for water over liquid) at the specified mud temperature (Eq. (6.1)) (Austin and Goldstein, 2000).

$$N_{\text{SUBLIMATED}} = P_{\text{Vapor}} \times \pi R^2 \times \Delta t / \sqrt{2\pi kT(t)M_{H_2O}} \quad (6.1)$$

where  $R = 30 \times 10^3$  m is the radius of our sublimating crater,  $\Delta t$  is the timestep size used in the calculations,  $T(t)$  is the surface temperature inside the crater, and  $M_{H_2O}$  is the molecular mass of water ( $M_{H_2O} = 2.99 \times 10^{-26}$  kg).

In order to sublimate the water molecules in the two specified timescales, the following two temperature profiles for the crater surface temperature were arbitrarily chosen for the fast release (Eq. (6.2)) and the slow release (Eq. (6.3)), respectively. Again, these functions are only used to sublimate the water in the specified timescales and cannot be related to any specific physical process.

$$T_{\text{FAST}}(t) = 260 \times e^{-7.45 \times 10^{-4} t} \quad (6.2)$$

$$T_{\text{SLOW}}(t) = 183 \times e^{-9.78 \times 10^{-8} t} \quad (6.3)$$

From the SOVA and DSMC simulations of the early stages of the impact event we estimated that ~1% of the comet mass remained within the 20 km radius interface 21 s after the 45° oblique impact of a 1 km radius comet at 30 km/s (See Section 5.4.2). In the present simulations, we look at the migration of  $4.65 \times 10^{10}$  kg, or that 1% of the total comet mass, from the point of impact to the lunar cold traps using 100 million simulated molecules. In the present section, the effects of the sublimation rate from the crater as well as the effect of location of the point of impact are being studied. We first present the results for the low density transient atmospheric flow for fast sublimation from the crater at three different initial impact point

locations: at the 45S° latitude at local midnight (Case 1), at the 45N° latitude at local noon (Case 2), and at the North Pole (Case 3) (Table 6-1). We also compare these results to the slow release of water from a crater located at the 45N° latitude at local noon (Case 4). Finally, we present the deposition results obtained for each scenario. The present simulations were run up to three months after impact for all cases.

Table 6-1 Summary of the initial conditions used for Cases 1 to 4. Note that the subsolar point is assumed to be at longitude 0°.

Case Number	Latitude	Longitude	Release Time
Case 1	45S°	180°	10 minutes
Case 2	45N°	0°	10 minutes
Case 3	0°	0°	10 minutes
Case 4	45N°	0°	30 Earth days

#### 6.4.1 Low Density Transient Atmospheric Flow

In the present section, we first study the influence of the location of the impact point on the transient atmospheric flow by comparing our results for Cases 1, 2, and 3 at several points in time. The atmospheric water vapor densities and the mass of water stuck to the surface per square kilometer are presented in Figure 6-6 to Figure 6-9, ten minutes, one hour, one day and seven days after the beginning of the release for Cases 1, 2, and 3. Note that the scale of the color contours for density is different ten minutes after impact from the scale used at later times. We are not showing the flow collision rate contours in the present section but we observed that the present simulations were collisional near the impact crater early on and that at later times the flow was only collisional near the dawn terminator.

Ten minutes after the beginning of the release, all three sublimating flows exhibit the characteristics of a simple unsteady expansion plume into a vacuum (Figure 6-6). The flow appears to be nearly axisymmetric with some low density flow surrounding a much denser core. In our present model, the sublimation rate increases exponentially with temperature (due to the

vapor pressure component in Eq. (6.1)), and by the end of the release the temperature inside the crater has dropped by almost 100 K. Therefore, most of the water molecules are released into the atmosphere in the first couple of minutes, and on the first ballistic hop this material will also reach further distances on average than the later material. As the early water vapor starts to fall back to the lunar surface, it has very limited interactions with the rising water molecules so no canopy shock is observed above the sublimating crater. The absence of a shock is different from steady state Ionian volcanic plumes (Zhang *et al.*, 2003). The absence of a canopy shock is at least partially related to the model used to sublimate water from the impact crater and some other model may produce a different initial flow pattern. However, we are interested here in the capture rate of water molecules in the polar cold traps so the initial flow pattern is not of great concern in the present simulations.

While the model for the release of the water molecules is the same for all three cases, the plume observed in Case 2 is taller (up to 700 km above the lunar surface) than the plumes observed in Cases 1 and 3 (up to 600 km above the lunar surface). This has been attributed to the fact that some of the water has already fallen back to the lunar surface (see surface contours in Case 1) and in Case 2 has already been sublimated back up. In Case 2, the local surface temperature of the Moon near the crater, at  $\sim 380$  K, is actually larger than the assumed mud temperature within the crater, initially at 260 K (close to the temperature at  $0^\circ$  latitude 50 cm below the surface (Vasavada *et al.* (1999))), so water molecules will have higher thermal velocities after accommodating to the local surface temperature than after their initial hop.

Different deposition patterns are observed for the three different impact point locations. The densest deposits are observed for Case 1 with as much as  $5 \times 10^5$  kg/km<sup>2</sup> of water being stuck to the lunar surface which would be equivalent to 5 mm of snow (with an assumed density of 100 kg/m<sup>3</sup>) covering that entire region. In Case 1, all of the molecules falling back to the cold surface appear to stick to the surface forming a concentric deposition pattern. Most of the water landed near the impact crater but some material reached as far as  $\sim 650$  km from the crater. In Case 2, no molecules are stuck to the surface because of the relatively warm surface temperatures surrounding the impact crater and because the water molecules have not yet had time to migrate to the nightside over several hops. Case 3 is an intermediate case where half of the molecules are stuck while half have been re-emitted into the atmosphere ten minutes after the beginning of the release.

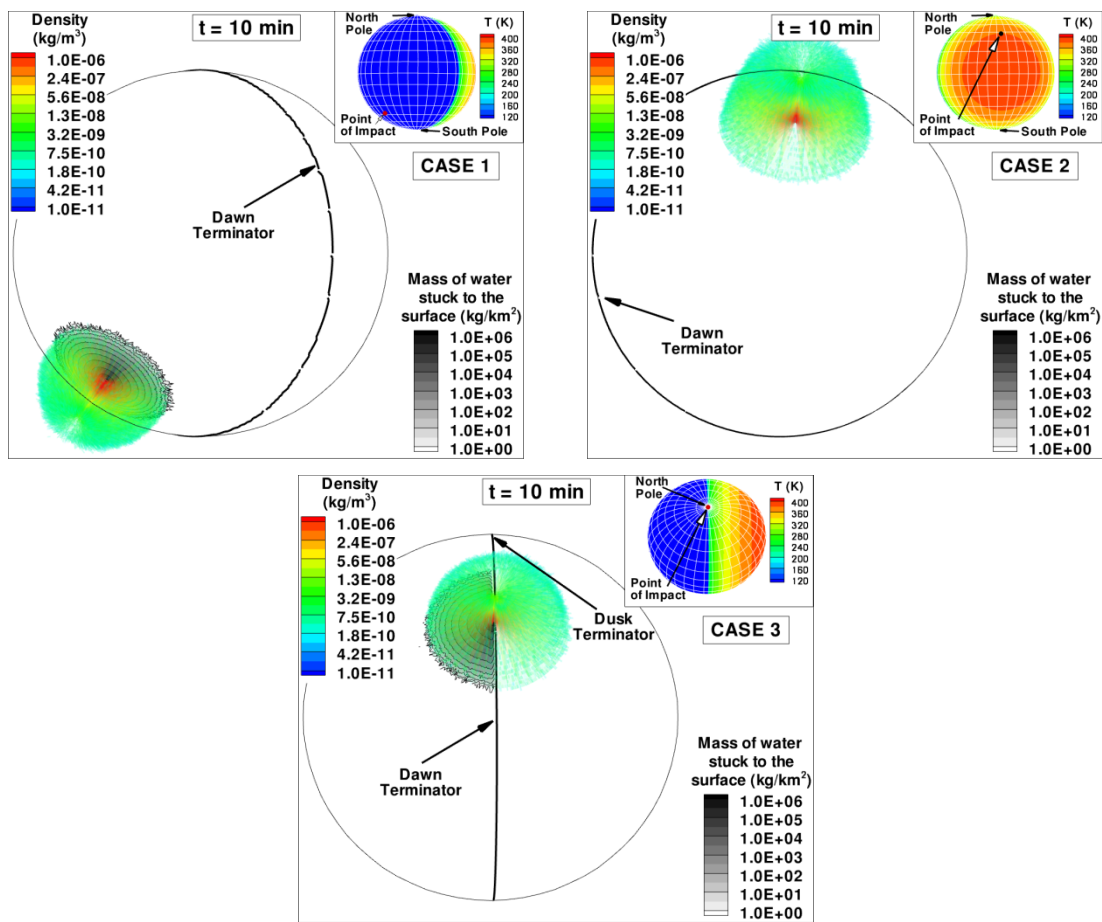


Figure 6-6 Translucent density contours (colored) for the atmospheric flow with superimposed grayscale contours for the mass of water stuck to the surface per square kilometer 10 minutes after impact for Cases 1, 2, and 3. Note that the inset picture indicates the location of the impact point at that time relative to the subsolar point.

One hour after the sublimation began the atmospheric flows have evolved very differently for all three cases (Figure 6-7). In Case 1, only a small fraction of the sublimated water has reached the sunlit part of the lunar atmosphere so most of the water is still stuck on the nightside of the Moon. The water molecules are again deposited into concentric circles with the densest deposits ( $\sim 6 \times 10^5$  kg/km<sup>2</sup>) being observed near the impact crater. At that time, some of the water has been deposited as far as 2000 km from the impact crater and some has even reached the cold traps near the South Pole. The atmosphere is most extended in Case 2 protruding far onto the

nightside. In several regions, maroon contours can be observed which are due to the present graphic representation where atmospheric cells containing water are set as translucent. The “maroon” contours are observed when some dense (red) region is seen through a more rarefied part of the atmosphere (green). Therefore, the densest atmospheres are observed near the terminator and in the regions near the point of impact. The surface contours show that water preferentially landed near the North Pole, which is the shortest distance from the point of impact to the nightside. In Case 3, the top of the atmosphere does not extend as high above the surface as in Case 2 but it also covers the entire lunar dayside. The densest atmospheric flow is observed near the impact crater one hour after the beginning of the release. Also, most of the water stuck on the nightside is located near the lunar North Pole with some additional water beginning to deposit near the terminator.

One day after the release began the atmospheric flows are very similar to that observed one hour after the beginning of the release with some noticeable thinning of the dayside atmospheres observed in Cases 2 and 3 (Figure 6-8). In Case 1, most of the water remains stuck on the nightside of the Moon, mostly in concentric circles around the impact crater, but now some thin deposits can also be observed near the terminator. In Case 2, the atmospheric density and also the extent of the atmosphere have noticeably decreased compared to one hour after the beginning of the release with the densest flow being observed near the terminator. The deposition pattern has also noticeably changed with the thickest deposits being observed near the entire terminator and mostly decreasing with distance from the terminator. The asymmetry due to the high latitudinal location of the impact crater, which was observed initially in the deposits, has mostly disappeared one day after impact. Finally, in Case 3, in addition to some thinning of the atmosphere, the most noticeable feature is the asymmetry observed between the dawn and dusk regions of the nightside. Near the dawn terminator, the densest deposits are observed at the terminator. Near the dusk terminator, however, the densest deposits are located a few hundred kilometers away from the terminator. This phenomenon is due to both the rotation of the Moon and the initial flowfield. Most of the water is deposited on the nightside in Case 3 within hours, near the North Pole and the dawn and dusk terminators. Then, as the Moon rotates, the deposits near the dusk terminator end up further into night. At the same time, the deposits near the dawn terminator see the sun rise over their location and sublimate before condensing back on the nightside, mostly again near the dawn terminator.



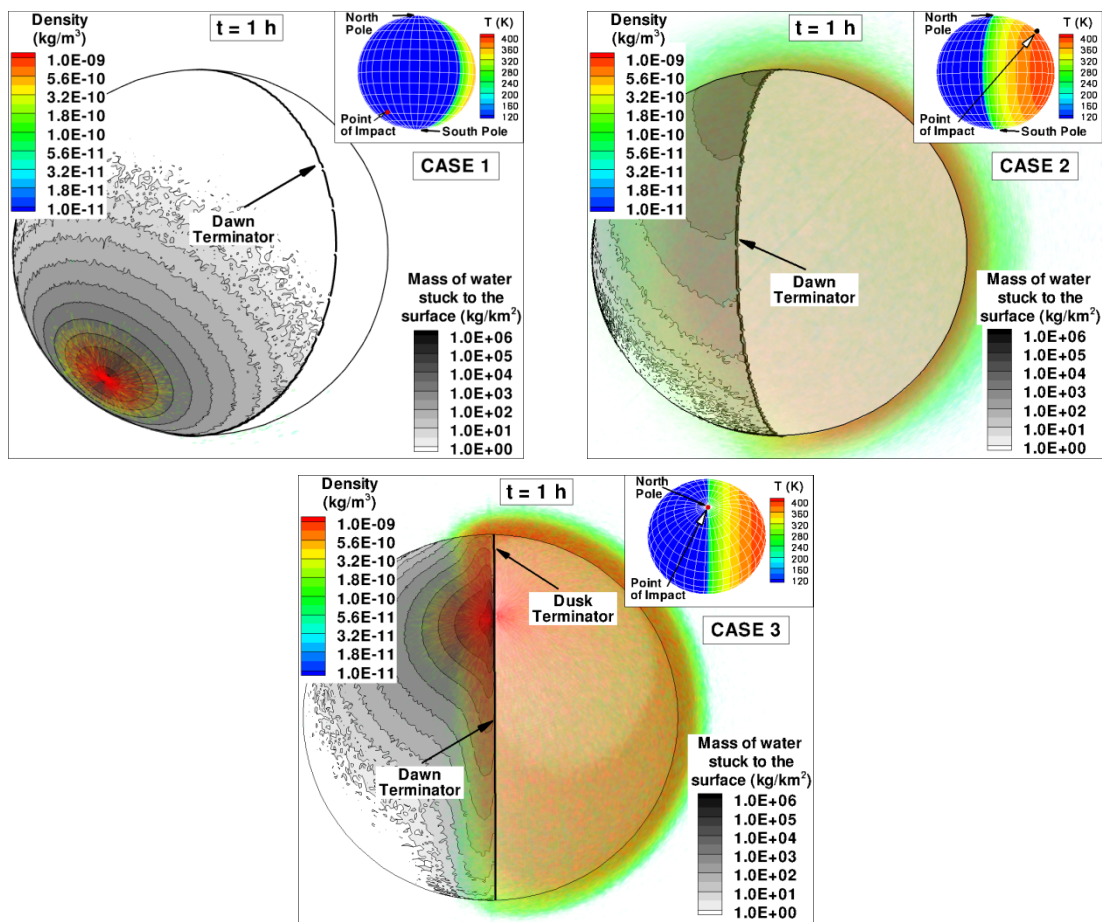


Figure 6-7 Translucent density contours (colored) for the atmospheric flow with superimposed grayscale contours for the mass of water stuck to the surface per square kilometer one hour after impact for Cases 1, 2, and 3. Note that the inset picture indicates the location of the impact point at that time relative to the subsolar point.

Seven days after the beginning of the release, the impact points for Cases 1 and 2 are now located near the dawn and dusk terminators, respectively (Figure 6-9). At that time Case 1 has the fullest atmosphere mostly localized near the impact crater and southern dawn terminator. A small fraction of the water molecules have, however, travelled to the northern hemisphere and some thicker deposits are observed near the terminator north of the equator. At that time, the densest deposits are still observed near the point of impact. In Case 2, almost no water molecules are present in the dusk atmosphere. The deposition map for this case is the most uniform North to

South with the thickest deposits being located more than one thousand kilometers away from the terminator along the equator near local midnight (Figure 6-10). In Case 3, the low density atmosphere is densest on the dawn side of the Moon. The deposits on the dawn side continue to be depleted as the sun rises above them. Simultaneously, the fresh deposits near the dusk terminator are much thinner ( $\sim 200 \text{ kg/km}^2$ ) than the initial deposits ( $\sim 5 \times 10^5 \text{ kg/km}^2$ ).

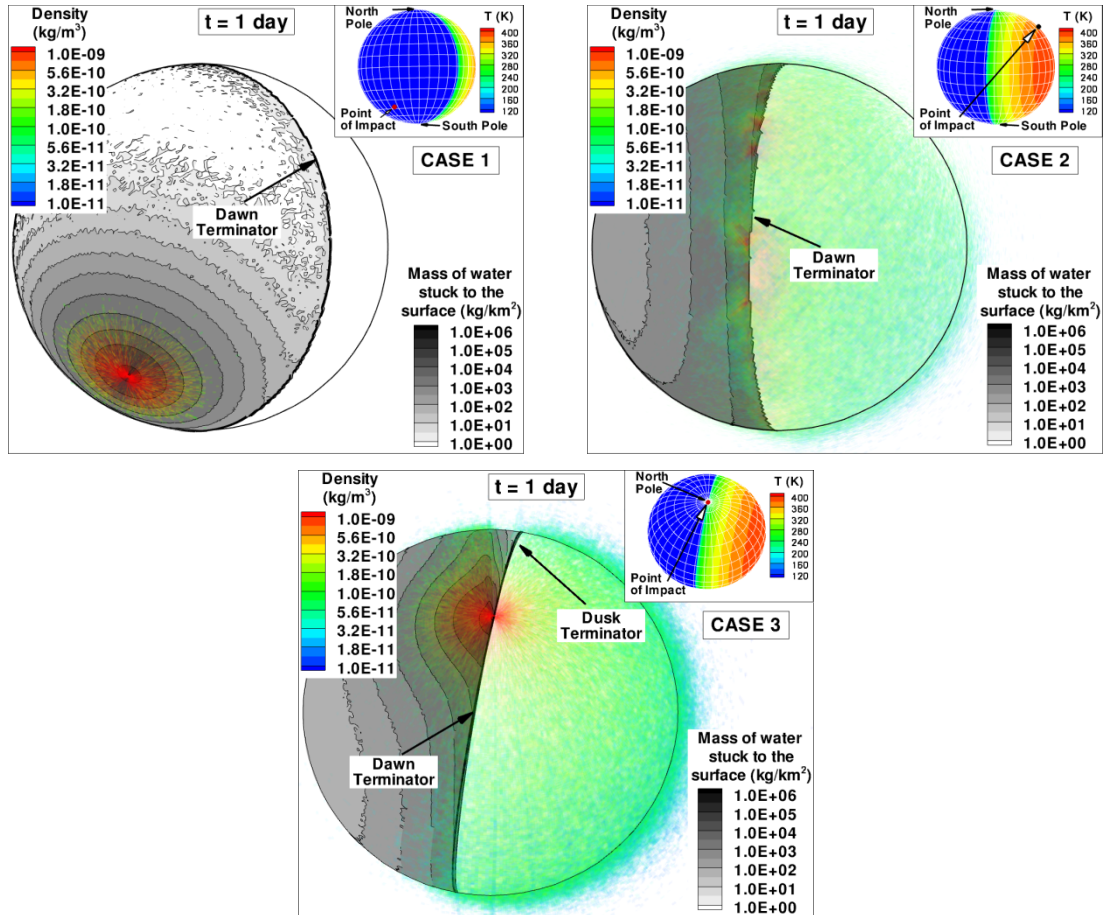


Figure 6-8 Translucent density contours (colored) for the atmospheric flow with superimposed grayscale contours for the mass of water stuck to the surface per square kilometer one day after impact for Cases 1, 2, and 3. Note that the inset picture indicates the location of the impact point at that time relative to the subsolar point.

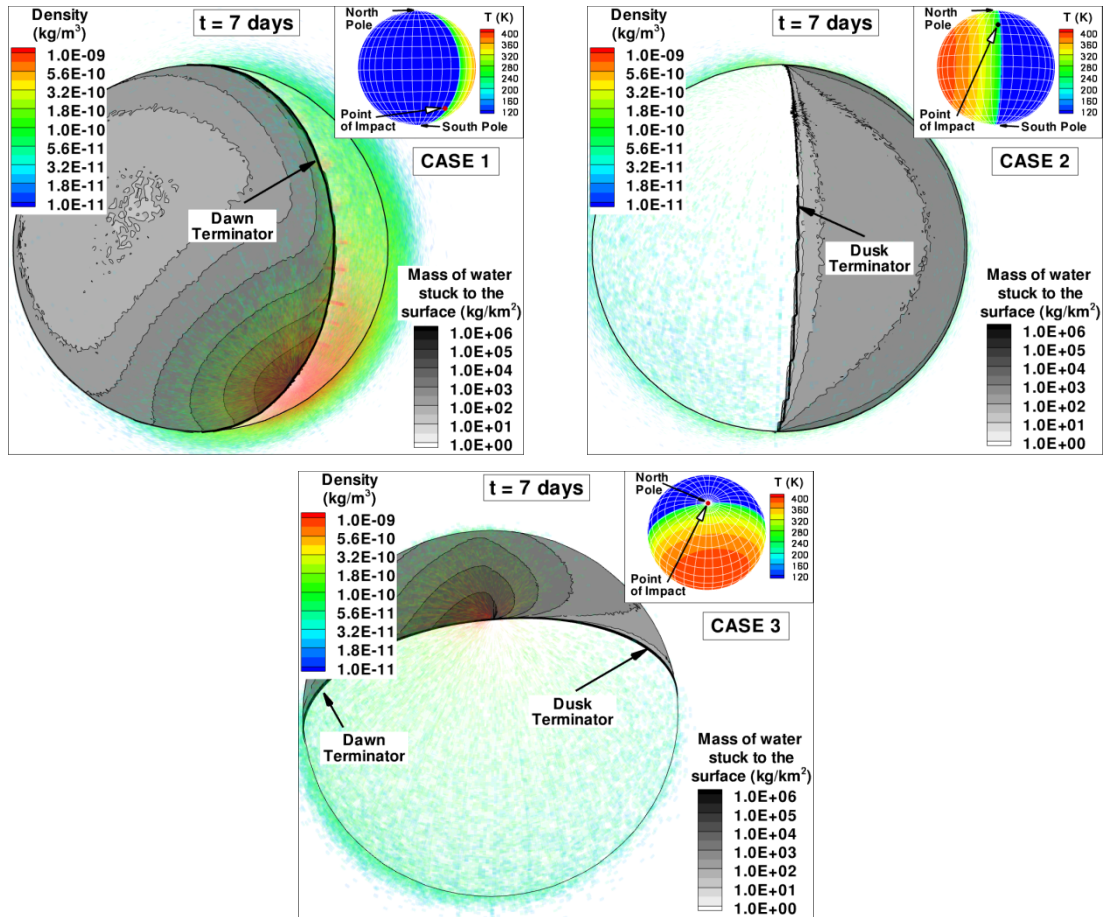


Figure 6-9 Translucent density contours (colored) for the atmospheric flow with superimposed grayscale contours for the mass of water stuck to the surface per square kilometer seven days after impact for Cases 1, 2, and 3. Note that the inset picture indicates the location of the impact point at that time relative to the subsolar point.

For several days after the release of the water from the crater, the location of the point of impact is a very important factor in the characteristics of the developing atmospheric flow. Impact locations on the nightside provide nearly negligible atmospheric flow until the sun rises above the initial deposition rings. After that time, a relatively dense atmosphere is observed near the impact crater that then expands to the entire dayside hemisphere. The main early water deposits are, however, found mostly near the impact crater. For impact craters located on the

dayside, the early atmosphere is very thick near the impact crater and near the terminators. However, most of the water rapidly condenses on the nightside of the Moon relatively uniformly across the southern and northern hemispheres. The atmospheric flow at later times is mostly localized near the dawn terminator. For an impact crater located at the North Pole, the atmospheric flow is somewhat similar to the flow observed for dayside impact crater locations. The water deposits are however noticeably different between the two cases. For an impact crater located at the North Pole, most of the water is deposited in the northern hemisphere and within a thin North-South band that was initially located at the dusk terminator.

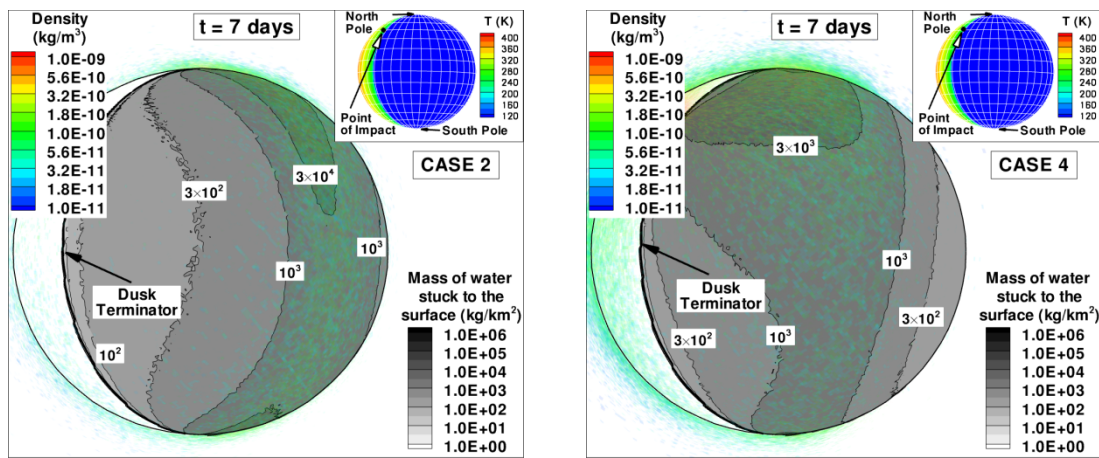


Figure 6-10 Translucent density contours (colored) for the atmospheric flow with superimposed grayscale contours for the mass of water stuck to the surface per square kilometer seven days after impact for Cases 2, and 4. Note that the inset picture indicates the location of the impact point at that time relative to the subsolar point.

In order to study the influence of the sublimation rate from the crater on the atmospheric flow and deposition pattern, we compared our results seven days after the beginning of the release for Cases 2 and 4 in Figure 6-10. Note that at that time, most of the water has been sublimated in both Cases (black lines in Figure 6-12). The atmospheric flow is much more noticeable in the slow release case (Case 4) on the entire dayside hemisphere and more particularly near the impact crater. In addition, the thicker water deposits for Case 4 are mostly localized on the northern lunar hemisphere while the deposits for Case 2 were much more uniform across the equator.

#### 6.4.2 Time Evolution of the Ice Deposits in the Polar Cold Traps

The previous section showed that both the impact point location and the release time influence the early transient atmospheric flow as well as the early deposition pattern of water on the nightside of the Moon. The objective of the present section is to study the influence of these parameters on the trapping of water molecules in the polar cold traps.

Figure 6-11 shows line plots for mass remaining on the Moon, mass destroyed and mass captured in the polar cold traps as a function of time for Cases 1, 2, and 3. Note that in Figure 6-11, the black “mass released” line represents 1% of the comet mass. Initially, both destruction and capture rates are highly dependent on the impact point location. For impact points located on the nightside (Case 1), the number of water molecules photodestroyed is initially a factor of five less than it is for impact points located on the dayside (Case 2). Note that molecules are destroyed even for Case 1 because the point of impact is close enough to the terminator that some parts of the plume are in the sunlight. The destruction numbers for the polar impact (Case 3) are found somewhere between Cases 1 and 2 early on as was expected. As the Moon rotates, however, the number of molecules destroyed increases rapidly in Case 1 as soon as some of the primary deposits become illuminated and water vapor sublimates into the lunar atmosphere. As time further increases, however, the total numbers of molecules lost become similar for all three cases due to the fact that the capture rate is much smaller than the destruction rate in the present simulations.

Similar to the destruction rate of in-flight water molecules, the capture rate of water in the cold traps is also highly dependent initially on the impact point location. In Case 1, most of the water is initially captured by the South Pole cold traps and only a small fraction is captured by the North Pole cold trap. As the Sun rises above the primary deposition pattern, a circum-lunar flow establishes itself and the capture rate for both South Pole and North Pole cold traps increases (for  $t > 4$  days). Both rates increase similarly so three months after impact more than six times as many molecules have been trapped at the South Pole than at the North Pole. At that time  $\sim 0.05\%$  of the comet mass has been captured by the cold traps in Case 1.

In Case 2, the number of molecules trapped at both North and South Poles is very similar a few days after the beginning of the release. While the number of molecules landing near the North Pole versus the South Pole is greater early on (Figure 6-7), the much larger trapping area near the South Pole ( $4575 \text{ km}^2$  at the South Pole versus  $1257 \text{ km}^2$  at the North Pole)

“compensates” for the differences. Later on, when the distribution of molecules on the nightside is more uniform across the equator, the number of molecules captured at the South Pole increases more rapidly than at the North Pole. Three months after impact, the mass of water captured by the cold traps is similar to that observed in Case 1, at  $\sim 0.05\%$  of the comet mass. The distribution of trapped molecules is, however, more uniform between the North and South Poles with only 70% of the water being trapped at the South Pole.

In Case 3, a large fraction of the trapped molecules can be found at the North Pole cold trap early after the beginning of the release. The number of molecules trapped at the South Pole only increases after a few hours after impact but very rapidly this number becomes greater than the one obtained in Case 1. Because around half of the impact crater molecules for Case 3 land on the daytime hemisphere, it only requires a few hours and a few hops for them to reach the South Pole. On the other hand, in Case 1, molecules have to wait for the Moon to rotate for the primary deposits to become illuminated. This process takes about one day after which the number of captured (and of destroyed) molecules rapidly increases. In Case 3, as time goes on, however, the trapping rate at the South Pole increases more rapidly than at the North Pole ( $t > 4$  days). Three months after impact, almost 0.06% of the water has been trapped, 63% of which is found in the North Pole cold trap.

Overall, the number of water molecules captured in the polar cold traps seems to depend more on the position of the point of impact relative to the cold traps location than on the time at which the comet hit the lunar surface. Cases 1 and 2 were located at opposite ends of our parametric field but the retention rate obtained three months after impact was actually of the same order in both cases. In Case 3, the number of molecules captured after three months is somewhat greater than the number trapped in Cases 1 and 2. Because Case 3 was located at the North Pole, a greater number of molecules landed in a cold trap directly after being released and therefore have a lower probability to photo-react before being captured. The number of molecules captured in the cold traps has, however, not reached an asymptote at that time so small differences may be observed in the final retention number.

If we assume that the transient atmospheric flow is established on the Moon three months after the beginning of the release, similar to the vapor plume simulations, we can estimate how much water is retained on the Moon months later. Assuming that the destruction and capture rates remain nearly constant from three months after impact on, we estimate that the fraction of the



initial comet mass captured in the polar cold traps should be equal to  $\sim 0.06\%$ ,  $\sim 0.06\%$  and  $\sim 0.08\%$  for Cases 1, 2, and 3, respectively. This amounts to a mass captured of water between  $2.79 \times 10^9$  kg and  $3.72 \times 10^9$  kg.

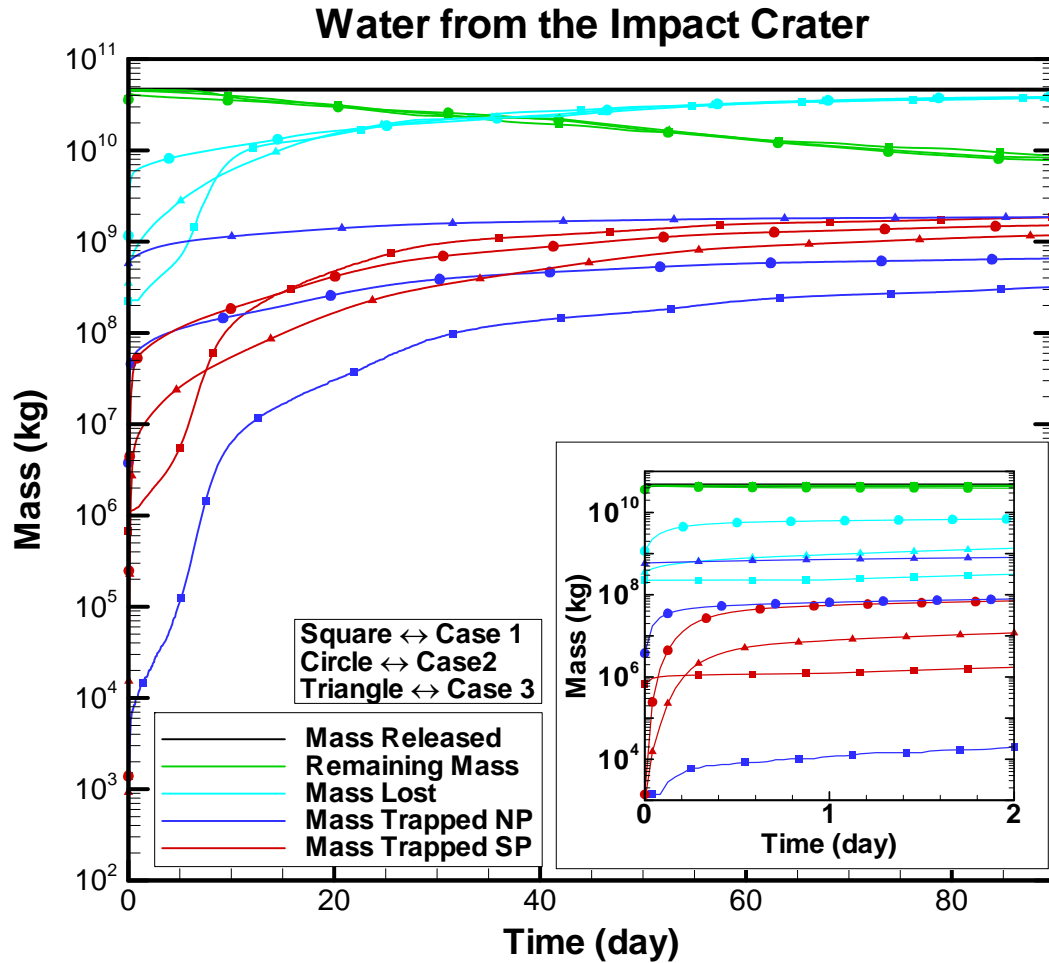


Figure 6-11 Line plots of the mass of water released (black line), remaining on the Moon (green lines), destroyed (light blue lines), and captured in the cold traps (red and blue lines for the cold traps located at the South Pole and North Pole, respectively) as a function of time. The square symbols represent Case 1, the circle symbols represent Case 2 and the triangle symbols represent Case 3. The inset figure zooms in early times. Note that the mass released (black line) is equal to 1% of the comet mass.

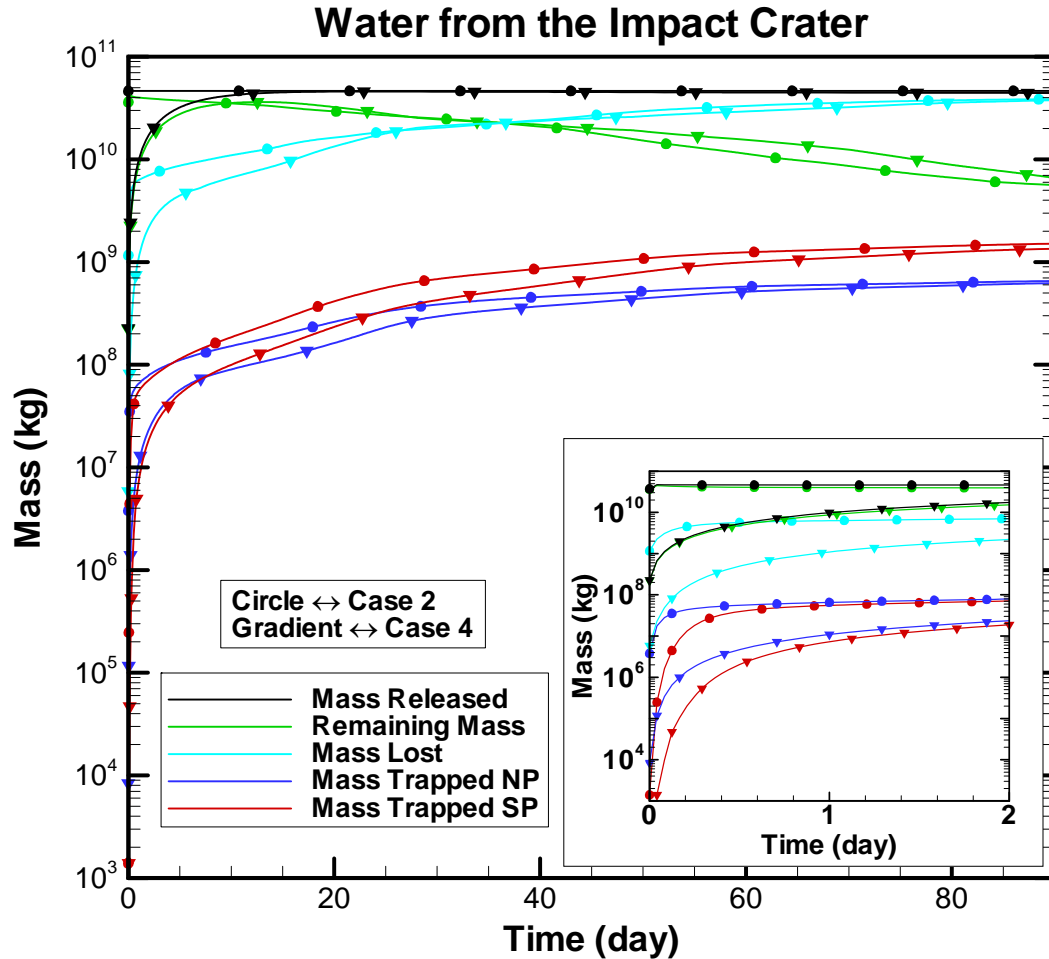


Figure 6-12 Line plots of the mass of water released (black line), remaining on the Moon (green lines), destroyed (light blue lines), and captured in the cold traps (red and blue lines for the cold traps located at the South Pole and North Pole, respectively) as a function of time. The square symbols represent Case 2, and the circle symbols represent Case 4. The inset figure zooms in early times. Note that the mass released (black line) is equal to 1% of the comet mass.

The influence of the release rate of water from the impact crater is studied in Figure 6-12. In Case 4, the number of molecules released continues to increase as a function of time until one month after the beginning of the release, at which time 1% of the comet mass has been sublimated from the impact crater. For both impacts on the dayside hemisphere of the Moon, the number of molecules initially captured is similar across the South Pole and North Pole cold traps.



Later on, however, more water is captured at the South Pole than at the North Pole. In addition, more water is captured initially in Case 2 than in Case 4 but at later times ( $t > 60$  days), similar numbers have been captured in both cases. We attribute the initial differences to the observed water deposits on the nightside at early times (Figure 6-10). Because the captured number for Case 4 seems to converge to that observed in Case 2, the final capture rates for both cases are expected to be nearly identical.

By combining our results for the vapor plume water and for the impact crater water (for Case 1) we find that at least 0.14% of the comet mass, or  $6.51 \times 10^9$  kg of water, is captured in the polar cold traps. With a trapping surface area of  $5832 \text{ km}^2$ , the deposits are equivalent to  $1.12 \text{ kg/m}^2$  or an ice thickness of  $\sim 1$  mm. This number may be slightly larger, however, in the case of a comet impact near the lunar poles (as more water is captured in Case 3 than in Case 1).

Ong *et al.* (2010) estimated that the total water mass flux to the Moon due to comet impacts over one billion years was between  $1.9 \times 10^5$  to  $6.0 \times 10^6$  kg/year. They then estimated the fraction of water retained on the Moon by normalizing their modeled fraction of water retained as function of velocity by the probability that an impact occurs at a fixed velocity. Note that the mass retained refers to the mass left on the Moon after impact and not the mass captured inside the cold traps. They considered comet sizes from 500 m to 34 km in diameter which have similar impact physics. Therefore, they extended their modeled fraction of water retained as function of velocity for the impact of a 1 km diameter ice sphere comet to the entire range of comet sizes. Using these assumptions, they found that  $1.2 \times 10^{13}$ – $3.9 \times 10^{14}$  kg of water has been retained on the Moon. In their simulations, Ong *et al.* found that 1.5% of the comet mass would be retained after a vertical impact at 30 km/s. In the present simulations, we find that for a 30 km/s  $45^\circ$  oblique impact, the mass of water retained was equal to  $\sim 3\%$  of the comet mass (after  $\sim 3$  hours). Therefore, we can estimate the mass of water retained on the Moon over one billion years by correcting their modeled fraction of water retained using our initial retention rate estimates. Using this approach, we find that 9.6% of the water mass delivered to the Moon is retained. Therefore, the total mass of water retained on the Moon before migration over one billion years is  $1.8 \times 10^{13}$ – $5.8 \times 10^{14}$  kg. From our simulations, we find that  $\sim 5\%$  of the water molecules remaining on the Moon are actually captured in the cold traps or  $9.0 \times 10^{11}$ – $2.9 \times 10^{12}$  kg over one billion

years. The fraction of water destroyed inside the cold traps was estimated to be 94.4% (Crider and Vondrak, 2003), so only  $5.0 \times 10^{10}$ – $1.6 \times 10^{11}$  kg should be present inside the polar cold traps after one billion years. From the Lunar Prospector data, Feldman *et al.* (2000) estimated that as much as  $1.98 \times 10^{11}$  kg of water ice may be present at the lunar poles. Our current estimates are therefore consistent with the Lunar Prospector observations.

## **Chapter 7**

### **Conclusions**

#### **7.1 SUMMARY**

The primary purpose of this study was to model the water vapor flow produced by a comet impact on the Moon using the Direct Simulation Monte Carlo (DSMC) method. Toward that end, our DSMC solver was modified to simulate the cometary water from the time of impact until it is either lost due to escape, destroyed by photodestruction processes, or captured inside one of the lunar polar cold traps.

In order to model the complex unsteady flow induced by a comet impact, a 3D spherical version of the DSMC solver was created. The spherical geometry used in our domain enables us to model a smooth lunar surface. Molecules move under a variable gravity field, and molecules in flight may be lost due to photodissociation or photoionization. Molecules landing on the lunar surface stick to the surface for a given residence time based on the local surface temperature. Chemistry in the atmosphere or on the surface, radiative cooling, photoabsorption in the atmosphere and condensation processes not on the surface were ignored. Several additional features related to the modeling of a comet impact were added to our code including the addition of cold traps near the lunar poles, and the implementation of a rotating surface temperature map around any axis in order to simulate different impact locations.

A parallel version of the DSMC solver was implemented in order to simulate the early impact continuum flow as well as the full planetary atmosphere which develops later. In the present implementation, we used the MPI method, so the DSMC simulations can be run on either distributed or shared memory systems with the limitation that each processor must have I/O access. The domain decomposition among processors was done in the azimuthal direction and was static for a given calculation. The number of MPI communication calls was limited to four per timestep. Superlinear speed-up was achieved for most cases up to 100 processors when simulating either a hemispherical expansion or the early stages of a comet impact event.

The DSMC code was also modified to take, as input, the solution from the SOVA hydrocode for the impact event at a fixed interface. Because the DSMC method cannot model the physical phenomena involved during the impact event, such as phase changes and surface deformation, the present simulations used the data provided by the hydrocode simulations of the impact event as input. The vapor plume produced during the impact event was supersonic in the near field just after impact so we chose a unidirectional coupling where macroscopic data from the SOVA domain were transferred at a hemispherical interface into the surrounding DSMC domain. Data from the DSMC domain were not transferred back into the SOVA domain. The interface geometry was provided by the SOVA computations in Cartesian coordinates but any other given geometry can be used in the present DSMC code. The Cartesian cells were used as reservoir cells where molecules were created based on the cell macroscopic data as provided by the SOVA hydrocode.

In addition, a sequential unsteady multi-domain approach was also added to the previous implementation in order to follow the water from the near field to the far field. In the comet impact simulations, molecules reach altitudes greater than 25 times the Moon radius and the resolution used for these large scale simulations cannot also resolve the early continuum flow observed in the near field. Molecules that exit the inner domain are saved to a file that is later read in as input to the simulations inside a larger domain. Again, this sequential approach is appropriate in the present simulations because the flow is supersonic at the domain boundaries. Both timestep size and cell size can differ between two successive domains.

Because the near field of the water vapor plume produced by a large comet impact is continuum, we implemented a collision limiting scheme in order to limit the computational cost of our simulations. In the continuum regions of the flow, the cell and timestep sizes are so large that billions of collisions would need to be computed at each timestep in each cell. Instead we used a two level collision limiting scheme that accurately models the flow in the continuum and transitional regimes before reverting back to the regular DSMC collision scheme in the more rarefied regions. This feature was tested for an unsteady hemispherical flow against simulations using the regular DSMC collision routine at a relatively large Knudsen number ( $Kn \sim 0.001$ ). Good agreement was obtained between the regular and collision-limited simulations but the collision-limited solution was five times faster than the regular DSMC computation. The collision limiter gives much greater speed-up for the cometary impact simulations.

The present implementation was initially tested on a simple unsteady hemispherical expansion flow into a vacuum. For these simulations, the data at the interface were provided by a 1D analytical model instead of the SOVA solution. Cell size and timestep size used in the simulations were much greater than the mean free path and mean collision times but were similar to the parameters used in the comet impact simulations. Even with this coarse resolution, good agreement was obtained downstream of the interface for density, temperature and radial velocity. Freezing of the vibrational modes was also observed in the transitional regime as the flow became collisionless.

For our study, we chose the initial conditions for our comet impact to be fairly representative of the most probable impact event: the 45° oblique impact of a 1 km radius ice sphere at 30 km/s. The DSMC simulations simulated the evolution of the water vapor from the SOVA hemisphere until it is either destroyed or captured in a cold trap months after impact. The DSMC results were tested in the near field against the SOVA solution downstream of the interface. Good agreement was obtained for the density and velocity contours but the DSMC solution appeared to be hotter than the SOVA solution downstream of the interface.

Initially, most of the water vapor moves radially out through the downrange portion of the interface with velocities up to 50 km/s. Because of the very high velocities early on, most of the water crossing the 20 km in radius hemispherical interface under seven seconds is lost due to planetary escape. The shape of the plume is initially very complex but fairly rapidly (in less than 3 s) the downrange edge of the plume takes on the shape of an inverted cone as observed in impact experiments. As more water vapor crosses the interface a secondary low density plume can be observed uprange of the main high density plume five seconds after impact. Simultaneously, rocky material, that will later form the central peak observed in large crater impacts, rises from the center of the expanding crater. This rocky material pushes water out of its way forcing the main plume into a thin ring of high density material at a fixed altitude. Overall, the extent of the plume is greater uprange of the point of impact but because most of the uprange material has a low density, even at later times most of the water vapor is moving downrange of the point of impact. From nine seconds after impact on, most of the water vapor crosses the interface with velocities slower than the escape velocity. Overall, the flow is highly supersonic so the plume mostly expands radially out with time and very little broadening of the plume due to thermal motion can be observed up to a few tens of seconds after impact. The plume is also

relatively cold with the hottest gas being the water vapor that crossed the interface early after impact (in less than one second). In addition, the plume is nearly entirely continuum up to several tens of seconds after impact. The cell and timestep resolutions used in the present simulations are too coarse to resolve the mean free path of the flow. However, the cell resolution is fine enough to capture the gradients of the flow and should provide a fairly accurate model of the vapor plume flowfield.

Most of the water vapor plume escapes the gravity well of the Moon within the first few hours after impact. For such a large comet impact, only  $\sim 3\%$  of the comet mass remains on the Moon after impact. Of this total mass 2% crossed the SOVA interface under 21 s while the remaining 1% was still within the interface at the end of the SOVA computations. As the Moon rotates, the molecules begin to migrate until they are destroyed or captured in a cold trap. In our model, we chose to use a conservative approach where the total mass captured in the polar cold traps should be a lower limit estimate as to the actual mass captured. In particular, we ignored recombination processes for the photo-dissociation products as well as possible shielding of molecules in the lower layers of the vapor cloud from solar photons. A parametric study of the impact point location shows that the capture rate is mostly dependent on the number of molecules that are able to reach the cold traps in one hop. Therefore, impacts near the lunar poles provide the thickest deposits inside the lunar cold traps. Of the 3% of the water remaining on the Moon after impact, only a small fraction,  $\sim 0.14\%$  of the comet mass, actually reaches the cold traps. Based on the surface area of the cold traps used in the present simulations,  $\sim 1$  mm of ice will have accumulated in the polar cold traps after impact. Using the results presented by Ong et al. (2010) and Crider and Vondrak (2003), we estimated that between  $5.0 \times 10^{10}$  to  $1.6 \times 10^{11}$  kg of water should have accumulated inside the polar cold traps after one billion years. From the Lunar Prospector data, Feldman *et al.* (2000) estimated that as much as  $1.98 \times 10^{11}$  kg of water ice may be present at the lunar poles. From the Chandrayaan mission, it was estimated that at least  $6 \times 10^{11}$  kg of water ice was present in the lunar cold traps (at [http://www.nasa.gov/mission\\_pages/Mini-RF/multimedia/feature\\_ice\\_like\\_deposits.html](http://www.nasa.gov/mission_pages/Mini-RF/multimedia/feature_ice_like_deposits.html)). Therefore, our current estimates are consistent with both the Lunar Prospector and Chandrayaan observations.

## 7.2 FUTURE WORK

The following ideas can be considered in the future as possible extensions and additions to the present work.

A parametric study focusing on the size of the impactor, its velocity and impact angle can be used to constrain the total mass of water deposited and captured on the Moon over its history. Also, the influence of the physical model should be studied in more detail with a particular emphasis on the following: the shielding of the molecules from photodestruction processes during their transport, the condensation of water within the plume and the interactions of the water with the rock. Various surface areas for the cold traps can also be considered in order to study its influence on the transient atmosphere.

Because most of the plume is in the continuum domain and still hypersonic far away from the point of impact for several seconds after impact, the use of some intermediate Euler solver between SOVA and DSMC may be considered. Such approach should produce some noticeable savings on computational time.

## **Appendices**



## **Appendix A**

### **Parallel Computing**

#### **A.1 PARALLEL COMPUTING**

Since the implementation of the very first computer, the increase in computing power has been outpaced by the computational cost of the numerical problems that we wish to solve. The differences between two generations of computers generally involve upgrades of computing components such as the CPU, cache and main memory modules. Unfortunately, some computations cannot be run on even the newest machines because the size of the problem is too large and/or the run time would be too long to complete. In the past few decades, research has moved in a different direction: studying the collaborative use of multiple computational units to solve the largest and most complex problems. Today's most commonly used parallel computers follow the Multiple-Instruction Multiple-Data (MIMD) model. In such architecture, the system is composed of multiple independent CPUs, or processors, that can execute their own programs at their own pace while working on one overall task. Examples of MIMD computers include clusters, constellations and networks of workstations. The MIMD computers are usually further divided into two categories the shared and distributed memory systems. Whatever parallel computer is chosen to run the computation on, its architecture has to be well understood in order to take full advantage of the system. Therefore, both shared and distributed memory architectures are described in more details in the following sections.

In a shared memory computer, several processors are connected to a pool of memory through a network forming a node. In order to obtain the fastest machine possible, the cache of the processors must be large and the latency and bandwidth of the network have to be small and large, respectively. The network can be bus-based, which is cheaper but has a limited bandwidth, or switch-based, which is more expensive but more scalable. One of the most common node architectures uses crossbar switches that connect several processors to several independent memory modules. By connecting several crossbars together, a shared memory computer with a

larger number of processors can be created. However, these computers have an unpredictable non-uniform access to memory when a variable is stored on a different crossbar than the one the processor is on. Also, a complication inherent to the shared memory systems is that if a processor accesses a shared variable in its cache, the value may not be current. Several protocols had to be implemented over the years in order to prevent this problem. The method of choice to run a program on a shared memory system is to use the OpenMP commands. OpenMP is a series of compiler directives that indicate which portions of the code have to be simulated in parallel. No details are generally required as to how to divide the work among processors, which makes simulations on a shared memory computer relatively easy to program.

In the distributed memory architecture, each processor has access to its own local memory forming a processor/memory pair. Because the memory is no longer shared, data must be manually decomposed among processors and information must be transferred between processors during the simulation. Therefore, research on distributed memory supercomputers usually focuses on the interconnect network used to link the processor/memory pairs. In theory, the most efficient system is a fully connected network where any pair is connected to all the other pairs. Unfortunately, as the number of processors increases, the cost of a fully connected network becomes prohibitive and is therefore never implemented. The networks most resembling a fully connected network are dynamic networks, which use crossbar switches in between the pairs, or special static networks such as “hypercubes”, which make use of wires in between the pairs. However, these networks are rarely used for the largest supercomputers due to cost and scalability constraints. The relatively simpler “mesh” and “torus” static or “fat-tree” dynamic networks are the most commonly used as they provide an acceptable number of direct neighbors and a relatively short path between any two pairs. The method of choice to run a simulation on a distributed memory system is to use the Message Passing Interface (MPI) method. The MPI implementation provides functions that enable communication of data between processors. Unfortunately, the MPI method is harder to implement than the Open MP method because data must be manually decomposed among processors and must be sent explicitly across processors.

Most of today’s machines are hybrids between the two architectures (shared vs. distributed memory) where nodes of processors are linked together through an interconnect network. If the number of processors in a node is smaller/larger than the number of nodes, the computer is called a cluster/constellation. As of 2010, only two of the top 500 largest

supercomputers are constellations, the others follow the cluster architecture. If the number of processors to be used for one's simulation is equal to or less than the number of processors on a node (usually up to 16 processors), the computations should be run on a node using the OpenMP commands, therefore taking advantage of the fast access to memory and the relative ease of programming. On the other hand, if the computations require a large number of processors, the simulations will have to be run on a several nodes using the MPI implementation. In order to be flexible in the number of processors that we wish to use for our simulations (possibly up to a few hundred), we chose to run our parallel DSMC code on the Lonestar and Ranger clusters at TACC and we therefore used the MPI implementation for the parallelization of the code. Lonestar has 1300 computing nodes that each has 2 Xeon Intel Duo-Core 64-bit processors for a total of 5200 processors. Each processor has a frequency of 2.66 GHz and each node has 8 GB of memory. Nodes are interconnected in a "fat-tree" network with "InfiniBand" switches providing a 1GB/s bandwidth. Ranger has 3936 computing nodes that each has 4 AMD Opteron Quad-Core 64-bit processors for a total of 62976 processors. Each processor has a clock rate of 2.3 GHz and each node has 32 GB of memory. Nodes are again interconnected in a "fat-tree" network with "InfiniBand" switches providing a 1GB/s bandwidth.

## **A.2 THE MESSAGE PASSING INTERFACE (MPI) METHOD**

Initially, parallel codes were machine dependent and had to be modified to run on different supercomputers. In order to address this issue, in the early 90s, the MPI method was implemented with the main goal of being portable to most supercomputers. Since then, MPI has become the most widely used approach for parallel programming on distributed memory systems. On such machines, because the memory is not shared, each processor only has access to the data stored locally. Therefore, for parallel computations on distributed memory systems, data must be decomposed among processors and information must be transferred between processors during the simulation when required. The MPI method is a library of definitions and message-passing functions that provides ways to communicate information between processors (Pacheco, 1997).

First, the MPI library has several environment functions that set up the parallel architecture. Such functions serve the purpose of letting processors know how many processors are running the simulation and what the rank of each processor is. The rank of a processor is especially important for MPI parallel codes based on the single-program multiple-data (SPMD)

programming model. In this commonly used model, the program algorithm is composed of branching statements based on processor rank, so each processor ends up executing its own individual program. In simulations where one processor handles all the I/O (LeBeau, 1999), that one processor executes a different program from all the other processors.

In addition to the environment functions, communication functions and MPI datatypes were implemented in order to explicitly transfer data between processors. When writing a parallel MPI code, programmers have to decide where and what information must be transferred between processors but all communications must include a message between communicants. The message has to be represented as a MPI datatype such as the predefined integer and double types. Sometimes, the message can be more complex than a single integer or double so the library was set-up so that complex MPI structures can also be built from the predefined MPI datatypes similar to the common C structures. Depending on the problem, two or more communicants can be involved in a communication. The simplest communication functions are the MPI\_Send and MPI\_Receive functions that enable the unidirectional transfer of data from one processor to another one. Several other functions were also implemented in the library in order to handle the complex global communications where all processors can send and receive data at once, such as MPI\_Alltoall and MPI\_Alltoallv that are used in the present implementation of the DSMC code (see Section A.3).

### **A.3 IMPLEMENTATION**

The DSMC method is well suited to parallelization because the molecules only interact through collisions with other molecules in their cell (Dietrich and Boyd, 1996, LeBeau, 1999). Therefore, a parallel implementation of the DSMC method only requires a decomposition of the physical domain among the processors. Once the computational domain is distributed among the processors, each processor follows the classic DSMC algorithm (i.e. creates, moves, indexes and collides molecules).

The algorithm for our parallel DSMC implementation is presented in Figure A-1. The present parallel simulations were run on the Texas Advanced Computing Center (TACC) supercomputers for which all processors have I/O access. Therefore, the algorithm shown in Figure A-1 was used by all the processors. First, the parallel environment was set up so the

processors could communicate with each other and each processor was given a rank (myID). Then each processor read the input file (filename.inp) providing, among other things, the overall domain boundaries. In order to take advantage of the parallel I/O capabilities of TACC's supercomputer, each processor was assigned individual input and output data files. The filenames for the required I/O files were created based on the input file name and processor rank.

In the present simulations, we decided that the physical domain was to be divided among processors in the azimuthal direction so each processor would simulate a piece of pie (close-up simulations) or a melon slice (full planet simulations). The geometry of the decomposition was known to all the processors so molecules that crossed the boundaries of a processor but remained in the overall domain would be sent to the appropriate processor. The number of communications had to be kept to a minimum for parallel efficiency so an MPI structure was created for the molecules to be sent across processors. Similarly to the serial simulations (Figure 3-1), memory was allocated for the cell, Moon's surface, and molecule structures. However, additional space was also required for the buffer structures used for communications. In addition, in order to limit the number of memory allocation calls made during the simulations, the molecule structure was pre-allocated in the parallel simulations, therefore modifying the dynamic allocation used in the serial code. Once all the parameters were initialized, each processor began to loop over timesteps: creating, moving, indexing, and colliding its own set of molecules.

For the comet impact simulations, communications of molecules between processors occurred after both the creation and the move steps. Because of the geometry of our interface, some of the Cartesian SOVA cells were split among several processors. For these cells, molecules were only created inside one of the processors (see Appendix B) and the molecules created outside of the boundaries of that processor had to be sent to the appropriate processor. Also, after the molecules were moved, some of the molecules which had crossed to another processor domain had to be transferred. In most DSMC codes (Dietrich and Boyd, 1996, LeBeau, 1999), molecules that crossed into another processor are first moved to the processor boundaries. After being transferred, they are moved by the remaining timestep. This process was repeated until molecules were moved by a full timestep. In the present simulations, the molecules were moved by a full timestep before being sent across. In the rare occurrence of a molecule crossing the

bottom wall after crossing into another processor, that molecule was deleted. All other cases where multiple walls were being crossed were handled correctly using the full timestep to move the molecules. For both the creation and move steps, the number of global communications was limited to two per timestep per phase. First, the molecules were saved to a buffer structure at the end of the creation/move step. Then, all the molecules going from a given processor to another given processor were grouped together. A first global communication (MPI\_Alltoall) sent across the number of molecules that a given processor was to receive from each of the other processors, and then molecular data was sent across in a single second communication (MPI\_Alltoallv) in order to minimize the overhead due to communication latency.

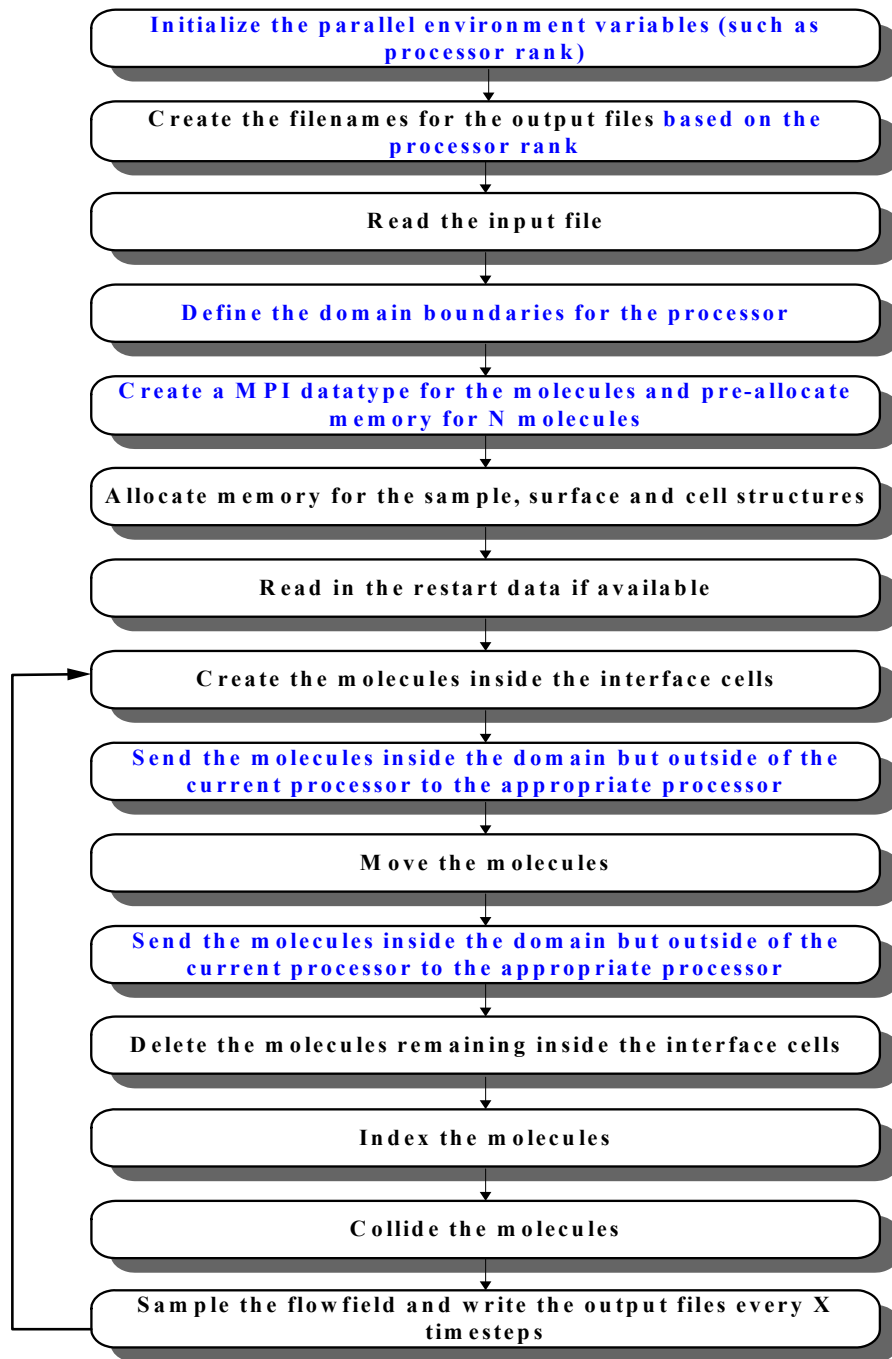


Figure A-1 Schematic of the DSMC algorithm used by all processors for the parallel comet impact simulations. Note that the steps related to the parallel implementation are shown in blue.

## **Appendix B**

### **Preprocessing of the SOVA Data**

#### **B.1 OVERVIEW**

The SOVA output provided by Dr. Pierazzo gives us data for all the interface cells at each timestep that are used as input to our DSMC comet impact simulations. All the SOVA simulations were run at the Planetary Science Institute (PSI) at the University of Arizona. First, the SOVA files were transferred from the cluster at PSI to the machines in the CFDLAB at the University of Texas. An initial decision was made that the SOVA output files (mat-flow) would be written in ASCII format in order to be able to easily verify the validity of our pre-processing code. This format was, however, kept all along and the SOVA files proved to be very large and had to be zipped in order to be transferred. The listing of the SOVA files used as input to the DSMC simulations of the 45° impact event is presented in Figure B-1. A total of 35 files were required for the simulations of the first 21 s of the impact. Initially, each SOVA output file provides 0.5 s worth of data, but after 16 s each file provides 1 s worth of data. The total size of the zipped files adds up to 142 GB with the smallest unzipped file being 8.1 GB (mat-flow-3.dat) and the largest unzipped file (mat-flow-19.dat) being 69 GB. These files are currently stored on TACC's file system Ranch.

The content of each SOVA output file is presented in Figure B-2. For a given timestep, the cell number, cell location, cell velocities as well as the target and projectile concentration, density, pressure, temperature, and energy were provided. However, the DSMC simulations only required the cell location, the velocities as well as the water density and temperature. The cell size and the time interval between outputs, which is not constant in the SOVA simulations, were also required for our DSMC calculations. Therefore, some preprocessing of the SOVA data was required first to compute the information required for the DSMC calculations but also to limit the size of the files that would be use as input to the DSMC simulations.



-rw-r--r--	1	larignon G-25002	2.5G	Jul 19 2007	mat-flow-1.0.dat.gz
-rw-r--r--	1	larignon G-25002	2.1G	Jul 19 2007	mat-flow-1.5.dat.gz
-rw-r--r--	1	larignon G-25002	3.4G	Sep 6 2007	mat-flow-10.5.dat.gz
-rw-r--r--	1	larignon G-25002	3.1G	Sep 6 2007	mat-flow-10.dat.gz
-rw-r--r--	1	larignon G-25002	2.6G	Sep 17 2007	mat-flow-11.5.dat.gz
-rw-r--r--	1	larignon G-25002	3.3G	Sep 17 2007	mat-flow-11.dat.gz
-rw-r--r--	1	larignon G-25002	4.8G	Sep 17 2007	mat-flow-12.5.dat.gz
-rw-r--r--	1	larignon G-25002	3.6G	Sep 17 2007	mat-flow-12.dat.gz
-rw-r--r--	1	larignon G-25002	4.3G	Aug 7 14:32	mat-flow-13.5.dat.gz
-rw-r--r--	1	larignon G-25002	5.4G	Jun 24 2008	mat-flow-13.dat.gz
-rw-r--r--	1	larignon G-25002	3.7G	Aug 7 14:49	mat-flow-14.dat.gz
-rw-r--r--	1	larignon G-25002	5.2G	Sep 29 09:44	mat-flow-15.5.dat.gz
-rw-r--r--	1	larignon G-25002	8.9G	Aug 25 09:02	mat-flow-15.dat.gz
-rw-r--r--	1	larignon G-25002	4.7G	Sep 29 10:51	mat-flow-16.dat.gz
-rw-r--r--	1	larignon G-25002	8.3G	Aug 27 11:28	mat-flow-17.dat.gz
-rw-r--r--	1	larignon G-25002	7.7G	Sep 17 13:14	mat-flow-18.dat.gz
-rw-r--r--	1	larignon G-25002	10.0G	Oct 2 15:30	mat-flow-19.dat.gz
-rw-r--r--	1	larignon G-25002	1.9G	Jul 19 2007	mat-flow-2.0.dat.gz
-rw-r--r--	1	larignon G-25002	1.6G	Jul 24 2007	mat-flow-2.5.dat.gz
-rw-r--r--	1	larignon G-25002	7.9G	Oct 8 20:43	mat-flow-20.dat.gz
-rw-r--r--	1	larignon G-25002	7.7G	Oct 8 22:54	mat-flow-21.dat.gz
-rw-r--r--	1	larignon G-25002	1.1G	Jul 24 2007	mat-flow-3.0.dat.gz
-rw-r--r--	1	larignon G-25002	2.5G	Jul 24 2007	mat-flow-3.5.dat.gz
-rw-r--r--	1	larignon G-25002	3.9G	Jul 24 2007	mat-flow-4.0.dat.gz
-rw-r--r--	1	larignon G-25002	3.9G	Jul 24 2007	mat-flow-4.5.dat.gz
-rw-r--r--	1	larignon G-25002	3.6G	Jul 24 2007	mat-flow-5.0.dat.gz
-rw-r--r--	1	larignon G-25002	3.3G	Jul 24 2007	mat-flow-5.5.dat.gz
-rw-r--r--	1	larignon G-25002	3.0G	Jul 24 2007	mat-flow-6.0.dat.gz
-rw-r--r--	1	larignon G-25002	2.7G	Jul 24 2007	mat-flow-6.5.dat.gz
-rw-r--r--	1	larignon G-25002	2.5G	Jul 24 2007	mat-flow-7.0.dat.gz
-rw-r--r--	1	larignon G-25002	2.3G	Jul 24 2007	mat-flow-7.5.dat.gz
-rw-r--r--	1	larignon G-25002	2.1G	Jul 25 2007	mat-flow-8.0.dat.gz
-rw-r--r--	1	larignon G-25002	2.4G	Jul 25 2007	mat-flow-8.5.dat.gz
-rw-r--r--	1	larignon G-25002	2.6G	Jul 25 2007	mat-flow-9.0.dat.gz
-rw-r--r--	1	larignon G-25002	3.2G	Jul 25 2007	mat-flow-9.5.dat.gz

Figure B-1 Listing of the SOVA files provided for the DSMC simulations of the 45° impact event.

Because the I/O operations in a computational code are among the slowest operations, limiting their number will decrease computational time. The SOVA output data was preprocessed so all the data that would not be used in the DSMC simulations was removed. This was done two ways: the useless cell data (such as the cell number and the target data) were deleted and the cells

that did not contain water or that had both water and rock were not taken into account. Such a process provided us with output files containing the required cell data for our DSMC simulations at every timestep. In addition to deleting the unnecessary data, the pre-processing code also computed the timestep size for the current timestep as well as the size of the interface cells. In the preprocessed data, the number of cells varied from one timestep to the next so at the beginning of each timestep both the time interval to the next timestep and the number of interface cells to read were provided (Figure B-3).

```
TIME= 0.600461841 Flow Boundary= 20.0
Cell(178 1 266 ) 49.977 0.000 19899.973 0.000 0.000 0.000
0.000 0.0000E+00 0.0000E+00 0.0000E+00 0.0000E+00
0.000 0.0000E+00 0.0000E+00 0.0000E+00 0.0000E+00
```

Figure B-2 Example of the first few lines at the beginning of a new timestep in the SOVA output files. The first line indicates the time at which the output has been provided and the next three lines provide the macroscopic data inside a given interface cell.

```
zone 0.000835 45684 20.0009
11850 5550 14950 1050.63 404.199 100.533 0.15 364.2 150 150 150
```

Figure B-3 Example of the first two lines at the beginning of a new timestep in the DSMC input files. The first line indicates the time interval, number of interface cells to read for that timestep and the time at which the output has been provided. The next line provides the cell location, velocities, density, temperature and cell sizes for a given interface cell.

The listing of the preprocessed DSMC input files (impact\_new.dat) is presented in Figure B-4. The size of the zipped processed files was then 27.5 GB, with the largest file unzipped file being impact150\_new.dat at 6.0 GB and the smallest being impact030\_new.dat at 366 MB. Note that the largest preprocessed file is not the largest SOVA output file as several other parameters come into play in the preprocessed file size such as the number of interface cells with pure water during that time.

-rw-r--r--	1	larignon cfd	435M	2009-06-16 10:20	impact010_new.dat.gz
-rw-r--r--	1	larignon cfd	226M	2009-06-16 10:20	impact015_new.dat.gz
-rw-r--r--	1	larignon cfd	171M	2009-06-16 10:21	impact020_new.dat.gz
-rw-r--r--	1	larignon cfd	156M	2009-06-16 10:22	impact025_new.dat.gz
-rw-r--r--	1	larignon cfd	101M	2009-06-16 10:22	impact030_new.dat.gz
-rw-r--r--	1	larignon cfd	290M	2009-06-16 10:23	impact035_new.dat.gz
-rw-r--r--	1	larignon cfd	514M	2009-06-16 10:25	impact040_new.dat.gz
-rw-r--r--	1	larignon cfd	648M	2009-06-16 10:30	impact045_new.dat.gz
-rw-r--r--	1	larignon cfd	715M	2009-06-16 10:33	impact050_new.dat.gz
-rw-r--r--	1	larignon cfd	695M	2009-06-16 10:36	impact055_new.dat.gz
-rw-r--r--	1	larignon cfd	668M	2009-06-16 10:37	impact060_new.dat.gz
-rw-r--r--	1	larignon cfd	648M	2009-06-16 10:38	impact065_new.dat.gz
-rw-r--r--	1	larignon cfd	602M	2009-06-16 10:39	impact070_new.dat.gz
-rw-r--r--	1	larignon cfd	571M	2009-06-16 10:40	impact075_new.dat.gz
-rw-r--r--	1	larignon cfd	528M	2009-06-16 10:41	impact080_new.dat.gz
-rw-r--r--	1	larignon cfd	637M	2009-06-16 10:42	impact085_new.dat.gz
-rw-r--r--	1	larignon cfd	713M	2009-06-16 10:43	impact090_new.dat.gz
-rw-r--r--	1	larignon cfd	890M	2009-06-16 10:45	impact095_new.dat.gz
-rw-r--r--	1	larignon cfd	872M	2009-06-16 10:47	impact100_new.dat.gz
-rw-r--r--	1	larignon cfd	990M	2009-06-16 10:49	impact105_new.dat.gz
-rw-r--r--	1	larignon cfd	945M	2009-06-16 10:50	impact110_new.dat.gz
-rw-r--r--	1	larignon cfd	698M	2009-06-16 10:52	impact115_new.dat.gz
-rw-r--r--	1	larignon cfd	910M	2009-06-16 10:53	impact120_new.dat.gz
-rw-r--r--	1	larignon cfd	1.2G	2009-06-16 10:55	impact125_new.dat.gz
-rw-r--r--	1	larignon cfd	1.3G	2009-06-16 10:58	impact130_new.dat.gz
-rw-r--r--	1	larignon cfd	941M	2009-08-09 20:12	impact135_new.dat.gz
-rw-r--r--	1	larignon cfd	760M	2009-08-24 20:58	impact140_new.dat.gz
-rw-r--r--	1	larignon cfd	1.8G	2009-08-28 14:16	impact150_new.dat.gz
-rw-r--r--	1	larignon cfd	988M	2009-09-29 22:16	impact155_new.dat.gz
-rw-r--r--	1	larignon cfd	872M	2009-09-30 17:18	impact160_new.dat.gz
-rw-r--r--	1	larignon cfd	1.5G	2009-09-17 20:23	impact170_new.dat.gz
-rw-r--r--	1	larignon cfd	1.2G	2009-10-01 22:06	impact180_new.dat.gz
-rw-r--r--	1	larignon cfd	1.4G	2009-10-08 23:30	impact190_new.dat.gz
-rw-r--r--	1	larignon cfd	973M	2009-10-09 14:05	impact200_new.dat.gz
-rw-r--r--	1	larignon cfd	860M	2009-10-10 21:26	impact210_new.dat.gz

Figure B-4 Listing of the DSMC input data files used in the simulations of the 45° impact event.

The reservoir cell boundary condition in the DSMC method requires the knowledge of the geometry of the interface so the molecules that did not exit the creation cells can be deleted. For that reason, the SOVA output data is also preprocessed to provide a grid file that contains the location and size of all of the interface cells. After a molecule has been moved, the code searches

through that file in order to determine if the molecule is still within the interface and therefore should be deleted. This file is very small (8.2 MB) and associated with the SOVA input file we have all the data required for the DSMC impact simulations.

## **B.2 PARALLEL SIMULATIONS**

In order to take advantage of the parallel I/O capabilities of TACC supercomputers, the present comet impact event simulations have been run with individual files for each processor. This approach was applicable to the present problem as we used a static domain decomposition for our parallel simulations. The advantages of using individual input data files are twofold. First, if all the I/O computing was done by one processor, all the other processors would be idle during that time therefore decreasing the efficiency of the parallel implementation. Also, when molecules that did not exit the creation cells have to be deleted, a search algorithm is used to see if the molecules are outside of the interface. If the number of cells to search through is smaller noticeable speed-up can be achieved.

Because the SOVA cells are Cartesian and the DSMC cells are spherical, the input data and grid files will contain different cells. In our approach, the input data file only contains cells that have their cell center within the processor boundary. This implementation prevents the creation of molecules by several processors for the same SOVA cell. It requires however, that we transfer molecules created outside of the boundaries of the processor at the end of the creation step to the appropriate processor. The grid file, however, needs to have all the SOVA cells that have any part within the boundaries of the processor in order to verify if a molecule exited the creation interface by the end of the timestep.

## Appendix C

### Spherical Coordinates Calculations needed for the Move Step

#### C.1 PREDICTOR-CORRECTOR SCHEME

In most DSMC calculations, molecule movement is assumed to occur on scales where the influence of gravity can be neglected. For our planetary application problem, however, the influence of gravity on the molecular movement cannot be ignored and has to be modeled. Note that gravity is actually ignored in the SOVA simulations but this was deemed acceptable due to the relatively short timescale ( $< 1$  min) and relatively small domain ( $< 30$  km) used in the hydrocode computations as compared to our DSMC simulations (timescale  $\sim$  months and domain size  $\sim$  thousands of kilometers). We, however, ignored both Coriolis and centrifugal forces in our simulations because the Moon is a slow rotator. Similarly, the gravitational influence of the Earth and the Sun are ignored. For our simulations, the initial assumptions were that for relatively small distances travelled during one timestep the acceleration that a molecule undergoes during flight can be approximated by the gravity field at the initial location of the molecule and the velocity of the molecule used to calculate the new position of the molecule is constant. However, when the distance travelled by a molecule during one timestep becomes large, that initial assumption breaks down and a predictor-corrector scheme must be implemented.

While molecular positions are given in spherical coordinates, the molecular velocities ( $V_x, V_y, V_z$ ) are Cartesian so the movement of the molecules is done in the Cartesian coordinate system. For a molecule initially at the location  $(r_0, \theta_0, \varphi_0)$  in the spherical coordinate system, its Cartesian coordinates are:

$$\begin{aligned} X_0 &= r_0 \sin(\theta_0) \cos(\varphi_0) \\ Y_0 &= r_0 \sin(\theta_0) \sin(\varphi_0) \\ Z_0 &= r_0 \cos(\theta_0) \end{aligned} \tag{C.1}$$

The gravity components in the Cartesian coordinate system are given by:

$$\begin{aligned}
 g_X &= -g \sin(\theta_0) \cos(\varphi_0) \frac{Radius_{Moon}^2}{r_0^2} \\
 g_Y &= -g \sin(\theta_0) \sin(\varphi_0) \frac{Radius_{Moon}^2}{r_0^2} \\
 g_Z &= -g \cos(\theta_0) \frac{Radius_{Moon}^2}{r_0^2}
 \end{aligned} \tag{C.2}$$

where  $g$  is the gravity at the surface of the Moon and is equal to  $1.62 \text{ ms}^{-2}$ .

The new position of a molecule at the end of the timestep,  $\Delta t$ ,  $(X_l, Y_l, Z_l)$  in Cartesian and  $(r_l, \theta_l, \varphi_l)$  in spherical coordinates, is given by twice integrating Newton's second law over time:

$$\begin{aligned}
 X_1 &= X_0 + V_X \times \Delta t + \frac{1}{2} \times g_X \times \Delta t^2 \\
 Y_1 &= Y_0 + V_Y \times \Delta t + \frac{1}{2} \times g_Y \times \Delta t^2 \\
 Z_1 &= Z_0 + V_Z \times \Delta t + \frac{1}{2} \times g_Z \times \Delta t^2
 \end{aligned} \tag{C.3}$$

and

$$\begin{aligned}
 r_1 &= \sqrt{X_1^2 + Y_1^2 + Z_1^2} \\
 \theta_1 &= \tan^{-1} \left( \frac{\sqrt{X_1^2 + Y_1^2}}{Z_1} \right) \\
 \varphi_1 &= \tan^{-1} \left( \frac{Y_1}{X_1} \right)
 \end{aligned} \tag{C.4}$$

The updated velocities at the end of the timestep  $(V_{Xl}, V_{Yl}, V_{Zl})$  are given by:

$$\begin{aligned}
 V_{X1} &= V_X + g_X \times \Delta t \\
 V_{Y1} &= V_Y + g_Y \times \Delta t \\
 V_{Z1} &= V_Z + g_Z \times \Delta t
 \end{aligned} \tag{C.5}$$

For planetary scale problems, molecules may move over thousands of kilometers during a simulation. Also, the timescales of interest may be up to weeks or months. Therefore for our full planetary simulations, the timestep and cell size have to be relatively large. In addition, the post-impact velocities of our molecules can be up to tens of kilometers per second, so molecules may move over hundred of meters in one timestep. Under these conditions, approximating the acceleration that the molecule undergoes during flight to the acceleration at its initial location may not provide an accurate solution. In order to improve our solution we implemented a “predictor-corrector” scheme for the movement step of the molecules. First, we calculate the midway point by using half the timestep in Eq. (C.3):

$$\begin{aligned} X_{1/2} &= X_0 + V_X \times \frac{\Delta t}{2} + \frac{1}{2} \times g_X \times \left(\frac{\Delta t}{2}\right)^2 \\ Y_{1/2} &= Y_0 + V_Y \times \frac{\Delta t}{2} + \frac{1}{2} \times g_Y \times \left(\frac{\Delta t}{2}\right)^2 \\ Z_{1/2} &= Z_0 + V_Z \times \frac{\Delta t}{2} + \frac{1}{2} \times g_Z \times \left(\frac{\Delta t}{2}\right)^2 \end{aligned} \quad (C.6)$$

and

$$\begin{aligned} r_{1/2} &= \sqrt{X_{1/2}^2 + Y_{1/2}^2 + Z_{1/2}^2} \\ \theta_{1/2} &= \tan^{-1} \left( \frac{\sqrt{X_{1/2}^2 + Y_{1/2}^2}}{Z_{1/2}} \right) \\ \varphi_{1/2} &= \tan^{-1} \left( \frac{Y_{1/2}}{X_{1/2}} \right) \end{aligned} \quad (C.7)$$

Then we compute the acceleration due to gravity at that location:

$$\begin{aligned} g'_X &= -g \sin(\theta_{1/2}) \cos(\varphi_{1/2}) \frac{Radius_{Moon}^2}{r_{1/2}^2} \\ g'_Y &= -g \sin(\theta_{1/2}) \sin(\varphi_{1/2}) \frac{Radius_{Moon}^2}{r_{1/2}^2} \\ g'_Z &= -g \cos(\theta_{1/2}) \frac{Radius_{Moon}^2}{r_{1/2}^2} \end{aligned} \quad (C.8)$$

Finally, the location of the molecule at the end of the timestep is calculated by using the midway point acceleration:

$$\begin{aligned} X_1 &= X_0 + V_X \times \Delta t + \frac{1}{2} \times g'_X \times \Delta t^2 \\ Y_1 &= Y_0 + V_Y \times \Delta t + \frac{1}{2} \times g'_Y \times \Delta t^2 \\ Z_1 &= Z_0 + V_Z \times \Delta t + \frac{1}{2} \times g'_Z \times \Delta t^2 \end{aligned} \quad (C.9)$$

and  $(r_I, \theta_I, \varphi_I)$  are given by Eq. (C.4).

The updated velocities at the end of the timestep ( $V_{X1}, V_{Y1}, V_{Z1}$ ) are given by:

$$\begin{aligned} V_{X1} &= V_X + g'_X \times \Delta t \\ V_{Y1} &= V_Y + g'_Y \times \Delta t \\ V_{Z1} &= V_Z + g'_Z \times \Delta t \end{aligned} \quad (C.10)$$

## C.2 SURFACE TEMPERATURE MAP

The surface temperature at a given point on the surface of the Moon is related to its relative angle to the subsolar point,  $\delta$ . In a given spherical coordinate system, the angle between two points,  $A = (\varphi_A, \theta_A)$  and  $B = (\varphi_B, \theta_B)$ , is given by:

$$\cos(\delta) = \sin(\theta_A) \sin(\theta_B) [\sin(\varphi_A) \sin(\varphi_B) + \cos(\varphi_A) \cos(\varphi_B)] + \cos(\theta_A) \cos(\theta_B) \quad (C.11)$$

In order to take advantage of the fine grid near the axis of symmetry of the domain, we fixed the impact point at  $(\theta = 0^\circ, \varphi)$  in the reference frame presented in Figure C-1, called the Old reference frame  $(X_{OLD}, Y_{OLD}, Z_{OLD})$ . In the Old reference frame, the origin is at the center of the Moon; the  $Z_{OLD}$ -axis passes through the impact point and the  $X_{OLD}$ -axis is in the plane of symmetry of our impact. One of the objectives of our simulation was to run multiple simulations of the same impact conditions for different impact locations. To do so, we decided to rotate the surface temperature map in order to reflect the actual latitude and longitude picked for the impact location. Or more explicitly, the North Pole of the Moon is defined in the Old reference frame by the following angles  $(\theta_{NP}, \varphi_{NP})$ . In order to assign the correct values for the temperature at each



surface cell, we need to know the relative location of the cell center to the North Pole of the Moon and/or the subsolar point. Therefore, we created a New reference frame where the  $Z_{NEW}$ -axis passes through the North Pole and the  $X_{NEW}$ - and  $Y_{NEW}$ -axes are in the orbital plane of the Moon. In this frame, the coordinates of a point are given by the angles  $(\Theta, \Phi)$  and the location of the subsolar point is given by  $(\Phi_{SS}, \Theta_{SS} = \pi/2)$  (Figure C-1).

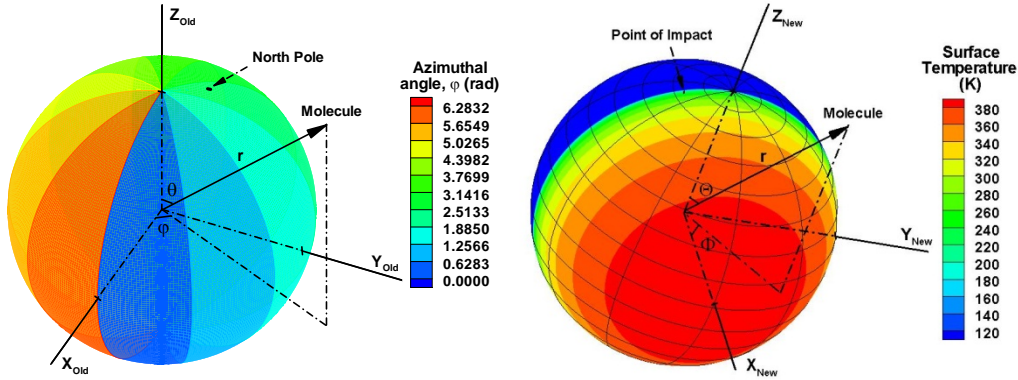


Figure C-1 Coordinates of the same molecule in the Old (left) and New (right) reference frames. The Old reference frame (left) has the point of impact located at the axis of symmetry of the spherical domain. In the left figure, the surface contours represent the azimuthal angle  $\phi$ . Because the domain decomposition for the parallel simulations is made in the Old reference frame, each color represents the domain simulated on one processor. The New reference frame (right) has the North Pole of the Moon at the axis of symmetry of the spherical domain. In the right hand side figure, surface temperature contours are plotted with superimposed latitude and longitude lines.

The rotation between the Old  $(X_{OLD}, Y_{OLD}, Z_{OLD})$  and the New  $(X_{NEW}, Y_{NEW}, Z_{NEW})$  reference frames is as follows:

$$\begin{aligned}\overrightarrow{X_{NEW}} &= \cos(\varphi_{NP}) \cos(\theta_{NP}) \overrightarrow{X_{OLD}} + \sin(\varphi_{NP}) \cos(\theta_{NP}) \overrightarrow{Y_{OLD}} - \sin(\theta_{NP}) \overrightarrow{Z_{OLD}} \\ \overrightarrow{Y_{NEW}} &= -\sin(\varphi_{NP}) \overrightarrow{X_{OLD}} + \cos(\varphi_{NP}) \overrightarrow{Y_{OLD}} \\ \overrightarrow{Z_{NEW}} &= \cos(\varphi_{NP}) \sin(\theta_{NP}) \overrightarrow{X_{OLD}} + \sin(\varphi_{NP}) \sin(\theta_{NP}) \overrightarrow{Y_{OLD}} + \cos(\theta_{NP}) \overrightarrow{Z_{OLD}}\end{aligned}\tag{C.12}$$

or inversely:

$$\begin{aligned}
\overrightarrow{X_{OLD}} &= \cos(\varphi_{NP}) \cos(\theta_{NP}) \overrightarrow{X_{NEW}} - \sin(\varphi_{NP}) \overrightarrow{Y_{NEW}} + \cos(\varphi_{NP}) \sin(\theta_{NP}) \overrightarrow{Z_{NEW}} \\
\overrightarrow{Y_{OLD}} &= \sin(\varphi_{NP}) \cos(\theta_{NP}) \overrightarrow{X_{NEW}} + \cos(\varphi_{NP}) \overrightarrow{Y_{NEW}} + \sin(\varphi_{NP}) \sin(\theta_{NP}) \overrightarrow{Z_{NEW}} \\
\overrightarrow{Z_{OLD}} &= -\sin(\theta_{NP}) \overrightarrow{X_{NEW}} + \cos(\theta_{NP}) \overrightarrow{Z_{NEW}}
\end{aligned} \tag{C.13}$$

The relationship between the spherical  $(\theta_{OLD}, \varphi_{OLD})$  and Cartesian coordinates  $(X_{OLD}, Y_{OLD}, Z_{OLD})$  in the Old reference frame, for a point at the surface of the Moon, is given by:

$$\begin{aligned}
X_{OLD} &= Radius_{Moon} \cos(\varphi_{OLD}) \sin(\theta_{OLD}) \\
Y_{OLD} &= Radius_{Moon} \sin(\varphi_{OLD}) \sin(\theta_{OLD}) \\
Z_{OLD} &= Radius_{Moon} \cos(\theta_{OLD})
\end{aligned} \tag{C.14}$$

Similarly, in the New reference frame, the relationship between the spherical  $(\theta_{NEW}, \Phi_{NEW})$  and Cartesian coordinates  $(X_{NEW}, Y_{NEW}, Z_{NEW})$ , for a point at the surface of the Moon, is given by:

$$\begin{aligned}
X_{NEW} &= Radius_{Moon} \cos(\Phi_{NEW}) \sin(\theta_{NEW}) \\
Y_{NEW} &= Radius_{Moon} \sin(\Phi_{NEW}) \sin(\theta_{NEW}) \\
Z_{NEW} &= Radius_{Moon} \cos(\theta_{NEW})
\end{aligned} \tag{C.15}$$

By replacing Eqs. (C.14) and (C.15) in Eq. (C.13), we find:

$$\begin{aligned}
&\cos(\varphi_{OLD}) \sin(\theta_{OLD}) = \\
&\cos(\varphi_{NP}) \cos(\theta_{NP}) \cos(\Phi_{NEW}) \sin(\theta_{NEW}) - \sin(\varphi_{NP}) \sin(\Phi_{NEW}) \sin(\theta_{NEW}) + \\
&\cos(\varphi_{NP}) \sin(\theta_{NP}) \cos(\theta_{NEW}) \\
&\sin(\varphi_{OLD}) \sin(\theta_{OLD}) = \\
&\sin(\varphi_{NP}) \cos(\theta_{NP}) \cos(\Phi_{NEW}) \sin(\theta_{NEW}) + \cos(\varphi_{NP}) \sin(\Phi_{NEW}) \sin(\theta_{NEW}) + \\
&\sin(\varphi_{NP}) \cos(\theta_{NP}) \cos(\theta_{NEW}) \\
&\cos(\theta_{OLD}) = -\sin(\theta_{NP}) \cos(\Phi_{NEW}) \sin(\theta_{NEW}) + \cos(\theta_{NP}) \cos(\theta_{NEW})
\end{aligned} \tag{C.16}$$

The location of the subsolar point in the New reference frame is given by the following coordinates ( $\Phi_{SS}$ ,  $\Theta_{SS} = \pi/2$ ). By plugging these coordinates in the previous equation, we find:

$$\begin{aligned}\cos(\varphi_{SS}) \sin(\theta_{SS}) &= \cos(\varphi_{NP}) \cos(\theta_{NP}) \cos(\Phi_{SS}) - \sin(\varphi_{NP}) \sin(\Phi_{SS}) \\ \sin(\varphi_{SS}) \sin(\theta_{SS}) &= \sin(\varphi_{NP}) \cos(\theta_{NP}) \cos(\Phi_{SS}) + \cos(\varphi_{NP}) \sin(\Phi_{SS}) \\ \cos(\theta_{SS}) &= -\sin(\theta_{NP}) \cos(\Phi_{SS})\end{aligned}\tag{C.17}$$

Using Eq. (C.11), we find that the angle between one of our grid points  $P = (\varphi_P, \theta_P)$  and the subsolar point is:

$$\begin{aligned}\cos(\delta) &= \sin(\theta_{SS}) \sin(\varphi_{SS}) \sin(\theta_P) \sin(\varphi_P) + \sin(\theta_{SS}) \sin(\varphi_{SS}) \cos(\varphi_P) \cos(\varphi_P) \\ &\quad + \cos(\theta_{SS}) \cos(\theta_P)\end{aligned}\tag{C.18}$$

or, by replacing Eq. (C.17) into Eq. (C.18) and after reorganizing

$$\begin{aligned}\cos(\delta) &= \cos(\theta_{NP}) \cos(\Phi_{SS}) \sin(\theta_P) \cos(\varphi_{NP} - \varphi_P) + \sin(\Phi_{SS}) \sin(\theta_P) \sin(\varphi_P - \varphi_{NP}) \\ &\quad - \sin(\theta_{NP}) \cos(\Phi_{SS}) \cos(\theta_P)\end{aligned}\tag{C.19}$$

In order to account for the rotation of the Moon around the Sun, we assumed that the Moon rotates around its polar axis. Using this assumption, the longitude of the subsolar point is time dependent and varies as:

$$\Phi_{SS} = -[2.463 \times 10^{-6} \times i \times \Delta t] + \text{Const}\tag{C.20}$$

where  $i$  is the timestep number,  $\Delta t$  is the timestep size and  $\text{Const}$  is a constant.

## C.2 LOCATION OF THE COLD TRAPS

The locations of the cold traps that we are using in our calculations are in the New reference frame. However, we need to know their locations in the Old reference frame in order to verify if a molecule landed inside these craters. To save on computational time, at each timestep, we first want to know if a molecule that just landed on the Moon's surface is actually near the

Poles. In our simulations, we only consider molecules that have arrived within  $10^\circ$  of the Poles, an angle within which our craters fully lie. In order to verify this first assumption we use Eq. (C.1) for the angle between the North ( $\theta_{NP}$ ,  $\varphi_{NP}$ ) or South ( $\theta_{SP} = \pi + \theta_{NP}$ ,  $\varphi_{SP}$ ) Pole and the molecule location ( $\theta_{mol}$ ,  $\varphi_{mol}$ ).

North Pole:

$$\cos(\delta) = \sin(\theta_{NP}) \sin(\theta_{mol}) \cos(\varphi_{NP} - \varphi_{mol}) + \cos(\theta_{NP}) \cos(\theta_{mol}) \quad (C.21)$$

South Pole:

$$\cos(\delta) = -\sin(\theta_{NP}) \sin(\theta_{mol}) \cos(\varphi_{NP} - \varphi_{mol}) + \cos(\theta_{NP}) \cos(\theta_{mol}) \quad (C.22)$$

A molecule is considered for possibly being caught by a cold trap if the angle  $\delta$  calculated using Eqs. (C.21) or (C.22) is smaller than  $10^\circ$ , which is equivalent to:

$$\cos(\delta) > 0.985 \quad (C.23)$$

If the previous equation is valid for either the North Pole or the South Pole, the code starts to loop over the list of cold traps for that Pole. For each cold trap, the code first calculates the distance between the molecule and the center of the cold trap ( $\theta_{CT}$ ,  $\varphi_{CT}$ ), using Eq. (C.16) into Eq. (C.11):

$$\begin{aligned} \cos(\delta) = & \sin(\theta_{mol}) \sin(\theta_{CT}) \times [\cos(\theta_{NP}) \cos(\varphi_{CT}) \cos(\varphi_{NP} - \varphi_{mol}) + \sin(\varphi_{CT}) \sin(\varphi_{mol} - \varphi_{NP}) + \\ & \cos(\theta_{CT}) \times \{\cos(\theta_{NP}) \sin(\varphi_{NP}) \sin(\varphi_{mol}) + \sin(\theta_{NP}) \cos(\varphi_{NP}) \cos(\varphi_{mol})\}] \\ & + \cos(\theta_{mol}) \times [\cos(\theta_{NP}) \cos(\theta_{CT}) - \sin(\theta_{NP}) \sin(\theta_{CT}) \cos(\varphi_{CT})] \end{aligned} \quad (C.24)$$

The molecule will be within the cold trap if:

$$\cos(\delta) > \cos\left(\frac{Radius_{CT}}{Radius_{Moon}}\right) \quad (C.25)$$

### C.3 SHADOW CALCULATIONS

While molecules are in-flight in the sunlit part of the atmosphere around the Moon, they might be destroyed due to photo-dissociation or photo-ionization processes. In order to determine if a molecule is in the sunlit part of the domain or in the shadow of the Moon (Figure C-2), the code calculates the angle between the subsolar point and the molecule (Eq. (C.19)):

$$\begin{aligned} \cos(\delta) = & \cos(\theta_{NP})\cos(\Phi_{SS}) \sin(\theta_{mol}) \cos(\varphi_{NP} - \varphi_{mol}) \\ & + \sin(\Phi_{SS}) \sin(\theta_{mol}) \sin(\varphi_{mol} - \varphi_{NP}) - \sin(\theta_{NP}) \cos(\Phi_{SS}) \cos(\theta_{mol}) \end{aligned} \quad (C.26)$$

Using this equation a molecule will be in the shadow of the Moon if:

$$\cos(\delta) < 0 \text{ AND } \cos(\delta - \pi/2) \times r < Radius_{Moon} \quad (C.27)$$

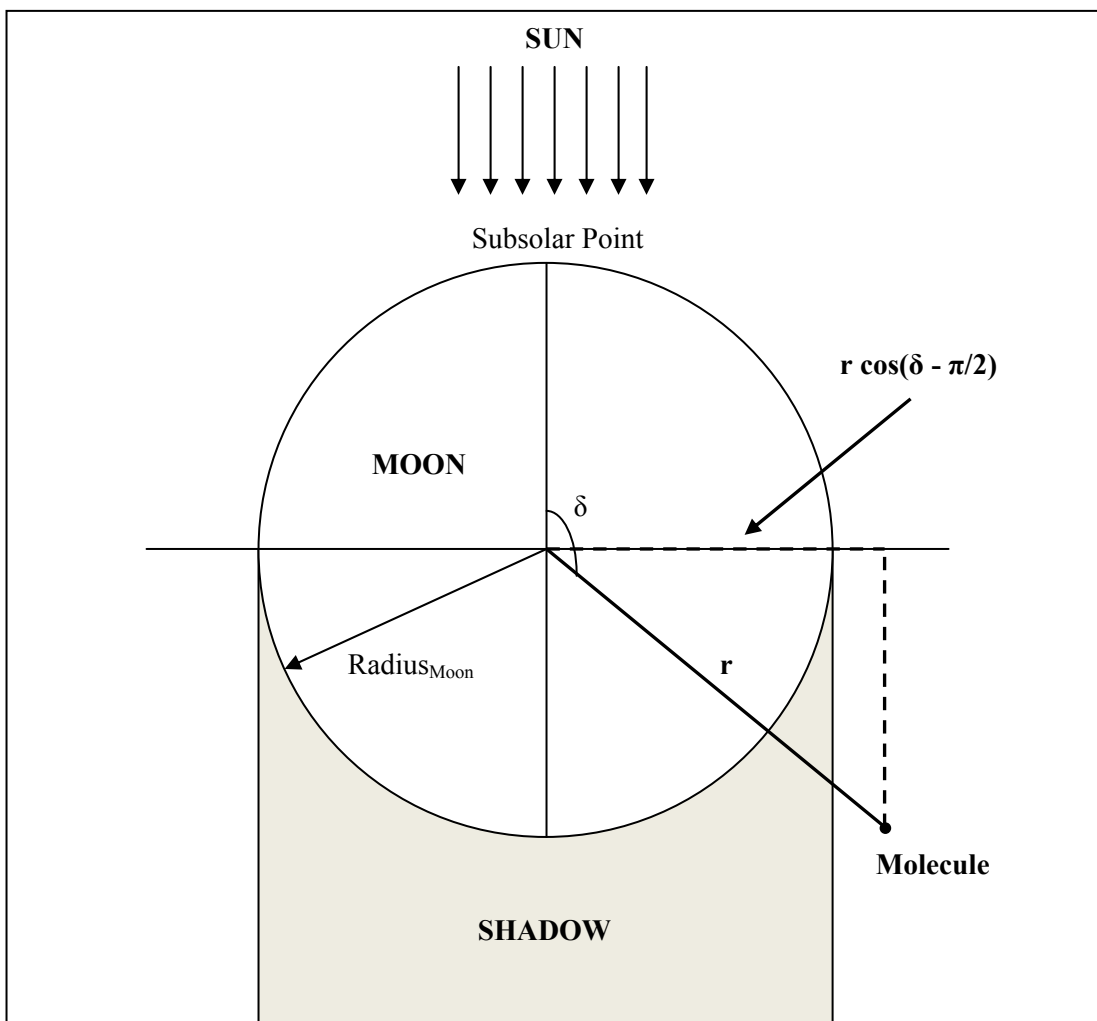


Figure C-2 Schematic of the conditions under which a molecule will be in the sunlit part of the atmosphere versus in the shadow of the Moon.

## Appendix D

### SOVA Solution in the Plane of Symmetry for the 45° Impact

The SOVA simulations run by Dr. Elizabetta Pierazzo have been used as input to our DSMC simulations. In addition to providing data at the transfer hemisphere, the SOVA runs output density contours in the plane of symmetry of the impact as a function of time. These SOVA pictures are presented for the 45° oblique impact of a 1 km in radius ice sphere on the Moon at 30 km/s in the current section.

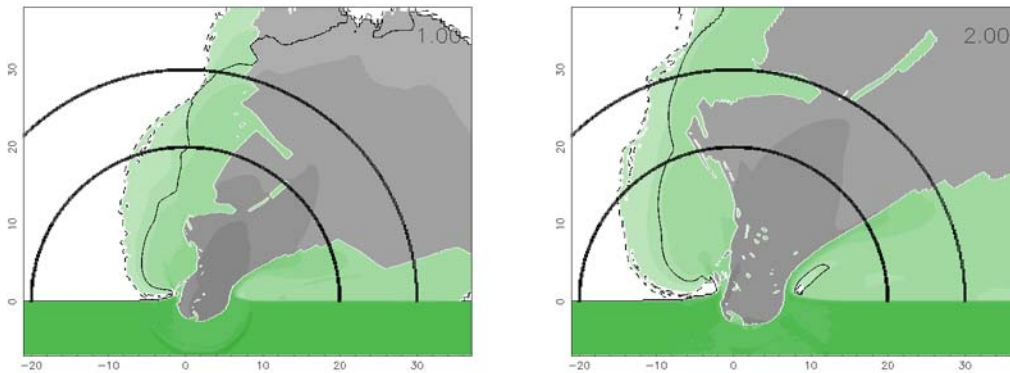


Figure D-1 Density contours 1 and 2 s after the beginning of the impact in the plane of symmetry of the impact. Note that the axes are in kilometers. The green and grey contours represent the rock and water densities, respectively. The darker contours represent denser material. The black lines represent the interface at which the SOVA data is provided for the DSMC simulations.

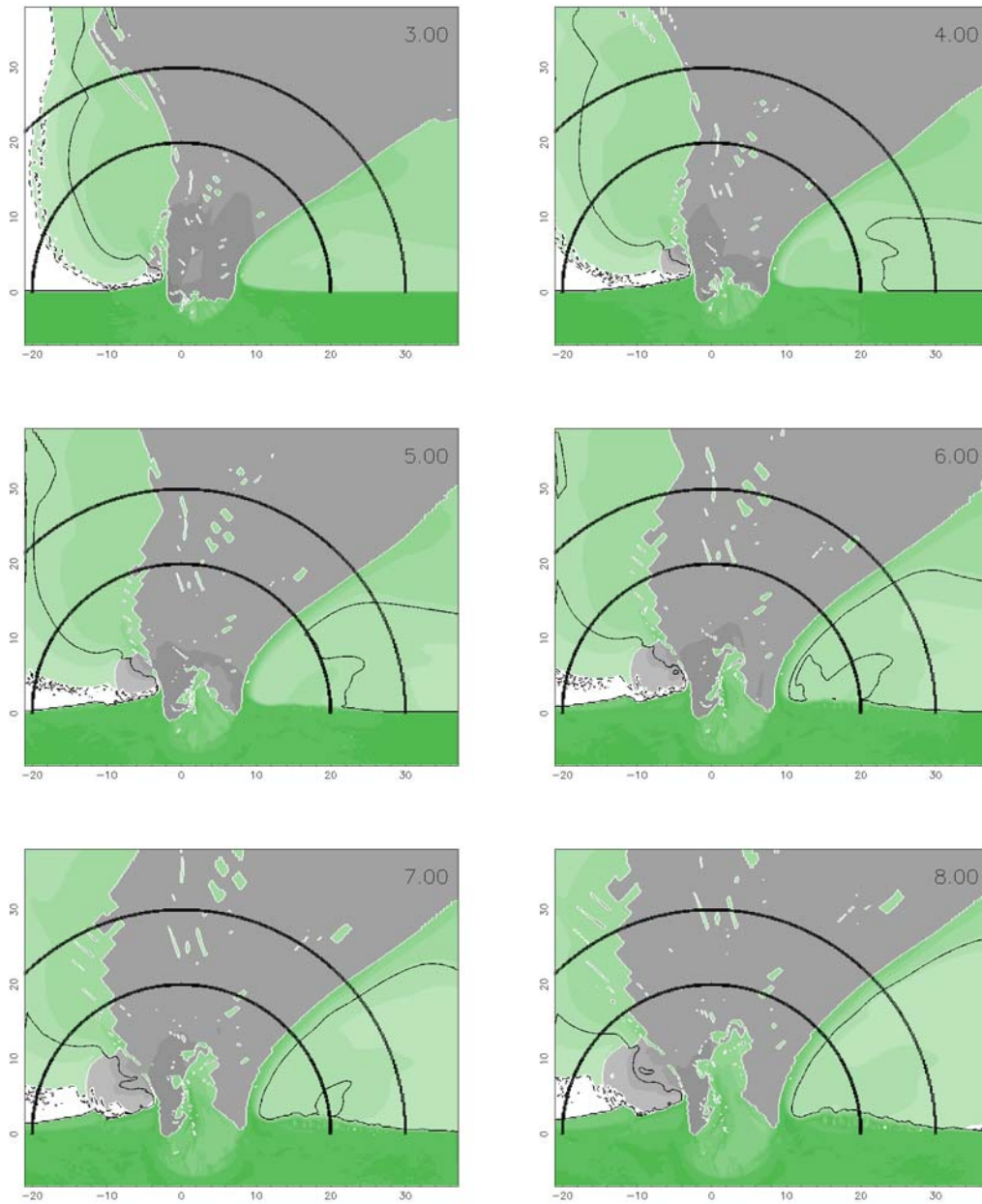


Figure D-2 Density contours 3, 4, 5, 6, 7, and 8 s after the beginning of the impact in the plane of symmetry of the impact. The green and grey contours represent the rock and water densities, respectively. The darker contours represent denser material. The black lines represent the interface at which the SOVA data is provided for the DSMC simulations.



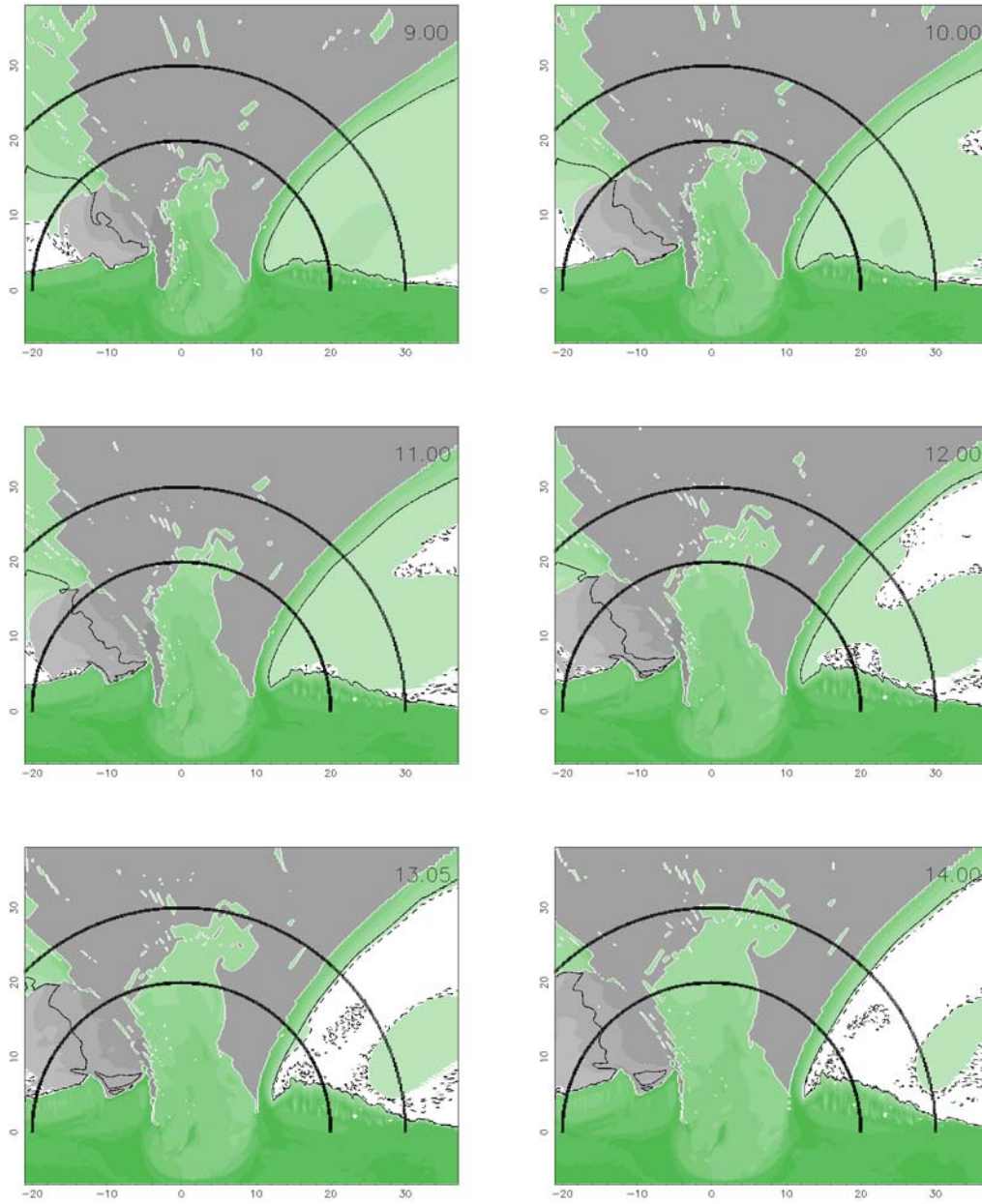


Figure D-3 Density contours 9, 10, 11, 12, 13, and 14 s after the beginning of the impact in the plane of symmetry of the impact. The green and grey contours represent the rock and water densities, respectively. The darker contours represent denser material. The black lines represent the interface at which the SOVA data is provided for the DSMC simulations.

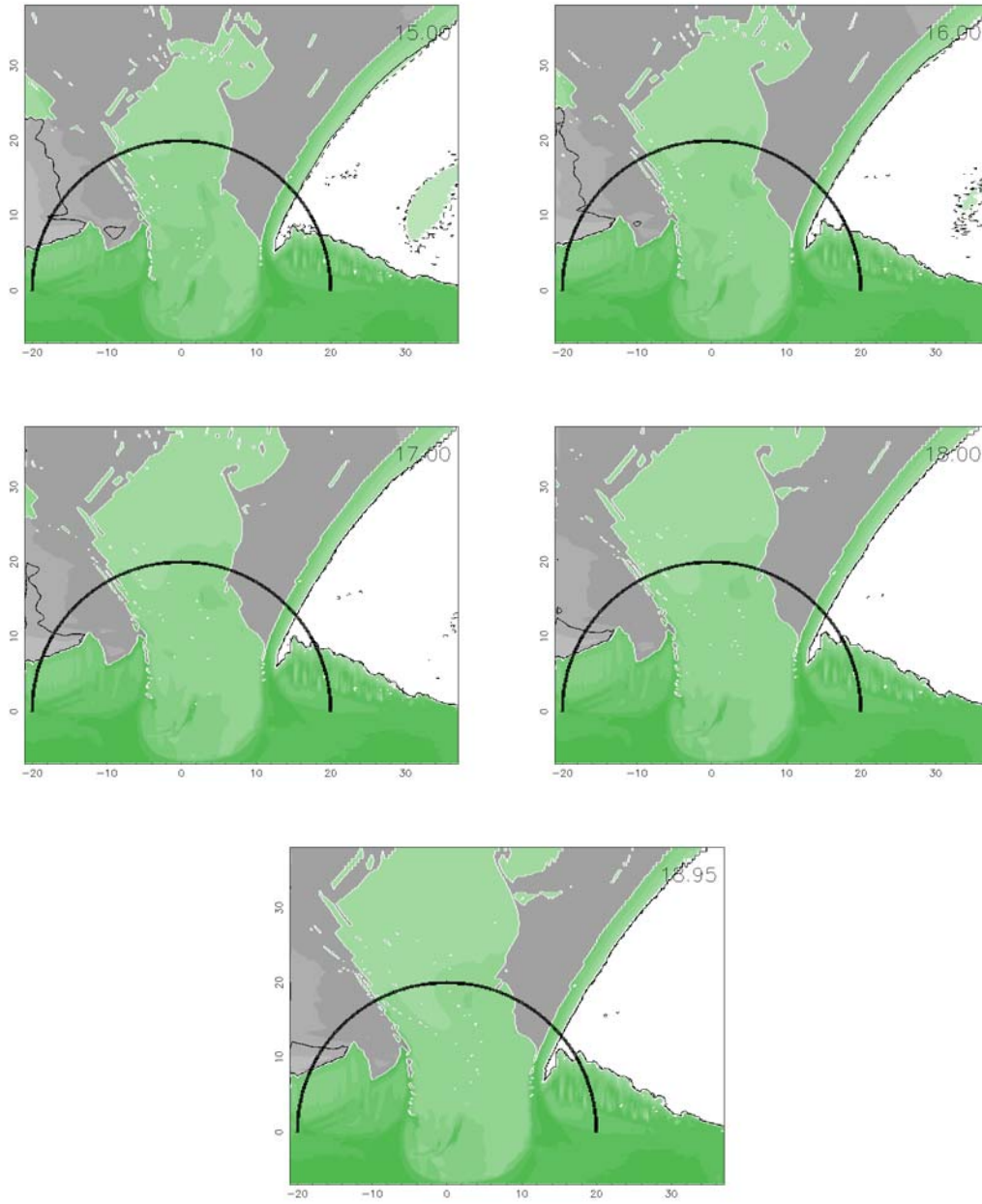


Figure D-4 Density contours 15, 16, 17, 18, and 19 s after the beginning of the impact in the plane of symmetry of the impact. The green and grey contours represent the rock and water densities, respectively. The darker contours represent denser material. The black lines represent the interface at which the SOVA data is provided for the DSMC simulations.

## **Appendix E**

### **Number of Molecules per Cell for the 45° Impact**

The number of molecules per cell is shown in Figure E-1 to Figure E-7 for both the near-field and far-field computations of the 45° oblique impact event. These figures show that the high density plume is well resolved in the near field (more than 4 molecules per cell) while the low density regions of the plume may be slightly under-resolved. As the flow expands, however, the entire plume is much better resolved because each successive domain uses bigger cells as compared to the previous one.

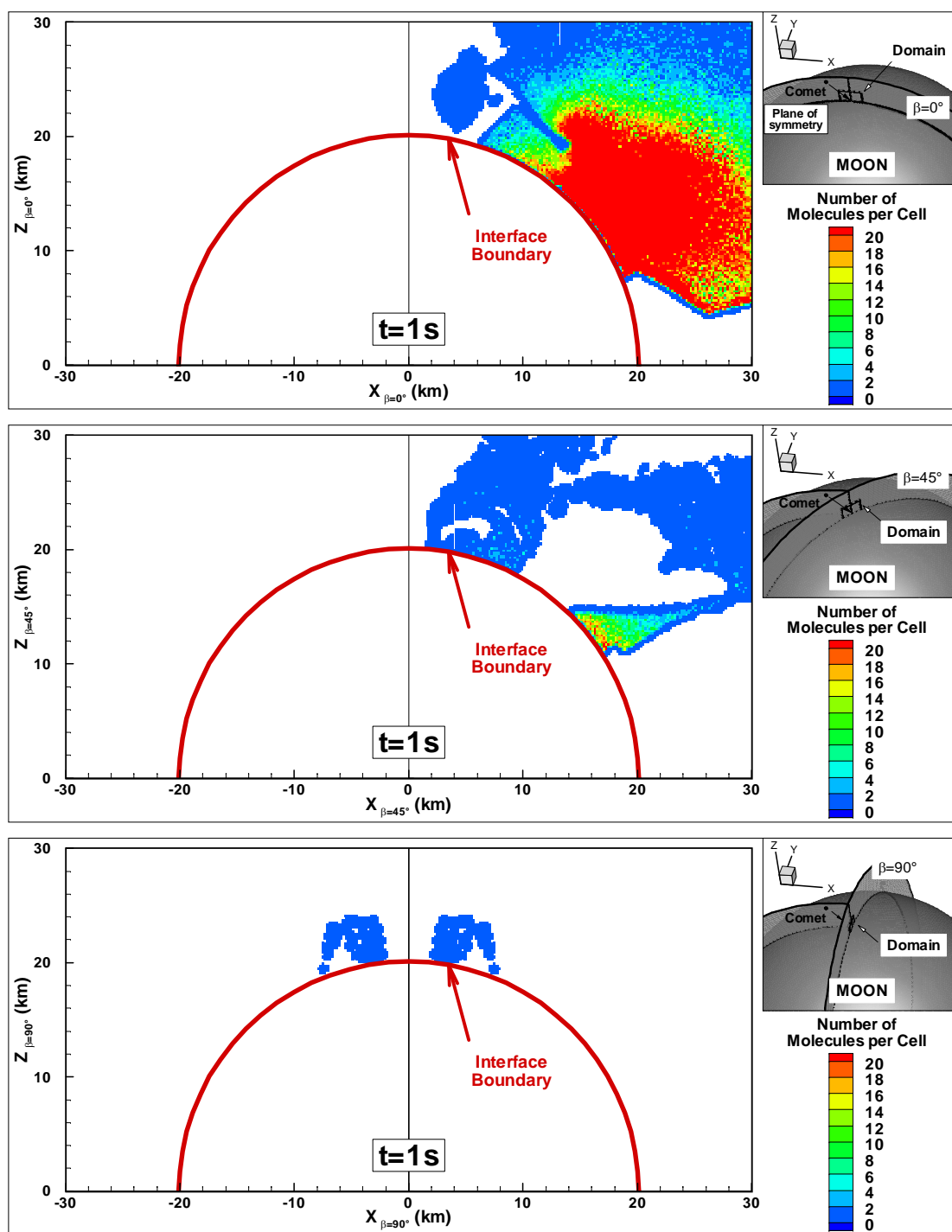


Figure E-1 Near-field number of molecules per cell contours 1 s after impact in the plane of symmetry (top), 45° off the symmetry plane (middle) and perpendicular to the plane of symmetry (bottom).

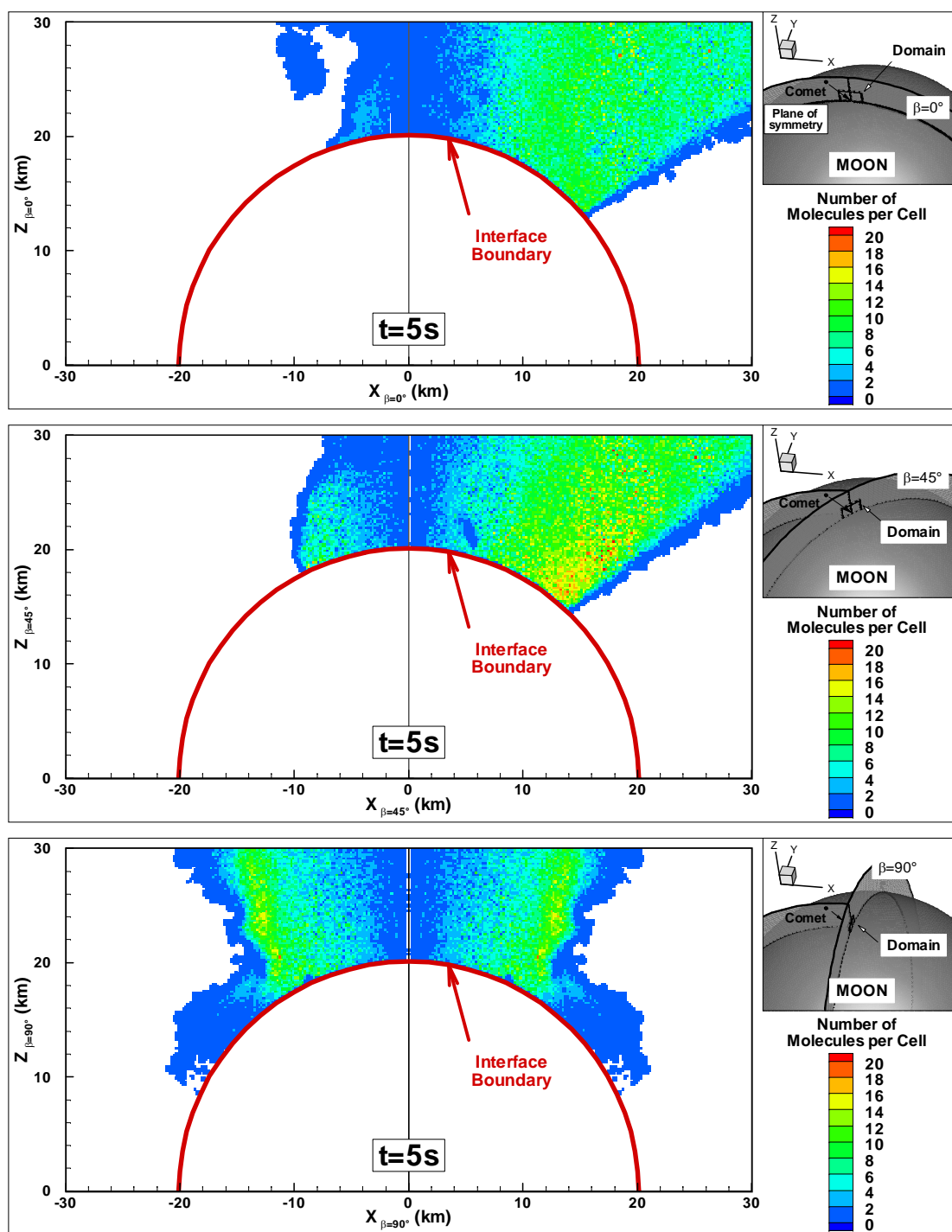


Figure E-2 Near-field number of molecules per cell contours 5 s after impact in the plane of symmetry (top),  $45^\circ$  off the symmetry plane (middle) and perpendicular to the plane of symmetry (bottom).

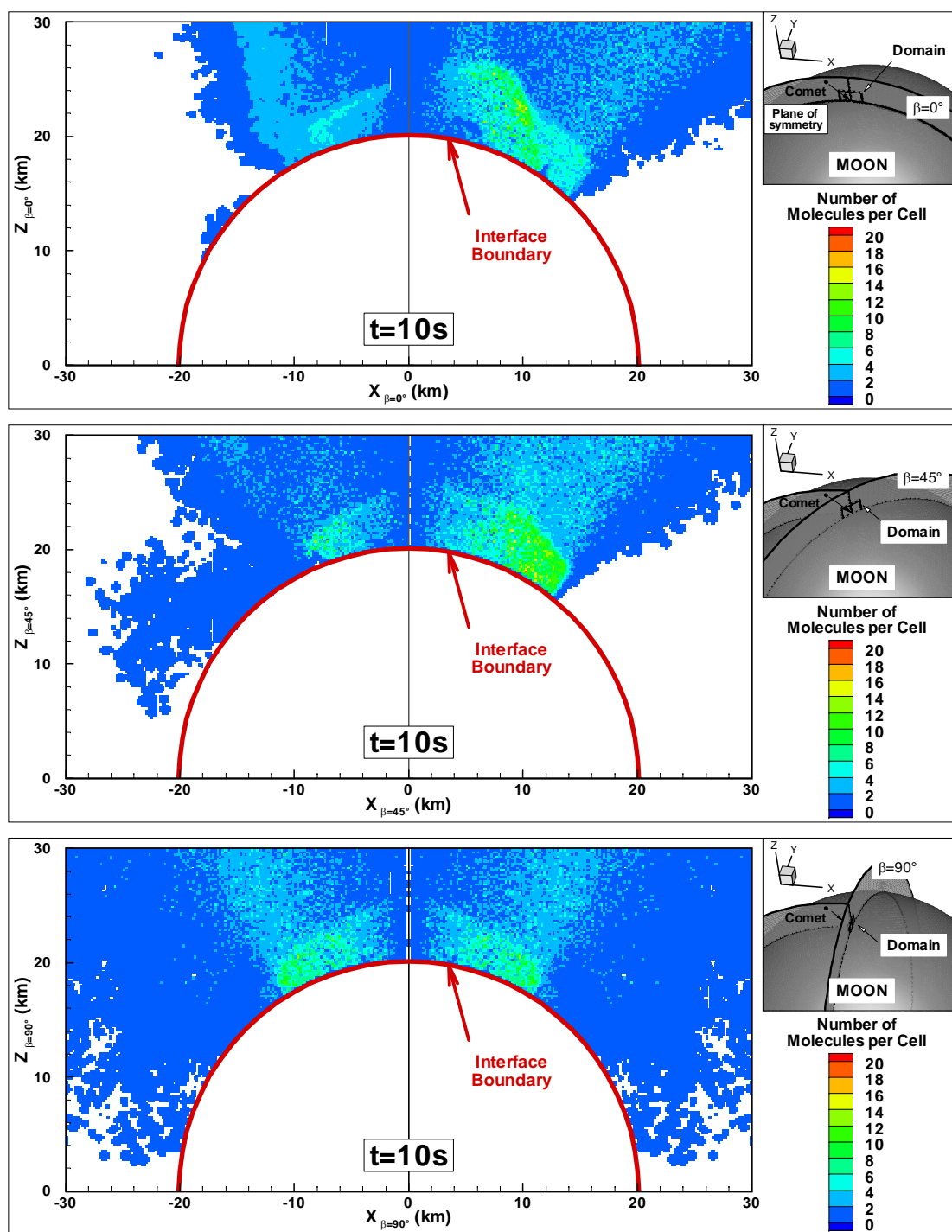


Figure E-3 Near-field number of molecules per cell contours 10 s after impact in the plane of symmetry (top), 45° off the symmetry plane (middle) and perpendicular to the plane of symmetry (bottom).

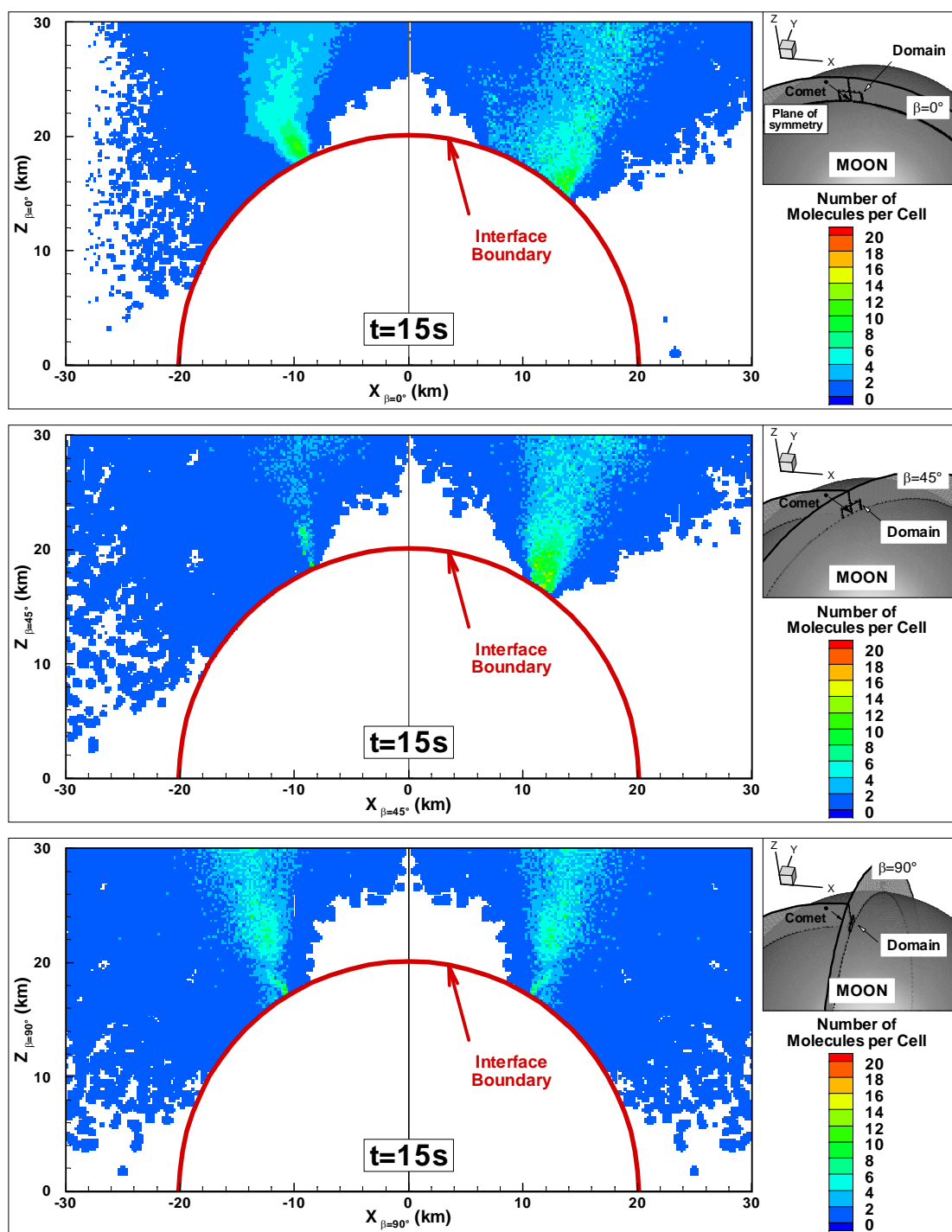


Figure E-4 Near-field number of molecules per cell contours 15 s after impact in the plane of symmetry (top),  $45^\circ$  off the symmetry plane (middle) and perpendicular to the plane of symmetry (bottom).

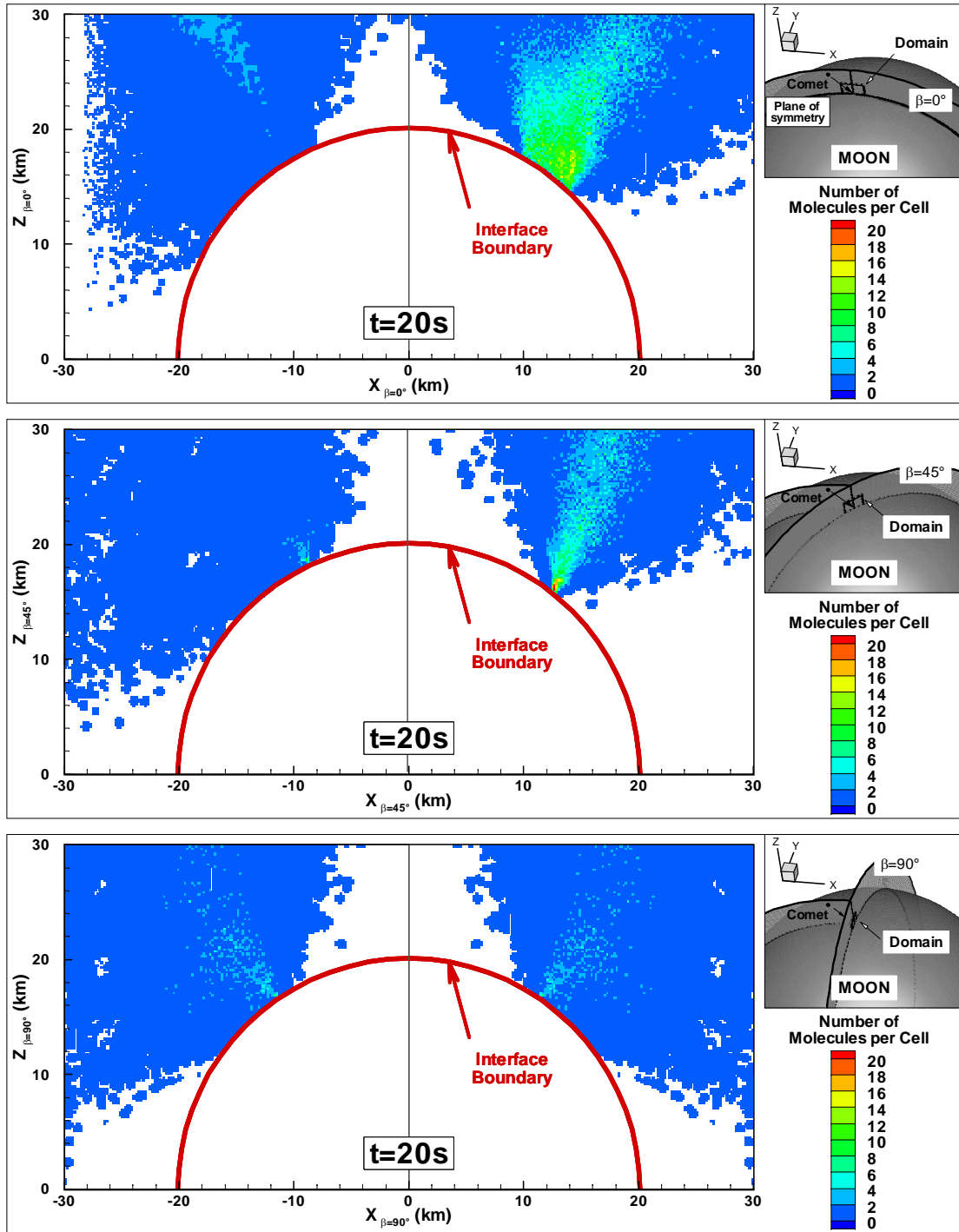


Figure E-5 Near-field number of molecules per cell contours 20 s after impact in the plane of symmetry (top), 45° off the symmetry plane (middle) and perpendicular to the plane of symmetry (bottom).



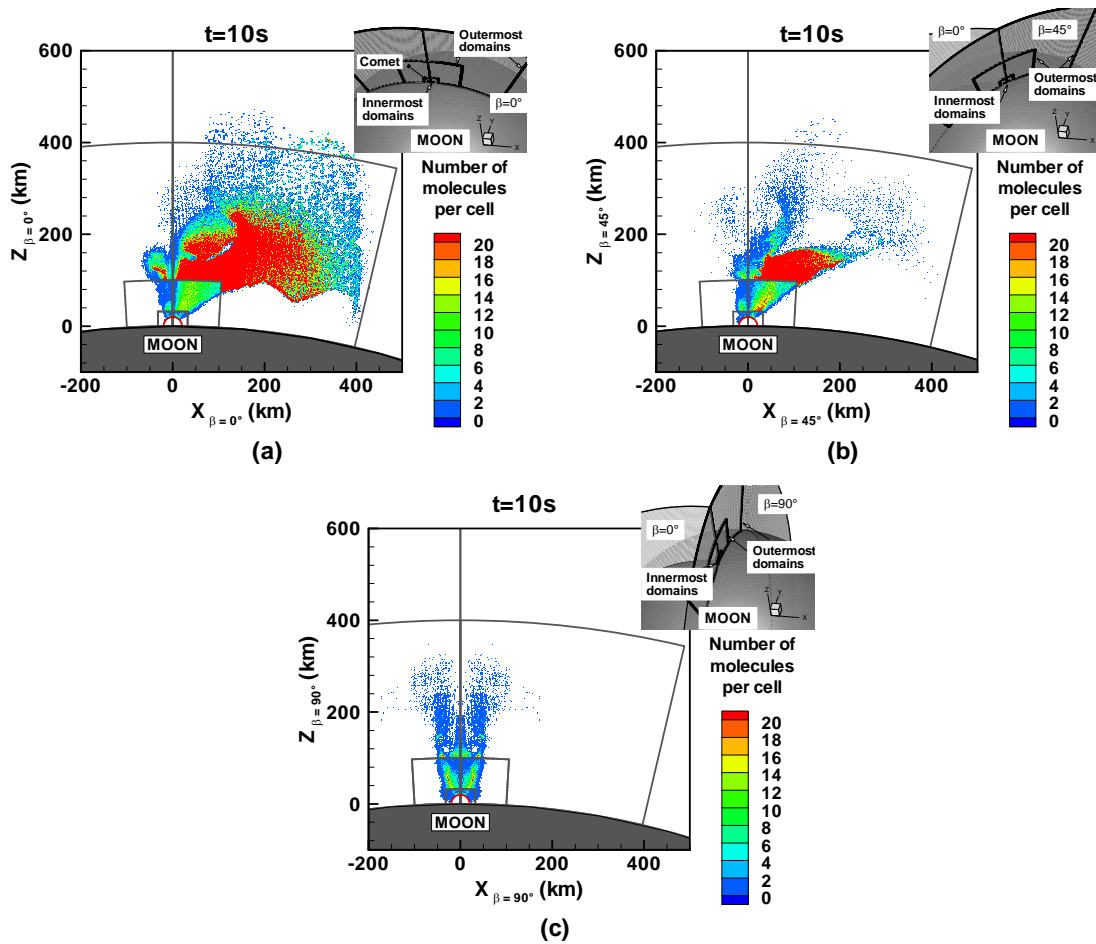


Figure E-6 Number of molecules per cell contours 10 s after impact in: (a) the symmetry plane, (b)  $45^\circ$  off the symmetry plane and (c) perpendicular to the plane of symmetry. Note that because the cell size increases from one domain to the other, the number of molecules per cell is non-uniform across domains.

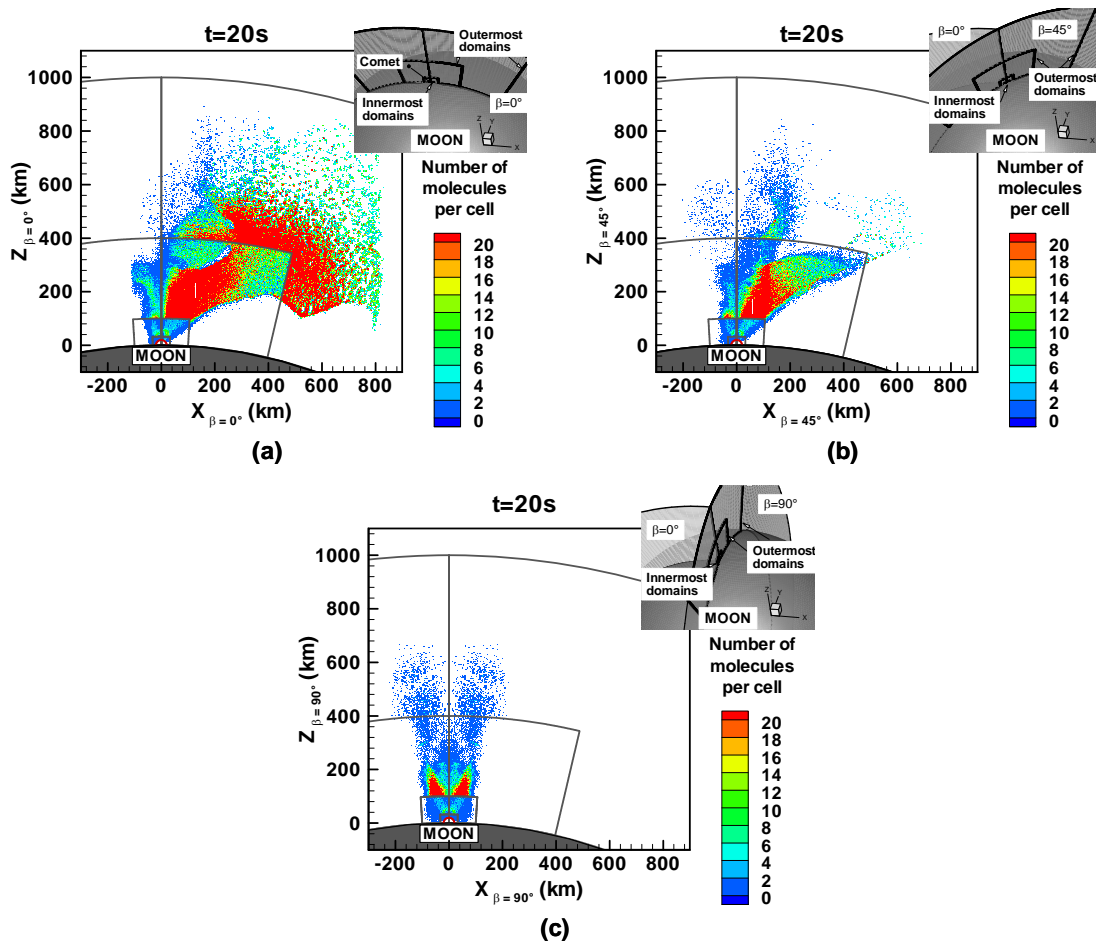


Figure E-7 Number of molecules per cell contours 20 s after impact in: (a) the symmetry plane, (b)  $45^\circ$  off the symmetry plane and (c) perpendicular to the plane of symmetry. Note that because the cell size increases from one domain to the other, the number of molecules per cell is non-uniform across domains.

## References

Arnold, J. R., "Ice in the lunar polar regions," *Journal of Geophysical Research*, Vol. 84, pp. 5659-5668, 1979.

Artemieva, N. A., and Shuvalov, V. V., "Numerical simulation of high-velocity impact ejecta following falls of comets and asteroids onto the Moon," *Solar System Research*, Vol. 42, No. 4, pp. 329-334, 2008.

Austin, J. V., and Goldstein D. B., "Rarefied gas model of Io's sublimation driven atmosphere," *Icarus*, Vol. 148, pp. 370-383, Dec. 2000.

Berezhnoi, A. A., and Klumov, B. A., "Lunar ice: Can its origin be determined?," *JETP Letters*, Vol. 68, No. 2, pp. 163-167, July 1998.

Bergemann, F., and Boyd, I. D., "DSMC simulation of inelastic collisions using the Borgnakke-Larsen method extended to discrete distributions of vibrational energy," in: Shizgal, B.D., Weaver, D.P. (Eds.), *Rarefied Gas Dynamics: Theory and Simulations. Progress in Astronautics and Aeronautics*, pp. 174-183, 1994.

Bird, G. A., "Breakdown of translational and rotational equilibrium in gaseous expansions," *AIAA Journal*, Vol. 8, No. 11, pp. 1998-2003, Nov. 1970.

Bird, G. A., "Molecular gas dynamics and the direct simulation of gas flow," *Oxford University Press*, New York, 1994.

Bird, G. A., "A criterion for the breakdown of vibrational equilibrium in expansions," *Physics of Fluids*, Vol. 14, No. 5, pp. 1732-1735, May 2002.

Bird, G.A., “Sophisticated DSMC,” Notes from *DSMC07 Meeting*, Available at: <http://www.gab.com.au/Resources/DSMC07notes.pdf>, Santa Fe, New-Mexico, pp. 28-29, Sep. 2007.

Burt, J. M., and Boyd, I. D., “A hybrid particle approach for continuum and rarefied flow simulation,” *Journal of Computational Physics*, Vol. 228, No. 2, pp. 460-475, Feb. 2009.

Butler, B. J., “The migration of volatiles on the surfaces of Mercury and the Moon,” *Journal of Geophysical Research*, Vol. 102, No. E8, pp. 19,283-19,291, Aug. 1997.

Bykov, N. Y., Lukyanov, G. A., Bulgakov, A. V., and Bulgakova, N. M., “Modeling of vapor expansion under pulsed laser ablation: Time-of-flight data analysis,” *Rarefied Gas Dynamics: 24<sup>th</sup> International Symposium*, AIP Conference Proceedings, Vol. 762, pp. 373-378, 2005.

Campbell, B. A., Campbell, D. B., Chandler, J. F., Hine, A. A., Nolan, M. C., and Perillat, P. J., “Radar imaging of the lunar poles,” *Nature*, Vol. 426, pp. 137-138, Nov. 2003.

Campbell, B. A., and Campbell, D. B., “Regolith properties in the south polar region of the Moon from 70-cm radar polarimetry,” *Icarus*, Vol. 180, No. 1, pp. 1-7, Jan. 2006.

Campbell, D. B., Campbell, B. A., Carter, L. M., Margot, J.-L., and Stacy, N. J. S., “No evidence for thick deposits of ice at the lunar south pole,” *Nature*, Vol. 443, pp. 835-837, Oct. 2006.

Clark, R. N., “Detection of Adsorbed Water and Hydroxyl on the Moon,” *Science Express Reports*, 10.1126/science.1178105, Sep. 2009.

Crider, D. H. and Vondrak, R. R., “The solar wind as a possible source of lunar polar hydrogen deposits,” *Journal of Geophysical Research*, Vol. 105, No. E11, pp. 26,773-26,782, Nov. 2000.

Crider, D. H., and Vondrak, R. R., "Hydrogen migration to the lunar poles by solar wind bombardment of the Moon," *Advance Space Research*, Vol. 30, No. 8, pp. 1869-1874, 2002.

Crider, D. H. and Vondrak, R. R., "Space weathering effects on lunar cold trap deposits," *Journal of Geophysical Research*, Vol. 108, No. E7, Jul. 2003.

Dietrich, S., and Boyd, I. D., "Scalar and parallel optimized implementation of the Direct Simulation Monte Carlo method," *Journal of Computational Physics*, Vol. 126, No. 2, pp. 328-342, July 1996.

Eke, V. R., Teodoro, L. F. A., and Elphic, R. C., "The spatial distribution of polar hydrogen deposits on the Moon," *Icarus*, Vol. 200, No. 1, pp. 12-18, March 2009.

Elphic, R. C., Eke, V. R., Teodoro, L. F. A., Lawrence, D. J., and Bussey, D. B. J., "Models of the distribution of hydrogen at the lunar south pole," *Geophysical Research Letters*, Vol. 34, L13204, July 2007.

Feldman, W. C., et al., "Major compositional units of the Moon: Lunar Prospector thermal and fast neutrons," *Science*, Vol. 281, pp. 1489-1493, Sep. 1998.

Feldman, W. C., Lawrence, D. J., Elphic, R. C., Barraclough, B. L., Maurice, S., Genetay, I., and Binder, A. B., "Polar hydrogen deposits on the Moon," *Journal of Geophysical Research*, Vol. 105, No. E2, pp. 4175-4195, Feb. 2000.

Fleagle, R. G., and Businger, J. A., "An introduction to atmospheric physics," *International Geophysics Series, Academic Press*, Vol. 25, New York, pp. 69-72, 1980.

Frenkel, Z., "Theorie der adsorption und verwandter erscheinungen," *Z. Physics*, Vol. 26, pp. 117-138, 1924.

Garcia, A. L., and Wagner, W., "Generation of the Maxwellian inflow distribution," *Journal of Computational Physics*, Vol. 217, No. 2, pp. 693-708, Sep. 2006.

Goldstein, D. B., Nerem, R. S., Barker, E. S., Austin, J. V., Binder, A. B., and Feldman, W. C., "Impacting lunar prospector in a cold trap to detect water ice," *Geophysical Research Letters*, Vol. 26, No. 12, pp. 1653-1656, June 1999.

Haruyama, J., Ohtake, M., Matsunaga, T., Morota, T., Honda, C., Yokota, Y., Pieters, C. M., Hara, S., Hioki, K., Saiki, K., Miyamoto, H., Iwasaki, A., Abe, M., Ogawa, Y., Takeda, H., Shirao, M., Yamaji, A., and Josset, J.-L., "Lack of exposed ice inside lunar south pole Shackleton crater," *Science*, Vol. 322, pp. 938-939, Nov. 2008

Hensley, S., Gurrola, E., Rosen, P., Slade, M., Jao, J., Kobrick, M., Wilson, B., Chen, C., and Jurgens, R., "An improved map of the lunar south pole with Earth based radar interferometry," *Radar Conference 2008, IEEE*, pp. 1-6, May 2008.

Hodges, R. R., "Exospheric transport restrictions on water ice in lunar polar traps," *Geophysical Research Letters*, Vol. 18, No. 11, pp. 2113-2116, Nov. 1991.

Hodges, R. R., "Reanalysis of Lunar Prospector neutron spectrometer observations over the lunar poles," *Journal of Geophysical Research*, Vol. 107, No. E12, Dec. 2002.

Huebner, W. F., Keady, J. J. and Lyon, S. P., "Solar photo rates for planetary atmospheres and atmospheric pollutants," *Astrophysics and Space Science*, Vol. 195, pp. 1-294, 1992.

Ingersoll, A. P., Svitek, T., and Murray, B. C., "Stability of polar frosts in spherical bowl-shaped craters on the Moon, Mercury and Mars," *Icarus*, Vol. 100, No. 1, pp. 40-47, Nov. 1992.

Kannenber, K. C., and Boyd, I. D., "Three-dimensional Monte Carlo simulations of plume impingement," *Journal of Thermophysics and Heat Transfer*, Vol. 13, No. 2, pp. 226-235, April-June 1999.

Langmuir, I., "The Evaporation, condensation and reflection of molecules and the mechanism of adsorption," *Physical Review*, Vol. 8, No. 2, pp. 149-176, 1916.

Larsen, P. S., and Borgnakke, C., "Statistical collision model for simulating polyatomic gas with restricted energy exchange," in Becker, M., Capitelli, M. F. (Eds.), *Rarefied Gas Dynamics*, CFVLR Press, PorzWahn, Germany, 1974.

Lawrence, D. J., Feldman, W. C., Elphic, R. C., Hagerty, J. J., Maurice, S., McKinney, G. W. and Prettyman, T. H., "Improved modeling of Lunar Prospector neutron spectrometer data: Implications for hydrogen deposits at the lunar poles," *Journal of Geophysical Research*, Vol. 111, E08001, Aug. 2006.

LeBeau, G. J., "A parallel implementation of the Direct Simulation Monte Carlo method," *Computer Methods in Applied Mechanics and Engineering*, Vol. 174, pp. 319-337, July 1999.

Li, Z., Zhong, J., Levin, D. A., and Garrison, B. J., "Kinetic nucleation model for free expanding water condensation plume simulations," *Journal of Chemical Physics*, Vol. 130, No. 17, 174309, May 2009.

Lilley, C. R., and Macrossan, M. N., "Methods for implementing the stream boundary condition in DSMC computations," *International Journal for Numerical Methods in Fluids*, Vol. 42, No. 12, pp.1363-1371, Aug. 2003.

Macrossan M. N., and Geng, X., "Detecting equilibrium cells in DSMC to improve the computational efficiency," *Rarefied Gas Dynamics: 25<sup>th</sup> International Symposium*, St. Petersburg, Russia, 21-28 July 2006, pp. 361-366, Siberian branch of the Russian academy of sciences, 2007.

McConnochie, T. H., Buratti, B. J., Hillier, J. K. and Tryka, K. A., "A search for water ice at the lunar poles with Clementine images," *Icarus*, Vol. 156, No. 2, pp. 335-351, April 2002.

McGlaun, J. M., Thompson, S. L., and Elrick, M. G., "CTH: A three-dimensional shock wave physics code, *International Journal of Impact Engineering*, Vol. 10, No. 1-4, pp. 351-360, 1990.

Margot, J. L., Campbell, D. B., Jurgens, R. F. and Slade, M. A., "Topography of the lunar poles from radar interferometry: A survey of cold trap locations," *Science*, Vol. 284, pp 1658-1660, 1999.

Melosh, H. J., "Impact cratering – A geologic process," *Oxford University Press*, New York, pp. 46-86, 1989.

Morgan, T. H. and Shemansky, D. E., "Limits to the lunar atmosphere," *Journal of Geophysical Research*, Vol. 96, No. A2, pp. 1351-1367, Feb. 1991.

Moses, J. I., Rawlins, K., Zahnle, K., and Dones, L., "External sources for Mercury's putative ice deposits," *Icarus*, Vol. 137, No. 2, pp. 197-221, Feb. 1999.

Moss, J. N., Boyles, K. A., and Greene, F. A., "Orion aerodynamics for hypersonic free molecular to continuum conditions," *14<sup>th</sup> AIAA/AHI International Space Planes and Hypersonic Systems and Technologies Conference*, AIAA Paper 2006-8081, 2006.

Nadiga, B. T., "An Euler solver based on locally adaptive discrete velocities," *Journal of Statistical Physics*, Vol. 81, No. 1-2, pp. 129–146, 1995.

Nanbu, K., "Theoretical basis on the direct Monte Carlo method," *Rarefied Gas Dynamics: 15<sup>th</sup> International Symposium*, Grado, Italy, June 16-20 1986, *Proceedings*, Vol. 1, Teubner, Stuttgart, pp. 369-383, 1986.



Ngalande, C., Lilly, T., Killingsworth, M., Gimelshein, S., and Ketsdever, A., “Nozzle plume impingement on spacecraft surfaces: Effects of surface roughness,” *Journal of Spacecraft and Rockets*, Vol. 43, No. 5, pp. 1013-1018, 2006.

Noda, H., Araki, H., Goossens, S., Ishihara, Y., Matsumoto, K., Tazawa, S., Kawano, N., and Sasaki, S., “Illumination conditions at the lunar polar regions by KAGUYA (SELENE) laser altimeter,” *Geophysical Research Letters*, Vol. 35, L24203, Dec. 2008.

Nozette, S., Lichtenberg, C. L., Spudis, P., Bonner, R., Ort, W., Malaret, E., Robinson, M., and Shoemaker, E. M., “The Clementine bistatic radar experiment,” *Science*, Vol. 274, pp. 1495-1498, Nov. 1996.

Nozette, S., Spudis, P. D., Robinson, M. S., Bussey, D. B. J., Lichtenberg, C., and Bonner, R., “Integration of lunar polar remote-sensing data sets: Evidence for ice at the lunar south pole,” *Journal of Geophysical Research*, Vol. 106, No. 10, pp. 23,253-23,266, Oct. 2001.

Ong, L., Asphaug, E. I., Korycansky, D., and Coker, R. F., “Volatile retention from cometary impacts on the Moon,” *Icarus*, 2010.

Pacheco, P. S., “Parallel programming with MPI,” *Morgan Kaufmann Publishers*, San Francisco, California, pp. 89-110, 217-278, 1997.

Papp, J. L., Wilmoth, R. G., Chartrand, C. C., and Dash, S. M., “Simulation of high-altitude plume flow fields using a hybrid continuum CFD/DSMC approach,” *42<sup>nd</sup> AIAA/ASME/SAE/ASEE Joint Propulsion Conference and Exhibit*, Sacramento, 2006.

Pierazzo, E. and Melosh, H. J., “Hydrocode modeling of Chicxulub as an oblique impact event,” *Earth Planetary Science Letters*, Vol. 165, pp. 163-176, 1999.

Pierazzo E. and Melosh, H. J., "Understanding oblique impacts from experiments, observations, and modeling," *Annual Review of Earth Planetary Science*, Vol. 28, pp. 141-167, 2000.

Pierazzo, E. and Melosh, H. J., "Hydrocode modeling of oblique impacts: the fate of the projectile," *Meteoritics & Planetary Science*, Vol. 35, pp. 117-130, 2000.

Pierazzo, E., and Collins, G., "A brief introduction to hydrocode modeling of impact cratering," in Dypvik, H., Burchell, M., and Claeys, P. (Eds.), *Cratering in marine environments and on ice*, pp. 323-341, 2004.

Pieters, C. M., Goswami, J. N., Clark, R. N., Annadurai, M., Boardman, J., Buratti, B., Combe, J.-P., Dyar, M. D., Green, R., Head, J. W., Hibbitts, C., Hicks, M., Isaacson, P., Klima, R., Kramer, G., Kumar, S., Livo, E., Lundeen, S., Malaret, E., McCord, T., Mustard, J., Nettles, J., Petro, N., Runyon, C., Staid, M., Sunshine, J., Taylor, L. A., Tompkins, S., and Varanasi, P., "Character and Spatial Distribution of OH/H<sub>2</sub>O on the Surface of the Moon Seen by M<sup>3</sup> on Chandrayaan-1," *Science Express Reports*, 10.1126/science.1178658, Sep. 2009.

Roveda, R., Goldstein, D. B., and Varghese, P. L., "Hybrid Euler/Direct Simulation Monte Carlo calculation of unsteady slit flow," *Journal of Spacecraft and Rockets*, Vol. 37, No. 6, pp. 753-760, Nov-Dec 2000.

Sandford, S. A., and Allamandola, L. J., "Condensation and vaporization studies of CH<sub>3</sub>OH and NH<sub>3</sub> ices: Major implications for astrochemistry," *The Astrophysical Journal*, Vol. 417, pp.815-825, Nov. 1993.

Schroeder, D. V., "An introduction to thermal physics," *Addison Wesley Longman*, New York, pp. 166-168, 1999.

Schwartzentruber, T. E., Scalabrin, L. C., and Boyd, I. D., "Hybrid particle-continuum simulations of nonequilibrium hypersonic blunt-body flowfields," *Journal of Thermophysics and Heat Transfer*, Vol. 22, No. 1, pp. 29-37, Jan.-March 2008.

Sedov, L. I., "Similarity and Dimensional Methods in Mechanics," *Academic Press*, London, pp. 271-281, 1959.

Shoemaker E. M., "Physics and astronomy of the Moon," ed. Z. Kopal, *Academic Press*, New York, pp. 283-359, 1962.

Shuvalov, V. V., "Multi-dimensional hydrodynamic code SOVA for interfacial flows: Application to the thermal layer effect," *Shock Waves*, Vol. 9, pp. 381-390, 1999.

Simpson, R. A. and Tyler, G. L., "Reanalysis of Clementine bistatic radar data from the lunar south pole," *Journal of Geophysical Research*, Vol. 104, No. E2, pp. 3845-3862, Feb. 1999.

Stacy, N. J. S., Campbell, D. B. and Ford, P. G., "Arecibo radar mapping of the lunar poles: A search for ice deposits," *Science*, Vol. 276, pp.1527-1530, June 1997.

Stanyukovich, K. P., "Unsteady motion of continuous media," *Pergamon*, New York, 1960.

Starukhina, L. V., and Shkuratov, Y. G., "The lunar poles: Water ice or chemically trapped hydrogen?," *Icarus*, Vol. 147, No. 2, pp. 585-587, Oct. 2000.

Stern, S. A., "Lunar atmosphere: history, status current problems and context," *Reviews of Geophysics*, Vol. 37, No. 4, pp. 453-491, Nov.1999.

Stewart, B., Pierazzo, E., Goldstein, D., Varghese, P., Trafton, L., and Moore, C., "Parallel 3D Hybrid Continuum/DSMC Method for Unsteady Expansions Into a Vacuum," 47<sup>th</sup> *AIAA Aerospace Sciences Meeting*, AIAA Paper 2009-266, Orlando, Florida, Jan. 2009.

Sunshine, J. M., Farnham, T. L., Feaga, L. M., Groussin, O., Merlin, F., Milliken, R. E., and A'Hearn, M. F., "Temporal and Spatial Variability of Lunar Hydration as Observed by the Deep Impact Spacecraft," *Science Express Reports*, 10.1126/science.1179788, Sep. 2009.

Taylor, S. R., "Lunar science: A post-Apollo view," *Pergamon Press*, New York, 1975.

Titov, E. V., and Levin, D. A., "Extension of the DSMC method to high pressure flows," *International Journal of Computational Fluid Dynamics*, Vol. 21, Nos. 9–10, pp. 351–368, Oct.-Dec. 2007.

Tzuk, Y., Barmashenko, B. D., Bar, I., and Rosenwaks, S., "The sudden expansion of a gas cloud into vacuum revisited," *Physics of Fluids A*, Vol. 5, No. 12, pp. 3265-3272, Dec. 1993.

VanGilder, D. B., Chartrand, C. C., Papp, J., Wilmoth, R. and Sinha, N., "Computational modeling of nearfield to farfield plume expansion," *43rd Joint Propulsion Conference & Exhibit*, Cincinnati, AIAA 2007-5704, July 2007.

Vasavada, A. R., Paige, D. A., and Wood, S. E., "Near-surface temperatures on Mercury and the Moon and the stability of polar ice deposits," *Icarus*, Vol. 141, No. 2, pp.179-193, Oct. 1999.

Vashchenkov, P. V., Kudryavtsev, A. N., Khotyanovsky, D. V., and Ivanov, M. S., "DSMC and Navier–Stokes study of backflow for nozzle plumes expanding into vacuum," *Rarefied Gas Dynamics: 24th International Symposium*, AIP Conference Proceedings, Vol. 762, pp. 355-360, 2005.

Vincenti, W. G., and Kruger, C. H., "Introduction to physical gas dynamics," *Krieger Publishing Company*, Malabar, Florida, p380, 1965.

Vondrak, R. R., "Creation of an artificial lunar atmosphere," *Nature*, Vol. 248, pp. 657-659, April 1974.

Walker, A. C., Gratiy, S. L., Goldstein, D. B., Moore, C. H., Varghese, P. L., Trafton, L. M., Levin, D. A., and Stewart, B., “A Comprehensive Numerical Simulation of Io’s Sublimation-Driven Atmosphere,” *Icarus*, pp. 409-432, May 2010.

Watson, K., Murray, B. C. and Brown, H., “The Behavior of volatiles on the lunar surface,” *Journal of Geophysical Research*, Vol. 66, pp. 3033-3045, Sep. 1961.

Wu, J.-S., and Tseng, K.-C., “Parallel DSMC method using dynamic domain decomposition,” *International Journal for Numerical Methods in Engineering*, Vol. 63, pp. 37-76, Feb. 2005.

Zel’Dovich, Y. B. and Raizer, Y. P., “Physics of shock waves and high-temperature hydrodynamic phenomena,” *Academic press*, New York, Vol. 2, pp. 571-584, 1967.

Zhang, J., Goldstein, D. B., Varghese, P. L., Gimelshein, N. E., Gimelshein, S. F. and Levin, D. A., “Simulation of gas dynamics and radiation in volcanic plumes on Io,” *Icarus*, Vol. 163, No. 1, pp. 182-197, May 2003.

Zhang, J., Goldstein D. B., Varghese P. L., Trafton L. M., Miki K., and Moore C., “Numerical modeling of ionian volcanic plumes with entrained particulates,” *Icarus*, Vol. 172, No. 2, pp. 479-502, Dec. 2004.

Zhong, J., Zeifman, M. I., Levin, D. A., and Gimelshein, S. F., “Direct Simulation Monte Carlo modeling of homogeneous condensation in supersonic plumes,” *AIAA Journal*, Vol. 43, No. 8, pp. 1784-1796, Aug. 2005.

## **Vita**

Bénédicte Stewart was born on September 11, 1980 in Cannes, France to Lydie and Yann Larignon. She joined the graduate program in Aerospace Engineering at the University of Texas at Austin in 2002. In 2004, she graduated with a M.S. in Aerospace Engineering from UT and a M.S. in Engineering from Ecole Centrale de Lille, France. Her research at the University of Texas at Austin in relation with this dissertation has been supported in part by the NASA Planetary Atmospheres program.

Permanent address:     438 Shadow Creek Drive  
                                 Seabrook, TX, 77586

This manuscript was typed by the author.